HAKONE XV

International Symposium on High Pressure Low Temperature Plasma Chemistry

with joint COST TD1208 workshop Non-Equilibrium Plasmas with Liquids for Water and Surface Treatments

Book of Contributed Papers

Masaryk University

Hakone XV: International Symposium on High Pressure Low Temperature Plasma Chemistry

with joint

COST TD1208 workshop

Non-Equilibrium Plasmas with Liquids

for Water and Surface Treatment

Book of Contributed Papers

11th – 16th September 2016

Brno, Czech Republic

Masaryk University

Brno 2016

Contact Address
Department of Physical Electronics
Faculty of Science
Masaryk University
Kotlarska 2
611 37 Brno
Czech Republic
Phone: +420 549 498 239
E-mail: hoder@physics.muni.cz
http://www.physics.muni.cz/kfe/

Editors
Mirko Černák, Tomáš Hoder

International Scientific & Organizing Committee

Ronny Brandenburg (Germany)
Mirko Černák (Czech Republic) - chair
Nicolas Gherardi (France)
Tony Herbert (Ireland)
Haruo Itoh (Japan)
Masuhiro Kogoma (Japan)
Kirill V. Kozlov (Russia)
Štefan Matejčík (Slovakia)
Jerzy Mizeraczyk (Poland)
Cristina Paradisi (Italy)
Henryka D. Stryczewska (Poland)
Hans-Erich Wagner (Germany)
Koichi Yasuoka (Japan)
Indrek Yögi (Estonia)
Ulrich Kogelschatz (Switzerland) - honorary member
Matti Laan (Estonia) - honorary member
Chobei Yamabe (Japan) - honorary member

Reading and Advisory Committee

Zdeněk Bonaventura
Antonín Brablec
Jan Čech
Pavel Dvořák
Jaroslav Hnilica
Tomáš Hoder
Ondřej Jašek
Vít Kudrle
Zdeněk Navrátil
David Pavliňák
Jozef Ráheľ
Dana Skácelová
Petr Synek
David Trunec
Jan Voráč

Local Organizing Committee

Mirko Černák (chair)
Tomáš Hoder (vice-chair)
Monika Dušková
Jana Kršková
Tomáš Morávek
Dana Skácelová

WELCOME TO HAKONE XV

Dear colleagues,

on behalf of the International Scientific Committee and the Local Organizing Committee, we would like to thank you for attending the 15th International Symposium on High pressure Low Temperature Plasma Chemistry in Brno – HAKONE XV. It is jointly organized by the Masaryk University (CEPLANT, Department of Physical Electronics, Faculty of Science) and The Union of Czech Mathematicians and Physicists Brno, Czech Republic.

The series of High Pressure Low Temperature Plasma Chemistry Symposiums was initiated in Hakone (Japan, 1987). The following meetings were held in Kazimierz Dolny (Poland, 1989), Strasbourg (France, 1991), Bratislava (Slovakia, 1993), Milovy (Czech Republic, 1996), Cork (Ireland, 1998), Greifswald (Germany, 2000), Pühajärve (Estonia, 2002), Padova (Italy, 2004), Saga (Japan, 2006), Oléron Island (France, 2008), Trenčianske Teplice (Slovakia, 2010), Kazimierz Dolny (2012) and Zinnowitz (Germany, 2014). The scope of the conference, originally devoted to theoretical mechanisms of dielectric barrier and corona discharges for ozone synthesis, basic oxidants generation and applications in water treatment and environment protection, expanded significantly during the coming years. Gradually the area of HAKONE interest has been extended to new emerging and innovative fields of research and development, like biomedical plasma application, alternative materials, fuels and other interdisciplinary plasma topics.

After exactly 20 years, the HAKONE conference returns to the Czech Republic and we are glad to host this event here in Brno. Brno is an old city being one of the capitals in Moravia already from 11th century. As the second largest city in Czech Republic it is also an important centre for technology and research. There are several universities in the city and research institutes. There are also many famous scientists connected directly to Brno, e.g. Gregor Johann Mendel, Ernst Mach or Kurt Gödel. We believe that such venue will be a perfect ambient for HAKONE XV.

Unfortunately, this will be the first HAKONE conference without our colleague, friend and one of the founders of the HAKONE symposium, Dr. Ulrich Kogelschatz. He passed away in June this year. The HAKONE XV conference is therefore dedicated to the memory of Ulrich Kogelschatz – an outstanding scientist and good friend to many of us.

In the name of ISC, LOC and with best wishes
Mirko Černák and Tomáš Hoder

WELCOME TO COST ACTION TD1208 ELECTRICAL DISCHARGES WITH LIQUIDS FOR FUTURE APPLICATIONS

The COST Action TD1208 Electrical Discharges with Liquids for Future Applications is a worldwide research network connecting currently about 100 research groups form more than 30 mainly European countries. It covers studies in the fields of electrical discharges generated directly in liquid phase as well as gaseous discharges interacting with liquids using many different discharge configurations and very broad range of power supplies. A wide spectrum of fundamental phenomena such as breakdown in the liquid phase, discharge physics, generation of active species and the consequent liquid chemistry induced by them are studied experimentally. Existing models are being improved using newly measured or calculated basic kinetic data and new complex kinetic physical-chemical models are under development.

Besides the fundamental research, many applications are being investigated. The main application fields are in water treatment, where plasmas interacting with liquids can help at the decomposition of harmfully removable hazardous chemicals like dyes, pesticides, hormones, pharmaceutics etc. Another broad field of applications is in material sciences for surface treatment and nanoparticles synthesis where new alloy materials can be produced with high efficiency. However probably the applications with greatest potential are in biomedicine since virtually all biological matter contains water. Here, applications ranging from the simple sterilization of surfaces to the direct therapeutic use of plasma on wounds or selective cancer cell killing.

The workshop Non-Equilibrium Plasmas with Liquids for Water and Surface Treatment, which is connected to HAKONE XV gives a unique opportunity to demonstrate the application fields, mentioned above, to other plasma scientists using atmospheric pressure discharges in gaseous phase, many in relevant areas. Thus new links can be established leading to an acceleration of the research progress across atmospheric plasma physics and plasma chemistry.

František Krčma and Bill Graham
Chair and vice-chair of COST Action TD1208

In memory of
Ulrich Kogelschatz

Ulrich Kogelschatz passed away after a short severe illness on June 25, 2016. He lived for science to the end of his life. Our community has lost an outstanding scientist, supporter and friend.

Ulrich Kogelschatz was born in 1937 in Germany. He obtained his academic education from 1957 to 1967 at Kiel University. During this period he also studied at Wesleyan University in Connecticut (USA) for one year as a Fulbright scholar. After finishing his doctoral dissertation in Kiel on the dynamics of electromagnetically impelled convergent cylindrical shock waves, he joined the NASA Langley Research Center in Virginia (USA) until 1969. In the same year, he started work as a senior scientist at the Brown Boveri Corporate Research Center at Baden (Switzerland), later named ASEA-Brown Boveri corporate research centre. In his early years in Baden, he made important contributions to the plasma physics of high-voltage circuit breakers and corona discharges and to their application in electrostatic precipitators for power plants.

From the 1970's, Ulrich Kogelschatz investigated dielectric barrier discharges for various applications. The first application was the generation of ozone. He and his collaborators clarified experimentally the fundamental properties of individual plasma filaments and complemented the experimental data with detailed numerical modelling of the reaction kinetics in these plasmas. These results enabled a significant performance improvement to existing technical ozonizers. At that time, nobody expected that basic research on a discharge known about for more than 100 years could have such far-reaching technological and economic consequences.

Later, Ulrich realized that this type of highly nonthermal plasma could be used for the efficient generation of incoherent excimer radiation. Once again he made several important contributions, both in terms of fundamental research and in transferring this knowledge to technical applications. These resulted in the development of high-power excimer lamps and the development of plasma displays. The success of the dielectric barrier discharge stimulated major activity in the field of high-pressure, low-temperature plasma chemistry, such as the conversion of exhaust gases and CO_2 and the production of hydrogen from hydrocarbons. All these topics are still technologically and scientifically relevant and under research today, much of such research based on work done by Ulrich.

He retired from ABB in 2000 but continued his work in plasma science. He joined the University of Minnesota in Minneapolis (USA) and later the Université de Sherbrooke (Canada), working on nanoparticle treatment by means of dielectric barrier discharges. He also worked on photochemical generation of ozone. He supervised several PhD students, participated in conferences and published several review articles. In 2005, he and collaborators published the book „Non-Equilibrium Air Plasmas At Atmospheric Pressure", today a compulsory reference for everybody working in this field.

One of his most inspiring and relevant publications is entitled „Industrial innovation based on fundamental physics" which makes the point, as exemplified by Ulrich's outstanding scientific work, that basic research can be combined with investigation of applications to deliver economically, socially and humanistically important technical devices and solutions. Recognizing his achievements, Ulrich Kogelschatz was awarded the A. H. von Engel prize in 2001 and the Rudolf Seeliger Prize in 2011.

Ulrich Kogelschatz was one of the founders of our International Symposium on High Pressure, Low Temperature Plasma Chemistry in 1987 in Hakone (Japan) and participated in all previous 14 meetings from the beginning of Hakone, often accompanied by his wife, Dagmar. From 2008 to 2014 he was the chairman of the International Scientific and Organising Comittee and, due to his personal activity, our HAKONE has become an ever more interesting, attractive and universally recognized international conference. It is now the duty and privilege of Ulrich's colleagues and successors to follow where he has led and to retain the quality and characteristic of HAKONE and our HAKONE community, so much of which is due to Ulrich.

Many colleagues at this meeting will remember that Ulrich was knowledgeable about almost every publication in our field, clearly having read it with the keenest scientific intellect and assessing colleagues' work with the   highest respect and the broadest mind. To work scientifically and to discuss results was always a joy for him and a pleasure and revelation for those with whom he interacted. For his contribution to science and the sum of human knowledge, his kindness to and respect for all colleagues and his unfailing generosity and good humour he will be universally missed.

The International Scientific Committee
In September 2016, Brno, Czech Republic

SYMPOSIUM SPONSORS

2.45 GHz SURFACE WAVE PLASMA SOURCES

STANDARD DOWNSTREAM SET-UP

▸▸ *HV Switch mode power supply*

Magnetron head

Sliding short-circuit

Isolator

3-stub tuner

Downstream

Argon 1 mbar

| 230 W | 280 W | 350 W | 500 W | 1000 W | 2000 W |
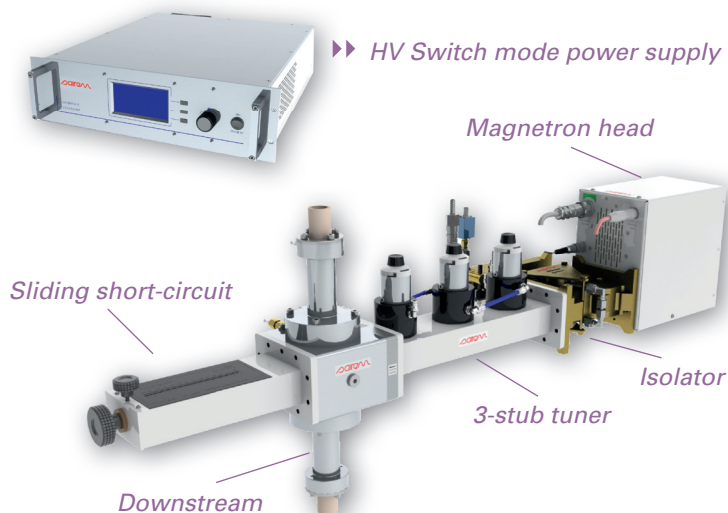
DOWNSTREAM

Pressure range	10^{-2} mbar to atmospheric pressure
Gas type	Ar, N_2, O2, H_2, CH_4, He, air, ...
Maximum power	6 kW
Application type	Creation of radicals, reactive species, surface activation, PECVD, gas abatement, gasification, sterilization, nanopowder synthesis

SURFAGUIDE

Pressure range	10^{-2} mbar to atmospheric pressure
Gas type	Ar, N_2, O_2, He, air, ...
Maximum power	6 kW
Application type	Creation of radicals, reactive species, surface activation, PECVD, gas abatement, gasification, sterilization, atmospheric high temperature chemistry

S-WAVE

Pressure range	10^{-2} mbar to atmospheric pressure
Gas type	Argon or argon based gas mixture at atmospheric pressure. All gases at reduced pressure
Maximum power	300 W
Application type	Creation of radicals, reactive species, surface activation, elementary analysis

KEY POINTS & BENEFITS

▸ Over dense plasmas, high ions and active species densities

▸ High temperature plasmas at atmospheric pressure

▸ Extremely wide operating pressure range: large application spectrum

▸ Electrodeless: independence of targets and substrate bias voltage

CONTACT US

commercial@sairem.com
www.sairem.com

rougevert

Your partner in Microwave & Radio Frequency professional solutions

HIDEN ANALYTICAL

Plasma
Characterisation

Positive & Negative Ion Analyser

EQP

EQP mass and energy analysers measure key plasma parameters providing the detailed information you need to understand your plasma:

▶ ion mass and energy analysis

▶ RF, DC, ECR & pulsed plasma

▶ neutrals & neutral radicals
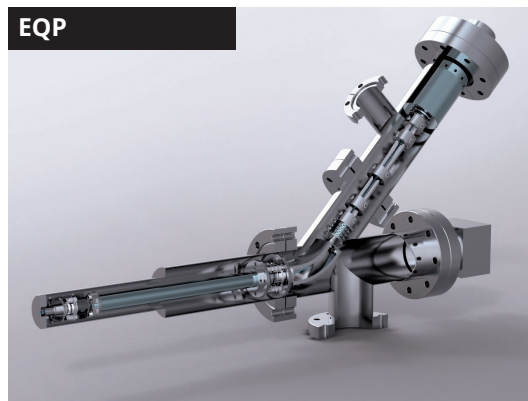
Electrostatic Langmuir Probe

ESPion

Hiden ESPion advanced electrostatic Langmuir plasma probes are the instruments of choice for industrial and academic plasma research:

▶ electron temperature distribution

▶ ion & electron density

▶ plasma uniformity
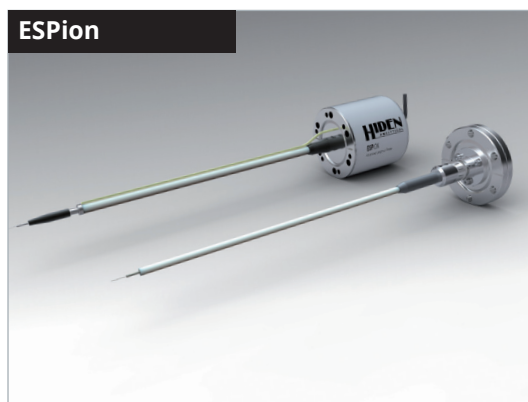
Atmospheric Plasma Ion Analyser

HPR-60 MBMS

The Hiden HPR-60 Molecular Beam Sampling Mass Spectrometer is a compact, mobile gas analysis system for the measurement of atmospheric and near-atmospheric plasma and reactive processes in applications including:

▶ atmospheric plasma jets

▶ flame chemistry

▶ dielectric barrier discharges
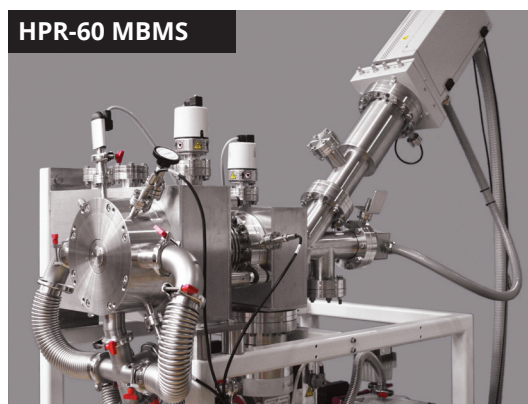
DIFFUSE COPLANAR SURFACE BARRIER DISCHARGE PLASMA
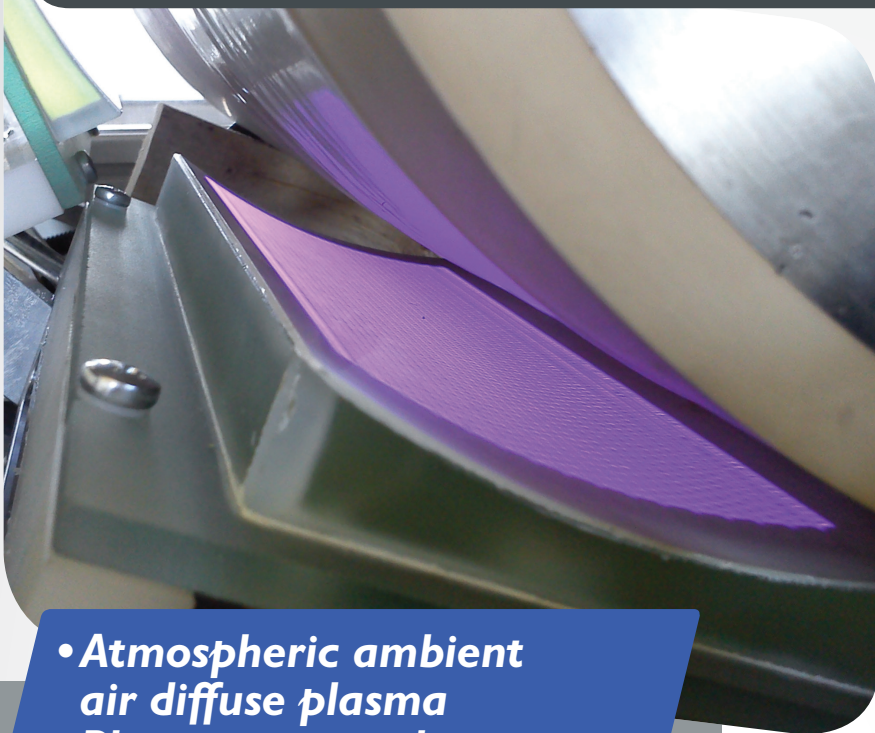
- **Atmospheric ambient air diffuse plasma**
- **Planar or curved geometry**

- Plasma area of one unit: 20 × 8 cm
- Power of one plasma unit > 400 W
- High plasma power density ~ 100 W/cm³
- Permanent hydrophilization
- Treatment speed: 3 – 100 m/min
- **Suitable for in-line treatment of flexible polymeric and metallic foils, paper, flexible glass, etc.**

Water contact angle [°] — untreated, plasma treated for 3 s
PP, PEN, PET, PMMA, PU, PTFE, Aluminium, Glass
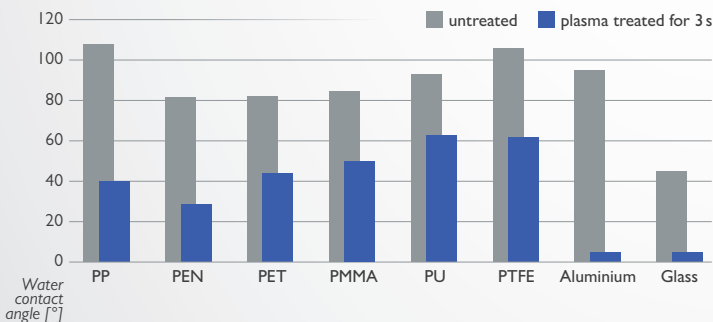
CEPLANT   ROPLASS robust plasma systems

Masaryk University, Czech Rep.

R&D Centre for Low-Cost Plasma and Nanotechnology Surface Modifications (CEPLANT), *www.ceplant.cz*

Robust Plasma Systems (ROPLASS), *www.roplass.cz*
info@roplass.cz

We offer:

- Comparative studies of plasma treatment with various commercially available systems at CEPLANT with your samples (rigid or flexible)
- Hand-held or continuous plasma treaters available from www.roplass.cz
- Integrated roll-to-roll plasma treatment line

TABLE OF CONTENTS

POSTER PRESENTATIONS

POSTER PRESENTATIONS

ORAL PRESENTATIONS

POSTER PRESENTATIONS

**TOPIC 5: GENERATION OF RADIATION IN HIGH PRESSURE
DISCHARGES**

POSTER PRESENTATION

TOPIC 6: DEPOLLUTION AND ENVIRONMENTAL APPLICATIONS

ORAL PRESENTATION

POSTER PRESENTATIONS

POSTER PRESENTATIONS

INVITED LECTURES

PLASMA BASED CO₂ CONVERSION:
A COMBINED MODELING AND EXPERIMENTAL STUDY

<u>A. Bogaerts</u>[1], R. Snoeckx[1], A. Berthelot[1], S. Heijkers[1], W. Wang[1], S. Sun[1], K. Van Laer[1], M. Ramakers[1], I. Michielsen[1,2], Y. Uytdenhouwen[1,2], V. Meynen[2], P. Cool[2]
[1]*Research group PLASMANT, Department of Chemistry, University of Antwerp, Universiteitsplein 1, B-2610 Antwerp, Belgium*
[2] *Research group LADCA, Department of Chemistry, University of Antwerp, Universiteitsplein 1, B-2610 Antwerp, Belgium*

E-mail: annemie.bogaerts@uantwerpen.be

In recent years there is increased interest in plasma-based CO_2 conversion. Several plasma setups are being investigated for this purpose, but the most commonly used ones are a dielectric barrier discharge (DBD), a microwave (MW) plasma and a gliding arc (GA) reactor. In this proceedings paper, we will show results from our experiments in a (packed bed) DBD reactor and in a vortex-flow GA reactor, as well as from our model calculations for the detailed plasma chemistry in a DBD, MW and GA, for pure CO_2 as well as mixtures of CO_2 with N_2, CH_4 and H_2O.

Keywords: CO_2 conversion; modeling; experiments; DBD plasma; MW plasma; GA plasma

1   Introduction

The impact on global warming due to greenhouse gas emissions is one of the largest environmental problems of the 21st century. One way to reduce the greenhouse gas concentrations (mainly CO_2 and CH_4) is to convert them into value-added chemicals and liquid fuels. However, the classical methods for CH_4 and CO_2 conversion, such as dry reforming of CH_4 with CO_2 (DRM) and thermal dissociation of CO_2 (i.e., reactions (1) and (2)), require a large amount of energy:

(1) $CH_4 + CO_2 \rightarrow 2\ CO + 2\ H_2$ $\Delta H° = 247$ kJ mol^{-1}
(2) $CO_2 \rightarrow CO + \frac{1}{2}\ O_2$ $\Delta H° = 283$ kJ mol^{-1}

Therefore, there is increased interest in alternative reforming techniques in pursuit of milder reaction conditions with reduced energy costs. Atmospheric pressure plasmas offer unique perspectives, because they can induce chemical reactions within gases with a reduced energy cost at ambient pressure and temperature, because mainly the electrons in the plasma are heated by the applied electric power, and these electrons can subsequently activate the gas by ionization, excitation and dissociation collisions.

Several different types of plasma setups can be used for CO_2 conversion, but the most common types are dielectric barrier discharges (DBDs), microwave (MW) plasmas and gliding arc (GA) discharges. In our group PLASMANT, we study the plasma-based CO_2 conversion, either in pure CO_2 or mixed with another gas, by means of modelling the plasma chemistry in these three different plasma types, as well as experimentally in a DBD and a GA plasma. This proceedings paper gives an overview of our recent work.

2   Experimental

As mentioned above, we do experiments with a DBD reactor as well as a GA reactor. The cylindrical DBD reactor consists of an inner (grounded) electrode and a coaxial alumina (or

quartz) tube, with inner and outer diameter of 17 and 22 mm, respectively. This tube is covered by a stainless steel mesh electrode, connected to an AC high voltage power supply. The inner electrode is a stainless steel rod with variable diameter, to allow investigating different gap sizes. For instance, using an inner electrode with diameter of 8 mm yields a discharge gap of 4.5 mm, which we fill with beads of various sizes (typically between 1 and 2 mm diameter) and various materials (i.e., silica, alumina, zirconia and barium titanate). However, by increasing the diameter of the inner electrode, we also investigate the performance of a microgap DBD reactor, with discharge gaps of 250, 500 and 1000 μm, and bead sizes varying between 100 and 900 μm. For comparison, we also perform experiments in an empty DBD reactor. The outer electrode has a length of 90 mm, which defines the length of the discharge. The gas flow rate is controlled with a mass flow controller (EL-flow of Bronkhorst). The total current is recorded by a Rogowski-type current monitor (Pearson 4100) while a high voltage probe (Tektronix P6015A) is used to measure the applied voltage. To obtain the charge generated in the discharge, the voltage on the external capacitor is measured. All the electrical signals are sampled by a four-channel digital oscilloscope (Picotech PicoScope) and the discharge power is obtained by a control system used to calculate the area of the Q-U Lissajous figures. The output gas composition is analysed online by gas chromatography. A schematic picture of the setup is illustrated in Figure 1.
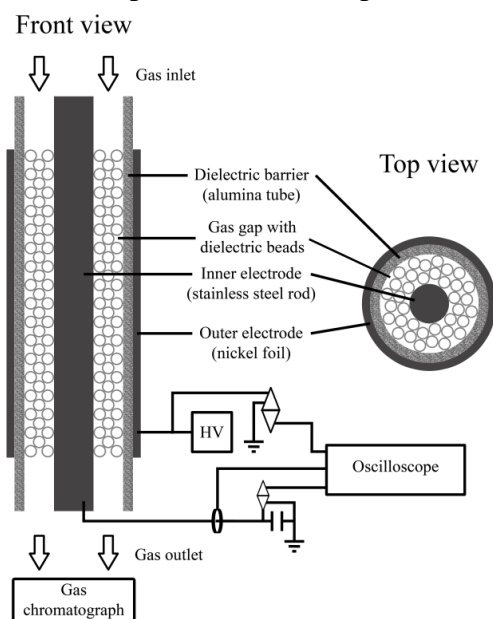
Fig. 1: Scheme of the packed bed DBD setup [1].

The GA reactor used in our work is a three-dimensional gliding arc reactor designed at Drexel Plasma Institute (Philadelphia), in which the gas enters through a tangential inlet so that a vortex flow is obtained. The plasma is stabilized in the center of the reactor by this vortex flow and the gas flow is forced to go through the plasma (see Figure 2). Moreover, it is also possible to insert an additional gas through an axial inlet. A diagram of the experimental system is shown in figure 2. The reactor is powered by a DC current source type power supply. The plasma voltage and current are measured by a high voltage probe and a current sense resistor of 10 Ω, respectively. With these values the plasma power can be calculated. In the reactor tube, which is placed after the gliding arc, a thermocouple is inserted to measure the temperature of the outflowing gas. The output gas composition is again analysed online by gas chromatography.
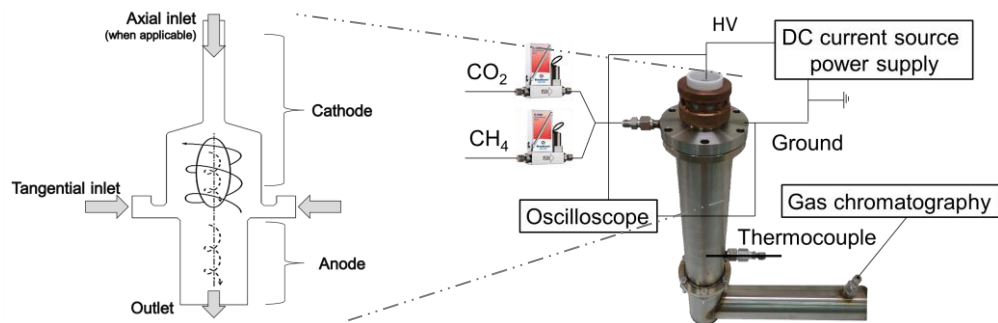
Fig. 2: Scheme (left) and picture (right) of the vortex-flow GA setup [2].

3 Model description

To improve the application of plasma-based CO_2 conversion, a good insight in the underlying mechanisms is desirable. We try to obtain this by computer modeling. We focus especially on the plasma chemistry in the three most commonly used plasma setups for this purpose, i.e., a DBD, a MW and a GA plasma. We try to model these plasma setups with 2D or 3D fluid models, but when focusing on the detailed plasma chemistry, a 0D chemical kinetics model is more appropriate, in terms of calculation time. This model solves the continuity equations for the various plasma species, based on production and loss terms, as defined by the chemical reactions:

$$\frac{dn_i}{dt} = \sum_j \left\{ \left(a_{ij}^{(2)} - a_{ij}^{(1)} \right) k_j \prod_l n_l^{a_{ij}^{(1)}} \right\} \tag{1}$$

where $a_{ij}^{(1)}$ and $a_{ij}^{(2)}$ are the stoichiometric coefficients of species i, at the left and right hand side of a reaction j, respectively, n_l is the species density at the left-hand side of the reaction, and k_j is the rate coefficient of reaction j (see below). For each species included in the model, i.e., different types of molecules, radicals, ions, excited species, as well as the electrons, a separate balance equation is solved. Typically, up to 100 different species are considered, which react among each other in up to 1000 different chemical reactions.

These balance equations yield the time-evolution of the species densities, averaged over the plasma reactor volume. Indeed, this 0D model only accounts for time-variations, while spatial variations, due to transport in the plasma, are not considered. However, based on the gas flow rate, we can translate the time-variation into a spatial variation, i.e., as a function of distance travelled through the plasma reactor. In this way, we can account for spatial variations of input power or gas temperature inside the plasma reactor.

Besides the species densities, also the average electron energy is calculated in this model, based on an energy balance equation, again with energy source and loss terms as defined by the chemical reactions. The average electron energy is used to calculate the energy-dependent rate coefficients of the electron-induced processes, such as ionization, excitation and dissociation. The rate coefficients of the other chemical reactions, i.e., between the neutral species or ions, depend on the gas temperature and are calculated from Arrhenius equations, using data adopted from literature.

We developed a 0D chemical kinetics model for different gas mixtures relevant for CO_2 conversion, i.e., pure CO_2 [3-6], CO_2/CH_4 [7,8], CO_2/N_2 [9,10] and CO_2/H_2O [11]. Depending on the gas mixture under consideration, different species need to be considered in the model. Details can be found in the cited references. The models for CO_2/CH_4 and

CO_2/H_2O were only applied to a DBD reactor, while the models for pure CO_2 and CO_2/N_2 were developed for a DBD and a MW (and GA) plasma. In the latter two cases, a lot of attention was paid to the behavior of the vibrational levels of CO_2 (and N_2), because of their important role in energy-efficient CO_2 conversion.

4   Results and Discussion

Results will be presented for experiments in a (packed bed) DBD and a vortex-flow GA in pure CO_2, focusing on the conversion and energy efficiency at different conditions and reactor setups. The modeling will focus on the detailed plasma chemistry, i.e., the role of vibrationally excited CO_2 levels, playing a key role in energy efficient CO_2 conversion, as well as the relative importance of various processes responsible for CO_2 conversion, linking this to the energy efficiency in the various types of plasma setups.

For the modeling results on the CO_2/CH_4 and CO_2/H_2O mixtures in a DBD reactor, we will focus on the production of value-added chemicals. The main products formed are a mixture of H_2 and CO, or syngas, with a tuneable H_2/CO ratio depending on the gas mixing ratio. The production of oxygenated compounds, such as methanol, formaldehyde, etc, is very limited. On the other hand, in the CO_2/H_2O mixture, significant amounts of H_2O_2 could be produced. A detailed chemical kinetics analysis allows to elucidate the different pathways leading to the observed results, and to propose solutions on how to further improve the formation of value-added products.

Finally, we also studied the plasma chemistry in a CO_2/N_2 mixture, both in a DBD and in a MW plasma reactor, to investigate the effect of this important impurity in effluent gases on the CO_2 conversion, energy efficiency and product formation. The presence of N_2 up to 50 % in the mixture barely influences the effective (or overall) CO_2 conversion and energy efficiency, because the N_2 metastable molecules (in the DBD) and the vibrational levels (in the MW plasma) enhance the absolute CO_2 conversion, and this compensates for the lower CO_2 fraction in the mixture. Higher N_2 fractions, however, cause a drop in the CO_2 conversion and energy efficiency. Moreover, in the entire CO_2/N_2 mixing ratio, several harmful compounds, i.e., N_2O and NO_x compounds, are produced in the range of several 100 ppm. The reaction pathways for the formation of these compounds are again explained based on a kinetic analysis, which allows proposing solutions on how to prevent the formation of these harmful compounds.

References
1. K. Van Laer et al., Energy Technol. 3, 1038 (2015)
2. M. Ramakers et al., paper in preparation
3. R. Aerts et al., J. Phys. Chem. C 116, 23257 (2012)
4. T. Kozák et al., Plasma Sources Sci. Technol. 23, 045004 (2014)
5. T. Kozák et al., Plasma Sources Sci. Technol. 24, 015024 (2015)
6. R. Aerts et al., ChemSusChem 8, 702 (2015)
7. R. Snoeckx et al., J. Phys. Chem. C 117, 4957 (2013)
8. R. Snoeckx et al., RSC Advances 5, 29799 (2015)
9. S. Heijkers et al., J. Phys. Chem. C 119, 12815 (2015)
10. R. Snoeckx et al., Energy & Environm. Sci. 9, 999 (2016).
11. R. Snoeckx et al., Energy & Environm. Sci. 2016 (submitted)

CONFINED ATMOSPHERIC PLASMA SOURCES FOR ACTIVATING GASES, LIQUIDS AND TISSUE

A. M. Lietz, J. Kruszelnicki, M. J. Kushner

University of Michigan, Ann Arbor, MI 48109-2122 USA

E-mail: lietz@umich.edu, jkrusze@umich.edu, mjkush@umich.edu

The propensity for atmospheric pressure plasmas (APPs) to become unstable has motivated many strategies for obtaining quasi-steady state or pulse-periodic operation. Many such strategies rely on confinement or close-by surfaces to stabilize the plasma. These discharges are then defined by their confining boundaries, which in turn impacts their activation of gases, liquids and tissue. In this paper, results from computational modeling will be used to illustrate strategies for confining APPs to enhance chemical reactivity, and how that reactivity is impacted by the confinement.

Keywords: atmospheric pressure plasmas, microdischarges, plasma-liquid interactions, plasma jets

1   Introduction

The development of low temperature, atmospheric pressure plasmas (APPs) has been challenged by a compromise between discharge stability, uniformity, and power deposition. The propensity to form arcs and non-uniformities typically increases as specific power deposition (W/cm^3) increases. One strategy to meet this challenge is microplasma based devices. In microplasmas, the surface-to-volume ratio of the discharge is large which enables surface processes, such as thermal conduction and recombination, to stabilize the plasma.

The microplasma is a subset of a class of APPs more generally described as *confined*. In confined plasmas, physical or electrical boundaries lend stability to the discharge to enable higher power deposition, continuous wave (cw) or pulse-periodic operation. To some degree, plasma jets are confined discharges. In these devices, a rare gas seeded with a small fraction of a reactive gas flows through a tube and into the ambient, producing a plume of the rare gas surrounded by air. [1] The discharge is initiated in the tube, and propagates as an ionization wave (IW) into the confined plume. To some degree, packed-bed-reactors (PBRs) are also confined discharges. [2] In these devices, small regions of intense electric field in the gas phase are produced by deliberate (or fortuitous) arrangements of high permittivity materials (or beads). The resulting volumetric IWs and surface ionization waves (SIWs) along the surface of the beads are stabilized by their small dimensions or their proximity to surfaces. The high production of ions, radicals and photons enabled by confined APPs is then instrumental in activating gases, liquids and biological materials (tissue).

In this paper, results from computational investigations of confined APPs will be discussed with the goal of providing insights to their stabilizing properties and ability to activate gases, liquids and tissue. The motivating applications are environmental, as represented by PBRs for remediation and fuel-reforming, and biotechnology, as represented by plasma jets for activating liquids and treating tissues. The model used in this investigation is *nonPDPSIM*, a 2-dimensional plasma-hydrodynamics and plasma chemistry model which incorporates neutral flow and surface chemistry, and which extends plasma transport into liquids.

2   Confined Atmospheric Plasmas

The first example of confinement-enhanced stability of an APP is streamer propagation through a packed bed reactor. In this example, quartz beads ($\varepsilon/\varepsilon_0$ = 4), 1.8 mm in diameter, were arranged between two co-planar electrodes separated by 1 cm. The beads are separated by 430 microns or 700 microns, as is shown in Fig. 1. A single pulse of -30 kV was applied to the top electrode for 25 ns with the bottom electrode being grounded. Propagation of a negative streamer through the PBR is shown in Fig. 1. In this geometry, there is natural electric field enhancement at the vertical poles of the beads and a reduction in the electric field at the horizontal equators. These electric field enhancements guide the initial avalanche and radical formation towards the poles of the top beads, and continue to initiate secondary discharges near the poles of beads lower in the PBR. This general trend is followed for both bead spacings. However, the closer proximity of the beads (more confinement) creates regions of higher electric field enhancement which produces a different manner of discharge propagation. When there is more confinement, the discharge takes the form of standing filaments and SIWs with a higher propagation velocity of the IWs. Aside from a strong cathode-seeking restrike, which forms near the central bead, surface discharges are dominant in the less confined geometry. The more highly confined geometry with higher electric field enhancement produces higher rates of initial radical formation. Regions having stationary filamentary discharges in the more confined arrangement support increased radical production of: O_3 26%, NO 76% and OH 113%.
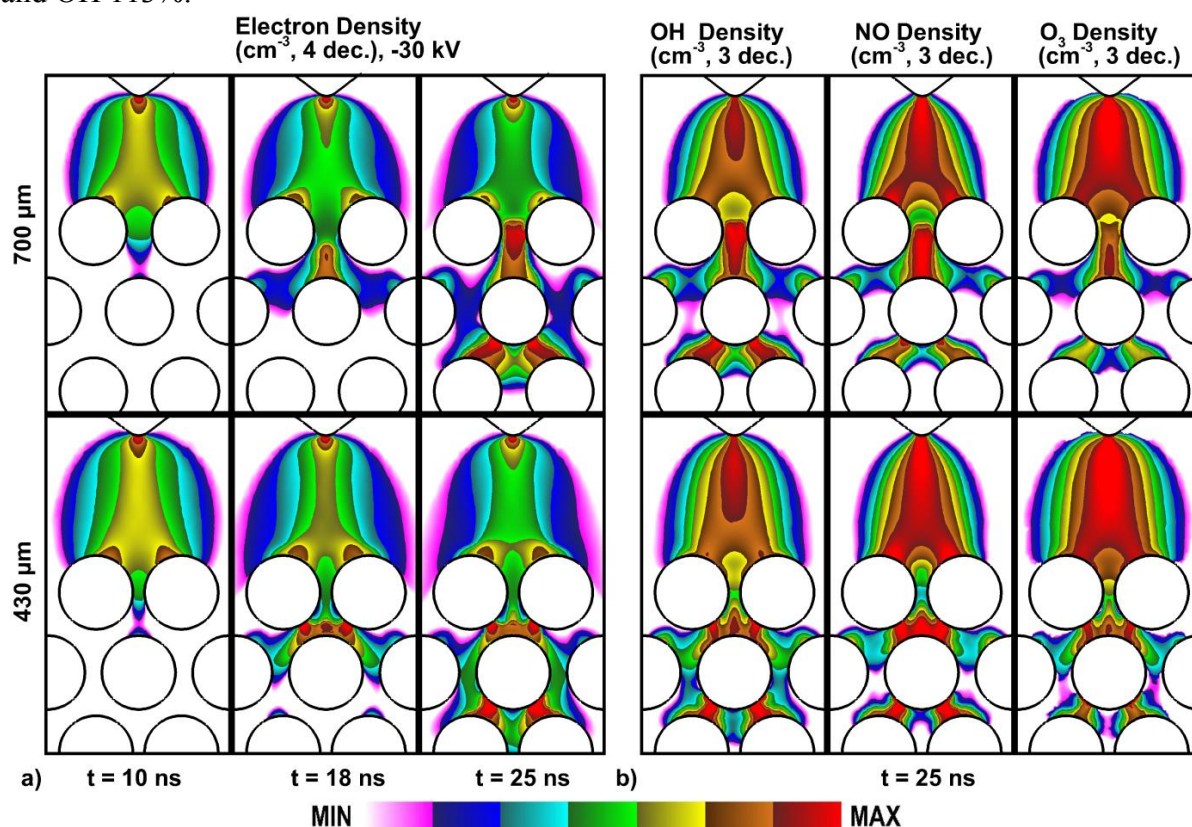
Fig. 1: Plasma properties for a single pulse, initial avalanche through a PBR having (top) 700 μm or (bottom) 430 μm separation between the beads. (a) Electron densities and (b) radical densities. Maximum densities are: [e] 10^{13} cm^{-3}, OH 7×10^{11} cm^{-3}, NO 1×10^{12} cm^{-3}, and O_3 1×10^{11} cm^{-3}.

A second example of control of APPs through confinement is the multi-jet plasma comb (MJPC) originating from a single ionization wave, first developed by Robert, et al. [3]. The MJPC consists of an otherwise conventional plasma jet that is capped at one end and which has an array of holes. The IW propagating through the tube launches a sequence of daughter IWs into the ambient air from each hole. In this example, simulations were performed of an MPJC having holes of different sizes, 30 μm to 750 μm, to demonstrate control of the secondary IWs through confinement. Helium at 100 sccm having 0.001% air impurity is flowed through the tube having an inner diameter of 750 μm and out the holes into humid air, producing plumes of He, shown in Fig. 2. The electrodes consist of a biased ring inside the tube and a grounded ring outside of the tube, overlapping the powered electrode. When the -20 kV voltage is applied, an IW propagates along the length of the tube, and smaller IWs propagate out of the holes perpendicular to the original IW, shown in Fig. 2. The resulting MJPC could be used to treat a larger area than with a single source.
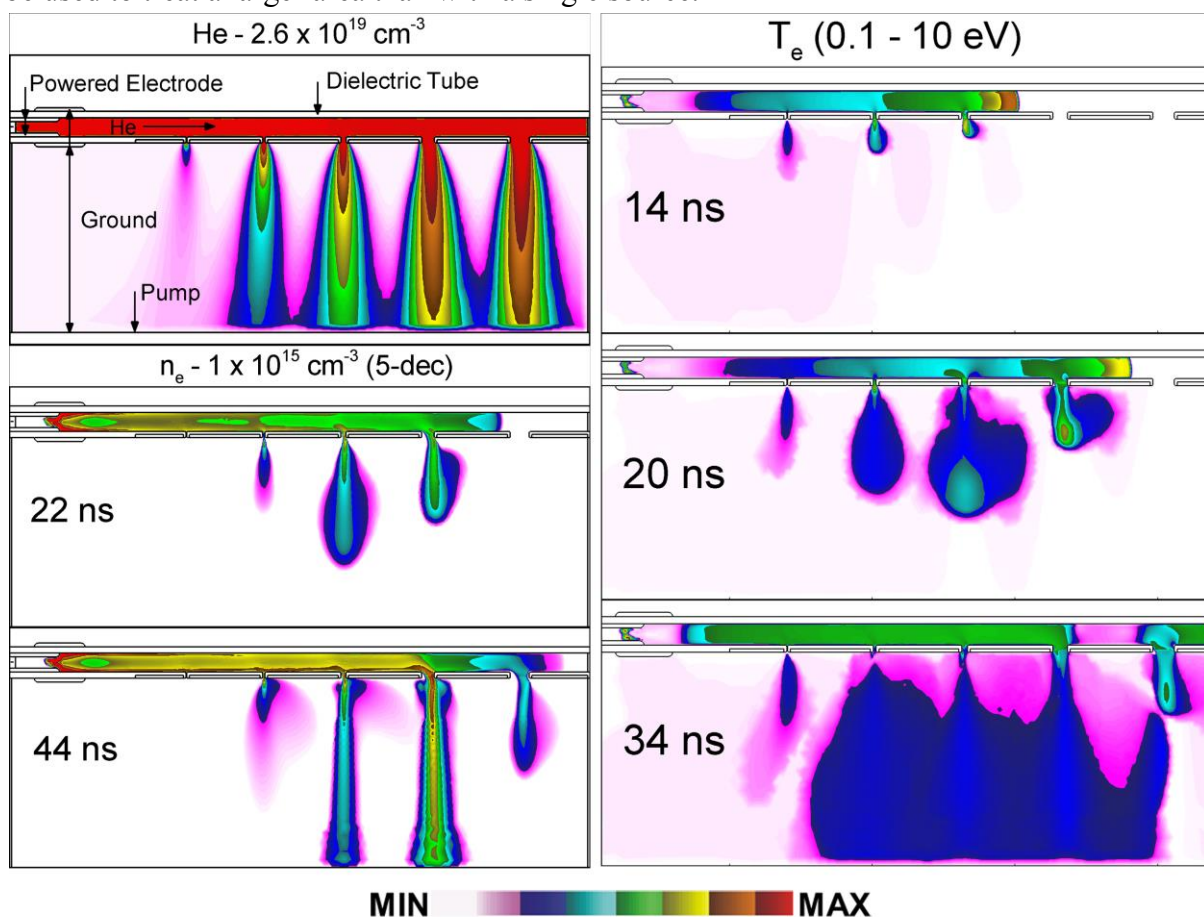
Fig. 2: Properties of the MJPC. (left) He plumes and electron density at 22 and 44 ns. (right) Electron temperature during propagation of the primary IW.

There are at least two ways in which the sizes of the holes and confinement may affect the propagation of the IWs in the MJPC. First, if a hole is smaller than the Debye length of the plasma in the IW, the plasma in the hole is entirely comprised of sheath without any bulk plasma. Second, the size of the hole determines the proportion of He in the humid air immediately outside of the tube. A larger hole, and therefore a larger He density, increases the likelihood of propagation out of the tube as a lower E/N (electric field/gas number density) is re-

quired to propagate in the He dominated plume. As a result, the IW does not propagate through the smallest hole, which is smaller than the Debye length of the plasma. The ionization wave that propagates out of the second hole is short and does not fully develop due to the high mole fraction of humid air in the plume. The third hole and those larger produce secondary ionization waves (teeth in the plasma comb) that reach the grounded surface below.

The electron temperature during the propagation of the IW is also shown in Fig 2. T_e is highest in the ionization wavefront, but decreases significantly after passing the fourth hole. It seems holes that are too large significantly attenuate the primary IW traveling in the tube. As the individual ionization waves contact the ground plane, they produce a restrike, resulting in higher T_e in the tube to the left of the hole. This restrike can disturb the propagation of subsequent teeth in the plasma comb. This process also may explain the low n_e and slow propagation of the rightmost tooth of the plasma comb in Fig 2.

The control of APPs through confinement does eventually imprint into the manner of activating species. This correlation between confinement and activation is illustrated by plasma jets to activate thin liquid layers in plasma medicine for sterilization and wound healing. For example, results from modeling are shown in Fig. 3 for an atmospheric pressure plasma jet sustained in He/O_2 = 99.5/0.5 flowing into room air activating a thin water layer. The plasma jet is generated by an ionization wave (the *plasma bullet*) that propagates through the He rich plume emanating from the jet and which produces a core of reactive oxygen species (ROS) on axis. Reactive nitrogen species (RNS) are preferentially produced off axis by mixing with air. The end result when these gas phase reactive species solvate into the liquid are regions which are dominated by aqueous ROS, regions which are dominated by a subset of the RNS, in this case aqueous NO, and a subset of RNS that are more uniformly distributed.

3 Concluding Remarks

Confinement of APPs is a method to promote stability, intensify the plasma and guide the plasma to optimally produce radicals, ions and photons to activate gases, liquids and tissue. Models of confined APPs are providing insights on methods to optimally deliver activated species.
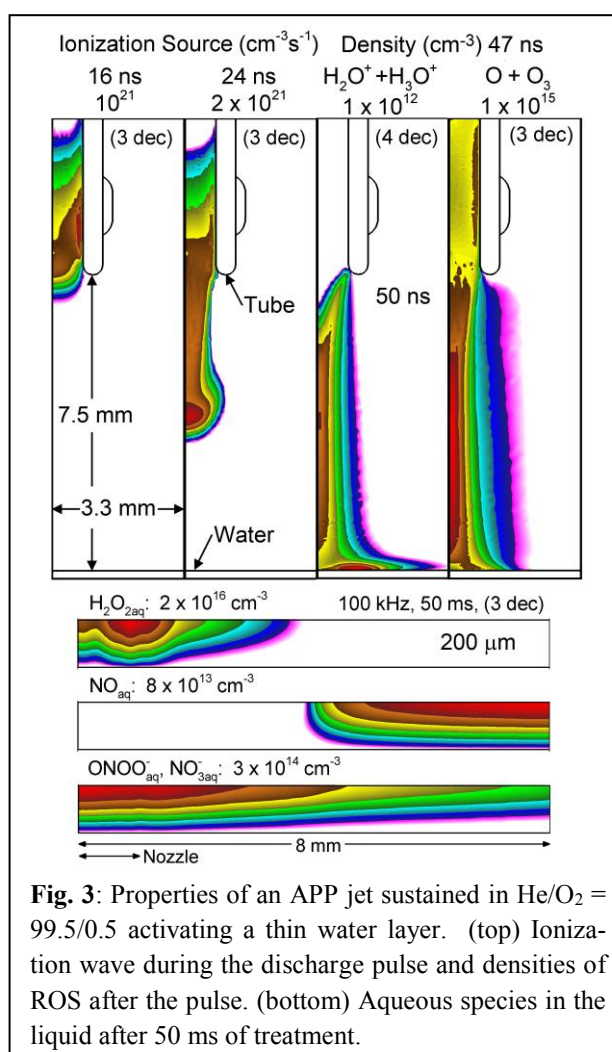
Fig. 3: Properties of an APP jet sustained in He/O_2 = 99.5/0.5 activating a thin water layer. (top) Ionization wave during the discharge pulse and densities of ROS after the pulse. (bottom) Aqueous species in the liquid after 50 ms of treatment.

4   Acknowledgments

References

1. R. Wang et al., Plasma Sources Sci. Technol. 25, 015020 (2016)
2. H. L. Chen et al., Ind. Engr. Chem. Res. 47, 2122 (2008)
3. E. Robert et al., Phys. Plasmas 22, 122007 (2015)

NON-THERMAL PLASMA COMBINED WITH CATALYSTS FOR ENVIRONMENTAL TECHNOLOGY

A. Mizuno, K. Takashima

Dept. Environmental and Life Sciences, Toyohashi University of Technology, Hibarigaoka 1-1, Tenpaku-cho, Toyohashi, 441-8580

E-mail: mizuno@ens.tut.ac.jp

In order to use NTP, selectivity and energy efficiency should be improved. For this purpose, combination of NTP and catalysts is effective. Several industrial applications have been developed, including a pulsed streamer corona combined with TiO_2 catalysts which has been commercialized successfully. A packed bed has been used to combine NTP and catalysts. An application is decomposition of VOC (volatile organic compounds). We have developed to initiate NTP in honeycomb catalyst. This honeycomb discharge could be used for various processes to combine NTP and catalyst.

Keywords: non-thermal plasma; plasma chemical process; barrier discharge; packed bed; surface discharge; gas cleaning

1   Introduction

Positive pulsed corona has been used to generate non-thermal plasma at atmospheric pressure [1]. With short pulsed high voltages, electrons migrate longer distance compared with ions having heavier mass, therefore, electrons are driven across larger voltage drop so that most of the input electrical energy is mainly transferred to the electrons. NTP in air produces reactive radicals such as O and OH. These radicals promote various chemical reactions. For environmental remediation such as exhaust gas cleaning, decomposition of VOCs and so on, NTP processes have been developed and various products have been commercialized [2-5]. For environmental applications, the NTP process should be efficient, low cost and compact, to be competitive with conventional processes. Combination of NTP with catalysts is a possible method to improve competitiveness of NTP system. In this review, several NTP-catalyst processes are introduced [6].

2   Generation of NTP combined with catalysts and examples of several applications

Figure 1-a shows the packed bed [7]. When an AC or a pulsed voltage is applied to the pellet layer, the voltage is devided mainly by the contact points of the pellets due to low permittivity of the air compare with the pellet. The partial discharge, therefore, takes place at each contact points. Figure 1-b is a packed bed reactor using insulating wall to avoid sparking. This reactor is successfully applied in cleaning of Diesel exhaust. With the complimental oxidation of NO by NTP at lower temperature condition, the plasma-catalyst process is effective for cleaning of diesel exhaust since selective catalytic reduction (SCR) process by ammonia works at lower temperature [8]. In addition, NO_2 converted from NO is more easily adsorbed for decomposition when gas temperature becomes high.

Honeycomb is a commonly used type of catalysts because of lower pressure drop and durability against vibration. It has been difficult to generate electrical discharge evenly inside a honeycomb. If discharge is generated inside a honeycomb, a larger surface area can

(a) Discharge in a packed bed   (b) Cylindrical packed bed reactor
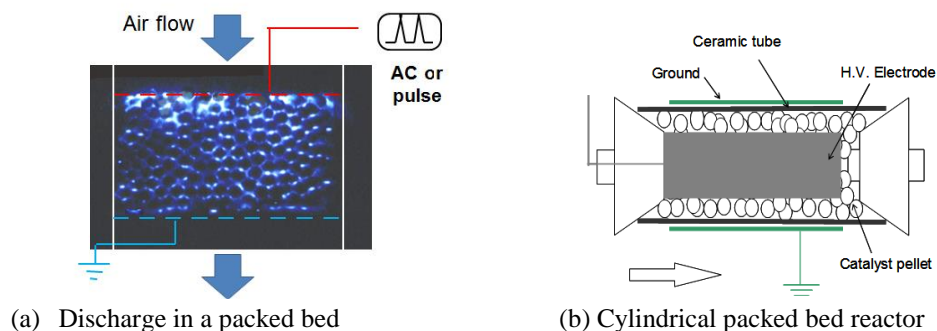
Fig. 1 Packed bed reactor for combination of NTP and catalyst

(a) Electrode configuration   (b) Discharge inside the glass tube
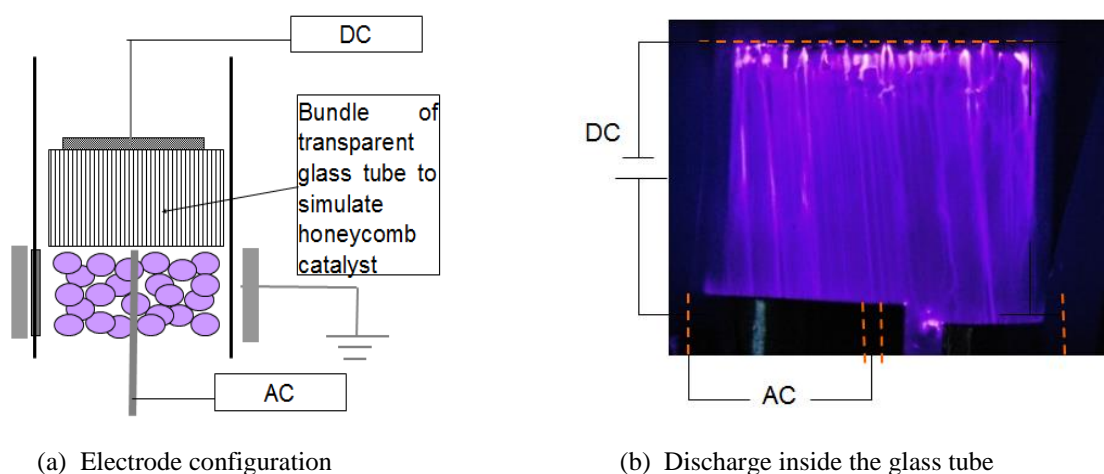
Fig. 2: Discharge inside a honeycomb.

be used for plasma chemical process. To realize the discharge in honeycomb catalysts, there are several important works recently reported. One is the superposition of surface discharge and AC discharge to obtain a large discharge volume [9]. Surface discharge is generated on the inner wall of a cylinder, and AC voltage is applied between the centered electrode and the electrode placed on the inner wall for the surface discharge. The other is a sliding discharge that has been used to cover the large surface area of wings of airplanes to stabilize airflow [10]. Surface discharge is generated using a pair of electrodes placed between a sheet of insulator film. The other electrode is set apart from the electrode for surface discharge on the film and energized with negative DC. From the surface discharge, streamers are extended by the DC electric field and cover the large surface area. Figure 2-a illustrates the plasma reactor for honeycomb [11]. A packed-bed discharge is used to form the preceding discharge. The γ-Al_2O_3 pellets (3 mm) are set in a quartz glass tube (inner diameter: 26 mm) with a stainless steel rod (diameter: 6 mm) at the center as a discharge electrode. The outer surface of the quartz glass tube is covered with an aluminum sheet of 15 mm length as a ground electrode. Bundled thin quartz glass capillary tubes are used to simulate a honeycomb catalyst and to observe the light emission. The inner diameter of the quartz glass capillary is 1 or 2 mm. Length is 20 mm. Diameter of the bundle is 26 mm and the bundle is inserted into the outer quartz glass tube.   A stainless steel mesh (1 6mesh) is placed on the upper end of the capillaries.   This stainless steel mesh is connected to a DC power supply to form the honeycomb discharge in the capillary. In the packed-bed, discharges are generated at contacting points of the γ-Al_2O_3 mm). The packed-bed discharge is used as the preceding

discharge. When DC high voltage is applied between the bundle of quartz glass capillaries, inside of the capillaries can be ionized, as if the AC discharge (packed bed discharge) is sliding into the capillaries by the DC electric field. Figure 2-b shows photographs of the discharge in the bundle of quartz glass capillaries of 1 mm inner diameter. Instead of using a packed bed discharge, a ceramic electrode can be used for initiating a honeycomb discharge. As shown in Figure 3, a flat plate electrode with holes for gas passages has been designed [12]. Inside the ceramic plate, an induction electrode is embedded, and the other electrode is printed on the surface. This ceramic electrode has many holes for gas passage. With AC application between the induction and the printed electrode, surface discharge takes place at the inner wall of each hole. This can be used to initiate a honeycomb discharge. With the application of –DC to the counter electrode placed across the honeycomb made of cordierite, honeycomb discharge can be generated.
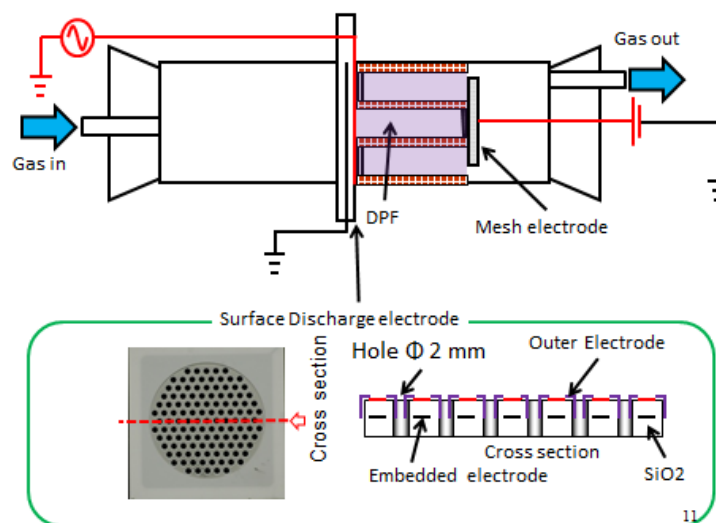
Fig. 3: Low temperature regeneration of DPF (Diesel Particulate Filter) using Honeycomb discharge.
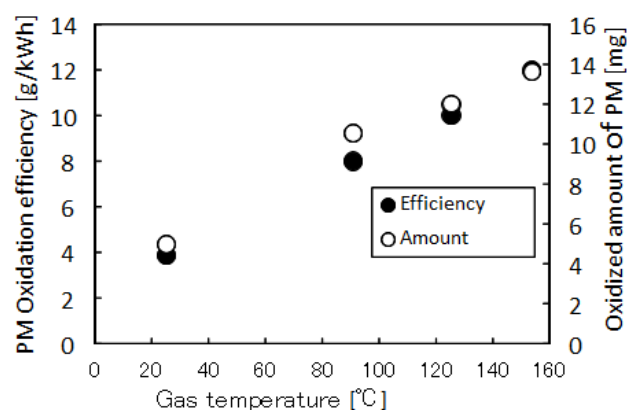
Fig. 4: PM oxidation efficiency using honeycomb discharge in DPF.

AC: 12.0 kV$_{P-P}$ Freq: 1.0 kHz   DC: 4.0 kV

Gas temp. : 23～150℃ Duration: 30min

Honeycomb discharge can be used to regenerate DPF (diesel particulate filter) by oxiding the trapped diesel particles[12]. Figure 3 shows the experimental setup. The flow rate of dry air was 5 L/min. The outlet gas from the regeneration reactor was analyzed by using a Fourier transform infrared spectroscope (FT-IR). The regeneration reactor was placed in a convection oven in order to control the ambient temperature. The oxidation efficiency was calculated from the weight change of the DPF before and after the regeneration. Figure 4 shows the oxidation efficiency versus ambient temperature. The applied voltage and the frequency of the surface discharge electrode were fixed at 12 kVp-p and 1.0 kHz, respectively. The applied voltage of the sliding discharge electrode was fixed at 4 kV in this experiment. The oxidation efficiency increased with increasing the ambient temperature. Oxidation efficiency was more than 11 g/kWh at 150 C. It should be added that, when the DPF was doped with Ag, the efficiency has been improved to 23 g/kWh.

3   Concluding remarks

NTP-Catalyst processes have been utilized for various enviromental applications such as cleaning of indoor air, VOCs, etc. Further understanding of the mechanism of activation of catalysts as well as reactions by radicals is challenging, but will lead to various applications.

References
1. A. Mizuno et al., IEEE Trans. Ind. Appl. 22, 516-522 (1986)
2. B. M. Penetrante, S.E.Schultheis, Eds., Non-thermal plasma Techniques for Pollution Control (NATO ASI Series Part A and Part B) (1993)
3. J. S. Chang et al., 19, 1152-1166, (1991)
4. T. Yamamoto et al., IEEE Trans. Ind. Appl. 28, 528-534 (1992)
5. A. Mizuno et al., IEEE Trans. Ind. Appl. 35, 1284-1288 (1999)
6. A. Mizuno, Catal. Today, 211, 2-8 (2013)
7. A. Mizuno et al., J. Electrostat. 25, 97-107 (1990)
8. S. Sato et al., SAE Technical Paper 2011-01-0310
9. K. Urashima et al., IEEE Trans. Ind. Appl. 33, 879-886 (1997)
10. E. Moreau, J. Phys. D: Appl. Phys. 40, 605 (2007)
11. S. Sato et al., J. Electrostat. 67, 77-83 (2009)
12. H. Hayashi et al., International Journal of Plasma Environmental Science and Technology, 6, 160-165 (2012)

MEASUREMENT OF ELECTRIC FIELD IN ATMOSPHERIC PRESSURE DISCHARGES USING STARK POLARIZATION SPECTROSCOPY

B. M. Obradović[1], N. Cvetanović[2], S. S. Ivković[1], G. B. Sretenović[1], V. V. Kovačević[1], I. B. Krstić[1], M. M. Kuraica[1]

[1] *University of Belgrade, Faculty of Physics, PO Box 368, 11001 Belgrade, Serbia*
[2] *University of Belgrade, Faculty of Transport and Traffic Engineering, Vojvode Stepe 305, 11000 Belgrade, Serbia*

E-mail: obrat@ff.bg.ac.rs

A short overview of the emission spectroscopy methods for measuring the macroscopic electric field in high pressure discharges is given. The occurrence of macroscopic electric field is a consequence of space charge build up. It is a common feature of discharge sheaths, streamer heads and double layers. The spectroscopic methods are based on polarization-dependent Stark splitting and shifting of atomic lines in the presence of a relatively strong electric field. For high pressure discharges Stark shifting of helium lines and their forbidden counterparts is used. The advantage of Stark methods is their ab initio basis which makes them independent on other plasma parameters. A different method for field measurement, based on helium line ratio, can be applied in cases where Stark method cannot be used.

Keywords: Stark polarisation spectroscopy; electric field measurements; atmospheric pressure discharges

1 Introduction

The occurrence of macroscopic, collective electric field is common in the laboratory plasma. It is a consequence of separation of charged particles that leads to space charge buildup and, in turn, to a directed macroscopic electric field governed by the Poisson equation. The region of significant macroscopic field occurs commonly in the so called sheath regions, the boundary layers where plasma is in contact with the confiding chamber or the electrodes. It is also present in the so called double layers and similar occurrences of directed collective field found both in the laboratory and astrophysical plasmas, for instance in atmospheres of outer planets. The formation of streamer heads is another example of a high field region. In all these cases, the electric field distribution in space and time, often determines the energy and flux of charged particles, thereby determining ionization rates and other characteristics of the bulk plasma. A number of experimental methods based on emission spectroscopy have been developed for measuring the macroscopic field in plasma sheaths, see for instance [1-3]. Methods are commonly based on Stark splitting and shifting of atomic lines in the presence of a relatively strong electric field. Compared to laser techniques [4-7], emission spectroscopy can only be used for higher values of the electric field and provides somewhat reduced spatial resolution but requires a simpler apparatus and offers ease of use, especially where higher line intensities are available. On the other side, the laser spectroscopy techniques are based on high lying Rydberg states which overlap at atmospheric pressure due to pressure broadening. The emission spectroscopy methods are mainly concentrated on the use of helium and

$$F(\lambda) = \sum_i f_i(\lambda, \Delta\lambda_i) \; ; \quad \Delta\lambda_i = S_i(E)$$

hydrogen lines and were applied to various types of discharges at lower [1-3] and higher pressure [8-10]. The advantage of these methods is their ab initio basis, hence they can be used for measuring electric field spatiotemporal distributions in diverse plasmas, independently of other plasma parameters and fulfillment of special conditions. Due to the Stark effect, hydrogen and helium lines are split into components with each component shifted in the field. For measuring the electric field from the line profile numerical fitting procedure can be established [11]. The model function for fitting is formed by assigning a line profile f to each component i while the field strength is implicitly incorporated in the function, via the component shift from the central wavelength given. Shift is defined by functional dependence on the field *S(E)*.

Fitting procedure has to be accommodated to the specific plasma conditions; due to different line broadening mechanisms. This paper is an illustration of emission spectroscopic field measurement in gas discharges. In the case of helium lines, along with the allowed line, additional lines appear in the spectra which are forbidden in the dipole approximation i.e. non-existent in the absence of field. Several examples of helium spectra obtained in our laboratory are presented.

2   Experimental
In our laboratory the Stark methods for measuring electric field were developed and applied to a wide range of discharges from low pressure glow to high pressure jet plasma. Use of ICCD cameras enabled spatiotemporal examination of electric field distribution. Details on experimental setups can be found in [9-11]. The gas flow and power supply are specific for each experiment. The radiation from the investigated region is projected by a lens to the entrance slit of a spectrometer. In order to obtain Stark shifts the radiation should be polarized using a polarizer at the entrance slit. Radiation is polarized either in the electric field direction (π-polarization) or orthogonally to the electric field direction (σ-polarization). The π-polarization is used more often due to larger shifts and a simpler interpretation of the measured spectrum. Typically, the direction of the electric field in the sheath region is orthogonal to the electrode surface.

3   Results and Discussion
Here, spectra from three different discharges will be presented. Namely, the low pressure glow discharge [2, 11], dielectric barrier discharge [8, 9] and atmospheric-pressure plasma jet [10]. The Grimm type low pressure DC abnormal glow discharge is characterized by relatively short cathode fall with high field strength and high intensity of spectrum lines. The dielectric barrier discharge operates at sinusoidal voltage and it usually operates at atmospheric pressure in a wide range of frequencies. Similarly, to glow discharge it contains a high field sheath and a low field region of bulk plasma. The atmospheric pressure plasma jet usually appears when noble gas flows through the primary discharge region, i.e. through the interelectrode space with the electrodes supplied by an AC or pulse high voltage. Discharge formed in this way poses all streamer characteristics. All discharges in presented examples operated in pure helium as working gas.

In a recent paper, Stark shifts of allowed lines and their forbidden counterparts is reexamined and calculated shifts are tabulated [11]. The He I 492.2 nm and 447.1 nm are the most used lines for field measurement. Fitting procedure can be applied that takes into account all of the components. This is especially important for low pressure discharges and/or at higher field values [11]. At higher pressures, only one forbidden and one allowed line commonly appear due to Van der Waals and resonant broadening. In this case the wavelength distance between the forbidden and allowed line can be used to calculate the field by applying peak to peak formula, see for instance [11]. The wavelength distance dependence on field may be incorporated in the fitting procedure or simply applied after the fit. It should be noted that line He I 492.2 nm (2^1P-4^1D) is the best choice for measurement in atmospheric pressure discharges since its forbidden counterpart (2^1P-4^1F) clearly appears in the spectrum, usually fairly separated.
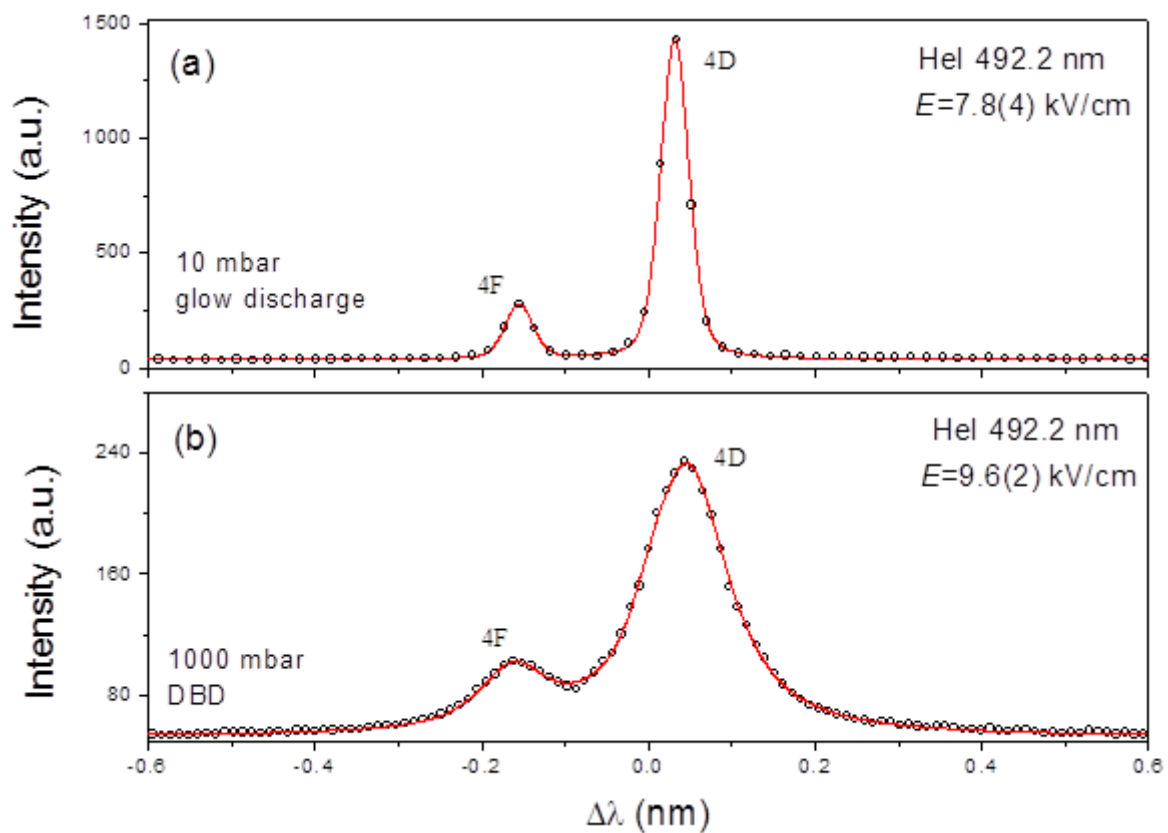
Fig. 1: Examples of He I 492.2 nm line from (a) a low pressure DC glow discharge and from (b) a dielectric barrier discharge at atmospheric pressure. Corresponding fits are shown as line graphs.

For the purpose of comparison, two examples of He I 492.2 nm spectra from a low pressure glow discharge and from a dielectric barrier discharge at atmospheric pressure are given in Fig. 1. At the atmospheric pressure discharge the overall fitting profile is comprised of two Pseudo-Voight functions and the widths of the profiles take into account the instrumental, resonant and Van der Waals broadening. These measurements were used to obtain the electric field spatiotemporal distribution in the discharge [9] which is important for modeling.

Another example is the same line from the atmospheric plasma jet where a different fitting procedure is performed, see Fig 2a. Namely the profile was fitted with two Voight functions

with Gauss component fixed as known from the instrumental and Doppler broadening. The electric field is then afterwards calculated from the wavelength distance of the two components.

An interesting fitted profile is shown in Fig. 2b. It shows a much higher field and incorporates a so called field-free component. Namely, the profile is obtained from the streamer head of the plasma jet. Intense radiation that is not shifted in the field is detected in the optical path. This component usually comes from the low field region for various reasons due to existence of emitting atoms that are not in the field. Therefore, a non-shifted component has to be included in the fit due to its overlap with the allowed component of the He I 492.2 nm line, see Fig. 2b. In this case, special care should be taken due to presence of three lines that have relative position correlated to the field strength. Here a different fitting method was used than in the original paper [10]. In the mentioned experiment, use of the Stark method in combination with the Abel inversion demonstrated the field minimum at the jet axes – an important result for understanding the plasma jet.
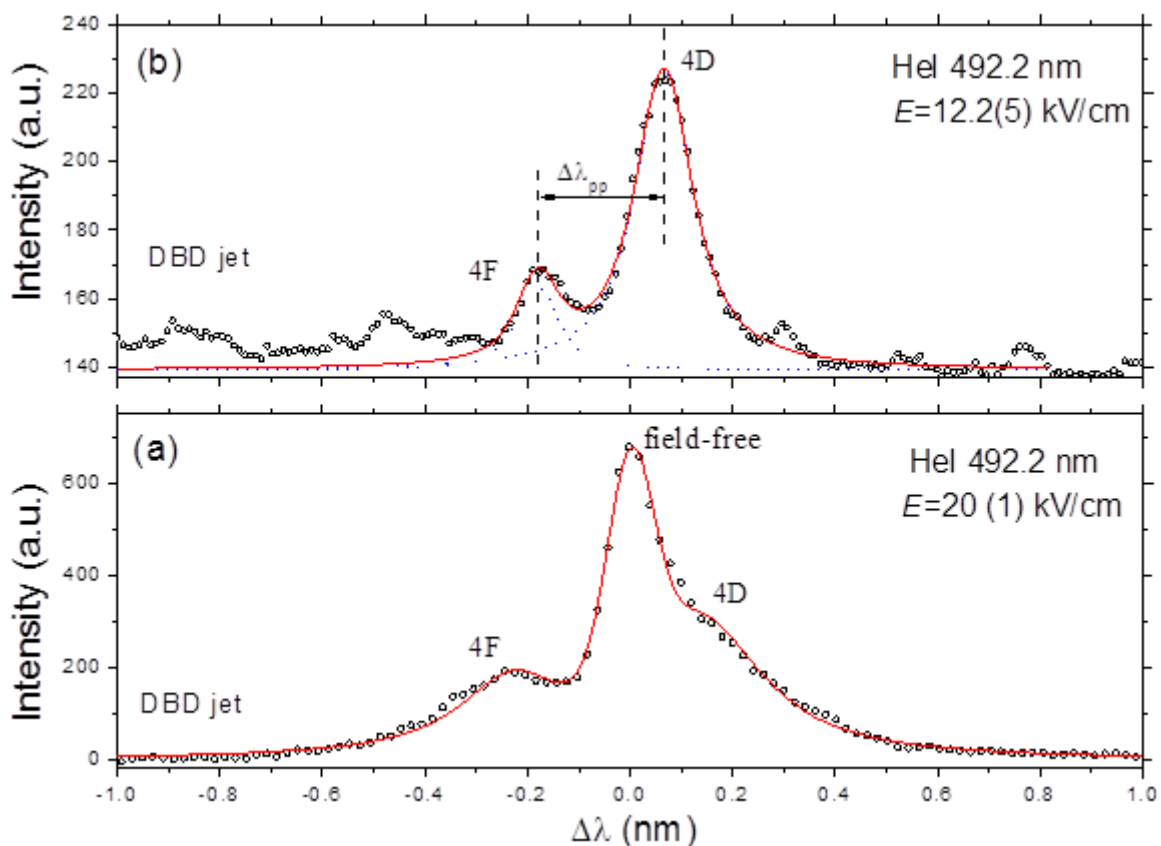
Fig. 2: Examples of He I 492.2 nm line from atmospheric plasma jet. (a) Fit for each component and the overall fit are shown as line graphs. (b) Example of He I 492.2 nm line from atmospheric plasma jet with strong field-free component with the overall fit. Corresponding fits are shown as line graphs.

Although Stark polarization spectroscopy is independent of energy distributions and densities of plasma particles it suffers from relatively low intensity of helium lines with forbidden counterparts, especially at atmospheric pressure discharges. Additionally, at atmospheric pressure, measurement of low field values is limited due to the overlap of the atomic line and its forbidden component caused by pressure broadening. The overcoming of this drawbacks

was the motivation for proposing another method for electric field measurement, based on line intensity ratio of two singlet atomic lines of helium (He I 667.8 nm and He I 728.1 nm) with respectable intensity [12]. Opposite to the exact, quantum mechanics based method of Stark splitting, the new method is based on the excitation rate dependence on the electric field, with recommended calibration.

Even though the method is postulated as a calibration method, by measuring the dependence of line intensity ratio on the electric field strength at specific discharge conditions, its physical background was investigated using a collisional-radiative model. This model provided the functional dependence of line intensity ratio dependence on local field strength. It was found that line ratio is directly connected to the local electric field strength and independent of electron density. The method was recommended only for high pressure (e.g. atmospheric) discharges where the local field approximation is valid and at regions with considerable electric field strength (>3 kV/cm) where excitation from metastables is negligible. The advantage of the method is the possibility of measuring lower electric field values and measuring at the time instances with lower light intensity. These advantages enabled additional investigations e.g. electric field evolution with discharge development. It was found that the dielectric barrier discharge in helium transforms from subnormal to glow-like with current increase [12].

4 Conclusion

The polarization dependent Stark emission spectroscopy is a powerful and practical tool for investigating the macroscopic field in electric discharges. Several experimental examples of the use of helium line Stark effect are presented. The line He I 492.2 nm is the best choice for measuring of the electric field spatiotemporal distribution in high pressure discharges. The important advantage of this noninvasive method is its ab-initio nature, making it independent of plasma parameters and fulfillment of special conditions. For measurement in conditions where Stark method cannot be used, a method based on helium line intensity ratio is recommended. This second method relies on local field approximation and therefore can only be used at relatively high (atmospheric) pressure.

References
1. B. N. Ganguly et al., J. Appl. Phys. 70, 621 (1991)
2. M. M. Kuraica et al., Appl. Phys. Lett. 70, 1521 (1997)
3. T. Wujec et al., J. Phys. D: Appl. Phys. 36, 868 (2003)
4. B. N. Ganguly et al., J. Appl. Phys. 61, 2778 (1987)
5. E. A. den Hartog et al., Phys. Rev.A 38, 2471 (1988)
6. U. Czarnetzki et al., Plasma Sources Sci. Technol. 8, 230 (1999)
7. S. Hussain et al., J. Phys. D: Appl. Phys. 39, 3788 (2006)
8. B. M. Obradović et al., Appl. Phys. Lett. 92, 191501 (2008)
9. S. S. Ivković et al., J. Phys. D: Appl. Phys. 42, 225206 (2009)
10. G. B. Sretenović et al., Appl. Phys. Lett. 99, 161502 (2011)
11. N. Cvetanović et al., J. Phys. D: Appl. Phys. 48, 205201 (2015)
12. S. Ivković et al., J. Phys. D: Appl. Phys. 47, 055204 (2014)

OPTICAL EMISSION DIAGNOSTICS FOR NANOSECOND MICRODISCHARGES AT ATMOSPHERIC PRESSURE

B.-D. Huang[1, 2], X.-M. Zhu[2], K. Takashima[3], Y.-K. Pu[1]

[1] *Department of Engineering Physics, Tsinghua University, Beijing 100084, P. R. China*

[2] *Institute for Plasma and Atomic Physics, Ruhr-University Bochum, Bochum 44780, Germany*

[3] *Department of Electronic Engineering, Tohoku University 6-6-05 Aoba Aramaki, Aoba-ku, Sendai, MIYAGI 980-8579, Japan*

E-mail: puyikang@mail.tsinghua.edu.cn

In this presentation, we will describe the techniques and results for measuring plasma discharge parameters of nanosecond pulsed discharges at atmospheric pressure by optical emission spectroscopy. Special attention is focused on the breakdown period of the discharges, which are generated between two parallel plate electrodes with very narrow gap. Information on the generation of high energy electrons, the propagation of ionization wave and the modification of the electric field profile can be clearly observed with spatial and temporal resolved measurement of emission line intensities. Advantages as well as challenges for this work will be discussed.

Keywords: optical emission spectroscopy; nanosecond discharges; breakdown; ionization wave

1   Introduction

Optical emission spectroscopy (OES) is a very useful tool for diagnosing discharge characteristics of atmospheric pressure nanosecond discharges. In this presentation, we will review the results from our recent work on the investigation of nanosecond discharges by using both spatially and temporally resolved spectra in the wavelength range of 400 nm to 800 nm.

Electron impact processes are the primary driving mechanism for the generation of active species in nanosecond discharges at atmospheric pressure. The main goal of our effort is to obtain electron density, effective electron temperature and even electron energy distribution in the discharge. Driven by a nanosecond high voltage pulsed power supply, the discharge characteristics are fast changing in time. The discharge usually consists of three periods: the breakdown, the quasi-stationary discharge, and the afterglow. It is our opinion that most high energy electrons are generated in the breakdown period, so we focus our attention on the discharge development in the breakdown period.

2   Principle

When performing optical diagnostics for this kind of discharges, one may question what kind of temporal resolution can be realized. This is a valid concern since the resolution depends not only on the exposure time of the detector, but also on the lifetime of the emission species. Another important question is about the spatial resolution. This is especially challenging since the dimension of these discharges is generally small in the category of microdischarges. The

last concern is how to relate the emission intensities to the electron density and the effective electron temperature.

In the breakdown period, the electron density is quite low ($<< 10^{14}$ cm^{-3}), the mean electron energy could be quite high (> 3 eV) under the influence of externally applied strong electric field, the characteristic time for discharge parameter evolution is ultra-short (sub-nanosecond), and the major excitation mechanism is the direct electron impact excitation, i.e. excitation from the atoms and molecules in ground state. In this period, the density of other excited species is too low to contribute to step-wise excitation and the contribution from recombination followed by collisional de-excitation from the Rydberg levels to lower levels is also insignificant in this initial stage of the discharge development. This is because both of these processes are generally related to low energy electrons ($< \sim 3$ eV) and have much longer characteristic time (order of tens or hundreds of ns). Therefore, the emission from an upper energy level truly reflects the existence of high energy electrons. Even though the natural lifetime of a particular excited level can be tens of a nanosecond or longer, the effective lifetime can be much shorter (~ 1 ns or shorter), due to strong collisional quenching at atmospheric pressure. One of the consequences of this effect is the enhancement of temporal resolution. For the same reason, the spatial resolution can also be increased. (This is the case for quasi-static states). A photon emitted from a certain location represents the presence of a local excitation process by electron impact.

In order to be able to "see" electrons with different energies, a mixture of two or more gas species with different excitation threshold energies can be used. In this way, in the breakdown period, a relative increase of the emission intensity emitted from a particular level is directly related to the number of high energy electrons capable of causing that excitation from the ground state. Therefore, the ratio of the change in emission intensities between two lines is proportional to the ratio of excitation rate coefficients for these two levels, which depends on the electron energy distribution or the effective electron temperature. Notice that the escape factor for the collected emission lines emitted from this kind of discharges in the breakdown period is not an issue, due to both the pressure broadening and low density of the lower levels.

Technically, the emission intensity of any given spectral line is extremely weak in the breakdown period. The requirement of both temporal and spatial resolution does not help the situation. This poses a serious threat to the signal to noise ratio for the collected emission intensities. A way out of this challenge is, for any given time window, to accumulate the emission over many tens of thousands of discharges. In order to retain meaningful time resolution, one needs to be able to generate repetitive discharge with extremely low jitter.

3   Results and Discussion

With all the above considerations, we investigate the breakdown process in atmospheric pressure nanosecond discharges with parallel-plate electrodes. The breakdown process evolves in a form of cathode directed ionization wave, which can be seen from the fact that the high optical intensity region firstly appears near the anode and propagates toward the cathode [1].

The temporally and spatially resolved electric field is obtained from the Stark splitting of the He I 492.1 nm line. Compared with the average electric field (voltage / gap width), the electric field is greatly enhanced at the ionization wave front and is significantly weakened within the plasma column behind the wave front, showing a clear structure of ionization wave propagation [2].

The spatial profiles and its temporal evolution for He II 468.6 nm, He I 667.8 nm, and Ar I 750.4 nm lines are obtained. It is found that the He II 468.6 nm line, which has very high excitation threshold energy (75.60 eV), has its peak intensity at the ionization wave front, where the electric field is strongest. However, the He I 667.8 nm and Ar I 750.4 nm lines, which have lower excitation threshold energy (23.07 eV and 13.48 eV, respectively), have their intensity peaks behind the ionization front (near the anode). It can be expected that from the wave front to the anode, the mean electron energy decreases while the electron density increases, resulting in the phenomenon that the intensity peaks for different these lines locate in the order of their excitation threshold energy.

Using a time dependent collisional–radiative model and the ratios of these lines, the evolution of $T_{e, high}$ and $T_{e, low}$ (representing the local slope in the high energy and low energy part of the EEPF, respectively) are obtained. The value of $T_{e, high}$ is much larger than that of $T_{e, low}$ (tens of eVs *v.s.* several eVs), which indicates that an elevated high energy tail in the EEDF is built up under the influence of strong electric field during the breakdown process (even though abundant newly generated low energy electrons also exist). During the breakdown process, the spatial distribution of the $T_{e, low}$ and the $T_{e, high}$ generally follows that of the electric field, i.e. the ionization wave front region has a much higher T_es compared the region behind the wave front. At the end of the breakdown period (when the discharge region or the wave front reaches the cathode), the location of the highest $T_{e, low}$ and $T_{e, high}$ is shifted away from the cathode sheath, where the electric field is strongest. In fact, it can be estimated that the energy relaxation length for electrons with hundreds of eV energy is in the order of ~ 100s μm in atmospheric pressure helium, which is comparable with the thickness of the cathode sheath. This indicates the existence of a non-local behavior for high energy electrons. Therefore, the fluid approximation (which basically assume a local relationship between the discharge parameters like ionization frequency and electron mobility with the electric field) may not be valid in a region with strong electric field or large field gradient. These arguments are also supported by the result from a simple Monte-Carlo simulation.

References
1. B. D. Huang et al., J. Phys. D: Appl. Phys. 48, 125202 (2015)
2. B. D. Huang et al., J. Phys. D: Appl. Phys. 49, 045202 (2016)

LATERAL PATTERNS IN GLOW-LIKE BARRIER DISCHARGES

L. Stollenwerk, R. Wild
[1]Institute of Physics, University Greifswald,
Felix-Hausdorff-Straße 6, 17489 Greifswald, Germany

E-mail: stollenwerk@physik.uni-greifswald.de

Gas discharge systems are well known for their formation of self-organised patterns. Beside the structuring along the current direction, which is investigated since the beginning of the scientific investigation of gas discharges, the formation of lateral structures in laterally uniform experimental setups has drawn the attention in the last decades. In this contribution, a short overview over lateral structures in barrier discharges, especially those working in the glow-like mode, is given. We will have a look at the mechanisms stabilizing lateral patterns as well as their classification within classical modes of operation. Furthermore, we want to give an overview over the variety of observed patterns and especially the more complex ones involving multiple breakdowns per half-cycle.

Keywords: barrier discharge; low-temperature discharge; pattern formation; dissipative solitons

1   Introduction

The barrier discharge is a long known discharge type and one of the oldest being used in industrial applications. Classically, this type of discharge is separated into two modes: the filamentary mode, dominated by streamer ignitions, and the diffuse mode, operating either as a Townsend discharge or a glow-like discharge. However, while developing systems with a small discharge gap – often a result of the increasing of the working gas pressure towards atmospheric pressure – a somehow intermediate mode of discharge arose. While both the shape of the overall current and the current density are typical for a glow-like discharge, the lateral current distribution becomes inhomogeneous. Usually, the lateral current distribution is spot like, similar to the current distribution of filamentary discharges. But also other shapes have been observed, some being complex but regular patterns of discharge spots, other rather irregular. In this contribution we shall give an overview over different patterns, the experimental conditions of their appearance, and the underlying physical mechanisms.

2   Experimental setup

Although the details of the experimental setups in different experiments differ, they have many things in common. A typical setup is sketched in Fig. 1(a). The discharge cell consists of two dielectric layers, usually glass, enclosing the discharge gap. The discharge gap is shorter than 1 mm, in this example 0.5 mm. The thickness of the dielectric layers in in the same order. The electrodes are applied on the outside of the dielectric layers. At least one of the electrodes has to be transparent so that the discharge can be observed in current direction. An ITO (Indium-Tin-Oxide) layer is usual. The other electrode may consist of metal. The diameter of the discharge area is much larger than the discharge gap; in this example a typical value of 40 mm is shown. The working gas varies in different experiments. Noble gases are common as well as nitrogen. The gas pressure varies from 100 hPa to atmospheric pressure.

The system is driven with an AC voltage of some hundred volts amplitude and a frequency in the range of several ten kHz to several hundred kHz.
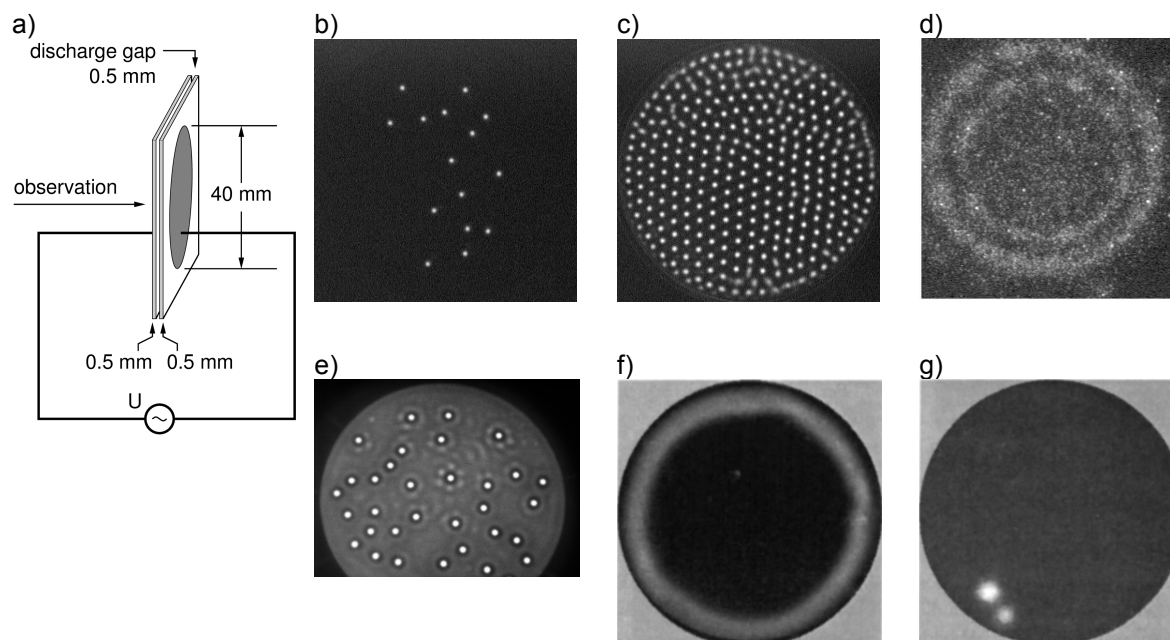
Fig. 1: (a) Sketch of the discharge cell with large aspect ratio. Both dielectric layers as well as the discharge gap have a typical thickness of 0.5 mm. The diameter of the discharge is several centimeters wide, typically 40 mm. At least one dielectric layer and the corresponding electrode is transparent, so the discharge can be observed in current direction. (b) few discharge spots [1]. (c) hexagonal arrangement of discharge spots [1]. (d) discharge forms a spot pattern during the first several breakdowns via an intermediate ring pattern [2]. (e) complex pattern consisting of multiple breakdowns per half-cycle [3]. (f) ring-like pattern observed with a long exposure time [4]. (g) same pattern as before observed with short exposure time; it consists of a fast moving pair of spots.

3   Examples for patterns and their mechanisms

The subfigures (b) to (g) of Fig. 1 show different examples of observed patterns. A loose arrangement of spot (b) is very common, as well as the hexagonal arrangement of spots (c). Both patterns can be converted to each other via a bifurcation. Fig. 1(d) shows a pattern consisting of two ring-like discharges at the boundary of the discharge area. This is not a stable pattern but an intermediate state while a pattern is forming during the first several breakdowns after the ignition of the system. (e) shows a rather complex pattern emerging in a multi-breakdown discharge. The oscillating tails of the discharge spots govern their interaction. Pattern (f) is a stable pattern and looks like a bright ring at the boundary of the discharge area. An observation with a short exposure time reveals two different discharge spots in fast motion along their axis.

4   Outlook

The understanding of the underlying mechanisms of pattern formation is in some cases well known, but in other cases rather poor. While the basic mechanisms for the spot-like appearance of the discharge are well investigated both in experiments and numerical simulations, the more complex patterns and their dynamic often are explained only on a qualitative level.

References

1. L. Stollenwerk et al., Eur. Phys. J. D 44, 133 (2007)
2. L. Stollenwerk et al., Phys. Rev. Let. 96, 255001 (2006)
3. A. L. Zanin et al., Gemen workshop 2001 (unpublished)
4. I. Brauer et al., Phys. Rev. Let. 84, 4104 (2000)

TOPIC 1: FUNDAMENTAL PROBLEMS OF HIGH PRESSURE DISCHARGES

ROLE OF THE He METASTABLE IN SELF ORGANIZED DBD AT ATMOSPHERIC PRESSURE

A. Belinger, N. Naudé, N. Gherardi

LAPLACE, Université de Toulouse, CNRS, INPT, UPS, France

E-mail: antoine.belinger@laplace.univ-tlse.fr

Depending on the operating conditions, different regimes can be obtained in a Dielectric Barrier Discharge (DBD): filamentary, diffuse/homogeneous or self-organized. For a plane-to-plane DBD operated at high frequency (160 kHz) and at atmospheric pressure in helium gas, we show that the addition of a small amount of nitrogen induces a transition from the homogenous regime to a self-organized regime characterized by the appearance of stable filaments at the exit of the discharge. In this paper, we detail the key role of the helium metastable in the transition from diffuse to self organized discharge.

Keywords: dielectric barrier discharge; self organization; helium; high frequency

1   Introduction

Similarly to what is observed in many other nonlinear systems, Dielectric Barrier Discharges (DBD) can exhibit self-organized (SO) patterns. This phenomenon may look like as a spatial organization of filaments [1] usually obtains in filamentary mode but other patterns have been observed: strip, inversed hexagonal, concentric ring [2–4]. The appearance and the dimension of these patterns suggest that these SO discharges ignited under a Townsend breakdown. Recently, a hexagonal superlattice pattern has been observed, which consists on several hollow rings equally distributed on the dielectric surface [5]. Observed with short exposure time photographs, a hollow ring is the composition of periodic-driven vibrating motion of discharge filament pairs. Therefore self-organized pattern is not necessary obtain within one discharge, but successive discharges could lead to a pattern. This confirms that self-organized denomination describes different kinds of discharge. This is certainly why it is obtained in a wide spectrum of experimental conditions: SO discharge pattern can thus be produced in one [6] or two dimensional discharge gap geometry [2], at low or at atmospheric pressure [3] and under a large range of temperature [7]. However, discharges leading to formation of SO pattern are most often produced in noble gases. In any case memory effect seems the cause of SO pattern: discharge ignites where charges have been previously deposited (the breakdown in this location being lower). Theses charges are deposited on the electrode in the same location (by the current of the discharge) or in the vicinity (by the low current (dark) between two filaments) of the previous discharge [8]. In this paper we focus on the structure of a 2D-DBD in helium at atmospheric pressure and on the role of the adding of nitrogen on the self-organization.

2   Experimental setup

The DBD is kept in a closed vessel to perform experiments in a well controlled atmosphere. The plasma reactor is pumped down to 10^{-3} mbar prior to any experiment, and then is filled up to atmospheric pressure using mixtures of helium and nitrogen. Two mass flow meters allow regulating the amount of helium and nitrogen. In order to renew the atmosphere, a gas flow is injected from one side of the discharge (longitudinal gas injection), keeping a constant pressure through a gentle pumping of the vessel.

The discharge is created between two plane electrodes, square with 3 cm side, each of them covered by a dielectric barrier. The high voltage (bottom) electrode is covered with an alumina plate 625 μm thick, the grounded one (top) with a glass plate 1.1 mm thick. Both dielectrics are separated by a 1 mm gas gap. So as to observe the discharge, the top electrode is made of a thin layer of ITO.

The DBD is powered with a high frequency (160 kHz) power supply (RFPP-LF 10) associated with a homemade matching network. Voltage is amplified using a transformer (ratio 1:20). The electrodes are connected to the secondary of the transformer. Light emission of the discharge is analyzed by optical emission spectroscopy and by short-exposure time photographs taken with an intensified CCD camera (PI-MAX-3, Princeton Instrument).

3   Modification of the discharge structure

The nitrogen proportion is increased step by step. That means that the discharge is first ignited in pure helium and remains switched on when increasing the N_2 content in order to see the transition between different discharge stages. For each step, analyses are performed after the steady state is reached. At low concentration of nitrogen, discharge is diffuse and spreads over the whole surface of the electrode (Fig. 1a). When N_2 concentration increases, the discharge area first decreases, but the discharge looks always diffuse. For a concentration around 1%, some microdischarges appear and coexist with a homogeneous discharge. As can be seen on Fig. 1.b, these filaments appear preferentially at the exit of the DBD (along the gas flow direction). When N_2 concentration increases again (Fig. 1.c), discharge may contain only filaments. In some case, these filaments can be arranged along strips which can be seen at naked eye (Fig. 3.a). This stage is rather unstable. For a higher N_2 concentration, discharge transits suddenly to a stable self-organized state (Fig. 1.d): the discharge is then composed of 1 mm^2 filaments regularly spaced by 2 mm and located on a "line" at the exit of the DBD.
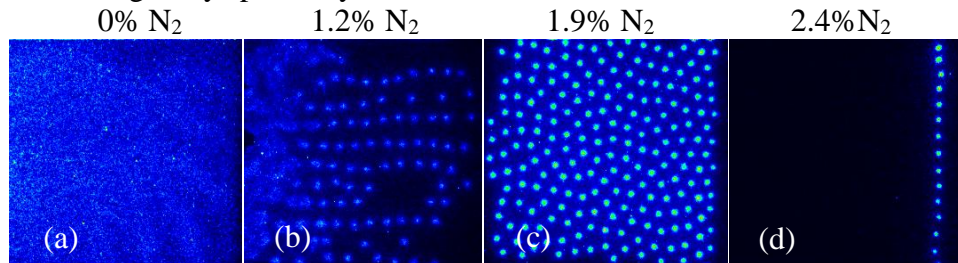
Fig. 1: discharge pictures for increasing concentration of N_2 in He. Exposure time is 6.25 μs (1 period). A 2 slm gas flow is injected homogeneously from the right of the picture to the left. (a): 100% He (b): 1.2% N_2 (c): 1.9% N_2 (d): 2.4% N_2.

The discharge is analysed by optical emission spectroscopy. We focus specifically on the emissions from N_2 (2nd positive system: SPS), He and N_2^+ (1st negative system: FNS) shown in Fig. 2a. In helium DBDs, the emission of the FNS (main band at 391 nm) is generally attributed to Penning ionisation from helium mestastable $He(2^3S)$, whereas the emission of the SPS of N_2 (main band at 337 nm) is attributed to direct electronic excitation [9]:

$$N_2 + e^- \rightarrow N_2\left(C^3\Pi_u\right) + e^-$$

$$N_2 + He\left(2^3S\right) \rightarrow N_2^+\left(B^2\Sigma_u^+\right) + e^- + He$$
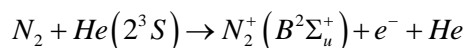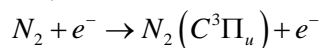
Hence, the relative concentration of helium metastable can be estimated from the ratios of the emission bands, knowing the electron concentration. We assume that the electron density can be estimated as proportional to the current density J. Hence, one can write:

$$\left[He\left(2^3S\right)\right] = \alpha \cdot [e^-] \cdot \frac{I(391)}{I(337)} \square\ J \cdot \frac{I(391)}{I(337)}$$

where J is calculated from the measured discharge current and from the area covered by the discharge (deduced from the pictures presented above). This method is valid until several assumption. First of all, N_2^+ is produced only by He^* and not by electronic ionisation (*i.e* N_2 concentration must be low). Secondly, the electronic temperature, the electronic density should be constant. This crude approximation prevents the comparison of the $[He^*]$ between the different regimes of discharge (α is clearly not constant).
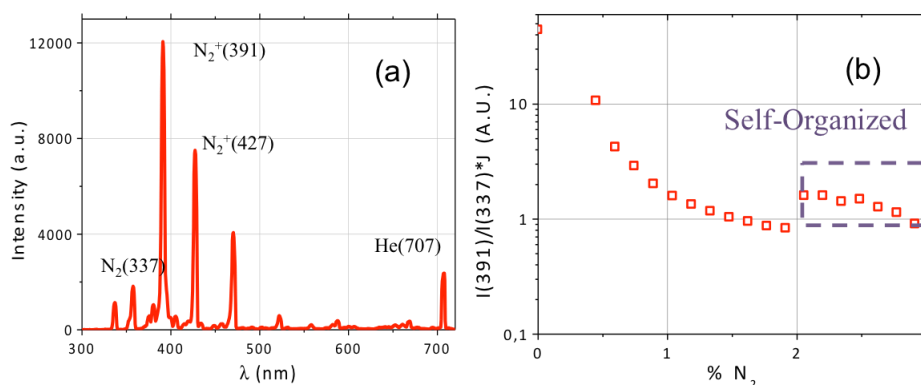
Fig. 2: (a) Typical optical emission spectrum of the dischage. (b) Relative concentration of helium metastable estimated from eq (1) vs N_2 amount.

As seen in Fig. 2.b, an increase of the relative nitrogen amount in the He/N_2 gas mixture logically results in a decrease of the He^* while the discharge stays in diffuse mode. For around 2% of nitrogen, the discharge switches in the SO mode (Fig. 1.d) and this transition seems to be associated with a small step increase (the y-axis is logarithmic) of the He^* content. However, one has to note here that during this transition the discharge current density strongly increases (not shown here) which indicates a change in the discharge regime. Thus the used approximation relating the current density with the electron concentration may be not anymore avaliable at this point.

For low concentrations of nitrogen (typically below 1%), Penning ionisation can produce electrons in the gap from one discharge to the following one (typical lifetime of He metastable is higher by one order of magnitude than the half period). He^* are dispersed over the whole area of the electrode and so the discharge is mostly diffuse. The transition to a filamentary discharge (presented in Fig. 1.c and Fig. 1.d) seems to occur when the He^* becomes too low. The transition to the self organized mode (presented in Fig. 1.d) is sudden and associated with a step of the N_2 concentration. When the N_2 concentration is increased (keeping the discharge running), the concentration of N_2 is higher at the entrance of the DBD than at the exit. Morovers every metastable (produced in the previous state) are pushed by the flow toward the exit. These both phenomena favour the ignition at the exit of the DBD. In this case discharge ignites where charges have been previously deposited. We have measured that the charge density is ten times greater at the discharge location (not shown here).

The state presented in Fig. 1-c, is of particular interest. For longer exposure time photographs, or at nacked eye, this state appears like SO strips (Fig. 3.a). Moreover, the pattern seems to depend on some uncontrollable experimental circumstance; in some case the discharge can even looks diffuse. In any case these patterns or strips consist in fact on discharge filaments in motion along the gas flow direction. Under special circumstance (very low flow, special dielectrics) the motion of the filaments towards the exit can be seen at nacked eye. This state is completely unstable: a little modification of the N_2 ratio results in the transition to the mode described in Fig. 1.d.

An important feature is that all these filaments ignite simultaneously and move slowly as presented in Fig. 3.b. This specific picture is the result of an acquisition of two periodes separated by a delay ΔT. This delay allows to observe the displacement of the filaments and then to calculate the velocity of the filaments. The red arrows indicate the displacement of a few of these filaments.
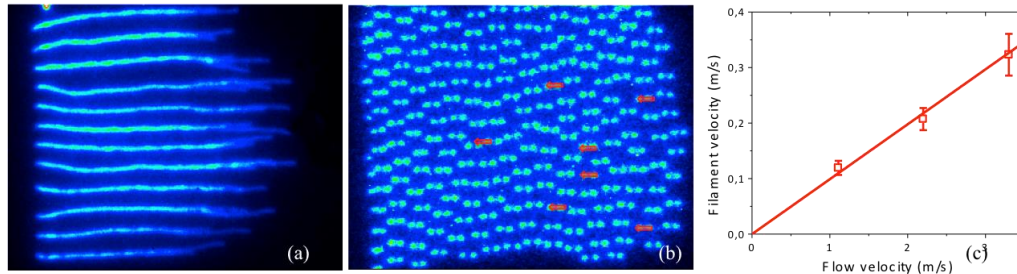
Fig. 3 : a: self organized strips (100 acqusition of one period delayed by 1 ms) external flow: 2slm. b: motion of the filament (2 acquisition delayed by 25 ms): external flow 6 slm. c: filament velocity versus flow velocity.

The gas flow can be modified in order to change the velocity of the gas. As we can seen in Fig. 3.c the velocity of the filament depends on the external gas flow. However, it is typically ten times lower than the velocity of the gas which indicates that a slow process governs this movement. This is probably the results of the combination of the He* displacement along the gas flow (due to the excitation frequency of the used power supply: 160 kHz, and knowing the mean gas velocity (1.1 m/s for 2 slm)), one can estimate that the metastables cross around 10 μm between two discharges) and the fact that the ignition of a microdischarge is favored by the charges deposited by the previous discharge (mechanism which tends to keeps the filaments at the same place). The He* displacement allows the motion of the filament and the electric charge slows down the displacement. As already described a slight increase of the N_2 concentration results in the transition to the SO mode, for which the ignition becomes possible only at the end of the discharge area.

4   Conclusion

Adding of nitrogen in a helium APGD sustained at high frequency (160kHz) tends to perturb the discharge uniformity which transits to a pattern made of filaments. For the lowest N_2 concentrations, discharge stays diffuse. Afterwards, filaments coexist with the diffuse discharge and above a threshold concentration only a few filaments are localized at the exit of the DBD. The helium metastables He(2^3S) play an important role in the transition of this different state. Indeed He* favours the diffuse mode and the addition of N_2 tends to decrease the concentration of He* and then to promote the appearance of filaments. Moreover, in the transition mode between diffuse and self organized regime, the He* metastable displacement along the gas flow is certainly responsible of the motion of the filaments.

References
1. I. Brauer et al., Phys. Rev. Lett. 84, 4104 (2000)
2. I. Radu et al., IEEE Trans. Plasma Sci. 31, 411 (2003)
3. W. Breazeal et al., Phys. Rev. E 52, 1503 (1995)
4. E. L. Gurevich et al., Phys. Rev. Lett. 91, 154501 (2003)
5. B. Li et al., J. Phys. Appl. Phys. 47, 055205 (2014)
6. B. Bernecker et al., J. Phys. Appl. Phys. 44, (2011) 262002
7. S. Stauss et al., Plasma Sources Sci. Technol. 22, 025021 (2013)
8. J. P. Boeuf et al., Appl. Phys. Lett. 100, (2012)
9. A. Ricard et al., Surf. Coat. Tech. 112, 1 (1999

EFFECT OF THE MODULATION ON A HELIUM DBD IN THE MEDIUM-FREQUENCY RANGE AT ATMOSPHERIC PRESSURE

J.-S. Boisvert[1,2], J. Margot[1], F. Massines[2]

[1] Département de physique, Université de Montréal, 2900 Blvd Édouard-Montpetit, H3T 1J4, Montréal (Qc), Canada
[2] PROMES-CNRS, Rambla de la Thermodynamique, 66100, Perpignan, France

E-mail: jean-sebastien.boisvert@umontreal.ca

In this paper, the electrical behavior and the gas temperature of a modulated dielectric-barrier discharge operated at 1.6 MHz are described as a function of the modulation frequency varied from 1 to 10000 Hz. It is shown that the gas temperature and the breakdown voltage are reduced when a modulation frequency higher or equal to 10 Hz is used. This effect is related to the gas renewal rate of 8.3 Hz (i.e. gas residence time of 120 ms). Beyond 100 Hz, the dielectric temperature decreases but this is accompanied by a significant decrease of the effective power.

Keywords: dielectric barrier discharge; medium frequency; modulation; gas temperature; helium

1   Introduction

Dielectric barrier discharge (DBD) devices are widely used to generate low-temperature atmospheric-pressure diffuse discharges. Surface modification and medicine are a few examples of fields in which DBDs are useful. However, one of the major disadvantages of diffuse DBDs is their low power density. One way to raise it is to increase the excitation frequency. Recent studies have shown that using excitation frequency in the medium-frequency (MF: 0.3 to 3 MHz) range allows the power density to increase by one order of magnitude in comparison to low frequency [1,2]. However, using a higher power density leads to higher gas temperature and surface heating. In this paper, we show to which extend the gas temperature and surface heating can be reduced in helium DBDs by modulating the applied power as well as the consequences of the modulation on the discharge behaviour.

2   Experimental

The plasma reactor consists of a plane parallel DBD with solid dielectrics on each electrode. The amount of impurities is minimized by the use of a mechanical pump connected to the chamber. Experiments are performed at atmospheric pressure (101.3 kPa) with a constant helium flow (99.999% purity) of 8.3×10^{-6} m^3/s through a 2 mm gap between the alumina solid dielectric surfaces (see figure 1). Medium frequencies can be obtained using a waveform generator (Agilent 33220A) and a power amplifier (Prâna GN500) connected to the discharge cell via non-commercial air core transformers [3]. Adjusting the capacity of the electrical circuit, it is possible to tune at 1.6 MHz. With the excitation frequency fixed at 1.6 MHz, the modulation frequency was varied from 1 Hz to 10 kHz with a duty cycle maintained at 50% (i.e. 50% with power on and 50% with power off). Time-resolved optical emission (230 to 920 nm) was recorded using a H10721-20 (optimized for VIS) Hamamatsu photomultiplier tube (PMT). A Princeton instrument Acton SP2500 spectrometer equipped with a PI-max 2 camera was used to record rotational spectra of $N_2(C^3\Pi_u \rightarrow B^3\Pi_g)$ in order to determine the gas temperature. In addition, a thermocouple was positioned on the dielectric surface.
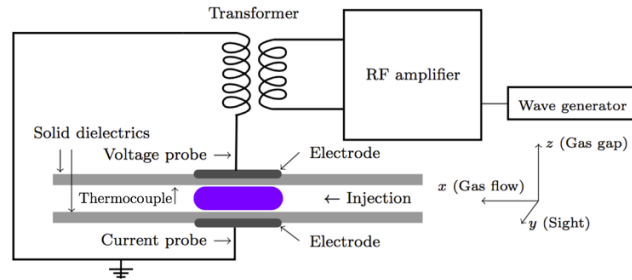
Fig. 1: Discharge cell and electrical circuit. The gas gap lies along the *z* axis, while the line of sight of the optical measurements is along the *y* axis.

3   Results and Discussion

As expected in a MF discharge two distinct modes can be sustained: the Ω mode and the RF-α mode [1]. Modulation of the discharge, implies that the discharge turns on and off frequently. First the discharge ignition is studied in figure 2 were waveforms are obtained by calculating the RMS voltage and current of each time-period of the excitation frequency. Even though the power density has to rise by one order of magnitude to yield the RF-α mode, the RMS voltage rises by less than 10%. On the other hand, the RMS current is almost quadrupled. In comparison to the Ω mode, the rise of the RMS current and of the light emission along with the RMS voltage drop indicates a faster breakdown in the RF-α mode.
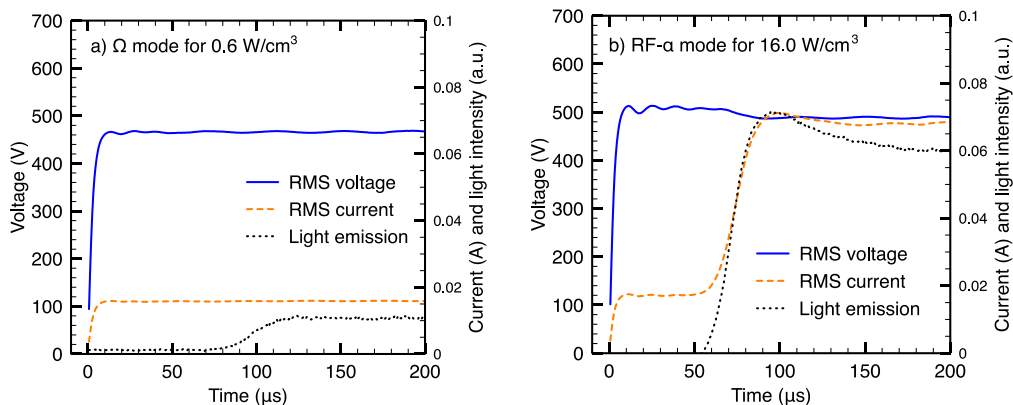
Fig. 2: Voltage, current and light emission waveform for the first 200 μs of the discharge with a modulation frequency of 1 Hz. The light emission was recorded with the photomultiplier tube. Left) The discharge is in the Ω mode at 0.6 W/cm³. Right) The discharge is in the RF-α mode at 16.0 W/cm³.

RMS voltage current characteristic curves are shown in figure 3. The characteristic curves are very similar for each modulation frequencies: the slope is the same in the Ω mode and in the RF-α mode. On the other hand, the RMS voltage is systematically lower at 100 Hz in the α mode. From the I_{RMS}-V_{RMS} curves, one can notice that according to the modulation frequency, the discharge ignition occurs at different voltage values. Accordingly, the breakdown voltage as a function of the modulation frequency is also plotted in figure 3. It drops by more than 15% when the modulation frequency increases from 1 to 100 Hz, i.e. when the time off changes from 500 to 5 ms. This could be explained by a higher electron temperature in the bulk enabling the discharge to be sustained at lower field values as reported for radio frequency discharge [4]. Above 100 Hz, the breakdown voltage can exceed that obtained at 1 Hz by almost 20%. As it will be discussed in the last paragraph of this section, this behavior is related to the effective power density that decreases at higher modulation frequency. Let us note that the transition voltage from the Ω mode to the RF-α mode displays a similar behavior to that of the breakdown voltage.
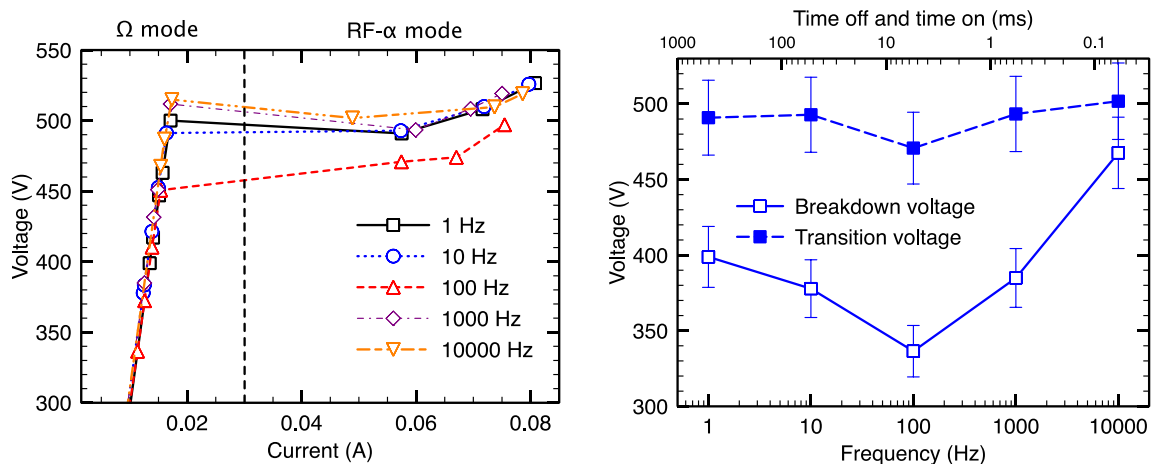
Fig. 3: Left) I_{RMS}-V_{RMS} curves for each frequency tested. The values are calculated from high resolution sampling recorded during the plateau in figure 2 (when the current and voltage are stable). Right) Breakdown and transition voltage for every modulation frequency. The time off between two pulses is also displayed on the plot for reference.

In order to estimate the gas temperature, the rotational temperature of $N_2(C^3\Pi_u \rightarrow B^3\Pi_g)$ transition with band head at 337.8 nm was used and compared with the temperature of the dielectrics. As reported previously [2], the rotational temperature increases very steeply with the power in the Ω mode and more slowly in the RF-α mode. The behavior is the same when the waveform is modulated. In order to compare different modulation frequencies, the temperature at both breakdown and transition are considered. Whatever the modulation frequency, the breakdown and the transition occur at very similar power: 0.49 W with a standard deviation of 0.03 W at breakdown and 11.0 W with a standard deviation of 1.1 W at transition.
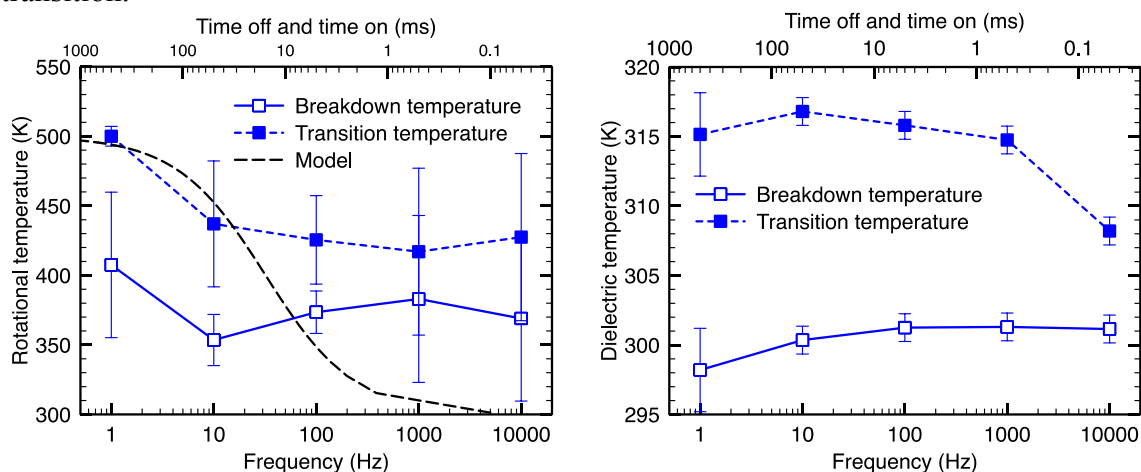
Fig. 4: Left) Rotational temperature of $N_2(C^3\Pi_u \rightarrow B^3\Pi_g)$ as a function of the modulation frequency for the breakdown and the transition. Right) Dielectric temperature as a function of the modulation frequency for the breakdown and the transition.

Figure 4 shows the rotational and dielectric temperatures at breakdown and transition as a function of the modulation frequency. In contrast with the gas temperature dependence on the duty-cycle [5], the measured temperatures are not decreasing when the off time delay increases. Actually, the rotational temperatures at both breakdown and transition tend to decrease between 1 and 10 Hz and then to remain constant. This can be explained by the time required for the gas to renew within the discharge zone, namely 120 ms. Indeed, when the discharge is on for less than 120 ms, the gas is heated during a fraction of the time that it

spends between the electrodes area. For instance, at 10 Hz, the discharge is on during 50 ms (i.e., 50 ms time off). Therefore, during the 120 ms that the gas spends in the discharge zone, the gas is only heated during 60 ms in average. On the other hand, at 1 Hz, the discharge is on during 500 ms and the gas is thus heated over 120 ms. As the rotational temperature can only be recorded when the discharge is on (camera exposure=1s), the recorded temperature is higher at 1Hz. Assuming that the power P is converted into gas heating according to $\Delta T = Pt/C_p \nu V$ and that the gas (during its residence time) is cooled by transferring its heat to the solid dielectric via Newton's law of cooling: $P_{cool}=hA\Delta T$, the variation of temperature can be estimated from $P_{cool} - P$, which yields

$$\Delta T = \frac{Pt}{C_p \nu V - hAt}$$

where t is the exposure, $A=0.001$ m^2 is the solid dielectric area over which heat transfer occurs, h is the heat transfer coefficient (estimated to 50 W/m^{2}K), V is the gas volume, $\nu=0.15$ kg/m^2 is the volumetric He mass density and $C_p=5200$ J/kgK is the heat capacity at constant pressure. The temperature calculated from the model is shown in figure 4 (P=10 W). Clearly, the temperature decreases as the modulation frequency increases to finally reach a stable value. Figure 4 also shows that the temperature of the dielectric at the transition tends to decrease when the modulation frequency is larger than 100 Hz. This is caused by the reignition time (the time it takes to light emission to reach its maximum or its plateau) that becomes significant above 100 Hz. For instance, figure 2 indicates that the reignition time can be up to 100 μs. Thus, when the modulation frequency is 10 kHz, the discharge is on during 50 μs. Therefore, the reignition time can no longer be neglected. Actually, the effective power should be considerably lower at this low effective duty-cycle (not taken into account in the measurement of the power), thus reducing heating. Another effect of this longer effective off time is the breakdown voltage discussed in figure 3. Since the reignition time is high for low applied voltage, it is natural that at very low voltage (about breakdown) the reignition would take longer than the time on (i.e., effective on time of 0 s), hence, higher breakdown voltage.

4   Conclusion

The effect of the repetition rate was studied in a time-modulated DBD generated at medium frequency (1.6 MHz). A modulation of about 100 Hz looks optimal as it enables to decrease the breakdown voltage and the gas temperature. More specifically, at 100 Hz, the rotational temperature is about 50 K lower than at 1 Hz. Moreover, the breakdown voltage is 15% lower than at 1 Hz. The reason for the higher rotational temperature below 10 Hz is, the discharge is on during a time too long for the gas renewal rate in the discharge zone to effectively reduce the temperature. On the other hand, above 1 kHz, the effective duty-cycle is significantly reduced by the reignition time, which decreases the effective power. Finally, the breakdown voltage reduction at 100 Hz might be related to a higher electron temperature. This assumption is presently under investigation using a collisional-radiative model to calculate the electron temperature from experimental spectra [6].

References

1. J.-S. Boisvert et al., in *Proceedings of the 22nd International Symposium on Plasma Chemistry*, Antwerp, 2015, edited by A. Bogaerts and R. van de Sanden, O-5-2

2. J.-S. Boisvert et al., J. Phys. D Appl. Phys. (submitted)

3. R. Bazinette et al., Plasma Sources Sci. Technol., 23, 035008 (2014)

4. X. Li et al., Plasma Sources Sci. Technol., 14, 1069 (2012)

5. J. J. Shi et al., Appl. Phys. Lett., 93, 041502 (2008)

6. R. K. Gangwar et al., Plasma Sources Sci. Technol., 25, 015011 (2016)

INFLUENCE OF THE CONCENTRATION OF H₂ ON THE STRUCTURE OF A NANOSECOND DISCHARGE IN DIFFERENT H₂/AIR MIXTURES AT ATMOSPHERIC PRESSURE FOR PLASMA ASSISTED COMBUSTION APPLICATIONS

S. Kobayashi[1], Z. Bonaventura[2], F. Tholin[3], N. Popov[4], A. Bourdon[1]

[1]LPP, UMR 7648, Ecole Polytechnique, route de Saclay, 91128 Palaiseau Cedex, France

[2]Department of Physical Electronics, Faculty of Science, Masaryk University, Brno, Czech Republic

[3]ONERA, DMPH Department, 29 avenue de la Division Leclerc, 92322 Châtillon cedex, France

[4]Skobel'tsyn Institute of Nuclear Physics, Moscow State University, Leninskie gory, Moscow 119991, Russia

E-mail: sumire.kobayashi@lpp.polytechnique.fr

This paper presents 2D simulations of nanosecond pulsed discharges in different H₂/air mixtures at atmospheric pressure. A fluid model is coupled with a detailed kinetic scheme to simulate the discharge dynamics between two point electrodes. For H₂/air mixtures with equivalence ratios between 0.3 and 2, it has been observed that major positive ions produced by the nanosecond discharge are N_2^+, O_2^+ and HN_2^+. The discharge dynamics is shown to vary only slightly with the equivalence ratio of the H₂/air mixture, which is of interest for plasma assisted combustion applications.

Keywords: plasma-assisted combustion; 2D simulations; nanosecond discharge; hydrogen-air mixture; detailed chemical kinetics

1 Introduction

Since a few years, nanosecond pulsed discharges have been extensively studied at atmospheric pressure as they efficiently produce many reactive chemical species at a low energy cost. This is of great interest for several applications and in particular for plasma assisted combustion. First studies on the influence of nanosecond discharges on combustion were focused on identifying the key kinetic mechanisms and gas heating processes. Different models have been developed in 0D [1-4] to compare results with experimental studies at low pressure in which the discharge is rather homogeneous. In these studies, the key role of dissociative reactions $N_2^* + O_2 \rightarrow N_2 + 2O$, involving different electronically excited states of N₂ has been put forward, both for the O atom production and also for the fast gas heating by nanosecond discharges. Recently, several numerical 1D and 2D simulations have been carried out to understand the influence of nanosecond pulsed discharges on the flame structure. As an example, Bak et al. [5] have simulated in 2D the plasma-assisted stabilization of a laminar premixed methane/air flame at atmospheric pressure. In [5], the plasma and combustion kinetics are solved simultaneously with as input a given Gaussian-shaped electric field. As at atmospheric and higher pressures, nanosecond discharges have usually filamentary structures, it is important to simulate self consistently the discharge phase. As far as we know there are

only few studies with the self-consistent 2D simulation of the nanosecond discharge at atmospheric or higher pressures for plasma assisted applications [6,7]. Takana et al. [6] have simulated in 2D a nanosecond pulsed DBD in lean methane-air mixture at 10 atm to be close to typical conditions in internal engines. Tholin et al. [7] have simulated in 2D a nanosecond discharge between two point electrodes for the ignition of a lean (equivalence ratio ϕ=0.3) premixed H_2-air mixture at atmospheric pressure. In [7] a self-consistent 2D fluid model for the nanosecond discharge was coupled to a 2D reactive Euler code to simulate all the spatial and temporal time scales of the nanosecond discharge and combustion ignition. As a first step in [7], it was assumed that H_2 has no influence on the discharge structure for a lean H_2/air mixture with an equivalence ratio of ϕ=0.3 and the discharge was simulated in air. Recent experiments [8] show that the fuel has an influence on the discharge structure. Therefore, in this work we propose to simulate the nanosecond discharge in H_2/air mixtures with different equivalence ratios (ϕ=0.3,1 and 2) at atmospheric pressure. The objective is to study the influence of the change of the mixture composition on the discharge structure and dynamics.

2   Model formulation

We use a classical 2D fluid model for a nanosecond discharge between two point electrodes separated by 2.5 mm [9]. A pulse voltage is applied with a rise time of 2 ns and then a voltage plateau of 5 kV. In a first step we assume no gas heating by the discharge. We focus on the study of the discharge dynamics until a conducting channel is formed between the two point electrodes. We have implemented a detailed kinetic scheme for H_2/air mixtures mostly given in [2] with 8 positive ions (N_2^+, H_2^+, O_2^+, N_4^+, HN_2^+, H_3^+, HO_2^+, HO_3^+), O^- and electrons. Electron transport parameters and electron impact rate coefficients for the different mixtures studied have been pre-calculated as a function of the reduced electric field using Bolsig+ [10].

3   Results and Discussion

Figure 1 shows the distribution of the absolute value of the electric field and the electron density at t=4.2 and 4.5 ns in a stoichiometric (ϕ=1) H_2/air mixture. As already observed in air [9], the discharge between two point electrodes consists of a positive ionization-wave and a negative ionization-wave propagating in the opposite direction. Both fronts impact each other at a connection time of t=4.5 ns. After the connection, the positive ionization-wave propagates very rapidly toward the cathode in the volume preionized by the negative discharge to form a conductive channel, bridging the interelectrode gap as in air [9].
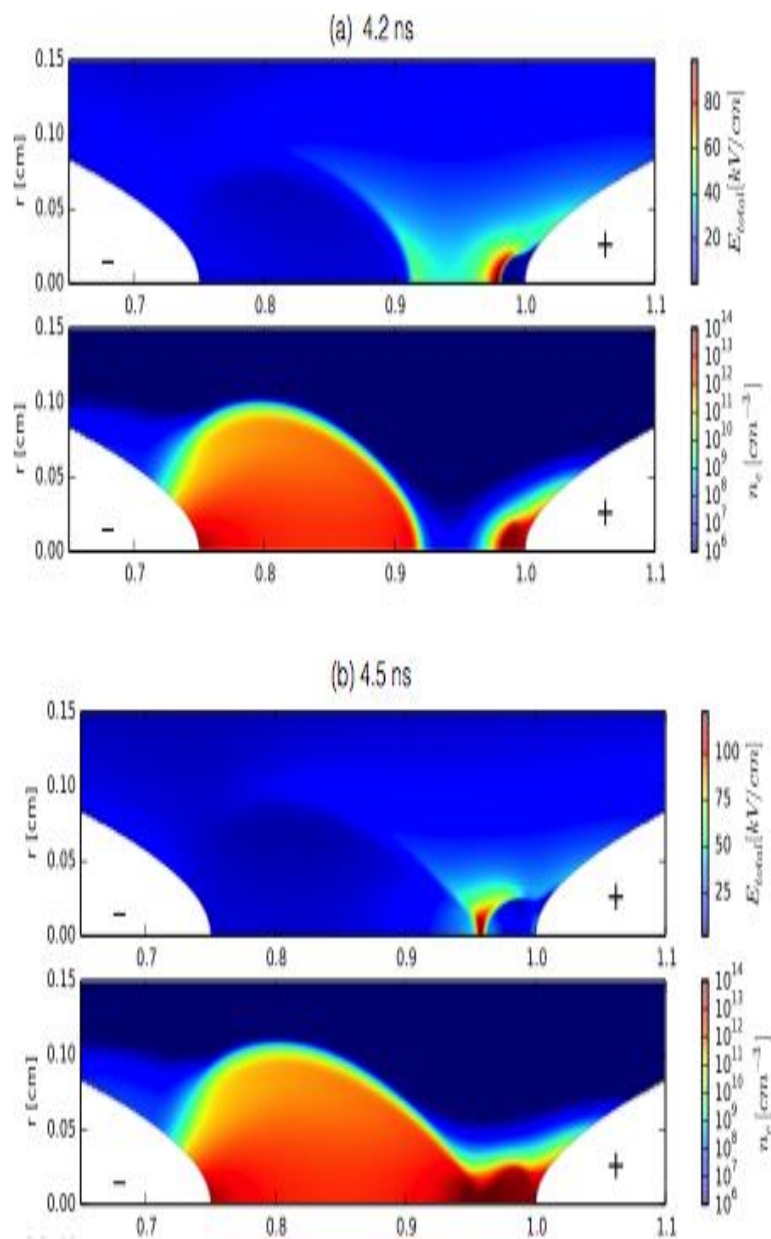
Fig. 1: Cross-sectional views of the magnitude of the electric field and electron density for the nanosecond discharge in a stoichiometric (ϕ=1) H_2/air mixture at t=4.2 and 4.5 ns.
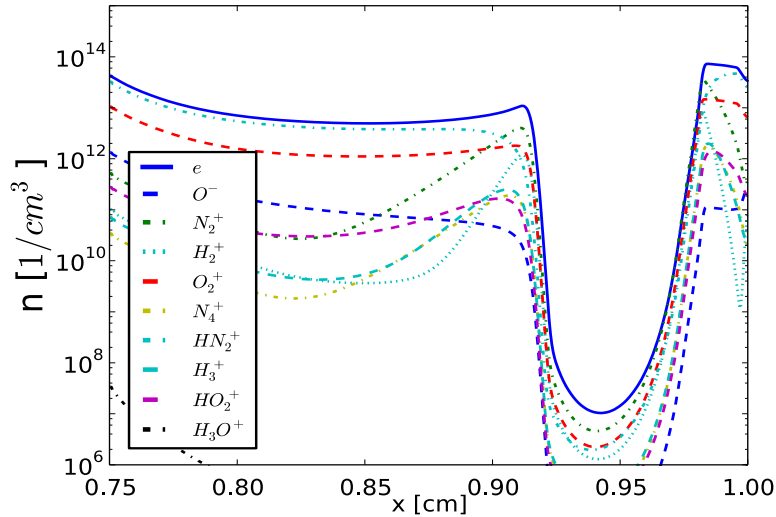
Fig. 2: Axial distribution of charged species densities at t=4.2 ns a stoichiometric (ϕ=1) H$_2$/air mixture.

Figure 2 shows the axial distribution of all the charged species at t=4.2ns. We note that in both discharge fronts where the electric field is the highest, N_2^+ is the major positive ion whereas in the discharge channels, the main positive ions are HN_2^+ and O_2^+. Figure 3 shows the 2D distribution of several ions at the connection time t=4.5ns. We clearly observe a non uniform distribution of the different ions in the interelectrode gap.
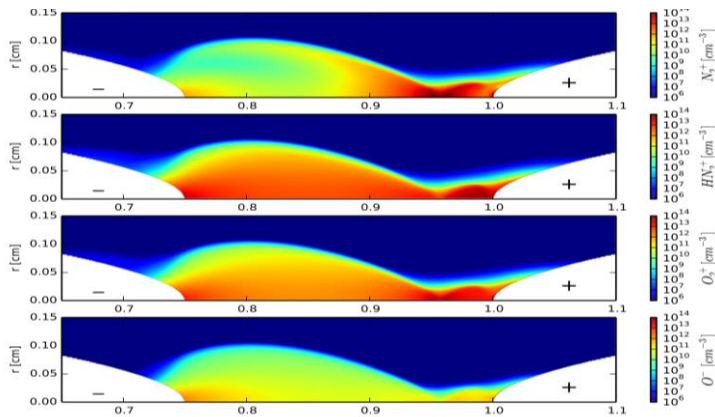
Fig. 3: 2D distributions of charged species densities at t=4.5 ns a stoichiometric (ϕ=1) H$_2$/air mixture.

It should be noted that extremely fast reaction of negative ions destruction $O^- + H_2 \rightarrow H_2O + e$ has no appreciable effect on the electron density, since the concentration of O^- ions is relatively small, see Figs. 2,3. Finally, we have compared the discharge characteristics for different equivalence ratios (ϕ=0.3,1 and 2). Table 1 shows the ignition times of both discharges and their connection time. We observe that the ignition time of the positive discharge and consequently the connection time increase, but only slightly, as the equivalence ratio ϕ increases from 0.3 to 2. These first results show that, the differences in the gas mixture composition and the changes in the electron transport parameters and electron impact rate coefficients for mixtures with equivalence ratios ϕ varying between 0.3 to 2, have only a very small influence on the discharge dynamics and structure. In a future work, we will study the gas heating by the nanosecond discharge and the production of radicals.

	Ignition time of the negative discharge	Ignition time of the positive discharge	Connection time of both discharges
ϕ=0.3	2.2ns	3.4ns	4.4 ns
ϕ=1	2.2ns	3.6ns	4.5 ns
ϕ=2	2.2ns	3.8ns	4.6 ns

Table 1: Ignition and connection times for different H_2/air mixtures with equivalence ratios of ϕ=0.3,1 and 2.

4   Conclusion

In this work, we have simulated 2D nanosecond pulsed discharges in different H_2/air mixtures at atmospheric pressure. A detailed kinetic scheme has been coupled to a 2D fluid model. Electron transport parameters and electron impact rate coefficients are calculated for different mixture compositions. We have shown that the dynamics of the discharge varies only slightly for H_2/air mixtures with equivalence ratios ϕ between 0.3 and 1.

References

1. S. Williams et al., in *42nd AIAA Aerospace Sciences Meeting and Exhibit*, Reno, NV, AIAA-2004-1012 (2004)
2. N. A. Popov, Plasma Physics Reports, 34, 376-391 (2008)
3. N. L. Aleksandrov et al., Proc. Combust. Inst. 32, 205-212 (2009)
4. I. N. Kosarev et al., Plasma Sources Sci. Technol. 22, 045018 (2013)
5. M. S. Bak et al., Combust. Flame 159, 3128-3137 (2012)
6. H. Takana et al., Plasma Sources Sci. Technol. 23, 034001 (2014)
7. F. Tholin et al., Combust. Flame 161, 1235-1246 (2014)
8. P. Tardiveau et al., Int. Journal of Plasma Environmental Science & Technology, 6,130 (2011)
9. F. Tholin et al., Plasma Sources Sci. Technol., 22, 045014 (2013)
10. G. Hagelaar et al., Plasma Sources Sci. Technol., 14, 722-33 (2005)

PRE-TOWNSEND PHASE OF COPLANAR BARRIER DISCHARGE

T. Morávek, Z. Navrátil, J. Čech, J. Ráheľ

1Masaryk University, Department of Experimental Physics, Kotlářská 2, 611 37 Brno, Czech Republic

E-mail: tomas.moravek@mail.muni.cz

Coplanar barrier discharge was used to study previously reported pre-Townsend phase luminescence on alumina with high permittivity coating in helium diffuse operation mode. The aim of this study was to obtain the spectrum of this discharge phase. Pre-Townsend phase was observed also in argon, proving that this phenomenon is presented also in the filamentary mode of discharge operation.

Keywords: DBD; helium; argon; pre-Townsend phase

1   Introduction

Electrical charge deposited by the microdischarge evolving on the dielectric barrier is the fundamental cause behind the non-thermal character of dielectric barrier discharges (DBD). Rapid build-up of counter electrical field created by deposited surface charge results in extremely short life-time of microdischarge, and therefore an insignificant heat transfer to the neutral gas. After the polarity change of DBD electrodes, deposited surface charge lowers the magnitude of external inception voltage. Furthermore, its presence is claimed to be responsible for the time jitter of consequent micro-breakdown and its magnitude [1]. It is clear, that any deeper understanding of the processes associated with deposited surface charge would provide an important insight into DBD microdischarge formation dynamics.

When we compare the time duration of single microdischarge (MD) event with the time lag between two consecutive MDs, we find out that deposited surface charge remains unaffected by active discharge environment for more than 90% of its time. During that time, deposited charge is free to migrate along the dielectric surface, or interact with ambient gas, which leads to its gradual relaxation. The presence of surface charge relaxation in He and He/N2 volume DBD was confirmed by direct assessment of surface electric field via electro-optic Pockels effect [2, 3]. However actual mechanism has not been addressed there, most likely due to lack of associated optical emission signal. In our recent article of [4] we were able to show, that in a diffuse mode of He coplanar DBD a specific type of luminescence wave with extremely weak optical emission can be observed. The luminescence wave preceded the formation of Townsend electron avalanching at the anode edge. A distinct feature of coplanar DBD comparing to the volume DBD, is that well defined domains of opposite polarity surface charges are simultaneously presented on the same dielectrics. We have concluded that the observed pre-Townsend phase luminescence is a manifestation of so called "backward discharge", which renders a partial surface charge recombination immediately before the change of electrode polarity.

In the presented work two still open questions related to our observation of backward discharge will be addressed: (1) spectral characterization of observed phenomenon; (2) the presence of detectable pre-Townsend phase in the coplanar DBD filamentary mode of operation.
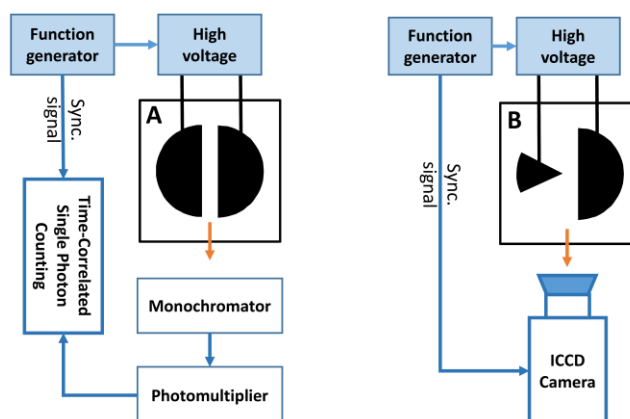
Fig. 1: Experimental set-up for: (A) spectroscopic measurement in diffuse mode configuration; (B) high-speed camera measurement in filamentary mode configuration.

2   Experimental

Coplanar electrode discharge consisted of pair of brass electrodes with adjustable rectangular electrode gap, which were immersed into insulation oil and covered by alumina dielectric plate (96% Al_2O_3; thickness 0.6 mm), coated with a high permittivity dielectric coating (ESL 4113-H; ε_r = 120–140). Two sets of metal electrodes were used: (A) single strip configuration with inter-electrode gap of 4.7 mm; (B) point-plain configuration with inter-electrode gap of 2.5 mm (Fig.1). The light coming out of the helium discharge was first spectrally resolved by monochromator SK1 (resolution 20 nm) and then analyzed by single photon counter (Becker-Hickl SPC-150) equipped with photomultiplier working in photon counting mode (PMC-100-4). The spectrum was measured with the step 20 nm to cover the spectral range 300-760 nm. A time-resolution of 200 ns was achieved by synchronization of the photon counter with the voltage signal. Phase-resolved images of argon discharge were captured using PI-MAX3 ICCD camera. External clock signal from function generator was used to synchronize the ICCD with the voltage signal.

3   Results and Discussion

Fig. 2A shows spectrally resolved measurement of helium discharge on alumina dielectric covered with high permittivity coating (HPC), which offered best contrast for observing extremely weak optical emission associated with pre-Townsend luminescence wave. In order to obtain the spectrum of the luminescence wave, the signal was integrated over time interval 60-69 µs, i.e., within the pre-Townsend phase for all measured wavelengths (Fig. 2B). The current state of spectral resolution does not allow us to resolve the presence of any particular spectral line. The highest intensity emission is observed in the area around 700 nm. This is present for the whole period of discharge which makes He line at 706.5 nm to be an unlikely explanation. Therefore, we propose that solid state fluorescence of alumina ceramics exhibiting sharp emission at 693 nm [5,6] is observed.

Experiments in argon filamentary mode confirmed the presence of pre-Townsend phase as well. Figure 3 shows that the associated emission starts approximately at -14 µs in the middle

of the inter-electrode gap and heads towards the wedged electrode (left side) inside the created discharge channel, where 0 µs represents the position of current maxima of the microdischarge event.
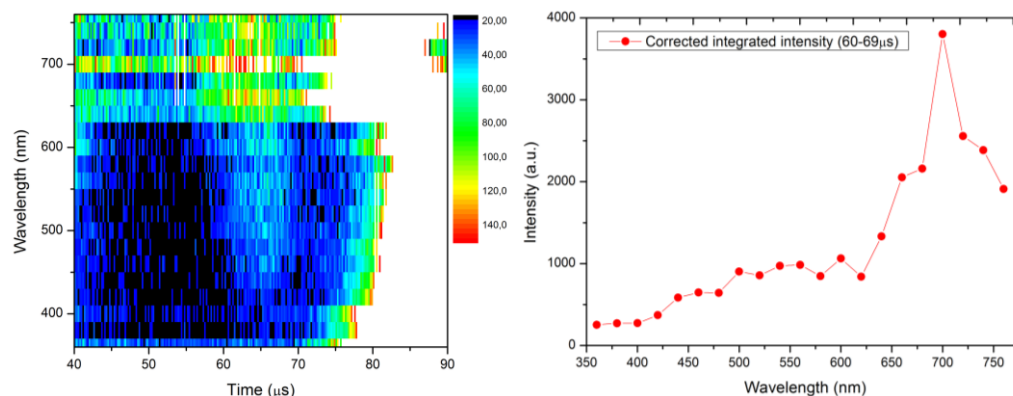
Fig.2: (A) Spectrally resolved evolution of helium discharge (B) Spectrum of pre-Townsend phase (set-up B).
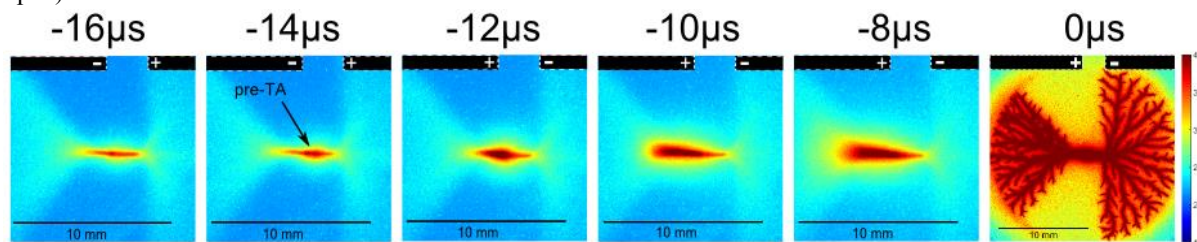
Fig. 3: ICCD plane view filmstrip of pre-Townsend phase for argon discharge (set-up B). Integration time 1µs per frame, 2300 accumulations. Last picture is a single shot of a fully developed discharge (please note the change in dimension scale).

4   Conclusion

Spectrally resolved measurement of helium discharge indicates that fluorescence of alumina ceramics contributes to the overall emission of the discharge even during its dark phase. At the moment, insufficient resolution does not allow us to detect any spectral lines in the pre-Townsend phase, therefore the spectrum appears continuous. Using a point-plain configuration of electrodes filamentary mode in argon was stabilized and the pre-Townsend phase was recorded.

References

1. Yu. Akishev et al., Plasma Sources Sci. Technol. 20, 024005 (2011)
2. R. Wild et al., J. Phys. D: Appl. Phys. 47 (43), 435204 (2014)
3. R. Tschiersch et al., J. Phys. D: Appl. Phys. 47 (36), 365204 (2014)
4. T. Morávek et al., Eur. Phys. J. Appl. Phys. xx: xx DOI: 10.1051/epjap/2016150538 (2016)
5. I. I. Milman et al., Radiat. Meas. 38, 443-446 (2004)
6. G. Molnár et al., Phys. Status Solidi A 179 (1), 249-260 (2000)

ELECTRICAL AND OPTICAL DIAGNOSTICS OF NANOSECOND REPETITIVELY PULSED MICRODISCHARGES IN AIR AT ATMOSPHRERIC PRESSURE

T. Orriere, N. Benard, E. Moreau, D. Pai

Institut PPRIME (CNRS UPR 3346, Université de Poitiers, ISAE-ENSMA).
SP2MI – Teleport2 Bd Marie & Pierre Curie BP 30179, 86962 Futuroscope, France

E-mail: thomas.orriere@univ-poitiers.fr, david.pai@univ-poitiers.fr

The aim of this work is to combine nanosecond repetitively pulsed discharges with microplasmas in a pin-to-pin configuration in air at atmospheric pressure. Discharge characteristics are studied by employing optical emission spectroscopy and electrical measurements. As the gap distance is decreased from the millimeter scale to 200 μm, differences in discharge properties include the emergence of atomic ion emission lines and much lower rotational temperature of N2(C).

Keywords: microplasmas; sparks; ultrafast heating; optical emission spectroscopy

1   Introduction

Non-thermal plasmas are useful for many applications such as biomedicine, aerodynamic flow control, nanomaterial synthesis, biological decontamination or surface treatment. In some of these areas, it is advantageous or necessary to operate in air at atmospheric pressure and at room temperature. Several methods have been developed to control the main characteristics of the plasma, two of which consist of confining the discharge in different ways. The first is temporal confinement with nanosecond repetitively pulsed (NRP) discharges, where a pulsed electric field optimizes dissociation or ionization rates, and thus the production of interesting plasma species [1]. Repeating these electric pulses at high repetition frequency (PRF) allows for the accumulation of these species. In air at atmospheric pressure, several regimes can be generated, and the spark regime has been shown to be the most reactive [2]. On the other hand, the heating rate is much higher for the NRP spark than for the other regimes, which can be a problem for heat sensitive materials and applications. The second method is to contain the discharge to the micrometer scale [3]. Confining the discharge in microplasma geometries, i.e. less than 1 mm in at least one dimension, could enable more control over the temperature because microplasmas can channel more energy towards plasma chemistry and less to heating, via a high electric field and enhanced surface processes. The high surface-to-volume ratio also increases heat transfer, enabling more control over the temperature.

Combining the NRP and microplasma regimes can increase the chemical activity and optimize the temperature for applications, as has been demonstrated in noble gases [4]. Our objective is to study NRP microplasmas in air at atmospheric pressure because of the relevance to applications. The mains characteristics are described with optical emission spectroscopy and voltage-current measurements.

2   Experimental setup

In this study, NRP spark discharges were generated in air at room conditions between two tungsten electrodes spaced by with a gap distance of 200 µm or 2 mm with a 100 µm radius of curvature, as shown in figure 1. Pulses 11-15 ns in duration and up to 14.5 kV in amplitude were produced by a pulse generator (FID Technology FPG 40-30 NK), and impedance matching was achieved using 200 Ω and 100 Ω resistances. The voltage V_{probe} was measured using a passive voltage probe (Lecroy PPE6kV, bandwidth 600 MHz). The current I_{probe} was recorded using a current transformer (Bergoz CT-D5.0, bandwidth 400 MHz). All signals were recorded with oscilloscope (Lecroy Wavesurfer 24 Xs-A, 200 MHz bandwidth). The measurements were synchronized with the plasma using a common trigger source (Stanford Research Systems DG645 or ARMEXEL PDG-2520).

Fig. 1: Schematic diagram of the experimental setup for plasma generation, voltage-current measurements, and optical emission spectroscopy.

Optical emission spectroscopy (OES) was performed with a spectrometer (Princeton Instruments SpectraPro 2500i) equipped with an ICCD camera (Princeton Instruments PI-MAX 4). The optical path was formed by two off-axis parabolic mirrors with focal lengths of 20 and 5 cm. The light converged onto a 600 µm diameter optical fiber bundle (Ocean Optics QP-600-2-SR-BX). Emission from the (0, 2) and (1, 3) bands of the N_2 (C → B) transition was studied with the 2400 gr.mm^{-1} grating, and the system was calibrated in relative intensity with a quartz tungsten halogen lamp (Oriel Instruments No.63355).

3   Results and Discussion

Fig. 2: (a) Short circuit experiment to determine the stray inductance, with the measured (black) and modeled (red) voltage across L_{stray} = 0.2 µH.   (b) Measured voltage (solid black) and current waveforms (solid red) of an NRP microplasma in air at atmospheric pressure, with d = 200 µm and PRF = 8 kHz. Also shown are the voltage across the discharge V_{plasma} (dotted black) and plasma current I_{plasma} (dotted red).

The procedure for electrical characterization begins with the definition of passive components in the circuit. The stray inductance formed by the lead wires and electrodes L_{stray} is measured with a short circuit experiment by contacting the needles. In this case, V_{probe} is considered as induced voltage across L_{stray}. Figure 2a shows the matching between V_{probe} and L.di/dt with L_{stray} = 0.2 μH. The voltage across the gap V_{plasma} is calculated with equation 1. The parasitic capacitance C = 2.4 pF formed by the electrodes is used to calculate I_{plasma} using V_{plasma}.

$$V_{plasma} = V_{probe} - L_{stray}\frac{dI_{probe}}{dt} \; ; \; I_{plasma} = I_{probe} - C\frac{dV_{plasma}}{dt} \tag{1}$$

Figure 2b shows typical waveforms for NRP microplasmas in air at atmospheric pressure. The plasma current reaches a maximum value of 36 A, and the discharge energy per pulse is 113±12 μJ. These values are in the range of NRP sparks in millimeter gaps [5], but in this case d = 200 μm. The reduced electric field E/N, calculated using the gas number density N for P = 1 atm and T = 450 K measured by OES at the beginning of the pulse (see figure 4), reaches a maximum value of 802 Td., which is much higher than that reported for millimeter-scale NRP sparks [5].
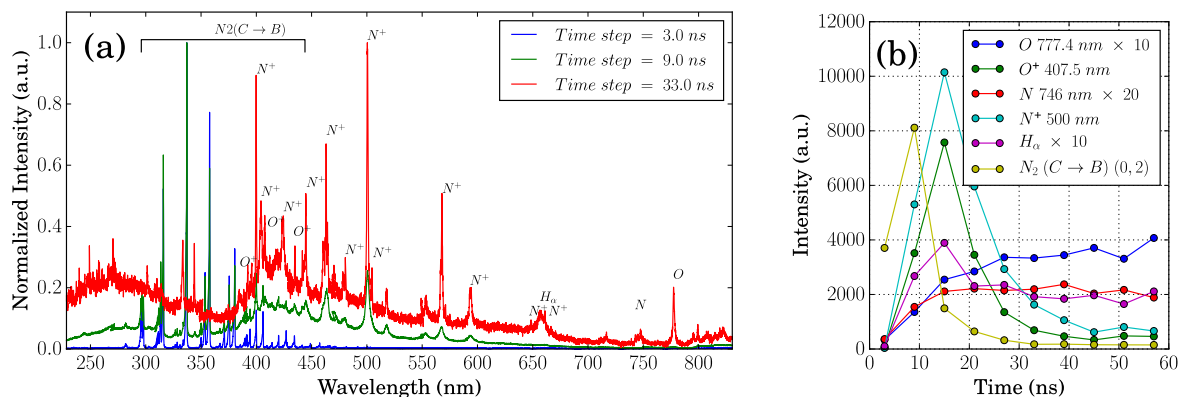
Fig. 3: (a) Measured optical emission spectra of an NRP microplasma in air at atmospheric pressure (PRF = 5 kHz, V_{probe} = 2.7 kV) for three time steps after the discharge, acquired using gate width = 6 ns and 200 accumulations on CCD. (b) Maximum emission intensity of plasma species as a function of time.

Figure 3 shows several time steps of the optical emission spectrum of the discharge at PRF = 5 kHz and V_{probe} = 2.7 kV. The activity in the spectrum can be described in three phases. First, the N_2 second positive and N_2^+ first negative systems begin emitting during pulse at t = 3 ns, similarly to previous studies of NRP discharges [5]. Second, there is the emergence of atomic ion lines O^+ and N^+ towards the end of the pulse at t = 9 ns. Finally, N, O and H_α lines appear well after the pulse at t = 21 ns. At the same time, there is also a continuum spectral component whose intensity varies together with that of the atomic ions. The principal difference in comparison to other studies with larger gaps is the absence of emission from the N_2 (B→A) transition and the appearance of neutral atomic species after the ions [5]. The presence of atomic ion species has already been reported for millimeter-scale NRP sparks generated in Propane-Air mixtures [6] and pure N_2 [7]. Like in these studies, our measurement is not spatially resolved and light near the electrodes can be collected. On the other hand, no atomic ions were observed in spatially resolved spectra from the middle of the discharge of a 4-mm gap NRP spark in atmospheric-pressure air [5].

Figure 4a presents the evolution of the rotational temperature of $N_2(C)$, determined by fitting experimental spectra to spectra modeled using Specair. Figure 4b presents two examples of spectral fits. To generate the discharge stably at high PRF without damaging the electrodes, the following pulse burst scheme was used for temperature measurements: bursts of 5 pulses at PRF = 30 kHz are repeated with a burst frequency of 300 Hz. For the 200 μm case, the temperature could be measured only at the first temporal step because the presence of the other species and continua overlapped the spectrum of N_2 at latter times. Figure 4a shows similar temperatures between the 200 μm and 2 mm cases for t = 9 ns and 12 ns of the first pulse of the burst. However, as the burst progresses, the 2 mm case evolves towards a high-temperature steady state with an initial temperature of about 2000 K, whereas that of the 200 μm case remains at only 550 K.
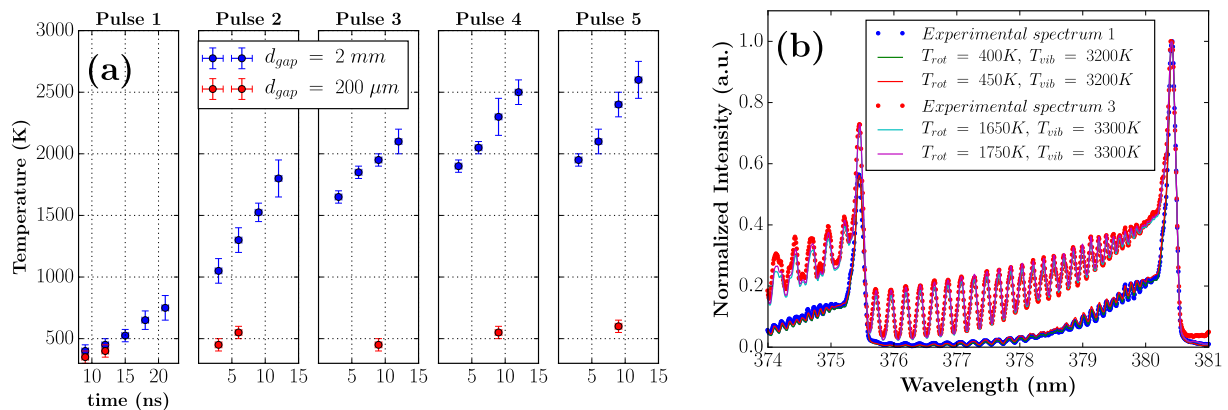
Fig. 4: Measured rotational temperature, deduced from the $N_2(C{\rightarrow}B)$ (0,2) and (1,3) bands: (a) evolution of the temperature in 2 mm and 0.2 mm configurations performed on 5 successive pulses and PRF = 30 kHz in burst mode. (b) Spectral fits for the first and the third pulse of the 2 mm discharge gap (526 ns).

4   Conclusion

We have characterized several similarities and differences of NRP microplasmas in air at atmospheric pressure with NRP sparks in millimeter-scale gaps. The reduce electric field is higher than in other studies with millimeter gaps [5]. OES of emission integrated over the entire discharge reveals the emission of O^+ and N^+ lines, possibly indicating chemical kinetics different from millimeter-scale NRP sparks. Moreover, rotational temperature measurements demonstrate a much lower initial temperature at the beginning of the pulse for d = 200 μm, which may imply significant differences in the inter-pulse heat transfer and chemical kinetics. However, due to the lack of spatial resolution so far, the roles of surface and microplasma effects on the temperature and plasma chemistry cannot yet be isolated.

References
1. D. Packan, Ph.D. thesis, Stanford University, (2003)
2. D. Z. Pai et al., Plasma Sources Sci. Technol. 19, 065015 (2010)
3. K. H. Becker et al., J. Phys. D: Appl. Phys. 39, R55 (2006)
4. X.-M. Zhu et al., J. Phys. D: Appl. Phys. 45, 295201 (2012)
5. D. L. Rusterholtz et al., J. Phys. D: Appl. Phys. 46, 464010 (2013)
6. S. V. Pancheshnyi et al., IEEE Trans. Plasma Sci. 34, 2478 (2006)
7. R. M. van der Horst et al., et al., J. Phys. D: Appl. Phys. 45, 345201 (2012)

PARALLEL OPERATION OF PULSED PINHOLE DISCHARGES FOR HYDROGEN PEROXIDE GENERATION

K. Yasuoka, R. Saeki, K. Ikeda

Tokyo Institute of Technology,2-12-1-S3-3 Ookayama, Meguro-ku Tokyo, Japan

E-mail: yasuoka@ee.titech.ac.jp

Multiple pulsed pinhole discharges have been developed to generate hydrogen peroxide for an ozone‑hydrogen peroxide advanced oxidation process. A ceramic plate with 10 very small holes was used as a diaphragm to separate the conductive water into two parts. Ten pinhole discharges were generated simultaneously in a solution with a conductivity of 30 mS/cm by applying bipolar rectangular voltages. A generation rate of 2.7 g/h and an energy yield of 2.3 g/kWh were obtained at 2 kV and 20 kHz. Within 40 min of operation with an ozone gas feed, 1 L of 400 mg_{TOC}/L acetic acid solution was mineralized by up to 82%.

Keywords: pulsed pinhole discharge; parallel operation; hydrogen peroxide; advanced oxidation

1 Introduction

Advanced oxidation processes (AOP) utilizing hydroxyl radicals are a promising method for mineralizing persistent organic compounds in wastewater. In particular, ozone–hydrogen peroxide (H_2O_2) AOPs are suitable for processing a large amount of wastewater with high total organic carbon (TOC) [1]. However, these systems require a continuous supply of H_2O_2, which necessitates the in-situ generation of H_2O_2. A plasma-based ozone–H_2O_2 system [2] has been proposed, in which H_2O_2 is generated by a pinhole discharge [3,4] driven by repetitive bipolar rectangular voltages. This report describes the formation of a pinhole discharge and parallel operation of pinhole discharges and presents the energy yield of H_2O_2 production, and acetic acid mineralization.

2 Experimental

Figure 1 presents a schematic of the experimental setup of an AOP system, which consists of an inverter circuit and a reactor in which the H_2O_2 and externally supplied ozone react to produce hydroxyl radicals. The reactor is divided into two parts by a 1-mm-thick ceramic plate with 10 pinholes (0.3 mm diameter). Sodium sulfate solution (1 L, 3 wt%) was poured into the reactor to measure the H_2O_2 concentration. An acetic acid solution mixed with phosphate buffer solution to a total volume of 1L was used as the water sample for AOP. The water sample was characterized by an organic content of 420 mg_{TOC}/L, conductivity of 30 mS/cm, and pH of 7.6. In the AOP experiments, ozone gas (180 g/m^3) was fed into both parts of the reactor at a flow rate of 1 L/min. The output voltage and frequency of the inverter were varied in the ranges of 2–4 kV and 10–20 kHz, respectively. A 19 or 39-nF series capacitor was inserted between the inverter circuit and the reactor to control the pulse width of the pinhole-discharge current. A bipolar voltage was applied to the center screws on both sides of the reactor. A cooling system was introduced to prevent the water from boiling.
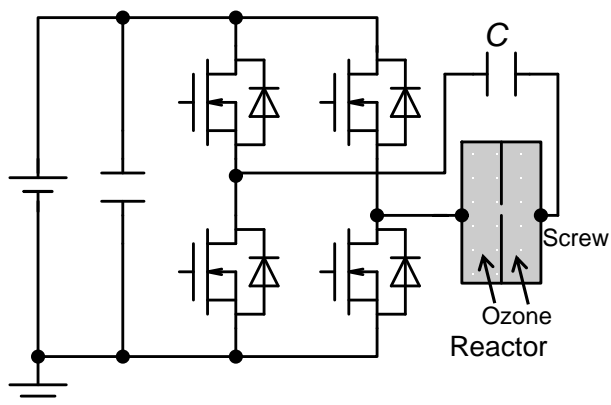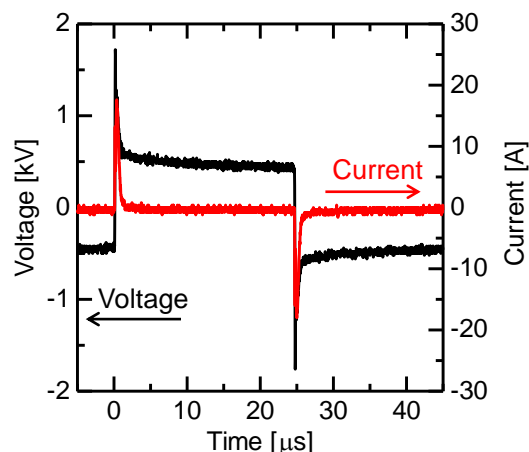
Fig. 1. Schematic of the experimental setup.   **Fig. 2.** Reactor voltage and current waveforms.

3   Results and Discussion

Figure 2 shows the voltage and current waveforms of the reactor over one cycle of 20-kHz bipolar voltages using the 19-nF series capacitor. Although the output voltage at the inverter was 1 kVp-p, the peak voltage at the reactor was approximately 1.7 kV due to the addition of the capacitor voltage. The initial peak of the current corresponds to the displacement current. The current duration was 3 μs with the 19-nF capacitor and 10 μs with the 39-nF capacitor.

The formation of the pinhole discharge and its emission spectra were observed using a single-hole reactor with the same configuration as the reactor shown in Fig. 1. At the beginning of the voltage application, pinhole discharge was not generated, as shown in Fig. 3(a). After 10 voltage cycles, a small bubble was generated due to the Joule heating of water in the hole. The bubbles expanded at 900 μs, as shown in Fig. 3(b), and then gradually shrank after 1000 μs. Finally, a pinhole discharge was generated in a small bubble at 1150 μs, as shown in Fig. 3(c). The generation ratio of the pinhole discharge for each voltage pulse was 80–90%. The average rotational temperature calculated from the OH radical spectrum was 4400 K. The rotational temperature varied from 4800 K in the initial discharge stage to 3500 K in the final stage. Based on this result, some of the water vapor inside the bubbles seems to dissociate into H, O, and OH before the discharge is initiated.

(a)   (b)   (c)
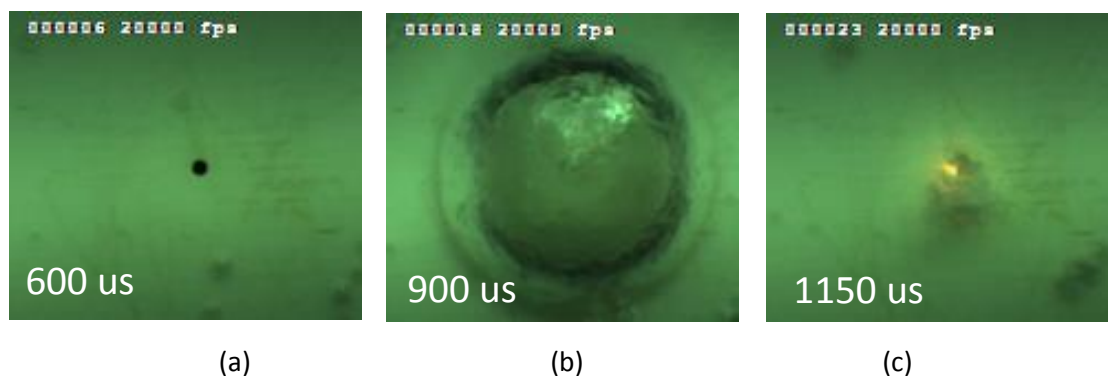
Fig. 3. Images of the pinhole without a bubble (a), with an expanding bubble (b), and with a pinhole discharge(c).

71

Figure 4(a) shows a photograph of the 10 parallel pinhole discharges in sodium sulfate solution with a conductivity of 30 mS/cm. The power input to the reactor was 557 W at 20 kHz. Hydrogen-α, hydrogen-β, and oxygen lines and a strong sodium line were observed. The small bubbles traveling upwards at the center of the photograph are the externally fed ozone bubbles. The other, larger bubbles were generated by the pinhole discharges.

(a)   (b)
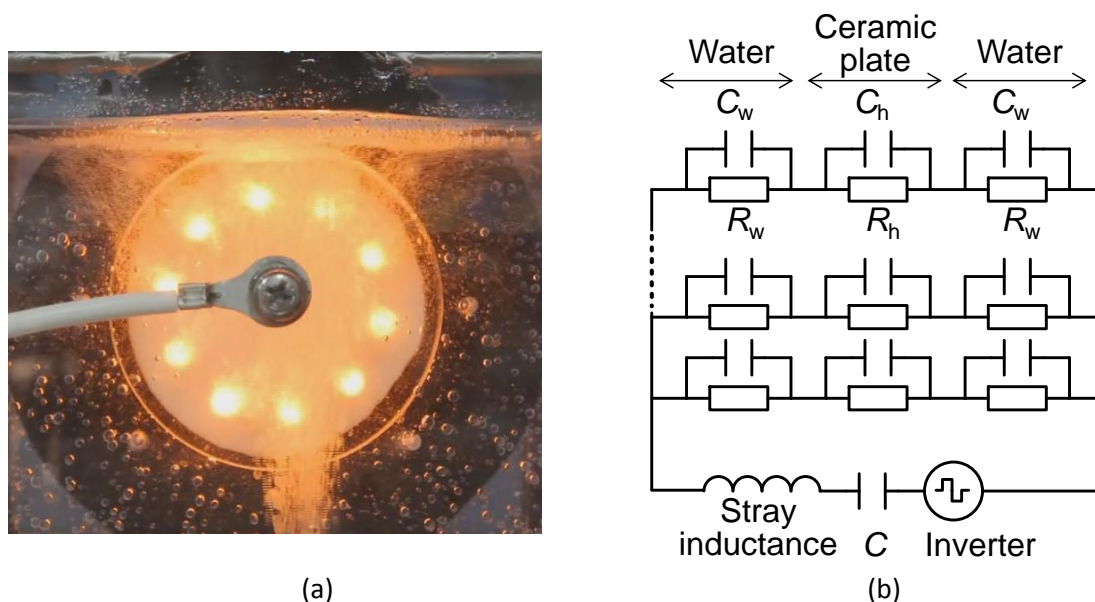
Fig. 4. Photo of the parallel operation of 10 pinhole discharges in Na_2So_4 solution (a) and equivalent circuit (b).

The equivalent circuit of the pinhole discharges is shown in Fig. 4(b). In this diagram, C_w, R_w and C_h denote the solution capacitance, solution resistance, and capacitance of the ceramic plate. R_h is the pinhole resistance, which varies with the plasma formation. The values of the circuit elements are ordered as follows: $C_h > C_w$, $R_h >> R_w$. The value of R_h without plasma was ~6 kΩ and the plasma resistance R_p was calculated as approximately 5 kΩ. When R_p is approximately equal to or greater than R_h, the current flows through a pinhole without a plasma formation, and another bubble is formed in the pinhole. In this way, the parallel operation of pinhole discharges is obtained.

The concentration of H_2O_2 in the sodium sulfate solution was measured for 1 min under various repetition frequencies and series capacitances. Figure 5 shows that the H_2O_2 concentration increased linearly with time in all cases. The pinhole discharge was generated upon the reversal of the applied voltage. The peak voltage, peak current, and current pulse duration were 2 kV, 13 A, and 10 μs, respectively, at 39 nF and 20 kHz. A H_2O_2 concentration of 45 mg/L, generation rate of 2.7 g/h, and energy yield of 2.3 g/kWh were obtained at an average discharge power of 1.2 kW. Leys et al. reported a generation rate of 0.31 g/h and an energy yield of 4.1 g/kWh in a solution with100 μS/cm with 50-Hz AC voltage [5]. Because our value is 100 times higher than that reported by Leys et al., more efficient generation is expected with decreasing current density.
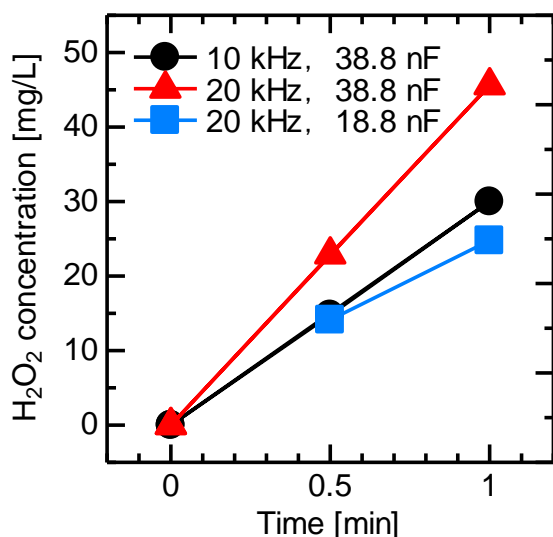
Fig. 5. H$_2$O$_2$ concentration versus operating time.
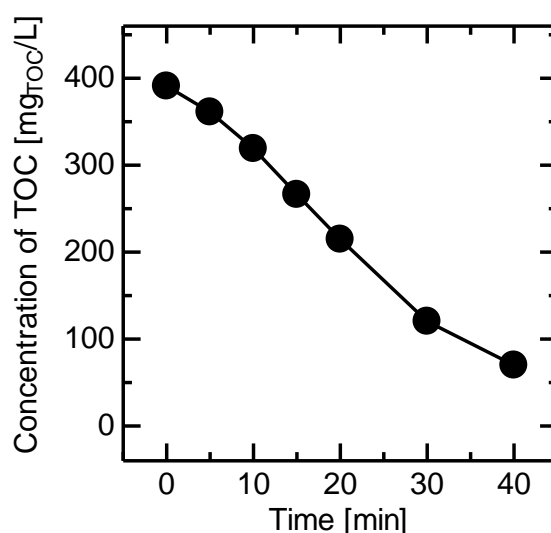
Fig. 6. TOC concentration in acetic acid solution versus operating time.

Mineralization of the acetic acid was conducted by feeding ozone gas into the reactor, which was operated at 1 kV and 10 kHz. Figure 6 shows the acetic acid concentration as a function of time. The phosphate buffer solution kept the solution pH at approximately 7. Within 40 min of operation, 1 L of acetic acid solution with an initial organic content of 400 mg$_{TOC}$/L was mineralized by up to 82%. The decomposition rate and energy efficiency were 0.48 g$_{TOC}$/h and 0.41 g$_{TOC}$/kWh, respectively.

4   Conclusion

Parallel operation of pinhole discharges was introduced to increase the hydrogen peroxide production rate for the ozone–hydrogen peroxide process in conductive solutions. A hydrogen peroxide concentration of 45 mg/L, generation rate of 2.7 g/h, and energy yield of 2.3 g/kWh were obtained at an average discharge power of 1.2 kW. By feeding the ozone gas into the reactor, 1 L of acetic acid solution containing 400 mg$_{TOC}$/L with a conductivity of 30 mS/cm was mineralized by up to 82% after 40 min of operation.

References
1. W. H. Glaze et al., J. Int. Ozone, 9, 335-352 (1987)
2. R. Saeki et al., J. Inst. Electrostat. Jpn., 40, 26-31 (2016) (in Japanese)
3. P. Lukes et al., Plasma Chem. Plasma Process. 33, 83-95 (2013)
4. E. Vyhnankova et al., Open Chem. 13, 218-223 (2015)
5. A. Y. Nikiforov et al., Plasma Sources Sci. Technol. 16, 273-280 (2007)

STUDY OF DYNAMIC BEHAVIOR OF PATHS OF DISCHARGE ON SERPENTINE PLASMA WITH VARIOUS GASES

S. Aoqui[1], R. Takanami[2], F. Mitsugi[2], H. Kawaski[3]

[1] Dep. of Computer & Information Sciences, Sojo Univ., Ikeda 4-22-1, Kumamoto, 860-0082, Japan
[2] Faculty of Eng. Kumamoto Univ., Kurokami 2-39-1, Kumamoto, 860-8555, Japan
[3] Dep. of Electrical & Electronics Eng., Sasebo National College of Tech., Okishin-machi 1-1, Sasebo, 857-117, Japan

E-mail: aoqui@cis.sojo-u.ac.jp

We renamed the plasma by gliding arc discharge serpentine plasma. In this study in order to investigate dependency by gas kind, we measured the dynamic behavior of plasma using a high-speed camera, high-speed current and voltage probe. It was confirmed that the behavior of plasma differed greatly between molecules and atoms.

Keywords: gliding arc discharge; atmospheric pressure plasma; plasma diagnostics; high-speed camera; serpentine plasma

1 Introduction

We have been studying about the basic and applications of atmospheric pressure discharge. Specially, there has been interest in the use of so-called gliding arc discharge (GAD) for various applications in material processing, gas conversion, water treatment, biological disinfection and agricultural applications [1-8]. As for GAD plasma, the consumption power is bigger than dielectric barrier discharge (DBD), creeping discharge and is smaller than Inductively Coupled Plasma (ICP). As for the atmospheric pressure discharge, small expense is required because it is easy to apply the scaling size law, it is convenient for large-scale large area processing. However, in the case of ICP, application is limited to a generated plasma or gas temperature, in general, to become over 5000 K. On the other hand, GAD plasma has a problem to be a nonequilibrium discharge. In other words, the discharge is not always maintained and repeats a discharge and extinction of arc. In GAD, a breakdown of atmospheric gas is generated at the shortest gap between two divergent electrodes. After the breakdown, the plasma keeps gliding along the same direction as the gas flow, which causes an increase of applied voltage, with a transition from thermal to non-thermal equilibrium until the applied voltage reaches a critical voltage that is needed for the next breakdown. The previous plasma disappears at the moment of the next breakdown. This cycle from the ignition to the gliding is repeated continuously. In recent years a lot of reports about the observation of GAD plasma were published by after the development of a high-speed camera [9,10]. There are very many papers using the argon gas. However, in industrial applications, the possibility of using the inert gas will be low, most of the investigation in inert gases is not effective when it is used with the GAD plasma. As for the atmosphere, oxygen (O_2), nitrogen (N_2), carbon dioxide (CO_2) and H_2O vapor are included as components, and gaseous properties should be totally different from inert gases. A high-speed camera was used to investigate the basic process of the GAD plasma in this study. Our fundamental study on the

simultaneous observation of the dynamic behavior of plasma path with a high-speed camera and the corresponding electrical properties for GAD revealed that the plasma path was 'serpentine' due to gas turbulence and reconnections were repeated frequently especially in high gas flow to suppress the increase of plasma power. Therefore, we distinguished this kind of non-equilibrium plasma from normal arc plasma and named it serpentine plasma.

2   Experimental

Fig. 1 shows the schematic illustration of experimental setup for the serpentine plasma system with UV assistance and equipment for observation of electrical properties and dynamic behavior. Two electrodes, which are made of iron, are 100 mm in height, knife-edge shaped and their shortest gap was 5 mm. The electrodes were set inside an acrylic chamber which has an outlet on the top for gas exhaust. Ar, N_2 and CO_2 were used to investigate the influence of gas flow rate. The gas flow rate was controlled with a digital flow instrument from 10 to 40 litter / min. We used a low-pressure mercury lamp (Hamamatsu, L937-01) as an UV source of which the photon energy for the main spectrum is about 5 eV. On the other hand, the work function of electrode materials is 3.91 eV, photoemission occurs by irradiated UV source. We do patent application about this method.
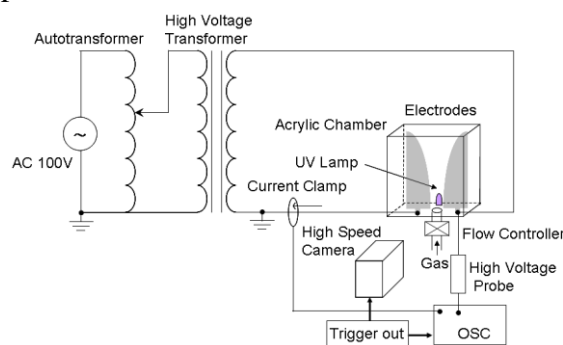
Fig. 1: Experimental setup of synchronized high-speed camera & I-V measurement system.

High voltage (sine wave, 60 Hz) was applied between two electrodes with a high-voltage transformer (VIC international, 120:1). Waveforms of applied voltage and discharge current were measured with a high-voltage probe (Tektronix, P6015A) and a current clamp (Tektronix, TCP2020), respectively. Both waveforms were captured with a digital oscilloscope (Lecroy WaveRunner 204Xi-A). Time-resolved digital photographs for plasmas were recorded by a high-speed digital camera (Nobby Tech. Ltd., Phantom V.1210) with the frame rate of 30,000 fps. The observation times for the digital oscilloscope and the high-speed camera were synchronized by an external trigger signal from a pulsed signal generator (Hamamatsu, C10149).

3   Results and Discussion

Fig. 2 shows gas flow rate dependency of current-voltage characteristics using CO_2, N_2 and Ar. The Black line is voltage and the left vertical axis shows the voltage the red line is current, and the right axis shows the current value. When flow rate increases, amplitude grows, and the vibration frequency becomes higher. However, as for the molecular gas of CO_2 and N_2, the temporal change was slower than Ar. Ionization energy is different depending on each gas. Each gas's ionization energy is as follows; CO_2: 14.0 eV, N_2: 14.53 eV,

Ar: 15.8 eV. However the breakdown voltage was measured in standard sphere gap, in the case of a knife-edge shaped electrode such as GAD, it is not applicable. Furthermore, in the system used for our experiment, that a low-pressure mercury lamp was used should be considered by assistance of discharge start.
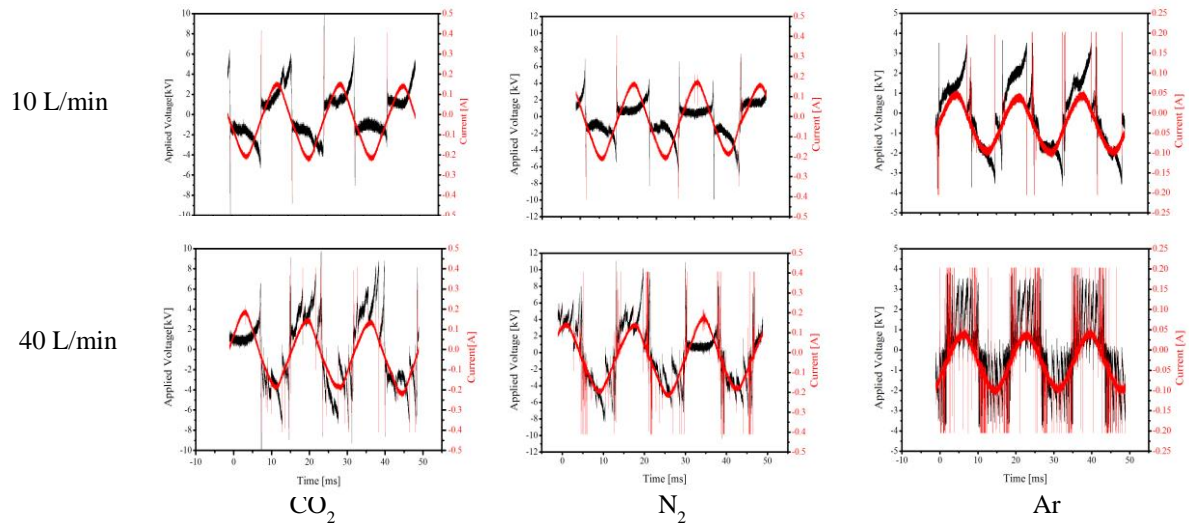
Fig. 2: Gas flow rate dependency of I-V characteristics of each gas

It would be connected with each other that an inert gas is easy to ionize in comparison with molecules and its voltage repetition frequency is high. But the relations with flow rate were unknown, and supposedly chilling effect by gas would be related.

Fig. 3 shows the synchronized measurement of the end of discharge (10.47 ms) and new breakdown (10.50 ms).
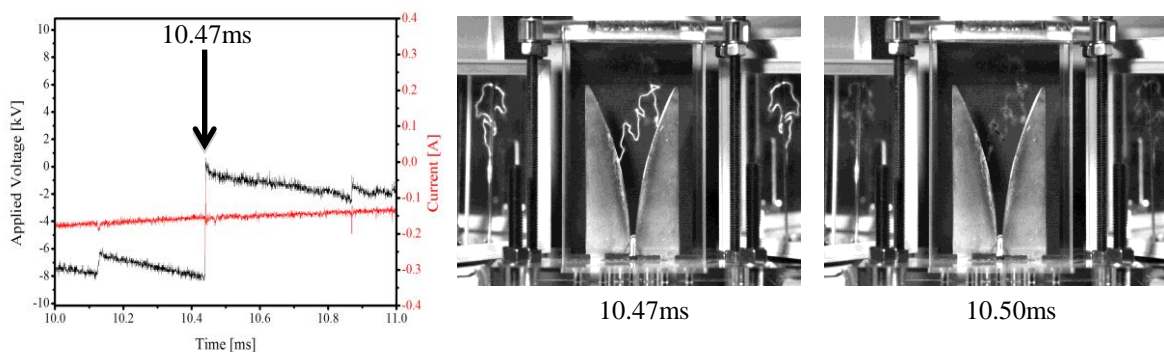
Fig. 3: Synchronized measurement of end of discharge (10.47 ms) and new breakdown (10.50 ms)

A trace of paths of 'fog-shaped' discharge was left with the image of 10.50ms, but the voltage rose and the current dropped pulsingly like the graph. Paths of discharge produce not only extinction of the arc but also re-connection. Fig. 4 shows re-connection of paths of discharge. The high-speed camera image was taken by a front, but mirrors were located on both sides, and a three-dimensional property of paths of discharge was identified. Paths of discharge did a re-connection during 10.17 ms from 10.20 ms. Fog-shaped trace was left like a case of the extinction of arc. The reason why the paths of electric discharge do a re-connection is not

clear, but we consider that discharge changed in a lower impedance state because the path was twisted for three dimensions. Fig.5 shows consumption power at 40 L/min. The product of I-V properties measured with a digital oscilloscope derived the power. Because I-V properties were not sine waves, it was not easy to demand from power accurately, but comparison between gases was possible. We should pay attention to the value of the vertical axis having a large difference. Power of CO_2 which was molecules was the biggest on the average of 50ms and becomes in order of N_2, Ar, He. It may be the condition that is close to AC arc in the case of molecules. In other words a thermionic emission condition is satisfied partially.
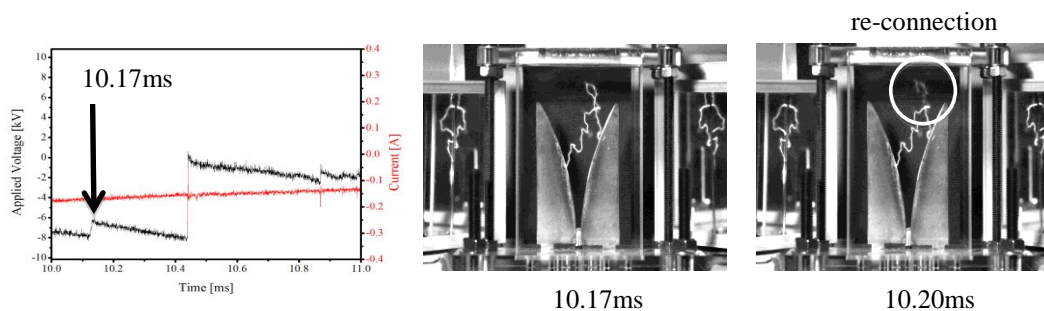
Fig. 4: High speed images of re-connection of paths of discharge (at N_2 40 L/min)
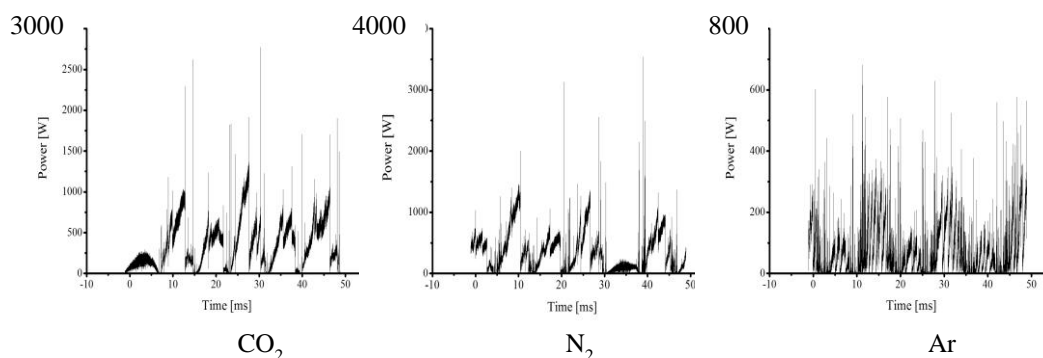
Fig. 5: Gas kind dependency of consumption power at 40 L/min.

4   Conclusion

A synchronous measurement was carried out with a high-speed camera and high-speed current and voltage probe. The dependency of gas kind was investigated in atmospheric pressure serpentine plasma. Plasma control with mixed gases for application is expected.

References

1. A. Fridman et al., Prog. Energy Combust. Sci. 25, 211-231 (1999)
2. K. Krawczyk et al., Plasma Chem. Plasma Process. 29, 27-41 (2009)
3. Z. Bo et al., J. Hazard. Mater. 166, 1210-1216 (2009)
4. L. Yu et al., J. Phys. Chem. A 114, 360-368 (2010)
5. R. Burlica et al., Ind. Eng. Chem. Res. 49 (14), 6342-6349 (2010)
6. C. M. Du et al., Plasma Chem. Plasma Process. 28 (4), 523-533 (2008)
7. M. S. Lim et al., Environ. Eng. Res. 17(2), 89-94 (2012)
8. F. Mitsugi et al., Przeglad Elektrotechniczny 88 (6), 105-107 (2012)
9. F. Mitsugi et al., The Eur. Phys. J.-Appl. Phys. 61(2), 24308 (2013)
10. F. Mitsugi et al., IEEE Trans. Plasma Sci. 42, 3681 (2014)

DYNAMICS OF ACCELERATING STREAMER IN BARRIER DISCHARGE IN AIR

T. Hoder[1,2], Z. Bonaventura[1], V. Prukner[2], M. Šimek[2]

[1]*Department of physical electronics, Masaryk University, Brno, Czech Republic*
[2]*Institute of Plasma Physics v.v.i., Department of Pulse Plasma Systems, Praha, Academy of Sciences of the Czech Republic, Czech Republic*

E-mail: hoder@physics.muni.cz

An accelerating streamer in barrier discharge is generated in 10 torr pressure air. Using the complex voltage waveform, the stable and reproducible discharge is triggered. From the ratio of two spectral bands of molecular nitrogen the electric field is determined in 2D. These results are well resolved in time and space thus suitable as a benchmark for computation of the streamer initiated plasma-chemistry in air.

Keywords: streamer; air; electric field

1   Introduction

The fundamental mechanism of the gas discharges in high-pressure air is called streamer. Streamer in atmospheric air is a contracted ionizing wave that propagates into a low- or non-ionized medium exposed to a high electric field. It is characterized by a self-generated field enhancement at the head of the growing discharge channel, leaving a trail of filamentary plasma behind. Such a wave phenomenon results from the space charge left by electron avalanches [1-3]. This mechanism takes place in discharges from 760 torr pressure in the laboratory plasmas or industrial applications to the few torr of upper atmosphere lightning phenomena [2,4,5]. The knowledge of the streamer's electric field is crucial for understanding the initial conditions leading to the induced atmospheric chemistry. More precisely, the detailed spatiotemporal evolution of the electric field of the running streamer head is of particular interest as that is the primary location of the high-energy electrons contributing to the chemical changes. In general, the experimental understanding of streamer dynamics and its initial phases are far from perfect. Streamers propagate with velocities reaching up to several percent of the speed of light making them truly a challenge for diagnostics. Joint theoretical and experimental understanding is important for air-plasma applications [2] as well as for lightning in upper atmosphere [4,5].

We investigate the triggered streamers in 10 torr pressure air. Using the simple kinetic scheme, we determine the electric field in the running streamer head in 2D. Our experimental results clarify the complete period of the streamer development − from its ignition to its approach to the cathode. The experimentally determined electric field profiles can be used as a benchmark for the streamer initiated plasma-chemistry in air [6].

2   Experimental

The reproducible stable streamers were generated in volume barrier discharge arrangement between two Macor covered electrodes of mutual distance of 4 cm. The synthetic air at 10 torr pressure filled the stainless steel chamber. The electrical characteristics obtained from the

current and applied voltage measurements using the methods published in [6-8] are shown in figure 1. Analyzing the emission of the second positive (337 nm band head wavelength) and the first negative (391 nm band head wavelength) systems the electric field distribution in time and space was determined with high resolution according to the methods presented recently in [6].
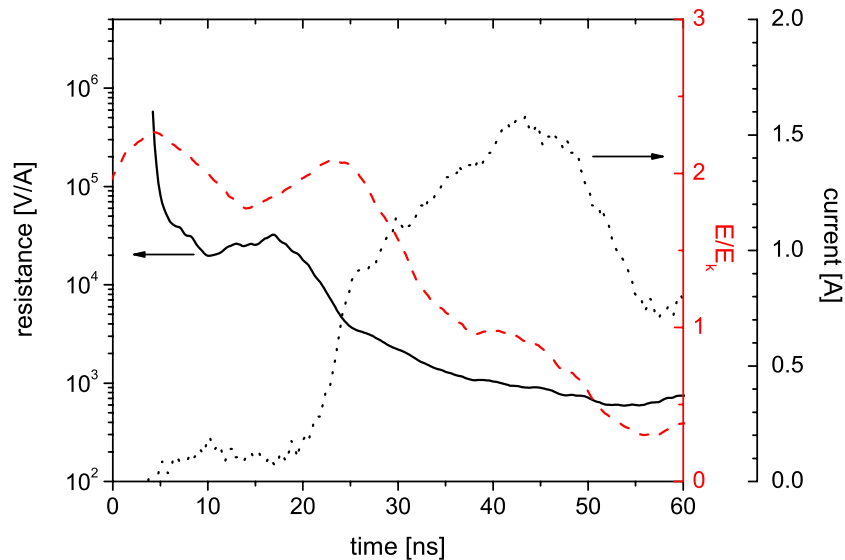
Fig. 1: Electrical characteristics of the triggered streamer discharge in 10 torr air. The electric field values (red line) are given as a factor of the critical breakdown field of 120 Td. The electric field is the spatially averaged magnitude over the whole gap computed from the instantaneous gap voltage and the gap dimension of 4 cm.

3   Results and Discussion

As it can be seen already from the analysis of the electrical measurements, the electrical resistance, current and the averaged electric field in the gap are changing rapidly during the discharge development. During the streamer propagation (i.e. between the 20th and 25th nanosecond) the current rises up to one Ampere and the resistivity of the gas falls over one order of magnitude. Consequently, the electric field in the gap decreases as the transient glow discharge is created. From the optical measurements, especially the axial scans of the temporally resolved streamer luminosity, the velocity of the streamer was determined. It reached the maximal value of approximately 8×10^6 m/s. From the radial scans of the emission of above mentioned spectral bands the radial development of the streamer electric field was determined. The maximal local value was 360 Td, i.e. a factor 3 higher than the breakdown field at given conditions.

4   Conclusion

Understanding the development of such a basic plasma parameter as the electric field one is able to determine the initiated plasma chemical changes under selected conditions. The pressure of 10 torr mimics the conditions in lower Earth atmosphere where ozone layer occurs and can be affected by lightning. Moreover, it is a suitable model-case for higher-pressure streamer discharges. As the streamer is the very first phase of many electrical breakdown phenomena, understanding the electric field values and the initiated chemistry is of the main importance to analyze the generated plasma thoroughly.

References

1. T. Hoder et al., J. Appl. Phys. 117, 073302 (2015)
2. E. Marode et al., Plasma Phys. Control. Fusion 51, 124002 (2009)
3. U. Ebert et al., Plasma Sources Sci. Technol. 15, S118-S129 (2006)
4. A. Luque et al., Nature Geophys. 757, 2 (2009)
5. J. Qin et al., Nature Commun. 5, 3740 (2014).
6. T. Hoder et al., Plasma Sources Sci. Technol. Phys. 2016 (under revision)
7. A. V. Pipa et al., Rev. Sci. Instrum 83 115112 (2012)
8. A. V. Pipa et al., Rev. Sci. Instrum 83 075111 (2012)

OPTICAL WAVE MICROPHONE MEASUREMENTS ON ATMOSPHERIC PRESSURE PLASMAS

F. Mitsugi[1], S. Kusumegi[1], T. Kawasaki[2], T. Nakamiya[3], Y. Sonoda[3]

[1]Kumamoto University, 2-39-1 Kurokami, Kumamoto 860-8555, JAPAN
[2] Nippon Bunri University, 1727 Ichigi, Oita, Oita 870-0397, JAPAN
[3]Tokai University, 9-1-1 Toroku, Kumamoto 862-8652, JAPAN

E-mail: mitsugi@cs.kumamoto-u.ac.jp

In this work, an optical wave microphone, which works based on Fraunhofer diffraction caused by phase modulation, was applied to detect pressure waves emitted from surface dielectric barrier discharges and plasma jets. Synchronized measurements of the optical wave microphone, electrical properties, plasma emission, and iodine-starch observation were carried out.

Keywords: plasma jet; optical wave microphone; pressure waves; iodine-starch method

1   Introduction

Our research focuses on the energetic distribution of electric discharges in atmospheric pressure, especially on the energy transfer from the discharge plasma to the atmosphere in the form of pressure waves including sound waves and shock waves. Because atmospheric pressure plasmas such as plasma jets are used in biomedical applications, the detection of pressure waves is important issue from practical and fundamental points of view. Therefore, the development of optical method detecting plasma-generated pressure waves is expected since conventional mechanical sensors can not be placed close to electrodes due to high electric field. An optical wave microphone, which works based on Fraunhofer diffraction of laser beam, is available to detect very slight phase modulation caused by pressure waves [1-7]. In this work, we introduce a fibered optical wave microphone that improves upon the conventional optical wave microphone with regard to signal-to-noise ratio. The fibered optical wave microphone was applied to plasma jets and surface dielectric barrier discharges synchronizing with high-speed camera observation and iodine-starch method [8].

2   Experimental

Figures 1 and 2 show schematic illustrations of the setups of the fibered optical wave microphone with synchronized systems of high-speed camera and iodine-starch method. The fibered optical wave microphone is composed of a fiber laser (637 nm, 7 mW, 1.5 mm in diameter), a lens (f=7.93 mm), a fiber (Single mode, diameter of core: 4.3 μm, 5 m), and a detector (Hamamatsu, S5935-01). Any electronic amplifier to gain signals was not used. We utilized plasma jet and surface dielectric barrier discharge devices as different types of plasma targets. The dielectric plate of the surface dielectric barrier discharge device is composed of Al_2O_3 ceramic substrate (15 mm in width, 37 mm in length, and 1.25 mm in thickness). The device of a dielectric barrier discharge plasma jet was made of a glass tube (8.0 mm in outer diameter, 2.5 mm in inner diameter) with wrapped powered and grounded electrodes (13 mm

in width) separated each other by 20 mm on the tube. The gas was supplied into the glass tube with the flow rate of 1-10 L/min. Sinusoidal high voltage was applied to the powered electrode of both devices using a function generator (NF, WF1948) with an amplifier (Trek, 10/40A). The high-speed camera used in this experiment (Photron, Phantom v1210) operates at a maximum frame rate of 100,000 frames per second. Streams of reactive oxygen radicals induced by the plasma jets were observed using a liquid iodine-starch reagent, which contains 0.3% potassium iodide and 0.5% starch in distilled water. When this liquid reagent is reacted with reactive oxygen species having oxidation potentials > 0.54 V, the color is changed from transparent to purple.
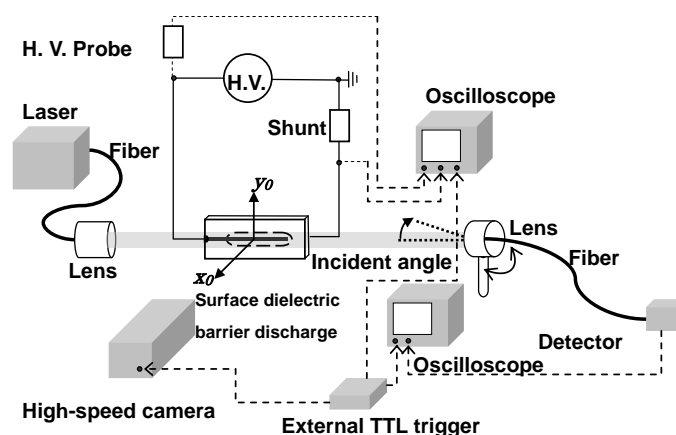
Fig. 1: A schematic illustration of the experimental setup for synchronized observation of fibered optical wave microphone and high-speed camera.
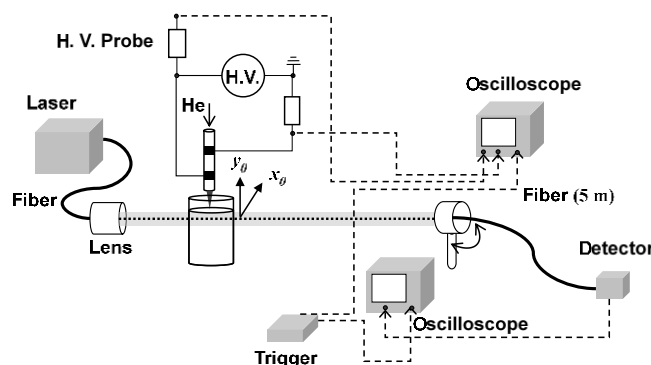
Fig. 2: A schematic illustration of the experimental setup for synchronized observation of fibered optical wave microphone and iodine-starch method.

3   Results and Discussion

The relationship between the electrical and optical properties of the surface dielectric barrier discharge can be explained by comparing the observed applied voltage waveform, current waveform, pressure waves and camera images. It was found that the incidence of a pulsed current corresponded to that of the observed pressure wave. Our experimental results show the numerous pulses in the current waveform are attributed to the generation of micro-discharges, generating micro-shock waves which are detectable using the fibered optical wave microphone.

For plasma jets, the relationship between pressure waves and streams induce inside the iodine-starch liquid was studied (Fig. 3). When the frequency of the applied voltage was set to the same frequency as the specific frequency of the glass tube, stronger pressure waves that have a single-frequency could be observed at the downstream of the device. The distribution of the pressure waves was limited within the diameter of plasma jets. When plasma jets were irradiated to the liquid reagent under same experimental conditions, plasma jet-induced narrow stream was observed in the liquid (Fig. 4). This narrow stream may be related to the pressure waves supplied into liquid phase from gas phase by the plasma irradiation. The phenomenon was not able to be observed when gas flow rates were higher than 5 L/min. although the intensity of pressure waves increased.
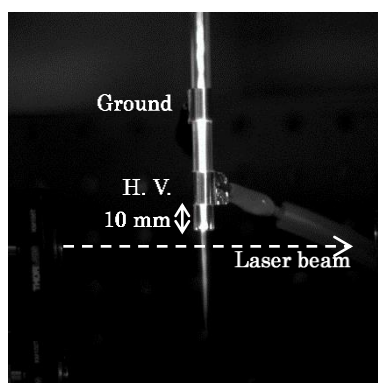
Fig. 3: A photograph of the experimental setup of the optical wave microphone and plasma jet.

Fig. 4: The plasma jet induced narrow stream after 5 s from plasma-on.

4   Conclusion

We investigated the relationship among the electrical properties, shock waves, and micro-discharge images of surface dielectric barrier discharges by simultaneously using a high-speed camera and fibered optical wave microphone. The following results were obtained.

(1) The pulses of the current reflect the generation of micro-discharges.

(2) The fibered optical wave microphone can detect the shock waves that originate from the micro-discharges.

(3) There was polarity dependence in the incidence of pulsed current. The number of current pulses in the negative half period increased compared to that in the positive half period.

(4) The number of observed pressure waves and micro-plasmas in the negative half period increased compared to that in the positive half period, reflecting the polarity dependence in the incidence of pulsed current.

For the experiments on plasma jets, the fibered optical wave microphone measurement was used in atmosphere to investigate frequency properties of the generation of pressure waves from plasma jets in advance of measurement of pressure waves in distilled water irradiated by plasma jets. Then, the detection of pressure waves inside distilled water was attempted. The following results were obtained.

(1) Optimum frequencies of the applied voltage to generated single-frequency pressure waves from plasma jets should be adjusted to specific frequencies of the glass tube that depend on gas flow rates. The optimum frequencies showed proportional increase with the gas flow rates.

(2) Pressure waves could be detectable even in the distilled water when the gas flow rate of 1 L/min. although the penetration of the pressure waves from atmosphere into the water was rather suppressed. A narrow stream of oxygen radicals was also induced at the same condition with an iodine-starch method. The phenomenon was not able to be observed when gas flow rates were higher than 5 L/min.

(3) Therefore, we suggest that the propagation of pressure waves in liquid is one of possibilities that relate with the narrow stream of oxygen radicals induced by plasma jets.

References
1. F. Mitsugi, Jpn. J. Appl. Phys. 51, 01AC10 (2012)
2. F. Mitsugi, Thin Solid Films 521, 132 (2012)
3. F. Mitsugi, Przeglad Elektrotechniczny 88, 105 (2012)
4. F .Mitsugi, Eur. Phys. J. Appl. Phys. 61, 24308 (2013)
5. T. Nakamiya, Eur. Phys. J. Appl. Phys. 61, 24310 (2013)
6. F. Mitsugi, Thin Solid Films 547, 81 (2013)
7. F. Mitsugi, IEEE Trans. Plasma Sci. 43, 2642 (2015)
8. T. Kawasaki, Jpn. J. Appl. Phys. 54, 086201 (2015)

ACOUSTIC SPECTRA CHARACTERISTICS OF HIGH PRESSURE PLASMA USING OPTICAL WAVE MICROPHONE

T. Nakamiya[1], F. Mitsugi[2], Y. Iwasaki[1], T. Ikegami[2],
Ryoichi Tsuda[1], Yoshito Sonoda[1]

[1]Graduate School of Industrial Engineering, Tokai University, 9-1-1,Toroku Higashi-ku, Kumamoto, Japan 862-8652
[2]Graduate School of Science and Technology, Kumamoto University, 2-39-1, Kurokami Chuo-ku, Kumamoto, Japan 860-0082

E-mail: nakamiya@tokai.ac.jp

We apply the new method to examine electric discharge sound using Fraunhofer diffraction effect of visible laser beam. This new system is called the optical wave microphone by us and is very useful for the detection of sound wave without disturbing the sound field. Applied voltage, current and the electrical discharge sound of Coplanar DBD (Dielectric Barrier Discharge) were measured, and examined the fundamental relationship between the discharge and the acoustic properties.

Keywords: discharge sound; high pressure plasma; Fraunhofer diffraction; optical wave microphone; laser

1 Introduction

Dielectric barrier discharge is very attractive for industrial applications because they can provide non-equilibrium plasma conditions at atmospheric pressure. Traditionally mainly used for industrial ozone production, DBD have been focused from practical applications such as surface treatment, pollution control including the removal of the environmental pollutant such as NOx, plasma actuator and the further applications are expected [1]. Future applications may include their use in greenhouse gas control technologies. The coplanar electrical discharge, where the electrode arrangements consist of two electrodes embedded inside a dielectric with a fixed electrode distance, is a kind of the DBD. The phenomenon clarification of coplanar DBD chiefly examines voltage, current, and luminescence. The example of using the electrical discharge sound is not seen as a means of the phenomenon clarification. To examine the fundamental characteristic of coplanar DBD, voltage, current signal, and the electrical discharge sound are measured, and examined the fundamental relationship between the coplanar discharge and the acoustic properties. However, it's not easy to detect the sound signal in plasma reactor by the conventional condenser microphone technique. Therefore, we have attempted to develop a new diagnostic method (optical wave microphone), in which sound wave is measured by an optical sensor based on a Fraunhofer diffraction effect [2,3] between the sound wave and laser beam. The optical wave microphone is very useful to detect not only audible sound but also ultrasonic sound wave without disturbing the sound field. In addition, the optical wave microphone has a potential to diagnostic the plasma state even during operation because this measurement system is totally insulated.

In this paper, we measured the ultrasonic wave emitted from the coplanar DBD using the optical wave microphone. The condenser microphone was also used for the comparison. The time-resolved waveforms of the applied voltage, the current and the ultrasonic wave were measured simultaneously and the relationships were analyzed.

2 Experimental

The coplanar DBD is generated in order to understand the relationship between the discharge and the acoustic properties. The electrode to generate the coplanar DBD consists of two-electrodes system embedded inside a dielectric with a fixed electrode distance. This type of discharge also has been used as an ozonizer but has recently attracted much attention because of its potential as a plasma actuator.

The top view and cross-section schematic diagrams of the electrode are shown in Fig. 1. The main part of coplanar DBD is a high-purity Al_2O_3 ceramic substrate (15 mm in width, 37 mm in length, and 1.25 mm in thickness) and is also used as the dielectric. The discharge plasma is generated on the surface.
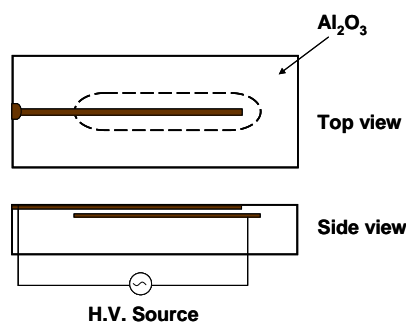
Fig. 1: Top view and cross section of electrodes module.

Figure 2 shows the experimental setup to detect the sound signal from coplanar DBD in the air. The high voltage is produced by the high frequency and high voltage power supply. The high voltage is applied to the electrode in atmospheric pressure. The sound signal (the audible sound wave and the ultrasonic wave) is generated by the discharge of the electrode. The discharge current is measured through the current transformer (frequency range = 1kHz～1MHz). The applied voltage, the voltage of current transformer of coplanar discharge and the acoustic signal is stored in the digital oscilloscope (Tektronix TDS3034).
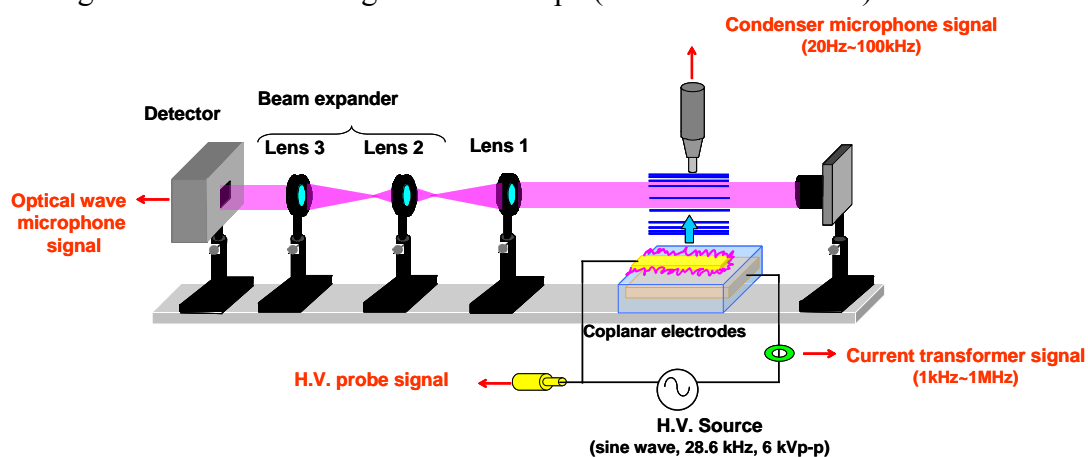
Fig. 2: Experimental setup to detect the coplanar discharge sound.

The acoustic signal is measured by the optical wave microphone and the condenser microphone (Rion, UC-29, 20-100 kHz). The condenser microphone is set up 2 cm away from the electrode and the proving laser beam (685 nm, 28 mW, φ2 mm) of optical wave microphone passed through 1cm above the discharge device. Therefore, the distance of the optical wave microphone and the condenser microphone is 1cm. The sound wave has reached to the optical wave microphone after a delay of 29.4μs from the condenser microphone when the sound speed is assumed to be 340 m/s.

The discharge sound crosses the laser beam between the laser beam and Lens1. The diffracted laser beam is performed the optical Fourier transform by the Lens1 and detected by the photodiode detector. The diameter of the laser which reaches to the photodiode detector is adjusted by the beam expander (Lens2 and Lens3).

3   Results and Discussion

Figure 3 shows time-resolved waveforms obtained from (a) the high voltage probe, (b) the current transformer, (c) the optical wave microphone and (d) the condenser microphone. The sampling frequency is 25 MHz. The sound signal of optical wave microphone after low-pass filter of 100 kHz is shown at Fig.3(c). The time delay from the sound emission to the detection
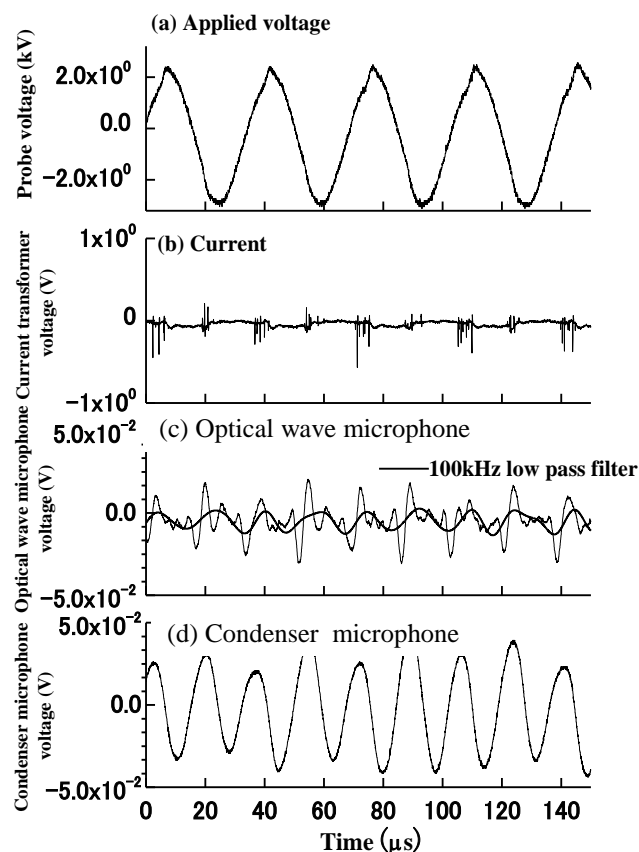
Fig. 3: Time-resolved waveforms of (a) High voltage probe, (b) Current transformer, (c) Optical wave microphone and (d) Condenser microphone. The treatment of digital low pass filtering (<100 kHz) is performed for (c).

is made correction in Fig.3(c) and (d) by considering the sound velocity and the distance between the device and the condenser microphone or the laser beam of the optical wave microphone. As can be seen in Fig.3(b), the current is composed of the pulsed discharge current and the displacement current which is caused by the capacitance of the ceramics of the device (6 pF). It is revealed from the comparison of the applied voltage and the current (Fig.3(a) and (b)) that the pulsed discharge current which has the pulse width of a few 100 ns flows for about 5 μs when the time derivative of the applied voltage exhibits almost maximum value. It can be said that the discharge occurs mainly two times in the one cycle of the applied voltage although there are the polarity dependencies which are well known in many reports. It is obvious that the discharge emits the ultrasonic wave because the result observed by the condenser microphone shows the typical waveform of compression wave (Fig.3(d)). The ultrasonic wave is generated when the pulsed discharge current flows as can be seen from Fig.3(b) and (c). The optical wave microphone could detect the ultrasonic wave from the discharge as shown in Fig.3(c). As can be seen from Fig.3(c), the waveform is rather different from that of the condenser microphone and the frequency resolution of the optical wave microphone is rather higher compared to that of the condenser microphone because the optical wave microphone is sensitive to the high frequency wave which the condenser microphone can not detect. The reason of the complex waveform of the optical wave microphone is still not understood. However, it is confirmed that the waveform after the low pass filter (< 100 kHz) treatment shows a good agreement with the waveform of the condenser microphone. In this time-resolved measurement, it was found that the ultrasonic wave was emitted from the coplanar DBD. In addition, it was revealed by employing the optical wave microphone that the ultrasonic wave was composed from high frequency components which may have relationship with the harmonics of the applied voltage and could not be observed by the condenser microphone.

4   Conclusion

We applied the new diagnostic method of the optical wave microphone to the coplanar dielectric barrier discharge. The time-resolved waveforms of the applied voltage, the current and the ultrasonic wave were stored. The obtained results are as follows.

(1) The emission of ultrasonic wave from the discharge which synchronizes with the pulsed discharge current was observed.

(2) The optical wave microphone was very useful to detect the ultrasonic wave over 100 kHz which condenser microphone could not be detected. The frequency components may have relationship with the harmonics of the applied voltage.

 (3) The waveform of the optical wave microphone after the low pass filter treatment showed a good agreement with the waveform of the condenser microphone.

References

1. J. Pons et al., J. Phys. D: Appl. Phys. 38, 3635 (2005)
2. Y. Sonoda et al., Plasma Phys. Control Fusion, 25, 1113 (1983)
3. T. Nakamiya et al., PRZEGLĄD ELEKTROTECHNICZNY, 2009, 5 (2009)

GLIDING ARC PLASMA CHANNEL EVOLUTION PECULIARITIES

L. Potočňáková[1], J. Šperka[1,2], J. Gregor[1], V. Kudrle[1]
[1]*Department of Physical Electronics, Masaryk University,*
Kotlářská 2, 61137 Brno, Czech Republic
[2]*Czech Metrology Institute, Okružní 31, 638 00 Brno, Czech Republic*

E-mail: nanai@mail.muni.cz

In this work, gliding arc was studied in both buoyancy and gas flow dominated regimes. It was shown that in latter case, the microdynamics of re-ignition can cause the movement of the plasma channel to become non continuous, even backstepping.

Keywords: gliding arc; flow dynamics; plasma channel; reignition

1   Introduction

One of the best known plasma sources is an electric arc, which is known and industrially employed for decades [1]. The arc got its name thanks to arc-like curved shape, originating in buoyancy acting on heated plasma channel. If the electrode geometry enables it, the plasma channel may start to slide upwards along these electrodes and thus forming a gliding arc [2]. When operated at high voltage and low current density, the gliding arc is closer to atmospheric pressure glow discharge than to typical arc as it is strongly nonisothermic.

The typical feature of gliding arc on divergent electrodes is the repetitive character of its lifecycle. The discharge starts at the shortest distance between the electrodes, then moves up and when it reaches maximum elongation, it extinguishes. In the very next moment, a new plasma channel is formed again at minimal electrode distance and the whole cycle is repeated.

One of the key parameters of the gliding arc is the speed of the plasma channel upward movement. It was previously shown [3] that both higher gas flow and stronger buoyant force acting on gliding arc can result in higher speed. However, closer examination reveals that the problem of plasma channel speed definition itself might be more complex.

2   Experimental

The gliding arc was generated between slanted copper electrodes with a minimum distance of 4.5 mm and an initial angle between them of 36°. These electrodes were connected to a current limiting high voltage transformer, in this experiment supplying 4 kV at 50 Hz AC. The electrode system was enclosed in nonconductive discharge chamber with argon gas inlet nozzle positioned at the bottom of the chamber, horizontally centred between the electrodes. Front and back walls of the chamber were made of heat resistant glass and allowed direct optical observation by digital camera capable of high speed (up to 1000 frames per second) video recording. More detailed description of the experiment can be found in [4].

3   Results and Discussion

In Fig. 1 (a), the evolution of gliding arc plasma channel in relatively low gas flow conditions (280 sccm) is shown. The red symbols show the instantaneous top, i.e. the vertical position of the highest point of plasma channel (horizontal position is here not considered). It can be seen, that in this case, the position is linearly dependent on time throughout the whole glide and gliding motion is continuous, until its quenching at maximum height (3.6 cm). The speed is constant at value of 0.25 m/s.
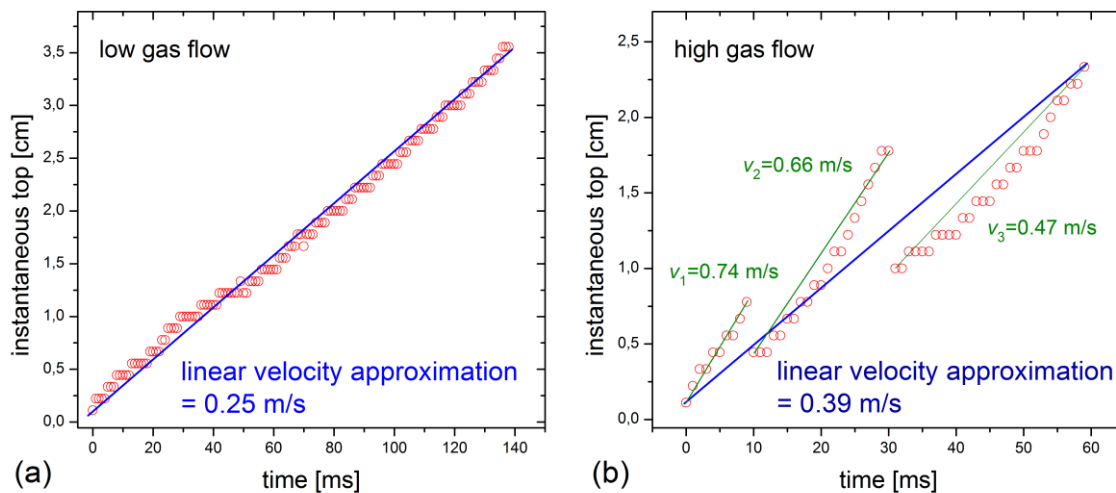
Fig. 1: Temporal evolution of the instantaneous top (i.e. highest point of the plasma channel) in two different flow rate conditions: (a) low gas flow rate = 280 sccm, (b) high gas flow rate = 1000 sccm.

The situation significantly changes by increasing the gas flow to higher rates (1000 sccm), as is seen in Fig. 1 (b). If the detailed evolution depicted by red symbols was ignored and the attention was only paid to the starting and ending points (linear blue line), the decrease in maximum height (2.3 cm) and increase in linear speed (0.39 m/s) would still be observed, just as expected [3] for an increased flow rate. However, in reality the upwards motion of plasma channel is disrupted by several drops in height and the actual speed (green colour) of the plasma channel in each segment of the evolution is higher than the linear approximation of the average speed. As the microdynamics of the plasma channel is governed by this higher, actual speed, the macroscopic approach in most of gliding arc studies, which neglects to look deeper into plasma channel evolution details, might in some cases lead to inaccurate results.

4   Conclusion

In this paper, the frame by frame image analysis of high speed camera recordings reveal more details about temporal evolution of the plasma channel of the gliding arc. Significant differences were found between low and high gas flow regime. While at low flow the channel moved upwards steadily and with constant speed, high gas flow can cause disruptions of the plasma channel followed by the reignition in lower position. This makes the distinguishing of the actual and globally perceived speed crucial for correct interpretation of glide arc qualities.

References

1. H. Edels, Proceedings of the IEEE-Part A: Power Engineering 108, 37 (1961)
2. A. Fridman et al., Progress in Energy and Combustion 25, 2 (1998)
3. L. Potočňáková et al., Plasma Sources Sci. Technol. 24, 2 (2015)
4. J. Šperka et al., Eur. Phys. J. D 67, 12 (2013)

A TREATISE ON THE DIFFUSIVENESS OF DIFFUSE COPLANAR SURFACE BARRIER DISCHARGE

J. Ráheľ, J. Čech, T. Morávek

[1]*Masaryk University, Department of Experimental Physics, Kotlářská 2, 611 37 Brno, Czech Republic*

E-mail: rahel@mail.muni.cz

Various aspects of uniform appearance of diffuse coplanar surface barrier discharge are discussed, leading to the conclusion, that generated plasma should be viewed as macroscopically, not microscopically uniform. For some particular condition however, a real diffuse operation mode can be stabilized. These conditions will be presented here.

Key words: coplanar DBD; diffuse DBD; DCSBD

1   Introduction

So called Diffuse Coplanar Surface Barrier Discharge (DCSBD) represents a particular type of coplanar DBD, characterized by mm-sized electrode geometry and operation at specific power density higher than 2 W/cm^2. From the time of its first appearance in 2002 [1], the DCSBD had proven its exceptional treatment efficiency for ample variety of solid materials: nonwovens fabrics [2], wood [3-5], powders [6], composite materials [7,8] etc. Nevertheless, the justification for using the term *diffuse* in its name is still challenged by informed critics. Their strongest argument states: current waveform of DCSBD exhibits multiple sharp peaks, which indicates the presence of streamer formation mechanism. Therefore, DCSBD differs from the APGD in helium or APTD in nitrogen, and naming it diffuse results in a terminology confusion. The standard (canonical) response to this argument is: (1) DCSBD indeed involves streamer mechanism formed discrete microfilaments, consisting of central filamentary stem and diffuse footprints propagating above the insulated power electrodes; (2) with increasing gap voltage, the diffuse part of plasma light emission strengthens compared to the filamentary plasma emission to the point when the diffuse part of generated plasma is dominant. The term diffuse does not refer to the actual microscopic uniformity of generated plasma, but to the macroscopic uniformity (i.e. optical appearance) created by merged diffuse footprints of individual microfilaments. Apparently, the controversy lies in different viewpoints on whether it is acceptable to use the term diffuse also for the macroscopically uniform DBD.

In the following contribution, we present new supporting pieces of evidence to the both sides of dispute. Using a high speed imaging technique, we are able to show real examples where DCSBD formed plasma fulfilled even the most stringent definition for being diffuse. On the other hand, several examples will be presented, where point (2) of the canonical argumentations is proven to be inaccurate. Finally, a new insight into the merit of dispute will be presented with the corresponding photographic material.

2   Experimental

High-speed ICCD camera PI-MAX3-1024i-SR-46-CM (Princeton Instruments) equipped with true-macro objective telelens (SIGMA 105/2.8 MACRO) was used to follow microscopic uniformity of DCSBD. Two distinct electrode configurations were used. Single electrode pair with inter-electrode gap of 4.7 mm (f=9.5 kHz) was used for experiments in helium and neon. Multiple strips electrode (1.5 mm wide; 1 mm gap; f=15 kHz) was used for tests in ambient air, nitrogen, argon and oxygen. In both cases 96% Al_2O_3 with the thickness of 0.635 mm was used as dielectric barrier. All experiments were performed at atmospheric pressure.

3   Results and Discussion

| (A) | (B) | (C) |
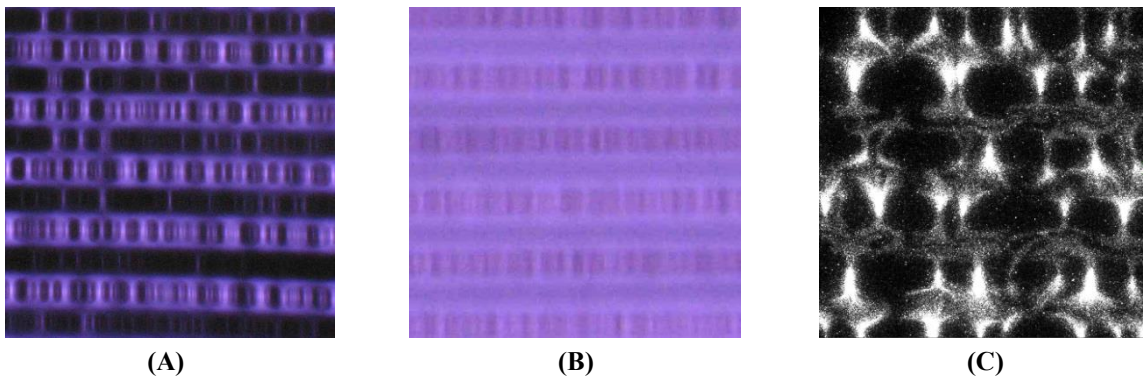
Fig. 1: DCSBD in air (14×14 mm): (A) individual microfilaments viewed by naked eye (exposure 1/8 sec); (B) diffuse appearance of fully energized DCSBD (exposure 1/8 sec); (C) high-speed camera measurement (exposure 10 μs).

Fig. 1A-B illustrates the line of canonical argumentation for air DCSBD. Upon increasing the applied voltage, diffuse parts of individual microfilaments (Fig. 1A) are fused together, forming uniform strips directly above the embedded electrodes (Fig. 1B). When we make high-speed camera snapshots of the interacting microfilaments, the spatial stratification of diffuse plasma becomes apparent (Fig. 1C). What the canonical argumentation took as a merged diffuse plasma has in fact a treeing structure above both positive and negative feed electrodes. The same observation has been made already in [9], although only for a single pair of coplanar electrodes. Observation in other gases (Fig 2) revealed, that the treeing of diffuse part is a common phenomenon, with the possible exemption of O_2 and H_2 [10], where the optical limits of our spatial resolution did not allow to resolve the presence of any kind of filamentary structure.

| (A) | (B) | (C) |
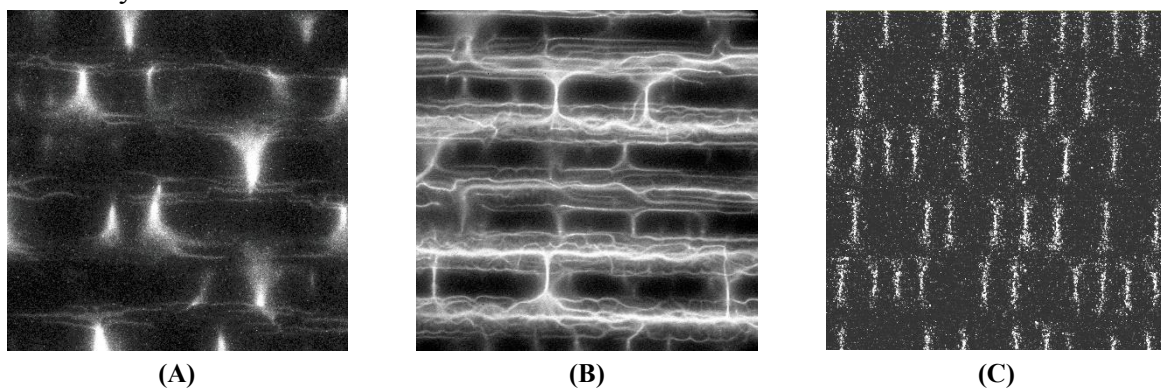
Fig. 2: High-speed camera snapshots showing treeing structures in (A) nitrogen and (B) argon. In oxygen (C) presence/absence of the treeing is uncertain.

Although the diffuse part of DCSBD is not diffuse at microscopic level, one cannot deny that to the naked eye DCSBD exhibits substantially higher degree of uniformity in comparison to volume DBD of the same power input and comparable inter-electrode gap. Further investigation by high-speed camera measurements revealed a lower tendency of coplanar DBD microfilaments to become spatially stabilized than the volume DBD does. According to our recent analysis [11], the inherent instability of coplanar microfilaments may originate from the presence of thermal body force due to the asymmetric cooling in the vicinity of dielectric barrier wall.

Our experiments performed in helium and neon showed, that the real diffuse mode, lacking thin microfilament channels and sharp current peaks, can be stabilized in these particular gases (Fig. 3). Details on their temporal development were reported in [10]. A quite peculiar feature of observed diffuse mode is the formation of striated emission region above the anode.
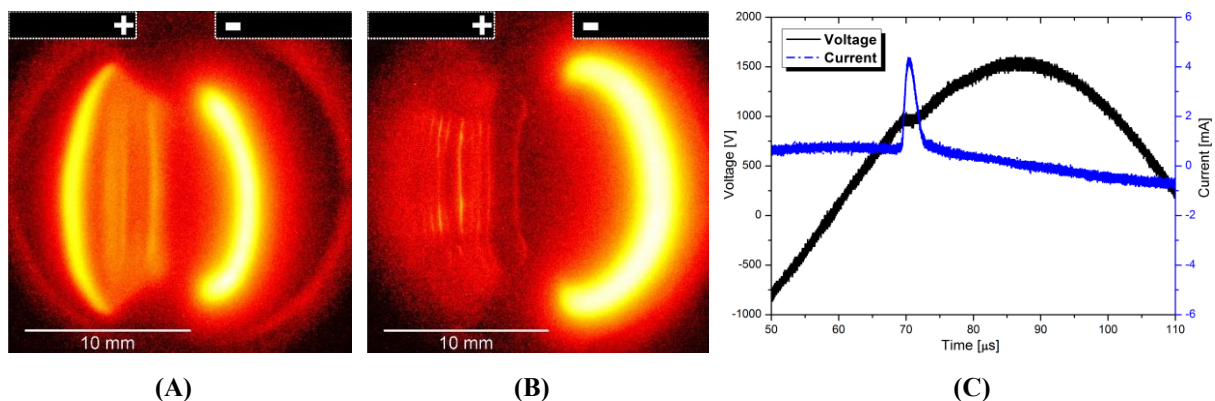
Fig. 3: Diffuse mode of coplanar DBD: (A) in helium; (B) in neon – both in artificial colors; (C) current-voltage waveform for helium.

With respect to the aforestated dispute, the necessity of introducing the new term of *real diffuse DCSBD* provides a supporting evidence of unfortunate choice of terminology in the past. There is however one aspect of DCSBD diffusiveness which we have omitted so far. In all above presented applications of DCSBD the discharge panel did not operate in the free space. Instead it was always brought into intimate contact with the surface of treated dielectric material, and the discharge was formed in an extremely narrow gap. The distortion of electric field within the gap results in the reduction of its tangential component with respect to the electrode surface, and enhancement of its normal component. In such narrow gap, the electron avalanche propagating in the normal direction may not have enough space to develop a critical size for the transition into the filamentary glow discharge.

Fig. 4 shows the manifestation of DCSBD constrained in such manner. The narrow gap of 0.1 mm was created between the Al_2O_3 discharge electrode and transparent sapphire wafer. For all tested gases (Fig. 4) we could see a continuous diffuse light emission emanating above the embedded electrodes. The effect was most pronounced in N_2, although the diffuse light emission co-exists with partial filamentary breakdown in the tangential direction. In air, partial breakdowns in tangential direction were less frequent. Nevertheless, for chosen width of the gap we could clearly see numerous tiny filamentary breakdowns in the normal

direction. In argon the treeing structures remained for the chosen gap width, but as can be seen at the central electrode, it was superposed on the emanating diffuse light. Our observations are in agreement with the electrostatic numerical model prediction, devised to explain observed strip-like structures on DCSBD treated Si wafers [12]. Results shown in Fig, 4 confirmed, that at

| (A) | (B) | (C) |
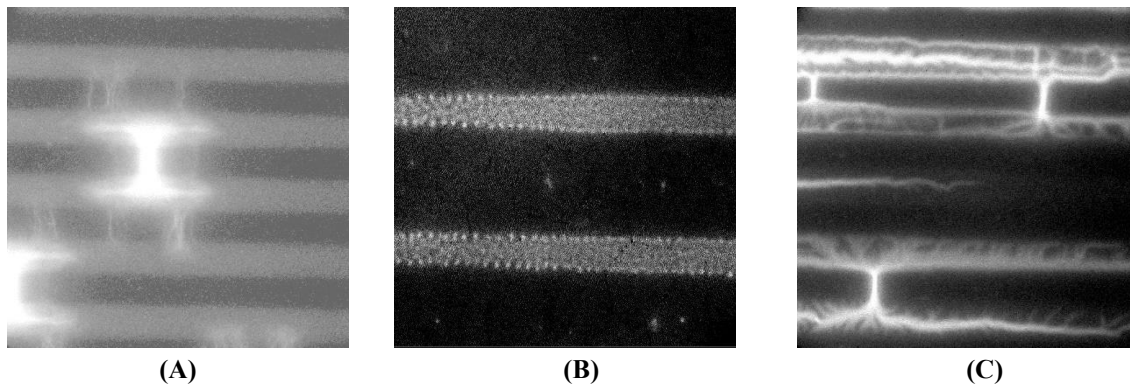
Fig. 4: High-speed camera view (exp. time 100 µs) on DCSBD formed in narrow gaps: (A) nitrogen; (B) air – magnified 2.5×; (C) argon.

optimized treatment conditions DCSBD is fully capable to form microscopically uniform diffuse plasma even for molecular gases.

4   Conclusion

The justification of using term diffuse based on the prevalence of diffuse microfilament part of free coplanar DBD is misleading. Presumably diffuse microfilament part has in fact a discrete filamentary structure. Visual uniformity of free DCSBD is chiefly due to the high spatial mobility of its microfilaments. Using helium or neon working gas, it is possible to stabilize a real diffuse regime of operation, which meets generally accepted definition of diffuse DBD regime. Nevertheless, in the case of real surface treatment the DCSBD is always constricted into the narrow gap between the plasma panel and treated surface. Our high-speed camera images gave a compelling evidence that microscopically uniform diffuse plasma can be naturally formed in such narrow gaps.

Acknowledgement

References

1. M. Šimor et al., Appl. Phys. Lett. 81 (15), 2716 (2002)
2. M. Černák et al., Plasma Phys. Controlled Fusion, 53 (12), 124031, (2011)
3. M. Odrášková et al., Plasma Chem. Plasma Process. 28 (2), 203 (2008)
4. C. Lux et al., Eur. J. Wood Prod. 71 (5), 539 (2013)
5. P. Král et al., Wood Sci. Technol. 49 (2) 319 (2014)
6. Z. Szalay et al., Ceramics International, 40 (8B), 12737 (2014)

7. P. Klímek et al., Composites Part B, 90(April), 188 (2016)

8. V. Prysiazhnyi et al., Surf. Coat. Technol. 258, p. 1082 (2014)

9. L. Hulka et al., G.J. Plasma Process. Polym. 2 (3), p. 222 (2005)

10. T. Morávek et al., in *Book of Contributed Papers HAKONE XIV*, 2014 Zinnowitz Germany, P1-01-09

11. J. Ráheľ et al., Eur. Phys. J. D, 70(92), (2016)

12. D. Skácelová et al., in *Book of Contributed Papers HAKONE XIV*, 2014 Zinnowitz Germany, P3-07-19

DIELECTRIC BARRIER DISCHARGE IN AIR ON SURFACE AND IN THE GAS GAP UNDER SINGLE NANOSECOND VOLTAGE IMPULSES

M. Sokolova[1], V. Voevodin[1], M. Malashin[2], I. Rebrov[2]

[1] National Research University "Moscow Power Engineering Institute"
Krasnokazarmennaya 14, 111250 Moscow, Russia
[2] Institute for Electrophysics and Electric Power of the Russian Academy of Sciences,
Dvortsovaya nab. 18, 191186 St.-Petersburg, Russia

E-mail: mvsokolova@mail.ru

A comparison of volume and surface DBD in air under single high voltage impulses of nanosecond duration is done. Some peculiarities of the memory effect manifestation in these conditions and effect of the voltage impulse front steepness on the discharge current amplitudes are analyzed. The influence of the surface charges was found to be identical for channel form of the SD and homogeneous form of VD.

Keywords: surface barrier discharge; volume discharge; impulse voltage; memory effect

1   Introduction

Numerous investigations of dielectric barrier discharge (DBD) were carried on in recent years as the discharge of this type is used in many plasma technologies. There are at least two basic electrode arrangements to generate DBD. First one which forms a volume barrier discharge (VD) can consist of two electrodes one of which (or both) is covered by a dielectric layer. The discharge between the electrodes develops as a volume stage in the gas gap and a subsequent surface stage on the barrier surface [1]. The second arrangement can consist of a dielectric plate with one electrode which forms the surface discharge (SD) on its one side and a second extended electrode on the reverse side. This last basic electrode configuration is used now relatively wide as a source of charge species in plasma chemical reactors. It has been shown previously in a range of works that both types of the DBD have many features that are alike in comparable conditions. One of the main features that are essential for both types of the DBD is the manifestation of a so called memory effect connected with the influence of charges on the barrier left from previous discharges on the development of the subsequent discharges [2]. The comparison of both types of discharge is done usually under a.c. or periodic impulse voltage. The aim of the present work was to compare experimentally VD and SD under single high voltage impulses of nanosecond duration and to analyze possible peculiarities of the memory effect manifestation in these conditions and to analyze possible influence on the discharge of the steepness of the voltage impulse front.

2   Experimental

All experiments were done with plane electrode arrangement in laboratory air at normal air conditions. A dielectric plate of Alumina 1 mm thick and 60x80 mm in dimensions was used as a barrier in the arrangement to form a SD. The discharge grounded electrode was either a strip of Ni 1 mm wide and 8 mm long or a small piece of foil of Al placed on one side of the barrier, while the high voltage electrode was a strip 8 mm wide with all boards covered by an epoxy layer to prevent appearance there of the surface discharge. The foil electrode had all its edges covered by an epoxy compound except for a small open section 1.5 mm long where the discharge could appear.

To form a VD two plane steel disk electrodes 30 mm in diameter were used. A dielectric barrier of Alumina 2 mm thick was placed on one of electrodes at a distance 1 mm from the other electrode. The Alumina barrier has been chosen in both cases as this material has very high surface resistance in normal air conditions.

Two different high voltage impulse generators were used. A so called cable generator used to investigate SD produced voltage impulses of 350 ns duration with 35 ns front duration and amplitudes up to 7 kV. The other generator used to form a VD could produce impulses of 600 ns duration, 75 ns rise time and amplitudes up to 20 kV. Oscillograms of voltage impulses and discharge currents at the front and at the falling part of the voltage impulses were registered by DPO 7354 oscilloscope with 3.5 GHz frequency bandwidth and LeCroy WaveRunner 104Xi-A oscilloscope with 2 GHz frequency bandwidth.

The current measuring element for SD was a low inductance shunt R = 11.5 Ohm. For VD the sensitivity of the measuring element was 0.64 A/V. It must be stressed that all oscillograms of SD in the figures are not inverted. So the polarity of the signals in the figures corresponds to the high voltage electrode and not to the corona one which is contrary to the VD case.

Special attention was paid to the neutralization of the surface charges before first high voltage application. A very soft grounded metallic brush was moved delicately over the barrier surface to neutralize the charges. The experiments have shown that neutralization of charges by means of grounded brush does not provide full charges removal. To do so the barrier surface has been washed with soaped water and dried for 1 hour under a flow of warm air.

It must be noted that the experimental conditions for SD provided a microdischarge channel form of the discharge whereas the VD was found to be of a homogeneous type.

3   Results and discussion

Different cases of the SD development were analyzed for $U_m = 4.1\text{-}4.2$ kV: a) a single voltage impulse of different polarity was applied to the discharge electrode with surface charge carefully removed from the barrier surface (fig.1 A, B); b) a sequence of voltage impulses of the same polarity were applied to the discharge electrode without a removal of the surface charge. This was done for a strip and for a small piece electrodes under voltage impulses of both polarities (fig. 3); c) a series of voltage impulses of variable polarity were applied in a succession to the discharge electrode. Several oscillograms for the last case with positive voltage impulse on the corona electrode are given in fig.1 (C, D, E). It must be noted that for every single application of a high voltage impulse two surface discharges are known to appear. It is seen in all oscillograms. So the charge left on the barrier after voltage impulse application is a resultant charge of two surface discharges.

Oscillograms show that current amplitudes of sequential SD are sensible to the very first change of polarity of the applied voltage impulse. It is especially related to the positive discharge. After about 6 or 7 discharges of positive polarity with intermittent discharges of negative polarity the positive current values for the front discharge become identical (fig. 2). So the surface charge distribution on the barrier surface becomes identical while there is a strong influence of the surface charge on the SD intensity after first change of the polarity.

For very first voltage impulse application the moment of SD appearance does not change if the amplitude of the applied voltage is the same (fig. 1) and corresponds to the rise part of the voltage impulse. With an increase of the voltage impulse amplitude from 4.1 to 5 kV it was

possible to check discharges that appeared with a much longer time delay relatively to the moment of voltage impulse application. This delay could be up to 150-200 ns. An increase of the impulse amplitude for the same front duration means an increase of the voltage impulse front steepness. It leads to an increase of the formation time of the discharge.

Typical oscillograms of VD current under positive voltage impulse given in fig. 4 show a much higher values of the discharge current than in the SD case. This difference can be connected with higher values of the applied voltage (nearly 18 kV for VD compared to 4.5 kV for SD) but the duration of the discharge in both cases is practically the same (40 ns).
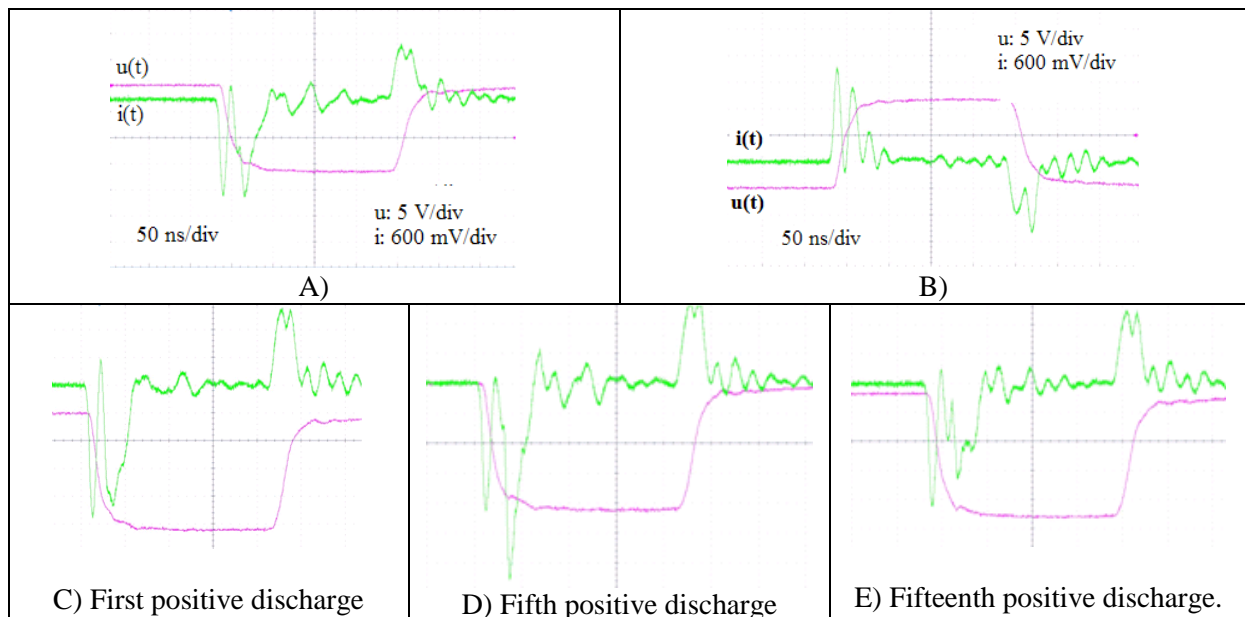
Fig. 1: Typical oscillograms of the SD currents. Cases A and B are for positive and negative voltage impulse. The surface charge was neutralized before the discharge. Cases C-E are for positive voltage impulses after a change of the polarity and without a neutralization of the charge. Channel sensibilities are the same as in fig. A
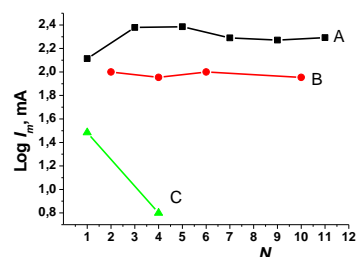
Fig. 2: Values of SD current amplitude as a function of the number of sequential discharges without a neutralization of the surface charge. A-positive impulses, strip electrode, B-negative impulses, C – positive impulses foil electrode
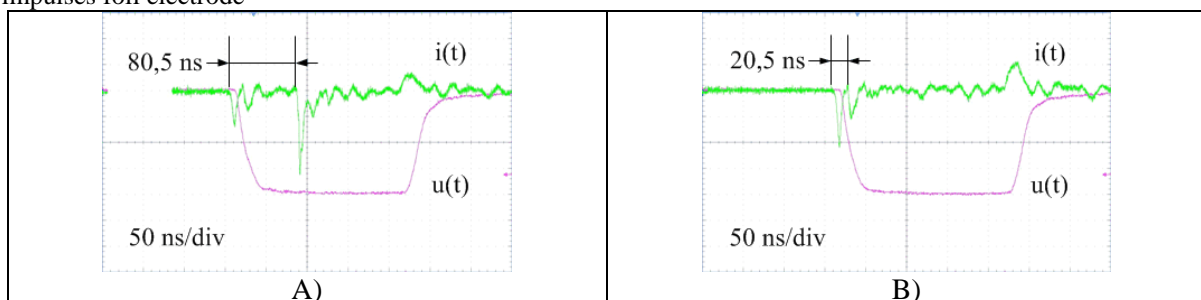
Fig. 3: Oscillograms of SD from small electrode edge under positive impulse voltage. A – first impulse application, B –after 4 discharges

A series of volume discharges (VD) under positive voltage impulses was registered for different numbers of sequential applications of voltage impulse. Oscillograms for three different cases are given in fig. 4 and correspond to first discharge (A) without a surface charge on the barrier, second discharge (B) with a charge and tenth discharge (C) with the charge on the barrier that was left on the surface under previous voltage impulses. In all cases investigated the result of a series of discharges of one polarity are the decrease of the current impulse amplitude and a decrease of time delay of the discharge appearance relative to the moment of voltage impulse application.
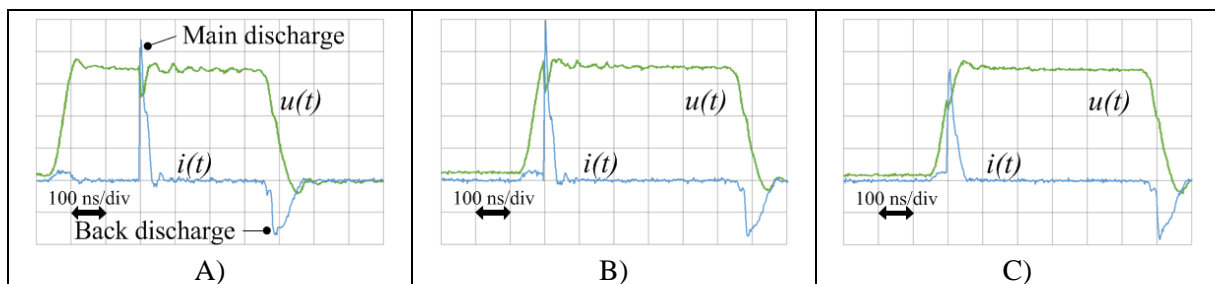
Fig.4: Oscillograms of VD under positive impulse voltage of positive polarity. A – first discharge, B – second discharge without a neutralization of surface charges, C – after several discharges without a neutralization of surface charges.

A difference in the mechanisms of the surface and volume discharge development described in [1] is connected with the gas gap that is bridged by the volume part of the DBD. According to [1] an increase of the applied voltage amplitude leads to an increase of the number of microdischarges in the gas gap while in the SD the length of the microdischarge channels is increased with higher applied voltage. Measurements made in the present work with nanosecond voltage impulses of different amplitude have shown that in the SD case the increase of the applied voltage leads mostly to an increase of the number of microdischarge channels and to their more intense branching.

4   Conclusions

It is shown experimentally that the time τ from the moment of nanosecond impulse voltage application relative to the moment of the discharge appearance (time of discharge delay) can in case of VD and SD significantly exceed the rise time of the voltage impulse if the barrier surface is free from surface charges. Charges left on the barrier during previous discharges influence the newly discharge appearance. This phenomenon known as a memory effect reveals itself in the same way under single nanosecond impulse voltages or their sequence as it is shown in investigations for a.c. or periodic impulse voltages of microsecond duration. The results of the present work show that memory effect reveals itself in a decrease of the ignition voltage of discharge appearance and in a decrease of the discharge current amplitude. The moment of the discharge appearance tends to be closer to the moment of the voltage impulse application. This effect is found to be present in both types of the discharge: channel form of SD and a homogeneous form of the VD.

The experiments show that the current amplitude and duration of the back discharge under nanosecond impulse voltage do not change with the number of previous discharges identically for VD and SD. The back discharge characteristics depend only on the polarity of the primary discharge at the voltage impulse front.

The complete removal of the surface charge and restitution of initial properties of the dielectric barrier surface can be achieved only after careful charge neutralization procedure.

References
1. V. I. Gibalov et al., J. Phys. D: Appl. Phys. 33, 2618 (2000)
2. F. Massines et al., Eur. Phys. J. Appl. Phys. 47, 22805 (2009)

GLIDING ARC BEHAVIOUR UNDER VARYING GAS FLOW FIELD

J. Šperka[1], J. Sluše[1], L. Potočňáková[2], V. Kudrle[2]

[1]*Czech Metrology Institute, Okružní 31, 638 00 Brno, Czech Republic*
[2]*Department of Physical Electronics, Masaryk University,*
Kotlářská 2, 61137 Brno, Czech Republic

E-mail: jsperka@cmi.cz

Many different types of gliding arc reactors have been constructed and operated under various experimental arrangements [1]. Several experimental studies demonstrated strong dependence of gliding arc performance on gas flow and gravity conditions [2, 3]. This contribution aims to show that exact knowledge of gas flow velocity field in gliding arc active zone is essential for traceability and reproducibility of gliding arc operation.

Keywords: gliding arc; wind tunnel; fluid dynamics; laser Doppler anemometry

1   Introduction

Atmospheric pressure gliding arc [4] is low cost and easy to build plasma source. It can be powered by alternating or direct current. The configuration of electrodes must allow the movement of the plasma channel. Although its name contains word "arc", it can be operated also at low current densities in mode with properties similar to non-equilibrium atmospheric pressure glow discharge. In this work, we report fundamental study on this plasma source under conditions that were not tested before. For this study, we used wind tunnel that is usually used in aerodynamic research to study the effects of air moving past solid objects.

In principle, there are two ways, how can experimentalist properly determine the gas flow phenomena and estimate the gas flow conditions in gliding arc operational volume. One approach is the employment of suitable diagnostics technique on existing experimental apparatus, e.g. the utilization of (i) dust particles as micro-probes and use of light scattering techniques, (ii) schlieren and shadowgraph techniques in transparent media or (iii) anemometry (laser Doppler, hot-wire, pilot tube, etc.). Another approach is the adaptation of existing experimental apparatus to configuration in which the gas flow conditions can be easily calculated/estimated. Numerical modelling of gas flow field can be performed in all cases.

2   Methodology and Experimental

In this contribution, we present results of gliding arc behaviour in different velocity fields. Gliding arc was ignited using alternating (50 Hz) high voltage with amplitude of 5-10 kV in air using steel electrodes with nearly quarter-elliptical shape, the dimension of one electrode was approximately 8 cm, the smallest distance between the electrodes was 1 mm. We used wind tunnel situated at Czech Metrology Institute (CMI) in Brno, manufactured by Westenberg engineering company (Type WK 845050-G, diameter of jet outlet 450 mm, length of measuring section 630 mm, flow velocity 0.3-50 m/s).
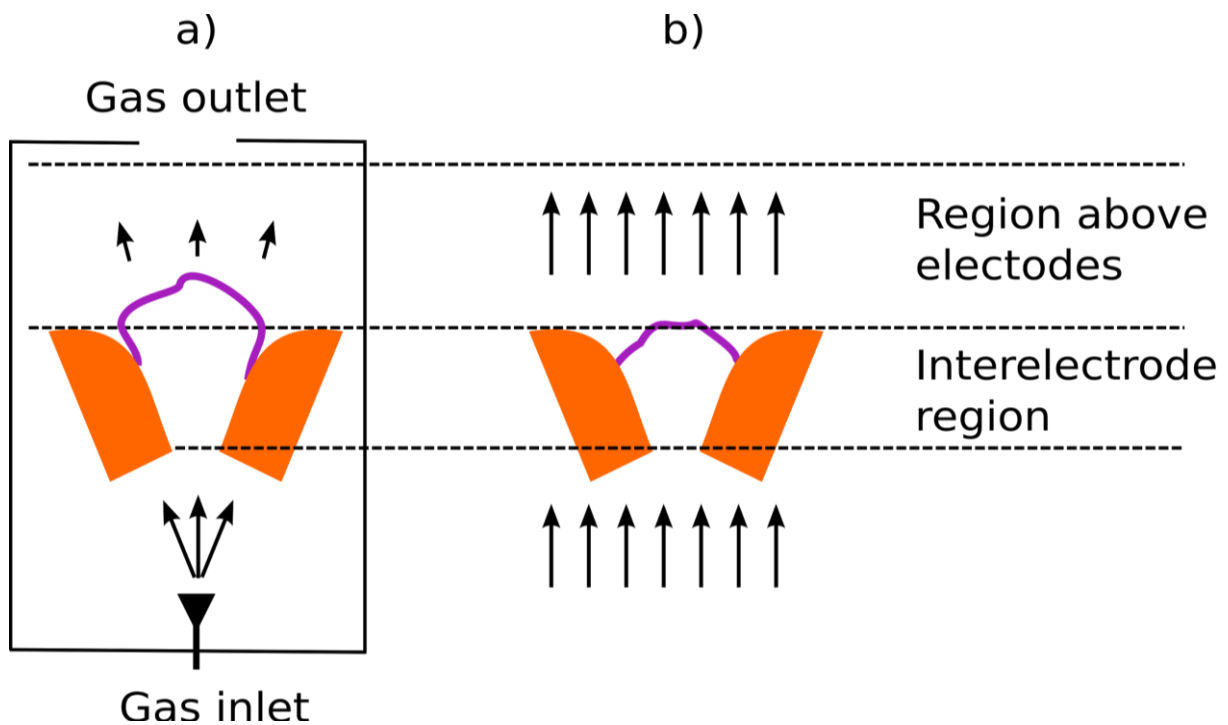
Fig. 1: Rough draft of two gliding arc experimental configurations, arrows denote flow velocity vectors: a) constricted configuration, b) non-constricted configuration with homogeneous gas flow.
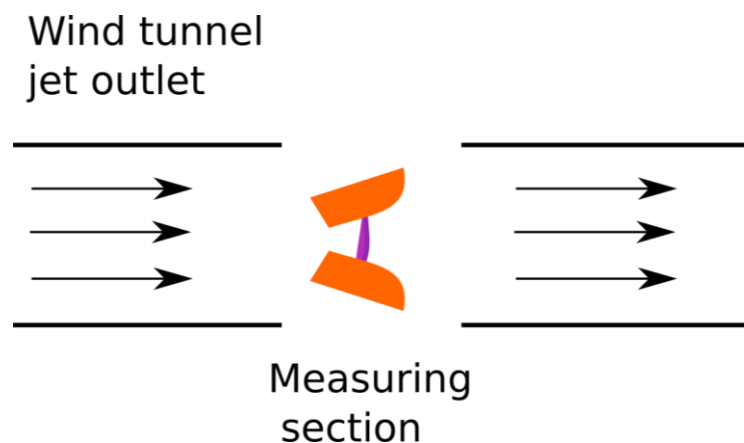
Fig. 2: Vizualization of gliding arc testing in wind tunnel, top view; arrows denote flow velocity vectors.

In the first research line, different flow conditions were achieved by using various inlet nozzles through which feed gas was applied to gliding arc constricted active volume (i.e. volume that was constricted by discharge chamber walls, see Fig. 1a). These inlet nozzles were custom made using 3D-printing technology (Original Prusa i3 printer). Laser scattering and schlieren technique were used to determine the gas flow conditions. Second research line deals with the adaptation of the gliding arc discharge setup that enabled the change of gas flow conditions in quantitatively expectable way in non-constricted configuration (i.e. gas flow and gliding arc discharge did not interact with the discharge chamber walls, see Fig. 1b). In this configuration, gas flow visualization was quantified using laser Doppler anemometry (LDA) measurement and numerical simulation (fluid dynamics OpenFOAM software) was verified by LDA, too. Optical images obtained by Casio EX-ZR100 high speed and Nikon

DSLR camera were processed using Gwyddion software [5]. Discharge channel moved perpendicularly to gravity vector to suppress buoyancy influence that was in this way less pronounced on optical images that were obtained from top view, see Fig. 2.

3   Discussion

Gliding arc on divergent electrodes has the following repetitive character of its life cycle: (i) it starts at the shortest distance between the electrodes, (ii) discharge channel moves due to gas flow and/or buoyancy (flow versus buoyancy dominated regimes; or combined regime) and (iii) it reaches its maximum elongation and extinguishes [4]. Whole life cycle is characterised by gliding frequency. The discharge channel can be in the first approximation considered as plasma column with characteristic length l. This length changes during its life cycle. Under flow dominated regime, the gas flow field is the most distinctive parameter that influences not only the gliding frequency, but also the geometrical properties of the plasma string. Predictably, one can distinguish several gliding arc regimes that correspond to various Reynolds numbers and gas flow conditions. Sequence of typical discharge channel geometrical forms was obtained using high speed camera recording and standard camera photography in the dependence on flow conditions.

4   Results and Conclusion

Wind tunnel proved to be fitting instrument for gliding arc testing under homogeneous gas flow. At relatively high gas flow speeds in wind tunnel and relatively high interelectrode distance, convective cooling was so pronounced that it even stopped the ignition of the discharge. This finding led us to the conclusion that for operation in strongly convectively-cooled environment, the power of the power source must be increased. Therefore, most of the measurements were performed at 10 kV. In most cases, the external gas flow is essential for gliding arc operation and applications. Hence, experiments in wind tunnel can lead to optimization of gliding arc operation. Moreover, this conclusion leads us to inquire if this technique would be interesting to be tested also on other atmospheric pressure plasma sources.

References
1. J. Zhu et al., J. Phys. D: Appl. Phys. 47, 29 (2014)
2. J. Šperka et al., Eur. Phys. J. D 67, 12 (2013)
3. L. Potočňáková et al., Plasma Sources Sci. Technol. 24, 2 (2015)
4. A. Fridman et al., Prog. Energy Combust. Sci. 25, 2 (1999)
5. D. Nečas et al., Open Phys. 10, 1 (2012)

TOPIC 2: MODELLING AND DIAGNOSTICS

NUMERICAL INVESTIGATION ON ATMOSPHERIC PRESSURE RADIO FREQUENCY NON THERMAL PLASMA TORCH

B. Bora

Comisión Chilena de Energía Nuclear, Santiago, Chile

E-mail: bbora@cchen.cl;biswajit.cpp@gmail.com

Different kind of non-thermal atmospheric pressure plasma sources have been reported in recent literatures for specific kinds of applications starting from biomedical application to material sciences. Realizing the important of the atmospheric pressure non-thermal plasma torch, an atmospheric pressure radio frequency non thermal plasma torch have been studied on the basis of nonlinear global model. The computational results show some interesting effects, like the different behavior of the plasma heating with distance between the electrodes. It is observed that the plasma heating is somehow complex dependence on the electrodes sizes.

Keywords: atmospheric pressure plasma; plasma torch; plasma modeling; CCRF plasma

1   Introduction

Different kind of non-thermal atmospheric pressure plasma sources (APPS) have been reported in recent literatures for specific kinds of applications starting from biomedical application to material sciences [1-3]. It also seems to have a great importance in plasma medicine. Depending on the particular applications the most used atmospheric pressure plasma sources are plasma needle, plasma pencil, radio frequency (RF) plasma torch, dielectric barrier discharge (DBD), barrier corona discharge (BCD) and plasma jet. It is known that in low pressure capacitively coupled radio frequency (CCRF) plasma a dc self-bias is generated due the geometrical asymmetry of the electrodes while operating by single frequency RF source. However, if the two electrodes are geometrically symmetrical, no such dc self-bias is generated while operating with single frequency RF sources. Very recently, it is reported that electrical asymmetry effect could be utilized to generate the dc self-bias even if the electrodes are symmetric in dual frequency low pressure CCRF plasma [4].

Realizing the important of the atmospheric pressure non-thermal plasma torch, a numerical modeling work on the basis of homogeneous discharge model have been carried out to optimize the design and understanding the influences of different physical parameters on the performance of the plasma torches. The model is implemented on the torch with cocentric cylindrical electrodes.

2   The Model

The schematic of the plasma torch based on concentric cylindrical electrodes along with the RF power source are shown in fig. 1. The schematic of the discharge in between two coaxial electrodes can be distinguished by two sheath capacitors near the electrodes and a bulk plasma column in between the two sheaths as shown in the fig.2. The model has been initially used to study the Ohmic and stochastic heating by plasma series resonance effect in

asymmetric low pressure CCRF plasma [5]. It was also used to experimentally measure the plasma series resonance heating and evaluate the plasma parameters from the electrical discharge characteristics [6-9]. The model has been later modified to study the dual frequency geometrically symmetric CCRF plasma by considering the second sheath at the grounded electrode [6-8, 10] in low pressure. It has been also used similar kind of model to evaluate the plasma parameters form electrical discharge characteristics of atmospheric pressure plasma torches and step ionization associated with atmospheric pressure plasma torch [8,9].

Considering the homogeneous plasma in between the two electrodes the schematic of the plasma discharge can be model as shown in fig 3. Where, $C_{s,k}$ (k=1, 2) is the sheath charges of the powered and grounded electrode and can be expressed as,

$$C_{s,k} = \frac{Q_{s,k}}{V_{s,k}} = \left(\frac{2e\varepsilon_0 n_e A_k^2}{V_{s,k}} \right)^{1/2} \tag{1}$$
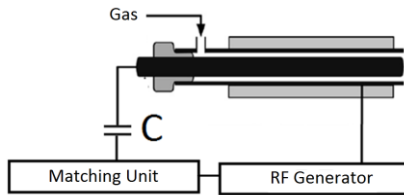
Fig. 1: Schematic of the plasma torch.
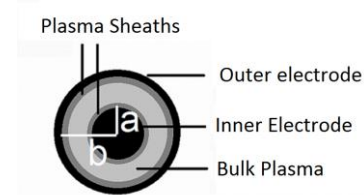
Fig. 2: Schematic of the discharge.
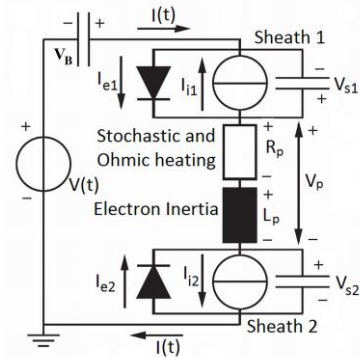
Fig. 3: Schematic of the model.

In the bulk of the plasma, the electron frequency, $\omega_{pe}^2 = n_e^2/\varepsilon_0 m$ (m is the mass of the electron) and the capacitance C_0 of a cylindrical electrode system can be used to express the inductance due to the inertia of the electron as [6-10],

$$L_p = \frac{1}{\omega_{pe}^2 C_0} = \frac{m\ln\left(\frac{b}{a}\right)}{2\pi n_e e^2 l} \tag{2}$$

Where a, b, and l are the inner radius, outer radius, and length of the cylindrical electrode system, respectively. The dependence of the current density on the electric field can thus be modeled by a generalized Ohm's law, as [5, 8-10].

$$R_p = \gamma L_p = \frac{d_{col}^2 \ln\left(\frac{b}{a}\right)}{l\pi e^2}\left(2\pi k m T_e\right)^{1/2} \tag{3}$$

107

Where, d_{col} is the electron neutral collision cross section, $\gamma = (8eTe/\pi m)^{1/2}$ is the electron mean thermal speed, and l_p is the length of the plasma bulk. The electron and ion current densities inside the both sheaths are taken to be $j_{e,k} = j_{eo}\exp(-Vs,k\ /Te)$ and $j_{io} = envB_{ohm}$, with $v_{Bohm} = (eT_e/M)^{1/2}$ the Bohm speed, M is the ion mass and $j_{eo} = en_e v_e$.

Applying Kirchhoff's law to CCRF plasma model as describe in fig. 3, we have obtained a set of four differential equations describing the two sheaths charge ($Q_{s,1}$, $Q_{s,2}$), the dc bias voltage (V_B) and rf current ($I(t)$) [5,6,10]

$$\frac{dQ_{sP}}{dt} = -\left[I(t) + A_P j_{i0} - A_P j_{eo} \exp\left(-\frac{Q_{sP}^2}{2e\varepsilon_0 n_e A_P^2 T_e} \right) \right] \tag{4}$$

$$\frac{dQ_{sG}}{dt} = -\left[-I(t) + A_G j_{i0} - A_G j_{eo} \exp\left(-\frac{Q_{sP}^2}{2e\varepsilon_0 n_e A_G^2 T_e} \right) \right] \tag{5}$$

$$\frac{dV_B}{dt} = -\frac{1}{C_B} I(t) \tag{6}$$

$$\frac{dI(t)}{dt} = \frac{1}{L_p}\left[V(t) + \frac{Q_{sP}^2}{2e\varepsilon_0 n_e A_P^2} - \frac{Q_{sG}^2}{2e\varepsilon_0 n_e A_G^2} + V_B \right] - v_{eff} I(t) \tag{7}$$

The plasma heating is calculated from the rf current considering the Ohmic heating by following equation.

$$\eta_{total} = \left\langle vL_p I_p^2 \right\rangle \tag{8}$$

The equations (4) – (7) are solved with the typical set of plasma parameters, V_{rf} =20 V, ω =2π x13.56 MHz, n_e=10^{16} m^{-3}, T_e = 1.5eV, M= argon ion mass, and $\gamma = K_m n_g$, where $K_m = 10^{-13}$ m^{3}s^{-1} is the rate coefficient, n_g (m^{-3}) =4.4x10^{24} p (Pascal) is the neutral gas density and p is the atmospheric pressure.

3   Results and Discussion
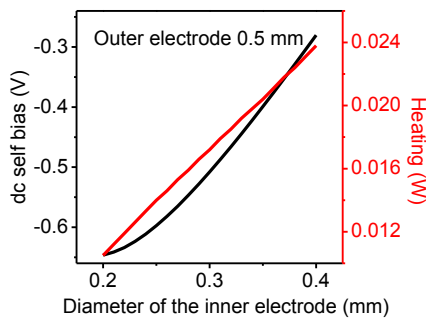
Fig. 4: Variation of dc self bias and heating with inner electrode size.
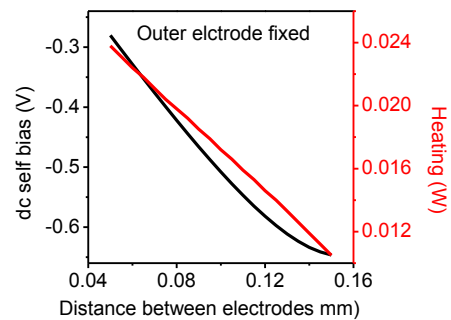
Fig.5: Variation of dc self-bias and heating with distance between the electrodes keeping the outer electrode fixed.

To study the influences of electrode sizes and the distance between the electrodes on the generation of dc self-bias and the plasma heating, the computations are performed for different electrodes sizes and distances. Two preliminary studies were carried out; one is the variation of the size of the inner electrode while the outer electrode kept constant, other is the

variation of the outer electrodes keeping the inner electrodes fixed. Fig. 4 shows the variation of the dc self-bias generated due to the asymmetry of the electrodes size and the heating with the inner electrode size. Fig. 5 shows the variation of the dc self-bias and the plasma heating with the distance between the electrodes. Although the amount of dc self-bias is small, almost a linear variation of dc self-bias and plasma heating is observed with the variation of the inner electrode size and distance between the electrodes. However, some nonlinear variation of the plasma heating is observed while varied the outer electrode size as shown in fig. 6. The computational results show some interesting effects, like the different behavior of the plasma heating with distance between the electrodes as shown in fig. 7. Although, the range of the distance between the electrodes (fig. 5 and fig.7) are same while investigating the influences of electrodes sizes, it is observed that the heating is not only depends on the distance between the electrodes but also depends on the electrodes dimensions.
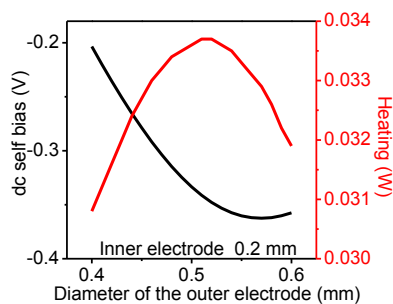
Fig. 6: Variation of dc self bias and heating with outer electrode size.
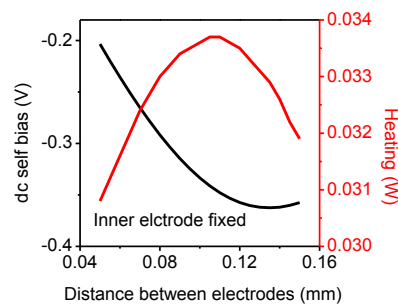
Fig. 7: Variation of dc self bias and heating with distance between the electrodes keeping the outer electrode fixed.

4   Conclusion

An atmospheric pressure radio frequency non thermal plasma torch have been studied on the basis of nonlinear global model. The computational results show some interesting effects, like the different behavior of the plasma heating with distance between the electrodes. It is observed that the plasma heating is somehow complex dependence on the electrodes size. A further numerical investigation is going on to study this complex dependence of the plasma heating on the electrodes sizes and distance between the electrodes.

References
1. A. Y. Gil et al., J. Appl. Phys., 101, 103307 (2007)
2. P. S. Le et al., Appl. Phys. Lett. 95, 201501 (2009)
3. S. Z. Li et al., Phys. Plasmas 13, 093503 (2006)
4. T. Mussenbrock et al., Phys. Rev. Lett. 101, 085004 (2008)
5. B. Bora et al., Phys. Plasmas 18, 103509 (2011)
6. B. Bora, Plasma Sources Sci. Technol. 24, 054002 (2015)
7. B. Bora et al., Phys. Plasmas 19, 064503 (2012)
8. S. Z. Li et al., Phys. Lett. A 360, 304 (2006)
9. B. Bora, Phys. Plasmas 22, 103503 (2015)
10. J. Schulze et al., J. Phys. D: Appl. Phys. 42, 092005 (2009)

INVESTIGATION OF SINGLE FILAMENTS IN A DIELECTRIC BARRIER DISCHARGE WITH ROTATING ELECTRODE

V. V. Andreev[1], R. Brandenburg[2], A. Sarani[2], M. Kettlitz[2]

[1]*Chuvash State University, Cheboksary, Russia*
[2]*Leibniz Institute for Plasma Science and Technology (INP), Greifswald, Germany*

E-mail: brandenburg@inp-greifswald.de

First experimental results on the investigation of single repetitive filaments in a DC-operated dielectric barrier discharge arrangement with a rotating dielectrically covered electrode in ambient air at atmospheric pressure are presented. The electrode arrangement consists of a metal pin electrode and a rotating electrode which is a plate electrode covered by glass. An additional electrode slides on the surface of the glass plate which discharges the remaining surface charges from the dielectric. Distinct differences from classical DBDs are observed.

Keywords: dielectric barrier discharge; time-correlated single photon counting; rotating electrode; DC high voltage

1   Introduction

The nature and physical parameters of dielectric barrier discharges (DBDs) is determined by the presence of dielectric material in the discharge gap and its properties. The charging of the dielectric barrier is responsible for the non-thermal regime as it limits the local energy dissipation. In an operating DBD residual surface charges are supposed to play a crucial role before the discharge inception phase [1, 2]. In a classical DBD, e.g. sinusoidal driven, surface charges can remain for several hours on the dielectric barriers after turn off [3] and can thus influence the distribution and development of the plasma in the following discharge cycles. For a filamentary DBD in helium admixed with nitrogen Bogaczyk et al. have demonstrated that distinct spots of positive and negative surface charges can exits more or less simultaneously on an electro-optic crystal utilized for the determination of surface charges by the Pockels effect [2]. Furthermore, an offset of the surface charge density after several AC cycles is obtained. In order to learn more about the role of surface charges in a DBD with usual dielectric materials such as glass a new experiment with a rotating dielectric barrier has been considered. It is motivated by a plasma-chemical reactor for ozone generation and a nanosecond pulse generator based on a DBD, which were presented by Andreev et al. [4-6]. The main idea is to have a rotating dielectric electrode so that remaining surface charges can be released by a second grounded electrode before a new discharge cycle starts. I.e. in contrast to classical DBDs, in particular single filament arrangements [1, 7] the filaments are ignited in a configuration without surface charges before discharge inception.

This contribution will give a description of the realized discharge arrangement. The single repetitive filaments where investigated by ICCD camera photos, electrical measurements and time-correlated single photon counting (TC-SPC), i.e. with sub-ns and sub-mm as well as spectral resolution [8].

2   Experimental

The electrode arrangement is similar as the one described in [5]. It consists of a fixed metal electrode pin with a radius of 0.65 mm and curvature radius of 0.325 mm which is energized by positive or negative DC high voltage of several kV amplitude. The grounded electrode is a disk of metal concentrically covered by a disk of glass with a thickness of 2 mm. The diameter of the glass disk is larger than the diameter of the metal disk (6 cm). The whole arrangement is rotating by means of a motor. Therefore, the disk assembly is concentrically mounted on the shaft of the motor. The circular speed of the motor is varied in a range of from 0 to 10000 rotations per minute (rpm). The grounding of the disk is performed via a sliding carbon brush electrode. The high voltage electrode is located off axis to the disk assembly. The gap between the point tip and the glass surface was fixed, with values between 1 and 3 mm. Opposite to the point electrode a second sliding grounded electrode is located. It is made of a flexible copper band. Figure 1 shows the schematic discharge arrangement.
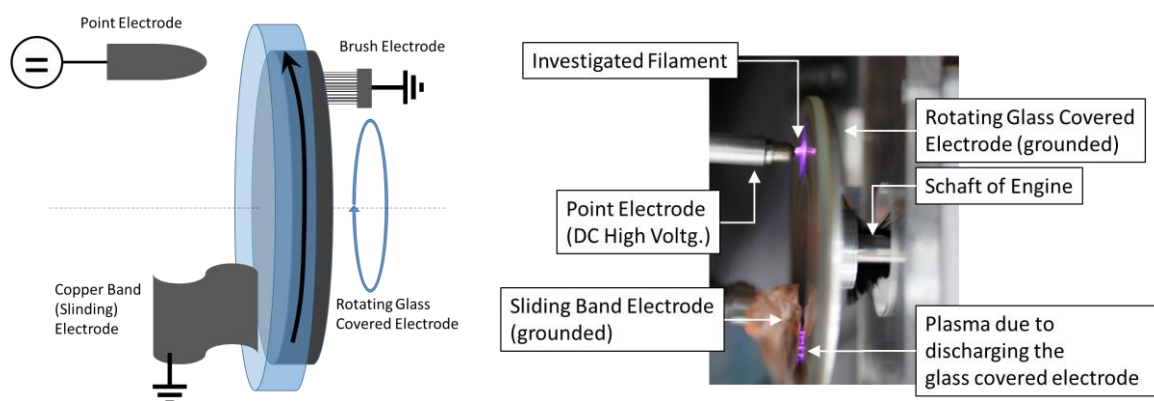
Fig. 1: Scheme (left) and photo (right) of the discharge arrangement with rotating dielectric electrode. The plasma is operated in still ambient air.

As shown on the photo in fig. 1, right part, there are two gas discharges observed. One is located between the point tip and the dielectric surface, and is the object of investigation. A second plasma zone is observed between the glass surface and the sliding copper band electrode. The remaining surface charges from the first discharge form an electric field between dielectric surface and copper band which is capable to cause a second gas discharge. This discharge was not investigated further except current measurements through the ground connection by means of a current monitor (Pearson 2877). An identical current monitor was used around the high voltage connection to the point electrode in order to measure the current in the first discharge.

The discharge at the point electrode was imaged to an ICCD camera (DiCAM-PRO) via a far field microscope (Questar QM 100) to record photos of the plasma with a short exposure time (in the range of microseconds). Since the plasma appears quite irregular and is of weak intensity as well as short duration and small scale the time-correlated single-photon counting technique is used for spatio-temporal resolved investigation of the discharge development. This technique has already been described elsewhere [1, 8]. Here the same setup, as presented in [9] was used.

3   Results and Discussion

The microdischarge current pulse amplitude and duration strongly depend on the polarity of the high voltage electrode and the distance between point electrode and glass surface. In case of positive polarity, the amplitude reaches a few hundred mA, while 5 times lower values are obtained for negative polarity. The amplitude is not significantly dependent on the rotational speed of the disk electrode for values exceeding 1000 rpm, but is decreased with declining the rotational speed below this value. As higher the distance (varied between 1 and 3 mm) as higher are the current pulse amplitude and duration. The duration of microdischarges is in the range of 100 ns. It is about 2 times longer in case of negative polarity compared to positive one. The rotational speed, the position of the point electrode (i.e. circular distance to the rotational axis) and the voltage amplitude define the number of microdischarges per unit of time. As higher the speed and as longer the distance the higher is the repletion rate. With 9000 rpm, a distance of 2 cm and a negative polarity voltage of 11.5 kV a mean repetition rate of about 3.6 kHz is reached. In case of low voltage amplitudes and rotational speeds it has to be mentioned that the discharge is very irregular, similar as known from Trichel pulse corona discharges, but the current pulse amplitude is much higher than for a Trichel pulse, namely about 35 mA. The higher the rotational speed and the voltage amplitude, the more regular appearing microdischarges are observed.
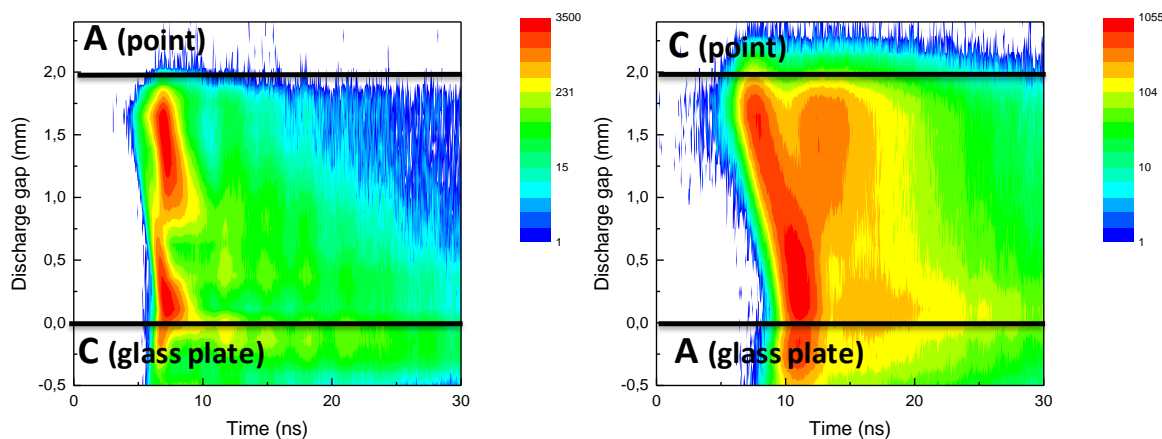
Fig. 2: TC-SPC results (number of counted photons) showing the development of microdischarges in a DBD arrangement with rotating dielectric electrode. Left: positive polarity of point electrode. Right: negative polarity of point electrode. Approximated positions of electrodes are given by lines; A is anode, C is cathode; emission of the 0-0 transition of the second positive system of nitrogen at 337 nm with a resolution of $\Delta\lambda=0.07$ nm.

In figure 2 two examples of observed spatio-temporal discharge development are presented. The radiation of the most intensive molecular band in the emissions spectrum of such discharges in air, namely the 0-0 transition of the second positive system of nitrogen at 337 nm is shown. The results compare the different polarities of the point electrode in a discharge configuration with 2 mm discharge gap and a voltage of 11.5 kV. The rotational speed was 7000 rpm. The discharge was operated in open atmosphere but with a gas flow of synthetic air of 150 sccm through the electrode arrangement. The abscissas are the time axis (time window of 30 ns with a resolution of 48 ps) and the ordinates are the axial discharge gap positions. The locations of the electrode surfaces are given in the diagrams (high voltage electrode always at top and dielectric at bottom).

For the positive polarity a cathode directed wave of radiation (positive streamer) starting from the middle of the gap followed by a second emission front (secondary wave) starting from the metal electrode are observed. This behavior is similar to a positive streamer corona [10]. For the negative polarity an anode directed wave of light (negative streamer) and a weaker glow in front of the cathode are observed. In both cases no pre-phase prior to the breakdown is investigated. The results suggest a pronounced influence of the surface charge dynamics on the discharge development in comparison with sinusoidal single-DBD cells with non-moving dielectric electrodes. In these case, a cathode directed streamer and an anode glow as well as a Townsend pre-phase were observed in asymmetric DBDs (one metal electrode and one dielectrically covered electrode) [1]. These differences suggest an important role of surface charges in the pre-phase of the microdischarge formation. To gain more information the investigation of different spectral lines and the systematic variation of the discharge configuration parameters are planned for future research.

4   Conclusion

A novel single filament DBD arrangement is presented. It enables the study of DC-operated DBDs of different polarities, where surface charges are discharged by a sliding electrode on a rotating dielectric electrode. This unique boundary condition has a significant impact on the discharge development as suggested by the first, preliminary TC-SPC results. Only in case of negative polarity a discharge development similar as known from classical single-DBDs with two fixed point electrodes is obtained. Further experiments on this discharge arrangement are motivated by the presented preliminary results.

References
1. T. Hoder et al., J. Phys. D: Appl. Phys. 43, 124009 (2010)
2. M. Bogaczyk et al., J. Phys. D: Appl. Phys. 45, 465202 (2012)
3. R. Brandenburg et al., J. Phys. D: Appl. Phys. 42, 085208 (2009)
4. V. V. Andreev et al., Plasma Phys. Rep. 37, 1053 (2011)
5. V. V. Andreev et al., Instr. and Exp. Techniques. 56, 299 (2013)
6. V. V. Andreev et al., Plasma Phys. Rep. 40, 481 (2014)
7. H. Höft et al., J. Phys. D: Appl. Phys. 47, 465206 (2014)
8. K. V. Kozlov et al., J. Phys. D: Appl. Phys. 34, 3164 (2001)
9. R. Brandenburg et al., In *Proceedings of the 22nd International Symposium on Plasma Chemistry*, Antwerp, 2015, edited by A. Bogaerts and R. van de Sanden
10. N. Ikuta et al., *In Proceedings of the 4th International Conference on Gas Discharges and their Applications*, Swansea, 1976, pp. 227-230

HELIUM RYDBERG MOLECULES KINETICS IN ATMOSPHERIC PRESSURE DISCHARGES

E. Carbone, Ch.-G. Schregel, D. Luggenhölscher, U. Czarnetzki

Institute for Plasma and Atomic Physics, Ruhr-University Bochum, 44780 Germany

E-mail: emile.carbone@rub.de

In high pressure discharges, neutral particle collisions play an important role on plasma kinetics. In high pressure pure helium discharges, the formation of helium molecules is qualitatively known but their kinetics are still poorly understood. In this contribution, the absolute density of helium Rydberg molecules is measured for the first time by a combination of laser photo-ionization and Thomson scattering experiments. The results are combined with electron and helium metastable densities measurements and compared with a kinetic model of the discharge. The source of He_2 molecules in the discharge and afterglow phases are identified with three-body association and recombination processes.

Keywords: helium kinetics; Rydberg molecules; atmospheric pressure plasmas; Thomson scattering; plasma modeling

1   Introduction

In the field of biomedical applications, atmospheric pressure helium discharges have been found to be the most promising plasma sources compared to argon plasmas mostly because they can be easily operated near room temperature and produce large amount of reactive species [1]. Most studies have focused up to now on argon and helium plasma jets in open environment where air entrainment inside the plasma jet makes any quantitative investigation of the plasma dynamics complex. Particularly, to understand and model plasma dynamics, it is necessary to work in pure gases due to the exponential increase in complexity when adding further species. Such impurities lead notably to strong changes in the temporal shape of the electron energy distribution function because of the extra inelastic electron energy losses.

In this contribution we present the experimental characterization of a nanosecond pulsed pure helium discharge in parallel plate configuration. Various diagnostic techniques are used to determine all important parameters of the discharge. A simple kinetic model is finally developed to discuss and describe the main production and destruction channels of excited neutral species in the afterglow.

2   Experimental
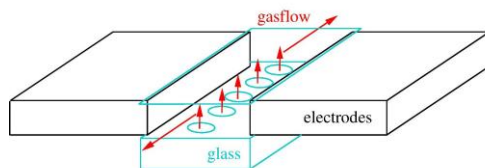
Fig. 1: Schematic diagram of the flow configuration of the parallel plate nanosecond pulsed discharge. The gap is 0.95 mm, the discharge length 2 cm and the Molybdenum electrodes have a thickness of 1.5 mm.

The discharge is a simple parallel plate pulsed DC discharge operated at 0.7 bar. The reactor consists of two molybdenum electrodes. A 800 sccm helium flow is blown into the gap through a glass plate below the electrodes forced outside via the sides by covering the electrodes with a thin glass plate (see figure 1 for more details). A rectangular 2.3 kV voltage pulse is applied for 150 ns to the powered electrode while the other one is grounded. The discharge is operated with a repetition frequency of 5 kHz to ensure stable conditions with low jitter. The electron density and electron energy velocity distribution function are measured by laser Thomson scattering (LTS). The triplet He (2 ^{3}S) metastable state is measured by laser diode absorption spectroscopy. From the analysis of the LTS data we measure also for the first time the absolute density of helium Rydberg molecules produced in the discharge. At high laser powers, one needs to be careful with photo-ionization, photo-detachment and laser heating of the electrons during LTS experiments [2]. We performed laser energy variation measurements. The measured electron temperature is found to be independent to laser energy as seen in figure 2 even at the peak electron density (100 to 120 ns) ruling out laser heating. In the afterglow, a significant increase of the electron density as a function of laser energy is observed with an overpopulation of the tail of the EVDF indicating
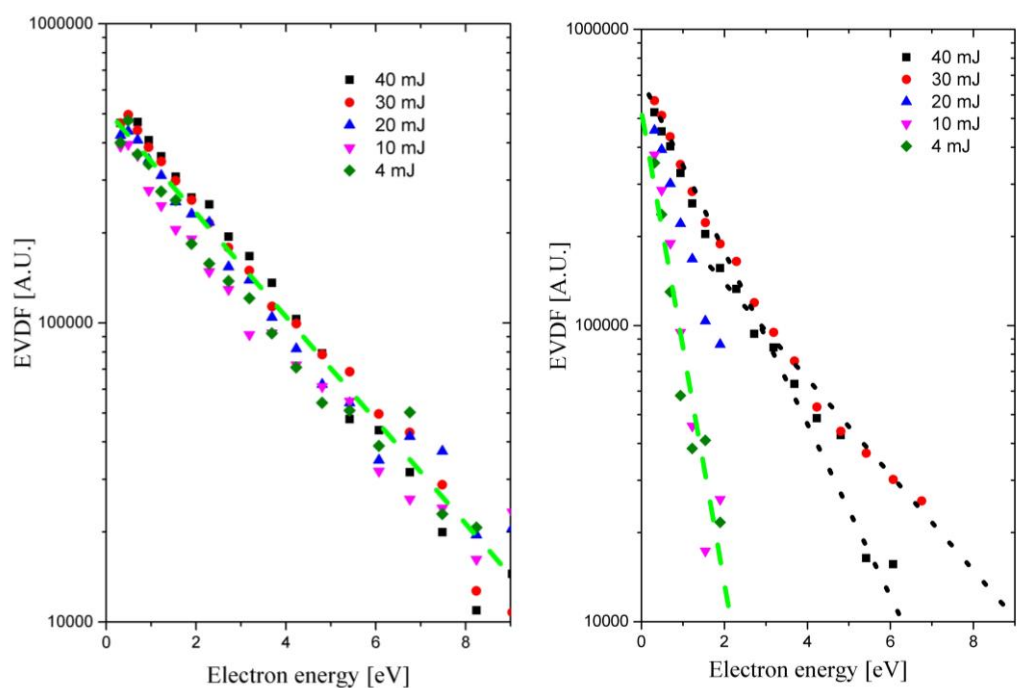
Fig. 2: Electron velocity distribution function at 100 ns (discharge regime) and 200 ns (afterglow period) as a function of the laser power. One can see that in the afterglow a significant number of extra electrons are produced by photo-ionization of Rydberg molecules.

photo-ionization of weakly bound electrons. After excluding possible contributions from impurities, these extra electrons are assigned to Rydberg molecules [3]. Fitting the photo-ionization saturation curves as a function of the laser pulse energy, absolute densities are finally obtained. The data are complemented with spatially and spectrally resolved optical emission spectroscopy of atomic and molecular helium lines.

3   Global plasma model

In the kinetic model, we consider several species in their ground state, namely helium atoms He, free electrons e⁻, the atomic ion He^+ and the molecular ions (He_2^+ and He_3^+). Additionally we consider a helium atomic metastable state He 2 ^{3}S and the helium metastable molecule He_2 $2s^3\Sigma_u^+$. For the excited neutral species, we consider two groups of lumped states both for helium atoms (He* and He**) and molecules (He_2^{rad} and He_2^{Ry}). These groups are defined consistently with their adiabatic interaction energy potential curves. The Rydberg molecules He_2^{Ry} correspond to all the molecular states which are formed by association processes (cf. reaction 1) above the He (3 ^{3}S) state. The He** atoms have higher potential energy than the ground state of He_2^+ [5]. The kinetic model is based on the numerical solution of a coupled set of balance equations solved using a forward Euler iteration scheme. The transport losses at atmospheric pressure are negligible compared to volume losses and the species balance equations reduce simply to the following form

$$\left(\frac{\partial n_j}{\partial t}\right) = P_j - n_j D_j$$

where P_j are the source terms via two or three body processes and D_j are the destruction processes by two or three body collisions. The energy balance of the plasma is not solved explicitly but taken into account via the electron density and total Rydberg density measured by Thomson scattering up to 120 ns and represented in figure 3. A source term is then self-consistently included for the electron and atomic excited states to represent the total amount of energy stored in the plasma species during the breakdown phase. At the start of the afterglow regime, defined as 120 ns and onwards, all species particle balances are solved self-consistently. All rate coefficients are taken from experimental measurements reported in the literature [4].

4   Results and Discussion

In figure 3, a comparison between the experimental results and the model are shown. One can find a good agreement, both for the decay of the electron density but also the source terms of
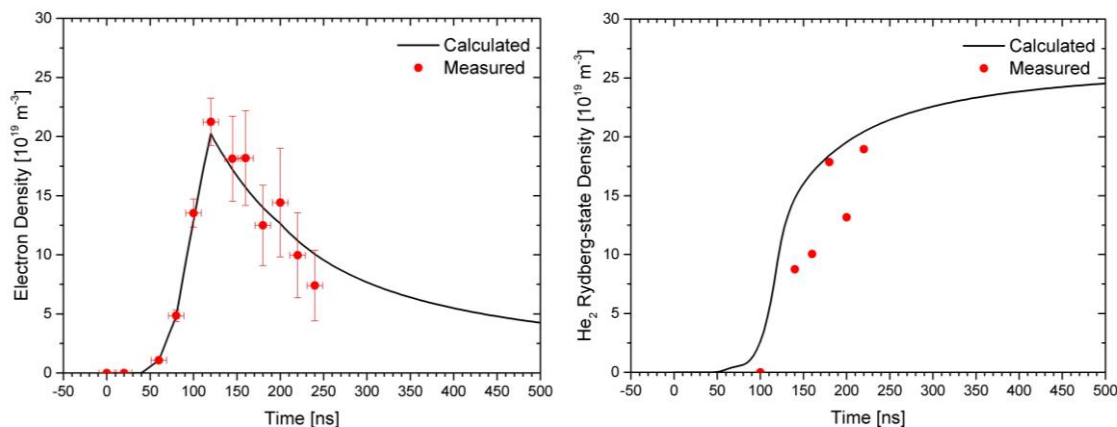
Fig. 3: Experimental electron and Rydberg molecule densities measured by Thomson scattering. The experimental results are compared with the output of a global plasma kinetic model for the main species produced in a pure helium discharge at high pressure.

the helium Rydberg molecules in the early afterglow. One can see that all the electrons recombine into Rydberg molecules but also that a significant amount of them are produced during the discharge phase as well. The analysis of the results from the model show that two processes governs the production. Three body association

$$He** + He + He \rightarrow He_2^{Ry} + He \qquad (1)$$
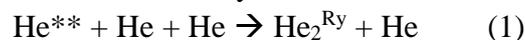
is the main process during the discharge phase. In the afterglow, neutral assisted three body recombination of He_2^+ takes over

$$He_2^+ + He + e- \rightarrow He_2^{Ry} + He. \qquad (2)$$

These reaction pathways have been suggested by some authors and even included into models (see for instance [7, 8]) but the absolute He_2^{Ry} density measurements allow to quantify for the first time the importance of different recombination pathways. The main other competing channel is identified as

$$He_2^+ + e- \rightarrow He\ 2\ ^3S + He \qquad (3)$$
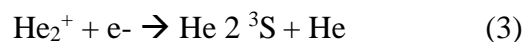
but is slower and He 2 ^{3}S density increases in the microsecond time scale in the afterglow. The measurements shown in figure 3 also show that the main recombination products of reaction 2 are Rydberg molecules.

5   Conclusions and perspectives

For the first time, we report experimental measurements of the absolute Rydberg states density in a high pressure helium discharge. The present work shows the importance of three body association processes in the kinetics of excited helium species. This process leads to the formation of helium molecules during discharge operation. In fact, this process can compete with auto-ionization processes [6] and more experiments are needed to evaluate their relative weights for the quenching of atomic helium species. In the late afterglow (t>500 ns), our measurements show that the loss channels of excited neutral species in pure helium discharges are not yet fully understood nor described yet. Indeed, our measurements also showed that the helium radiative and Rydberg molecules behave differently contrary to what has been usually assumed. Considering their large densities, Rydberg molecules are also expected to play an important role for controlling the background ionization degree in pulsed plasma operation.

References

1. J. J. Liu et al., J. Phys. D. Appl. Phys. 44, 345203 (2011)
2. E. Carbone et al., Plasma Phys. Control. Fusion, 57, 014026 (2015)
3. C. Schregel et al., Plasma Sources Sci. Technol. (submitted)
4. E. Carbone et al., Plasma Sources Sci. Technol. (submitted)
5. M. L. Ginter et al., J. Chem. Phys. 52(9), 4469 (1970)
6. H. C. Srivastava et al., Phys. Lett. A, 109(3), 101 (1985)
7. R. Deloche et al., Phys. Rev. A, 13, 1140 (1976)
8. Yu. B. Golubovskii et al., J. Phys. D. Appl. Phys. 36, 39 (2002)

COMPARISON OF EXPERIMENTAL AND THEORETICAL SPECTRA OF NON-SELF-SUSTAINED DISCHARGE IN N₂ AND AIR IN WIDE RANGE OF FIELD STRENGTH AND PRESSURE

I. Jõgi, E. Levoll, P. Paris, M. Aints
Institute of Physics, University of Tartu, W Ostwald str. 1, Estonia

E-mail: indrek.jogi@ut.ee

The optical emission of nitrogen and air discharges was investigated in wide range of reduced electric fields and pressures with the use of a non-self-sustaining Townsend discharge cell. The experimental spectra were compared with the theoretical spectra of nitrogen second positive system and first negative system. The calculations were based on a simple collisional-radiative model taking into account excitation by electron impact and de-excitation by radiative decay and quenching by N_2 and O_2. Reasonably good coincidence between experiment and theory was obtained. The choice of collisional quenching rate coefficients for $N_2^+(B\ ^2\Sigma_u^+, v=0)$ was discussed.

Keywords: nitrogen spectrum; reduced electric field; quenching rate coefficients

1 Introduction

Optical emission spectroscopy is an important tool for the characterization of air discharges. The emission of second positive system (SPS) originating from $N_2(C\ ^3\Pi_u)$ manifold and first negative system (FNS) originating from $N_2^+(B\ ^2\Sigma_u^+)$ manifold used in the estimation of reduced electric field strength, *E/N* [1,2] is of main importance. In addition to the electric field, the emission from these states is strongly influenced by the collisional quenching with air molecules, especially at atmospheric pressures [1]. Collisional quenching rate coefficients for $N_2(C\ ^3\Pi_u)$ vibrational states proposed by different authors are satisfactorily consistent while the collisional quenching rate coefficients for $N_2^+(B\ ^2\Sigma_u^+, v=0)$ vary up to 4 times [1].

The aim of present study was to evaluate the suitability of quenching rate constants proposed by different authors by registering the nitrogen emission spectrum in pure nitrogen and air at varying pressures and *E/N* values and comparing the results with the results calculated on the basis of theoretical model using the available data of quenching coefficients.

2 Experimental setup

A non-self-sustained Townsend discharge between parallel plate electrodes was used to carry out the experiments at well-determined *E/N* values. The experimental setup is depicted in figure 1 and detailed description can be found in [2]. The cathode was a semitransparent aluminum coating evaporated on a quartz plate while the anode was made from brass. The initial electrons were produced from the cathode by UV radiation of a mercury lamp equipped with an interference filter for λ= 253 nm. The diameter of the illuminated area of the cathode was 18 mm. The electric field strength between the electrodes was set by adjusting the distance between the electrodes and/or the applied voltage. The high voltage from Stanford Research Systems Inc. model P350 was applied to the cathode via a current limiting resistor *R*

= 396 MΩ. The anode was grounded via a Keithley 6485 picoammeter. The discharge current was fixed at 1 µA for measurements in nitrogen and 3 µA in air. Under these conditions, the space charge electric field created by charged particles remained below 1 % of the Laplacian field. The pressure in the discharge chamber was measured with the piezoelectric and micro Pirani transducer. Nitrogen with purity of 5.0 or synthetic air with purity of 4.0 was flowing through the chamber with the flow rate of 20 sccm. The experiments were carried out in the pressure range of 8 to 750 Torr and *E/N* range 200-2000 Td.
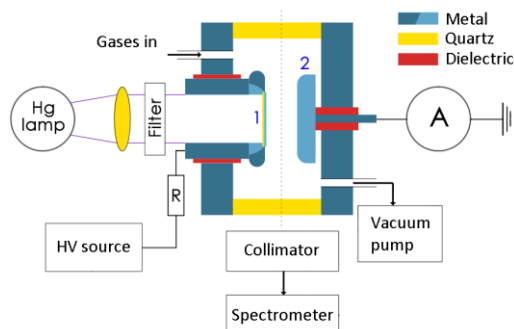
Fig. 1: Sketch of the experimental set-up. 1- semitransparent cathode, 2 - anode.

The emission originating from the discharge was registered through quartz windows. The collimator was used to focus the emission to a fiber which was attached to the Andor Mechelle ME5000 spectrometer. The spectrum in the range of 220-850 nm was collected for 10-15 minutes. The relative spectral sensitivity of the optical system was determined using a deuterium-halogen calibration source Ocean Optics DH-2000-Cal.

3   Results and Discussion

An example of emission spectrum obtained in pure nitrogen at 26 Torr and 584 Td is shown in figure 2. At all experimental conditions, only bands corresponding to nitrogen SPS and FNS systems in the spectral range of 270 to 470 nm were detectable in the spectra. The SPS(0,0) band at 337 nm had always highest intensity whereas the relative intensities of other bands varied depending on *E/N* value and pressure.

The integrated intensity of bands corresponding to different transitions was obtained by comparing the experimental spectrum of a band with the synthetic spectrum similarly to the procedure described in our previous paper [2]. An example of the measured SPS(0,0) band together with the simulated one is shown in the inset of figure 2.
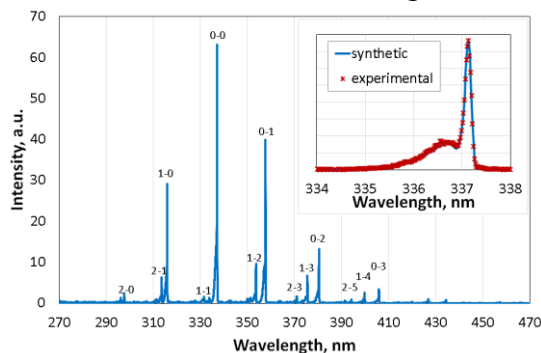
Fig. 2: Nitrogen spectrum at 26 Torr and 584 Td in pure nitrogen. The inset shows an example of the fit between experimental and synthetic spectrum of the SPS(0,0) band.

The collisional-radiative model used for the calculation of theoretical intensities of nitrogen SPS and FNS bands assumes that the excitation of $N_2(C\,^3\Pi_u, v=0\text{-}4)$ and $N_2^+(B\,^2\Sigma_u^+, v=0\text{-}2)$ states occurs through the electron impact from ground state $N_2(X\,^1\Sigma_g^+, v=0)$ while the losses are caused by spontaneous emission and collisions with N_2 and O_2 molecules. The excitation rates of respective N_2 states were calculated with Electron Energy Distribution Function (EEDF) obtained with the Boltzmann solver BOLSIG+ [3] and cross-sections of excitation processes obtained from the papers of Tabata and Shemansky [4,5]. The collisional quenching rate coefficients were obtained from Dilecce [1]. The steady state population of nitrogen states and relative emission intensity of bands were calculated by solving the respective system of equation presented in [6].

An example of the comparison of experimental and theoretical intensities of SPS and FNS bands is shown in figure 3. The intensities were normalized to SPS(0,0) band.
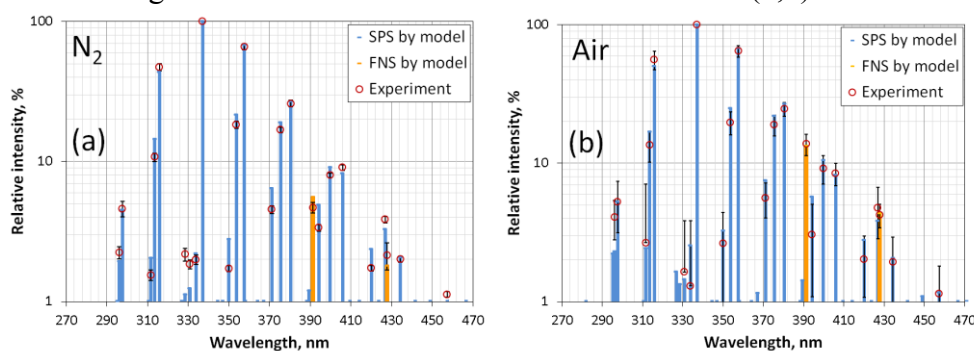
Fig. 3: Comparison of the relative intensities obtained by experiment and calculated by theoretical model for (a) N_2 at 15 Torr and 840 Td and (b) air at 15 Torr and 920 Td. Blue bars correspond to calculated intensity values of SPS and yellow bars to FNS. Experimental intensities are shown as red points with black error-bars.

In the limits of uncertainty the calculated intensities coincided with the measured intensities for transitions from $N_2(C\,^3\Pi_u, v=0)$ state. For transitions from $N_2(C\,^3\Pi_u, v=1\text{-}2)$ states the measured intensities were systematically lower than calculated intensities but the difference didn't exceed 20 %. This difference remains close to the measurement uncertainty when we take into account dispersion of data for calculation of EEDF and excitation rate constants. The relative intensities of bands originating from higher vibrational states remained below 5% where the measurement uncertainty became too large. For $N_2(C\,^3\Pi_u)$ states the dispersion of collisional quenching rate coefficients from different authors is less than our measurement uncertainty and the variation of quenching coefficients had minor effect on the calculation results. The available data for quenching rates of $N_2^+(B\,^2\Sigma_u^+, v=0)$ state differ up to 2-4 times and have much bigger impact on the results. Our calculated theoretical intensities had best coincidence with experimental intensities when the quenching rate coefficients determined with LIF method proposed by Dilecce [1] were used. Accounting the vibrational relaxation (cascade processes) [6] had only a small effect (less than 1%) on the intensity ratio of FNS and SPS bands.

Dilecce et al. [1] have highlighted that the quenching rates available in the literature have a clear dependence on the excitation method of $N_2^+(B\,^2\Sigma_u^+, v=0)$. The selective excitation methods (LIF) result in consistently higher quenching rate coefficients while methods based

on the pulsed discharge give smallest, up to 3 times lower values for these coefficients. Possible reasons for the smaller quenching rates obtained in the latter case could be continued electronic excitation or cascade from higher vibrational levels during the decay phase [1,7]. In our previous work [7], the duration of the excitation phase was sufficiently short to exclude the first effect. As concerning the cascade effects, there is no data available concerning the vibrational relaxation in $N_2^+(B\,^2\Sigma_u^+)$ manifold. However, our calculations showed that the relative population of the state v = 1 was more than an order of magnitude smaller than the population of v = 0 due to much smaller excitation cross-section and larger quenching rate coefficients. The population of higher levels was even smaller. As a consequence, the cascade effects should also have only a minor effect in the determination of quenching rate coefficients as well as in the population of the $N_2^+(B\,^2\Sigma_u^+, v=0)$ state.

Regardless of the cause of the differences between the quenching rate coefficients, it is reasonable to assume that the value of the quenching rate constant obtained under conditions of the current experiment should be the most suitable. However, the best coincidence was achieved with the coefficients determined by selective excitation method which had about 3 times higher values than coefficients determined by pulsed discharge method [7] under the conditions of the present experiment.

4   Conclusions

The emission spectra of nitrogen and air non self-sustaining Townsend discharges under different reduced electric field and pressure values were measured. The experimental spectra were reproducible in wide range of *E/N* and pressure, in air and pure nitrogen, with a simple collisional-radiative model where electron excitation rates of $N_2(C\,^3\Pi_u)$ and $N_2^+(B\,^2\Sigma_u^+)$ states were calculated with EEDF obtained by BOLSIG+ and de-excitation was calculated with Einstein coefficients and collisional quenching rate coefficients determined with LIF method [1]. Possible reasons for smaller values of $N_2^+(B\,^2\Sigma_u^+)$ collisional quenching rate coefficients obtained with the pulsed discharge method were discussed and reasons like cascading, or electron excitation, were argued to be of minor importance. The question about the dependence of collisional quenching rate coefficients for $N_2^+(B\,^2\Sigma_u^+)$ on the method of determination remains still open.

References
1. G. Dilecce, Plasma Sources Sci. Technol. 23, 015011 (2014)
2. P. Paris et al., J. Phys. D: Appl. Phys. 38, 3894 (2005)
3. G. J. M. Hagelaar et al., Plasma Sources Sci. Technol. 14, 722 (2005)
4. T. Tabata et al., Atomic Data Nucl. Data Tables 92, 375 (2005)
5. D. E. Shemansky et al., J. Geophys. Research 110, A07307 (2005)
6. G. Dilecce et al., Plasma Sources Sci. Technol. 16, S45 (2007)
7. F. Valk et al., J. Phys. D: Appl. Phys. 43, 385202 (2010)

EFFECTS OF PULSE VOLTAGE WAVEFORMS ON FAST GAS HEING IN AN ATMOSPHERIC PRESSURE STREAMER DISCHARGE: COMPARISON BETWEEN EXPERIMENTS AND NUMERICAL SIMULATION

A. Komuro, K. Takahashi, A. Ando

Department of electrical engineering, Tohoku University, 6-6-05Aramaki-Aza-Aoba, Aoba-ku, Sendai, Miyagi, Japan

E-mail: komuro@ecei.tohoku.ac.jp

Gas heating in an atmospheric pressure streamer discharge is one of the fundamental processes of atmospheric pressure plasma and it closely relates to the efficiency of radical productions. Understanding of the relation between applied pulse voltage waveforms and the fast gas heating phenomenon lead to improve the various applications of atmospheric pressure plasma. Schlieren visualization shows that the shock wave is produced by a streamer discharge and its strength was changed by the pulse voltage waveforms. Through the comparison between the experimental results and simulation results, the mechanism of gas heating is discussed.

Keywords: streamer discharge; numerical simulation; shock wave; fast gas-heating; chemical reaction

1   Introduction

Gas heating in atmospheric pressure plasmas is one of the important characteristics that influence the development of the discharge itself and the following by reducing the neutral gas density which changes the reduced electric field [1, 2]. In addition, an increase in gas temperature can affect the rate of chemical reactions and can induce turbulence phenomena starting from an initial laminar gas flow [3]. The studies of gas heating has been conducted by many researchers [4, 5], however, the interaction between the pulse voltage waveforms and the degree of gas heating has not been clearly elucidated yet. In this study, we performed both experimental and numerical works to understand the gas heating phenomenon and its relation with the pulse voltage waveform.

2   Experimental setup

Fig. 1 (a) shows the electrical circuit for generating a pulsed discharge. The charge stored in the capacitor is discharged using the spark gap switch. By changing the delay time between the LED trigger and the discharge pulse, a temporal variation of schlieren image is observed. Fig. 1 (b) shows the electrode configuration of the discharge reactor. The anode consists of 5 stainless needles which are arranged at 4 mm intervals. The gap between the anode and the cathode is 13 mm. The experimental setup for shlieren visualization is shown in Fig. 1(c). The Schlieren optical system is arranged with a gleen-color LED light source (OSRAM, LE-T-Q9WP), digital CMOS camera (Nikon, D5500), and two plano-convex lenses whose diameters and focal lengths are 50.8 mm and 1,000 mm, respectively.

3   Simulation model
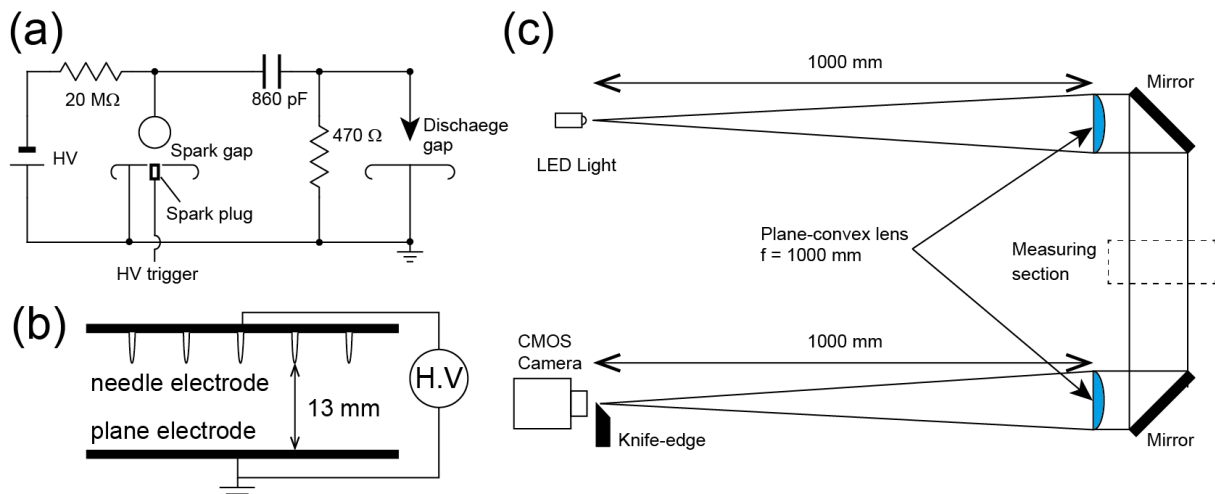
Fig. 1: (a) High voltage pulse generator circuit, (b) electrode configuration and (c) experimental setup for schlieren visualization.
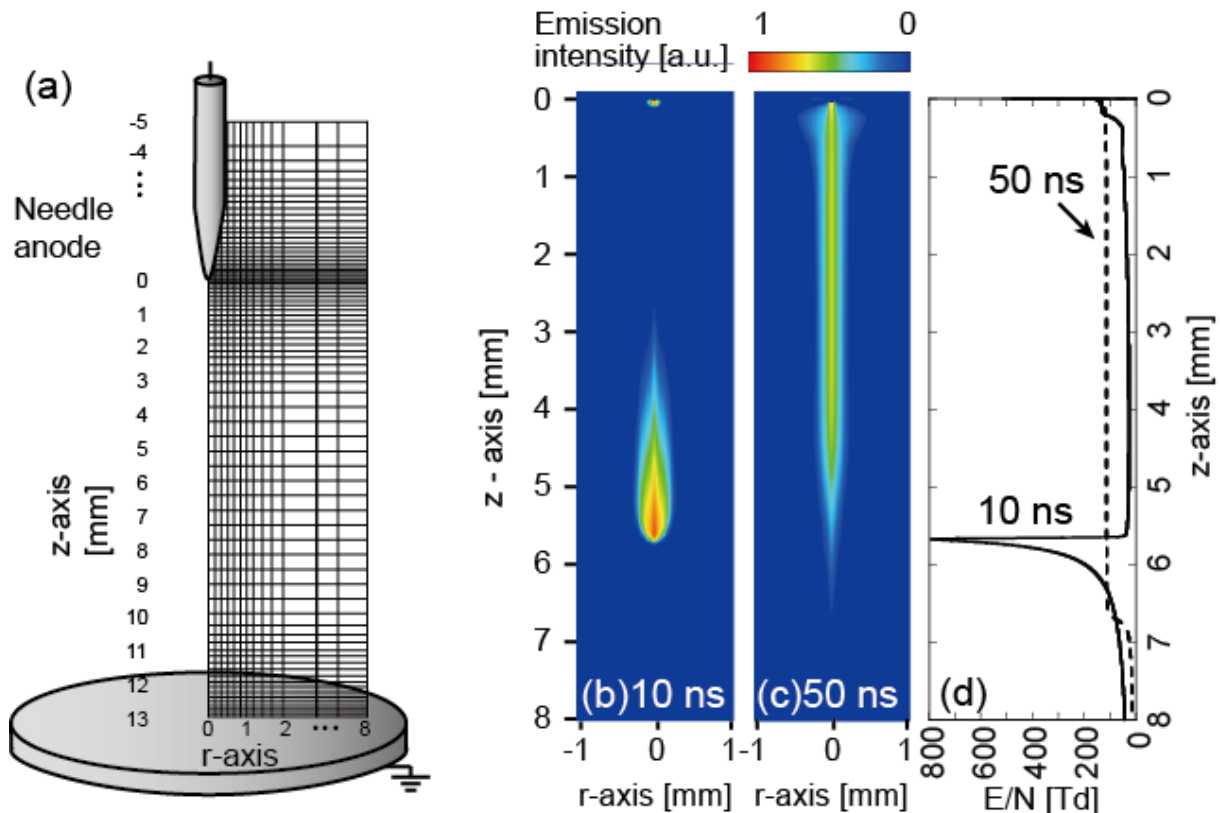
Fig. 2: (a) Schematic view of the calculation domain and mesh, (b) cross sectional views of instantaneous flux of photons emitted from $N_2(C^3\Pi_u)$ for a horizontal line of sight in $O_2(20\%)/N_2$ discharge at time t = 2 ns, (c) at t = 50 ns and (d) the corresponding axial distribution of reduced electric field (*E/N*) at each time.

The streamer model equations used in the present study consist of drift-diffusion equations for the electrons and ions and Poisson's equation. The transport and source parameters that involve electrons are calculated using the Bolsig+ solver [6] with published e-V cross sections [7]. A chemical reaction model that includes electron-impact collisions (excitation, ionization,
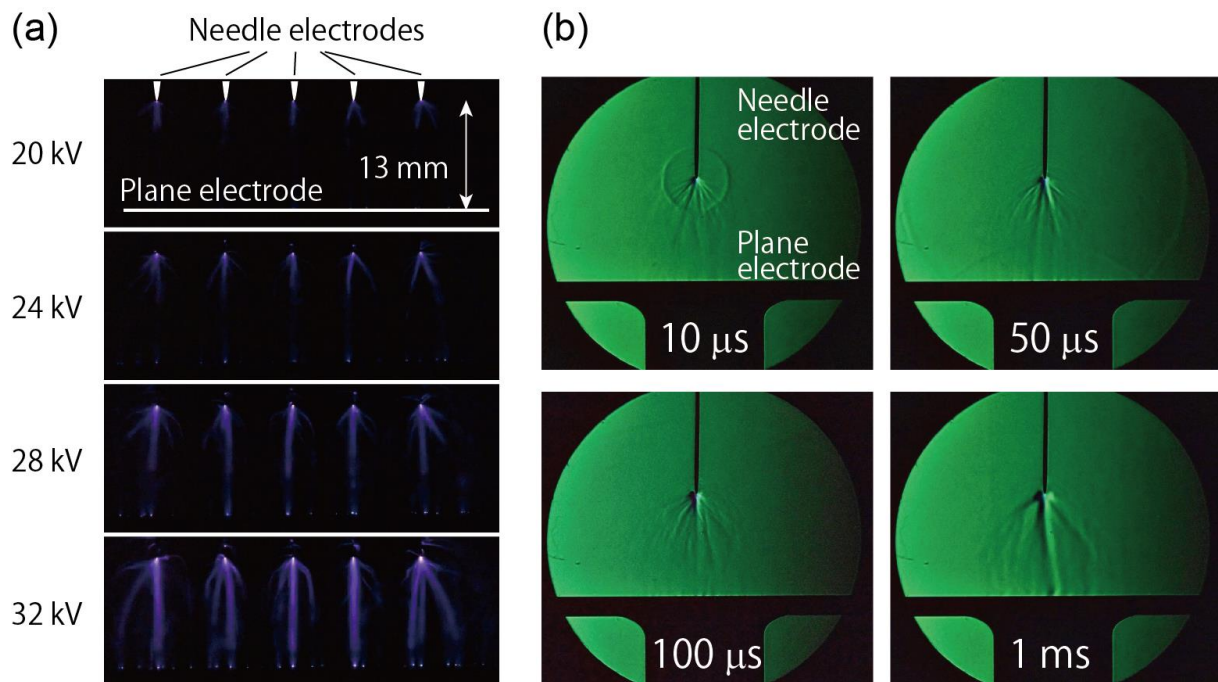
Fig. 3: (a) Time integrated photographs of streamer discharges in a 13 mm gap in air at atmospheric pressure at various peak pulse voltages and (b) temporal variation of schlieren images for 24 kV applied voltage.
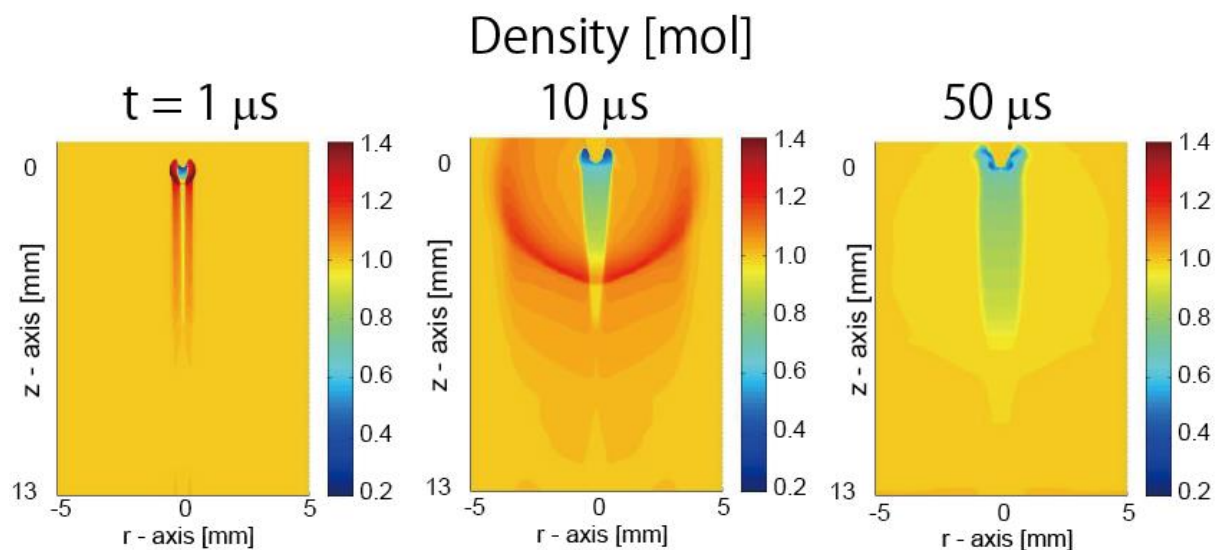
Fig. 4: Contour plot of the simulated gas density after the discharge (from 1 to 100 μs).

dissociation, recombination, attachment, and detachment), ion recombination, and the reactions of neutrals is used. The reactions considered here are described in detail in our previous paper [8, 9]. The Euler equation is coupled with the chemical reaction model and is solved to simulate the neutral gas flow. Photoionization is taken into account through three-exponential Helmholtz models. In this paper, the gas composition is set to be dry air at atmospheric pressure. The electrode geometry is a point-to-plane configuration with a gap of 13 mm as shown in Fig. 2 (a) which corresponds to the dimensions of the experimental setups. Fig. 2 (b) and (c) show the cross sectional views of instantaneous flux of photons emitted from $N_2(C^3\Pi_u)$ for a horizontal line of sight in $O_2(20\%)/N_2$ discharge at (b) time $t = 2$ ns and at (c) $t = 50$ ns. Fig. 2 (d) shows the axial distribution of reduced electric field

(E/N) at each time which is corresponding to the condition in Fig. 2 (b) and (c). Computational time step is fixed to 0.25 ps during 200 ns and then it is gradually increased up to 80 ps for coupling the discharge phenomenon with the gas fluid phenomenon. Details of the model equations, the numerical algorithms, and the computation acceleration techniques used in our study can be found in our previous reports [2].

4   Results and Discussion

Fig. 3 (a) shows time integrated photographs of streamer discharges. The peak voltages of applied pulse which are written in the left side of the photographs were changed by the charging voltage of the capacitor. The length of the streamer discharge gradually increases as the peak voltage increases. Fig. 3 (b) shows the schlieren images at time 10, 50, 100, 1000 μs after the discharges. At t = 10 μs, the spherical shapes which seems to be a shock wave is clearly observed. After expanding the spherical wave, the contrast of the streamer channel gradually increased. This phenomenon is already experimentally observed in [10]. Fig. 4 shows the temporal variation of the simulated gas density after the discharge. The spherical shock wave is observed at t = 10 μs. After the expanding of the shock wave, the gas density in the streamer channel decreases. As shown in Fig. 3 and Fig. 4, our simulation model qualitatively reproduces the experimental results. Now we are preparing both schlieren visualization and its simulation with various voltage waveforms. The results will be shown in this presentation.

5   Conclusion

In this study, we performed both experimental and numerical works to understand the gas heating phenomenon and its relation with the pulse voltage waveform. The schlieren visualization shows that the spherical shock wave is produced by a streamer discharges and its numerical simulation qualitatively reproduces the phenomenon. In this presentation, we will show the result of schlieren visualization and its numerical simulation with various voltage waveforms and discuss the results.

References

1. R. S. Sigmond, J. Appl. Phys. 56, 1355 (1984)
2. A. Komuro et al., J. Phys. D: Appl. Phys. 47, 155202 (2014)
3. M. Meziane et al., Int. J. Plasma. Environ. Sci. Technol. 6, 98 (2012)
4. F. Tholin et al., J. Phys. D: Appl. Phys. 46, 365205 (2014)
5. N. A. Popov, J. Phys. D: Appl. Phys. 44, 285201 (2011)
6. G. J. M. Hagelaar et al., Plasma Souces Sci. Technol. 14, 722 (2005)
7. Phelps database, www.lxcat.net, retrieved on March 30, 2016
8. A. Komuro et al., J. Phys. D: Appl. Phys. 45, 265201 (2012)
9. A. Komuro et al., J. Phys. D: Appl. Phys., 46, 175206 (2013)
10. R. Ono et al., Jpn. J. Appl. Phys. 43, 321 (2004)

ABSOLUTE OH DENSITY MEASUREMENTS IN SURFACE MICRO-DISCHARGE IN HE+H₂O AND AR+H₂O MIXTURES

D. Li[1,2], A. Nikiforov[2], N. Britun[3], R. Snyders[3,4], M. G. Kong[1,5,6], C. Leys[2]

[1]*State Key Laboratory of Electrical Insulation and Power Equipment, Center for Plasma Biomedicine, Xi'an Jiaotong University, Xi'an 710049, People's Republic of China,* [2] *Department of Applied Physics, Research Unit Plasma Technology, Ghent University, Sint-Pietersnieuwstraat 41, Ghent B-9000, Belgium*
[3] *Chimie des Interactions Plasma-Surface (ChIPS), CIRMAP, Universite de Mons, 20 Place du Parc,B-7000 Mons, Belgium*
[4]*Materia Nova Research Centre, Parc Initialis, B-7000 Mons, Belgium*
[5] *Frank Reidy Center for Bioelectrics, Old Dominion University, Norfolk, Virginia 23508, USA*
[6]*Department of Electrical and Computer Engineering, Old Dominion University, Norfolk, Virginia 23529,USA*

E-mail: anton.nikiforov@ugent.be

In this work, an array surface micro-discharge in He/Ar+H₂O, operating at peak-to-peak voltage of 14kV is investigated. The absolute OH density and its temporal-and-spatial dynamics are detected by broadband UV measurement and laser-induced fluorescence (LIF) spectroscopy. The absolute density of OH is about 10^{21}m^{-3} for Ar+H₂O mixture and about 10^{19}m^{-3} for He+H₂O mixture. The OH density reaches peak at 0.05% H₂O in Ar+H₂O.

Keywords: surface discharge; laser-induced fluorescence; absorption spectroscopy; hydroxyl radicals

1 Introduction

Atmospheric pressure non-equilibrium plasma has been widely used in many fields like biomedical applications, wastewater treatment and micro-chemical analysis systems [1,2]. Compared to low-pressure plasmas it is operating without expensive and size limited vacuum systems. Surface discharge is one type of atmospheric pressure non-equilibrium plasmas. It commonly consists of a plane HV electrode, a striped grounded electrode and a dielectric sheet sandwiched between the electrodes. Recently, a novel different structure of surface discharge source with mesh-array grounded electrode has been strongly investigated [2,3]. In this work, we used a hexagonal shape of mesh-array electrode to enhance plasma stability and spreading of the plasma over the whole area of the grounded electrode [3]. The plasma is generated on the surface of dielectric sheet near the grounded electrode, and it induces production of reactive species such as the OH radical in the gas phase which is transferred to treated materials far away from the grounded electrode.

Due to its high oxidation potential, OH is considered to play an important role in some applications like environmental remediation and biomedical treatment [1,3]. Therefore, it is meaningful to study OH density with high temporal and spatial resolution.

2   Experimental

In this work, an array surface discharge setup is used. The schematic diagram of the experimental setup is shown in FIG.1. The HV electrode is made of an aluminum plate of 4×4 cm^2, and the grounded electrode consists of a stainless steel mesh. Each mesh element has a hexagon shape, with sides of 4 mm in length, 0.76 mm in width and 0.5 mm in thickness. The sine power is applied with frequency of 20 kHz and peak-to-peak amplitude of 14 kV. To mix water vapour with gas, a homemade bubbler system is used. Two mass flow controllers (MKS instruments 4000) are employed to mix a flow of pure helium/argon and helium/argon saturated with water vapour. The total flow rate is fixed at 4 slm in all experiments. Broadband UV absorption measurement and laser-induced fluorescence (LIF) spectroscopy are applied to measure OH density and its temporal and spatial dynamics.
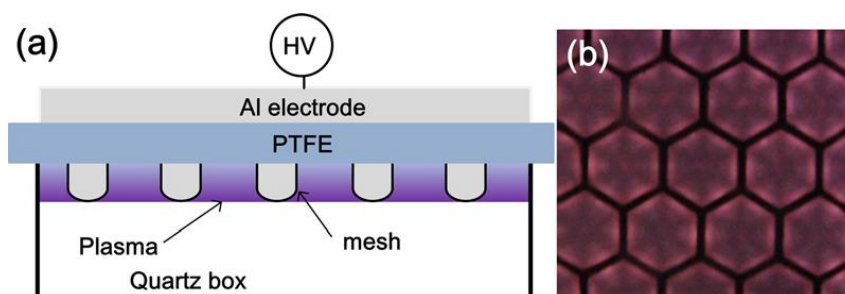
Fig. 1: Array of surface-confined plasmas with (a) its electrode unit; (b) 2.4×2.4 cm^2 area of an end-on image in helium.

3   Results and Discussion

From the discharge emission detection and LIF measurement, it is found that the level of OH(A) emission follows the discharge pulse, whereas OH(X) maintains the same level during the whole period of discharge, as it is shown in FIG.2. It indicates that OH(X) density is constant in each discharge cycle and life time of OH(X) radicals is longer than 50 μs which is duration of the applied voltage cycle shown in FIG.2.
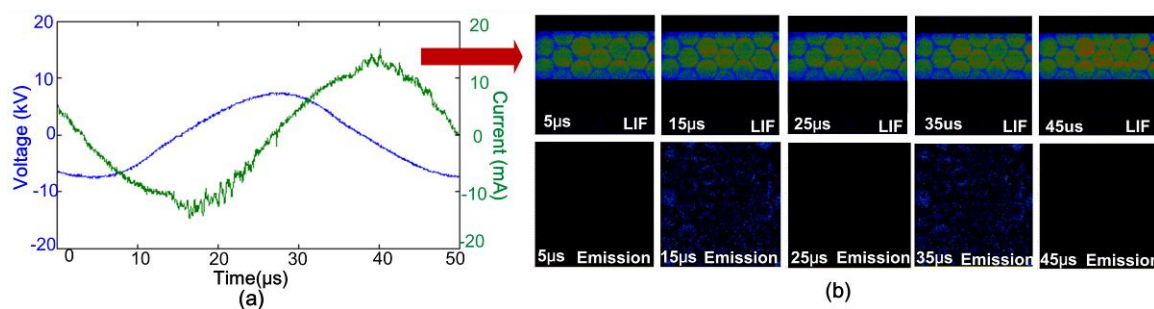
Fig. 2: Current-voltage characteristics in Ar+0.025%H$_2$O (a) the corresponding LIF images and 309nm emission images (b).

As found in the measurement, the decay time of LIF signal of excited states of OH (a) decreases with the increasing water concentration. This is explained by the fact that increasing water concentration enhances OH(A) quenching. Also the LIF measurement of the decay time allows estimating the impurity of air in the discharge. It is found that air impurity increases with the distance from the grounded electrode and it reaches its peak at 2 mm, after which it maintains a value around 0.45%.

In the broadband UV absorption measurement, the line integrated absorption of $P_1(2)$ rotational line is used for detection. With this line absorption, the Beer-Lambert law is used to determine OH density. Before that, the rotational temperature should be known, which is evaluated by fitting the emission of the OH(A-X) spectrum. As it is shown in FIG.3 the rotational temperature in Ar+H2O is about 20 Kevin higher than that in He+H2O but still very close to room temperature leading to possibility use the source in targeting biomedical application.
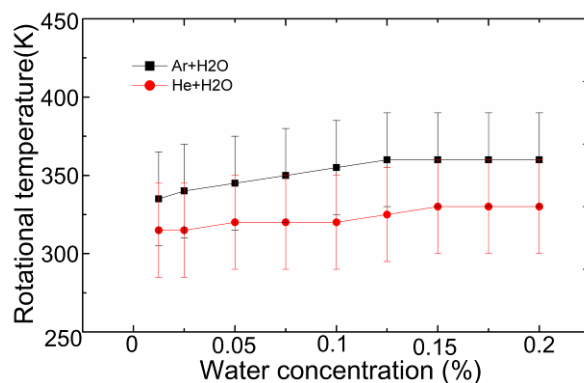
Fig. 3: Rotational temperature with increasing water concentration in the mixture of He+H_2O and Ar+H_2O

Based on broadband UV absorption of $P_1(2)$ line the absolute density of OH is $10^{21}m^{-3}$ for Ar+H_2O mixture and $10^{19}m^{-3}$ for He+H_2O mixture. We want to emphasise that an almost 20 times higher density is detected in Ar+H_2O discharge in comparison with He+H_2O in optimized mixtures with H_2O. This is significantly higher than what has been reported in the volume dielectric barrier discharge [4]. As noted in [4,5], the reason for the difference of OH density might be an increased role of metastables dissociation and charge exchange. We found that OH density keeps rising with increasing water concentration and it reaches its peak at 0.05%. Thereafter, the OH density starts to decrease. In the production of OH, the H_2O is a main precursor for OH. The increase of H_2O can help to enhance reactions like electron dissociation and dissociative attachment. However, H_2O is also an electronegative gas and it can weaken the discharge. When the H_2O concentration is too high, the discharge properties are changed due to presence of electronegative gas leading to a decrease of OH production.

4   Conclusion

In this work, broadband UV absorption measurement and laser-induced fluorescence (LIF) spectroscopy are used to measure OH density and its temporal and spatial dynamics in an array surface micro-discharge. The level of OH(A) emission follows the discharge pulse, but OH(X) maintains the same level during the whole period of discharge. The absolute density of OH is about $10^{21}m^{-3}$ for Ar+H_2O mixture and about $10^{19}m^{-3}$ for He+H_2O mixture and strongly depends on H_2O admixture. Ground state OH density is about 20 times higher in Ar+H_2O than that in He+H_2O. The density of OH reaches its peak at 0.05% H_2O in Ar+H_2O.

References
1. T. von Woedtke et al., Phys. Rep. 530 (4), 291-320 (2013)
2. T. Shibata et al., J. Phys. D. Appl. Phys. 47 (10) 105203 (2014)
3. M. Laroussi, IEEE Trans. Plasma Sci., 37(6):714-725 (2009)
4. G. Dilecce et al., Plasma Phys. Control. Fusion 53, 124006 (2011)
5. M. Miclea et al., J. Phys. D: Appl. Phys. 38 (11), 1709-1715 (2005)

TALIF MEASUREMENT OF ATOMIC HYDROGEN DENSITIES IN A COPLANAR SURFACE DIELECTRIC BARRIER DISCHARGE

M. Mrkvičková, J. Ráheľ, P. Dvořák, D. Trunec, T. Morávek

Department of Physical Electronics, Faculty of Science, Masaryk University,
Kotlářská 2, Brno 611 37, Czech Republic

E-mail: martinamrkvickova@gmail.com

The difficulties of employing two-photon absorption laser induced fluorescence (TALIF) technique for determination of atomic concentrations in close proximity of dielectric surface was successfully addressed. We present our experience from measurement of atomic hydrogen concentration in a coplanar surface dielectric barrier discharge.

Keywords: TALIF; surface DBD; atomic hydrogen

1   Introduction

Surface dielectric barrier discharges (DBDs) have been widely used for plasma treatment of solid surfaces or ozone generation. For development of efficient plasma sources, the knowledge of generated reactive species controlling the desired plasma processes is highly advantageous. However, determination of reactive species concentration in surface DBDs is a challenging task due to the low thickness of active discharge zone situated in the closest vicinity of the dielectric surface.

Suitable method for atomic concentrations measurement is two-photon absorption laser induced fluorescence (TALIF). The principle of the method is the excitation of diagnosed atoms in the ground state via simultaneous absorption of two laser photons and observing of the consequent fluorescent radiation. This fluorescent radiation has an intensity proportional to the atomic concentration. Method is well-described e.g. in [1], for atomic hydrogen measurements it was used e.g. in [2].

In this contribution we focus on employing TALIF technique in the close proximity to the surface of coplanar DBD. The interaction between laser beam and the dielectric surface poses several problems. First, the contact of laser beam with the dielectric can lead to discharge artificial breakdown, therefore, care must be taken to make the TALIF method non-invasive. This can be solved by synchronizing laser excitation with the DBD voltage cycle, so the laser shots are taken at the lowest internal field, insufficient to initiate the artificial breakdown [3]. Second, the laser beam is scattered on the DBD surface and induces fluorescence of the dielectric material, which both leads to detection of redundant signal, often exceeding the actual signal of measured particles. We bring the solution of this problem and present our experience from successful measurement of atomic hydrogen concentration above the dielectric surface.
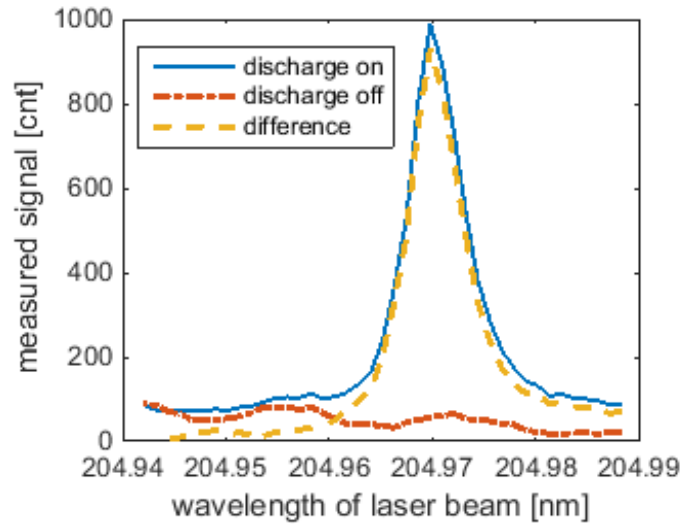
Fig. 1: Measured signal as a function of wavelength of the laser beam impinging the surface of coplanar DBD. Measurement with the discharge turned on (blue line) is compared with the measurement with the discharge turned off (red line), where the fluorescence of the dielectric can be seen. Difference of both signals (yellow line) should roughly correspond with the two-photon-absorption line of hydrogen atom. Displayed wavelengths are shifted approximately by 0.11 nm.

2 Problem solution

The problem of artificial breakdown was addressed by taking the measurements in the repetitive afterglow mode, where the magnitude of external voltage was insufficient to sustain development of artificial breakdown.

The problem with redundant signal was suppressed by a suitable choice of dielectric material for the DBD surface. We have proved successful to use quartz as a dielectric, because of its low UV absorption leading to low intensity of fluorescence of dielectric and smooth surface which minimizes scattering of the laser radiation to the detector. To minimize the contact of out-of-focus laser beam with the surface, we employed convexly curved surface.

Despite the use of silica, some amount of scattered light or a fluorescence of quartz was still detected when the laser beam touched its surface. This parasitic signal linearly depended on the energy of laser pulse. Therefore, following procedure was performed to distinguish the hydrogen fluorescence signal from other redundant signals. Besides a common dark frame S_{dark} measured without presence of any laser radiation, a detuned image $S_{detuned}$ was captured for each measurement. This signal $S_{detuned}$ was measured with the laser with similar value of energy, but detuned to wavelength that could not excite atomic hydrogen, while generating practically the same intensity of fluorescence of the dielectric. For our dielectric we selected the wavelength shifted by 20 pm from the center of hydrogen absorption line, with respect to the measurement demonstrated in the Fig. 1.

Pure fluorescence signal of hydrogen S can be calculated as

$$S = \left[S_{meas.} - S_{dark} - (S_{detuned} - S_{dark}) \cdot \frac{E_{L,meas.}}{E_{L,detuned}} \right] \cdot \left(1 + \beta E_{L,meas.}^2 \right) \tag{1}$$
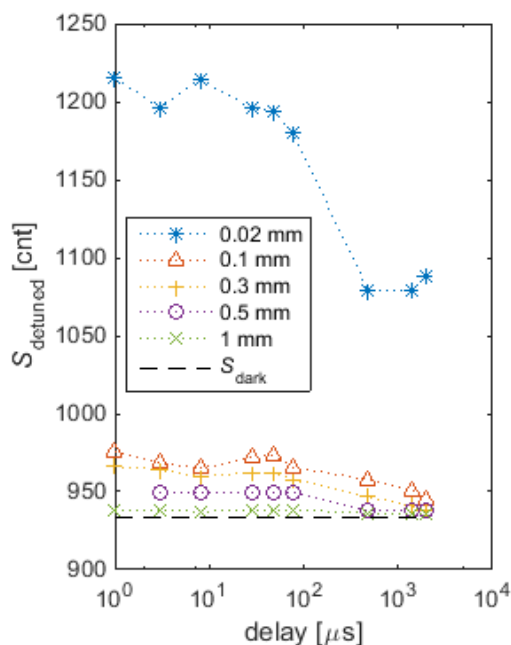
Fig. 2: Comparison of measured signals in a TALIF H measurement in surface DBD with laser tuned to or detuned from the centre of absorption line.
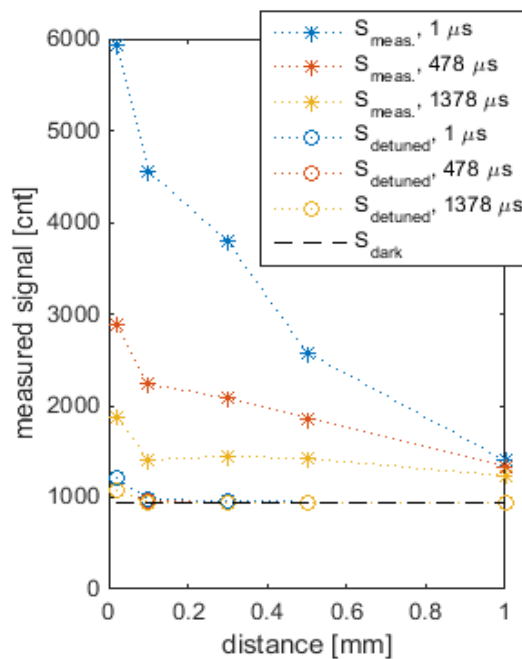
Fig. 3: Temporal development of signal with detuned laser in the DBD afterglow, in various positions above the dielectric.

where $E_{L,meas.}$ is the mean value of laser-pulse energies during the main (tuned) measurement, $E_{L,detuned}$ is the mean value of energies of detuned laser pulses. Expression $(1 + \beta E^2_{L,meas.})$ makes the correction of saturation effects: its meaning and determination is presented in [3] for single-photon laser induced fluorescence.

Fig. 2 and 3 show the comparison of signals measured with tuned or detuned laser for various times of discharge afterglow and various distances $(0.02 - 1 \text{ mm})$ from the dielectric surface. The signal with detuned laser accounted less than 20 % of the signal detected with laser tuned to absorption line, when measuring 0.02 mm above the dielectric surface. Laser diameter at the measurement point was less than 0.02 mm. For longer distances, the $(S_{detuned} - S_{dark})$ decreased to about 1 % of the $(S_{meas} - S_{dark})$. Fig. 3 shows temporal development of $S_{detuned}$ measured in the DBD afterglow. The signal slowly decayed in time. Possible explanation can be reducing the size of the dielectric during its cooling or changes of particles associated on the dielectric surface.

3 Atomic hydrogen concentration

Atomic hydrogen concentration was measured above the dielectric of coplanar surface dielectric barrier discharge in atmospheric pressure mixture of Ar + 2 % H2. The measurements were carried out in the afterglow phase of discharge powered by 33.33 kHz HV driving voltage. In the Fig. 4 we present some of our results: spatial distribution of atomic hydrogen concentration above one of powered electrodes at various time after the discharge extinction. The maximal concentration values reached 10^{22} m^{-3}. That value can be compared with results from atmospheric pressure volume DBD, where the concentration over 1021 m-3 was

measured [4]. The high concentration of hydrogen radicals in the coplanar surface barrier discharge is consistent with the fact, that the coplanar DBD produces thin discharge layer with high density of delivered power [5]. Our fit of concentration data by a numerical model described in [6] suggests, that the dielectric surface acts as a temporal source of atomic hydrogen in the afterglow phase.
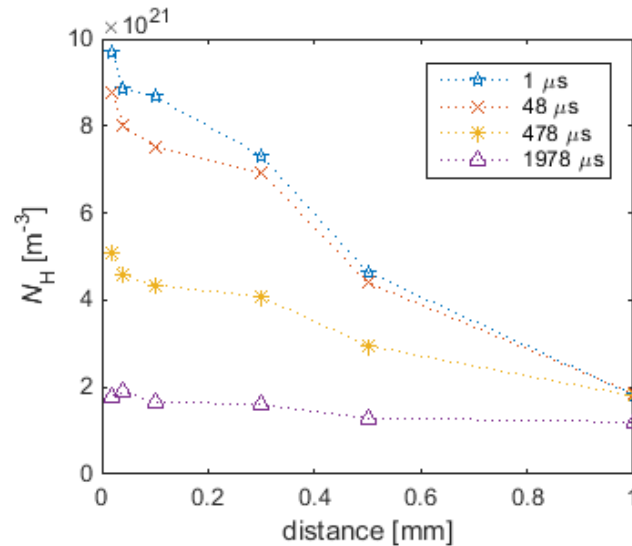
Fig. 4: Spatial distribution of atomic hydrogen concentration above one of the electrodes in the afterglow of the surface DBD. Concentrations are measured in various delays after the discharge extinction.

4   Conclusion

Concentration of atomic particles in the vicinity of dielectric surface of coplanar DBD can be investigated by TALIF measurement. Problems arising from the interaction between laser and the dielectric can be solved by a suitable choice of dielectric material and the proposed treatment of redundant signal.

References
1. K. Niemi et al., J. Phys. D: Appl. Phys. 34, 2330 (2001)
2. M. G. H. Boogaarts et al., Rev. Sci. Instrum. 73, 73 (2002)
3. J. Voráč et al., Eur. Phys. J. Appl. Phys. 71, 20812 (2015)
4. P. Dvořák et al., proposed to Plasma Sources Sci. Technol. (2016)
5. M. Černák et al., Plasma Phys. Control. Fusion 53, 124031 (2011)
6. M. Mrkvičková et al., submitted to Plasma Sources Sci. Technol. (2016)

ELECTRIC FIELD DEVELOPMENT IN γ-MODE RF APGD IN HELIUM

Z. Navrátil[1], R. Josepson[1], N. Cvetanović[2], B. Obradović[3], P. Dvořák[1]

[1]Department of Physical Electronics, Faculty of Science, Masaryk University, Kotlářská 2, 611 37 Brno, Czech Rep.
[2]Faculty of Transport and Traffic Engineering, University of Belgrade, Vojvode Stepe 305, 11000 Belgrade, Serbia
[3]Faculty of Physics, University of Belgrade, Studentski trg 12, 11001 Belgrade, Serbia

E-mail: zdenek@physics.muni.cz

Electric field strength in helium γ-mode RF (13.56 MHz) atmospheric pressure glow discharge was measured using Stark polarization spectroscopy. Time-correlated single photon counting was applied to record the temporal development of spectral profile of He I 492.2 nm line with a sub-nanosecond temporal resolution. Electric fields up to 32 kV/cm in the RF sheath, obtained from the fit of forbidden ($2\,^1P - 4\,^1F$) and allowed ($2\,^1P - 4\,^1D$) helium lines, are in agreement with the spatially averaged value of 40 kV/cm estimated from homogeneous charge density RF sheath model. The observed rectangular shape of the electric field time development is attributed to increased sheath conductivity by strong electron avalanches occurring in the γ-mode sheath at high current densities.

Keywords: radiofrequency discharge; atmospheric pressure; helium; electric field; Stark effect

1 Introduction

Non-thermal radio-frequency atmospheric pressure plasmas have become important tool for plasma treatment [1]. Homogeneous radio-frequency (13.56 MHz) atmospheric pressure glow discharge (α-mode RF APGD) can be obtained even using bare metal electrodes in helium, neon and argon [2-4]. The RF APGD transits into constricted γ-mode at higher RF power. The electric field in these discharges is mostly obtained by numerical modelling or estimated from the electrical measurements. The electric field of $1-5$ kV/cm was reported for α-mode helium discharge [4, 5]. Higher value (time-averaged 12 kV/cm) was calculated by 1D model in γ-mode RF sheath at current density of 106 mA/cm^2 [6]. In this work, electric field in γ-mode RF sheath was determined from the measurement of Stark splitting of helium 492.2 nm line profile [7]. This method has been already used for electric field measurement in atmospheric pressure helium barrier discharge [8].

2 Experimental

The RF APGD was generated between hemispherical bare metal electrodes inside a steel vacuum chamber. Brass electrodes, having 8 mm in diameter, were cooled by oil-cooling circuit. The discharge gap was 2 mm. The chamber was evacuated first down to 5 Pa by a rotary oil pump and then filled with helium (gas purity 5.0) up to atmospheric pressure. A gas flow of 200 sccm was kept constant during the measurement. The harmonic 13.56 MHz signal was generated by a function generator (Agilent 33220A) and amplified with RF power amplifier (Hüttinger TIS 0.5/13560). The amplitudes of AC voltage and current waveforms, measured by digital storage oscilloscope (LeCroy WaveRunner 6100A), were 240 V and 0.6 A, respectively.

The RF discharge was projected by a quartz lens onto a 20 μm optical slit with optical fibre located behind it. The slit was positioned into the maximal intensity of HeI 492.2 nm line at the driven electrode. A glass polarizer extracted the light polarized in the direction of the interelectrode axis. Temporally resolved measurement of helium HeI 492.2 nm line profile was performed by the method of time-correlated single photon counting (TCSPC, Becker & Hickl SPC-150 with PMT PMC-100-4). The photons were monochromatized by Jobin Yvon HR-640 monochromator (1200 gr/mm). Temporal resolution of 0.8 ns and spectral resolution of 0.075 nm were obtained with this setup.

3   Results and Discussion

The measured spectral profiles consisted of broad (tenths nm) and asymmetric allowed ($2\,^1P$ - $4\,^1D$) and forbidden ($2\,^1P$ – $4\,^1F$) helium lines. Whilst the role of Stark effect could be excluded, van der Waals and resonance broadening by helium ground state atoms broadened the allowed component only to FWHM of 0.06 nm. The broadening of the lines was therefore attributed to limited space resolution of the RF sheath (expected sheath thickness is approx. 50 μm) and to inclusion of components from different sheath regions into the measured profile. In order to determine the electric field, the measured profile was fitted by two pseudo-Voigt profiles for forbidden and allowed field-free non-shifted component with the wavelength distance related to the field strength [7].

The time development of electric field determined from the fit is plotted in Fig. 1 (black circles). The time development was almost rectangular with a maximum having approx. 30 kV/cm. As the spatial resolution was insufficient (as mentioned before), this value should be taken as the maximal electric field averaged over the RF sheath.
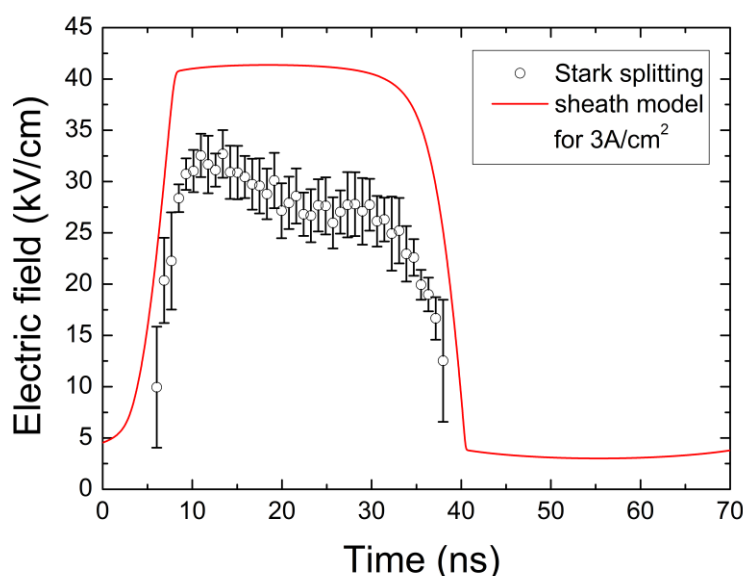
Fig. 1: Time-development of electric field strength at the driven electrode obtained from Stark splitting compared with the modelled spatially average electric field strength for total current density 3 A/cm². The average field strength is calculated as half the maximum value at the electrode.

In order to explain the observed development, homogeneous charge density model was used to calculate the electric field in the RF sheath. Neglecting the ion transport time through the sheath, current flowing from the electrode surface could be expressed as a sum of instantaneous components: displacement current, ion current and current of secondary electrons and electrons from the bulk plasma. Assuming total RMS current density j = 3 A/cm^2 according to the experiment, bulk electron density n_e = 10^{13} cm^{-3} [6] and secondary electron emission coefficient of the metallic electrode γ = 0.01, temporal and spatial development of the RF sheath was calculated. The average electric field value, taken as half of the maximal value at the electrode, is shown also in Fig. 1. It can be seen, that the experimental and calculated curves are in a relatively good agreement bearing in mind the difficulties of field measurement, current density determination, discharge non-uniformity and simplicity of the RF sheath model. The nearly rectangular shape of the electric field time development is caused by strong secondary avalanches crossing the γ-mode RF sheath at high current density. When the electric field is increased, secondary avalanches develop, increasing the sheath conductivity substantially. This prevents the sheath and the electric field from further growth.

4   Conclusion

The electric field in γ-mode RF APGD was determined both experimentally and numerically, reaching spatially averaged 30 – 40 kV/cm in the RF sheath at current density of about 3 A/cm^2. Although the results of both methods are in relatively good agreement, especially concerning the shape of the electric field waveform, numerical model expects higher maximal electric field (> 60kV/cm) at the electrode. Improvement of spatial resolution of the measurement is therefore necessary.

Acknowledgement

References

1. M. Laroussi et al., Plasma Process. Polym. 4, 777 (2007)
2. J. Park et al., J. Appl. Phys. 89, 20 (2001)
3. Z. Navrátil et al., Plasma Sources Sci. Technol. 23, 042001 (2014)
4. J. Laimer et al., Plasma Process. Polym. 3, 573 (2006)
5. T. Hemke et al., Plasma Sources Sci. Technol. 22, 015012 (2013)
6. J. Shi et al., IEEE Trans. Plasma Sci. 33, 624 (2005)
7. N. Cvetanović et al., J. Phys. D: Appl. Phys. 48, 205201 (2015)
8. B. M. Obradović et al., Appl. Phys. Lett. 92, 191501 (2008)

FLUID DYNAMICS IN ATMOSPHERIC-PRESSURE PLASMA JETS AND ITS IMPLICATIONS ON PLASMA CHEMISTRY

A. Obrusník[1], M. Gherardi[3], A. Stancampiano[3], E. Simoncelli[3], V. Colombo[3], L. Zajíčková[2]
[1]*Dept of Physical Electronics at Faculty of Science, Masaryk University, Brno, CZ*
[2]*Plasma Technologies at CEITEC, Masaryk University, Brno, CZ*
[3]*Dept of Industrial Engineering, Università di Bologna, Bologna IT*

E-mail: adamobrusnik@physics.muni.cz

This contribution investigates the gas dynamics in a helium atmospheric-pressure plasma jet. The model reproduces the formation of the laminar vortex which has previously been observed in Schlieren measurements. Additionally, the model takes into account heat transfer in the afterglow and evaporation of water from an aqueous substrate, so that the influence of evaporated water on the afterglow chemistry can be assessed.

Keywords: helium plasma jet; gas dynamics; afterglow chemistry; numerical simulation

1 Introduction

Atmospheric-pressure plasma jets (APPJs) have been subject to extensive investigations in the past years, mostly due to their potential biomedical (e.g. [1,2]) and material applications (e.g. [3]). The works focusing on the characterization of APPJs consist of either experimental ones, such as measurements of various active species [4], electron density [5], the electric field, or theoretical ones which employ numerical models in order to achieve deeper insight into the plasma sustainment mechanism [6], chemical reaction pathways [7] and gas dynamics phenomena.

This work complements the numerical studies of APPJs ignited in helium operating in ambient air by providing a model of gas dynamics which is coupled to a model of afterglow chemistry in an APPJ. Firstly, the work compares the gas dynamics simulations to Schlieren photography measurements presented earlier [8] and secondly, it illustrates the role of the non-uniform gas composition on the afterglow chemistry outside of the APPJ. The model also illustrates the role of water evaporation on the afterglow chemistry when the jet is in contact with a water-rich sample.

2 Model description

The numerical model that has been utilized has already been used and validated for different gas mixtures in argon atmospheric-pressure plasmas [9,10]. Most recently, it has also been utilized in a study on *E.coli* inactivation by a helium APPJ with air impurity, where it provided insight into the shape of the inactivation patterns and also helped to identify the key species responsible for the inactivation [11].

The model differs from the previously published versions in several aspects. As opposed to the argon/air models the transport properties of the components (helium/air) had to be

changed and a term corresponding to the buoyant force had to be added to the Navier-Stokes equation, so that it takes the form:

$$\rho_m(\mathbf{u} \cdot \nabla)\mathbf{u} = \nabla \cdot \left[\mu_m\left(\nabla\mathbf{u} + (\nabla\mathbf{u})^T\right) - \frac{2}{3}\mu_m(\nabla \cdot \mathbf{u})\right] + \rho_m\mathbf{g} \qquad (1)$$

where, ρ_m is the mixture density, μ_m is the mixture viscosity, $\mathbf{g}$ is the gravitational acceleration and $\mathbf{u}$ is the mixture velocity. Because the gas mixture is non-uniform and helium mixes with air outside of the plasma jet, μ_m and ρ_m are functions of the local gas composition. The local gas composition is obtained by solving two diffusion equations, one for the mass fraction of helium and one for the mass fraction of water vapour which is produced at jet-liquid interface. At this interface, the partial pressure of water is prescribed according to the empirical Antoine equation

$$\log_{10}(p_{H2O}[\text{Torr}]) = 8.07 - \frac{1730}{233.4 - T[°C]} \qquad (2)$$

The afterglow chemistry part of the model solves a transport-reaction equation for each of the 15 active species that have been considered (O, N, $O_2(^1\Delta)$, H, O_3, OH, HO_2, NO_2, NO_3, $O_2(^1S)$, NO, He*, N_2^+, H_2O^+, N^+) and which enter in total 127 reactions. The model assumes no electron-impact processes in the afterglow which is a rather strong approximation in some types of APPJs but qualitative insight into the processes is still possible. The reaction scheme was simplified from a comprehensive 0D model by Murakami *et al.* [7].

3   Results and Discussion

With regard to the gas flow in helium APPJs, the buoyant force is of key importance. Figure 1 shows the formation of a laminar vortex which is formed when a downward-facing helium jet impedes a planar surface, representing the treated sample. It is observed that a laminar vortex is formed in the proximity of the planar surface, which is a consequence of the sudden change of intertia of the helium stream and the buoyant force acting on it. Figure 1 also shows that the
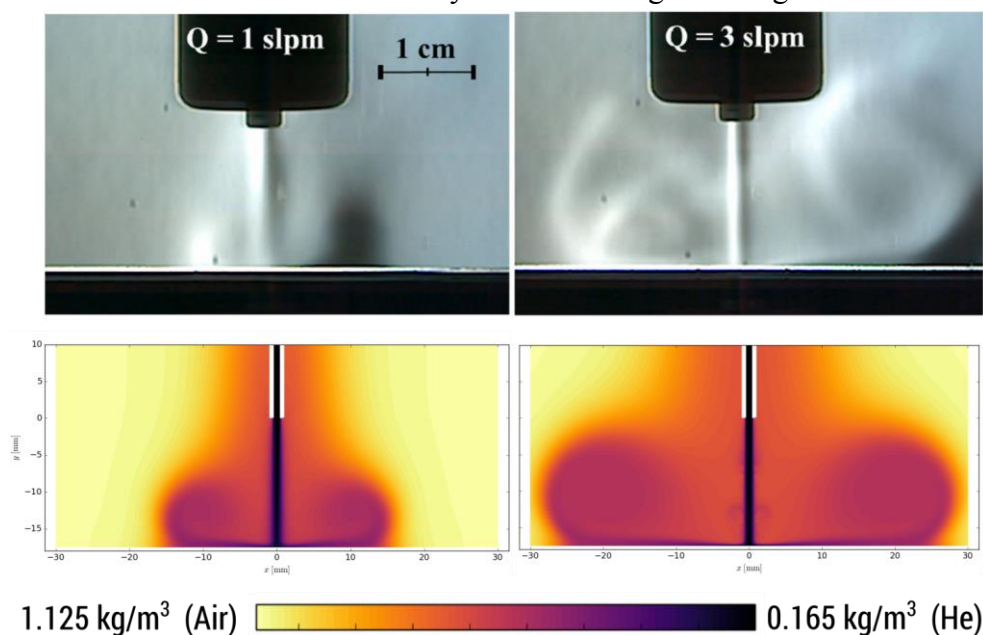
Fig. 1: Comparing Schlieren photography at two different flow rates of helium (above) with simulated mixture density (below) at same conditions – nozzle-sample distance of 18 mm, flow rates 1 slpm and 3 slpm respectively, laminar regime. Images are in the same scale, experimental data taken from [8]

size of the laminar vortex increases with the flow rate of helium through the jet and this was confirmed both in the simulation and in Schlieren measurements.

Additionally, the model allows us to study evaporation of water from the liquid surface and its influence on the afterglow chemistry. The two most important pathways, that the presence of water in the afterglow enhances, is the formation of nitric acid HNO_3 in the reaction

$$3NO_2 + H_2O \rightarrow 2HNO_3 + NO \tag{3}$$

And formation of nitrite NO_2^- and nitrate NO_3^-. In figure 2, we compare the molar fraction of water in the afterglow with solid and aqueous substrates. In this figure, it was assumed that the temperature at the nozzle outlet the afterglow is 40°C. In figure 3, the ratio of the rate of reaction (3) with and without the aqueous sample is plotted, showing that the reaction rate is increased by up to a factor of four.
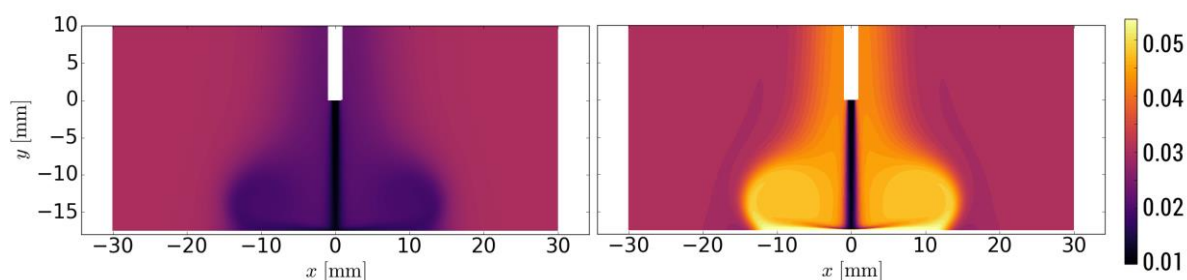
Fig. 2: Mole fraction of water with non-aqueous (left) and aqueous (right) sample exposed to the jet.
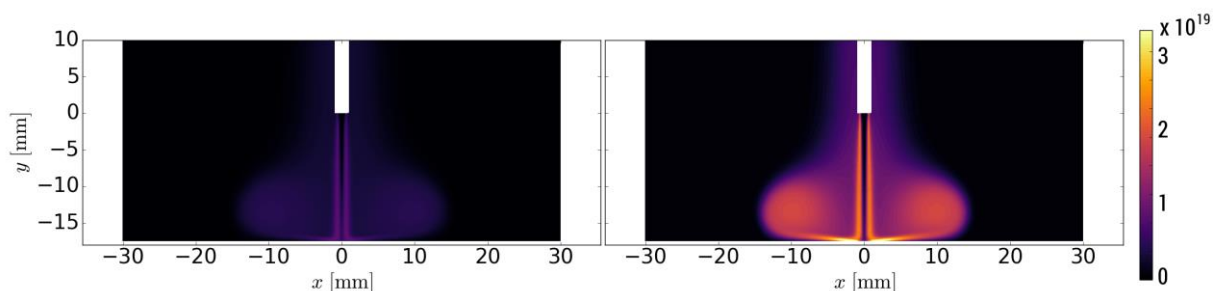
Fig. 3: Production rate of HNO_3 in the afterglow in $[1/(m^3 s)]$ with non-aqueous (left) and aqueous (right) sample exposed to the jet.

References

1. M. Laroussi, Plasma Process. Polym. 11, 1138 (2014)
2. X. Han et al., Eur. Phys. J. D 68, 46 (2014)
3. E. J. Szili et al., Plasma Process. Polym. 8, 38 (2011)
4. K. Niemi et al., Plasma Sources Sci. Technol. 20, 055005, (2011)
5. S. Hübner et al., Plasma Sources Sci. Technol. 24, 054005 (2015)
6. X. Y. Liu et al., Plasma Sources Sci. Technol. 23, 035007 (2014)
7. T. Murakami et al., Plasma Sources Sci. Technol. 23, 025005 (2014)
8. M. Boselli et al., Plasma Chem. Plasma Process. 34, 853 (2014)
9. J. Voráč et al., Plasma Sources Sci. Technol. 23, 25011 (2014)
10. P. Synek et al., Plasma Sources Sci. Technol 24, 025030 (2015)
11. K.-P. Arjunan et al., submitted to Plasma Processes and Polymers (2016)

SURFACE CHARGE MEASUREMENTS ON TRANSPARENT DIELECTRICS IN DIFFUSE AND FILAMENTARY BARRIER DISCHARGES

R. Tschiersch[1], S. Nemschokmichal[1], M. Bogaczyk[2], J. Meischner[1]

[1]*Institute of Physics, University of Greifswald, Felix-Hausdorff-Str. 6, 17489 Greifswald, Germany*
[2]*Leibniz Institute of Plasma Sci. and Technol., Felix-Hausdorff-Str. 2, 17489 Greifswald, Germany*

Email: robert.tschiersch@uni-greifswald.de

This work reports on the realization of surface charge measurements on transparent dielectrics that are frequently used in barrier discharge (BD) configurations. The method is based on the electro-optic Pockels effect of a bismuth silicon oxide (BSO) crystal covered with different transparent dielectrics, such as borosilicate glass, mono-crystalline magnesia or alumina which are known to have different secondary electron emission (SEE) coefficients. This advanced surface charge diagnostics was applied to diffuse and filamentary BDs, and the influence of using different dielectrics on the discharge development was carried out.

Keywords: barrier discharge; surface charges; transparent dielectrics; secondary electron emission

1   Introduction

The spatial surface charge distribution and its dynamics have significant influence on the general mechanism of barrier discharges (BDs), e.g., favoring the periodic discharge (re-) ignition (surface memory effect) as well as the discharge distinction [1,2], conserving the stability of laterally patterned BDs [3,4] and single discharge filaments, and acting as a source of weakly bound seed electrons that drive on the pre-ionization [5,6]. Mainly, this fundamental knowledge about the role of surface charges has been gained using the electro-optic Pockels effect of a bismuth silicon oxide (BSO) crystal. Although this method is already well-established, up to now it has been restricted to the BSO crystal exposed to the discharge. The present work achieves the next level by making this powerful method accessible to various transparent dielectrics which are commonly used for the operation of diffuse and filamentary barrier discharges, and which are most relevant from the theoretical point of view regarding plasma-surface interaction [7].

2   Discharge configuration and operating conditions

Figure 1(a) is a sketch of the concentric plane-parallel electrode configuration. The upper dielectric is a glass plate coated with an electrically conductive and transparent ITO layer.
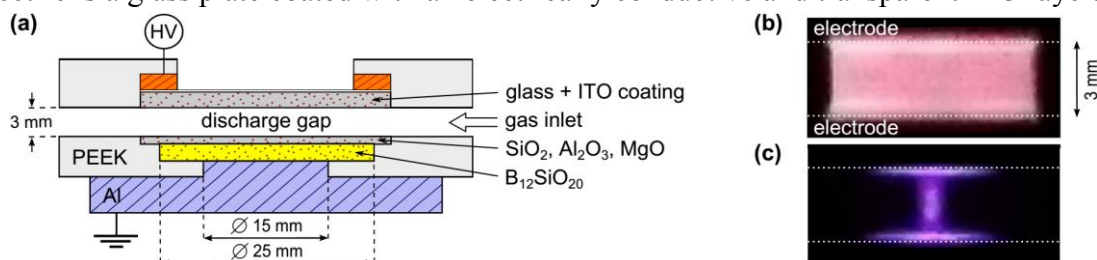
Fig. 1: Side-view of the discharge cell configuration (a) and photographs averaged over several breakdowns of a diffuse BD in He (b) and a self-stabilized discharge filament in He with 10% N_2 admixture (c), respectively.

This allows both the connection to the HV supply as well as the surface charge diagnostics from above. A 0.2 mm thin plate consisting of borosilicate glass, mono-crystalline magnesia, or alumina, respectively, covers the electro-optic BSO crystal which is placed on top of the grounded aluminum mirror. The discharge gap between both dielectrics is 3 mm. By varying the nitrogen admixture to helium and the pressure between 500 mbar and 1 bar, and by switching between the sine and square wave voltage at 2 kHz frequency, it was possible to operate both the diffuse discharge as well as self-stabilized discharge filaments. Figures 1(b) and 1(c) show representative photographs which are averaged over several discharge cycles.

3 Setup and methodologies

The experimental setup is illustrated in Figure 2. Surface charge diagnostics were combined and correlated with electrical measurements, optical emission spectroscopy and ICCD imaging at one discharge cell configuration under identical and well-defined operating conditions. Thereby, the discharge was comprehensively characterized regarding important volume processes and their interaction with the dielectric surface. The surface charge measurement is based on the electro-optic Pockels effect of the BSO crystal. Intensity changes of the LED light are detected spatio-temporally resolved by a high speed camera due to the birefringence of BSO depending on the amount and polarity of the deposited surface charges. Further details can be found elsewhere [1-4]. The surface charges accumulate on the thin dielectric plate covering the BSO crystal. Thus, the partial voltage drop across the BSO crystal, which solely determines the measured light intensity change, was recalculated using a capacitor model. Besides, the applied voltage and the total charge were measured using a HV probe and an external capacitor, respectively. The gap voltage and discharge current were recalculated using an electrical equivalent circuit. The discharge development in the volume was investigated by ICCD imaging with 0.05 mm spatial and 1 ns temporal resolution as well as by OES with spectral resolution of 0.5 nm.
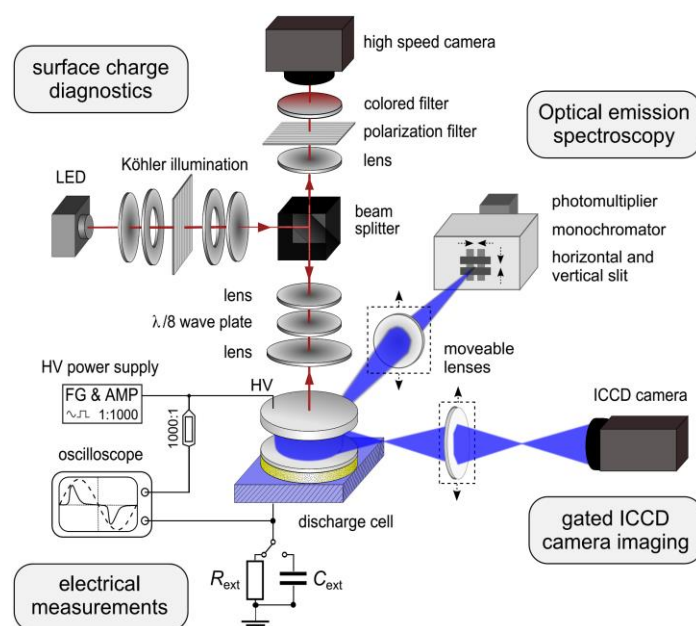
Fig. 2: Diagnostic setup: Combination of surface charge diagnostics, electrical measurements, ICCD imaging, and optical emission spectroscopy at one discharge cell configuration.

4   Surface charge measurements in diffuse and filamentary BDs

In figure 3(a), the discharge current $I_{dis}(t)$ and the transported charge $Q_{trans}(t) = \int I_{dis}(t) \, dt$ are compared with the dynamics of the spatially averaged surface charge $Q_{sur}(t)$ for the diffuse glow-like BD in helium. Just as observed for a BSO crystal exposed to the discharge [1,2], the transported charge agrees very well with the surface charge deposited on the borosilicate glass. Figure 3(b) shows the spatial surface charge distribution for the filamentary discharge in He with 10 % N_2 admixture. Initially, the discharge ignites in the microdischarge regime. However, by reducing the voltage amplitude, several self-organized discharge filaments arrange and, finally, one self-stabilized discharge filament remains due to the locally enhanced electric field across the gas gap at the position of the surface charge spots (surface memory effect), seen for positive and negative charge polarity in figure 3(b). Moreover, the surface charge profiles through the maximum positions are indicated by white lines and plotted on the left side. Since the incident positive ions have a significantly lower mobility than the incident electrons, the FWHM of the positive surface charge profile is smaller than for the negative polarity. These results show that the surface charge measurements were successfully extended to other, more common dielectrics covering the BSO crystal.
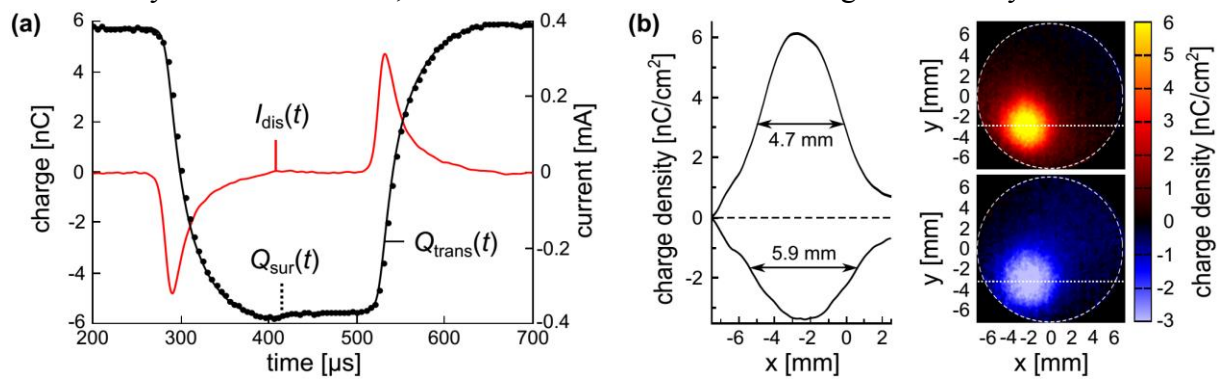
Fig. 3: Comparison between transported charge $Q_{trans}(t)$ and surface charge dynamics $Q_{sur}(t)$ for the diffuse BD in He (a). Spatial distribution (right) and profile through the maximum position (left) for positive and negative surface charges as the footprint of a self-stabilized discharge filament in He with 10% N_2 admixture (b).

5   Influence of different dielectrics on the discharge development

The diffuse glow-like BD in helium was also studied for mono-crystalline magnesia covering the BSO crystal. Both borosilicate (mainly composed of silica) and magnesia have nearly the same permittivity, but according to the literature [7], the trapping mechanisms as well as the binding energies of the surface electrons adsorbed to the dielectrics should significantly differ. Thus, it is most likely that the secondary electron emission (SEE) yield, predominantly caused by incident ions or thermal desorption in helium BDs, changes as well.

In figure 4, the electrical characteristics (a) and the phase-resolved spatially averaged surface charge (b) are compared between (boro-)silica (blue curves) and magnesia (red curves) as the anodic dielectric within the negative half-cycle of the gap voltage (i), and as the cathodic dielectric within the positive half-cycle (ii). For the first case, the discharge current, gap voltage, and surface charge dynamics clearly overlap which means that the anodic dielectric does not crucially influence the discharge. But, for magnesia instead of silica as the cathodic dielectric, the breakdown voltage is significantly reduced which corresponds to an earlier

discharge onset. In contrast to the anodic dielectric, the cathodic dielectric reveals an active part for the discharge development due to the residual surface electrons during the discharge pre-phase. The SEE yield depends only on the material properties at otherwise equal discharge conditions. Hence, the lower breakdown voltage indicates that magnesia has a larger effective SEE coefficient than silica, which is in accordance with the model in [7]. The relative effect is revealed by the surface charge dynamics in figure 4(b) too, however, the total amount of surface charges is still approximately the same. The larger current amplitude is compensated by the shorter current pulse duration.

In the case of the filamentary BD, the different dielectrics have no remarkable influence on the surface charge spots, since the spot dimensions are determined by the charge carrier mobilities in the volume. Also, the decay and radial transport of the surface charge occurs on the sub-second scale which clearly exceeds the discharge cycle [2].
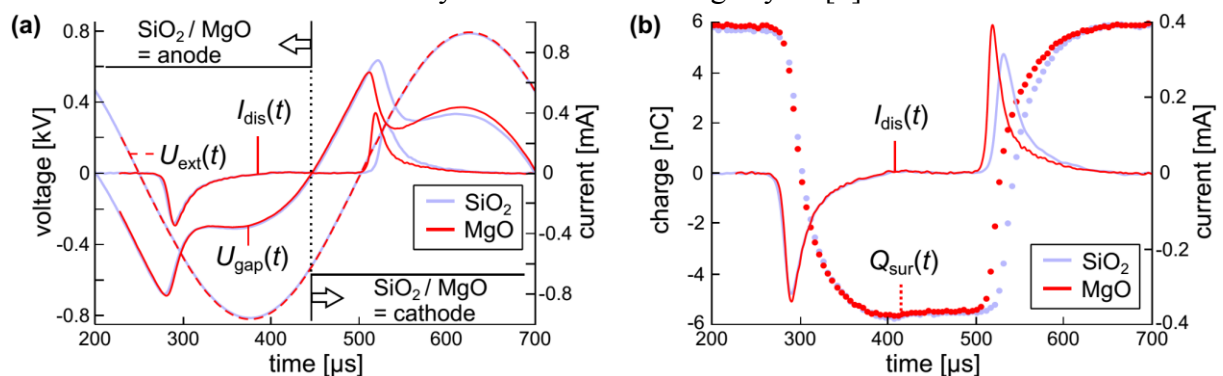
Fig. 4: Applied voltage $U_{ext}(t)$, gap voltage $U_{gap}(t)$, and discharge current $I_{dis}(t)$ (a), and spatially averaged surface charge $Q_{sur}(t)$ (b) for silica (gray curves) or magnesia (black curves) as the anodic dielectric within the negative half-cycle and as the cathodic dielectric within the positive half-cycle for the diffuse BD in helium.

6   Conclusion and outlook

The surface charge diagnostics based on the electro-optic Pockels effect of a BSO crystal was successfully extended to different transparent dielectrics in a plane-parallel barrier discharge configuration. The transported charge and deposited surface charge agree very well for both the diffuse as well as the filamentary BD. Further, a lower breakdown voltage was found for magnesia compared with silica as the cathodic dielectric which indicated that magnesia provides a larger secondary electron emission (SEE) yield. It is planned to investigate other dielectrics and to estimate the effective SEE coefficient by the comparison between the experiment and a 1D fluid simulation.

References
1. M. Bogaczyk et. al., J. Phys. D: Appl. Phys. 45, 465202 (2012)
2. R. Tschiersch et. al., J. Phys. D: Appl. Phys. 47, 365204 (2014)
3. L. Stollenwerk et. al., Phys. Rev. Lett. 98, 255001 (2007)
4. R. Wild et. al., New J. Phys. 16, 113040 (2014)
5. Yu. B. Golubovskii et. al., J. Phys. D: Appl. Phys. 35, 751-761 (2002)
6. S. Suzuki et. al., Plasma Sources Sci. Technol. 24, 055016 (2015)
7. R. Heinisch et. al., Phys. Rev. B 85, 075323 (2012)

WIDE-PRESSURE-RANGE COPLANAR BARRIER DISCHARGE

J. Čech, P. Sťahel, M. Zemánek, Z. Bonaventura
CEPLANT, Masaryk University, Kotlářská 2, 611 37 Brno, Czech Republic

E-mail: cech@physics.muni.cz

Single plasma source for wide-pressure-range applications was invented based on dielectric barrier discharge in coplanar geometry. In this paper the basic properties of this plasma source as well as the plasma parameters are presented for the working gas continuous pressure range from 10^1 Pa to 10^5 Pa. The current and voltage waveforms, discharge geometry and emission intensity are presented together with intended application.

Keywords: plasma source; dielectric barrier discharge; coplanar; atmospheric pressure; low pressure

1   Introduction

With the exception of plasma display panels [1] dielectric barrier discharges (DBD) have been studied mainly at atmospheric pressure conditions with respect to intended applications as industrial in-line plasma sources [2,3]. Recently the scientific interest was turned again also to the properties of DBDs at wider pressure range from super to sub-atmospheric pressure. The prominent position in this effort represents the surface DBD in plasma actuator design intended for applications in aeronautical industry [4] as the boundary layer flow control unit on wings or turbines. As a tool for basic plasma diagnostics [5] or a novel ionization source for mass spectrometry [6] also a sub-atmospheric volume DBD was studied.

To our best knowledge, beside plasma display panels the coplanar configuration of DBD (CDBD) was not studied at wider pressure range despite its interesting application as well as diagnostics capabilities. With respect to industrial applications the CDBD offers an open-geometry of electrodes generating the plasma layer suitable for treatment of materials of arbitrary thickness. The electrode system of CDBD also does not suffer from the plasma-chemical etching.

The intended adoption of CDBD as a source of radicals for plasma assisted atomic layer deposition and plasma cleaning applications lead us to investigate the behaviour and parameters of CDBD at wider than only atmospheric pressure conditions. The first results from the study of wide-pressure-range CDBD (WPR-CDBD) plasma source are given in this paper. The basic plasma source properties were characterized by the means of oscilloscopic measurements and the characterization of emission properties of generated plasma layer.

2   Experimental

The WPR-CDBD was derived from the DCSBD plasma source design [7] with insulation and cooling system suitable for operations at sub/super-atmospheric conditions. The model WPR-CDBD discharge cell consisted of three electrode pairs (1.5 mm thick with 1 mm gap)

embedded in glass-ceramics dielectrics (see [8]). External water cooling system was to dissipate power that exceeds the capacity of free-standing convective cooling. The WPR-CDBD design is highly favourable for clean environment or low-to-high pressure systems.
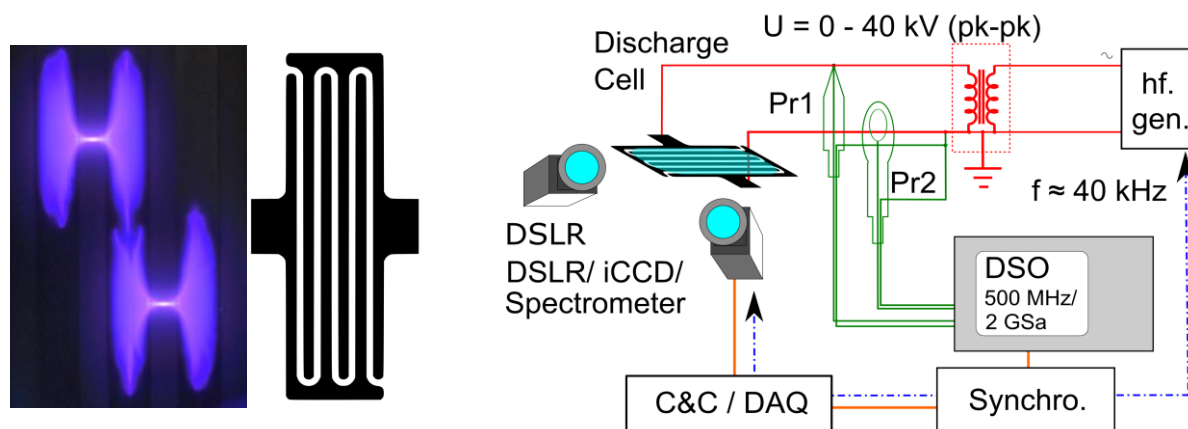
Fig. 1: Experimental setup of WPR/CDBD experiments. WPR-CDBD electrode geometry is given together with the image of two filaments at pressure approx. 20 kPa (left).

The WPR-CDBD discharge cell was placed in vacuum chamber made of a thick glass cylinder. On the top of the chamber the quartz glass square window was mounted. On the bottom the vacuum bushings for high-voltage cables and active water cooling circuit were mounted. Working conditions were maintained nitrogen gas flow (99.995%) using needle valve and rotary vane vacuum pump. The chamber pressure was monitored using Pirani and baratron gauges.

Experimental setup is given in Fig. 1. Custom-made sine-wave tuneable high-voltage (HV) generator was used to generate the discharge at 40 kHz frequency. Orbit Merret OM 402PWR was used to measure the input power. Voltage–current waveforms were recorded using HP24820A Infiniium (2-channel 500MHz/2GSa) digital storage oscilloscope coupled with HV probe Tektronix P6015A 1000:1 (labelled Pr1) and Pearson Current Monitor 2877 (labelled Pr2). For phase-locked imaging of discharge patterns Agilent 33220A function generator was used as the reference clock signal for HV generator and ICCD camera (Princeton Instruments PI-MAX3 1024i-SR-46-CM with SIGMA 105 mm 1:2.8 DG MACRO EX 1:1 macro lens). The ICCD camera was placed along axis of symmetry perpendicular to WPR-CDBD plasma layer. Dimensions of plasma layer were investigated using cross-imaging of the discharge pattern in top and side view using synchronized DSLR cameras (Nikon N80/SIGMA 105 mm 1:2.8 DG MACRO EX and N5100/NIKKOR 50 mm f/1.8D AF). For irradiance measurement the Newport Power Meter Model 1918-C equipped with 918D-UV-OD3 photodiode detector was used.

3   Results and Discussion

Three regimes of WPR-CDBD were found depending on the gas pressure. In low-pressure regime below approx. 1 kPa the discharge loses its filamentary character and it is characterized by single broad current pulse, see Fig. 2. At this regime WPR-CDBD appears homogeneous even at micro-scale (see ICCD image) and plasma layer could fill the entire

volume of the chamber. When the pressure is increased to approx. 1 to 10 kPa the discharge enters transitional regime characterized by spatially broadened individual micro-discharges and series of broad current pulses of significantly lower amplitude (see Fig. 3). In high-pressure regime above 10 kPa the discharge is clearly filamentary. With the pressure increase the surface discharges become significantly branched with sharp structures above electrodes and the regime is characterized by narrow current pulses of high amplitude (see Fig. 4).
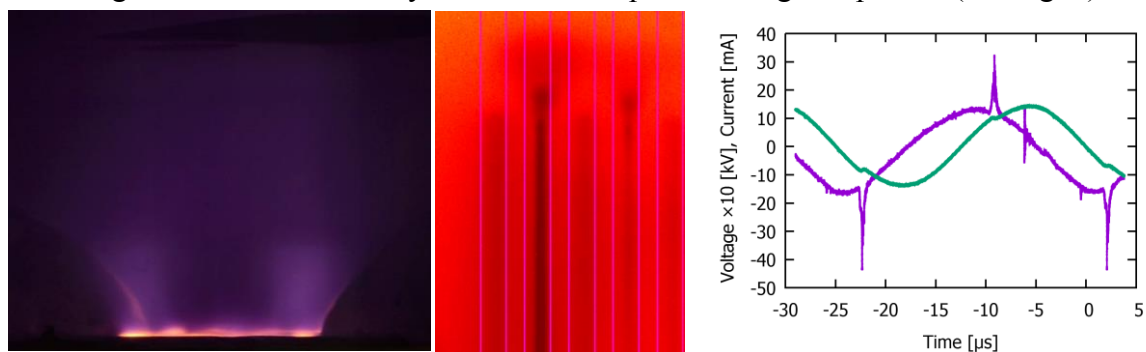
Fig. 2: Low-pressure mode of operation of WPR-CDBD, left-to-right: side-view, top-view (ICCD), C-V.
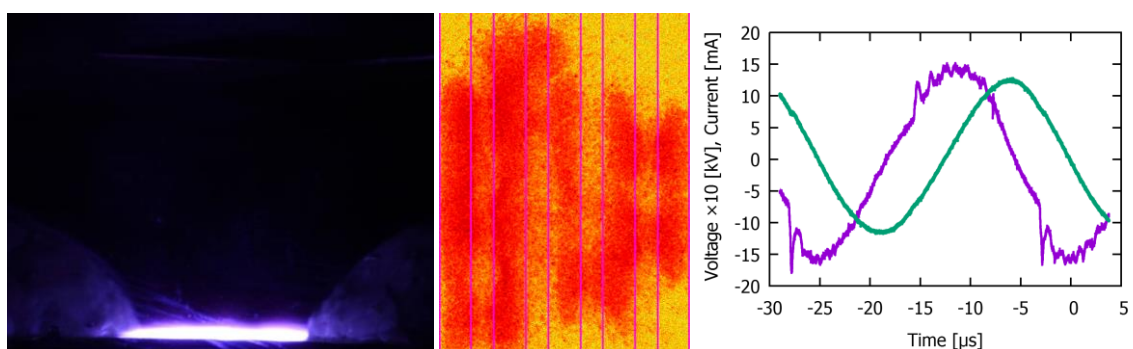
Fig. 3: Transitional mode of operation of WPR-CDBD, left-to-right: side-view, top-view (ICCD), C-V.
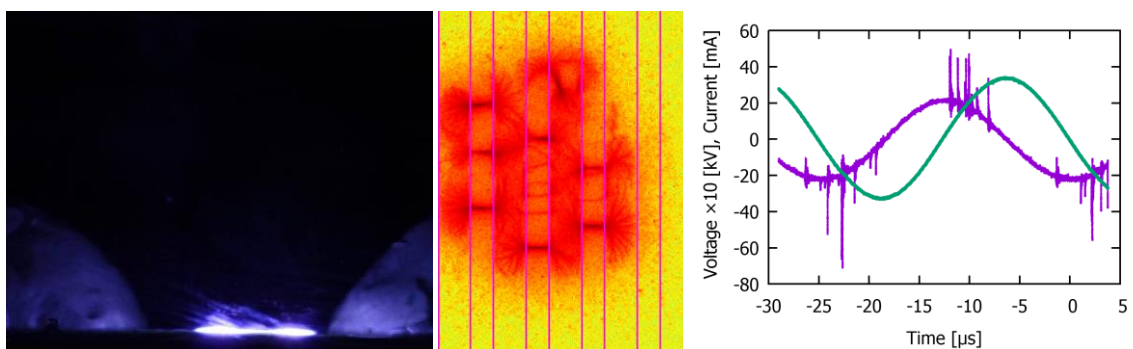
Fig. 4: High-pressure mode of operation of WPR-CDBD, left-to-right: side-view, top-view (ICCD), C-V.

The irradiation from approx. a half of WPR-CDBD surface was measured at the distance of approx. 7 cm from the discharge cell surface. The dependence of irradiation on the gas pressure and power input was investigated and it is given in Fig. 5 for pressures from 1 to 120 kPa, i.e. at the filamentary regime of discharge operation. Although the careful interpretation of the data and further study is necessary, we can comment on some common trends in the data. The discharge emission increases with the input power with a slight saturation at high power input. On condition that the spectral distribution of discharge emission does not vary significantly within studied power range, the irradiation increase could be explained by the regular increase of the number of individual microdischarges within

single discharge period [9], until the surface of the discharge cell is regularly covered and then the increase rate of irradiance drops. The ratio of irradiation per input power seems to decrease with increasing pressure, but further verification is needed.
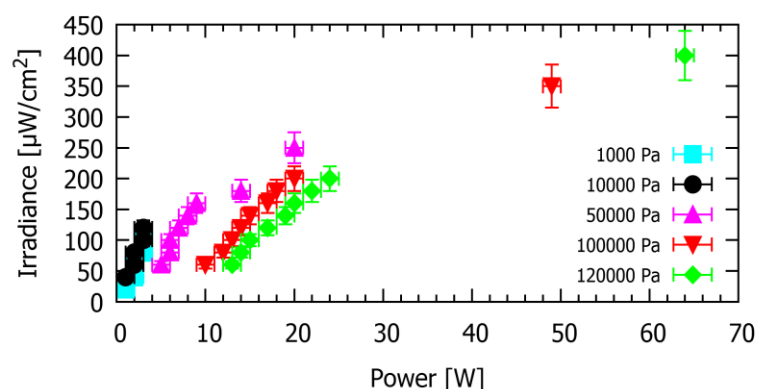
Fig. 5: Luminosity of WPR-CDBD as a function of input power and gas pressure for filamentary regime.

4   Conclusion

The wide-pressure-range plasma source based on the geometry of diffuse coplanar surface barrier discharge has been designed. The basic parameters of discharge generated in nitrogen were investigated. Three modes of operation were found: low-pressure (below 1 kPa), transitional (1-10 kPa) and high-pressure (above 10 kPa). At low-pressure mode the discharge exhibits a glow-like behaviour with plasma layer extending substantially to the half-space above surface of dielectrics (a homogeneous CDBD also at atmospheric pressure was reported recently [10]). With pressure increase the discharge collapses in filamentary mode with channel constriction and pronounced branching of surface discharges. The advantageous ability to manipulate the discharge regime and geometry using the gas pressure brings a high potential for intended applications of plasma-assisted cleaning and atomic layer deposition.

Acknowledgement

References
1. J. P. Boeuf, J. Phys. D: Appl. Phys. 36, R53–79 (2003)
2. U. Kogelschatz, Plasma Chem. Plasma Process. 23, 1-46 (2003)
3. M. Černák et al., Plasma Phys. Control. Fusion 53, 124031 (2011)
4. J. Soni et al., Appl. Phys. Lett. 102, 112908 (2013)
5. H. Höft et al., J. Phys. D: Appl. Phys. 47, 455202 (2014)
6. M. Sugiyama et al., Rapid Commun. Mass Spectrom. 27, 1005-10 (2013)
7. M. Šimor et al., Appl. Phys. Lett. 81, 2716 (2002)
8. J. Čech et al., Acta Polytechnica 54, 383-88 (2014)
9. J. Čech et al., Open Chem. 13, 528-40 (2014)
10. T. Morávek et al., Eur. Phys. J. Appl. Phys., (2016), DOI: 10.1051/epjap/2016150538 (in print)

CONCENTRATION OF ATOMIC HYDROGEN MEASURED IN A HEATED ATOMIZER BY TWO-PHOTON ABSORPTION LASER-INDUCED FLUORESCENCE

P. Dvořák[1], M. Talába[1], J. Dědina[2], J. Kratzer[2], A. Obrusník[1]
[1]Masaryk University, Faculty of Science, Brno, Kotlářská 2, Czech Rep.
[2]Institute of Analytical Chemistry of the CAS, v.v.i., Brno, Veveří 97, Czech Rep.

E-mail: pdvorak@physics.muni.cz

Concentration of free hydrogen atoms was measured by the two-photon absorption laser-induced fluoresence (TALIF) in an externally heated atomizer in a mixture of argon, hydrogen and oxygen at atmospheric pressure. Free hydrogen atoms were generated in a flame located at the end of a capillary that supplied O_2 into the Ar - H_2 mixture. The atomic hydrogen concentration in the order 10^{22} m^{-3} was found in the region around the flame. Optimal gas composition for atomic hydrogen production was found and an effect of gas flow on the atomic hydrogen distribution was observed.

Keywords: TALIF; hydrogen; flame, atomizer

1   Introduction

Atomic hydrogen belongs to the most reactive reducing agents that are commonly present in active environments like plasma or flames. Free hydrogen atoms play significant role in both volume gas phase reactions (e.g. methane dissociation $CH_4 + H \rightarrow CH_3 + H_2$ or oxygen reduction $O_2 + H \rightarrow OH + O$) and heterogeneous gas - solid surface reactions (e.g. reduction or etching). Similarly, they are expected to play a key role also in the decomposition of volatile hydrides in so-called atomizers. The atomizer is an analytical device used for sensitive detection of elements that can form volatile hydrides such as As, Se, Pb, Bi and Sb [1]. Prior to the atomization, the element to be determined is converted by a chemical reaction to the corresponding hydride that is introduced to the atomizer in the gaseous phase, usually together with argon carrier gas and co-generated hydrogen. In the atomizer, the hydride is decomposed and the resulting free atoms are detected by means of atomic absorption or fluorescence spectrometry. The atomization can be performed e.g. by plasma or by a flame. In this work, we present measurements of atomic hydrogen concentration in a heated atomizer containing a hydrogen - oxygen flame.

The presented work deals with measurements of free hydrogen atoms in an atomizer by means of two-photon absorption laser-induced fluorescence (TALIF). This method, described e.g. in [2,3,4], is based on excitation of measured species by simultaneous absorption of two laser photons with wavelength 205 nm and detection of the following fluorescence at 656 nm (Hα). In order to get concentration values, the calibration by TALIF of a known amount of krypton introduced to the atomizer is performed.

2   Experimental

Hydrogen atoms were detected in an externally heated atomizer, which is a T-shaped silica vessel with the rectangular optical arm with open ends and an inlet arm realized by a silica tube sealed to the center of the optical arm. The rectangular optical arm has inner dimensions 75 mm × 7 mm × 3 mm. The optical arm is externally heated to 820 °C employing a resistance wire coiled around. The inlet arm is used for supply of working gases: mixture of Ar and H_2 flowing directly through the tube, whereas O_2 is supplied to the atomizer via a thin capillary located inside the inlet arm with the capillary tip placed ca 1 mm above the inner surface of the wall of the optical arm (see figure 1). At the capillary tip a flame was ignited. Radical species produced in the optical arm can be detected by means of absorption or fluorescence.
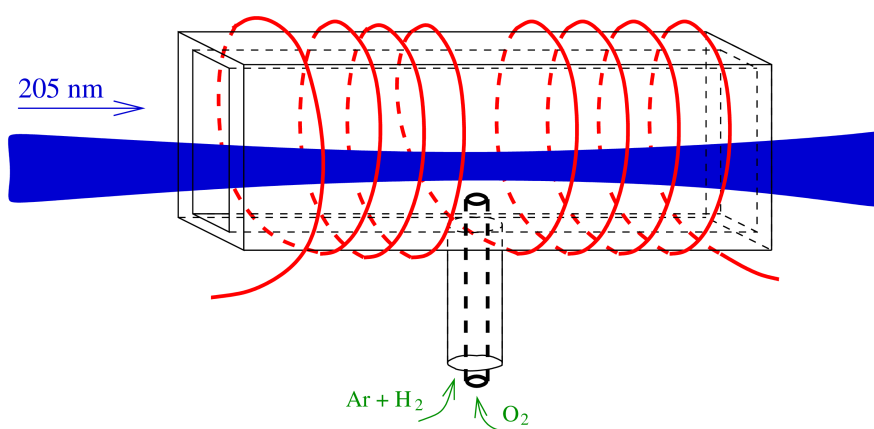
Fig. 1: Schema of the atomizer with a laser beam.

The laser beam, that was used for two-photon excitation of hydrogen atoms, was generated by a dye laser (Sirah) that was pumped by a Q-switched Nd:YAG laser (Spectra Physics). The frequency of the output beam of the dye laser (615 nm) was trippled (to 205 nm) by means of two nonlinear crystals and then focused to the center of the atomizer. The beam went through the optical arm (see figure 1). The duration of laser pulses was ca 8 ns, repetition rate 30 Hz and mean laser pulse energy was around 100 µJ.

The fluorescence of hydrogen atoms was detected by an ICCD camera (Princeton Instruments). Most of the light spontaneously emitted by heating wire, flame and ambient light sources was eliminated by an interference filter that was placed in front of the camera. The rest of the spontaneous light was eliminated by subtracting the signal measured by the camera when the laser beam was blocked in front of the atomizer. It was verified that the signals measured with no laser beam and with laser beam detuned from the frequency of the absorption line were identical. Consequently, no fluorescence of atomizer walls disturbed the presented measurement.

3   Results and Discussion

An example of measured atomic hydrogen concentration can be found in the figure 2, which shows a spatially-resolved dependence of atomic hydrogen concentration in the atomizer

center on the composition of the gas mixture. The atomic hydrogen concentration was below our detection limit when the flame at the capillary tip was not ignited. The flame can be ignited only at sufficient fractions of hydrogen and oxygen in the atomizer atmosphere. The actual flow rates of Ar and O_2 were 140 sccm and 3.2 sccm, respectively, whereas the flow rate of H_2 was varied. Under these conditions, the flame could not be ignited at hydrogen flow rates below ca 3 sccm. The atomic hydrogen concentration in the atomizer was found to be in the order 10^{22} m^{-3}. High concentration values were strongly localized to a few millimeter long area around the flame, that was positioned in the atomizer center. The H distribution is noticeably asymmetric, which is caused by a slightly asymmetric position of the O_2-supplying capillary demonstrating a strong influence of the gas flow pattern on the spatial distribution of atomic hydrogen.
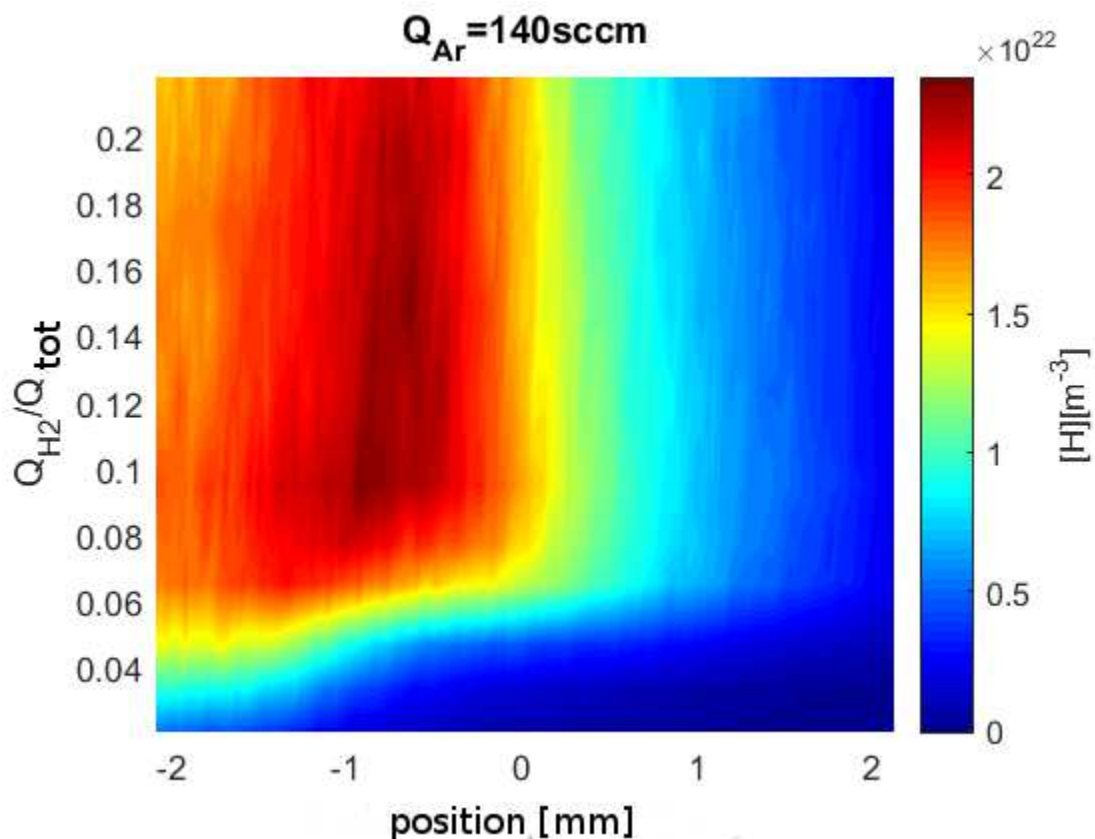
Fig. 2: Concentration of free hydrogen atoms in the atomizer center for various compositions of the Ar - H_2 mixture. The horizontal axis determines the horizontal position in the atomizer (along the laser beam). Zero position is located in the atomizer center.

4 Conclusion

The TALIF measurement was used to detect atomic hydrogen in the externally heated atomizer, where hydrogen atoms were produced by a hydrogen/oxygen flame burning in an Ar - H_2 / O_2 mixture. Measurements were realized at atmospheric pressure. The H concentration was in the order of 10^{22} m^{-3}, which is higher than the H concentration in a similar gas mixture in a volume dielectric barrier discharge [4]. However, in a comparison with the DBD, the atomic hydrogen distribution in the examined atomizer is strongly inhomogeneous with maximum in the vicinity of the flame.

Acknowledgement

References

1. J. Dědina et al., Hydride Generation Atomic Absorption Spectrometry (Chichester: Wiley, 1995)

2. M. Boogaarts et al., Rev. Sci. Instrum. 73, 73 (2002)

3. K. Niemi et al., J. Phys. D: Appl. Phys. 34, 2330 (2001)

4. M. Mrkvičková et al., submitted to Plasma Sources Sci. Technol. (2016)

MICROWAVE INTERFEROMETRY OF ATMOSPHERIC PRESSURE PLASMA JET

J. Faltýnek, J. Hnilica, V. Kudrle

Department of Physical Electronics, Masaryk University, Brno, Czech Republic

E-mail: kudrle@sci.muni.cz

Using numerical modeling the microwave interferometry was refined to enable the measurements of electron density in dense, filamentary atmospheric pressure plasmas. The approach includes the wave scattering, collision losses, inhomogeneities in probing electromagnetic field and other factors which are often neglected in plasma interferometry.

Keywords: plasma diagnostics; microwave interferometry; plasma jet

1   Introduction

As the electron concentration is very important parameter of any plasma, there are many well established methods for its determination, such as electric probes, optical spectroscopy, Thomson scattering or methods based on plasma permittivity in microwave region.

Plasma diagnostics using microwave interferometry has been extensively used for more than half century [1]. The full complexity of wave-plasma interaction can be significantly reduced by taking certain assumptions and approximations. Often, the principal simplification is the assumption of validity of the geometrical optics, i.e. neglecting the wave propagation phenomena inherent to the Maxwell equations. With current advances in numerical modeling, some of these simplifications can be abandoned and so the interferometric method can be used to study e.g. a plasma with dimensions comparable to the wavelength.

The atmospheric plasmas tend [2, 3] to form the filaments which are notoriously difficult to study by interferometry (and other methods, too), due to high electron density, high collision frequency, spatio-temporal instabilities and strong gradients. Therefore, the optical emission spectroscopy is currently the preferred diagnostics method.

In this contribution the results of interferometric measurements are combined with a numerical model of interaction between electromagnetic wave in waveguide (i.e. spatially inhomogeneous, non-planar and non-TEM) with small diameter high density plasma filament.

2   Experimental

The plasma source SAIREM Surfatron 80 plasma belongs to surface wave discharges [4] sustained by microwaves propagating along the plasma boundary and it is able to operate at atmospheric pressure, forming a plasma jet. The microwave generator is SAIREM GMP 20 KED with 2.45 GHz frequency and 2 kW maximum power. In present experiments, the output power is set to 250 W. The microwaves from the generator are fed to the surfatron via a waveguide, ferrite circulator, reflectometer, matching and coaxial cable.
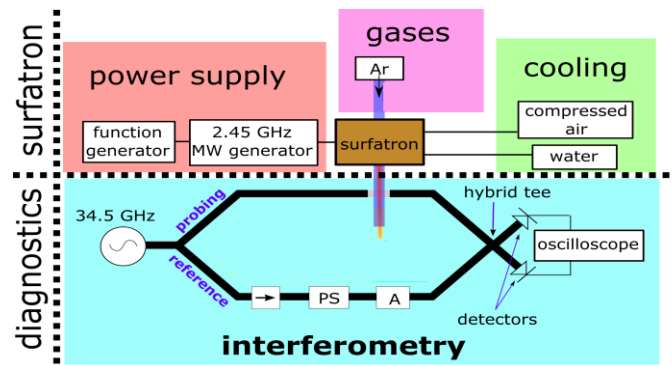
Fig. 1: Schematics of the experimental set-up.

Fused silica discharge tube (length 170 mm, inner diameter 1.5 mm, outer diameter 4 mm) passes through the surfatron and it is cooled by an external flow of compressed air (approximately 4 slm). The downstream (i.e. bottom) end of the discharge tube is 2 cm from the surfatron wave launching gap. Argon at flow rate of 1.45 slm (standard litre per minute) is used as the working gas.

The microwave interferometer is in Mach-Zehnder [5] configuration with quadrature detection, powered by 34.5 GHz (K_a 8 mm band) Gunn diode (SpacekLabs GKA-350). The whole interferometer is constructed of standard WR 28 waveguide. The discharge tube passes through a 8 mm hole drilled in a broader side of the probing arm waveguide, this crossing is 10 mm from the discharge tube end. The signal from both probing and reference arms is combined using the hybrid tee and detected by two microwave diodes (DKa-2N, Spacek Labs). The detector output signal is digitised by Agilent DSO 1022A oscilloscope using long buffers (approx. 25000 samples in each waveform).

3   Results and Discussion

Using the numeric model made in COMSOL Multiphysics, the full solution of Maxwell equations in a configuration identical to the experimental one is obtained. This solution includes also often neglected effects such as wave scattering, non-TEM waves or a propagation of the electromagnetic waves along the plasma filament. The main goal is to calculate the wave phase shift dependence on the plasma density. This then enables to get the plasma density from the experimentally measured phase shift.
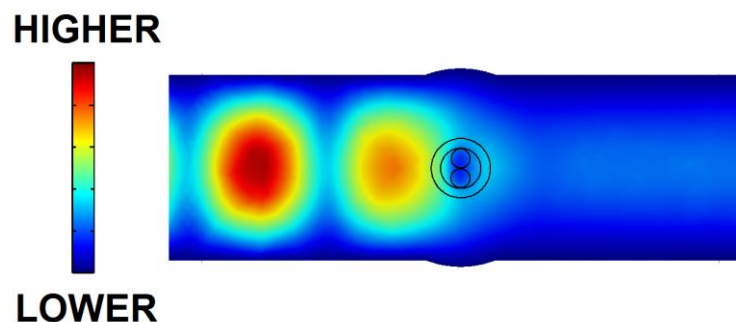
Fig. 2: Calculated electric field |E| in the interferometer probing arm affected by the discharge tube and two plasma filaments inside.

The influence of various factors, such as presence or absence of the discharge tube, number and position of filaments on the resulting phase shift was studied, too. It was found, that the results are rather insensitive to small, experimentally unavoidable, misplacements of the discharge tube or to the electron-neutral collision frequency, which is difficult to measure precisely.

Plasma density in the filaments is found in the range of $1 - 5 \times 10^{20}$ m^{-3} depending on the experimental conditions. These values are in good agreement with the values found by other authors [6,7] using similar experimental devices.

4   Conclusion

The developed numerical model is able to calculate the interaction of the electromagnetic wave with small diameter plasma filament in geometry close to the experimental configuration, including many parasitic effects which are often neglected. The results of the model, namely the phase shift is compared with the experimental results, giving together the sought parameter – the electron concentration in the plasma filament.

References

1. M. A. Heald et al., Plasma Diagnostics with Microwaves (New York: Wiley 1964)
2. J. Schafer et al., IEEE Trans. Plasma Sci. 39, 2350 (2011)
3. J. Hnilica et al., J. Phys. D: Appl. Phys. 47, 085204 (2014)
4. M. Moisan et al., Phys. Lett. A 50, 125 (1974)
5. L. Zehnder, Zeitschrift fur Instrumentenkunde 11, 275 (1891)
6. S. Dap et al., Plasma Sources Sci. Technol. 24, 065007 (2015)
7. M. D. Calzada et al., J. Appl. Phys. 88, 34 (2000)

MULTIRESOLUTION ON ARBITRARY DOMAINS FOR TIME-DEPENDENT PDE'S. APPLICATION TO STREAMER SIMULATIONS

P.-L. Lee[1], Z. Bonaventura[1], M. Duarte[2], A. Bourdon[3], M. Massot[4]

[1]Dept of Physical Electronics at the Faculty of Science, Masaryk University, Kotlarska 2, Brno, CZ
[2]CD-adapco, 200 Shepherds Bush Road, W67NL, London, United Kingdom
[3]LPP, CNRS, Ecole Polytechnique, UPMC, Paris XI, 91128 Palaiseau, France
[4]Centralesupelec, EM2C, UPR CNRS 288, Grande voie des vignes, 92295 Châtenay-Malabry Cedex, France

E-mail: pierre-louis.lee@supelec.fr , zbona@physics.muni.cz ,
maximuspy@gmail.com, anne.bourdon@lpp.polytechnique.fr ,
marc.massot@centralesupelec.fr

This contribution focuses on implementing immersed boundaries within a space-adaptive multiresolution technique in order to cope with arbitrary domains. The goal is to perform simulations of streamers in complex geometries while preserving the advantages of data compression and user-defined accuracy provided by the multiresolution algorithm.

Keywords: multiresolution; streamer simulation; immersed boundaries; poisson equation; adaptive mesh

1   Introduction

Electrical breakdown in air gaps often involves the development of fast ionizing waves that take the form of thin filaments called streamers. These complex and highly nonlinear phenomena precede the formation of sparks and leaders. Streamers are extremely difficult to reproduce with sufficient spatial and temporal resolution in experimental observations. Therefore, the appropriate interpretation of experimental data greatly relies on numerical models of the dynamics for the underlying physical-chemical phenomena. Non-thermal chemical activity of streamer discharges is of considerable interest for various scientific and industrial applications. Streamers can be mathematically modeled by drift-diffusion-reaction equations solved together with a Poisson's equation, and reveal an important time-space multi-scale character. The accuracy and robustness of the chosen numerical methods is then crucial. A combination of numerical techniques based on a second order, time-adaptive integration scheme and space-adaptive multiresolution was previously introduced in [1] to numerically simulate streamers. These techniques involve important efficiency gains in terms of CPU time and memory space while ensuring a time-space error control of the solution, and allow one to carry out computationally expensive parametric studies in reasonable time. Even though large, multi-dimensional computational domains can be successfully simulated with the present numerical tool [2], the adaptive multiresolution analysis is currently limited to simple geometries. The extension of this numerical framework to arbitrary domains constitutes then a natural enhancement of the methodology, paving the way to simulations of even more complex configurations.

2   The numerical method

In this work we aim at developing and implementing an efficient numerical procedure to account for arbitrary domains using the space-adaptive multiresolution scheme [3]. The final goal is to perform comprehensive simulations of streamers including electrodes of different geometries. The methodology is easily extensible to other applications. Adaptive Meshing Refinement (AMR) techniques have already been modified to cope with complex geometries (see, for instance, [4]) and these approaches are investigated, along with other immersed boundary techniques developed in the past for uniform grids. In our particular case the key underlying criterion for any development is that the proposed technique complies with the multiresolution theoretical framework developed in [3]. The latter involves numerical simulations within a user-defined prescribed accuracy, a key advantage of multiresolution analysis over other AMR methods.

3   Conclusion

This work presents an implementation of the effective numerical procedure to account for arbitrary domains and using the space-adaptive multiresolution scheme. Special care has to be taken to describe the domain boundaries for both the PDEs and the wavelet operations. The proposed numerical procedure is extensively tested on various arbitrary domains, to evaluate in particular its impact on the numerical accuracy. Simpler models are considered to assess the numerical performance for both time-dependent, parabolic PDEs and particularly the Poisson's equation.

References
1. M. Duarte et al., J. Comput. Phys. 231, 1002-1019 (2012)
2. M. Duarte et al., J. Comput. Phys. 289, 129-148 (2015)
3. A. Cohen et al., Math. Comp. 72, 183-225 (2003)
4. T. Guillet et al., J. Comput. Phys. 230, 4756-4771 (2011)

INVESTIGATION OF THE LOCAL CURRENT IN HOMOGENEOUS DIELECTRIC BARRIER DISCHARGE

N. Naudé, M.C. Bouzidi, V. Roustit, C. Tyl, S. Dap, A. Belinger, N. Gherardi

LAPLACE, Université de Toulouse, CNRS, INPT, UPS, France

E-mail: nicolas.naude@laplace.univ-tlse.fr

This work focuses on the development of a new electrical diagnostic to measure the local current in a Dielectric Barrier Discharge using a segmented ground electrode. By correlating these local electrical measurements with space resolved optical diagnostics, it will be possible to improve the understanding of phenomenon in homogeneous DBDs. A detailed study has been done for DBD in N_2 with small admixtures of NO and O_2. This paper is mainly dedicated to the technical feasibility study.

Keywords: dielectric barrier discharge; homogeneous discharge; atmospheric pressure; local current measurement

1   Introduction

Dielectric Barrier Discharges (DBD) have tremendous popularity for atmospheric pressure applications including thin-film coating, sterilization, treatment of flue and toxic gases, aerodynamic flow control, and energy-efficient lighting devices [1-3]. Depending on the gas, electrical parameters, and electrode configuration, these discharges can operate in the classical filamentary mode or in a homogeneous mode [4-5].

Due to their simplicity, electrical measurements (current and voltage) are widely used to characterize the homogeneous (and filamentary) DBDs. Combined with a simplified electrical circuit of the cell discharge, this allows *e.g.* (i) to calculate the temporal development processes of all internal electrical quantities in the discharge gap [6], (ii) to calculate the discharge power [3,6], (iii) to estimate the gas temperature [7]. Generally, the discharge current is measured as an integral over the entire electrode area and it is assumed that the current density is the same in any point of the electrode. However, due to gas flow circulation, to self-organization phenomenon, *etc.* this assumption is never perfectly true. The aim of this work is to measure the local current in a homogeneous DBD in nitrogen.

2   Experimental set-up

The experimental set-up has already been described in previous publication [8]. The DBD is kept in a closed vessel to perform experiments in a well controlled atmosphere. The plasma reactor is pumped down to 10^{-3} mBar prior to any experiment, and then is filled up to atmospheric pressure using mixtures of nitrogen (99,999% purity) purchased from Air Liquide. The discharge is ignited between two alumina plates separated by a 1mm gas gap and the discharge area is 3x3cm². In order to renew the atmosphere, a gas flow (1slm) is injected from one side of the discharge (longitudinal gas injection), keeping a constant pressure of 1 bar through a gentle pumping of the vessel.

The sinusoidal voltage power supply is made of a low-frequency generator providing the reference waveform, which is then amplified by a linear amplifier whose output is applied to the primary winding of a transformer in series with a 4Ω resistor. The electrodes are connected to the secondary of the transformer. The discharge is characterized by electrical measurements. The voltage applied to the electrodes is measured by means of a high voltage probe. The discharge current is measured through a 200Ω resistor in series with the electrodes. The current and the voltage applied to the electrodes are visualized on a digital oscilloscope. The discharge homogeneity is investigated by means of short exposure time pictures, which are taken with an intensified CCD camera synchronized with the power supply voltage.

3 Local current measurement

To measure the local current, the classical 3x3cm² ground electrode is replaced by a segmented electrode. This electrode is composed of 8 strips (3.4mm x 30mm) with 400μm between two strips. Each strip is connected to the ground trough a 1600Ω resistor to measure the discharge current using a data acquisition system from National Instruments (USB X series 6356 - 8 channels - 1.25 Mech/channel/s - 16 bits) connected to a computer (Figure 1).
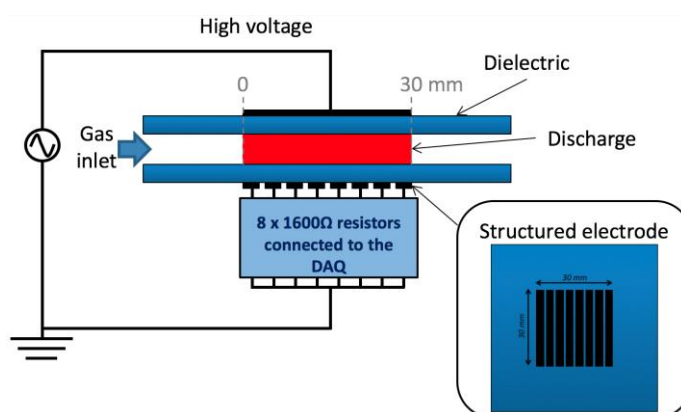
Fig. 1: Scheme of cell discharge with the local measurement system using a structured electrode with 8 strips.

Due to the presence of the dielectric and the tiny distance between two strips, the discharge behavior is not affected. This is confirmed by an electrostatic calculation using COMSOL© software. The figure 2 shows the electric potential in the gas gap near the segmented electrode. As we can see, the electric potential in the gas is not disturbed by the segmented ground electrode. This is also confirmed by a comparison of the total discharge current with and without segmented ground electrode (Figure 3).
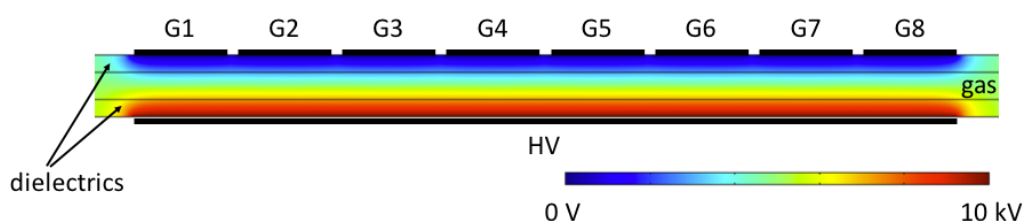
Fig. 2: Electric potential calculation (electrostatic modeling using COMSOL©). The electrodes G1 to G8 correspond to the 8 strips of the segmented electrode.
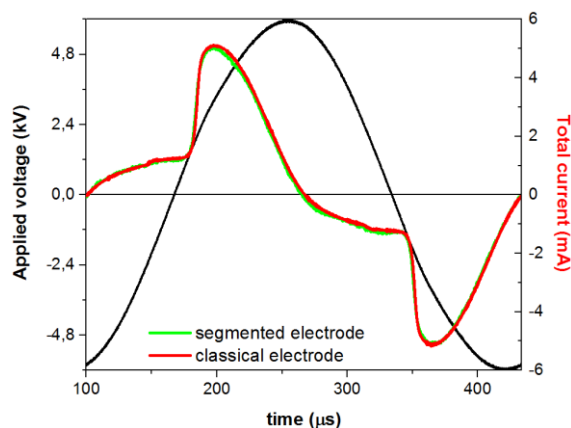
Fig. 3: Comparison of total current waveform with the segmented electrode and with the classical electrode (f=3kHz – V=12 kV_{CC}).

4   First results

The figure 4-a shows the applied voltage and the total current waveform for a homogeneous DBD in N_2 with 450 ppm of O_2. The figure 4-b shows the measured local current density evolution as a function of the position from the discharge entrance on a half-period of the applied voltage. In this condition, it is interesting to note that (i) the discharge ignited slightly later at the discharge entrance, (ii) therefore the current density is lower at the entrance, (iii) from 25mm to the end of the discharge a current is measured before the breakdown.

Then, by correlating these electrical measurements with optical diagnostics, it is possible to improve the understanding of phenomena taking place in homogeneous DBDs.

a)

b)
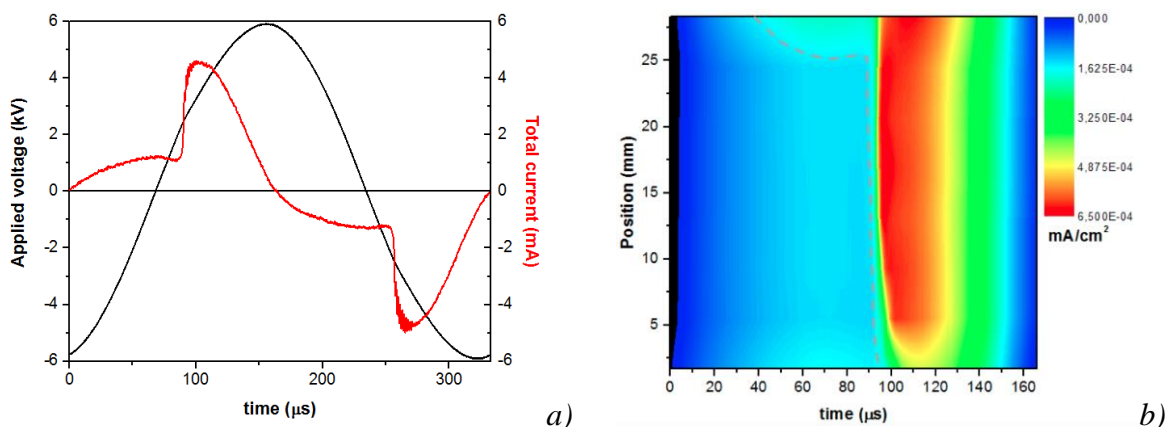
Fig. 4: Homogeneous DBD in N_2 with 450 ppm of O_2 (f=3kHz, V=12kV_{pk-pk}).
a) Applied voltage and total current waveforms, b) Experimental local current density evolution as a function of the position from the discharge entrance (1D measurements) on a half-period of the applied voltage.

A detailed study has been done for DBD in N_2 with small admixtures of NO and O_2. The aim is to improve the understanding of the mechanisms involved in the creation of seed electrons between two discharges: indeed, in order to induce a Townsend breakdown and to generate a stable discharge in N_2, it is necessary to have a memory effect which leads to the production of seed electrons just before the breakdown. In nitrogen-based discharges, the creation of seed electrons is correlated with the presence of $N_2(A^3\Sigma_u^+)$ metastable molecules created during the

previous discharge and remaining between two discharges. In presence of oxidizing gas, the associative ionization of $N(^2P)$ and $O(^3P)$ could explain the increase of stability observed when only a few tenths of ppm of O_2 or NO is added [9].

5 Conclusion

The technical feasibility of the local current measurement in a DBD has been demonstrated. The next step which is currently under study, is to measure the local current of the DBD with a ground electrode divided into 8x8 areas (Figure 5). This increases strongly the spatial resolution of this diagnostic. A special effort is made on the realization of the multi channel data acquisition system (especially on the sample rate).
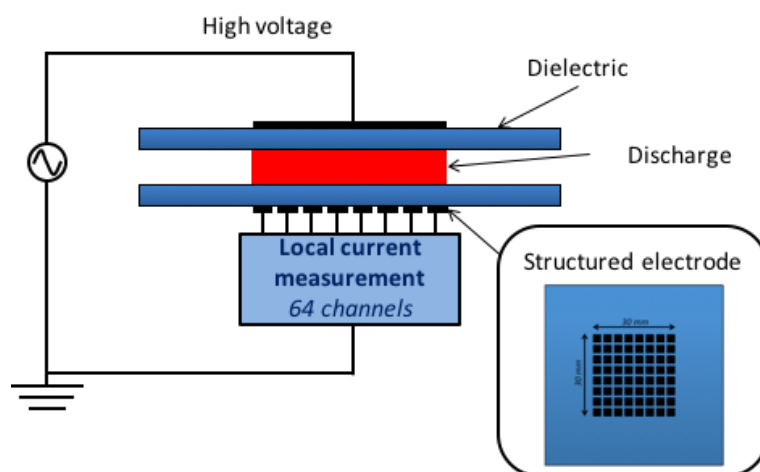
Fig. 5: Scheme of cell discharge with the local measurement system using a structured electrode with 64 squares.

Using this new electrical diagnostic, the influence of the gas gap and oxygen rate are studied and will be presented. The results will be correlated with optical diagnostics: ICCD imaging and optical emission spectroscopy (OES).

References
1. U. Kogelschatz, Plasma Phys. Control. Fusion 46, B63-B75 (2004)
2. F. Massines et al., Plasma Process. Polym. 9, 1041-1073 (2012)
3. H. E. Wagner et al., Vacuum 71 417-436 (2003)
4. U. Kogelschatz, Plasma Chem. Plasma Process. 23, 1-46 (2003)
5. F. Massines et al., Eur. Phys. J. Appl. Phys 47 (2009)
6. S. Liu et al., J. Phys. D: Appl. Phys. 36, 3144-3150 (2003)
7. N. Naudé et al., in *Proceedings of the 9th High Pressure Low Temperature Plasma Chemistry Symposium,* Padova, Italy (2004)
8. F. Massines et al., Plasma Phys. Contr. Fusion 47, B577-B588 (2005)
9. M. C. Bouzidi et al., in *Proceedings of the 14th High Pressure Low Temperature Plasma Chemistry Symposium,* Zinnowitz, Germany (2014)

SIMULATION OF LASER PHOTODETACHMENT OF NEGATIVE IONS IN HELIUM-OXYGEN BARRIER DISCHARGES AND COMPARISON WITH THE EXPERIMENT

S. Nemschokmichal, R. Tschiersch, J. Meichsner

Institute of Physics, University of Greifswald, Felix-Hausdorff-Str. 6,17489 Greifswald, Germany

E-mail: nemschok@physik.uni-greifswald.de

A 1D fluid simulation was developed to analyze the change of a diffuse helium-oxygen barrier discharge after the laser photodetachment of negative ions. The comparison of the measured and simulated parameter dependencies is used to draw conclusions about the negative ion densities in the pre-phase and during the discharge breakdown. Since the simulation turns out that the negative ion density in the simulation is too low to reproduce the laser photodetachment experiment, different additional production channels of negative ions and their ability to reproduce the measurements are discussed.

Keywords: barrier discharge; negative ions; laser photodetachment; fluid simulation

1 Introduction

Helium-oxygen discharges at atmospheric pressure are well established in industrial applications because of their ability to produce oxygen radicals under low power consumption. The use of oxygen in a discharge always causes the formation of negative ions, but the influence of negative ions on barrier discharges is poorly investigated. E.g., the attachment of electrons to oxygen reduces the effective ionization and might be responsible for the transition from the diffuse to the filamentary discharge regime when increasing the oxygen admixture. To investigate the influence of negative ions in helium-oxygen barrier discharges, a laser photodetachment experiment was realized [1]. It revealed that the laser photodetachment of the negative ions during the pre-phase of the discharge decreases the breakdown voltage which causes an earlier ignition of the following discharge pulse and less transported charges during the discharge. Surprisingly, no additional current due to the detached electrons was observed when firing the laser during the discharge current pulse. Furthermore, the experiment suggested that O^- and/or O_3^- are the dominating negative ions, but it cannot provide absolute densities of negative ions. This issue should be addressed by the simulation in combination with a detailed comparison with the experimentally determined parameter dependencies.

2 Setup

The 1D fluid simulation includes electrons, He^+, He_2^+, O^+, O_2^+, O_4^+, O^-, O_2^-, and O_3^- ions as charged particles. The regarded excited species and radicals are the helium metastable He^m, the helium excimer He_2, the oxygen atom O and its excited states $O(^1S)$ and $O(^1D)$, the oxygen molecule and its excited states $O_2(a)$, $O_2(b)$, and the ozone molecule O_3. The electron transport parameter depend on the reduced electric field strength E/n and are calculated by

BOLSIG+ [2, 3]. The desired cross sections for electron impact excitation and ionization are taken from lxcat.net and the associated databases. The rate coefficients for heavy particle collisions are mainly taken from [4].

As in the experiment, the simulation is performed for an admixture of 400 ppm oxygen to helium and a pressure of 500 mbar. The gap width is 3 mm and each electrode is covered by a 0.7 mm thick glass plate ($\varepsilon_r = 7.6$). The applied sinusoidal voltage has a frequency of 2 kHz and an amplitude of 700 V. The simulated laser photodetachment is shifted in time and position, and the laser pulse energy is varied.

3   Results

Two examples for the simulated laser photodetachment are presented in figure 1. Since the simulation of the laser photodetachment does not affect the discharge when using the commonly given attachment rates, some alternatives resulting in larger negative ion densities are discussed. The first, as shown in figure 1 (a), assumes the attachment rates to be 100 times larger, because there might be missing attachment processes by three particle collisions. For this case, the negative ion density exceeds the electron density by one order of magnitude, wherefore the laser photodetachment causes a large peak in electron density and an increase in pre-ionization before the breakdown. Hence, the ignition voltage reduces and the discharge ignites earlier as it was observed in the experiment
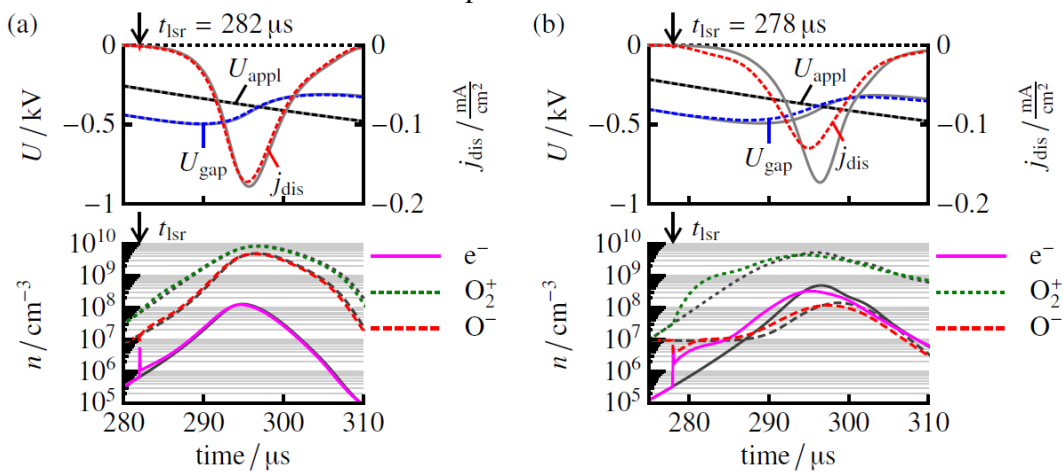
Fig. 1: Change in discharge characteristics after the laser photodetachment for a simulation with (a) 100 times larger attachment rates and (b) negative ion formation at the negatively charged dielectric.

A second considered process which might produce large negative ion densities is the formation of negative ions by a resonant charge transfer at the negatively charged dielectric. The laser photodetachment effect of such a situation is presented in figure 1 (b). The effect is even larger than for the 100 times larger attachment rates in (a), because the negative ion density is more than one order of magnitude larger than the electron density and the re-attachment of these electrons is improbable.

For both additional processes, the dependence of the laser photodetachment effect on the laser firing time is plotted in figure 2 in comparison with the experiment. Both show the increase of the laser photodetachment effect during the pre-phase, but the simulation with 100 times

larger attachment rates additionally shows a large effect during the discharge pulse. This was never observed in the experiments, which means that the electronegativity during the discharge pulse must be lower. Hence, if there are actually missing attachment processes in the simulation, their rate coefficients must have a maximum at low electric field strengths to cause a large electronegativity during the pre-phase, but not during the discharge breakdown. For the formation of negative ions at the negatively charged dielectric, only a very weak effect occurs during the discharge pulse because at this time the formation of negative ions is dominated by electron attachment in the volume. The comparison of both approaches shows that the negative ion density must exceed the electron density in the pre-phase but not during the discharge pulse to reproduce the measured time dependence of the laser photodetachment effect.
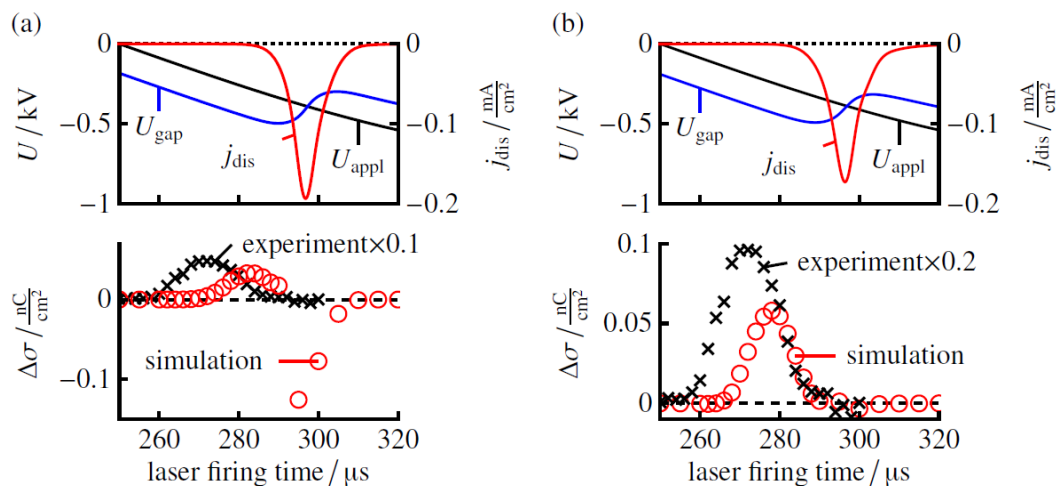
Fig. 2: Laser photodetachment effect depending on the laser firing time for a simulation with (a) 100 times larger attachment rates and (b) negative ion formation at the negatively charged dielectric.

4   Conclusion and outlook

The simulation of the laser photodetachment effect on the basis of commonly used rate coefficients and cross sections for attachment processes is not able to reproduce the results of the laser photodetachment experiment in [1]. The measured effect demands a larger negative ion density during the pre-phase of the discharge, whereas it must be lower than the electron density during the discharge breakdown and afterglow. A formation of negative ions at the negatively charged dielectric is able to increase the negative ion density in the pre-phase and to reproduce the measured time dependence of the laser photodetachment effect qualitatively. Besides the surface effect, the larger negative ion density during the pre-phase might also result from a volume attachment process which has its maximum at low electric field strengths as it is the case during the pre-phase of the discharge. The further discussion will show how these processes are able to reproduce further parameter dependencies (laser pulse energy, axial laser beam position) of the laser photodetachment effect.

References

1. R. Tschiersch et al., Plasma Sources Sci. Technol. 25, 025004 (2016)
2. G. J. M. Hagelaar, BOLSIG+ 6/2013, http://www.bolsig.laplace.univ-tlse.fr/
3. G. J. M. Hagelaar et al., Plasma Sources Sci. Technol. 14, 722 (2005)
4. D.-X. Liu et al., Plasma Process. Polym. 7, 846-865 (2010)

INSTANTANEOUS AND INTEGRATED ELECTRICAL PARAMETERS OF ATMOSPHERIC PRESSURE AC ROTATING GLIDING DISCHARGE

D. Hamazin, I. Veremii, O. Solomenko, V. Chernyak, K. Iukhymenko

Faculty of Radio Physics, Electronics and Computer Systems, Taras Shevchenko National University of Kyiv, 64/13, Volodymyrska Str., Kyiv, Ukraine

E-mail: denigam@gmail.com

This paper discusses electrical parameters of AC rotating gliding discharge operated at atmospheric pressure in argon with the addition of ethanol (in form of aerosol). In different times periods the discharge can be operated in either glow mode or arc discharge mode.

Keywords: rotating gliding discharge; AC power; plasma-chemistry; Lissajous figure

1   Introduction

Gliding electrical discharges have been known for a long time but it still arouses interest. The reason is those types of discharges are used in a wide range of applications, like plasma-chemical reforming of hydrocarbons into the synthesis-gas [1] and nanomaterials (nanoparticles, nanotubes, fullerenes, graphene nanofibers) generation [2]. It is more advantageous to use gliding rotation of plasma discharge instead of gliding it in one plane [3] to improve the discharge efficiency. Usually rotation can be caused by one of two reasons: due to the tangential gas injection [3] or due to the application of a magnetic field [4]. Gliding discharge dynamically changes its parameters over time as it was shown in [1]. These changes caused by the change in the plasma column length in gas stream with time. This "quasi-stationary" character of discharge is one of the most characteristic features of gliding discharges.

In both mentioned applications as a model hydrocarbon as a precursor for the production of the final product (e.g. carbon nanomaterials) [5], or as a model substance for reforming liquid fuels into synthesis gas [1, 4]. But in the case of work with hydrocarbons (or any others additional substances) it is important to consider its effect on electrical parameters.

That is why this research studies the properties of atmospheric pressure AC rotating gliding discharge in the vortex gas flow. Ethanol was used as a model hydrocarbon. Its aerosol was injected in the gas stream of investigated system. To study the change of electrical parameters, voltage and current waveforms were measured and analyzed.

2   Experimental

Photos of the shape of the discharge channel in argon with and without added ethanol aerosol and experimental setup scheme presented on Fig. 1. Prototype of experimental system was represented in [6] but it was modified for mentioned applications.
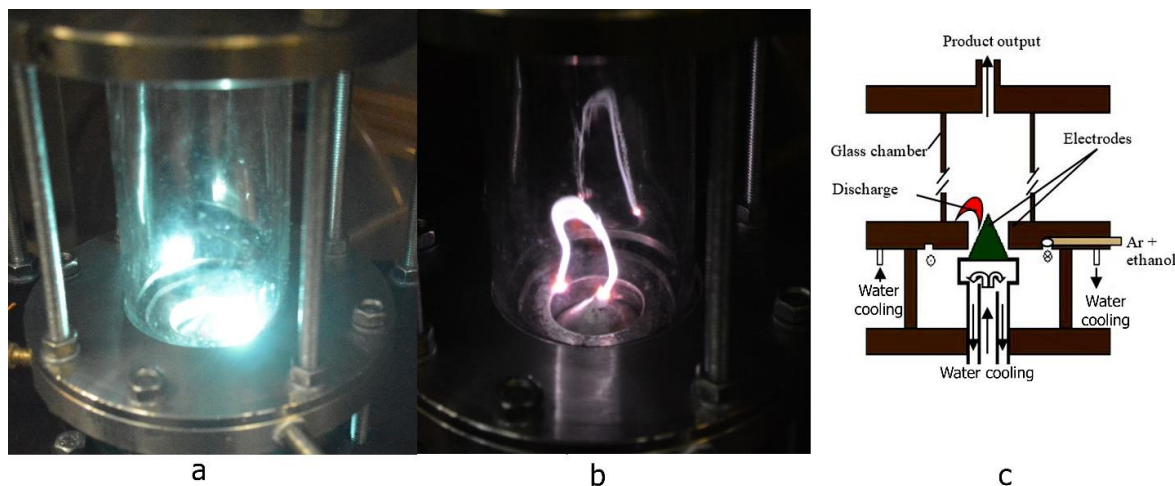
Fig. 1: the shape of the discharge channel in argon with added ethanol aerosol (a) and in the argon (b); experimental setup (c).

Compared to [6], the following changes were made to the system:
•   The system now uses a rotating gliding discharge (to increase the lifetime of the system [7]) (Fig 1, c);
•   The system is powered by the AC power source to prevent the formation of carbon deposits on the electrodes. The power supply was a step-up transformer (turns ratio - 28, the maximum current – 1 A). It was connected to the power line by an autotransformer (0-250V);
•   The metal chamber was replaced by glass for the visual observation of the discharge.
The rotation of the discharge is due to the vortex of the gas flow. The system worked at 50 Hz frequency. In pure argon (Fig 1, b) the length of the discharge channel changed over time. According to the results of visual observation (when the argon flow was about 10 L/min) this change was slower in compeer with current frequency. During one period of the current waveform, discharge length varied negligible. If ethanol (Fig. 1,a) is added to the system, the length of the discharge is reduced but it remained virtually unchanged with tike. This indicates that at zero current the discharge channel does not disintegrate.

The digital oscilloscope (ATTEN ADS2202CA, 200 MHz, 1 Gs/s) was used for the study of the electrical characteristics of the discharge. Using the oscilloscope instead of integrating measurement devices allows studying not only the root mean square (RMS) but also the instantaneous values of voltage and current. The voltage was measured by a divider (1:830, 0-1 MHz) and current using serial measuring resistor (3 Ohms, 0-1 MHz).

3   Results and Discussion
The current-voltage characteristics (CVC) of the discharge built using RMS voltage and current (Fig. 2) characterize the energy parameters of the system (power consumption). When operating without ethanol, the length of the discharge varies within a wide range. The discharge length decreases and becomes more stable by adding ethanol aerosol. In both cases the CVC were decreasing. By adding ethanol aerosol, the voltage to the discharge increased by approximately 3 times. Of interest is the fact that the plasma channel does not break at the current zero crossing twice over the period. The observed stability of the discharge suggests that the plasma does not decay during this transition. In this case, it is possible to build

Lissajous figures in a wide range of currents (from almost zero to peak value) using the instantaneous values of voltage and current.
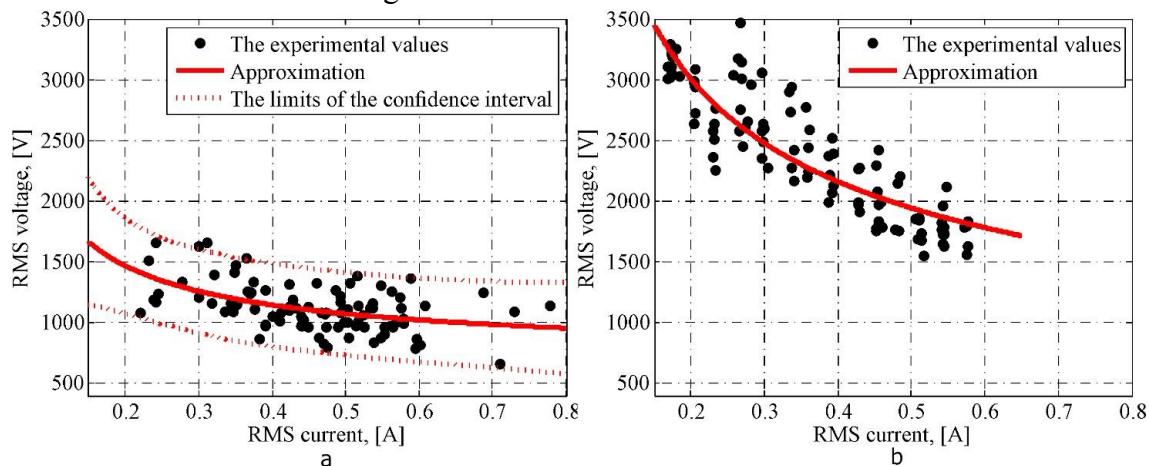
Fig. 2: CVC of the discharge in pure argon (a) and in argon with the addition of ethanol aerosol (b).

The typical shape of the voltage and current waveform in the system, as well as the Lissajous figure (CVC constructed using the instantaneous values), are shown in Fig. 3. The current corresponds to channel 1 (yellow curve) and voltage - to channel 2 (blue curve). Sweep synchronization was performed using AC line. Current channel is inverted.
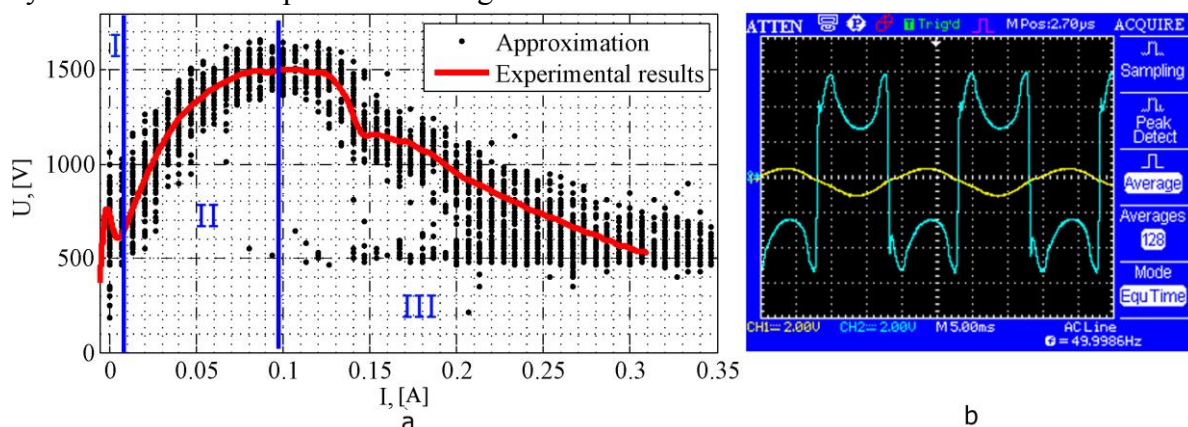
Fig. 3: Lissajous figure (a) and the waveform of current and voltage in the system (b) The voltage was measured by a divider (1: 830, 0-1 MHz), and current. in using measuring resistor (3 Ohms, 0-0.1 MHz). Current - the first channel (yellow curve, is inverted), the voltage - the second channel (blue curve). Waveform obtained by averaging 128 frames.

The current in the system remains nearly sinusoidal. When passing a zero value, no significant deviations from the sine wave were observed. This fact shows that the plasma decays insufficiently quickly to require the new breakdown. Lissajous figure of the discharge (fig 3a) was built for the first quarter period of current oscillations (time from the passing through zero to achieving the peak value). In addition, 3 areas can be distinguished on the characteristic:
•   Initial period until the voltage drops in the left part of the characteristic (I);
•   Rising part (II);
•   Falling part (III).

The local minimum of the voltage at the boundary between parts I and II obviously coincides with the beginning of the predominance of the ionization process over the recombination. At this moment shortly after the current value starts to rise from zero the degree of ionization increases due to the increase of electric power. As a consequence, the conductivity increased and the voltage in the discharge dropped.

The rising section of the Lissajous figure (II) corresponds to the abnormal glow discharge. Decreasing section (III) corresponds to the arc discharge. This conclusion is based solely on the features of CVC [8], other studies are still necessary for the final confirmation, spectral studies in particular. However, the presented data allow us to make an important conclusion: the studied discharge cannot be clearly attributed either to the glow or to the arc discharge. At different times, the discharge may have different characteristics.

4   Conclusion

Rotating gliding discharge, which is powered by the AC power supply, can not be clearly classified as one of the common discharge types. At various times, depending on the phase of the voltage (or current) supply, discharge characteristics correspond to either glow or arc discharge. In this case, it is possible to control the ratio between the durations of the phases of the glow and arc discharge, which can serve as a method of increasing the selectivity of nanomaterials production in such system.

References
1. A Czernichowski, Pure Appl. Chem. 66(6), 1301-1310 (1994)
2. E. Neyts et al., Chem. Rev., 115(24), 13408-13446 (2015)
3. A. Czernichowski, In *19th Int. Symp. on Plasma Chem. (ISPC-19)*, Bochum, Germany, (Vol. 31, p. 4) (2009)
4. A. J. Wu et al., IEEE Trans. Plasma Sci., 42(11), 3560-3568 (2014)
5. I. Veremii et al., Probl. Atom. Sci. Tech. 6 (94), 215-218 (2014)
6. R. A. Sheldon, Green chemistry and catalysis (John Wiley & Sons, 2007)
7. D. Chernolutsky et al., Probl. Atom. Sci. Tech. 6 (94), 175-178 (2014)
8. M. Druyvesteyn, Rev. Mod. Phys. 12(2), 87 (1940)

ELECTRICAL AND SPECTROSCOPIG INVESTIGATIONS OF BARRIER DISCHARGE AT TRIPLE JUNCTION

P. Synek, J. Voráč, T. Hoder

Department of Physical Electronics, Masaryk University,
Kotlářská 2, Brno, Czech Republic

E-mail: synek@physcis.muni.cz

Electrical and optical emission measurements and their results are presented for special case of the dielectric barrier discharge at the so-called triple junction. In our case the described discharge was operated in argon gas at atmospheric pressure with de-ionized water as liquid electrode and fused silica as dielectrics. High resolution temporal measurements of current-voltage characteristics were accompanied with phase resolved optical emission spectrometry and optical imaging. Preliminary results of spectral investigation were obtained and show strong non thermal distribution of OH states.

Keywords: plasma; dielectric barrier discharge; current-voltage characteristics; optical emission spectroscopy

1 Introduction

Discharges at triple junction are an interesting special case of the surface dielectric barrier discharges (DBDs) which occur at location where three electrically different states of matter are in contact. In most cases such interface is formed between a gas, a solid dielectric and a liquid. Such discharges working at atmospheric pressure were found as a promising tool for various applications (e.g. electrochemistry [1]) mostly due to their ability to produce highly reactive radicals without significantly increasing the gas temperature.

When sufficiently high voltage is applied to electrodes, electrical breakdown in gas occurs and a streamer is developed and propagates at high velocity. This can repeat several times and after a certain amount of charge is deposited on the dielectric, the polarity must be reversed to continue the discharge operation. Most common way to characterize DBDs is by measuring the current-voltage characteristics where current pulses corresponds to propagation of individual streamers and Q-V plots (Lissajous figures) which display the charge transferred through the gas gap and can be deduced as variation of measured charge during the discharge period. When coupled with equivalent circuit model they allow determining internal parameters as gap voltage, discharge (real) current, discharge (real) charge but only if the characteristic discharge capacitances are determined with high precision [2].

Optical emission spectroscopy (OES) has been largely utilized to obtain information about the plasma, mainly owing to the fact that it is a very sensitive and non-invasive method. The atomic spectra have been mostly used to extract information about the highly energetic electrons, whereas the spectra of diatomic molecules are usually believed to reflect the temperature of the neutral gas (e.g. [3]). However the plasmachemical processes in DBD are usually extremely rapid and may result is in strong non-equilibrium of states which while

advantageous for applications, makes these discharges difficult to diagnose. When supplied with suitable model, information about other parameters, such as local and instantaneous electric field may be obtained [4].

2   Experimental

The experimental setup comprises of function generator which supplies tunable signal to amplifier. Amplified signal is transformed to high-voltage and transfered to the electrode. The discharge chamber itself and its schematics are depicted in figure 1. Reactor chamber was flooded with deionized water (conductivity 5 µS/cm) so the grounded electrode was 1 mm under water surface. The discharge was operated at atmospheric pressure while reactor chamber being rinsed by 1 slm of argon gas flow.

Electrical measurements are done with voltage (Tektronix P6015A) and current probes (Tektronix CT2) which are connected to high resolution oscilloscope (Keysight DSO-S 204A). Chamber is equipped with quartz glass windows through which optical emission spectra were measured. We utilized 750 mm Andor spectrometer equipped with ICCD camera for phase resolved OES and low resolution Avantes spectrometer to obtain overview spectral profiles under different conditions.
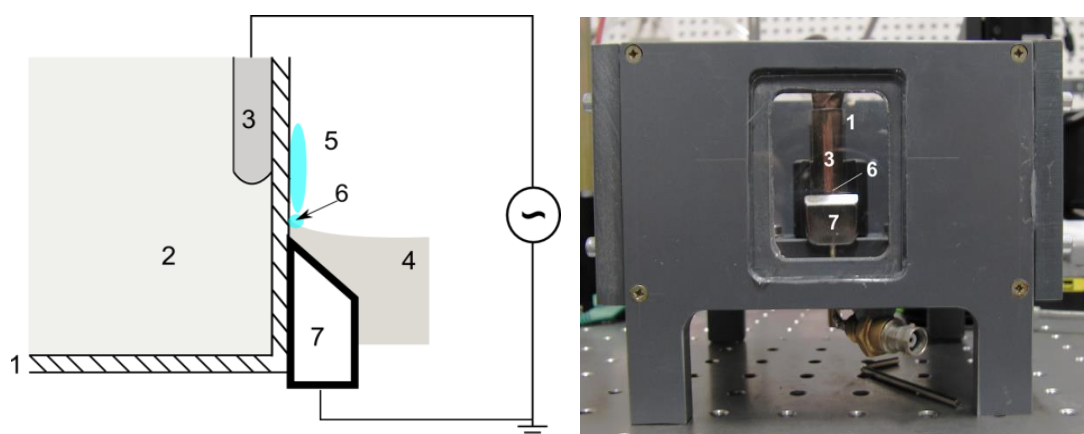
Fig. 1: Schematics (left) and photograph (right) of the experimental setup. 1-fused silica cuvette, 2 – transformer oil, 3 – copper foil, 4 – deionized water, 5 – discharge region, 6 – triple junction, 7 – submerged grounded electrode.

3   Results and Discussion

Discharge started to ignite at 8kV peak-peak voltage and further increase in voltage amplitude led to increase of the current pulses per period. In figure 2. voltage-current curves measured with 13kV peak-peak voltage are presented along with typical current pulse profile.

Q-V plot shown in fig. 3 is in accordance with expectations for surface DBD discharges [5] with distinct 'steps' which are caused by charge transfer through current pulses caused by discharges.
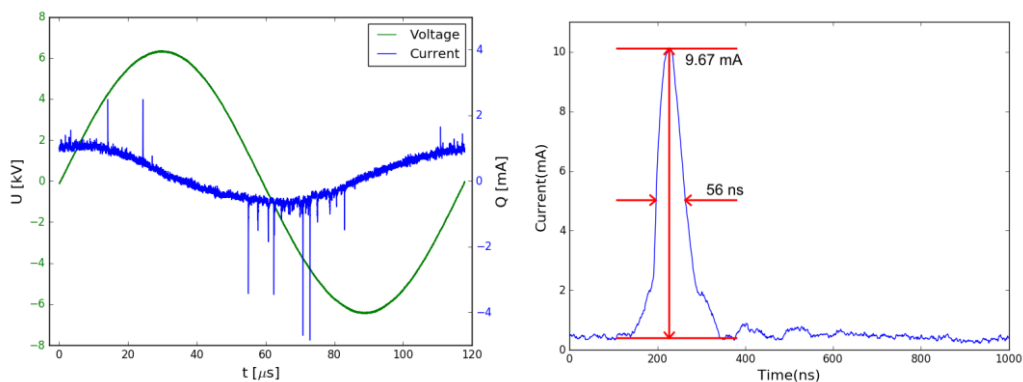
Fig. 2: Current and voltage curves of discharge accompanied by typical current pulse profile with FWHM and amplitude.
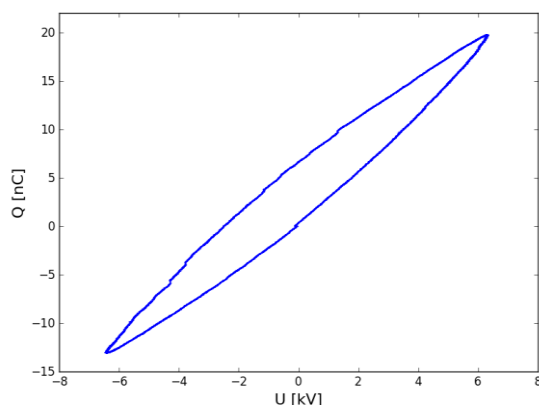
Fig. 3: Q-V plot of the discharge with noticeable steps at position of current pulses

Optical emission spectra (figure 4) show presence of argon atomic lines accompanied by oxygen triplets and weak H_α line. From molecular point of view the near UV region is predominantly populated by OH (A-X) vibration bands with weak N_2 (C-B) transition bands which originate from air impurities in the chamber.
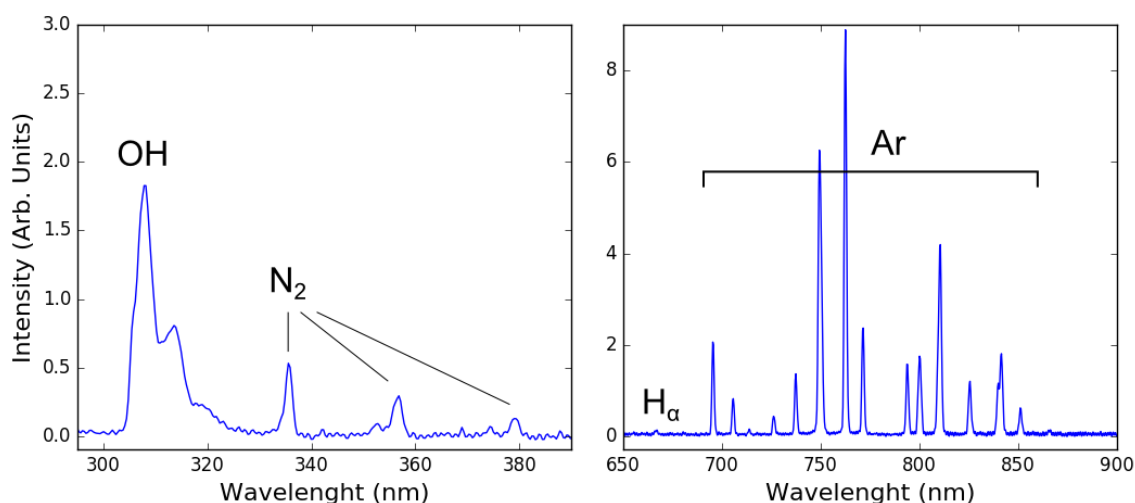
Fig. 4: Overlook of spectral emission components in the discharge measured on Avantes spectrometer

4   Conclusion

We have performed extended study of dielectric barrier discharge at triple junction using electrical and optical emission measurements. This yielded high resolution temporal measurements of current-voltage characteristics which were processed into Q-V plots determine chamber and discharge parameters. Electrical measurements were accompanied with phase resolved optical emission spectrometry and optical imaging. Our future plan is to tackle the problem of non-Boltzmann distribution in OH by determination of population of each individual state.

Acknowledgement

References

1. D. Pavliňák et al., Appl. Phys. Lett. 105 (2014) 154102
2. A. V. Pipa et al., Rev. Sci. Instrum. 83 (2012) 115112
3. M. Šimek, J. Phys. D: Appl. Phys. 47 (2014) 463001
4. T. Hoder et al., Plasma Sources Sci. Technol. 25 (2016) 025017
5. J. Kriegseis et al., J. Appl. Phys. 110 (2011) 013305

ADVANCED SPECTRA FITTING

J. Voráč, P. Synek, V. Procházka

Department of Physical Electronics, Faculty of Science, Masaryk University,
Kotlářská 2, 611 37 Brno, Czech Republic

E-mail: vorac@mail.muni.cz

A new method of spectral fitting is presented, where population of each state is treated independently. An example evaluation of OH (A-X) spectrum obtained in a microwave plasma jet at atmospheric pressure is presented. Two vibrational bands (0,0) and (1,1) are present in the emission. It appears that each vibrational state has a different rotational temperature.

Keywords: spectroscopy; fit; Boltzmann-plot

1   Introduction

Optical emission spectroscopy (OES) is a widespread method for investigating plasma discharges, mainly due to the fact that it is a very sensitive and non-invasive method. The spectroscopy of diatomic molecules can be used to obtain temperature of the neutral gas. If a suitable model is employed, also information about other parameters, such as local and instantaneous electric field may be obtained [1].

When evaluating an emission spectrum, the population distribution of upper states of a transition is investigated. If collisions are important for the energy balance, the population distribution follows the Boltzmann formula

$$n(|\mathrm{u}\rangle) \propto g_\mathrm{u} \exp\left(\frac{-E(|\mathrm{u}\rangle)}{k_\mathrm{B}\,T}\right) \tag{1}$$

where $|\mathrm{u}\rangle$ denotes the respective upper state, $n(|\mathrm{u}\rangle)$ its population, g_u is its degeneracy, k_B is the Boltzmann constant and T is temperature. Depending on the dominant collision partner of the investigated species, different temperatures can be found. Rotational distribution of certain diatomic molecules at elevated pressure may give the temperature of a neutral gas. The vibrational distribution of a diatomic molecule may provide a lower limit of electron temperature and atomic spectrum contains information about the highly energetic electrons.

A problem may arise when there is not a single process absolutely dominating the energy transfer. To visualise the population distribution, a so-called Boltzmann plot may be constructed, where the logarithm of populations (divided by their degeneracy) is plotted versus the upper energy of the states. If this plot shows a single straight line, the system is said to be in some sort of partial equilibrium. However, it may be difficult to determine the population of respective upper states from spectra, particularly when the instrumental resolution is low. This can be overcome by fitting a spectral simulation, where a temperature is given as an input parameter, to measured spectra. Fitting only several parameters (usually intensity and rotational, eventually also vibrational, temperature) reduces the computational

difficulty and increases the stability of results. On the other hand, it also hides any deviations from thermal distribution.

In this contribution, we present a novel approach to fitting molecular spectra, where the states are treated independently, i.e. the respective population of each rovibronic state is a parameter of the fit. First, an array of vectors is created, with each vector representing a spectrum for a special case, where only one state is populated. The optimization procedure is then looking for the linear combination of these vectors that fits the measurement best. Eventual line broadening is taken into account. In this way, also spectra taken with a moderate resolution instrument can be evaluated and Boltzmann plots may be constructed, revealing the nature of the rotational and, if more vibrational bands are measured, also vibrational distribution. The fitting procedure takes advantage of the fact that the spectral simulation is linear with respect to each state's population. Thus, even though the fit needs to cope with several tens or even hundreds of independent parameters, no iterative procedure needs to be employed and the calculation takes a few seconds on a moderate office computer.

2   Experimental

The presented spectrum was measured by a HR-640 monochromator with 1200 g/mm grating. The original detector was replaced by an ICCD camera PIMAX2 with 1024×256 pixels and 16-bit greyscale resolution.

The light was emitted by a surfatron discharge with modulated power, for details see [2]. The presented spectrum was taken during the rising edge of the power modulation, on the axis of the discharge, in the axial distance where a sharp increase of OH radiation was detected, which is attributed to a formation of a vortex structure [2]. In this region, the highly energetic plasma plume with relatively pure argon gas is rapidly mixed with the ambient air, resulting in strong production of OH(A) excited radicals. The spectral range from 305.5 to 328.3 nm was observed for (0,0) and (1,1) bands of OH(A-X) transition.

3   Results and Discussion

In Fig. 1 a measured spectrum and the respective fit is shown. A detail is depicted in Fig. 2 where also emission from both vibrational states (0 and 1) are shown separately. The number of measured points (i.e. pixels in the region of interest) was 718, the number of fit parameters in this case was 80, the resulting number of degrees of freedom was thus 638. The main result of this spectral fit is the relative population of each respective upper state. Logarithm of these populations (divided by the state's degeneracy, i.e. reduced) is plotted versus potential energy of the respective upper states in Fig. 3. This is commonly known as Boltzmann plot. The populations of states with $v' = 0$ appear to follow thermal distribution quite well. The resulting temperature is (3860 ± 92) K. The apparent populations of the states with $v' = 1$ are much more influenced by noise, nevertheless, a straight line can be fitted, with the resulting rotational temperature of (3097 ± 303) K. The reported uncertainty is the standard deviation of the fit. To span the 95% confidence interval, these should be multiplied by 2. In this particular case, the 2-sigma intervals slightly overlap, nevertheless it appears that the 2 vibronic states have different rotational temperature.
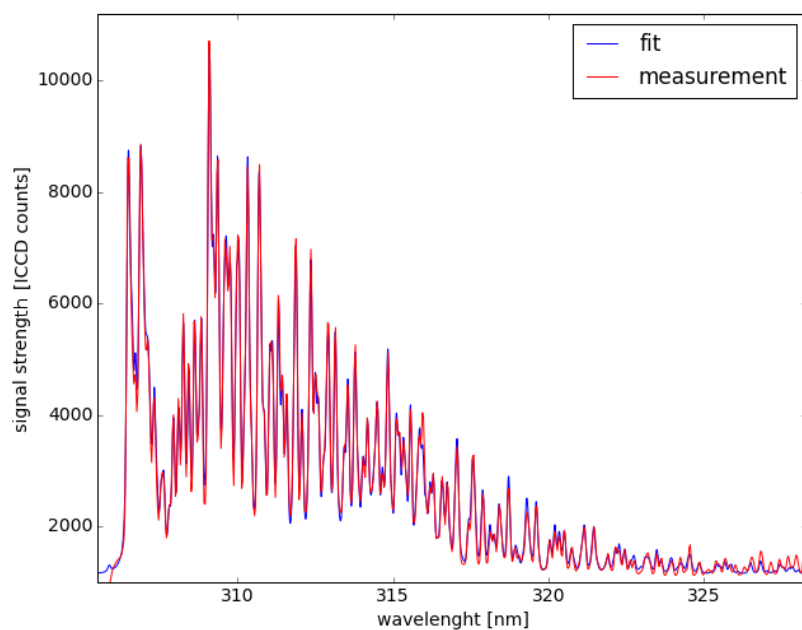
Fig. 1: Measured emission spectrum (red) and fit by states (blue). (0,0) and (1,1) bands are overlapping in this spectral region.
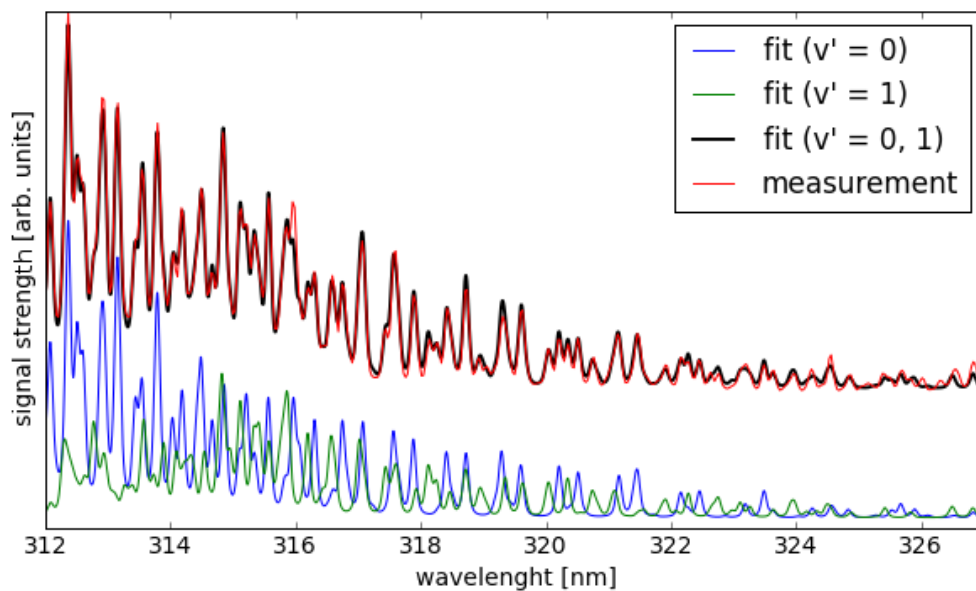
Fig. 2: Measured emission spectrum in detail (red) and fit (black). The blue and green line show resolved emission from vibrational states 0 and 1, respectively. An artificial offset is added for clarity.
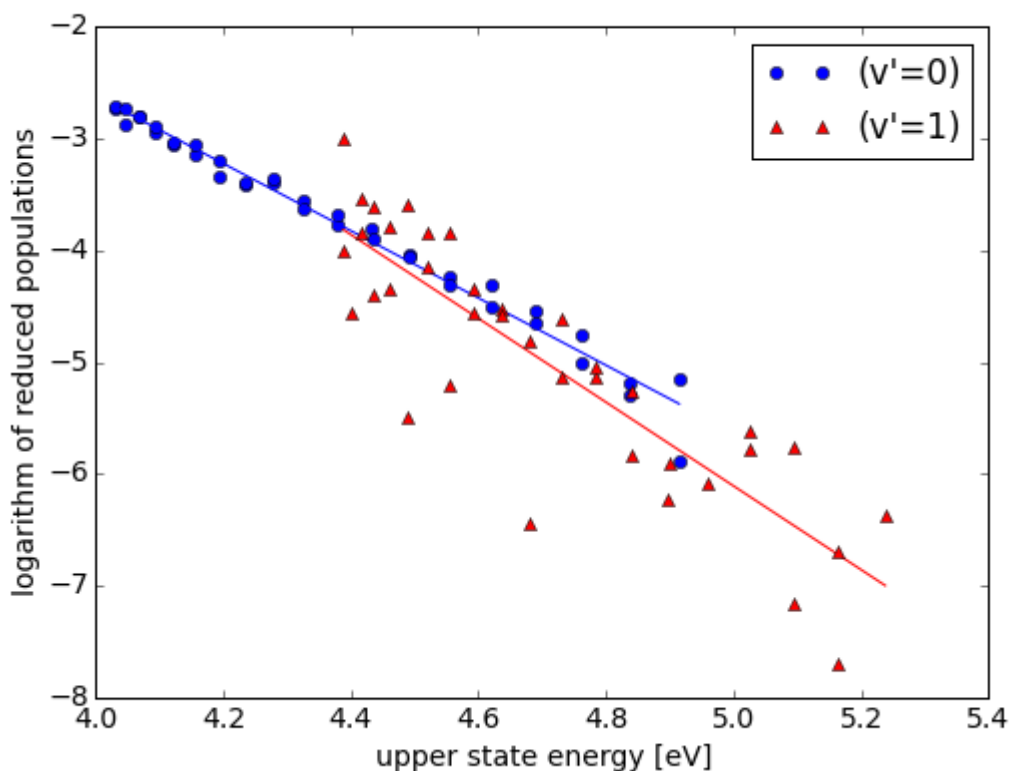
Fig. 3: Boltzmann plot with resolved upper vibrational states. The lines show linear fit for each vibrational band. The resulting temperatures are (3858 ± 92) K for ($v' = 0$) vibronic state and (3097 ± 303) K for state with ($v'=1$).

4 Conclusion

A novel method for spectral fitting is presented. Similarly to well established method of fitting spectral simulations with temperature as a parameter, the presented method takes into account also the line broadening (including instrumental) and can thus be used with moderate resolution spectra. On the other hand, it enables to evaluate the populations of each upper state independently, which may reveal eventual inequilibrium.

Acknowledgement

References
1. T. Hoder et al., Plasma Sources Sci. Technol. 25, 025017 (2016)
2. J. Voráč et al., Plasma Sources Sci. Technol. 25, 025018 (2016)

TOPIC 3: MOLECULAR SYNTHESIS AND DECOMPOSITION

PLASMA-CATALYTIC REFORMING OF OXYGEN-CONTAINING HYDROCARBONS

I. Fedirchyk[1], O. Nedybaliuk[1], V. Chernyak[1], V. Demchina[2]
[1]Taras Shevchenko National University of Kyiv, Address of First Author, Ukraine
[2]Gas Institute of NASU, Address of Second Author, Ukraine

E-mail: igor.fedirchyk@univ.net.ua

This research aims to investigate the conversion efficiency of the plasma-catalytic reforming of renewable oxygen-containing hydrocarbons. Reforming was conducted in a system that used low power rotating gliding discharge for the plasma generation. The samples of synthesis gas produced during the reforming of sunflower oil and ethanol were analyzed via the gas chromatography and mass spectrometry. The study obtained the reforming efficiency and the ratio between the chemical energy of the produced synthesis gas and the electrical energy spent on the reforming for the plasma-catalytic conversion of different raw materials.

Keywords: plasma-catalytic reforming; renewable hydrocarbons conversion; rotating gliding discharge

1 Introduction

From the point of sustainable development, chemical industry must move towards the efficient utilization of renewable raw materials, the avoidance of toxic and hazardous reagents, and the elimination of waste [1]. One of the main directions of such change lies in the transition from the fossil hydrocarbons to the renewable hydrocarbon raw materials produced from biomass. The main difference between the renewable and fossil hydrocarbons is in the presence of oxygen in most renewable raw materials. This poses problems to the traditional hydrocarbon processing technologies because the difference in raw material composition significantly decreases the efficiency and increases the amount of produced intermediates and waste. This often outweighs the advantages of renewable raw materials and increases their processing costs. The advancements of plasma chemistry gave birth to the new ways of renewable hydrocarbons processing, which take advantage of the high chemical reactivity of plasma species [2]. Most of the existing research on plasma-assisted hydrocarbon conversion deals with the plasma reforming, which offers high feedstock conversion rate but has low energy efficiency [2, 3]. The other approach to the hydrocarbon conversion, the plasma-catalytic reforming, uses low temperature atmospheric pressure plasma as a source of active species that initiate and accelerate the chain reactions of hydrocarbon reforming [2, 4]. In our study, we conducted the plasma-catalytic reforming of the liquid renewable oxygen-containing hydrocarbons. The study focuses on the reforming and energy efficiency of such conversions and on the ability to influence them using plasma.

2 Experimental

We studied the plasma-catalytic hydrocarbon reforming using a setup shown at Fig. 1. Ethanol and sunflower oil represented the oxygen-containing renewable hydrocarbons. Atmospheric air was used as an oxidant in the reforming process. The plasma generation takes

place in the discharge chamber (1) using low power (10 – 70 W) DC rotating gliding discharge. Plasma is injected by an air vortex into the pre-heated to 400 °C reaction chamber (2) through an aperture. The mixture of hydrocarbon, water steam, and air flows into the reaction chamber and mixes with the plasma species. The volume of reaction chamber is 0.2 L. The interaction between the plasma and the mixture results in the reforming of hydrocarbon and production of synthesis gas. Obtained synthesis gas cools down in the flowing water cooler (3). The non-gaseous reforming products are collected in the condenser (4). Produced synthesis gas was combusted in an open airspace using the plasma of transverse discharge (5) or in the water boiler.
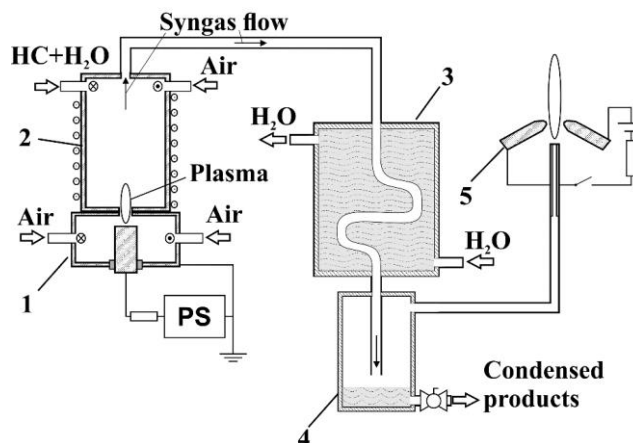
Fig. 1: Simplified schematic of the experiment.

The total airflow into the system corresponded to the amount of oxygen needed for the partial oxidation of injected hydrocarbon. The hydrocarbons were injected in quantity that was equal to 2, 5, and 8 kW of power released during their combustion. The flow of gaseous reforming products was determined using rotameters. The product composition was analyzed using gas chromatography and mass-spectroscopy. The behavior of the flame of combusted synthesis gas in response to the changes of discharge state was recorded on video.

3   Results and Discussion

The gas chromatography and mass spectrometry of produced synthesis gas showed that H_2, CO, CH_4, C_2H_4 are the main products of the plasma-catalytic conversion of the renewable oxygen-containing hydrocarbons. Nitrogen oxides were absent from the reforming products. This shows that nitrogen did not take part in chemical reactions, despite of its presence in the air used for the conversion. Typical composition of synthesis gas is shown at Fig. 2.
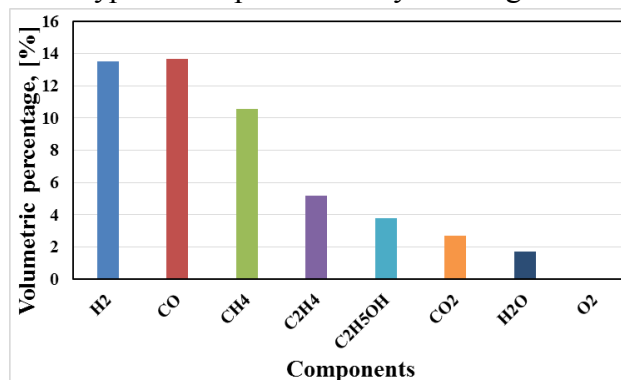
Fig. 2: Typical composition of produced synthesis gas.

The liquid collected in the condenser mostly contains ethanol and water, which are considered as the unreacted reagents in the calculations of reforming parameters. Liquid corresponds to less than 10 % of the reforming products.

The knowledge of the gaseous product composition allowed us to determine the value of the conversion efficiency of the conducted reforming and the ratio between the chemical energy of produced synthesis gas and the electric energy spent on plasma generation during the reforming. The energy spent on the heating of the reaction chamber is not present in the efficiency calculations, as it is not commonly used in the evaluation of the conversion efficiency of plasma-assisted reforming systems [5] and was not the focus of this study. It should be noted that the system could be pre-heated either by external heater or by combusting part of the hydrocarbon before launching the reforming process. The optimal obtained values are approx. 85 % for conversion efficiency and approx. 100 for the ratio between the chemical energy of produced synthesis gas and the electric energy spent on plasma generation during the reforming. The energy yield of hydrogen is approx. 300 $g(H_2)$/kWh, which is higher than in most existing systems for plasma-assisted hydrocarbon reforming [6].

The plasma-catalytic partial oxidation reforming of hydrocarbons was conducted at the temperatures of 400-450 ^oC, which is approximately two times lower than the temperature of the catalytic partial oxidation [7]. The reforming did not occur without the plasma generation in discharge. The interruption of the discharge caused the stop of the reforming in less than 5 seconds, which was indicated by the disappearance of the gaseous reforming products. The time between the ignition of the discharge and the start of reforming was less than 4 seconds. The existence of the reforming at the observed temperatures and its fast reaction to the presence of the discharge indicate that the plasma-catalytic approach allows to control the reforming processes with much higher chemical energy.

4   Conclusion
Plasma-catalytic reforming of renewable oxygen-containing hydrocarbons can offer high conversion efficiency and ratio between the chemical energy of produced synthesis gas and the electric energy spent on the reforming. Research showed that produced synthesis gas can be combusted in the commercial water boilers without reducing the energy conversion efficiency of a boiler.

References
1. R. A. Sheldon et al., Green chemistry and catalysis (Wiley-VCH, Weinheim, 2007)
2. A. A. Fridman, Plasma chemistry (Cambridge University Press, Cambridge, 2008)
3. O. A. Nedybaliuk et al., Probl. At. Sci. Technol. 6, (2012)
4. O. V. Solomenko et al., Probl. At. Sci. Technol. 1, (2015)
5. G. Petitpas et al., Int. J. Hydrogen Energy 32, (2007)
6. J. Mizeraczyk et al., Eur. Phys. J. Appl. Phys. (to be published)
7. F.-P. Nagel, D.Sc. thesis, ETH Zurich, 2008

MICROWAVE PLASMA SYNTHESIS OF IRON OXIDE NANOPARTICLES AND THEIR APPLICATIONS

O. Jašek, P. Synek, V. Kudrle

Department of Physical Electronics, Faculty of Science, Masaryk University,
Kotlářská 2, 611 37, Brno, Czech Republic

E-mail: jasek@physics.muni.cz

Microwave plasma synthesis is attractive way to produce nanostructured materials. Here we present synthesis of iron oxide nanoparticles in atmospheric and low pressure microwave discharges by decomposition of iron pentacarbonyl. In microwave plasma torch at atmospheric pressure crystalline phase of synthesized iron oxide nanoparticles could be purposely controlled by amount of O_2 flow in $Ar/Fe(CO)_5/O_2$ mixture. We were able to prepare high purity maghemite samples and also samples with high content (up to 30 percent) of rare epsilon-Fe_2O_3 phase. Low pressure surface wave discharge was used for synthesis of magnetite and maghemite samples and their functionalization was studied. Prepared nanoparticles were used in carbon nanotube growth, photoelectrochemical studies and labeling of stem cells.

Keywords: microwave plasma; iron oxide; nanoparticles; phase composition, maghemite

1 Introduction

Iron oxide based nanoparticles (INPs) are materials that drawn increasing attention in the scientific community in the recent decades [1]. INPs exhibit unique magnetic and chemical properties and are bio-compatible which give them potential for numerous medical applications. The former applications often utilize the superparamagnetic behavior of NPs with the diameter below 20 nm. They include, for example, selective drug delivery, magnetic resonance imaging or hypertermia treatment [2]. The most common methods of iron oxide NP synthesis are liquid chemical methods such as co-precipitation, micro-emulsion and hydrothermal synthesis [3]. Different synthetic approaches are represented for instance by flame pyrolysis, chemical vapor deposition or by plasma synthesis routes. At present, various types of plasmas have been used for NP synthesis, among them radio frequency (RF) thermal plasma, low pressure RF plasma, microwave (MW) plasma transferred or non-transferred direct current (DC) plasma arc, and atmospheric pressure glow discharge [4].

In this paper we discuss our results of INPs synthesis in microwave plasma systems in low and atmospheric pressure and their applications.

2 Experimental

In our work we use two microwave experimental setups for synthesis of iron oxide nanoparticles, microwave plasma torch (MPT) at atmospheric pressure and low pressure microwave surface wave discharge (LPSW).

Our current MPT setup consists of microwave generator operated at 2.45 GHz, 2 kW maximum power, from which microwave power was transmitted through water cooled ferrite circulator. Microwaves propagate through a rectangular waveguide WR340 which is gradually transformed to WR430 waveguide. Inside W430 rectangular waveguide, there is gradual transition to Π waveguide which is coupled to coaxial waveguide at λ/4. The central

conductor of the coaxial waveguide is prolonged to the discharge chamber, forming a nozzle. Teflon seal is mounted on the entrance to the reactor chamber as gas barrier. Reactor chamber consists of 8 cm quartz tube which is 15 cm long. Both ends are fixed to stainless steel caps by elastic silicon bands. Outlet is standard DN40KF flange connected to gas outlet ventilation. The gases are supplied to the discharge chamber through the nozzle which has two gas channels. Inner channel is in the nozzle axis and outer channel exits as a concentric slit. This way gas exiting outer channel follows curvature of the nozzle and enters discharge near a central nozzle exit. More details about the experimental setup and extensive discharge and carbon nanotubes deposition can be found in our previous publications [5, 6].

The powder was synthesized from iron pentacarbonyl vapors mixed with argon and oxygen. Iron pentacarbonyle was kept in a blower and 100 sccm of argon flowing above the liquid surface resulted in 1 sccm flow rate of $Fe(CO)_5$ vapors. $Ar/Fe(CO)_5$ was mixed with O_2 flow rate of 0, 5, 25, 150, 300, 500, 750 or 1,000 sccm and introduced into the torch by the outer nozzle channel. The inner nozzle channel supplied the majority of Ar flow, 560 sccm. The microwave power was 210 W. The deposition time was 15 minutes and after the deposition the powder was collected from the reactor walls.

LPSW setup consists of the microwave generator operated at 2.45 GHz frequency with maximum 2 kW microwave power. The flow of working gases (Ar, O_2) into the reactor was controlled by electronic flow-controllers. The plasma was excited in 1 m long, 2-4.5 cm diameter fused silica tube by means of a waveguide applicator (SURFG 439 by Sairem, France). The operating pressure was set by dynamic balance between the total gas flow and the throttling of a rotary vane pump. Typical pressure during synthesis was in the range of 0.5–3 kPa. Reactor scheme can be found in Fig. 1.
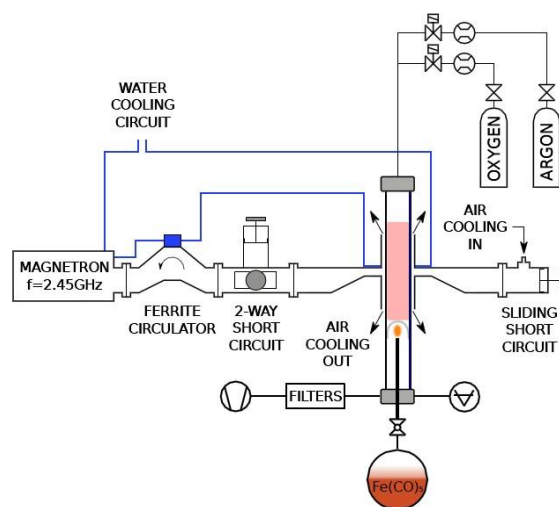
Fig. 1: Experimental setup for iron oxide synthesis in microwave surface wave discharge.

Typical deposition conditions for INPs in LSPW are following. Discharge is ignited in 280 sccm or Ar, with 500 W of microwave power and $Fe(CO)_5$ flow of 1.75 g/min. The $Fe(CO)_5$ injection point was situated 33 cm downstream from the launcher. Deposition time was 3 to 15 minutes. After the deposition, the reactor was filled with Ar and collected from reactor walls and filter placed downstream in front of the pumping system.

3   Results and Discussion

In microwave plasma torch we studied phase composition of iron oxide nanoparticle nanopowder in dependence on oxygen flow rate. Magnetite and maghemite phases could not be distinguished using the standard X-ray diffraction (XRD) analysis. Therefore, a combined XRD and Raman spectra analysis had to be applied, which is based on fitting of selected diffraction peaks and spectral features. According to XRD and Raman spectroscopy, the powder synthesized from $Ar/Fe(CO)_5$ consisted about 50 % of magnetite, Fe_3O_4, the rest being α-Fe and FeO. An increase in oxygen flow rate led to an increase in γ-Fe_2O_3 percentage, at the expense of α-Fe, FeO and Fe_3O_4. Almost pure γ-Fe_2O_3 was synthesized at oxygen flow rates 25–75x higher than the flow rate of $Fe(CO)_5$ [7]. A further increase in the oxygen flow rate led to α-Fe2O3 and ε-Fe2O3 production see Fig. 2.
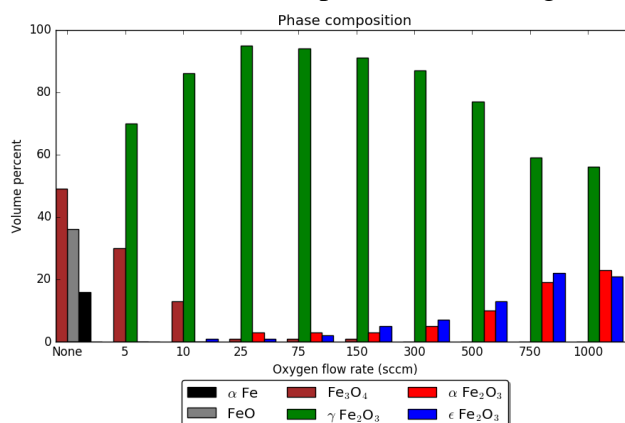
Fig. 2: Phase composition of iron oxide nanopowder in dependence on oxygen flow rate.

We also investigated photoelectrochemical performance of hematite layers deposited in microwave plasma torch. Quartz substrates (10 x 40 mm) with FTO conductive layer were placed 10 cm above the nozzle and we carried out short (10 seconds) deposition with following parameters: Ar 700 sccm, O_2 1000 sccm, Ar flow above $Fe(CO)_5$ 280 sccm, microwave power was 210 W. The layers were tested in photoelectrochemical cell (PEC) in following conditions: 1 M NaOH solution (pH 13.2), 5 $mV.s^{-1}$ scan rate, AM 1.5 100 mW cm^{-2} simulated sunlight. The response of the deposited layers can be seen in Fig 3. Deposited films were also doped by Sn by decomposition of $(CH_3)_4Sn$ in discharge but the generated current density did not reach values obtained by other authors [8].
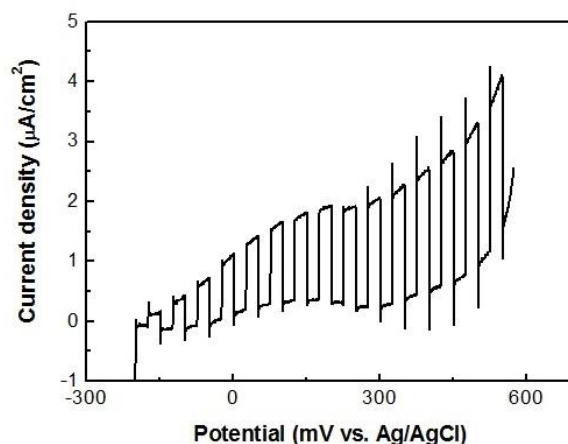
Fig. 3: Photoelectrochemical characteristic of hematite layer.

Maghemite is promising biocompatible material. Plasma synthesized maghemite nanoparticles present attractive alternative to nanoparticles prepared by chemical route. We studied interaction of different cell cultures including pluripotent cells with microwave plasma torch generated maghemite nanoparticles. Our data indicate that these nanoparticles have minimal toxic effects and can be used in regenerative medicine.

We used LPSW discharge for synthesis of maghemite and magnetite nanoparticles. We were able to increase magnetite phase content up to 90 % by modifying tube configuration, where instead of 2 or 4.5 cm diameter tube along the whole discharge length, we used 2 to 4.5 cm tube transition behind the applicator.

We have extensively used iron/iron oxide nanoparticles for carbon nanotube growth and applied such nanotubes for various sensors [9].

4   Conclusion

We have successfully prepared iron oxide nanoparticles in atmospheric pressure microwave plasma torch and low pressure surface wave discharge. We were able to change the phase of prepared nanoparticles at will and applied these nanoparticles in wider range of sensor, biomedical and photoelectrochemical applications. Further research is targeting better understanding of deposition process and extending the scope of applications.

Acknowledgements

References

1. D. Vollath, J. Nanopart. Res. 10, 39 (2008)
2. D. L. Huber, Small 5, 482 (2005)
3. S. Laurent et al., Chem. Rev., 108, 2064 (2008)
4. D. V. Szabo et al., Inorganics, 2, 468 (2014)
5. L. Zajickova et al., Pure and Applied Chemistry 82, 1259 (2010)
6. L. Zajickova et al., Plasma Process. Polym. 4, S245 (2007)
7. P. Synek et al, Plasma Chem. Plasma Process. 34(2), 327 (2014)
8. S. Kment et al., Catalysis Today 230, 8 (2014)
9. P. Majzlikova et al., Sensors 15(2), 2644 (2015)

PLASMA DIAGNOSTICS OF THE BARRIER DISCHARGES IN THE BINARY GAS MIXTURES OF ARGON AND ACETONE

K. V. Kozlov, E. A. Abramovskaia

Moscow State University, Department of Chemistry, Leninskie Gory 1/3, Moscow, Russia

E-mail: kozlov@kge.msu.ru

Barrier discharges in the gas mixtures of argon and acetone were operated in the filamentary mode or in the diffuse mode, depending on the acetone concentration and on the discharge gap width. Spatially and temporally resolved plasma diagnostics of these discharges was carried out by means of the technique of cross-correlation spectroscopy. The emission spectra of the discharges were found to contain argon lines as well as the bands of the excited molecules OH, CH, C_2, N_2 and CH_3COCH_3. The role of the metastable states of argon is discussed briefly.

Keywords: dielectric barrier discharge; cross-correlation spectroscopy; acetone; argon.

1   Introduction

In the binary gas mixtures "noble gas + molecular precursor" used as feeding gases to generate plasmas in barrier discharges (BDs), the greater the concentration of molecular precursor, the lower the mean value of electron energy [1]. This statement can be regarded as a hypothesis that should be verified experimentally. In the case of its validity, the variation of the chemical composition of the feeding gas mixture seems to be the simplest method to control the selectivity of the process of molecule decomposition (dissociation) by direct electron impact, provided that this molecule contains chemical bonds with considerably different energies. For example, the authors [2] have demonstrated that the selectivity of the decomposition of hexamethyldisiloxane (HMDSO) in the BD can be controlled by the variation of the feeding gas mixture composition (HMDSO + Ar + N_2). In order to test the applicability of this method to an arbitrary binary system "noble gas + molecular gas with different bond energies", we have undertaken the systematic study of the BD plasma properties in the mixtures of argon and several volatile organic compounds. In this paper, we report our first experimental results concerning the gas mixtures of argon and acetone. Acetone was chosen as a precursor mainly for two reasons. First, it is one of the simplest organic compounds with chemical bonds of essentially different energies. Second, the mixtures of argon and acetone are of particular interest due to the results of the authors [3] who demonstrated that under certain experimental conditions, the BD can be operated in the diffuse ("glow-like") mode.

2   Experimental

The experimental set-up for spatially resolved spectroscopic measurements and the CCS-method are described in detail elsewhere [4]. In order to localize repetitive microdischarges at a fixed position, a discharge cell consisting of two semi-spherical electrodes (radius of curvature R = 7.5 mm, see fig.1, both covered with glass) was used. The BD was operated by

sinusoidal voltage at a frequency within the range 2-7 kHz. The discharge gap width (the distance between the electrode tips) was variable within the range 0.5 – 11.0 mm.

3   Results and Discussion

In our experiments, the shape (in particular, the diameter) of the visible discharge channel was found to depend strongly on two parameters, namely on the concentration of acetone and on the discharge gap width. The BD operation modes for which the visible diameter of the discharge channel was approximately equal to or greater than the distance between the electrode tips we denoted as a diffuse mode. The difference between the diffuse and filamentary modes is clearly seen by a naked eye (see fig.1).
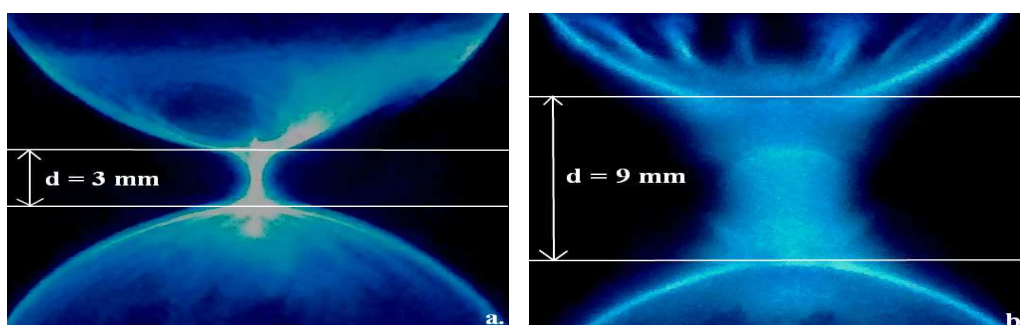
Fig. 1: Typical examples of the filamentary mode (a) and of the diffuse mode (b) of the discharge operation. Acetone concentration: (a) 10 ppm, (b) 1000 ppm. Discharge gap widths are indicated on the photos.

The dependencies of the BD operation mode upon the discharge gap width and upon the acetone concentration are shown in fig.2-a. Since the transition between diffuse and filamentary modes was found to be continuous, sometimes it was difficult to distinguish between them. That is why we denoted such BD operation modes as "transition mode" in fig.2-a. As it is clearly seen from these results, under the experimental conditions being considered, the diffuse mode of the BD was observed within the limited concentration range of acetone (0.04% − 0.3%) and for relatively broad discharge gaps (d > 4-5 mm). It seems interesting to mention that the dependencies of the burning voltage of the BDs (peak-to-peak values) on the content of acetone demonstrate profound minimums in the same concentration range (compare fig.2-a and fig.2-b).
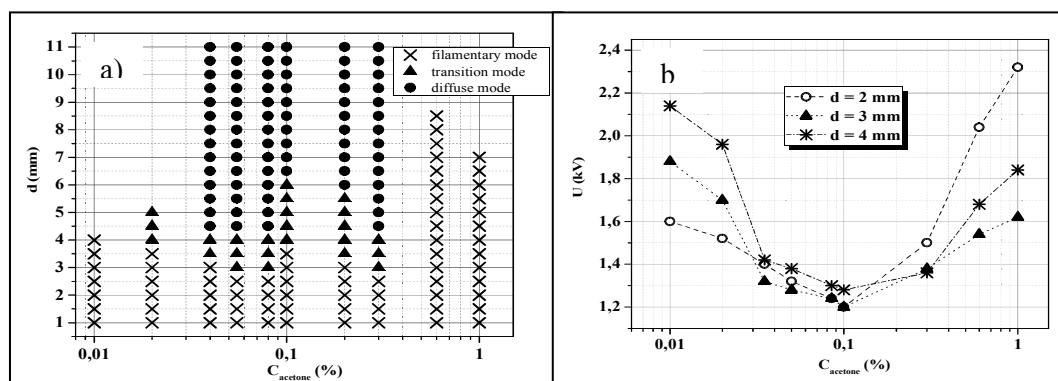
Fig. 2: Dependences of the barrier discharge operation mode (a) and of the burning voltage (b) on the acetone concentration and on the discharge gap width (see explanations in the text). Feeding voltage frequency f = 6.2 kHz, voltage amplitude was maintained at the minimal possible value (equal to burning voltage).

In our experiments, we used argon of the purity 99.997%, containing up to 10 ppm of N_2. Unfortunately, we could not avoid certain increase in humidity of the feeding gas during its passage through the gas preparation system, so the concentration of water at the entry to the discharge cell was about 200 ppm. That is why the BD spectrum even in pure argon (see Fig.3) besides the argon lines

$$Ar^{**} \rightarrow Ar^{*} + h\nu \qquad\qquad (696\ nm < \lambda < 775\ nm) \qquad\qquad (1)$$

contains also the bands of OH radical and of molecular nitrogen:

$$OH(A^2\Sigma^+)_{v=0} \rightarrow OH(X^2\Pi)_{v'=0} + h\nu \qquad\qquad (\lambda = 309\ nm) \qquad\qquad (2)$$

$$N_2(C^3\Pi_u)_{v=0} \rightarrow N_2(B^3\Pi_g)_{v'=0} + h\nu \qquad\qquad (\lambda = 337\ nm) \qquad\qquad (3)$$

For the low concentrations of acetone ($< 0.1\%$), the following spectral bands can be observed

$$CH(A^2\Delta)_{v=0} \rightarrow CH(X^2\Pi)_{v'=0} + h\nu \qquad\qquad (\lambda = 431\ nm) \qquad\qquad (4)$$

$$CH(B^2\Sigma^+)_{v=0} \rightarrow CH(X^2\Pi)_{v'=0} + h\nu \qquad\qquad (\lambda = 389\ nm) \qquad\qquad (5)$$

$$C_2(A^3\Pi_g)_{v=0} \rightarrow C_2(X^3\Pi_u)_{v'=0} + h\nu \qquad\qquad (\lambda = 515\ nm) \qquad\qquad (6)$$

For very high acetone concentrations (10%), the BD spectrum consists of the few comparatively weak argon lines and of three broad bands in the range 350-600 nm. The latter spectral bands can be attributed to the luminescence of acetone molecules.
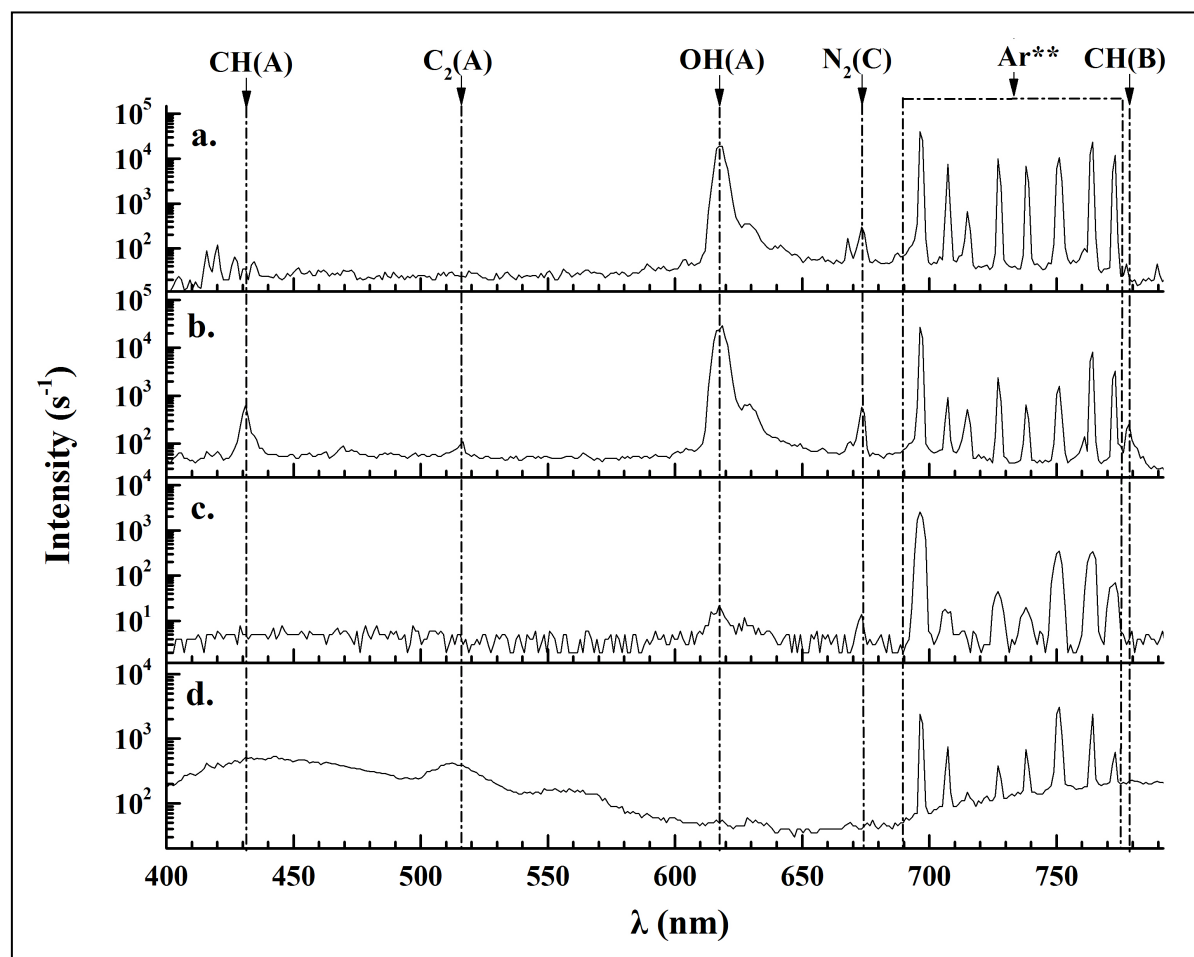
Fig. 3: Emission spectra of the barrier discharges in pure argon (a) and its mixtures with acetone (b,c,d). Concentrations of acetone: (b) 40 ppm, (c) 0.3%, (d) 10%. Experimental conditions: f = 2 kHz, d = 2 mm. All these spectra were registered using diffraction grid 600 mm^{-1}, therefore the UV signals were recorded in the 2nd order of the diffraction grid.

Typical example of the radiation kinetics registered by means of the technique of cross-correlation spectroscopy in the BD in the gas mixtures of Ar and acetone is presented in Fig.4. The signals of Ar (λ = 696 nm), OH-radical (λ = 309 nm), and CH-radical (λ= 389 nm) were chosen as spectral indicators for corresponding radiating species.
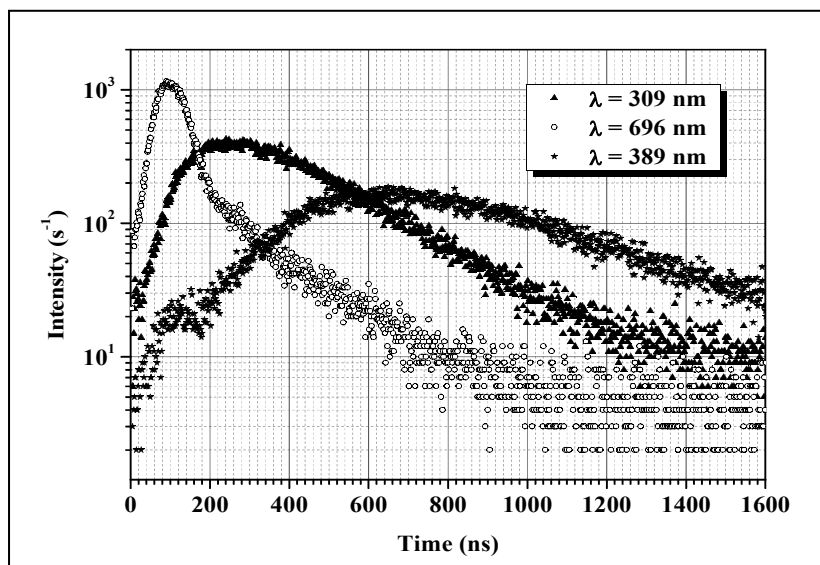
Fig. 4: Radiation kinetics of the barrier discharge plasma for selected spectral indicators. Experimental conditions: acetone concentration 10 ppm, feeding voltage frequency f = 2 kHz, discharge gap width d = 3 mm. Kinetic curves were recorded in the center of the discharge gap.

To explain the behavior of experimental kinetic curves obtained for different acetone concentrations, we carried out a detailed analysis of the radiation kinetics in the system being considered (including computer modeling). As a result of this analysis, a simplified kinetic model was proposed that provided reasonable agreement between the results of kinetic modeling and experimental data. According to this model, radiation kinetics shown in fig.4 can be explained as follows. For the time period 0-200 ns the dominant excitation process is direct electron impact, and then the metastable states of Ar begin to play a leading role.

4 Conclusion

Barrier discharges in the gas mixtures of argon and acetone can be operated either in the filamentary mode, or in the diffuse mode. Under experimental conditions being considered, the diffuse mode is observed within the limited concentration range of acetone (0.04% − 0.3%) and for the discharge gap width d > 4-5 mm. Detailed analysis of discharge emission spectra and of the observed radiation kinetics in a wide range of acetone concentration leads to the conclusion, that chemical composition of the feeding gas mixture exerts strong influence on the electron energy distribution and, consequently, on the efficiency and selectivity of acetone decomposition in the barrier discharge plasmas.

References

1. K. V. Kozlov et al., in *Proceedings of the 10th International Symposium on High Pressure Low Temperature Plasma Chemistry (HAKONE-X)*, Saga, Japan, 2006, p. 124
2. A. Sonnenfeld et al., Plasmas and Polymers 6, 237 (2001)
3. K. Urabe et al., Jap. J. Appl. Phys. 50, 11R, 116002 (2011)
4. P. A. Tatarenko et al., Moscow University Chemistry Bulletin, 65, 6, 350 (2010)

HYDROGEN PRODUCTION FROM ETHANOL USING DIELECTRIC BARRIER DISCHARGE

B. Ulejczyk[1], M. Zbrowska[1], D. Bala[1], Ł. Nogal[2], M. Młotek[1], K. Krawczyk[1]

[1] *Warsaw University of Technology, Faculty of Chemistry, Noakowskiego 3, 00-664 Warszawa, Poland*
[2] *Warsaw University of Technology, Faculty of Electrical Engineering, Pl. Politechniki 1, 00-661 Warszawa, Poland*

E-mail: bulejczyk@ch.pw.edu.pl

Hydrogen production from a water-ethanol mixture in dielectric barrier discharge was investigated. The effect of the water/ethanol molar ratio on hydrogen production and energy yield was studied. In the reactor with 7 cm^3 of active volume the maximum production of hydrogen was 0.082 mol./h with an energy yield of 21.15 mol. (H_2)/kWh. Besides H_2, the reaction products were CO, CH_4 and a small amount of CO_2.

Keywords: dielectric barrier discharge; ethanol; hydrogen

1   Introduction

Hydrogen (H_2) is considered the fuel of the future, which can be obtained from renewable sources such as biomass. The biomass has to be processed, for example in ethanol fermentation. Thus formed ethanol can be then converted into H_2 by steam reforming, oxidative steam reforming, partial oxidation or decomposition [1-5]. The highest H_2 production can be obtained through steam reforming of ethanol, which can be expressed by the reaction

$C_2H_5OH + 3H_2O \rightarrow 6H_2 + 2CO_2$

However, there are other reactions, which reduce the yield of H_2 production from ethanol, such as:

$C_2H_5OH + H_2O \rightarrow 4H_2 + 2CO$
$C_2H_5OH \rightarrow H_2 + CH_4 + CO$
$2C_2H_5OH \rightarrow 3CH_4 + CO_2$
$CO + 3H_2 \rightarrow CH_4 + H_2O$
$CO + H_2 \rightarrow H_2O + C$
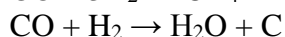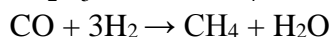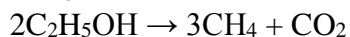
Generally, the process of ethanol steam reforming is performed on various catalysts. However, there are some problems like the use of high temperatures (above 300°C), the use of excess water, and carbon deposition [1-3]. The carbon deposit deactivates the catalyst. The high temperature and the use of excess water cause energy consumption to be high due to heating of the reactants. The process of ethanol steam reforming can be performed in non-equilibrium plasma at lower temperatures [6, 7].

In this paper, we are presenting results of using the dielectric barrier discharge in the process of ethanol steam reforming. Dielectric barrier discharge barrier discharge is a well-known method of non-equilibrium plasma generation. This discharge is used in the synthesis of ozone decomposition of pollutants and surface modification [8-10].

2   Experimental

Ethanol steam reforming was performed in the reactor which is shown in Fig. 1. The grounded electrode was made by applying a silver paste on a quartz tube. An outer diameter of the quartz tube was 54 mm and the wall thickness was 2 mm. The reactor has a grooved

high-voltage electrode. The distance between the high-voltage electrode and the quartz tube ranged from 1.5 to 5 mm respectively from top and bottom of the grooves. The active volume of the reactor (gas volume) was 7 cm^3.
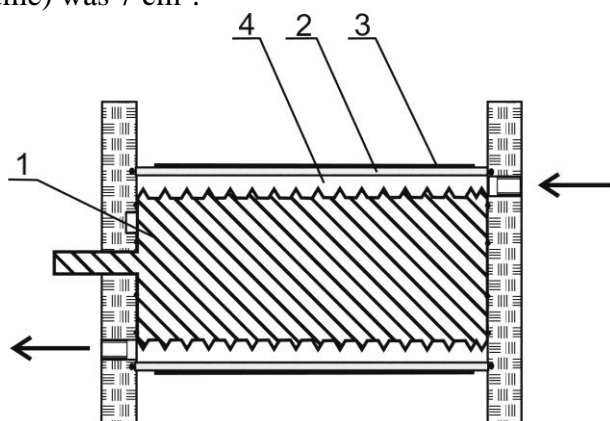
Fig. 1: Scheme of the reactor. 1 – high-voltage electrode, 2 – grounded electrode, 3 – dielectric barrier, 4 – gas space.

The reactant mixture water/ethanol molar ratio fed into the reactor ranged from 1 to 3. The total flow of reactant mixture was kept at 20 g/h. The reactants were evaporated in the reactor. The temperature of the reactor was 100-120°C.

The reactor was powered by a power supply systems of 15 kHz of frequency. The current-voltage curves were recorded by using oscilloscope Tektronix TDS 3052 with a Tektronix P6015A voltage probe and a Tektronix TCP312 current probe with a Tektronix TCP A300amplifier (Fig. 2).
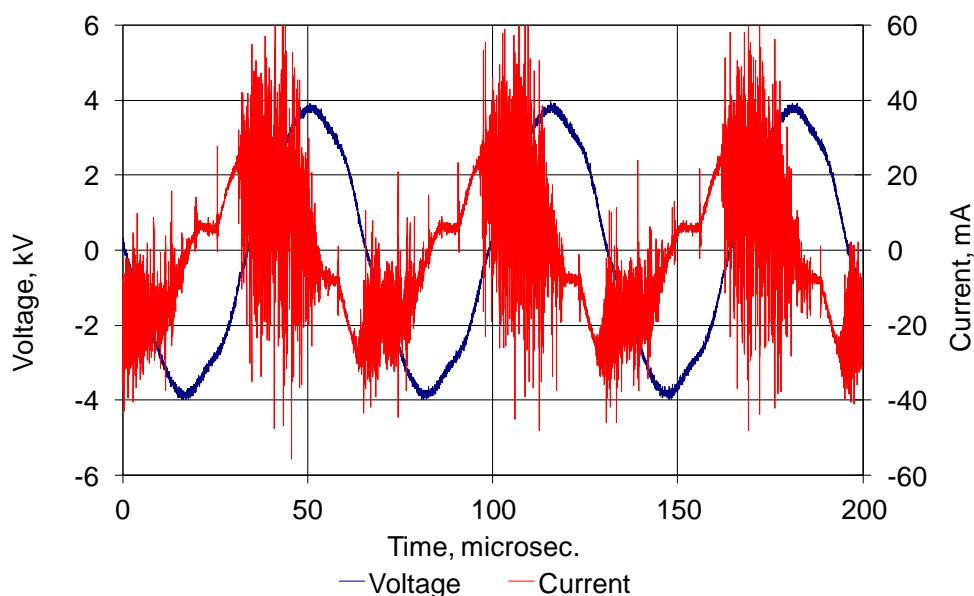
Fig. 2: Typical current-voltage curve of the discharge.

The energy yield was calculated in accordance with the formula:

$$Y = \frac{G}{P} \qquad (1)$$

Y – energy yield, mol (H$_2$)/kWh
G – hydrogen flow rate at the outlet, mol/h
P – discharge power, kW

H_2, CO, CO_2, CH_4 concentrations were analyzed using a Hewlett-Packard HP 6890 gas chromatograph with a TC detector and packed column with ShinCarbon ST 100/120.

3   Results and discussion

The effects of the water/ethanol molar ratio on H_2 production rate and energy yield are show in Figs. 3 and 4. The highest production of hydrogen was achieved when the water/ethanol molar ratio was 1. For this water/ethanol molar ratio the energy yield of hydrogen production was also the highest. Production of hydrogen and energy yield decreased with the increasing water/ethanol molar ratio.

Besides H_2, CH_4 and CO, as well as a small amount of CO_2 were formed. This means that the major chemical reactions in the dielectric barrier discharge were:
$C_2H_5OH + H_2O \rightarrow 4\,H_2 + 2\,CO$
$C_2H_5OH \rightarrow H_2 + CH_4 + CO$
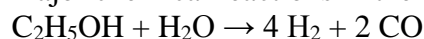
Typically, CO_2 production increases with increasing water vapor. However, in this case it did not happen. CO_2 production was similar for all used water/ethanol molar ratios. CO and CH_4 productions were the smallest when the water/ethanol molar ratio was 3. However, it is connected to the decrease of the H_2 production. Probably this is due to the increase of energy consumption for heating greater amounts of water vapor at the expense of the energy consumed in the chemical reactions.
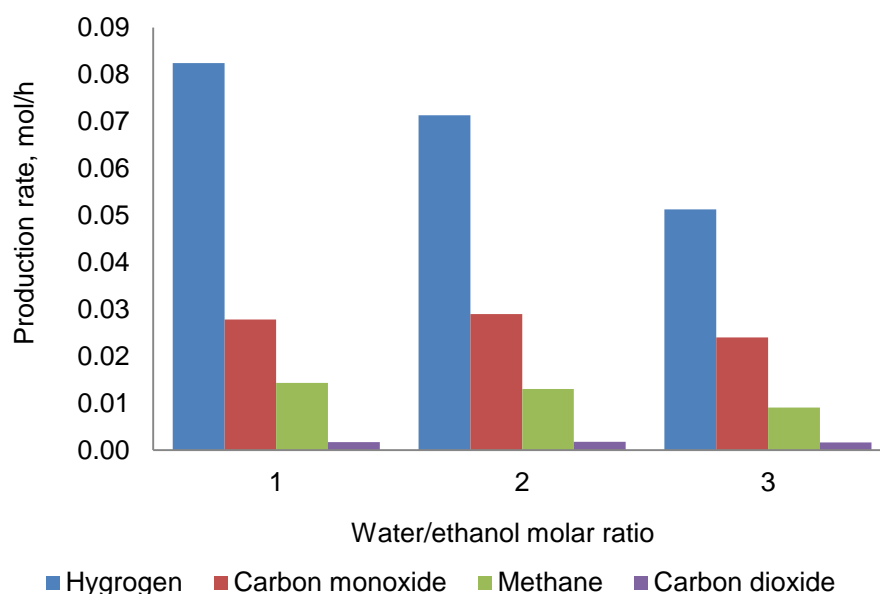
Fig. 3: H_2, CO, CH_4 and CO_2 production rate dependence on water/ethanol molar ratio.
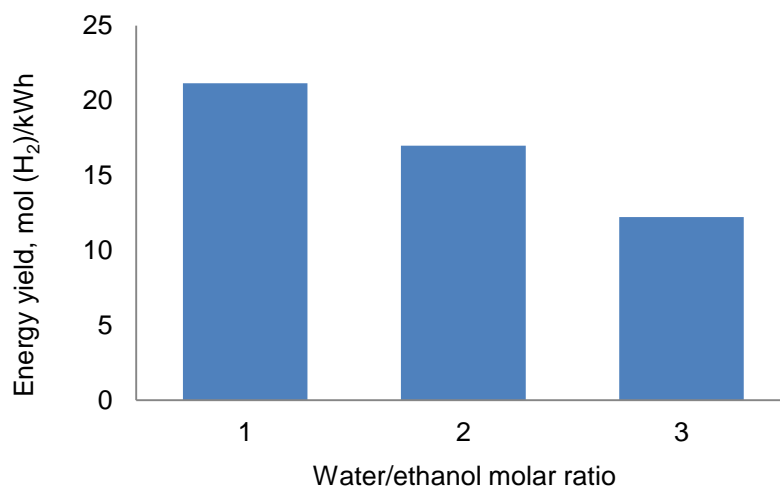
Fig. 4: Energy yield dependence on water/ethanol molar ratio.

4   Conclusions

The process of ethanol steam reforming in dielectric barrier discharge should be performed at low water/ethanol molar ratios. The dominant chemical reactions lead to the formation of H_2, CO and CH_4. The increase in the molar ratio of water/ethanol did not cause significant changes in the chemical reactions, but decreases the energy yield of the production of H_2.

References
1. M. N. Barroso et al., Int. J. Hydrogen Energy 39, 8712 (2014)
2. B. Bej et al., Cat. Today 237, 80 (2014)
3. R. Roldan, Int. J. Hydrogen Energy 40, 2035 (2015)
4. T. Mondal et al., Int. J. Hydrogen Energy 40, 2529 (2015)
5. G. Carotenuto et al., Cat. Today 203, 163 (2013)
6. B. Hrycak et al., Open Chem. 13, 317 (2015)
7. R. Rincon et al., Int. J. Hydrogen Energy 39, 11441 (2014)
8. S. Jodzis, Przem. Chem. 95, 219 (2016)
9. B. Ulejczyk et al., Opem Chem. 13, 509 (2015)
10. T. Opalińska et al., IEEE Trans. Plasma Sci. 37, 943 (2009)

INVESTIGATION OF THE EFFECT OF ON- AND OFF-TIME ON THE DISSOCIATION OF CO_2 IN A PULSED MICROWAVE DISCHARGE

T. Verreycken[1], P. M. J. Koelman[2], D. C. M. van den Bekerom[1], J. M. Palomares-Linares[1], S. Ponduri[1], J. van Dijk[2], G. J. van Rooij[1], M. C. M. van de Sanden[1], W. A. Bongers[1]

[1]*FOM Institute DIFFER – Dutch Institute for Fundamental Energy Research, P.O. Box 6336, 5600 HH Eindhoven, The Netherlands*
[2]*Department of Applied Physics, Eindhoven University of Technology, P.O. Box 513, 5600 MB Eindhoven, The Netherlands*

E-mail: t.verreycken@differ.nl

It is investigated in a pulsed microwave discharge if and how the CO_2 dissociation efficiency can be tuned. By applying power modulation, the discharge parameters can be influenced and heating can be reduced, which could influence the reaction mechanism in the plasma. In this work, the on- and off-time are experimentally varied for a fixed peak power. The on-time ranges between 50 ns and 50 µs. The dissociation degree is determined in the exhaust of the microwave reactor. Interestingly, no clear effect on the dissociation efficiencies is observed for the investigated on- and off-times.

Keywords: CO_2 conversion; pulsed microwave discharge; solar fuels

1   Introduction

Recently, there has been a revival of research on CO_2 dissociation for solar fuel production [1-5]. CO_2 dissociation is of interest not only because of environmental reasons but also for storage of renewable energy which is intermittent. If we want to increase the share of renewable energy in our energy consumption, amongst other things energy storage and flexible power plants are necessary [6]. Plasma-assisted dissociation can address intermittency and can be used to convert excess renewable electricity to CO, which can be further converted to storable fuels such as methane.

It is shown theoretically and experimentally that a microwave discharge can provide a high energy efficiency for CO_2 conversion (up to 80% for subsonic gas flow [7]), which is believed to be due to its low electron temperature T_e [4, 7]. For $T_e \approx 1$ eV, most of the discharge energy is transferred from plasma electrons to CO_2 vibrations [7]. By stepwise vibrational excitation up to the dissociation energy of CO_2 (5.5 eV), efficient dissociation can be obtained. Other, less efficient ways of CO_2 dissociation are thermal dissociation and dissociation by electronic excitation which requires more energy than the dissociation energy. To have a high energy efficiency, it is then key to enhance dissociation by vibrational excitation [2]. When power is applied, vibrational levels are primarily populated by electron excitation (so called eV transfer) [4]. Subsequently, relaxation takes place among the vibrational levels which results in population of high vibrational levels of CO_2 (VV transfer), which might result in dissociation. On the other hand, vibrational levels are depopulated due to transfer to translational degrees of freedom (VT transfer). This process is more likely to occur at a high gas temperature. A possible way to reduce the loss of vibrational to translational energy is

repetitively switching off the plasma before the gas temperature gets too high. Ideally, the modulation is chosen so that during the on-time vibrational levels are sufficiently populated and relax towards higher vibrational levels. This is expressed in an increase in vibrational temperature [3-4]. When the vibrational temperature saturates, the power pulse needs to be switched off. And before VT transfer becomes important and vibrational population is lost, the power pulse needs to be restarted. In this work, the on- and off-time in a pulsed CO_2 microwave discharge are varied. For these measurements, the peak power is kept constant to avoid an influence of the instantaneous power level and thus electron density and eV transfer during the power pulse.

2   Experimental

A pulsed microwave (2.5 GHz) discharge is operated in a quartz tube (ø 30 mm) which is inserted in a WR340 waveguide (figure 1). CO_2 gas is injected tangentially at the top of the quartz tube with a total flow rate of 1.9 slm. A swirl gas flow is created which keeps the plasma away from the tube walls. The pressure p in this work is maintained at 160 mbar. For a gas temperature T_g of 3000 K [8] the residence time t_r of the gas in the reactor can be estimated as

$$t_r = \frac{pV}{Q_{CO_2} kT_g} = 14 \text{ ms} \,, \tag{1}$$

where Q_{CO2} is the particle flow rate in molecules s^{-1} and the volume of the reaction zone V is calculated from the waveguide height and tube diameter. The residence time is significantly longer than the pulse duration.
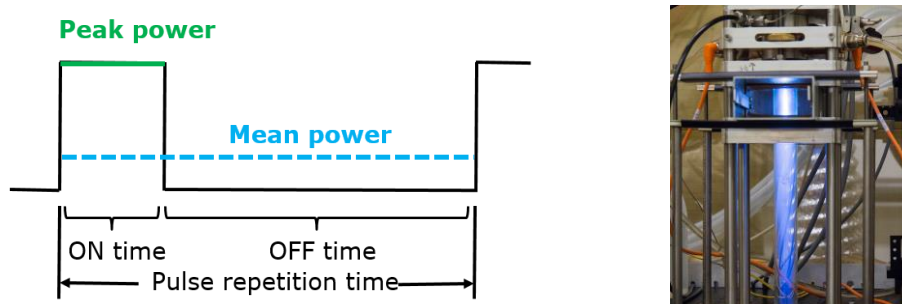
Fig. 1: Left: Duty cycle scheme of the power modulation. Right: Picture of the microwave reactor.

The off-time is varied for a fixed on-time. This is done for on-times of 50 ns, 500 ns, 5 µs and 50 µs. During the duty cycle scan, the peak power P_{peak} is kept constant. According to

$$\text{duty cycle} = \frac{\text{on} - \text{time}}{\text{pulse repetition time}} \tag{2}$$

and

$$P_{\text{mean}} = \text{duty cycle} \cdot P_{\text{peak}} \tag{3}$$

the mean power then changes due to the change in off-time (see also figure 1).

Concentrations of CO and CO_2 are determined in the exhaust of the reactor with a residual gas analyzer. This data is interpreted as follows. The process of CO_2 dissociation is summarized by [7]

$$CO_2 \rightarrow CO + \frac{1}{2}O_2 \qquad \Delta H = 2.9 \text{ eV/molecule} \qquad (4)$$
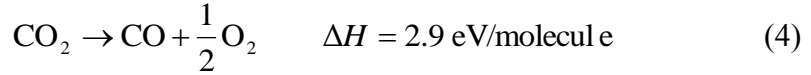
Assuming that no atomic carbon is produced, the conversion degree can be calculated as

$$\alpha = \frac{[CO]}{[CO_2] + [CO]} \qquad (5)$$

and the energy efficiency η as

$$\eta = \alpha \cdot \frac{\Delta H}{SEI}, \qquad (6)$$

where SEI is the specific energy input in eV molecule^{-1}, i.e. the average energy delivered per CO_2 molecule

$$SEI = \frac{P_{mean}}{Q}, \qquad (7)$$

where P_{mean} is the mean power in W and Q the gas flow rate in slm.

3   Results and Discussion

The conversion degree and energy efficiency measured for varying off-time at two different on-times are shown in figure 2. They are plotted as a function of mean power and SEI. The peak power is 550 W. For comparison, measurements are performed in continuous operation with equal mean powers (but different peak powers than in the modulated measurements). For the series with continuous power, the measurements at the two highest mean powers were repeated at the end of the measurement series. These measurements resulted in a higher energy efficiency and give an indication of the accuracy. It needs to be checked if there is an influence of a heating up of the reactor. In addition, the plasma volume needs to be monitored to correct the measured energy efficiencies for a possible change in power density in the plasma.

A lower estimate of the characteristic time for VT transfer is 1 μs for T_g about 3000 K [4]. It is then expected that in the case of 50 ns pulses, longer off-times would result in more time for VV relaxation and thus more efficient dissociation. This is however not observed in figure 2.
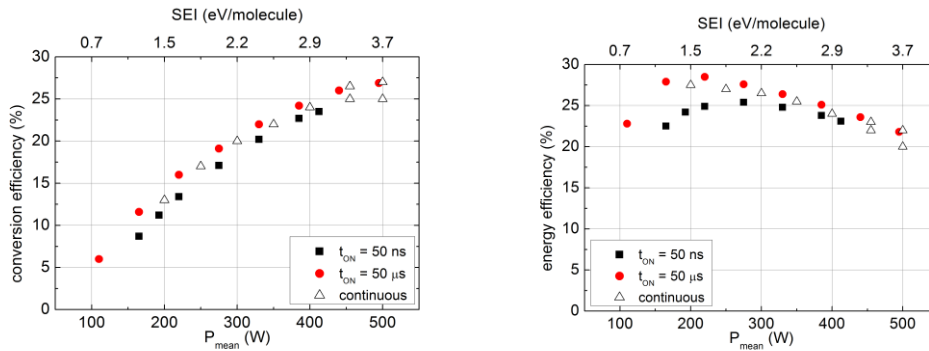
Fig. 2: Measured conversion and energy efficiency as a function of mean power and specific energy input for various on-times. SEI and P_{mean} are changing due to a varying off-time, as the peak power and flow rate are kept constant (see equations 2, 3 and 7). $P_{peak} = 550$ W and $Q = 1.9$ slm. Multiple measurements for continuous power at $P_{mean} = 455$ W and 500 W give an indication of the accuracy.

Taking the experimental accuracy into account, there is no clear influence of the plasma on-time on the energy efficiency. For a pulsed microwave argon plasma at 20 mbar it is said that with increasing repetition frequency (i.e. shorter on-times), the electron density slightly decreases whereas the electron temperature slightly increases [9]. A lower electron density would result in a lower population of vibrational levels [4] and hence a lower dissociation due to vibrational excitation. However, simulations in the current work suggest that the peak electron density is not dependent on the on-time for the current conditions and frequency range investigated. Only if the plasma is switched off before the peak density can be obtained, the electron density is naturally lower, which in fact can also influence the electron densities in [9]. More simulations and time resolved optical emission spectroscopy measurements are being performed to gain insight in the chemistry in the modulated discharges. In addition, accurate in-situ measurements of e.g. gas temperature T_g, vibrational temperature T_{vib} and vibrational level populations are required to investigate the reaction mechanism responsible for dissociation.

4   Conclusion

A power modulated CO_2 microwave discharge is investigated for plasma on-times between 50 ns and 50 μs. No clear effect has been observed of the on- and off-time on the measured energy and conversion efficiency. Possibly, even shorter pulses are required to switch off the plasma power before the vibrational temperature is saturated and gas heating is important. Accurate time and spatially resolved measurements of e.g. T_g and T_{vib} are necessary to determine if and how modulation can be used for tuning CO_2 dissociation.

References
1. T. Nunnally et al., J. Phys. D: Appl. Phys. 44, 274009 (2011)
2. G. J. van Rooij et al., Faraday Discuss. 183, 233-248 (2015)
3. T. Silva et al., Plasma Sources Sci. Technol. 23, 025009 (2014)
4. T. Kozák et al., Plasma Sources Sci. Technol. 23, 045004 (2014)
5. T. Kozák et al., Plasma Sources Sci. Technol. 24, 015024 (2015)
6. H. Wirth, Fraunhofer ISE, Recent Facts about Photovoltaics in Germany, 2015
7. A. Fridman, Plasma Chemistry (Cambridge University Press, Cambridge, 2008)
8. N. den Harder, Ph.D. thesis, FOM Institute DIFFER, 2016
9. E. Carbone et al., Plasma Sources Sci. Technol. 24, 015015 (2015)

ANALYSIS AND COMPARISON OF THE CO₂ AND CO DIELECTRIC BARRIER DISCHARGE SOLID PRODUCTS

I. Belov[1, 2], S. Paulussen[1], A. Bogaerts[2]

1 VITO, Sustainable Materials Management, Mol, Belgium
2 University of Antwerp, PLASMANT, Antwerp, Belgium

E-mail: igor.belov@vito.be

The CO and CO_2 Dielectric Barrier Discharges (DBD) and their solid products were analyzed keeping similar energy input regimes. Gas chromatography analysis revealed the presence of CO_2, CO and O_2 mixture in the exhaust of the CO_2 DBD, while no O_2 was found when CO was used as a feed gas. It was shown that the C_2 Swan lines observed with optical emission spectroscopy were distinct in the CO plasma while they were not observed in the CO_2 emission spectrum. Also the solid products of the plasmas exhibited remarkable differences. Nanoparticles with a diameter between 10 and 300 nm, composed of Fe, O and C (Fe:O:C~13:50:30) were produced by the CO_2 DBD, while microscopic dendrite-like carbon structure (C:O~73:27) were formed in the CO plasma. The growth rate in the CO_2 and CO DBDs was evaluated to be on the level of 0.15 mg/min and 15 mg/min, respectively. The difference of the CO and CO_2 discharges and their products might be attributed to the oxygen content in the latter (6.4 mol.% O_2 in the exhaust) and subsequent etching of the carbonaceous film.

Keywords: CO_2 decomposition; CO disproportionation; dielectric barrier discharge

1 Introduction

The transformation of CO_2 into a chemical feedstock or a solid product presents an attractive approach towards the mitigation of carbon dioxide. In this work we study the phenomenon of carbonaceous solid product formation in pure CO_2 and CO Dielectric Barrier Discharge (DBD) systems, which represent a popular non-thermal plasma approach to carbon dioxide decomposition [1]. Interestingly, coke formation is mostly not observed in DBD reactors when working with CO_2 [2]. In contrast to the CO_2 DBD, a rather intensive deposition process was demonstrated for low-pressure DC and microwave plasmas [2,3], as well as atmospheric pressure DBD's [5] when working with CO. In our previous work [6] the deposition of a slightly conductive coating on the reactor walls was observed in the CO_2 DBD which was correlated with the modification of the discharge behavior. In order to identify the difference between the CO_2 and CO plasmas, the discharges were compared by means of electrical characterization, GC and OES. These measurements were coupled to solid products analysis (FTIR, XRD, EDX) in order to obtain the information regarding possible synthesis mechanisms.

2 Experimental

The experimental setup is schematically shown in figure 1. In case of the MD configuration (figure 1), a cylindrical discharge gap of 0.5 mm is obtained between a grounded stainless steel central electrode and a dielectric tube made of borosilicate glass. A stainless steel mesh is wrapped at the outside of the dielectric tube, acting as an outer electrode and at the same time defining the length of the plasma (215 mm). The process is monitored by a 25 MHz

PicoScope 2205 digital oscilloscope. The energy input in the discharge is controlled by setting the power of the generator and calculating the corresponding value (equation 1):

$$P_{Input} = \frac{1}{T} \int_0^T I(t)U(t)dt \qquad (1)$$
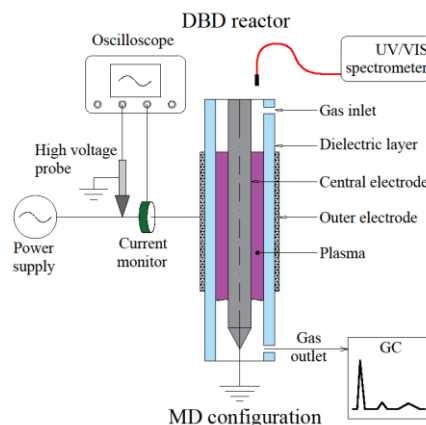
Fig. 1. Experimental setup of the tubular dielectric barrier discharge reactor.

The gaseous products of the reaction are analysed by gas chromatography (Trace-GC, Interscience), equipped with a Thermal Conductivity (TCD) and Flame Ionization (FID) detector. A UV/VIS (180-750 nm) survey fiber spectrometer (Avantes, AvaSpec 2048) with 2.3 nm FWHM resolution is used for monitoring the process, collecting light through a 6 mm collimating lens, located downstream the reactor parallel to the electrode axis.

3   Results and Discussion

3.1 Discharge Characterization

The electrical signals of CO_2 and CO discharges obtained at similar power are compared in Figure 2. It can be seen that the CO_2 plasma issues high-amplitude (up to 0.5-1 A) sparse current pulses in the positive half-cycle (HC) and a more stable filamentary regime in the negative HC. This behaviour is observed for electronegative gases in general (O_2, CO_2) [6]. The carbon monoxide discharge current (cf. figure 2,b) was symmetrical as 35-50 mA amplitude current bursts where measured in both HCs.
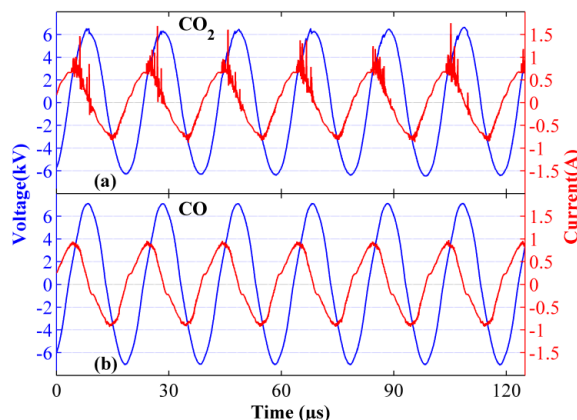
Fig. 2. Electrical signal of the (a) CO2 and (b) CO DBD; (Discharge power: 600W; gas flow rate: 1 SLM; frequency: 50kHz.)

The gas mixture at the reactor exhaust was evaluated by means of GC. At 600W power input and 1 SLM gas feed flow around 20% of initial CO_2 was converted into CO (13.8 mol.%) and O_2 (6.4 mol.%), the CO:O_2~2.1 ratio being close to the stoichiometric one. At similar conditions the CO discharge yielded 1.2 mol.% of CO_2. Interestingly, no molecular oxygen was found by GC in the exhaust of the CO DBD.

OES measurements revealed presence of Fe lines in the spectrum of the CO_2 DBD. Besides a more prominent Fox CO_2/CO_2^+ system, the CO 3rd positive band, CO Angstrom bands, and a continuum part with a maximum at about 450 nm were found. No distinct CH or C_2 lines were observed during the CO_2 experiments, not even at the highest energy input regimes. Contrary to that, C_2 Swan bands dominated the spectrum of the CO discharge.

The CO:O_2 ratio close to stoichiometric 2 indicates dominance of the overall reaction 2 for the CO_2 DBD, while the presence of the Fe lines reflects intensive ablation of the electrode surface. The formation of CO_2 (while no O_2 was found) and observations of the bright C_2(S) bands might be associated with the disproportionation reaction 3 occurring in the CO discharge.

$$CO_2 \rightarrow CO + 0.5\,O_2 \qquad\qquad (2)$$
$$CO + CO \rightarrow C + CO_2 \qquad\qquad (3)$$

Table 1 summarizes the discharge properties and characterization of the solid samples obtained in the CO and CO_2 DBDs, at 600 W input power and 1 SLM gas flow rate.

Table 1. Summary of properties of the solid samples obtained in CO and CO_2 DBD plasmas, respectively, at 600 W input power and 1 SLM gas flow.

Discharge characterization	CO DBD	CO_2 DBD
GC	CO(98.8%), CO_2(1.2%)	CO_2(79.8%), CO(13.8%), O_2(6.4%)
OES	C_2(Swan), CO(A), CO(3B)	CO(A), CO_2(Fox), CO(3B), Fe lines
Material characterization		
Production rate, mg/min	ca. 15	ca. 0.15
EDX	C:O=73:27	Fe:O:C=13:50:30
Particle size (SEM)	1-5 μm	10-300 nm
FTIR	C=O,C=C,C-O	Fe-O, C=C, C-O
XRD	Amorphous phase, (001),(002)	Fe_3O_4, Fe
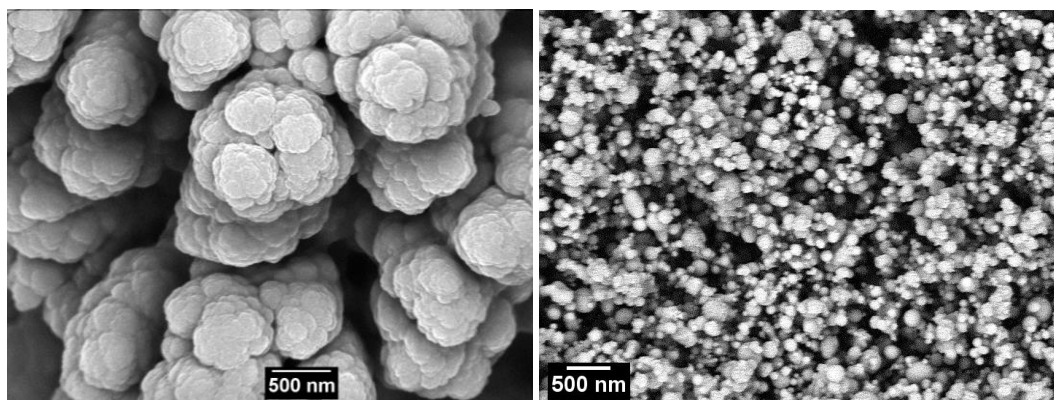
Fig. 3. SEM images of the 600W-1 SLM CO (left) and CO_2 (right) discharge products

3.2 Material Characterization

The solid products of the CO_2 and CO DBD were collected from the inner surface of the dielectric tube in the form of powder. A striking difference appeared in the deposits production rate, as the production rate via the CO discharge being two orders of magnitude larger than the CO_2 DBD (ca. 15 mg/min. vs 0.15 mg/min, respectively). To obtain more information regarding the possible mechanism of the deposition process, SEM imaging, EDX, FTIR and XRD techniques were applied for material characterization.

The morphology of the corresponding solid products is presented on figure 3. A microscopic dendrite-like carbon structure (C:O=73:27) was formed in the CO discharge. The FTIR spectrum revealed the presence of C=O, C-O and C=C groups, indicating the polymeric nature of the material. XRD analysis demonstrated that the sample is mostly composed of amorphous structures.

A coating of the spherical nanoparticles, composed of Fe, O and C (Fe:O:C=16:60:30) was deposited in the CO_2 discharge. The FTIR spectrum was largely dominated by the Fe-O signal while the presence of C=C and C-O groups was not so prominent. XRD analysis revealed the presence of Fe_3O_4 and Fe phases of crystalline structure.

4   Conclusion

CO and CO_2 discharges and their solid products were analyzed and compared. The striking difference of the CO and CO_2 discharges and their products might be attributed to the high oxygen content in the latter (6.4 mol.% O_2 in the exhaust). Intensive oxidation and ablation of the metal electrode surfaces are the results of that. Contrary, the disproportionation and polymerization dominates the material growth processes in the CO plasma.

References

1. S. Paulussen et al., Plasma Sources Sci. Technol. 19, 034015 (2010)
2. F. Brehmer et al., J. Appl. Phys. 116, 123303 (2015)
3. S. Mori et al., Diam. Realt. Mat. 17, 999 (2008)
4. S. Mori et al., Diam. Realt. Mat. 18, 678 (2009)
5. R. Geiger et al., J. Phys. D: Appl. Phys. 44, 274005 (2011)
6. I. Belov et al., Plasma Sources Sci. Technol. 25, 015023 (2016)

PREPARATION OF THE CARBIDES OF BORON AND SILICON FROM THEIR FLUORIDES AND METHANE IN RF-ARC HYDROGEN PLASMA

R. A. Kornev, P. G. Sennikov, A. D. Bulanov

G.G. Devyatykh Institute of Chemistry of High-Purity Substances of RAS

49 Tropinin Str., Nizhny Novgorod, 603950, Russia

E-mail: kornev@ihps.nnov.ru

Feasibility study of the synthesis of the carbides of boron and silicon by plasma chemical hydrogen reduction of their fluorides BF_3 and SiF_4 in RF-arc discharge at atmospheric pressure has been carried out. By-products of plasma chemical reactions were investigated. The samples of carbides were prepared and characterized.

Keywords: boron carbide; silicon carbide; RF-ARC hydrogen plasma

1 Introduction

The carbides of boron and silicon refer to refractory compounds with unique properties and are widely used in modern technologies.

Nuclear reactor engineering is the important field of application of boron carbide which is connected with unique high capture cross section of thermal and fast neutrons by [10]B isotope [1]. The main interest in silicon carbide is due to its application in high-power electronic devices [4]. Compared with silicon, commonly used in modern electronics, the silicon carbide has by several times larger energy gap [5], by 10 times higher electrical strength [6], by three times higher heat conductivity [7], and the increased radiation resistance [8]. The methods for preparation of different structural modifications of the carbides of boron and silicon can be divided into two groups: the solid phase including chemical reactions between the initial substances in elementary form or in the form of compounds at high temperature [9] and the gas-phase based on the synthesis of carbides by the method of chemical deposition from the gas phase [10-13]. It should be noted that in the case of boron carbide the boron trichloride (less often, diborane) and methane are used as the initial substances, and in the case of silicon carbide the methylsilanes and some other substances are used.

In the present work the gas-phase method was selected for preparation of the carbides of boron and silicon. In the first case the boron trifluoride and methane were taken as the precursors and in the second case the silicon tetrafluoride and methane. Their molecules are very stable (the binding energy of B-F and Si-F are equal to 7.8 and 7.2 eV, respectively) and that is why the plasma sustained by one or another discharge should be used for conversion of the fluorides into elementary forms or other compounds (PECVD method).

The goal of the present work is to investigate the plasma chemical synthesis of the carbides of boron B_4C and silicon SiC in hydrogen plasma of fluorides sustained by radio-frequency arc discharge (RFA) at atmospheric pressure and preparation of their bulk samples.

2   Experimental

In this work the fluorides of boron and silicon with the content of the main substance not less than 99.9% were used. Hydrogen of special purity grade was used as the plasma-forming gas: the content of hydrogen not less than 99.9999%; of oxygen $2\cdot10^{-5}$%, of argon $2\cdot10^{-5}$%, of nitrogen $8\cdot10^{-5}$%, of water vapors $1\cdot10^{-4}$%, and methane with purity of 99.999% was used as the carbon-containing precursor. The used high-pressure RFA (P > 200 torr) is characterized by high strength of current $1 - 10^2$ A and by relatively low voltage $10 - 50$ V. The experiments were carried out at the total pressure in reactor equal to 760 torr. Consumption of plasma-forming gas H_2 as well as of gas-reagents SiF_4, BF_3 and CH_4 during the experiment was determined by mass-flow controllers and was maintained constant equal to $H_2 - 350\pm5$ cm^3/min.; $SiF_4 - 60\pm5$ cm^3/min.; $BF_3 - 60\pm5$ cm^3/min.; CH_4 - 40 ± 5 cm^3/min. The molar ratio of $H_2/SiF_4/CH_4$ and $H_2/BF_3/CH_4$ was maintained constant being equal to 9/1, 5/1. The plasma chemical reactor is a quartz glass tube inside which the rod electrodes are placed connected with RF generator via matching device. The total degree of conversion of fluorides was determined by analyzing the IR spectra of exhaust gases with accuracy of 0.1% mole (Bruker Vertex 80v spectrometer). The X-ray analysis of the prepared samples was conducted on diffractometer XRD-7000. Morphological investigations of the prepared samples were carried out by scanning electron microscopy. SEM images were obtained by SUPRA 50VP and NEON 40 electron microscopes were used. The element composition of samples was determined by energy-dispersive X-ray spectrometer (Oxford Instruments).
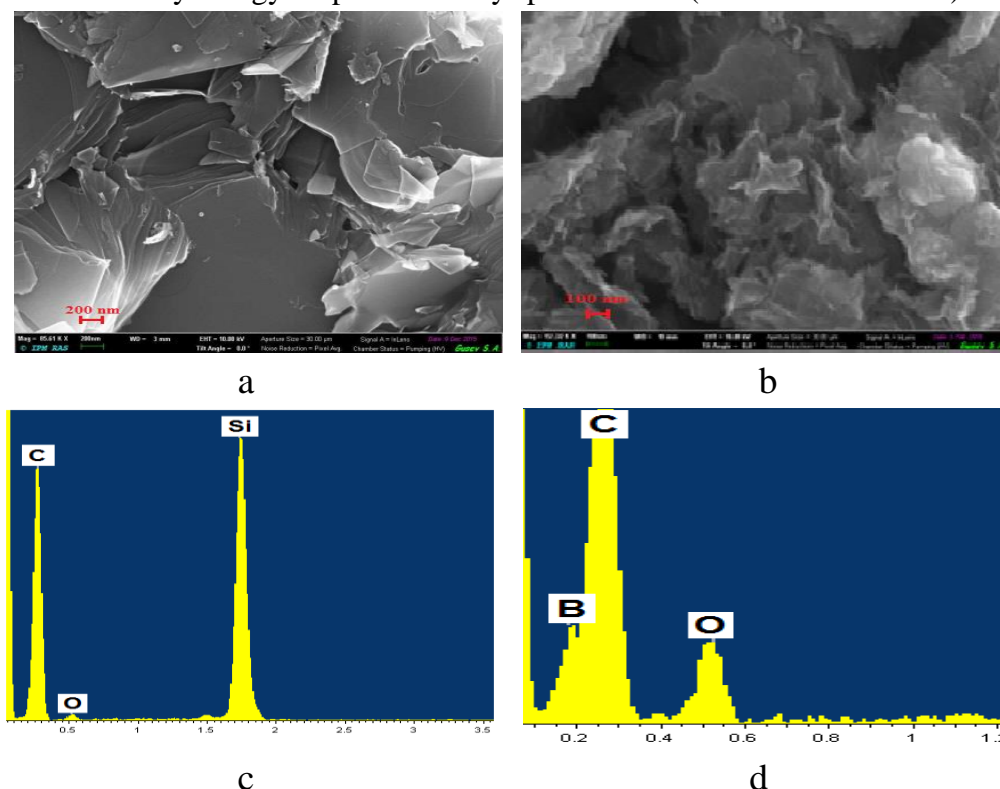
Fig. 1: The morphology of the samples of B_4C (a) and SiC (b) and their elemental composition (c) and (d).

3   Results and Discussion

Solid carbides of silicon and boron were grown on electrodes in the form of polycrystals in cylindrical form and simultaneously the fine soot was deposited on the walls of plasma chemical reactor. During plasma chemical reduction of boron fluoride as a by-product, the oily liquid was condensed on the walls of reactor/ We believe that that is a partially hydrolyzed (after the contact with atmosphere of the open reactor) coordination compound of boron fluoride with hydrogen fluoride $F_3B \cdot FH$ (the data of IR and NMR spectroscopy). Trifluorosilane, registered in IR spectra of exhaust gases, is a secondary silicon-containing product during synthesis of silicon carbide. Ethylene, acetylene, carbon dioxide, tetrafluoromethane and hydrogen fluoride are other products of plasma chemical transformations (free hydrogen fluoride is not observed during the synthesis of boron carbide).

Fig. 1 gives the morphology of the samples of B_4C, SiC and their elemental composition. The samples of the carbides of boron and silicon (Fig.1 a,b) have a layered structure. It can be assumed that growth of B_4C and SiC takes place in layers. As our observations indicate, the initial deposition of graphite layer on electrode surface is the required condition for carbides growth. Graphite is deposited on the surface of electrode, heated up to $900 - 1400^0C$, as a result of pyrolysis of methane forming dendrites. Intensity of electric field and its gradient on the formed dendrites are high making it possible to polarize the molecule SiF_4 or BF_3 and facilitates the deposition of Si or B layers. Then again the deposition of graphite takes place. That is why the samples, grown in these conditions, should contain substantial amount (up to 30%) of free carbon which is proved by the data of X-ray fluorescent (Fig. 1 c,d) and phase (Fig. 2 a,b) analysis.
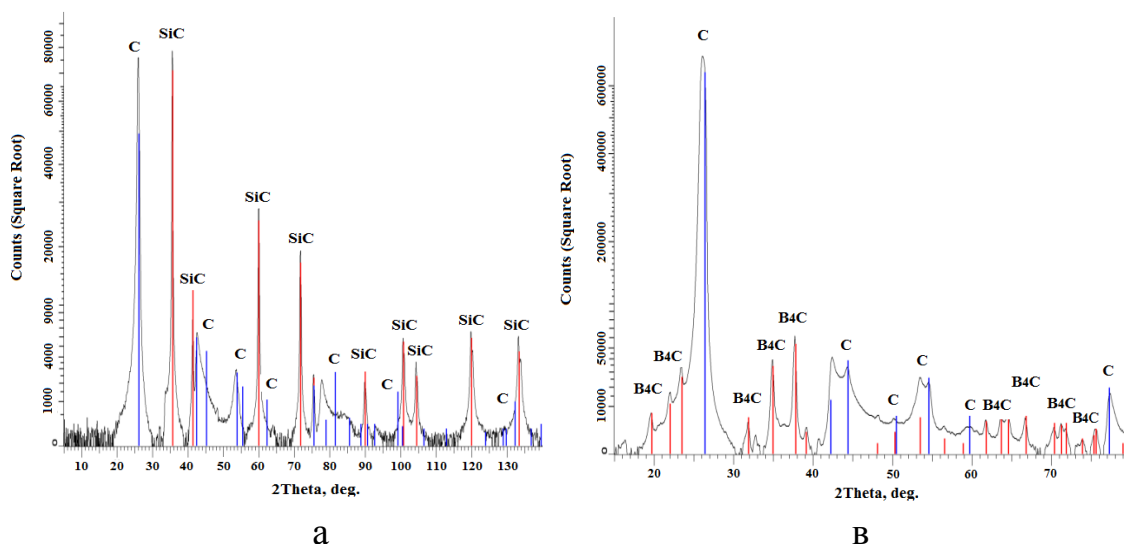
Fig. 2: The X-ray analysis of the samples SiC (a) and B_4C (в).

4   Conclusion

The samples of the carbides of boron and silicon were prepared by PECVD method using methane, the fluorides of boron and silicon as the initial compounds. Their morphology, phase and impurity composition were investigated. The main gas-phase and solid phase by-products of the synthesis of carbides were determined.

References

1. J. M. Blum et al., Energie nuclearie. 14, 33 (1972)
2. B. W. Robertson et al., Appl. Phys. Lett., 80, 3644 (2002)
3. O. I. Buzhinskij et al., Fusion Engineering and Design 45, 34 (1999)
4. I. C. Kizilyalli et al., IEEE Electron Device Lett. 26, 404 (2005)
5. H. Matsunami et al., Mater. Sci. Eng. 20, 125 (1997)
6. M. Bakowski et al., Phys. Stat. Sol. (a) 162, 421 (1997)
7. F. Christin, Adv. Eng. Mater. 4, 903 (2002)
8. E. Lypez-Honorato et al., J. Nucl. Mater. 392, 219 (2009)
9. B. Chang et al., Mater. Res. Soc. Symp. Proc. 848, FF9.28.1 (2005)
10. J. Berjonneau et al., J. Electrochem. Soc. 153, 795 (2006)
11. A. O. Sezer et al., Mater. Science and Eng. B79, 191 (2001)
12. M. Karaman et al., Mater. Res. Soc. Symp. Proc. 886, 0886-F11-11.1 (2006)
13. D. A. Petti et al., Nucl. Eng. Design 222, 281 (2003)

SYNTHESIS OF GRAPHENE SHEETS USING MICROWAVE PLASMA TORCH DISCHARGE

J. Toman, O. Jašek, J. Jurmanová

Department of Physical Electronics, Faculty of Science, Masaryk University, Kotlářská 2, 611 37, Brno, Czech Republic

E-mail: jasek@physics.muni.cz

In this work a synthesis of two-dimensional graphene related materials (GRM) in microwave plasma torch (MPT) discharge was studied. The MPT discharge operates at atmospheric pressure conditions in argon atmosphere. The discharge was driven by a microwave generator set to standard frequency of 2.45 GHz. Liquid ethanol vapours were led to the discharge by carrying gas - argon, was selected as a precursor. Decomposition of ethanol, at specific deposition conditions, led to synthesis of graphene flakes. Created samples were analysed using Raman spectroscopy and electron microscopy. The discharge was examined by optical emission spectroscopy.

Keywords: microwave plasma; torch discharge; graphene flakes

1   Introduction

Recently, there has been increased interest in using plasma techniques for creating graphene-based materials like carbon nanotubes (CNT), nanofibres, graphene, nanoribbons or nanoflakes. The production of graphene-based materials requires specific conditions such as sufficiently high energy of atomic and molecular species supplied to the growth zone and balanced influx of carbon particles. One of the most used techniques to provide suitable conditions for graphene synthesis is chemical vapour deposition (CVD) [1, 2]. However, this technique requires a very high temperature ranging from 1000 °C to 1300 °C and transfer of deposited films onto non-metallic substrates. Alternatively, plasma-enhanced chemical vapour deposition (PECVD) has been developed to synthesize graphene on a relatively large scale. The unique chemically active plasma environment provides suitable conditions for creating high yields of clean and highly ordered graphene sheets with well controlled structural qualities. Many applications exploit the ability of plasmas to break down complex molecules considering that plasma systems provide simultaneously high temperatures and a highly reactive environment [3, 4].

2   Experimental

The experimental equipment consisted of a microwave (MW) generator, working at a frequency of 2.45 GHz, 2 kW maximum power, with a standard rectangular waveguide, transmitting the MW power through a coaxial line to a hollow nozzle electrode. Ferrite circulator protected the generator from the reflected power by re-routing it to the water load. Matching of the plasma load to the line impedance was achieved by a 3-stub tuner. The gases are supplied to the discharge chamber through the nozzle which has two gas channels. The inner channel, in the nozzle axis, is used for introduction of working gas - argon and subsequent ignition of plasma. The outer channel is used for introduction of carrying gas with precursor vapors into the plasma environment. Reactor chamber consists of a quartz tube, 8cm

in diameter, which is 15 cm long. Both ends are fixed to stainless steel caps by elastic silicon bands. A schematic view of the experimental set-up with a detailed view of the nozzle configuration is shown in Fig. 1. More details about the experimental set-up, discharge characteristics and deposition of other carbon nanostructures can be found in previous publications [5, 6].
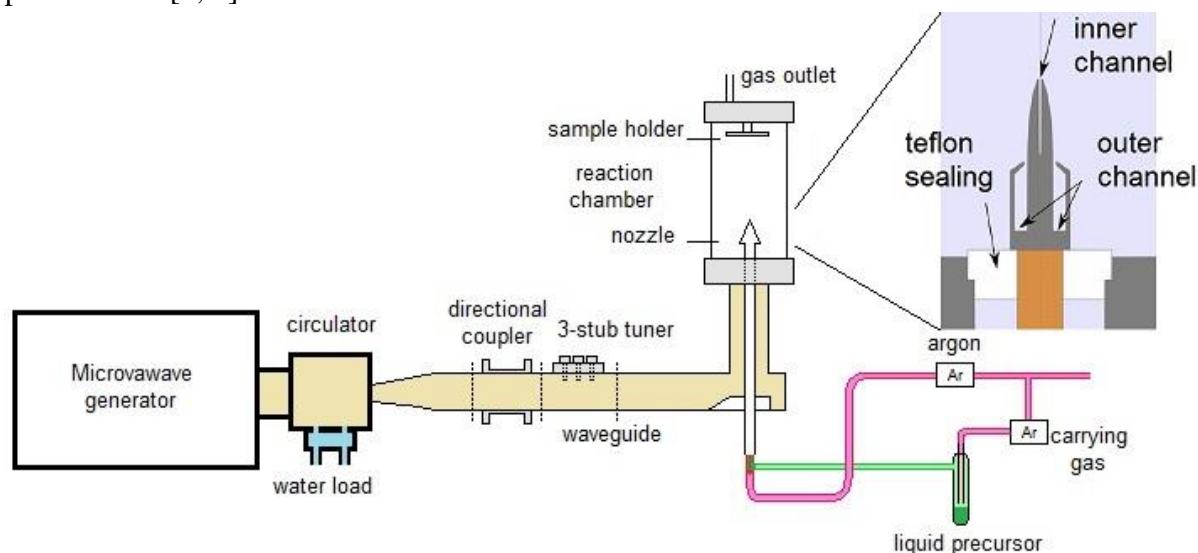
Fig. 1: Experimental setup for synthesis of graphene flakes by decomposition of ethanol precursor in microwave plasma torch discharge with a detailed view of the nozzle [7].

3   Results and Discussion

Optical emission spectra of argon plasma with ethanol vapours used as precursor at atmospheric pressure conditions is shown in Fig. 2. As a direct product of ethanol decomposition, molecular lines of C_2 molecule (Swan system) and CN molecule are dominant. Since we were not directly working with nitrogen, CN molecule is a result of residual nitrogen from atmosphere. We can also observe typical spectral lines of atomic argon at higher wavelengths (700 – 800 nm) and atomic hydrogen (H_α) at 656 nm.
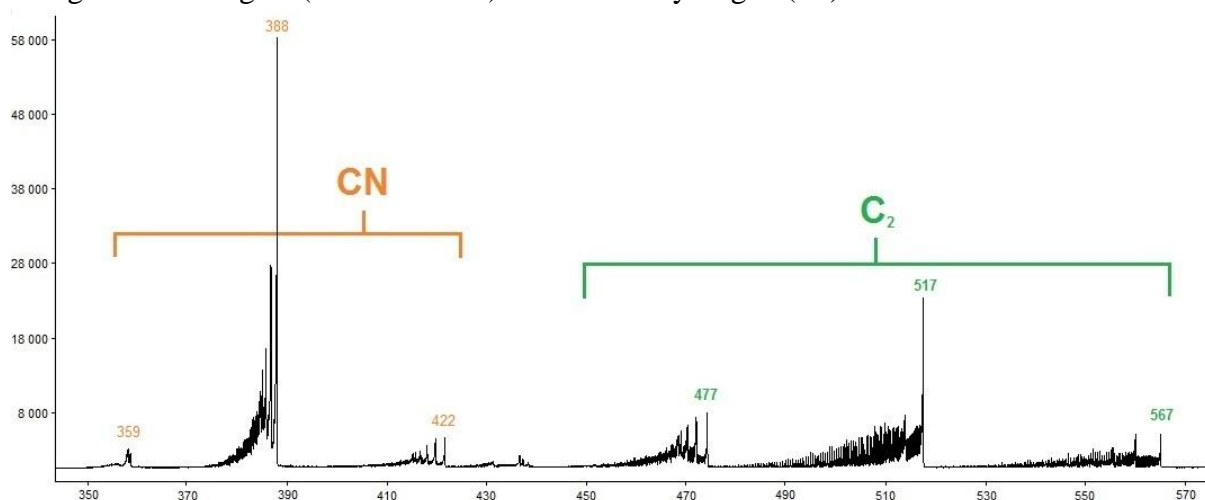
Fig. 2: Typical optical emission spectra of an argon / ethanol discharge at atmospheric pressure conditions.

Variation in deposition conditions, the microwave power P, the flow of working gas through inner channel Ar_c and the flow of carrying argon with ethanol vapours Ar_b resulted in change

of deposited material. The mixture with ethanol could be introduced to the discharge through inner or outer channel of the nozzle. We also tried to maximize the active surface for evaporation of liquid precursor by bubbling. Fig. 3 shows the final product of experiment named GV61 with Raman spectra. The deposition conditions were: t=5min., P=210W, Ar_c=420sccm, Ar_b=400sccm The SEM image shows, that the deposited material consists of layered structures, approximately 500 nm in diameter. Raman spectroscopy, as a versatile tool for graphene material analysis, suggests that prepared graphene flakes consist of 4 graphene layers.
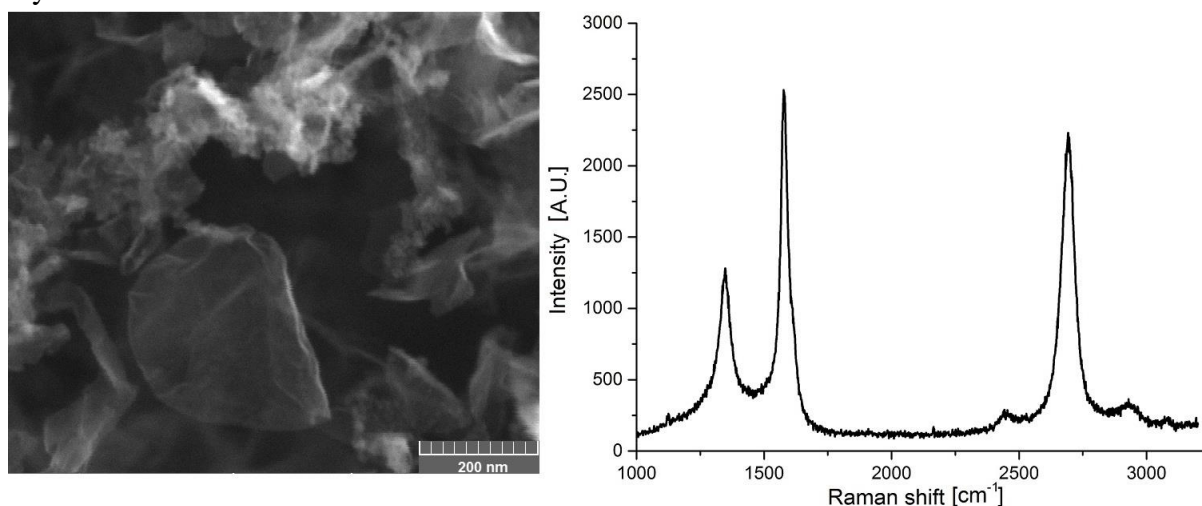
Fig. 3: Scanning electron microscopy (SEM) of prepared graphene flakes with Raman spectroscopy of deposited material.

As mentioned before, different approaches were used to introduce ethanol vapours into reaction chamber, which affected the amount of precursor participating in the synthesis, dynamics of the plasma jet and gas dynamics in the reaction chamber. The mixture of Ar_b carrying ethanol vapours were introduced either to inner or outer channel of the nozzle. Fig. 4
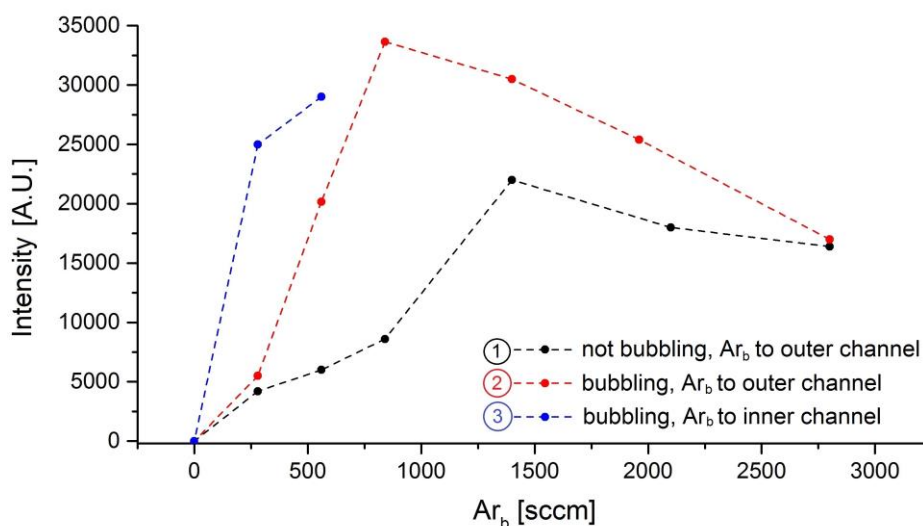
Fig. 4: Intensity of C_2 line at 517 nm as a function of argon flow for 3 different ways of introducing the gas mixture into the reaction chamber.

represents intensity of the most intensive spectral line of C_2 Swan system at 517 nm as a function of Ar_b flow for three different combinations of bubbling/not bubbling of liquid

precursor, introducing it to inner/outer channel of the nozzle. The graph shows, how these combinations influence the amount of carbon precursor participating in graphene synthesis. We also observed a significant impact on the plasma jet dynamics, while introducing the Ar_b mixture into the inner channel of the nozzle.

4   Conclusion

We successfully synthesised graphene flakes in microwave plasma torch at atmospheric pressure conditions. Prepared structures consist of 4 layers of graphene and the width is approximately 500 nm in diameter. Due to the layered structure and high surface area of prepared material, applications in the field of sensors are of increased interest for our future research.

Acknowledgements

References

1. K. Keun Soo et al., Nature 457, 706-710 (2009)
2. Xuesong Li et al., Science 324, 5932 (2009)
3. E. Tatarova et al., Appl. Phys. Lett. 103, 134101 (2013)
4. A. Dato et al., Nano Lett. 8, 2012-2016 (2008)
5. L. Zajickova et al., Plasma Process. Polym. 4, S245 (2007)
6. O. Jasek et al., J. Phys. Chem. Solids 68, 738 (2007)
7. P. Synek et al., Plasma Sources Sci. Technol. 24, 2 (2015)

TOPIC 4: OZONE GENERATION AND APPLICATIONS

EFFECT OF NITROGEN SPECIES ON OZONE GENERATION BY ATMOSPHERIC PRESSURE HOMOGENEOUS DIELECTRIC BARRIER DISCHARGE

N. Osawa, T. Tsuji, Y. Yoshioka
Kanazawa Institute of Technology, 7-1 Ohgigaoka Nonoichi Ishikawa, Japan

E-mail: n.osawa@neptune.kanazawa-it.ac.jp

We investigated the effect of nitrogen species on ozone generation characteristics by an atmospheric pressure homogeneous dielectric barrier discharge (Atmospheric Pressure Townsend Discharge: APTD). In this experiment, pure O_2 and various N_2 and O_2 mixed gases were used as the source gas of ozone generator. Using an ozone monitor and FTIR, we found that since excited N_2 molecules can produce additional O atoms for ozone generation, the highest ozone yield was obtained by using 80% N_2 and 20% O_2 mixed gas in this experiment.

Keywords: homogeneous dielectric barrier discharge; ozone; nitrogen species; FTIR analysis

1   Introduction

A Dielectric Barrier Discharge (DBD) type ozone generator is widely used for room air treatment, sterilization, deodorizing etc. In this type of ozone generator, air or O_2 is used as source gas. So far, we succeed in generating a homogeneous DBD in air, N_2 and O_2 at atmospheric pressure [1] and clarified that the DBD is a kind of Atmospheric Pressure Townsend Discharge (APTD). After the success, we applied the APTD to air-fed ozone generators and investigated the effect of by-products suppression in ozone gas. As the results, we found that concentrations of HNO_3, N_2O_5 and N_2O in ozone gas by APTD type ozone generators were lower than those of by filamentary DBD type ozone generators at the same ozone concentration [2]. Therefore, we concluded that the APTD can suppress by-product generation by air-fed ozone generators. We also applied the APTD to an O_2-fed ozone generator to investigate the ozone yield [3]. However, the maximum ozone yield of the O_2-fed ozone generator was almost the same as that obtained by air-fed ozone generators. In this paper, in order to clarify why the maximum ozone yield by APTD did not increase, we investigated the effect of the admixture ratio of N_2 and O_2 in source gas.

2   Experimental setup

Fig. 1 shows experimental setup. O_2 (absolute humidity: 119.3 mg/m^3, purity: 99.5%) and N_2 (absolute humidity: 119.3 mg/m^3, purity: 99.95%) were used as source gas of ozone generator. Total flow rate of mixed gas was fixed to 2.0 L/min using two mass flow controllers (SEC-400mk3, Horiba, Ltd.). The admixture ratio of N_2 and O_2 was changed by changing flow rates of N_2 and O_2 gases. Ozone concentration was measured by an UV absorption type ozone monitor (EG-3000B/01, Ebara Jitsugyo Co., Ltd.). Nitrogen oxides were analyzed by an FTIR (IR Affinity-1, Shimadzu corp.) with a gas cell (optical path length: 3 m, Gemini Scientific Instruments). A.C. high voltage was applied to the ozone generator by a step-up transformer. The maximum applied voltage and frequency were 13.6 kVp and 50 Hz respectively. The

applied voltage (*V*) and the current were measured by an oscilloscope (TDS-2024B, Tektronix, Inc.) using a high voltage probe (EP-50K, Pulse Electronic Engineering Co., Ltd.) and a differential probe (700924, Yokogawa Electric Corporation) respectively. An integral of the current (charge *q*) was measured from the voltage drop across an integral capacitor (0.1 μF). Besides, the discharge power was calculated by multiplying the area of *V–q* Lissajous figure by power frequency. Alumina barrier (Material code: A473, thickness: 1 mm, Kyocera corp.) was used as the barrier material of electrodes. The gap length was fixed to 2 mm. The electrode size was 62 cm^2.
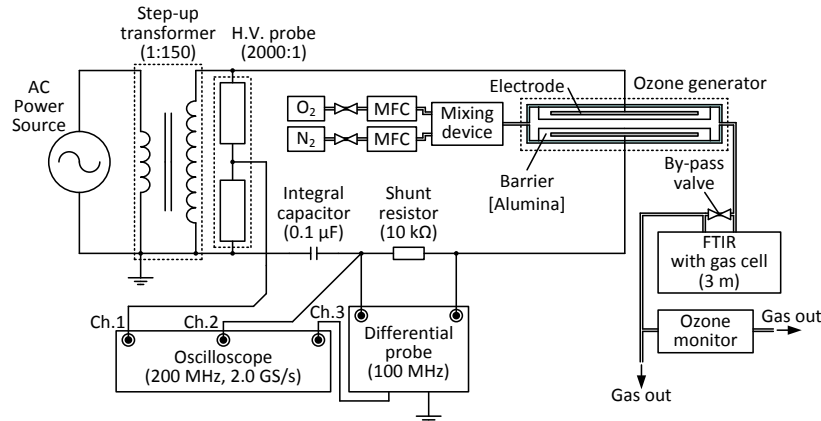
Fig. 1: Experimental setup.

3   Results and Discussions

3.1 Discharge characteristics

Fig. 2 shows discharge characteristics by different admixture ratio of N_2/O_2. From Fig. 2(a), discharge started at around 1 ms and 11 ms. Discharge inception time of 100% N_2 was faster than that of 100% O_2. Because electric fields required for Townsend breakdown of O_2 gas is lower than that of N_2 gas [4]. During discharge, the current flowed continuously and had no pulse. As can be seen in this figure, the APTD generated not only in 100% N_2 and 100% O_2, but also N_2/O_2 mixed gas. Fig. 2(b) shows *V-q* lissajous figures. All of the figures show a parallelogram. Discharge sustaining voltage (V_g) increased with increasing N_2 content. On the other hand, the amount of charge during discharge (dq) decreased with increasing N_2 content. Fig. 2(c) shows the change of discharge power and specific input energy (SIE) as a function of N_2 content. They were almost unchanged except at 100% N_2.
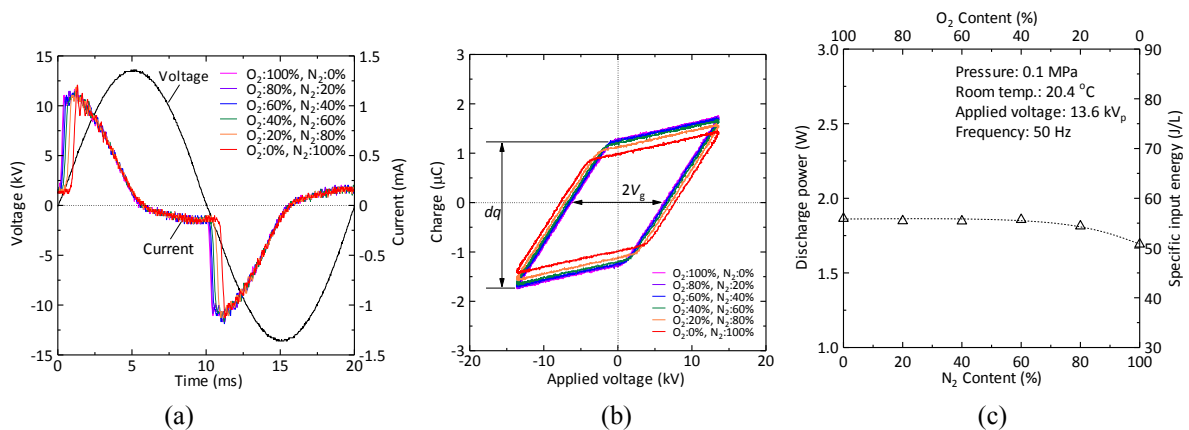
Fig. 2: Discharge characteristics. (a) Voltage and current waveforms, (b) Lissajous figures, and (c) discharge power and specific input energy at various N_2 contents.

3.2 Ozone generation characteristics

Fig. 3 shows the ozone concentration and the yield at various N_2 contents in source gas. Fig. 3(a) shows that ozone concentration increased with increasing N_2 content. It is well known that in case of filamentary DBD type ozone generators, ozone concentrations increase with increasing O_2 content [5], However, the highest ozone concentration by the APTD type ozone generator was obtained at 80% N_2 content. Fig. 3(b) shows that ozone yield increased with increasing N_2 content.
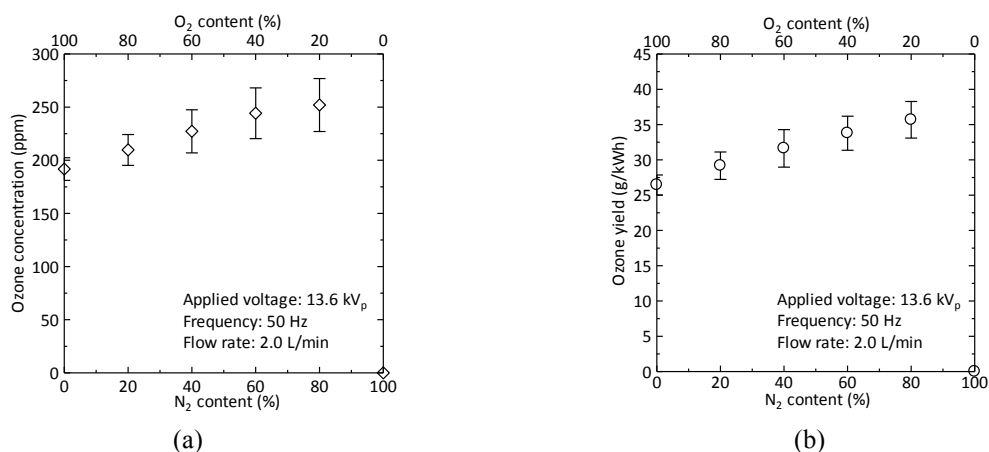
Fig. 3: Ozone generation characteristics. (a) Ozone concentration, and (b) ozone yield.

3.3 Gas analysis by FTIR

In order to clarify why the highest ozone concentration and yield were obtained at 80% N_2 content in source gas, we analyzed the absorbance spectra of 320ppm ozone gas generated by filamentary DBD and APTD by the FTIR.

Fig. 4 shows the absorbance spectra of 320ppm ozone gas. In case of filamentary DBD, HNO_3, N_2O, NO_2 and N_2O_5 were detected as by-products, on the other hand, in case of APTD, HNO_3, N_2O and N_2O_5 were detected as by-products.
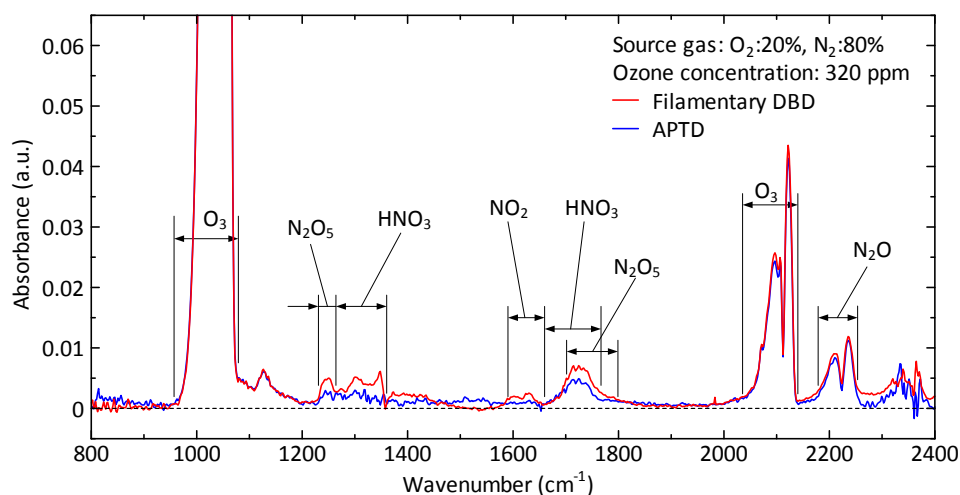
Fig. 4: Absorbance spectra of 320ppm ozone gas generated by 80% N_2 and 20% O_2 mixed gas.

In general, dissociation of O_2 and N_2 by electron impact (R1-3) and subsequent NOx formation (R4-8) occur by the following reactions [6].

N₂ dissociation: $e + N_2 \rightarrow 2N + e$ (9.1 eV) ....(R1)

O₂ dissociation: $e + O_2 \rightarrow O_2(A^3\Sigma_u^+) + e \rightarrow O(^3P) + O(^3P) + e$ (6.1 eV) ......(R2)

O₂ dissociation: $e + O_2 \rightarrow O_2(B^3\Sigma_u^-) + e \rightarrow O(^3P) + O(^1D) + e$ (8.4 eV) ......(R3)

NO generation: $N + O_2 \rightarrow NO + O$ ....(R4)

NO₂ formation: $O + NO + M \rightarrow NO_2 + M$ ....(R5)

$NO + O_3 \rightarrow NO_2 + O_2$ ....(R6)

NO₃ formation: $NO_2 + O_3 \rightarrow NO_3 + O_2$ ....(R7)

N₂O₅ formation: $NO_2 + NO_3 + M \rightarrow N_2O_5 + M$ ....(R8)
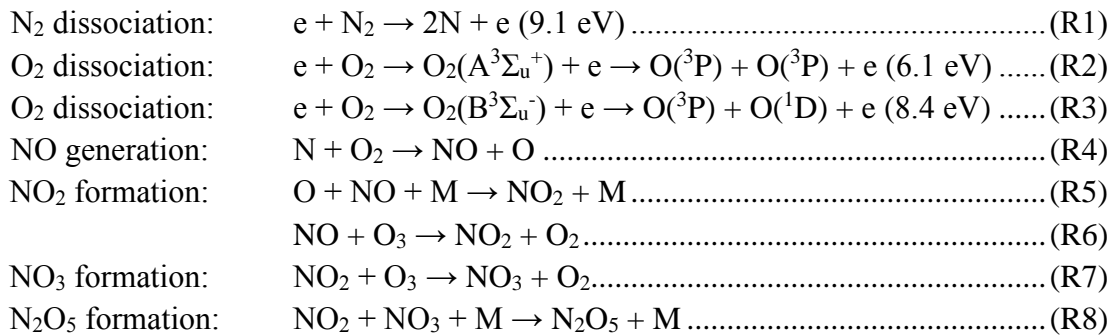
Because the reduced electrical field (E/n) of APTD is lower than that of streamer head of filamentary DBD [7], N₂ dissociation reaction (R1) is weak and the subsequent NOx formation (R4-8) are small. Therefore, the intensities of absorbance spectra of NO₂ and N₂O₅ by the APTD type ozone generator were lower than that of by filamentary DBD type ozone generator.

Since the E/n of APTD is low, N₂ excitation reactions (R9, R10) seem to be dominant in comparison with N₂ dissociation (R1).

N₂ excitation: $e + N_2 \rightarrow N_2(A^3\Sigma_u^+) + e$ (6.17 eV)......................................(R9)

$e + N_2 \rightarrow N_2(B^3\Pi_g) + e$ (7.35 eV) ....(R10)
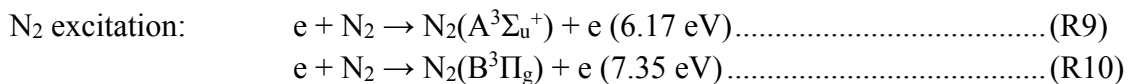
These excited N₂ molecules can produce additional O atoms for ozone generation (R11, R12). Therefore, ozone yield increased with increasing N₂ content in source gas.

Additional O atom generation: $N_2(A, B) + O_2 \rightarrow N_2 + 2O$...........................(R11)

$N_2(A) + O_2 \rightarrow N_2O + O$...............................(R12)
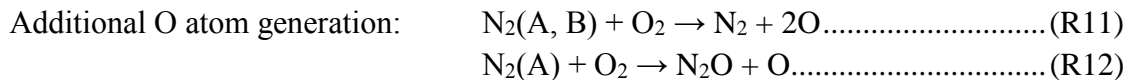
4   Conclusions

1. Discharge inception time of 100% N₂ was faster than that of 100% O₂. Because electric fields required for Townsend breakdown of O₂ gas is lower than that of N₂ gas.

2. Ozone concentration increased with increasing N₂ content. In this experiment, the highest ozone concentration by the APTD type ozone generator was obtained at 80% N₂ content.

3. Because the E/n of APTD is low, N₂ excitation reactions seem to be dominant in comparison with N₂ dissociation. Since these excited N₂ molecules can produce additional O atoms for ozone generation, ozone yield increased with increasing N₂ content in source gas.

References

1. N. Osawa et al., IEEE Trans. Plasma Sci. 40, 1 (2011)

2. N. Osawa et al., J. Adv. Oxid. Technol. 17, 2 (2014)

3. Y. Nakai et al., in *Proceedings of the 19th International Symposium on Plasma Chemistry*, Philadelphia (2011)

4. A. Fridman, Plasma Chemistry (Cambridge university press, 2008)

5. H. Kishida et al., T. IEE Japan 114, 8 (1995)

6. M. Laroussi et al., Non-equilibrium Air Plasmas at Atmospheric Pressure, (IOP Publishing, Bristol, 2005)

7. N. Osawa et al., Eur. Phys. J. Appl. Phys. 61, 2 (2013)

STUDY OF O$_2$ AND O$_3$ REACTIONS WITH ELECTRODE SURFACE IN OZONIZER

D. Trunec[1], V. Mazánková[2], J. Mierna[2], I. Manduchová[2], F. Krčma[2]

[1]*Department of Physical Electronics, Masaryk University, Kotlářská 2, Brno, Czech Republic*
[2] *Institute of Physical and Applied Chemistry, Brno University of Technology, Purkyňova 118, Brno, Czech Republic*

E-mail: trunec@physics.muni.cz

In this contribution the study of O$_2$ and O$_3$ reactions with electrode surface in an ozonizer is presented. The electrode surfaces in ozonizer were treated in the discharge with pure (99.9999%) oxygen for long time. Then the discharge was switched off and pure oxygen or oxygen with ozone reacted with treated electrodes for different time periods. Then the ozone concentration at the ozonizer output was measured by the absorption spectroscopy. It was found that the molecular oxygen reacts with oxygen atoms adsorbed on electrode surfaces producing ozone. On the other hand the ozone concentration in switched off ozonizer stays constant for long time.

Keywords: ozone; surface reactions; dielectric barrier discharge

1   Introduction

The plasma surface interactions are of considerable importance for a wealth of discharge phenomena. The surface oxidation on Pyrex of NO into NO$_2$ by adsorbed O atoms was studied by Guaitella et al. [1]. The surface recombination of oxygen atoms in O$_2$ plasma was studied by Lopaev et al. [2]. It has been also observed that the ozone concentration in high purity (99.99995%) oxygen-fed ozonizers decreases from the initial level to almost zero during several hours. This phenomenon is known as Ozone Zero Phenomenon [3]. This phenomenon is probably caused by surface processes at ozonizer electrodes. Explanation of this phenomenon can bring deeper insight into surface processes in ozonizer and it is also important for the models of ozone production in dielectric barrier discharges. Marinov et al. [4] also directly observed ozone formation on SiO$_2$ surfaces in oxygen discharges.

2   Experimental

A cylindrical ozonizer was used in this study. Outer electrode was made of stainless steel and it was maintained at earth potential. The internal diameter of the outer electrode was 24 mm. The outer electrode was covered by alumina dielectric, which was 2.85 mm thick. The inner cylinder is a high-voltage electrode and it was made of stainless steel. The external diameter of the inner electrode was 17 mm. The discharge gap was 0.65 mm. The length of the ozonizer was 240 mm. The water flowed trough outer electrode, the water temperature was controlled to be constant during the experiments. Extremely high-grade oxygen of 99.9999% was led into the ozonizer through the mass flow controller, the oxygen flow was set to 2 l/min. The ozone produced in the ozonizer was leaded to absorption cell, where the ozone concentration was measured using absorption spectroscopy.

3   Results and Discussion

In the first set of experiments the discharge in pure oxygen in ozonizer was burning for 5 min, then the discharge was switched off and the ozonizer was flowed by argon for 3 min. After this the ozonizer was flowed by oxygen for 1 min and then the ozonizer filled by oxygen was closed at the input and at the output by the valves for the reaction time t_r. After the elapse of time t_r the oxygen flow through ozonizer was restored and the concentration of produced ozone flowing through absorption cell was measured. The measured ozone concentrations are shown for different reaction time t_r in Fig. 1. The ozone amounts calculated from these time dependences are shown in Fig. 2. The amount of produced ozone increases with time t_r, at short times the amount of ozone increases quickly, at reaction times longer than 2 min the amount of ozone increases slowly.
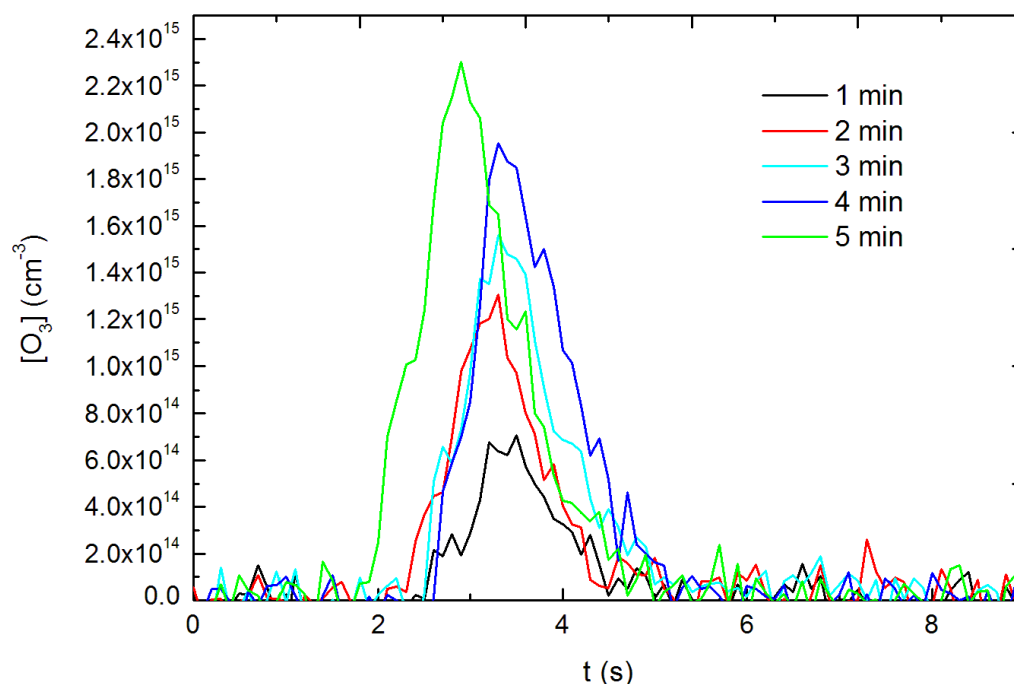
Fig. 1: The time dependences of ozone concentration in absorption cell for different reaction time t_r.

In the second set of experiments the discharge in pure oxygen in ozonizer was burning again for 5 min, then the ozonizer filled by oxygen with ozone was closed at the input and at the output by the valves simultaneously with switching of the discharge. After the elapse of time t_r the oxygen flow through ozonizer was restored and the concentration of ozone flowing through absorption cell was measured. The measured concentrations of ozone are shown in Fig. 3. It can be seen from this figure that ozone concentration in the ozonizer does not decrease with time t_r.

In the third set of experiments the mixture of 95% oxygen and 5% of nitrogen was used as working gas for the discharge in ozonizer. The discharge in this mixture was burning for 5 min. Then the discharge was switched off, the ozonizer was flowed by oxygen for 1 min and then the ozonizer filled by oxygen was closed at the input and at the output by the valves for the time t_r. The results of these experiments are shown again in Fig. 2. The dependence of created ozone amount versus reaction time t_r shows again two slopes – steeper one at short

times t_r and gradual one at longer times. Surprisingly amounts of created ozone are higher than the ozone amounts in the case of pure oxygen discharge.
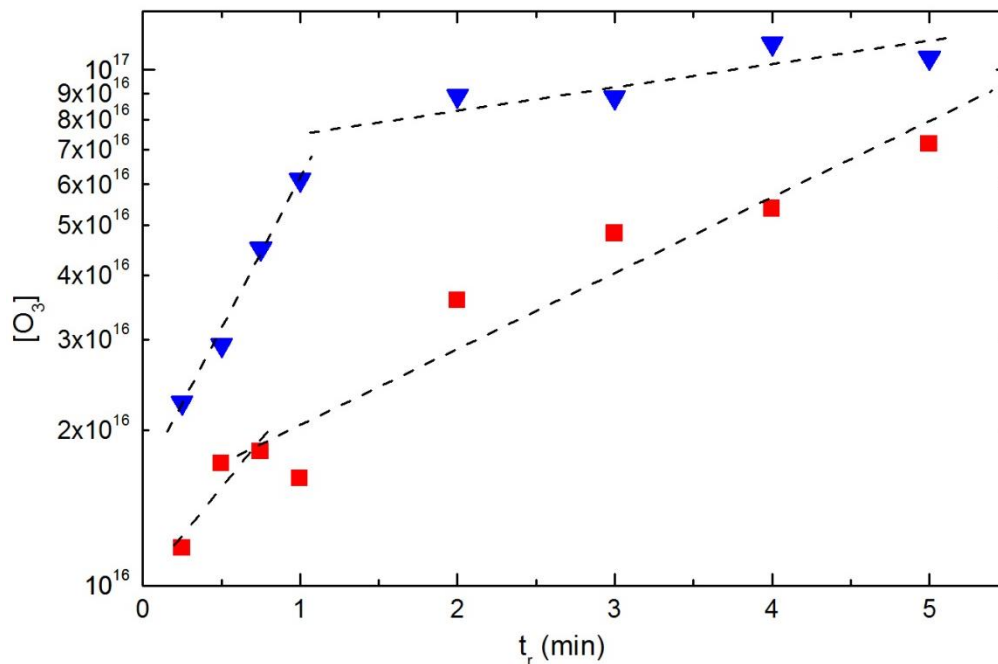
Fig. 2: The dependence of ozone amount on reaction time t_r. Squares – first set of experiments, pure oxygen discharge; triangles – third set of experiments, discharge in the mixture of 95% oxygen and 5% nitrogen.
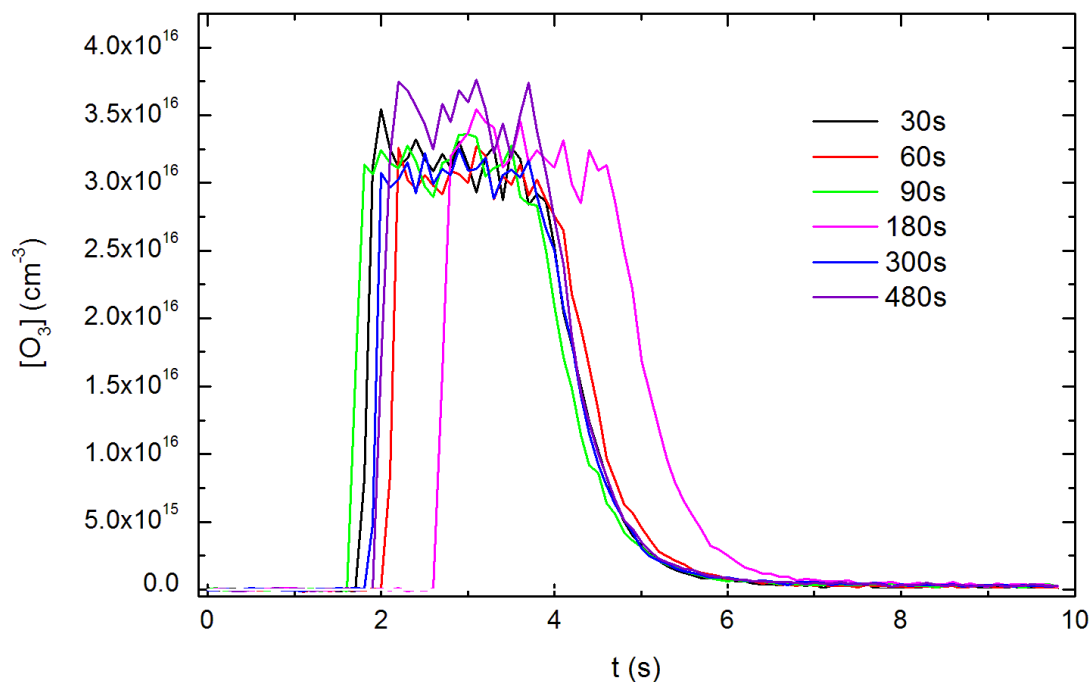
Fig. 3: The time dependence of ozone concentration in absorption cell at second set of experiments.

4   Conclusion

The experiments proved the creation of ozone on electrode surfaces which were treated in oxygen or oxygen/nitrogen DBD discharge. The measured time dependence of produced amount of ozone has two slopes, steeper one at shorter times and gradual one at longer times. This suggests that there is also a process in which the ozone is destroyed or the number of active sites with absorbed oxygen atoms on electrode surface decreases significantly.

5   Acknowledgement

References
1. O. Guaitella et al., Plasma Sources Sci. Technol. 19, 045026 (2010)
2. D. V. Lopaev et al., J. Phys. D: Appl. Phys. 44, 015202 (2011)
3. M. Taguchi et al., in *Book of Contributed Papers of 12th International Symposium on High Pressure Low Temperature Plasma Chemistry*, Bratislava, Slovakia, 2009, p. 291
4. D. Marinov et al., J. Phys. D: Appl. Phys. 46, 032001 (2013)

PLASMA CHEMISTRY OF OZONE IN DBD DISCHARGES

E. A. Abramovskaia [1], K. V. Kozlov[1], Yu. A. Mankelevich[2], A. Yu. Poroykov[2],
T. V. Rakhimova[2], D. G. Voloshin[2]

[1]*Lomonosov Moscow St. University, Chemical Dept., Leninskie gory 1/2, Moscow, Russia*
[2] *Lomonosov Moscow St. University, SINP, Leninskie gory 1/2, Moscow, Russia*

E-mail: e.abramovskaya@chemmsu.ru

Measured dynamics of emission intensity of nitrogen second positive system in single plasma filament of air DBD with ozone additions was compared with the modeling results. Electron energy distribution function and plasma chemical kinetics for 31 charged and neutral species of N_2/O_2 plasma was calculated at electric field levels and pulse durations typical for single plasma filament development and decay stages. Admixed ozone fraction was varied in the range of 0-1%. In the experiments, pronounced effect of ozone on nitrogen emission was observed even at minimal addition of ozone (0.1%). The calculated results show more gradual influence of added ozone on excited nitrogen $N_2(C^3\Pi_u)$ concentrations.

Keywords: ozone; dielectric barrier discharge; 0-D plasma chemical kinetics model

1   Introduction

Ozone is widely used as an oxidizing agent in a medical practice, a water purification technology, gaseous pollution control and some other industrial technologies [1]. In particular, the so called dielectric barrier discharge (DBD) type ozone generators are commonly used where plasma is formed by plurality of repetitive micro-discharges. Plasma in such micro discharges is substantially non-equilibrium and unsteady. The measured and monitored parameters of ozonizers, such as the concentration of ozone, energy input, electrode temperature, etc. represent the averaged values what complicates the numerical simulation of processes occurring in the ozonizer and comparison of experimental results with the calculated ones.

To overcome these difficulties and to provide an adequate comparison between theoretical model and experimental results it is very effective to conduct experiments with localized single barrier discharge. The evolution dynamics in both time and space of such discharges can be readily determined, and the data obtained in the experiment can be directly compared with results of computer simulations. Moreover, such experimental approach allows also studying the effect of the admixed ozone concentrations on micro discharge development. The role of ozone in DBD ozonizers plasma is not yet completely clear in spite of potential importance and possibility of ozone to affect plasma chemistry and electron energy distribution function (EEDF).

2 Effects of ozone on plasma chemistry and EEDF in oxygen DBD ozonizers. Saturation of ozone productivity at high specific energies.

Ozone dissociation by electron impact (reaction (1) below) was considered as a key process which could limit maximal ozone concentrations in case of significant (on order of magnitude) excess of O_3 dissociation rate coefficient k_{O_3} over coefficient k_{O_2} of O_2

dissociation by electron impact [2]. However, recent modeling [3] accounting O_3 dissociation with cross-sections from [4] showed that typical ratios k_{O_3}/k_{O_2} in DBD ozonizers are lower, $k_{O_3}/k_{O_2} \sim 3$. In addition, there are other important reactions of O_3 with excited atomic $O(^1D)$ and molecular $O_2(b^1\Sigma)$ oxygen, reactions (2) and (3), respectively, with comparable contributions in ozone destruction as it seen from calculated dynamics of single plasma filament development and decay in 5% O_3/O_2 gas mixture (figure 1). Reactions (1) – (3), in contrast to reaction (4), are not the reactions of odd oxygen loss. The dominating part of the produced atomic oxygen $O(^3P)$ (further denoted as O) recombines to ozone in three body reaction (5).

$$O_3 + e \rightarrow O + O_2 + e, \qquad O + O_2(a^1\Delta) + e \ \text{ or } \ O(^1D) + O_2(a^1\Delta) + e \qquad (1)$$
$$O_3 + O(^1D) \rightarrow O + O + O_2 \qquad (2)$$
$$O_3 + O_2(b^1\Sigma) \rightarrow O + O_2 + O_2 \qquad (3)$$
$$O_3 + O \rightarrow O_2 + O_2 \qquad (4)$$
$$O + O_2 + M \rightarrow O_3 + M \qquad (5)$$
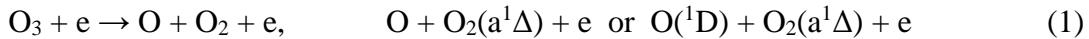
0-D plasma chemical kinetics model [3, 5] with input specific energies typical for a single filament in atmospheric pressure DBD ozonizers was used for calculations of charge and neutral species dynamics. Figure 1 shows the dynamics of O and O_3 production and reactions rates $R1 - R5$ of reactions (1) – (5), respectively, in 5% O_3/O_2 mixture at gas temperature T=300 K and reduced electric field E/N=155 Td applied for t_{pulse}=26 ns. This model pulse duration is required for avalanche increase of electron concentration from background level n_{0e}=6.5×10^4 см$^{-3}$ up to characteristic maximal concentrations $n_e \sim 5 \times 10^{13}$ см$^{-3}$ [2]. Balance analysis of ozone production/loss rates $R1 - R5$ shows that these gas-phase losses are insufficient for explanation of the observed saturation of maximal ozone concentrations $[O_3]_{max} \sim (5\text{-}15\%)[O_2]$ in DBD ozonizers at high input specific energies. To resolve this contradiction the ozone heterogeneous loss as a reason of $[O_3]_{max}$ saturation was considered in [3, 5, 6] and the mechanism of O_3 loss at the passivated surface of Al_2O_3 dielectrics was proposed on the base of DFT calculations [3]. Ozone decomposition on the electrode surface is an origin of the ozone-zero phenomenon as it was revealed in [7].
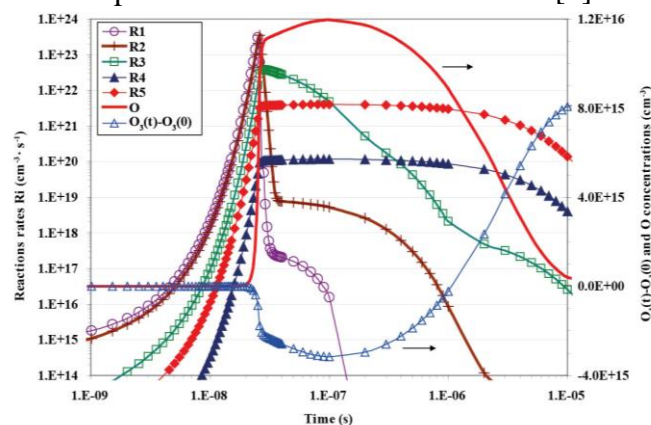
Fig. 1: Calculated dynamics of O concentration, O_3 concentration change ($O_3(t)$-$O_3(t=0)$) and reactions rates R1–R5 of reactions (1) – (5) in single plasma filament development and decay in 5% O_3/O_2 mixture

In addition to reactions (1) – (5) the interactions of O_3 molecules with electrons (attachment, excitation, ionization) could affect the EEDF at high ozone concentrations. Significant influence of electron energy losses in inelastic collisions with O_3 molecules on plasma

chemical kinetics and EEDF was revealed recently in numerical calculations [2]. In particular, these losses reduce total gas ionization rate and slow down the electron avalanche rise, e.g. the required pulse time was t_{pulse}=14.5 ns for pure O_2 vs mentioned above t_{pulse}=26 ns for 5% O_3/O_2 mixture. Therefore, any possibility to detect directly an effect of varied ozone additions on DBD plasma characteristics (Section 3) is important per se and for additional verification of plasma chemical and electron kinetics.

3   Effects of ozone in air DBD ozonizers. Experimental data and model results.

Experimental data were taken from [8]. Temporal distribution of the luminosity of the barrier discharge plasma was detected at wavelength of 337.1 nm, which corresponds to the 0-0 transitions of the second positive of nitrogen:

$$N_2(C^3\Pi_u)_{v'=0} \rightarrow N_2(B^2\Pi_g)_{v''=0} + h\nu \qquad (\lambda=337.1 \text{ nm}) \qquad (6)$$

The increase of the ozone concentration leads to the decrease of the light pulse duration as shown at figure 2. The sharpest decrease occurs when the concentration of ozone changes from 0% to 0.1 %.
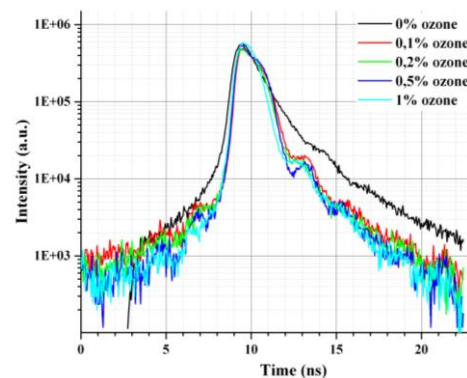
Fig. 2: Evolution of light emission from the barrier discharge in dry air with ozone admixtures at atmospheric pressure: a) spectral band of the 0-0 transition of the second positive system of N_2 (λ = 337.1 nm)

The measured emission dynamics (figure 2) was compared with the calculated behavior of $N_2(C^3\Pi_u)$ concentration in single plasma filament with ozone additions $X(O_3)$ = 0, 0.1 and 1%. The details of plasma-chemical kinetics are described in [3, 5, 9]. Here we varied the applied electric field E_{pulse} and pulse parameters: duration t_{pulse} of the main pulse $E(0<t<t_{pulse})=E_{pulse}$ and the rate of field drop at $t>t_{pulse}$.

Initial electron concentration $n_e(t=0)$ at the starting moment of the emission collection and $X(O_3)$ dependence of $n_e(t=0)$, as well as dynamics of E decay due to charges deposition on the dielectrics, are not known experimentally and theoretically. These uncertainties complicate direct comparison of the measured and calculated emission growth and decay. Therefore we did not aim to reach quantitative coincidence with the measured dynamics and focused on the possibility of qualitative description of base trends and relative intensity changes (emission drop on more than two orders of magnitude for $X(O_3)$=0 and three orders for $X(O_3)$=1%, figure 2).   In the experiments, remarkable influence of ozone on nitrogen emission was observed at the minimal ozone addition $X(O_3)$=0.1%. In contrast, the calculated influence of ozone was more gradual with $X(O_3)$ as it seen from figure 3. The emitting $N_2(C^3\Pi_u)$ molecules are produced mainly by electron impact excitation of N_2 ground state. $N_2(C^3\Pi_u)$

state is depopulated mainly in reactions $N_2(C^3\Pi_u) + O_2 \rightarrow O + O(^1D) + N_2$ and $N_2(C^3\Pi_u) + N_2(v) \rightarrow N_2(B^2\Pi_g) + N_2(v'>v)$ with the order of magnitude lower contribution of emission reaction (6). It is possible that some other important processes and effects of ozone in N_2/O_2 mixtures are not taken into account in the model.
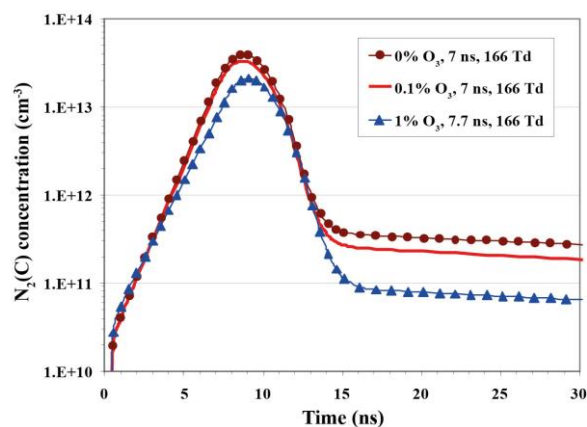
Fig. 3: Calculated dynamics of $N_2(C^3\Pi_u)$ concentration in single plasma pulse in air at 1 atm and various ozone fraction $X(O_3) = 0$, 0.1% and 1%. Applied reduced field in main pulse E/N=166 Td, pulse duration t_{pulse}=7 ns

4   Conclusion

Dynamics of nitrogen emission intensity of the band $N_2(C^3\Pi_u) \rightarrow N_2(B^2\Pi_g)$, ($\lambda$=337.1 nm) from single plasma filament in air DBD with ozone additions in the range $X(O_3) = 0$-1% was measured and compared with computer simulation based on 0-D plasma chemical kinetics model for single filament in atmospheric pressure DBD type ozone generators.

Acknowledgement

References

1. B. Eliasson et al., IEEE Trans. Plasma Sci., 19, 1063 (1991)

2. V. V. Lunin et al., Physical chemistry of ozone, (Moscow State University press, Moscow, 1998)

3. Yu. A. Mankelevich et al., Plasma Phys. Reports (2016) (in press)

4. M. Gupta et al., J. Phys. B: At. Mol. Opt. Phys. 38, 4057 (2005)

5. Yu. A. Mankelevich et al., Russ. J. Phys. Chem. A. 90, N9 (2016)

6. A. V. Zosimov et al., Russ. J. Phys. Chem. A 90, N8 (2016)

7. M. Taguchi et al., Plasma Process. Polym. 4, 719 (2007)

8. O. S. Shepelyuk, Spatio-temporal structure of the micro discharge in the ozonizer and its role in the synthesis of ozone from the air (PhD thesis, Lomonosov Moscow State University, 1999)

9. A. N. Vasiljeva et al., J. Phys. D: Appl. Phys. 37, 2455 (2004)

NON-CHEMICAL OZONE STERILIZATION SYSTEM AND ITS APPLICATION TO GREENHOUSE AGRICULTURE

K. Ebihara[1], S. Baba[2], F. Mitsugi [3], T. Ikegami [3], S. Aoqui[4],
Y. Yamashita[5], T. Yamashita[5], H. D. Stryczewska[6], J. Pawlat[6]

[1]Environment and Energy Laboratory, [2] Densoken Co.Ltd., [3]Kumamoto University ,[4]Sojo University,
[5]Sanwa hi-tech Co.Ltd., [6]Lublin University of Technology

E-mail: ebihara@environment-lab.com

Application of non-chemical ozone sterilization system to the greenhouse agriculture was studied. The sterilization characteristics of the developed ozone-mist sterilization system was shown for harmful insects including aphids. The half-life time and the diffusion length of ozone in the greenhouse were shown.

Keywords: ozone-mist; sterilization; aphid; non-chemical; greenhouse

1   Introduction

Ozone gas is a powerful oxidation agent that could kill microorganisms without having detrimental effects on the environment. Ozone-mist sterilization we have proposed is a potential alternative to the synthetic pesticides that deplete biodiversity and fertility in the green house. We have developed a portable ozone–mist sterilization system which is designed for agriculture farmers who engage in non-chemical agriculture under poor infrastructure of electrical power supply [1, 2]. This system has remarkable advantages in agricultural operation: (1) kill living small insects, worms, bacteria and viruses at high sterilization rate(~90%) in short operation time(10~20 sec); (2) oxygen gas and water as original materials produce an ozone-mist creating pesticide radicals which kill microorganism; (3) secure farmer health from ozone exposure; (4) leave no harmful residues on the product.

There is the urgent need of non-chemical sterilization technique to secure safety and security of food harvested in green house. Although corps grown in the greenhouse may be protected from common field pests and many diseases, there are still particular problems such as pests, infectious viruses and fungi being parasitic on the plant and in the soil. The ozone–mist sterilization method is a new method suitable to the green house agriculture.

Here, we studied the potential of the ozone-mist sterilization to treat pests, bacteria and pathogens living in the green house. We show basic sterilization effect of pests using the developed ozone-mist system at various sterilization conditions. Fundamental characteristics involving spatial and temporal diffusion of ozone in the green house was also investigated experimentally.

2 Experimental

The ozone sterilization system (Pecoshower#5) used here is composed of an ozone generator, a water-mist supply system, an AC-DC inverter connected to Li-ion batteries, a lightweight oxygen vessel (FRP) with a pressure regulator, a water tank and a movable spray rod with ozone-mist nozzle. Fig.1 shows the portable ozone-mist sterilization system. High dense ozone is generated by two types of surface dielectric barrier discharges (flat-plate and

Fig.1 Portable ozone-mist sterilization system

cylindrical electrodes). The AC electric power for the high frequency generator was supplied from the AC-DC inverter with Li-ion batteries. High dense ozone of 112 g/m^3 and 86 g/m^3 at an oxygen flow rate of 1 liter/min were generated using the cylindrical type and the flat-plate type, respectively. A compact chamber and a practical greenhouse were used to estimate the half-life time and the diffusion length of ozone in air at various conditions.

3 Results and Discussion

Basic experiments were carried out to estimate time-resolved death rate of a typical pest (aphid) at various sterilization conditions. Sample aphids were settled in a plastic container (ϕ50mmx20mm) which has an inlet tube connected to the ozone sterilization system. The behavior of the aphids during ozone treatment was observed by using a video camera and the number of death aphids was accounted on the time-resolved image flame on the video files. Fig.2 shows the death rate of aphids by gaseous ozone treatment at different ozone concentrations of 86 g/m^3 (O$_2$ flow rate: 1 liter/min) and 68 g/m^3 (O$_2$ flow rate:2 liter/min). In the case of 86g/m^3, 100% sterilization rate was attained at a treatment time of 85 sec.
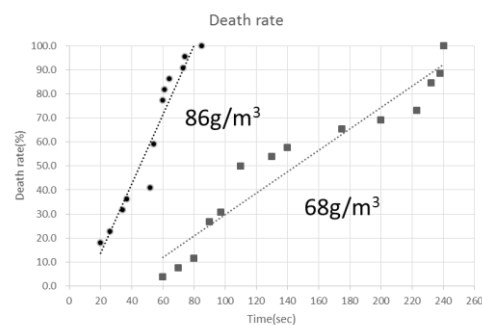
Fig.2 Death rate of aphids at 86g/m^3 and 68g/m^3.

In the case of the ozone-mist treatment, statistical analysis is introduced to obtain sterilization rate using many experimental runs for aphids. The ozone-mist mixture was generated with a specially designed splay nozzle under a condition of ozone concentration of 86 g/m^3 (O$_2$: 1 liter/min) and water-mist flow rate of 0.3 liter/min. Fig.3 shows the normal distribution function F(x) of sterilization rate for different treatment times of 5 sec and 10 sec. Number of aphids treated at each run is about 20. It is shown that most probable sterilization rate is 87% for 10sec and 81% for 5sec. We

Fig.3 Normalized distribution function (F(x) of sterilization rate at treatment time 5sec and 10sec.

also confirmed that 100% sterilization is realized at a treatment time of 20 sec. These results show the sterilization effect comparable to a conventional treatment using a synthetic pesticide of Acephate (Orthoran).

When ozone reacts with water-mist, the highly reactive radicals are generated and, specially, hydroxyl radical (*OH$^-$) has high redox potential of 2.86 V comparable to fluorine F (2.87 V), O$_3$ (2.07 V) and chlorine Cl (1.36 V). Gaseous ozone and the derivative radicals in ozone-mist mixture such as *OH$^-$ are taken into the aphid body through spiracles, travel via the trachea and reach the cells [1]. As a result, the aphid may be killed by molecular ozone and related radicals acting on proteins and organelles of the cell.

Ozone-mist treatment also provides the biological effects on plants depending on both ozone-mist conditions and treatment duration. It is shown that a positive effect of an increased leaf area, enlarged shoot size and root length of plant such as tomato occurs when a low gaseous ozone of a concentration (a few ppm) exposes under short repeated duration (2-3 minutes) for several days [3]. Our preliminary study on the ozone-mist treatment was performed for several plants. When eggplant seedlings were treated by ozone-mist of the same conditions as in Fig.3, the 10 sec treatment caused foliar injury showing color change of the leaves. However, apparent damages were not observed for the 5 sec treated sample. The mixture rate between ozone and water-mist, the flow rate and the treatment duration are essentials to optimize sterilization in each plant growth phase under keeping ozone stress-induced growth. Further studies are needed to identify the biological phenomena of these preliminary results.

Fig.4 The half-life time measurement system.

The half-life time (HLT) of ozone is the amount of time that takes to reduce the initial concentration by half. The practical half-life time of ozone in air is variable and usually less than 30 minutes based on the temperature, relative humidity, air movement and presence of contaminations. The HLT of ozone also depends on the level of ozone concentration at the environment. The experimental and theoretical study showed that the HLT of ozone is 22 minutes at initial concentration of 225μ g/m^3 and 36 minutes at 160μ g/m^3 in the indoor environment (volume: 46 m^3, temperature:20°C, relative humidity: 36%) [4]. We carried out the HLT measurement of our sterilization system in a small plastic chamber (size: 241mmx331mmx90mm, temperature: 25°C, relative humidity: 65%) as shown in Fig.4. Fig.5 shows the HLT measurement of our sterilization system under various conditions in the chamber. The saturated value of ozone concentration in the chamber was 34 g/m^3 at an oxygen flow rate of 1 liter/min, 33 g/m^3 at 2liter/min and 24 g/m^3 at 3 liter/min, respectively. The ozone concentration in Fig.5 was measured after terminating ozone supply from the ozone generator. The resulting HLT is 7.5 min for 34g/m^3, 22 min for 33 g/m^3 and 7 min for 24 g/m^3.

Fig.5 Half-life time of ozone in a chamber. Initial ozone concentrations are 33 g/m^3(■),34 g/m^3(●) and 24g/m^3(▲).
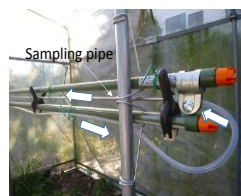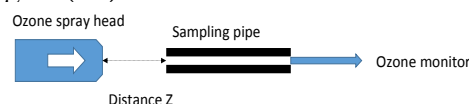
Fig.6 Spatial ozone diffusion measurement in a green house.

Spatial diffusion of ozone was investigated using a practical greenhouse (width 2.7 m, depth 4 m, height 2.2 m) as shown in Fig.6. High dense ozone was introduced into the greenhouse through a Teflon pipe. A sampling stainless pipe (length 2 m and height 1.5 m) connected to the ozone monitor was placed at a position (z) apart from the outlet of the ozone Teflon pipe. The distance (z) between a tip of the ozone sampling pipe and the ozone outlet pipe was changed to measure diffusion length of ozone in the greenhouse. Fig.7 shows the ozone concentration as a function of the distance (z) at various oxygen flow rate under temperature 25°C and relative humidity 65%. It is shown that the ozone concentration gradually decreases with distance and is reduced to small values at 10 cm. Spatial diffusion length of 14-30 cm was obtained using natural logarithm expression of these data. This result of the ozone diffusion length is useful to design the non-chemical agricultural greenhouse.
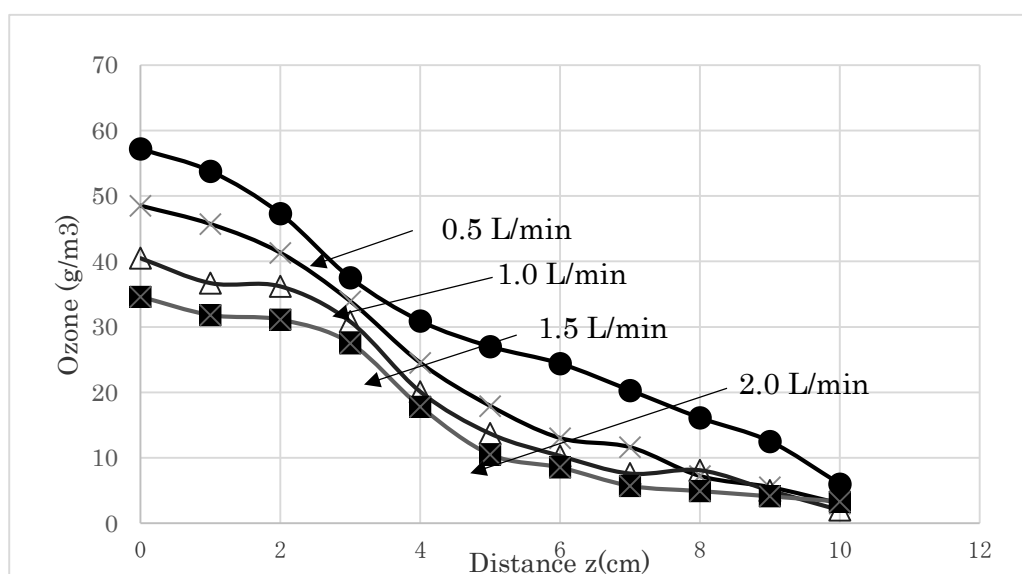
Fig.7 Ozone concentration as a function of the distance (z) at various oxygen flow rates.

4 Conclusion
The ozone-mist sterilization system we have developed was used to clarify the sterilization effect on harmful insects and the spatial and temporal characteristics of ozone in the closed space. The sterilization rate of 87% for aphids was achieved within a short treatment time of 10 sec. It is shown that the half-life time of ozone in air is 7.5-22 minutes and that the ozone diffusion length in the practical greenhouse is 14-30 cm. These results provide promising and useful information to design non-chemical agriculture operating in a greenhouse.

Acknowledgement

References
1. K. Ebihara et al., Eur. Phys. J.Appl.Phys.,61,24318, 1-5 (2013)
2. K. Ebihara et al., Int. J. Environ. Sci. Te. 10, 1 (2016)
3. N. Sudhakar et al., Aust. J. Crop. Sci. 2(1), 33-39 (2008)
4. S. Bycenkiene et al., Lith. J. Phys. 49, 335-339 (2009)

EXPERIMENTAL STUDY OF DIELECTRIC BARRIER DISCHARGE IN MIXTURES OF CARBON DIOXIDE AND OXYGEN

F. Pontiga[1], K. Hadji[2], M. Guemou[2], H. Moreno[1]

[1]*Dpt. Física Aplicada II, Universidad de Sevilla, Av. Reina Mercedes 4a, 41012 Sevilla, Spain*
[2]*Lab. de Génie Electrique et des Plasmas, Université Ibn Khaldoun, Tiaret, 14000, Algeria*

E-mail: pontiga@us.es

Carbon dioxide decomposition in mixtures of CO_2 and O_2 has been experimentally investigated using dielectric barrier discharge, with special interest on O_3 and CO productions. Experiments have been conducted at different frequencies and operating voltages, and the concentration of O_3 and CO have been measured by means of absorption spectroscopy in the UV and in the IR regions. According to the observations, the production of both species can be substantially increased by adding molecular oxygen to carbon dioxide, even in small proportions.

Keywords: dielectric barrier discharge (DBD); carbon dioxide; oxygen; carbon monoxide; ozone.

1 Introduction

Carbon dioxide emissions constitute a great concern because of its implications for the global temperature rise of Earth. Therefore, member countries of the Intergovernmental Panel on Climate Change (IPCC) have agreed to impose more stringent restrictions on CO_2 emissions to the atmosphere in the coming year. In this scenario, reprocessing of CO_2 emissions by plasma treatment can help to mitigate this problem, while producing valuable chemicals for the industry, such as ozone and carbon monoxide [1-3]. However, direct production of ozone from carbon dioxide gives poor results, due to the absence of enough molecular oxygen in the background gas. Therefore, in this work we explore the possibility of increasing ozone production by mixing carbon dioxide with small amounts of oxygen.

2 Experimental

The DBD reactor consisted of two stainless steel circular electrodes, 20 mm in diameter, covered with fused silica glasses of 1 mm of thickness. The gap between the two dielectrics was fixed at 2 mm. High purity CO_2 (99.995%) and O_2 (99.995%) were used to prepare the gas mixture, and the total gas flow was kept constant ($Q = 100$ cm^3/min) with the help of digital mass flow controllers (Alicat). High voltage (20 kVpp to 24 kVpp) was applied to one of the electrodes using a high voltage amplifier (Trek 20-20C-HS). The frequency of the AC voltage was varied in the range 50-500 Hz. The other electrode was connected to a monitor capacitor ($C_m = 1$ μF), and the voltage drop across the capacitor was measured using a digital oscilloscope (Tektronix DPO7254). The concentration of ozone and carbon monoxide in the effluent gas was sampled periodically using UV/VIS and IR spectrophotometers (Thermo Evolution 300, Bruker Vertex 70).

2 Results and Discussion

Figures 1 and 2 show the measurements corresponding to ozone and carbon monoxide productions as a function of the averaged energy density, P/Q, where P is the averaged
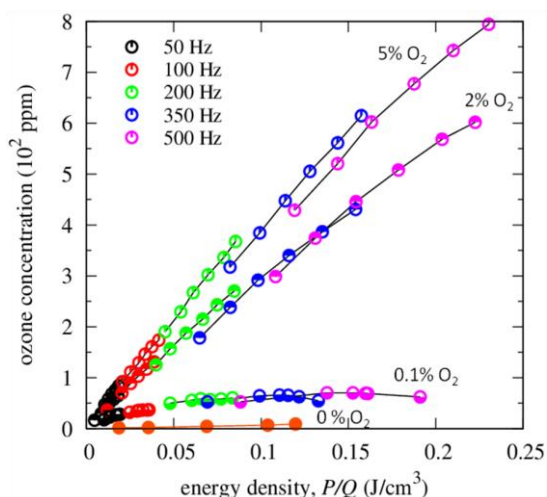
Fig. 1: Ozone concentration as a function of the energy density for different ratios of O_2/CO_2 in the gas mixture.
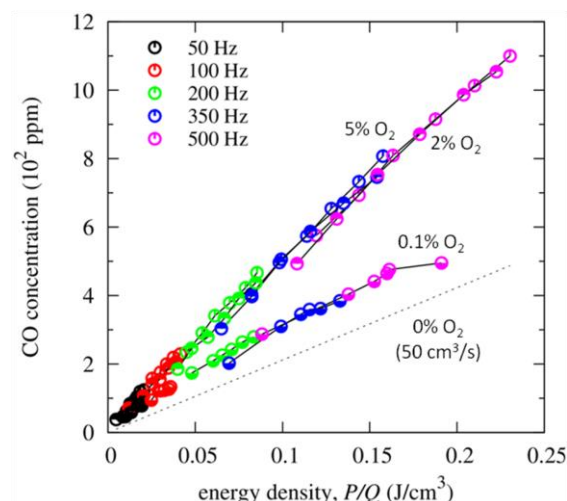
Fig. 2: CO concentration as a function of the energy density for different ratios of O_2/CO_2 in the gas mixture.

electrical power and Q is the gas flow rate. Regarding ozone (Fig. 1), the admixture of oxygen boosts importantly ozone production with respect to the case of using 100% CO_2, even with admixtures of oxygen of the order of 5% or lower. Moreover, ozone production increases steadily with the augmentation of the energy density, except for very low oxygen admixtures (< 0.1 O_2) for which a saturation is observed. It is also interesting to compare the production of ozone in a mixture of CO_2 and O_2 with the one obtain in pure O_2: for a gas flow rate of 200 cm^3/min and using the same experimental set-up, it was found that ozone production in pure O_2 increases linearly with the energy density at a rate of 2×10^4 ppm/(J/cm^3). Therefore, using a mixture with 5% of O_2, the direct production of ozone due to the presence of O_2 can be estimated to be 10^3 ppm/(J/cm^3). However, according to the results shown in Fig. 1, the measured rate of ozone production is more than 3.5 times the expected value, due to the contribution of CO_2. Similarly to ozone, the addition of O_2 also favors production of carbon monoxide (Fig. 2) by, at least, a factor of two. Its concentration increases very linearly with the energy density and no saturation was observed in the range of tested energy densities.

4 Conclusion

The decomposition of CO_2 using DBD can be substantially increased by mixing CO_2 with O_2 in small percentages. In mixtures with 2-5% of O_2, the production of CO was doubled, as compared with pure CO_2. Moreover, the production of O_3 was three times higher than the one expected according to the proportion of O_2 in the gas mixture.

Acknowledgements

References

1. G. Horváth et al., J. Phys. D: Appl. Phys. 41, 225207 (2008)
2. F. Brehmer et al., J. Appl. Phys. 116, 123303 (2014)
3. R. Aerts et al., ChemSusChem. 8, 702 (2015)

SURFACE LOSS RATE OF OZONE FOR VARIOUS MATERIALS IN A PHOTO-ABSORPTION CELL

S. Suzuki[1], K. Teranishi[2], A. Oda[1], I. M. Rusinov[3], H. Itoh[1]

[1] *Chiba Institute of Technology, 2-1-1 Shibazono, Narashino, Chiba, 275-0023, Japan*
[2] *The University of Tokushima, 2-1 Minamijyousanjima-cho,Tokushima, 770-8506, Japan*
[3] *Sofia University 'St. Kliment Ohrdski', Faculty of Physics, 5 James Bourchier Blvd. 1164 Sofia, Bulgaria*

E-mail: susumu.suzuki@it-chiba.ac.jp, haruo.itoh@it-chiba.ac.jp

We determined the fundamental coefficients i.e. the diffusion coefficient of ozone in oxygen and the reflection coefficient of ozone at surface that could be expressed the surface loss rate of ozone. Moreover, the rate coefficient for collisional disappearing of ozone with oxygen in the cell is determined simultaneously.

Keywords: ozone; surface loss rate; effective lifetime

1   Introduction

We investigated the loss process of ozone in an ozone-oxygen mixture contained in an enclosed cell [1-3] in the pressure range of 20 – 1000 Torr and temperatures of 293 –353 K [4] related to the investigations on the ozone generation process including ozone zero phenomena [5, 6] and construction of ozone generator using a piezoelectric transformer [7].

In the present paper, we report the surface loss rate of ozone in the cell made from stainless steel, polytetrafluoroethylene (PTFE), boron nitride, alumina and aluminium cells based on the Hg I photo-absorption method using ultraviolet (UV) light with a wavelength of 253.7 nm [1-4]. The observed trace of ozone concentration decreases exponentially with time, and we evaluate the time constant of the decaying curve. The time constant is equivalent to the effective lifetime of ozone in the cell. Then we determine the equivalent diffusion coefficient of ozone in oxygen together with the reflection coefficient of ozone at the surface in the cell and the collisional decompotion reaction rate coefficient of ozone by oxygen. In particular, both of the former values among them are important coefficients in the fields not only the ozone kinetics, but also the practical ozone application.

2   Experimental apparatus and method

The HgI photo-absorption method was used to measure the ozone concentration. Figure 1 shows the schematic diagram of the simplified double-beam method developed by us [4]. The detailed operations of the measuring system and their handling procedure were already described in the previous paper [4]. The cell was made of stainless steel and the both ends were sealed with quartz windows. The cell had a length of 200 mm and an inner diameter of 24 mm.

Before the start of measurement, no ozone was present in the photo-absorption cell. The sample and reference intensities $I_{in}(0)$ and $I_{ref}(0)$ are measured. Subsequently, ozone was introduced into the cell and the measurement was started to monitor the intensities of the light transmitted through the cell $I_{out}(t)$ and the reference signal of the incident light intensity $I_{ref}(t)$ as functions of time t. When $I_{ref}(t)$ deviated from $I_{ref}(0)$, the ratio $I_{ref}(t)/I_{ref}(0)$ was employed
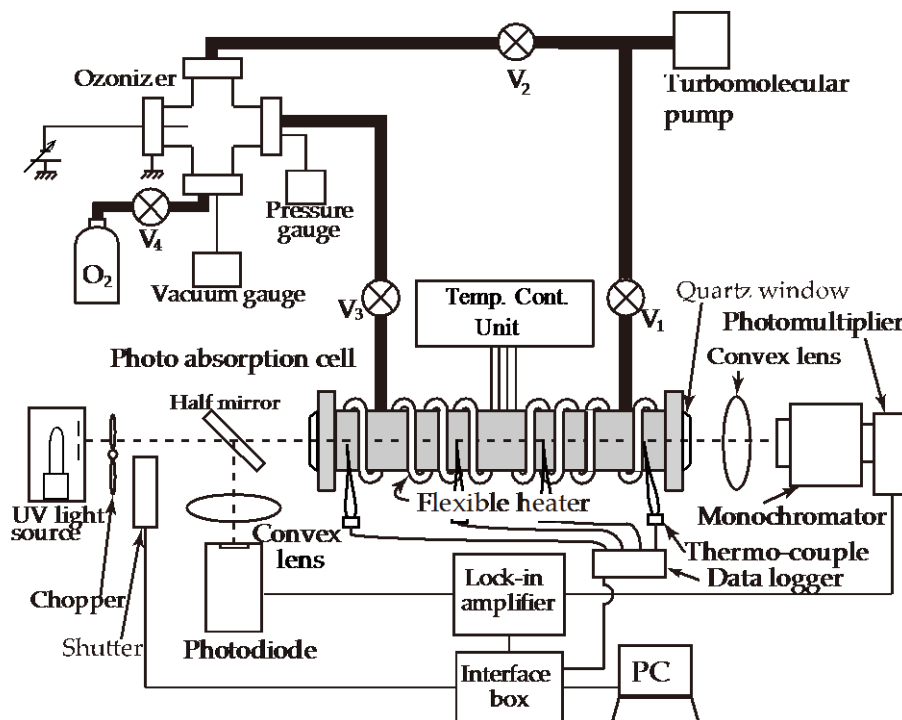
Fig. 1: Experimental apparatus. Ozone is formed in an ozonizer by corona discharge.

to correct the drift of the intensity $I_{in}(t)$. We obtained the correct incident light intensity by multiplying $[I_{ref}(t)/I_{ref}(0)]$ and $[I_{in}(0)]$. Then, the ozone concentration at time t was obtained as [4]

$$c(t) = \frac{1}{\sigma L} \ln\left[I_{in}(0) \frac{I_{ref}(t)}{I_{ref}(0)} \frac{1}{I_{out}(t)} \right] \qquad (\text{cm}^{-3}). \quad (1)$$

The temperature was controlled using a pair of flexible heaters, which were wound around the cell and a temperature controller unit. The temperature of the cell was monitored by four pieces of thermocouples attached to the cell and a data logger. In this experiment, the temperature was varied in the range of 293 K to 423 K.

3 Results and Discussion
3.1 Ozone effective lifetime
The obtained ozone effective lifetime in the stainless steel cell is shown in Fig. 2. The effective lifetime curves shift downward with increasing gas temperature while maintaining a similar dependence on the gas pressure. The solid lines were drawn by a curve-fitting procedure based on the theory proposed by us [8-10] using the observed values of the ozone effective lifetime τ. The inverse of τ is expressed by the following eq. (2).

$$\frac{1}{\tau} = \frac{D_e}{p_0} \left\{ \left(\frac{v_1}{a} \right)^2 + \left(\frac{q_1}{L} \right)^2 \right\} + k N_0 p_0 = \frac{1}{\tau_s} + \frac{1}{\tau_g} \qquad (\text{s}^{-1}) \qquad (2)$$

Then, the three coefficients could be used to express the loss rate of ozone in the cell, i.e., the equivalent diffusion coefficient of ozone molecules in oxygen D_e, the reflection coefficient of ozone molecules at the surface of the cell R, and the collisional decompotion reaction rate

coefficient of ozone by oxygen k were simultaneously determined by the curve fitting procedure of eq. (2) to the observed effective lifetimes τ.

In Fig. 2, the dotted straight lines indicate the effective lifetime of ozone, which were drawn under the assumption that the reflection coefficient of ozone at the surface is zero; therefore, the effective lifetime is proportional to the gas pressure at low gas pressures. The intersection of the dotted lines with the vertical axis at $p_0 = 1$ Torr gives the reciprocal of the equivalent diffusion coefficient $1/D_e$ for each temperature. The increment of the effective lifetimes from the values indicated by the dotted lines to the values shown by the solid lines expresses the reflection coefficient R at the surface of cell for each gas pressure and temperature. The collisional decompotion reaction rate coefficient of ozone by oxygen rate coefficient k is also determined from the analysis. The variations of these values are illustrated in Fig. 3. Thus, the equivalent diffusion coefficient D_e and the reflection coefficient R were utilized as the fundamental coefficients to express the loss rate of ozone at the surface of cell. The observed reflection coefficient of ozone at the stainless steel surface was approximately 0.99974; thus, then the surface loss probability of ozone is $s = 1 - R = 2.6 \times 10^{-4}$. This value is in good agreement with the value of $s = 1 - R = 2.6 \times 10^{-4}$ obtained in a previous experiment [4]. The value was also consistent with the results of Horvath *et al.* [11].
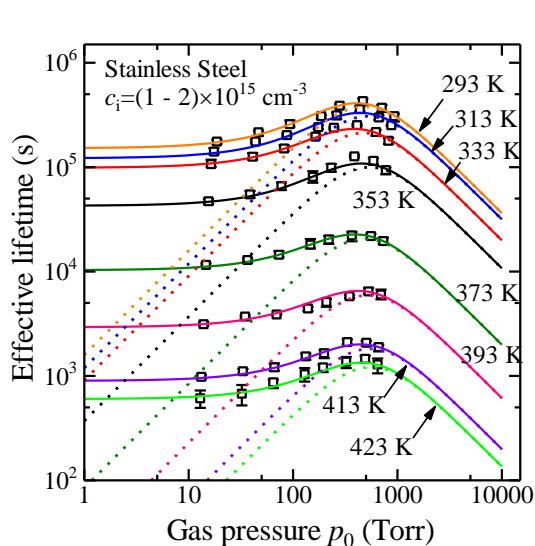
Fig. 2: Observed effective lifetime of ozone in the cell plotted against gas pressure. c_i is initial concentration of ozone.
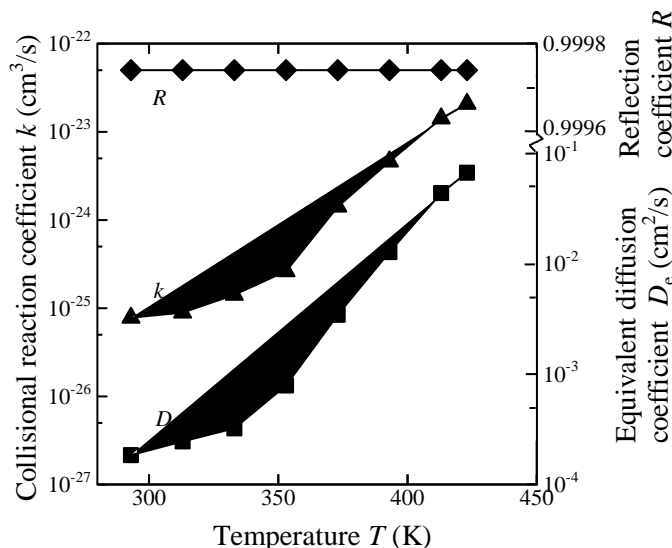
Fig. 3: Observed values of D_e, R, and k plotted against gas pressure in stainless steel cell.

3.2 Surface loss rate of ozone

The loss rate of ozone at the stainless-steel surface is about $(2 - 5) \times 10^{-6}$ s^{-1} at 293 K as shown in Fig. 2. The surface loss rate of ozone $1/\tau_s$ is expressed as shown in the eq. (2). The observed loss rates which are the inverse of the effective lifetime plotted by each symbols are in good agreement with theoritical values indicated by solid lines as shown in Fig. 4. In the low gas pressure, the surface loss rate draws an almost flat, then decreases gradually with an increase in the gas pressure and reach the bottom. After drawing the bottom of valley, the loss rate increases with the increase in the gas pressure. This part is corresponding to the ozone loss rate in the gas phace expressed by the second term on the right-hand side of eq. (2). However, the collisional decompotion reaction rate coefficient of ozone by oxygen rate coefficient k will be discussed at another opportunity. These loss rate curves shift upper with the increase in gas

temperature. It is concluded that the ozone loss rate for the boron nitride cell is the largest, in contrast, the stainless steel cell is the smallest among them in the present experiment.
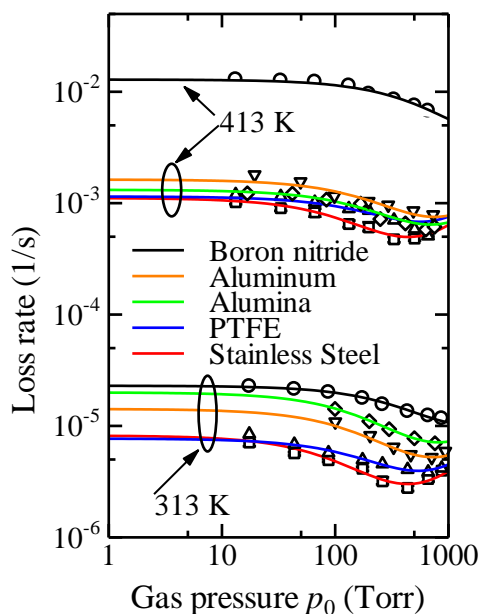
Fig. 4: Relationship between ozone loss rate and gas pressure in several materials.

4   Conclusion

We investigated the temperature dependence of the effective lifetime of ozone in several materials of cell after a sufficient aging process. We showed that the material with the smallest ozone loss rate was the stainless steel.

References

1. H. Itoh et al., Ozone: Sci. Eng. 26, 487-497 (2004)
2. H. Itoh et al., Plasma Processes and Polymers 2, 227-231 (2005)
3. H. Itoh et al., Ozone: Sci. Eng. 33, 106-133 (2011)
4. H. Itoh et al., Ozone: Sci. Eng. 34, 370-377 (2012)
5. T. Takano et al., IEEJ Trans. FM 125(6) 508-514 (2005) [in Japanese]
6. M. Taguchi et al., Plasma Processes Polym. 4, 719-727 (2007)
7. K. Teranishi et al., Plasma Sources, Sci. Technol. 18, 045011 (2009)
8. S. Suzuki et al., J. Phys. D: Appl. Phys. 25, 1568-1573 (1992)
9. S. Suzuki et al., Jpn. J. Appl. Phys. 39, 1333-1337 (2000)
10. S. Suzuki et al. J. Phys. D: Appl. Phys. 49, 185202 (2016)
11. G. Horvath et al., Plasma Chem. Plasma Process. 30, 43-53 (2010)

TOPIC 5: GENERATION OF RADIATION IN HIGH PRESSURE DISCHARGES

ATMOSPHERIC PRESSURE MICROPLASMA SYSTEM WITH VORTEX GAS FLOW

O. Solomenko, O. Solomenko, V. Chernyak, V. Lendiel, D. Hamazin, D. Kalustova

Faculty of Radio Physics, Electronics and Computer Systems, Taras Shevchenko
National University of Kyiv, 64/13, Volodymyrska Str., Kyiv, Ukraine

E-mail: *elanka@ukr.net*

Atmospheric pressure DC microdischarge system with vortex gas flow was investigated in the work. Current-voltage characteristics of the microjet there carried for evaluation of discharge power. The plasma parameters inside and outside the microdischarge system was evaluated by emission spectroscopy method, such as component composition and the temperatures of excited electronic, vibrational and rotational levels of plasma components. It was found that nitrogen was the main component of microdischarge plasma. Also NO, OH and N_2^+ (in some working regimes) molecular bands were presented.

Keywords: microdischarge; non-isothermal plasma; plasma-chemistry

1 Introduction

The development of atmospheric pressure microplasma jet is highly promising and perspective today. Numerous plasma components: such as activated components of oxygen or nitrogen (components of working gas or outside atmosphere), charged particles, electric fields and even UV radiation leads to different reactions in plasma volume and on the treated tissues. Among those discharges the microdischarges pose the greatest relevance. Important advantage of these systems is its compactness (plasma is not limited by the sizes of electrodes). The ability to adjust the size of the plasma jet allows localizing area of microplasma jet influence. Other advantage of microdischarge systems is low gas (rotation) temperature. This fact leads to higher selectivity in case of plasma-chemistry usage. Its allow using of microdischarge systems for various applications except plasma-medicine (which is very popular today), for example: nanoparticle synthesis [1], surface activation and treatment of low-melting materials [2-3]. This research studies the properties of atmospheric pressure DC microdischarges in the vortex gas flow.

2 Experimental

The Fig. 1 shows a schematic of atmospheric pressure axially symmetric design microdischarge plasma generators. The internal high-voltage electrode (1) was made in the form wire (d ~ 3.5 mm) with rounded cone-shape ending (d ~ 0.5 mm and high ~ 13.0 mm). Big part of the internal electrode (except cone-shape ending) covered by dielectric tube (2). Also from the body system it was separated by dielectric layer (3). Internal high-voltage electrode had water cooling (4). The role of the second external electrode (that was grounded) performed building (5) of this design. The microdischarge (6) was burning between internal electrode and disc/cap (7) with hole in the middle. The output diameter (from which microjet was blown out) was varied from d = 0.5 mm to d = 2.0 mm with step of 0.5 mm.
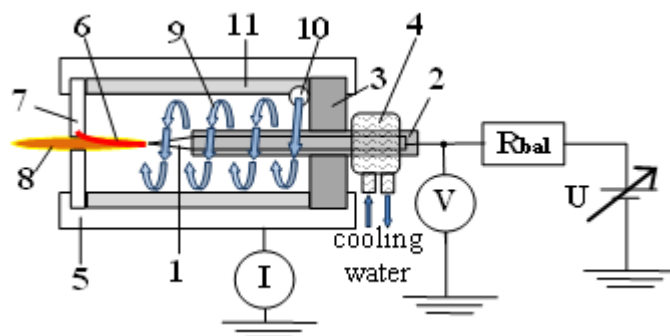
Fig. 1: Schematic representation of atmospheric pressure microdischarge plasma generator.

Both electrodes were made from copper. The jet (8) was blown over from microdischarge system through the outlet in grounded electrode by the vortex gas flow (9). The working gas (air) was fed through the channel (10) tangentially to the internal dielectric (quartz cylinder) wall (11), thus forming a reverse vortex flow in dielectric camber. Plasma jet can rotate under the influence of the gas flow, gliding over the surface of the grounded electrode. Also it should be mentioned, that outside metal construction (4) have round holes/windows. It was made fore the observation and diagnostic of plasma inside the system. The system can work horizontally, vertically or any other position (angle).

Current-voltage characteristics of the microjet there carried for evaluation of discharge power. The plasma parameters inside and outside the microdischarge system was evaluated by emission spectroscopy method. Optical emission spectroscopy of plasma-generated microplasma jet was made by CCD-based spectrometer Solar TII (S-150-2-3648 USB) in the wavelength range of $200 \div 1100$ nm with spectral resolution of approximately 0.2 nm. Also microplasma jet behavior was studied by photo and video registration methods.

3   Results and Discussion

The current-voltage characteristics (CVC) measurements of microdischarge were performed for different air flows (G = $0 \div 3$ L/min). The measurement results of CVC with the positive potential of the high voltage electrode in case then interelectrode distance was 1.0 mm and output diameters d = 1.0 mm are presented in Fig. 2. The CVC behavior and absence on electrode material (Cu) in plasma emission spectra (which will be described below) gives us the opportunity to assume that microplasma jet of this system is glow discharge. The extreme points on the ordinates axis correspond to the breakdown voltage. Also it should be mentioned that gas flow velocity weakly affect CVC behavior.

Photo and video observation was used for studying of microplasma jet behavior during the distance between electrodes was changed (it was increased from 0.5 mm to 5.5 mm in case of 1 L/min air flow, to the 5.0 mm in case of 2 L/min and to 3.5 mm in case of 3 L/min air flow). The example of photos of working microplasma system in case of 3.5 mm interelectrode distance, output diameters d = 1.0 mm and air flows G = 1 L/min presented in Fig. 3. It was notice that an increase of interelectrode distance led to the increase of discharge power and affected on microplasma jet length (z). In case of the smallest studied gas flow (1 L/min) the

plasma jet was the longest (in compare with bigger studied gas flows at the same interelectrode gaps) but it takes higher discharge power (Fig. 4).
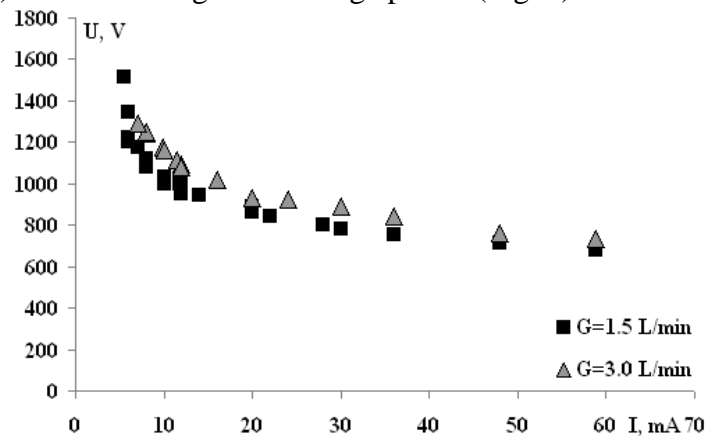
Fig. 2: Current-voltage characteristics of the microdischarge which were blowing through the hollow d=1 mm with gas flow G = 1.5 and 3 L / min. Working gas – air.
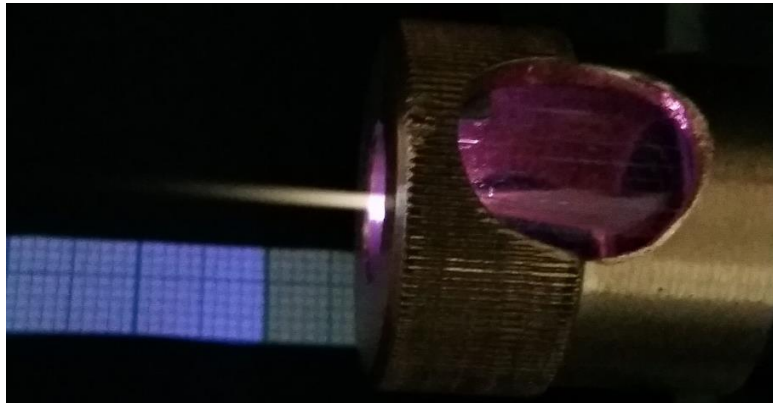
Fig. 3: The example of photos of working atmospheric pressure microplasma system in case of 3.5 mm interelectrode gap, output diameters d = 1.0 mm and air flows G = 1 L/min.
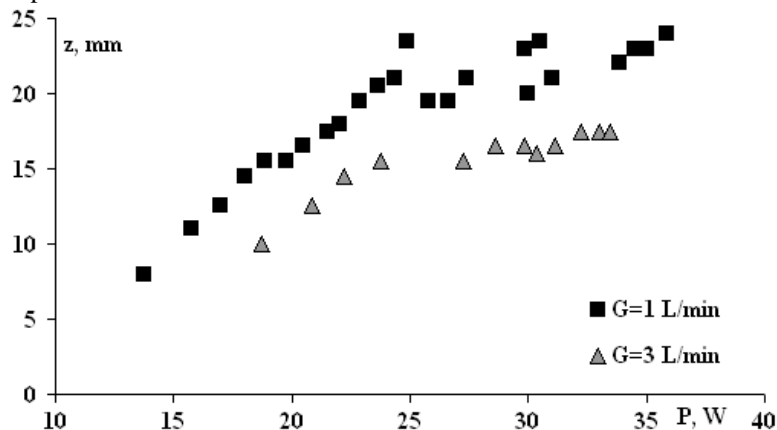
Fig. 4: The dependence of microplasma jet length (z) from discharge power increasing by the increasing of interelectrode distance in case of different gas flow (1 and 3 L/min).

Typical emission spectrum (at wavelength ranges 230÷450 nm and 600-1050 nm) of microdischarge inerelectrode plasma in case of discharge current I=25 mA, interelectrode distance l=1.0 mm, output diameter d = 1.0 mm and air flow G = 1 L/min presented in Fig. 5. The intensity of UV part of emission spectra is by 3-4 orders more intense than its IR part. Emission spectra of the microplasma are multicomponent and contain atomic oxygen

multipletes and molecular bands of NO, OH, N_2 (B-A) and N_2 (C-B). Also in cases of low gas flow velocity (or even its absence) and small interelectrode distance N_2^+ was noticed.
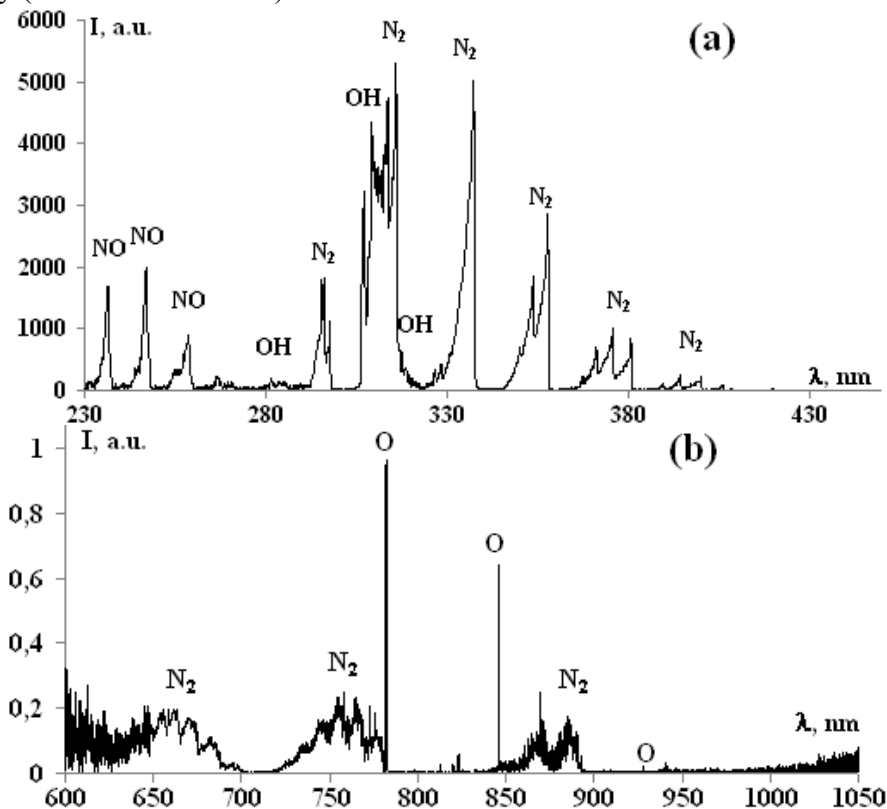
Fig. 5: The typical emission specter of microdischarge interelectrode plasma in case of I=25 mA, l=1.0 mm, d = 1.0 mm and G = 1 L/min at wave length ranges: 230÷450 nm (a) and 600-1050 nm (b).

Experiments show that microdischarge highly non-isothermal ($T_e^* \approx 13000$ K, $T_v^* \approx 4500$ K and $T_r^* \approx 1500 \div 2500$ K depends from working regime) and increasing of interelectrode distance leads to the increasing of rotational temperatures.

4 Conclusion

It was noticed, that increasing of interelectrode distance leads to the increasing of discharge power and microplasma jet length. Also in case of the smallest studied gas flow the plasma jet was the longest. The analysis of interelectrode plasma shows that microdischarge is highly non-isothermal and increasing of interelectrode distance leads to the increasing of rotational temperature.

References

1. S. Ghosh et al., J. Vac. Sci. Technol. A 33, 021312 (2015)
2. C. Oliveira et al., American Journal of Condensed Matter Physics, 4(3A): 19-27 (2014)
3. M. S. Oliveira, Jr, et al., Surface Eng. 26 N 7 519-524 (2010)

TOPIC 6: DEPOLLUTION AND ENVIRONMENTAL APPLICATIONS

NOx REMOVAL WITH DIELECTRIC BARRIER DISCHARGE AND WET ABSORPTION

M. S. Kang, J. Hwang

Department of Mechanical Engineering, Yonsei University, South Korea

E-mail: mskang90@yonsei.ac.kr

An experimental study of NOx removal with dielectric barrier discharge and wet absorption was performed. NO has low solubility to water while NO_2 has relatively high solubility to water. Generally, more than 90% of NOx is emitted with the form of NO. In this study, NO was oxidized to NO_2 by reacting with O_3 generated from a lab scale dielectric barrier discharge reactor. Then NO_2 was absorbed by a wet absorber. For the absorbant, 0.5 M NaOH solution was used. Maximum NOx removal efficiency was 85%.

Keywords: non-thermal plasma; DBD; NOx removal; ozonization; wet absorption

1   Introduction

NOx is considered as major air pollutant from combustion or waste incineration process. In military troops of South Korea, a large quantity of propellant has been waste due to the expiration of missiles or the rejection of propellant during manufacturing. For this, the South Korea has a plan to construct an incineration facility for expired propellant. As propellants contain large amount of nitrogen, they produce large amount of NOx during their combustion. Therefore, NOx removal process is important in incineration of waste propellant.

Selective catalytic reduction (SCR), and selective non-catalytic reduction (SNCR) are widely used in plant scale NOx removal process. However, these methods require certain temperature to reduce NOx which leads to operation cost rise. On the other hand, wet absorption method is relatively free from these constraints. In addition, wet absorption can remove NOx, SOx and particulate matter simultaneously. Wet absorption method uses aqueous absorbant like Urea(aq)[1,2], NaOH(aq)[3-5] to absorb NOx in the solution. Therefore, solubility to water is an important factor to reduction efficiency of wet absorption. NOx consists of NO and NO_2. NO_2 has high solubility to water. However, NO has relatively low solubility to water. Generally, more than 90% of NOx is emitted with the form of NO. Therefore, to achieve high removal efficiency by wet absorption, additional treatment is required which converts NO to NO_2 before the wet absorption process. For this, strong oxidizing additives like $NaClO_2$ [1-3, 5-7], $KMnO_4$[1], NaClO[1] and H_2O_2[1, 8] are widely used with absorbant in wet absorption process. However, some of these oxidizing additives have toxicity and their leakage can cause new environmental problem.

Therefore, several studies have been conducted on two stage NOx removal process using O_3 as NO oxidizer, and wet absorber as NOx remover. Sun et al. [9] investigated the simultaneous absorption of NOx and SO_2 from flue gas with pyrolusite slurry combined with gas-phase oxidation of NO using ozone. They used ozone injection to convert NO to NO2.

They achieved 75 % NOx removal efficiency. Wu et al. [10] conducted study of a photocatalytic oxidation and wet absorption combined process for removal of nitrogen oxides. They achieved 72.6 % NOx removal efficiency by applying photocatalytic oxidation process
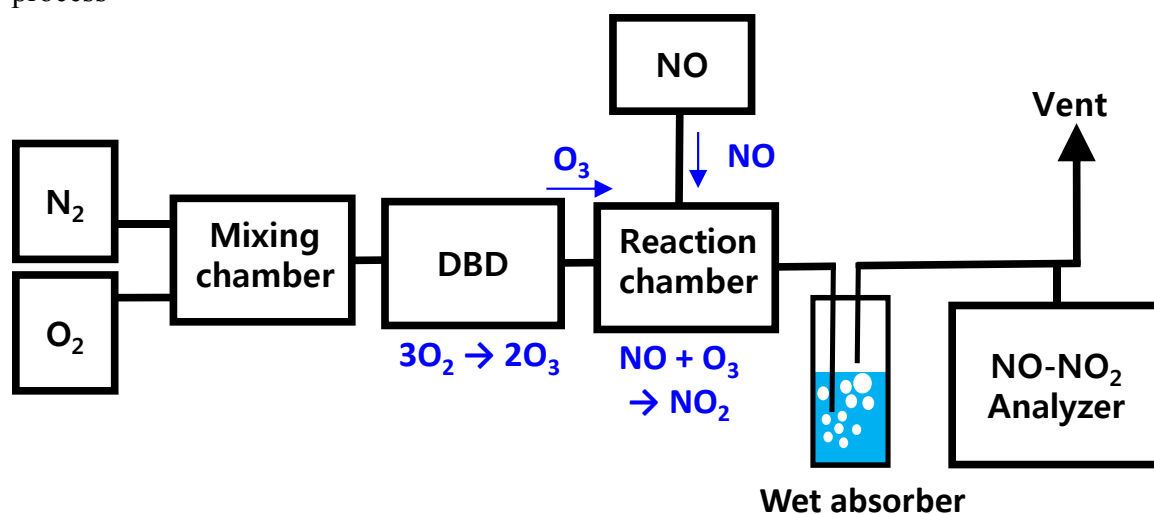
Fig. 1 Experimental setup of wet absorption process.

with the wet absorption. Mok et al. [11] investigated the removal of sulfur dioxides by using ozone injection and absorption reduction technique. They converted NO to NO_2 by injecting ozone produced by dielectric barrier discharge (DBD) reactor. They achieved 95% NOx removal efficiency.

In this study, experiment on NO removal with DBD reactor and wet absorption was conducted. DBD reactor produced O_3 to oxidize NO to NO_2 and NO_2 was removed in wet absorber using 0.5 M NaOH absorbant. At the applied power of 0.01 kW – 0.04 kW, NO oxidation efficiency and NOx removal efficiency were tested.

2   Experimental

Schematic of the experimental setup is shown in Fig. 1. The setup consists of DBD reactor, high voltage AC power supply, gas feeding system, and gas measurement system. 25 mm diameter, 150 mm length packed-bed type DBD reactor was used in this study. 5 mm diameter copper electrode was used as inner electrode, SUS mesh was used as outer electrode. Inside of the outer SUS mesh, quartz tube was used as dielectric barrier and 3mm diameter quartz beads were packed in the quartz tube. The experiment was performed using high-voltage AC power supply (KSC Korea Switching, Korea) which can provide 0 ~ 40 kV peak voltage sine wave AC power having 60 Hz ~ 1 kHz frequency. A 100 MHz digital oscilloscope (TDS 1012, Tektronix, USA), and current probe (i1000s AC Current clamp, Fluke, USA) were used to measure the voltage and current. Gas feeding system consisted of NO (1000ppm balanced with N_2), N_2 (99.99%), and O_2 (99.99%) supply, flow meter (MFC), and mixing chamber. Chemiluminescence gas analyzer (9110EH, Teledyne, USA) was used to measure NO and NO_2 concentration.

N$_2$ and O$_2$ entered the mixing chamber and DBD reactor. In the DBD reactor, O$_3$ was generated by decomposing oxygen. Then at the reaction chamber, NO and O$_3$ was mixed and NO was oxidized to NO$_2$ by reacting with O$_3$. NO$_2$ was removed by wet absorber using wet absorbant (0.5M NaOH). NOx concentration of the outlet was measured by the NO-NO$_2$ analyzer. Total gas flow rate was set to 3 LPM. Initial NO and O$_2$ concentrations were set to 330 ppm and 10%, respectively. For the frequency of 0.5 kHz, and the power of 0.01 kW - 0.04 kW, the applied power versus NO oxidation efficiency and NOx removal efficiency were compared.

(a) NO oxidation efficiency   (b) NOx removal efficiency
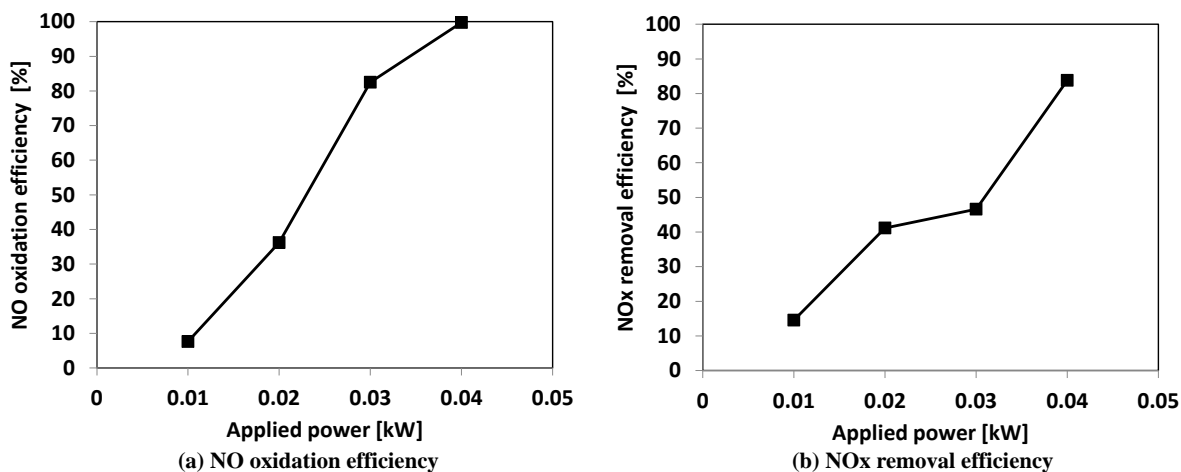
Fig. 2 NO oxidation efficiency and NOx removal efficiency versus applied power

3   Results and Discussion

Fig. 2 shows NO oxidation efficiency and NOx removal efficiency vs applied power. As shown in Fig. 2 (a), NO oxidation efficiency increased by increasing applied power. NO oxidation efficiency was calculated by measuring NO-NO$_2$ concentration at the outlet of the reaction chamber. Maximum 99% NO oxidation efficiency was achieved when the applied power was 0.04 kW. When NO passes reaction chamber, NO is oxidized to NO$_2$ by reaction (1).

$$NO + O_3 \rightarrow NO_2 + O_2 \tag{1}$$

As applied power to DBD reactor increased, O$_3$ concentration generated from DBD reactor also increased. Therefore, more NO was converted to NO$_2$. Maximum 99% NO oxidation efficiency was achieved when the applied power was 0.04 kW. NOx removal efficiency increased by increasing applied power. As applied power to DBD reactor increased, the portion of NO$_2$ in the gas increased. NO$_2$ has higher water solubility than NO. Therefore, as power increased, more NOx is removed by wet absorber. Maximum 85% NOx removal efficiency was achieved when the applied power was 0.04 kW.

4   Conclusions

Experimental study on NOx removal with DBD plasma and wet absorber was conducted. NO oxidation efficiency at the various power input (0.01 kW – 0.04 kW) was observed. NO oxidation efficiency increased as the power input increased. Maximum NO oxidation efficiency was 99%. NOx removal efficiency at the various power input (0.01 kW – 0.04 kW)

was observed. NOx removal efficiency increased as power input increased. Maximum NOx removal efficiency was 85%.

Acknowledgements

References

1. P. Fang et al., Chem. Eng. J. 168 (2011)
2. J. Wei et al., J. Ind. Eng. Chem. 15 (2009)
3. H. Chu et al., Water Air Soil Poll. 143 (2003)
4. E. Sada et al., Ind. Eng. Chem. Proc. DD. 18 (1979)
5. M. P. Jakubiak et al., Chem. Proc. Eng. 33 (2012)
6. T. Chien et al., J. Hazard. Mater. B80 (2000)
7. T. Chien et al., J. Environ. Eng-Asce. (2003)
8. E. Myers et al., Environ. Eng. Sci. 19 (2002)
9. W. Sun et al., J. Hazard. Mater. 192 (2011)
10. Z. Wu et al., Chem. Eng. J. 144 (2008)
11. Y. Mok et al., Fuel Process. Technol. 87 (2006)

CO₂-CONVERSION IN DIELECTRIC BARRIER DISCHARGES: INFLUENCE OF NITROGEN ADMIXTURE ON CHEMISTRY AND DISCHARGE PHYSICS

M. Schiorlin, A. Sarani, R. Klink, R. Brandenburg

Leibniz Institute for Plasma Science and Technology (INP), Greifswald, Germany

E-mail: brandenburg@inp-greifswald.de

Plasma assisted carbon capture utilization by using of excess energy from renewable sources is an approach to reduce CO_2 emission and conserve electrical energy as chemicals. This paper reports about the effect of the admixture of nitrogen to CO_2 in different Dielectric Barrier Discharge (DBD) configurations. The effect of admixture on the conversion of CO_2 to CO was systematically investigated in a coplanar DBD at atmospheric pressure. The energetic yield of CO generation resulted in values up to 60 g/kWh, where the highest energy yield was achieved in a gas mixture CO_2/N_2=30/70 and not in pure CO_2. In order to correlate these results with the discharge physics the spatio-temporal resolved development of single filaments in different CO_2/N_2 gas mixtures and corresponding discharge current pulses were investigated in a single filament volume DBD. The results show an optimized energy input into single filaments for gas compositions with 10 to 30 % CO_2 and a significant quenching of the luminosity by CO_2 molecules.

Keywords: carbon dioxide conversion; carbon capture usage; nonthermal plasma; dielectric barrier discharge; Time-Correlated Single Photon Counting

1 Introduction

Global warming is one of the most important issues for the 21st century and – besides the improvement of efficiency of energy consumption – technologies for the abatement of greenhouse gases are needed [1]. Plasma assisted carbon capture utilization by using of excess energy from renewable sources is an approach to reduce CO_2 emission and conserve electrical energy as chemicals [2]. Different approaches on CO_2 reforming by means of plasmas, also combined with catalyst have already been studied [3] and the progressive use of renewable energies can be seen as a cheap source of energy for plasma operation, in particular when temporary energy surpluses are obtained. This contribution reports about two connected activities studying the effect of nitrogen admixture to CO_2 in a non-thermal plasma at atmospheric pressure. In many off-gases CO_2 is mixed with other compounds, in particular nitrogen is present (e.g. combustion processes). The chemical processes were studied in a coplanar Dielectric Barrier Discharge (DBD). This discharge type offers compact design and good scalability. To study the discharge physics in the mentioned gas mixtures the single DBD arrangement as describe e.g. in [4] was used.

2 Experimental

The coplanar DBD consist of a dielectric plate in which both electrodes are embedded [5]. In detail it is a rectangular ceramic base body made of a mixture of silicon and aluminum oxide (125 x 35 x 2.4 mm). Two copper electrodes are comb-shaped interleaved at intervals of 0.5 mm next to each other on the base body. The electrodes are covered by the same material

as the body material. As seen in Figure 1 a, at the two ends of the ceramic base plate, the electrodes are not covered by dielectric for its contacting to the high-voltage power supply. Since both electrodes are covered with a dielectric, erosion and oxidation processes at the metal electrodes can be excluded. The coplanar DBD electrode arrangement was mounted in a gas-tight housing and flushed with gas mixtures containing CO_2 and N_2. The effluent gas was analyzed with an FT-IR, an oxygen sensor and an ozone monitor for quantitative analysis. High voltage and charge where measured via high voltage probe and measuring capacitor respectively and recorded with digital storage oscilloscope. The injected discharge energy per AC cycle and the discharge power were determined by charge-voltage-plots. To vary the discharge power the frequency was varied while the voltage was kept constant at 17 kV_{pp}. Details can be found in [6].
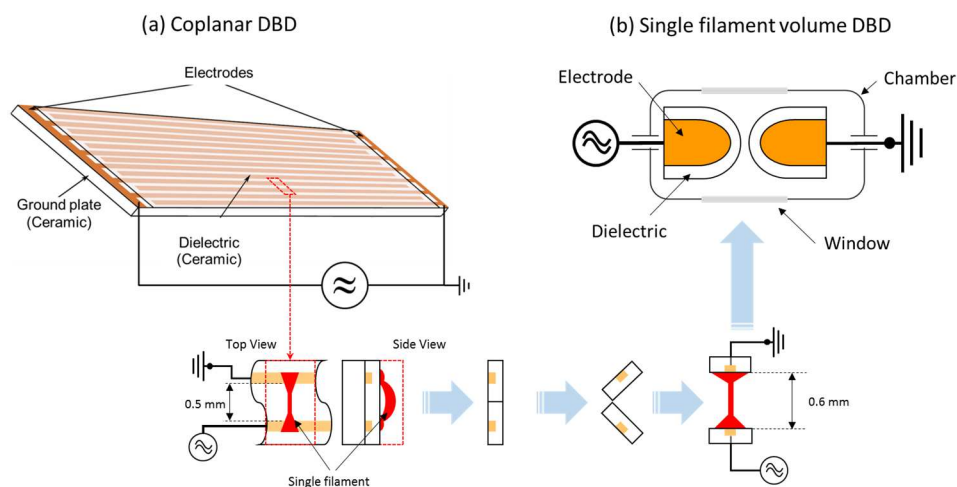
Fig. 1: Scheme of the discharge arrangement: (a) coplanar DBD and (b) single filament DBD. Bottom part visualizes the common aspects between both discharge types.

To study the discharge development in a well-localized repetitive filament, a similar DBD arrangement as described in [4] (see figure 1 b) with a discharge gap of 0.6 mm was used. It is a symmetric single filament DBD operated by sinusoidal voltage with frequency of 7.3 kHz, and voltage peak to peak amplitude in the range of 13-14 kV. The voltage amplitude was adjusted in order to generate only one single filament per every half period of the applied voltage. This value depends on the actual gas composition. For this experiments the CO_2 content in N_2 was varied in the range 1 % to 75 %. The geometry and electric field configuration of both discharge arrangements are very different (see lower part of figure 1 and [7]), but both electrodes are dielectrically covered and the lengths of the filaments are comparable. It is not the aim to compare the two different DBD arrangements but to learn about the discharge behavior in gas mixtures of CO_2 and N_2. Therefore, the filament evolution was measured by means of time-correlated single photon counting [8] with the set-up described in [9].

3   Results and Discussion

Figure 2 shows the production of CO and the corresponding energy yield (EY) as a function of the specific input energy (SIE) for the coplanar DBD. The CO concentration increased with

SIE for all gas mixtures being investigated. At the same SIE, changing the CO_2 concentration in N_2 from 10% to 30% resulted in the maximum CO production (Figure 2, left). The concentration of CO was similar for CO_2 concentrations between 30% and 50%. In pure CO_2 the lowest amount of CO was obtained. Beside CO oxygen and ozone were identified as products of the plasma chemistry. No N_xO_y or other products were registered by FT-IR analysis. Figure 2, right reports the value of energy yield as a function of SIE. The EY decreases with SIE. At the same value of SIE, changing the CO_2 concentration in N_2 from 10% to 30% results in higher EY, but EY is decreasing for CO_2 concentrations between 30% and 50%. In pure CO_2 the lowest EY is obtained. Additionally, an effect on the flowrate was obtained at the lowest CO_2 fraction of 10% and the highest value of EY which is attributed to the gas retention time in the reactor.
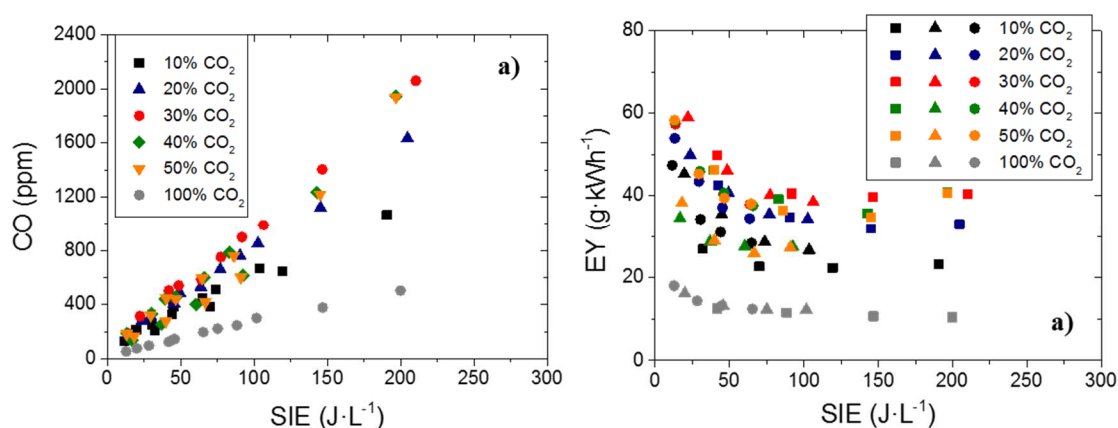
Fig. 2: Chemical conversion of CO_2 into CO in coplanar DBD. Left: CO generation as a function of specific input energy SIE (discharge power divided by gas flow), right: EY of CO generation in different gas mixtures.

The energy efficiency of CO_2 dissociation by means of coplanar DBD can be improved by admixing nitrogen. The energy efficiency evaluated through EY results in values up to 60 g/kWh, where the highest value is achieved with 30% CO_2. At a fixed value of CO_2 concentration, the highest energy efficiency is achieved at the lowest SIE and conversion rate, while the highest conversion rate is achieved at highest SIE and lowest energy efficiency as reported also by other works, e.g. [10, 11].
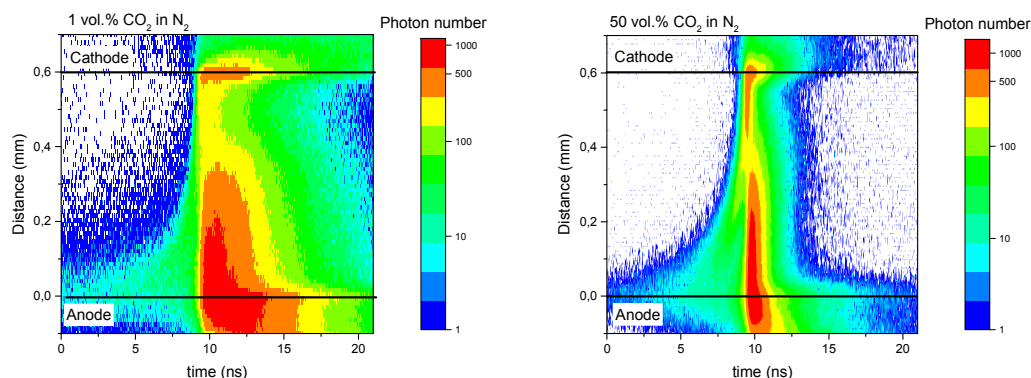
Fig. 3: Spatio-temporal distributions of filament luminosity (337 nm) for 1 and 50 % CO_2 in N_2 (approximate positions of electrodes shown by lines).

Results of the electrical characterization of the single filament volume DBDs showed a filamentary character for all gas compositions being investigated. The spatio-temporal distribution of the single DBD luminosity for the spectral band of the second positive system of molecular nitrogen (wavelength 337 nm, i.e. 0-0 transition) is shown in figure 3 for two different gas compositions. In both gas mixtures the overall discharge development is similar as in air: (i) weak pre-phase at the anode, (ii) propagation of a cathode directed ionization front (positive streamer), (iii) bulk plasma in front of the anode [7, 8]. The velocity of the streamer is in the same range as in N_2/O_2 gas mixtures, namely 10^6 m/s. Higher admixture of CO_2 in N_2 results in a shorter duration of luminosity but not in a principal change of the overall discharge development. This can be attributed to quenching of excited states by CO_2 molecules as well as electron attachment on electronegative CO_2. Both aspects have to be analyzed in context with electrical analysis of filaments. Furthermore, other spectral lines have to be investigated and the energy input in single filaments for the different gas compositions has to be determined.

4   Conclusion

The admixture of N_2 to CO_2 in a DBD reactor has significant effects on the plasma chemistry and the discharge physics. Changing the CO_2 concentration in N_2 from 10% to 30% resulted in the maximum CO production as well as the highest energy yield for CO (up to 60 g/kWh). The lowest amount of CO and lowest energy yield was generated in pure CO_2.

The investigation of single filament volume DBDs shows that the breakdown and development of filaments is similar as in O_2/N_2 DBDs. An increase of CO_2 to nitrogen leads to shorter discharge pulses which can be caused by electron attachment and collisional quenching of the excited state.

References

1. M. L. Parry et al., Climate Change 2007: Impacts, Adaptation and Vulnerability. (Cambridge University Press, Cambridge, 2007)
2. A. P. H. Goede et al., EPJ Web of Conferences 79, 01005 (2014)
3. M. Kraus et al., Phys. Chem. Chem. Phys. 3, 294 (2001)
4. T. Hoder et al., J. Phys. D: Appl. Phys. 43, 124009 (2010)
5. M. Šimor et al., Appl. Phys. Lett. 81, 2716 (2002)
6. M. Schiorlin et al., submitted to Eur. J. Appl. Phys. (2016)
7. T. Hoder et al., Contrib. Plas. Phys. 49, 381-387 (2009)
8. K. V. Kozlov et al., J. Phys. D: Appl. Phys. 34, 3164 (2001)
9. R. Brandenburg et al., In *Proceedings of the 22nd International Symposium on Plasma Chemistry*, Antwerp, 2015, edited by A. Bogaerts and R. van de Sanden
10. G. Zheng et al., Plasma Chem. Plasma Process. 23, 59 (2003)
11. F. Brehmer et al., J. Appl. Phys. 116, 123303 (2014)

CONVERSION OF TAR IN COUPLED PLASMA-CATALYTIC SYSTEM

M. Młotek, B. Ulejczyk, J. Woroszył, I. Walerczak, K. Krawczyk
^{1}*Warsaw University of Technology, 3 Noakowskiego Street, 00-664 Warsaw, Poland*

E-mail: mmlotek@ch.pw.edu.pl

In plasma of gliding discharge coupled with a catalyst, a high toluene conversion may be obtained. The study was carried out at atmospheric pressure, in a gas composition such as obtained during pyrolysis of biomass. When applying a reactor with RANG 19PR catalyst and a CO (0.13), CO_2 (0.12), H_2 (0.25), N_2 (0.5) and 3100 ppm of toluene flow rate was 1000 Nm^3/h conversion of toluene was higher than 80%. In coupled plasma-catalytic system the methanation of carbon oxides was observed.

Keywords: nonequilibrium plasma; tars decomposition; gliding discharge; plasma catalytic system

1   Introduction

Pyrolysis and gasification are now rapidly developing technologies for efficiently harvesting the energy contained in biomass. Biomass is currently considered the most promising source of renewable energy. The two most common processes applied in conversion of chemical energy contained in biomass into useful energy are pyrolysis or gasification [1]. As a result of these processes gaseous fuel is formed, which can be used to drive engines and turbines. However, there are restrictions to the applicability of the obtained gas. The gaseous fuel derived from the dry processes cannot be directly used in turbines, which require a concentration of tars below 0.05 g/m^3. Therefore, before using pyrolysis gas, it needs to be subjected to purification, which removes tars and VOCs.

There are many technologies used for the purification of pyrolysis gas from volatile organic compounds and tars. The following methods can be distinguished: catalytic oxidation, filtration and biofiltration, adsorption on activated carbon, electrostatic precipitation, and plasma techniques [1]. One method of purifying gas after pyrolysis is plasma techniques, including the gliding discharge. The aim of the study was to investigate the possibility of decomposition of toluene in the plasma and in a coupled plasma-catalytic system, as well as to determine the change in gas composition during the process.

2   Experimental

Toluene is used as a tar model compound. The conversion of toluene was investigated in three-phase gliding discharge reactor (Fig. 1) at normal pressure. The reactor is made of a quartz–glass tube of 60 mm in diameter and contained three converging duralumin electrodes. The gas inlet is located at the bottom, between the electrodes. The applied power supply consists of ferroresonant transformers energized from transistor inverter allows for design of poly–phase multi–electrode reactor systems. The electric power supplied to the gliding reactor was in the range of 1–2 kW and it was measured by an energy meter.

For the experiments NiO/Al_2O_3 (RANG 19PR industrial catalyst for methanation of carbon oxides) was used. During the selection of catalysts, the results of our previous studies and data from literature concerning the problem of conversion of toluene were taken into account. To obtain catalyst particles suitable for research in the above mentioned reactor, the industrial

catalyst with a diameter of 5 mm was crushed and the collected fraction 1.6 - 3.15 mm was used.

The gas temperature measured at the vessel axis over the upper ends of the electrodes reached 270–500°C, depending on the discharge power and presence of catalyst. The process of toluene decomposition was tested for gas flow rate 1000 Nl/h. Tests in homogeneous system were conducted in a wide range of initial concentrations of toluene 2000-4300 ppm. The initial concentration of 3100 ppm toluene was chosen for further studies with the coupled plasma-catalyst system.
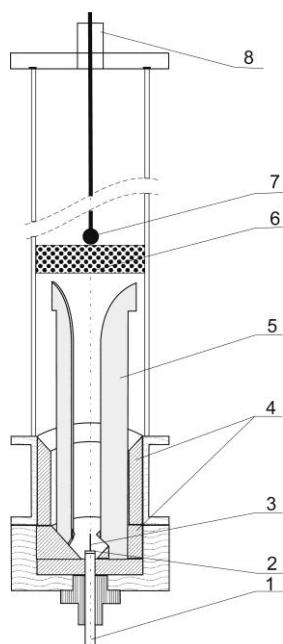
Fig. 1. Three – phase gliding discharge reactor. 1 – gas inlet, 2 – gas nozzle, 3 – starting electrode, 4 – ceramic lining, 5 – electrode, 6 – bed of catalyst, 7 – thermocouple, 8 – gas outlet.

The gaseous products of reaction were analyzed by gas chromatography using Thermo-Scientific Trace 1300 with HP5 column and an FID detector. Inorganic products (CO_2 and CO) were analyzed by Agilent 6890N with a Shin carbon column and the following detectors: TCD and FID. Water vapor was determined by an APAR moisture meter.

Toluene conversion was calculated using the equation:
$$x[C_7H_8] = \frac{W_0[C_7H_8] - W[C_7H_8]}{W_0[C_7H_8]}$$

where: $x[C_7H_8]$ – overall conversion of toluene;
$W_0[C_7H_8]/mol*h^{-1}$, $W[C_7H_8]/mol*h^{-1}$– toluene flow rate at the inlet and outlet respectively.

3   Results and Discussion

The measurements of toluene decomposition were performed in a homogeneous and a plasma-catalytic system. In the plasma-catalytic system a fixed bed of the nickel catalyst, RANG 19PR, was used. The study was carried out using a gas stream with the initial composition of 0.13 CO_2, 0.12 CO, 0.25 H_2, 0.5 N_2 and containing 2000-4300 ppm toluene. The following products of the reaction were detected: CO_2, CO, H_2, CH_4, C2-C3 hydrocarbons, H_2O and trace amounts of C4 hydrocarbons.

In gliding discharge reactor the effect of power and the initial concentration of toluene in the inlet stream on the conversion were studied. The highest conversion, i.e. 68%, was achieved

at the lowest initial concentration of toluene (2000 ppm) On the basis of the obtained results it was found that the conversion decreases with the increase of initial concentration of toluene in the inlet stream and increases with increasing power of the gliding discharge (Fig. 2). It was observed that in the coupled plasma-catalytic system the amount of carbon oxide and hydrogen decreased, but methane was detected in the outlet gas mixture. In the plasma-catalytic system significant quantities of methane as a result of the methanation of carbon oxides were observed in the outlet gas stream (Fig 4).
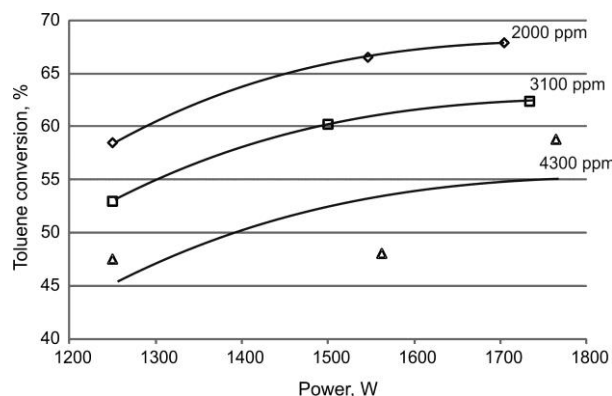
Fig. 2. Effect of power on toluene conversion in homogeneous system. The initial concentration of toluene 2000, 3100 and 4300 ppm.
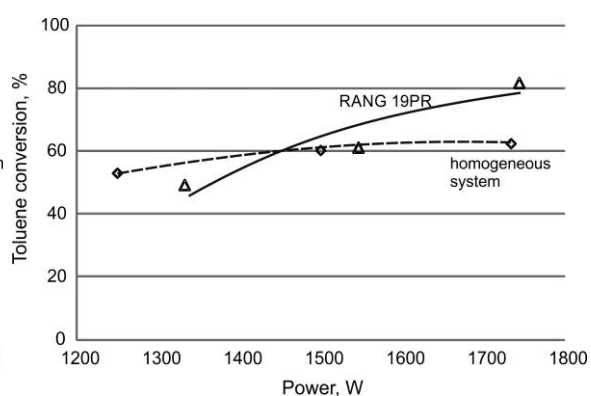
Fig. 3. Effect of power on toluene conversion. 3100 ppm of toluene. Gas flow rate 1000 Nl/h. $\diamond$ - homogeneous system, $\triangle$ - RANG 19PR (commercial catalyst).
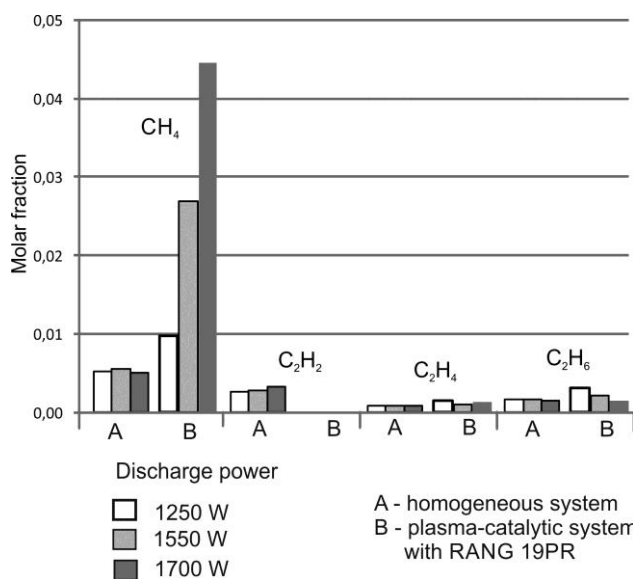
Fig. 4. Molar fractions of methane and C2-C4 hydrocarbons in the outlet stream after a plasma-catalytic process of toluene decomposition in a simulated post-pyrolysis stream.

4   Conclusion

On the basis of study and observation it has been found that the gliding discharge is an effective technique for decomposition of toluene in the pyrolysis gases with low toluene concentrations.

In plasma-catalytic system with RANG-19PR (industrial catalyst for methanation of carbon oxides) a higher toluene conversion was obtained than that in the homogeneous system. A small amount of hydrocarbons C2 - C4 was also observed. The presence of NiO/Al_2O_3

(RANG19PR) in the plasma zone increased the conversion of toluene and mathanation of carbon oxides. The maximum conversion of toluene was 89%.

Acknowledgment

References
1. A. V. Brigwater, Biomas Bioenergy 38, 68 (2012)

GLIDING DISCHARGE REACTOR FOR CONVERSION OF STABLE CHEMICAL COMPOUNDS

M. Młotek, J. Woroszył, I. Walerczak, B. Ulejczyk, K. Krawczyk
Warsaw University of Technology, 3 Noakowskiego Street, 00-664 Warsaw, Poland

E-mail: mmlotek@ch.pw.edu.pl

The experimental results showed that a higher toluene conversion may be obtained in a new type of gliding discharge reactor. The study was carried out in air at atmospheric pressure in a reactor with 6 electrodes and a flow rate in the range 4.5-6 Nm^3/h of air containing 180-2600 ppm of toluene. Under these conditions a conversion of approx. 50% was achieved for small specific energy of about 7700 kJ/mol.

Keywords: nonequilibrium plasma; gliding discharge; plasma catalytic system

1   Introduction

A serious problem, which significantly limits the application of the gasification process for the production of electricity, is the presence of tars (higher hydrocarbons) in the gas, which contaminate the surfaces of internal combustion engines or gas turbines. Toluene is typically one of the most important aromatic volatile organic compounds (VOCs) [1].

Over the last decade non-thermal plasma has been used as a new method of conversion of very stable chemical substances [2]. The efficacy of the reaction in non-equilibrium plasma depends on the power supply, electron energy, gas flow rate and concentration of compounds. The shape of the discharge space and the residence time have a large impact on the process.

Processes in non-equilibrium gliding discharge plasma are mainly studied in reactors with high-voltage electrodes that are located in tube-shaped or in vertical, conical chambers which widen upwards. Another solution are reactors, in which the central electrode has a conical shape and is placed in a metal tube that acts as the second electrode and reactors, in which a central conical electrode is used and the flow of the plasma is shaped by an external magnetic field (swirling motion). There are also other known solutions, in which a rotating central electrode [3] is implemented to cause movement of the plasma in the space between the electrodes. In addition, in gliding discharge reactors the gas can, regardless of the movement along the channel, move in a spiral motion in the reaction chamber. Moreover, "tornado" type reactors and those with at least two spiral electrodes of variable diameter increasing along the wall of the reactor, are currently used [4].

In the above mentioned reactors cannot operate with large gas streams, because a part of the stream may bypass the reaction zone. This does not allow their implementation on a pilot- or technical scale. In other words, their biggest drawback is that they cannot be up-scaled. Moreover, high power cannot be applied because it can cause an electric breakdown once the breakdown voltage is reached. In contrast, it is possible to use high power discharge in the reactor presented in this work and the chemical processes can easily be performed on a larger scale.

The purpose of this work was to study the effect of the gas flow rate and specific energy on the conversion of toluene as a model aromatic volatile organic compound. The following

paragraphs present the design of the reactor and some results of studies on the kinetics of toluene conversion in a large-scale gliding discharge reactor.

2   Experimental

In this study a new design of a discharge reactor (Fig. 1) was used. Steel electrodes arranged in the grooves of a ceramic tube are connected to a source of high voltage. The intake system was closed from the bottom with a ceramic part (1), which is resistant to high temperatures and allows the attachment of the central electrode (4), as well as prevents an uncontrolled electrical breakdown between the central electrode and the housing of the reactor.

The gas stream was fed (7) tangentially to the outer wall so that the gas was not introduced directly at the central electrode and swept the inner wall of the ceramic pipe (2) with high voltage electrodes (3), which significantly improved the hydrodynamics of the gas flow through the reactor. The edge of the center electrode and the tapered edge of the inner wall of the reactor forms an angle of 2.5°. The swirling motion of the gas stream facilitates access of reagents to the discharge channel, which begins in the space between the electrodes, thereby increasing the yield of chemical reactions under the influence of the gliding discharge. The rotating plasma reactor is powered by three high-voltage transformers. The frequency of voltage change was 40 Hz.
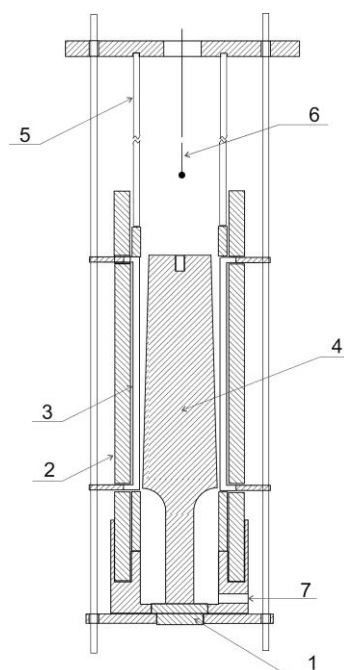
Fig. 1. Reactor for toluene decomposition. 1 – ceramic fitting, 2 – ceramic pipe, 3 – electrode, 4 – central electrode, 5 – quartz tube, 6 – thermocouple, 7 – gas inlet.

Fig. 2. A gliding discharge reactor equipped with six high voltage electrodes.

For the toluene conversion studies, the gas components were determined by two chromatographs: Chrompack CP-9001 with an HP-5 column and Flame Ionized Detector for analysis of hydrocarbon content (up to C7) and Chrompack CP-9002 with Carboplot P7 column and a Thermal Conductivity Detector for H_2, CO and CO_2 content analysis.

2.1 Parameters and definitions:

The toluene concentration in the inlet gas was calculated with mass flow rate of toluene.

$W_0[C_7H_8]$, $W[C_7H_8]$ — toluene flow rate at the inlet or outlet, respectively [mol/h],

Overall toluene conversion

$$X_{C_7H_8} = \frac{W_{0[C_7H_8]} - W_{[C_7H_8]}}{W_{0[C_7H_8]}}$$

Specific energy

$$E_V = \frac{P \cdot 3600}{W_{0[C_7H_8]} \cdot 1000}$$

P – power [W]

3 Results and Discussion

Measurements were conducted for three gas flow rates: 4.5 Nm^3/h, 5 Nm^3/h and 6 Nm^3/h, and toluene concentration in the range 180-2600 ppm. The discharge power was constant (1100-1200 W). The main products of toluene conversion were carbon dioxide and water. Traces of C2-C4 and methane have been observed.

Based on the obtained results it was concluded that the highest conversion of toluene was noted for the flow of carrier gas of 4.5 Nm^3/h. The toluene conversion decreases with the increase of the air flow rate (Fig. 3). The smallest toluene conversion was obtained with the highest carrier gas flow rate, i.e. 6 Nm^3/h. This is due to a shorter residence time of the
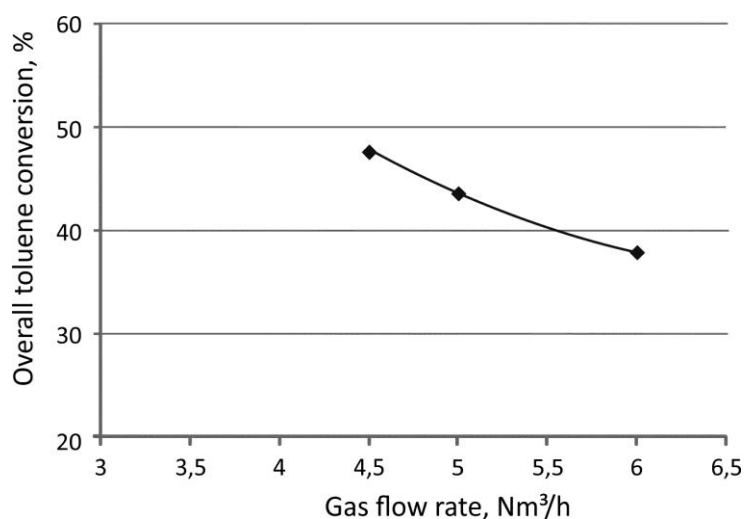
Fig. 3. Effect of gas flow rate on toluene conversion; discharge power 1150 W, 1260 ppm of toluene.
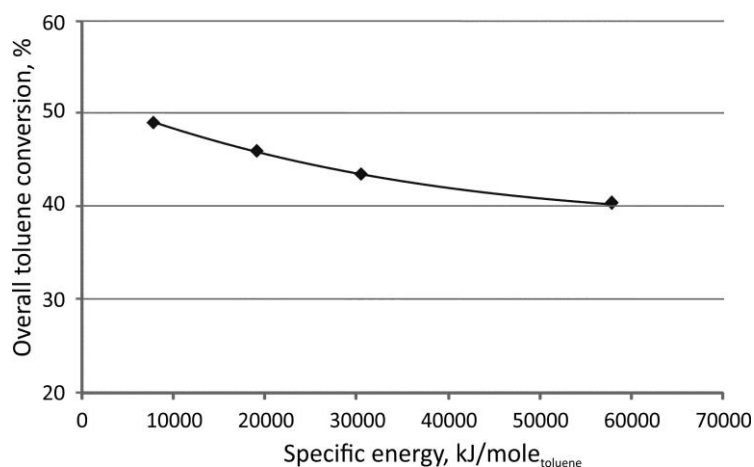
Fig. 4. Effect of the specific energy on toluene conversion; discharge power ~ 1100 W, gas flow rate 4.5 Nm^3/h.

The decrease of the toluene conversion with increasing of the specific energy was observed (Fig. 4).The highest conversion of toluene was 50% for a specific energy of 7700 kJ/mol. An

increase of the toluene conversion with increasing concentration of toluene in the inlet stream was observed. This phenomenon was caused by the increase of the temperature in the discharge zone as a result of the progress of an exothermic reaction, i.e. toluene oxidation.

It should be noted that with the increase of the initial concentration of toluene the temperature of the outlet gases increases. For a gas flow rate of 6 Nm^3/h and initial concentration about 180 ppm it was 140°C, whereas for the initial concentration of 2000 ppm it was 170°C. The highest temperature, i.e. 245°C was obtained when the gas flow rate of 4.5 Nm^3/h and an initial toluene concentration 2600 ppm were used.

4   Conclusion

The studies of toluene conversion in a reactor with a novel design have shown that in this system the toluene conversion may be 50% for a specific energy of 7700 kJ/mol. The new reactor contains a set of 6 wire electrodes and can be used to decompose toluene. The new design of the reaction space in which the power density is much higher is a new solution, which allows for considerably lower power consumption in the gliding discharge.

References:
1. A. M. Vandenbroucke et al., J. Hazard. Mater. 195, 30-54 (2011)
2. K. Schmidt-Szałowski et al., Chem. Eng. Res. Des. 89, 2643-2651 (2011)
3. E. Hnatiuc et al., *In Contributed papers of XIV-th Symposium on Physics of Switching Arc*, Brno, Czech Republic, 2001, p. 58
4. C. S. Kalra et al., Rev. Sci. Instrum. 76, 025110 (2005)

TOPIC 7: SURFACE PROCESSING AND TECHNOLOGY

Ar-H2 PLASMA SURFACE TREATMENTS OF SILICON WAFERS AT ATMOSPHERIC PRESSURE

B. Hergelová[1,2], M. Eichler[1], K. Nagel[1], C.-P. Klages[1]

[1] *Fraunhofer IST, Braunschweig, Germany*

[2] *Faculty of Mathematics, Physics and Informatics, Comenius University, Bratislava, Slovakia*

E-mail: beata.hergelova@ist.fraunhofer.de

We investigated the effects of exposing silicon wafer surfaces to direct or afterglow Ar-H2 plasmas of atmospheric-pressure volume dielectric barrier discharges. Direct plasma treatment introduced Si-H but also Si-O functionalities, which were stable in time. Afterglow H atom treatment did not introduce Si-H functionalities, neither in combination with UV radiation from a separate Ar DBD source, but the UV radiation was able to oxidize the surface. Direct and also afterglow plasma treatment on the other hand removed the Si-H functionalities created be HF dipping, that means H atom recombination takes place leaving behind reactive radicals.

Keywords: silicon wafer; dielectric barrier discharge; direct and post-discharge treatment; hydrogen containing plasma; Si-H bond formation

1   Introduction

Functionalization of Si wafers is an important process for subsequent Si wafer processing. Hydrosilylation, where Si-H functional groups react with unsaturated carbon bonds [1], can be used for functionalization with amino groups, to be used for DNA attachment or surface metallization [2, 3]. Low-pressure RF hydrogen plasma treatment may help to clean Si wafers from organic contaminants and create Si-H or Si-OH functionalities for bonding [4].

In the present study we investigated the interaction of Si surfaces with direct and afterglow Ar-H2 DBDs at atmospheric pressure. In the plasma of an Ar-H2 DBD several reactive features are formed: H atoms, Ar metastables, excited states of H2, electrons, radiation and, from oxygen-bearing impurities (O_2 and H_2O), OH, O atoms, and excited oxygen species. On the other hand, behind the plasma zone in the afterglow region very reactive species will decay and only longer living species like H or O atoms, O_3, and H_2O and OH may be present for a few ms, depending on the composition of the gas phase. There are several proposed mechanisms for the chemical interaction of H_2 and H with SiO_x surfaces at higher temperature [5], and the interaction of Ar-H2 plasma was also already investigated in low pressure plasma with additional heating [6], but there is less knowledge about atmospheric pressure plasma created using dielectric barrier discharge (DBD) [7]. From our previous work we know that Si-H bonds can be formed in Ar-H2 DBD plasma, but the mechanism is not understood [8].

2   Experimental

As samples we used one-side polished p-type (100) Si wafers. Before the plasma treatment the Si wafers were pre-treated in several different ways: used as received; annealed 3 hours in an oven at 350 °C or dipped for 1 min in 1% HF and then rinsed with deionized water.

Two identical tunnel-like DBD reactors were used as plasma sources for direct and afterglow plasma treatment. For combined treatment by Ar DBD UV emission and Ar-H$_2$ afterglow treatment they were connected as shown in Fig. 1. The distance between electrodes was 3 mm. On both electrodes there was 1 mm borosilicate glass and the gap for discharge propagation was 1 mm. The operating frequency in Ar-H$_2$ plasma was 36.7 kHz, peak-to-peak voltage varied between 10-15 kV and the power density between 10 and 20 Wcm^{-3}. The average gas speed in the horizontal DBD tunnel was 3 ms^{-1}. We used 4% of H$_2$ in Ar gas mixture (99.99%) or pure Ar treatment (99.999%).

To investigate the chemical structure, ATR-FTIR measurements were done on a Thermo Scientific Nicolet iS10, using a Ge ATR crystal at 42° incidence angle. Data were collected in the range 4000-650 cm^{-1}, with 64 scans at a resolution of 2 cm^{-1}. To qualitatively investigate the spectra we applied baseline correction and subtraction of reference sample spectra.

The silicon oxide layer thickness was estimated by means of spectroscopic ellipsometry (SE) using an SE850 (SENTECH Instruments) with SPECTRA RAY 3 software.
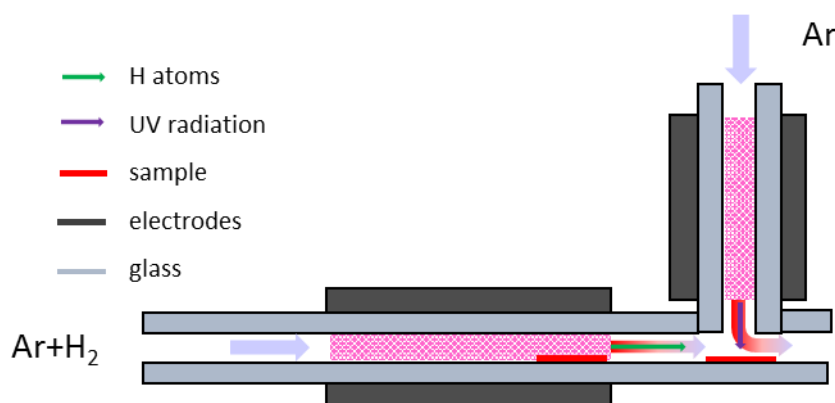
Fig. 1: Volume DBD plasma treatment arrangement of direct and afterglow plasma treatment (bottom DBD) with the possibility of simultaneous UV treatment from an Ar plasma (upper DBD).

3   Results and Discussion

First we investigated the development of functional groups on the as-received Si wafer surface with a native SiO$_x$ layer in direct plasma (Fig. 2 left). Already after 15 s a peak at 2250 cm^{-1} appeared, indicating the presence of H-SiO$_3$ moieties generated by H introduction into SiO$_x$. After longer treatment a broader Si-H peak was formed at 2100 cm^{-1}, tentatively deconvoluted to following functionalities: HSiSi$_3$ at 2090 cm^{-1}, H$_2$SiSi$_2$ at 2110 cm^{-1}, HSi(Si$_2$O) at 2130 cm^{-1}, HSi(SiO$_2$) at 2200 cm^{-1} and HSiO$_3$ at 2250 cm^{-1} [9, 10]. With (100) Si as a substrate, we do not expect to see H$_3$SiSi at 2140 cm^{-1}. Structure and intensity of the Si-H peaks remained stable for 1 month. It was possible to introduce Si-H functionalities also on Si wafers annealed in air for 3 h at 350 °C.

During direct plasma treatment we saw additional peak intensity of Si-O vibrations at 1240 cm^{-1}, indicating oxidation and change of the SiO$_x$ stoichiometry towards x = 2. Plasma-treated Si wafers could have oxidized after exposure of the active surface with created radicals to air before ex-situ FTIR and SE measurements. But because thicker oxide layers

were formed with longer treatment time, as we saw by SE measurement (Fig. 2 right), we may conclude, that oxidation took partially place already during plasma treatment - probably by residual humidity and/or oxygen present in the Ar-H_2 gas mixture.

To investigate, if Si-H bonds can be created within SiO_x by reaction with H atoms, we placed the leading edge of the Si sample 5 mm behind the active plasma into the postdischarge region, where H atoms are known to be still present at high gas flows. We saw no difference in an FTIR spectrum of a sample treated for 10 min. According to calculations of El-Sayed [11] interstitial H atoms should be able to break strained Si—O bonds in continuous amorphous silicon dioxide. Addition of two H atoms would create Si-OH and Si-H bonds. The lack of Si-H formation observed so far is possibly due to unsufficient access of H atoms to strained bonds expected to be present at the interface between silicon and its oxide.
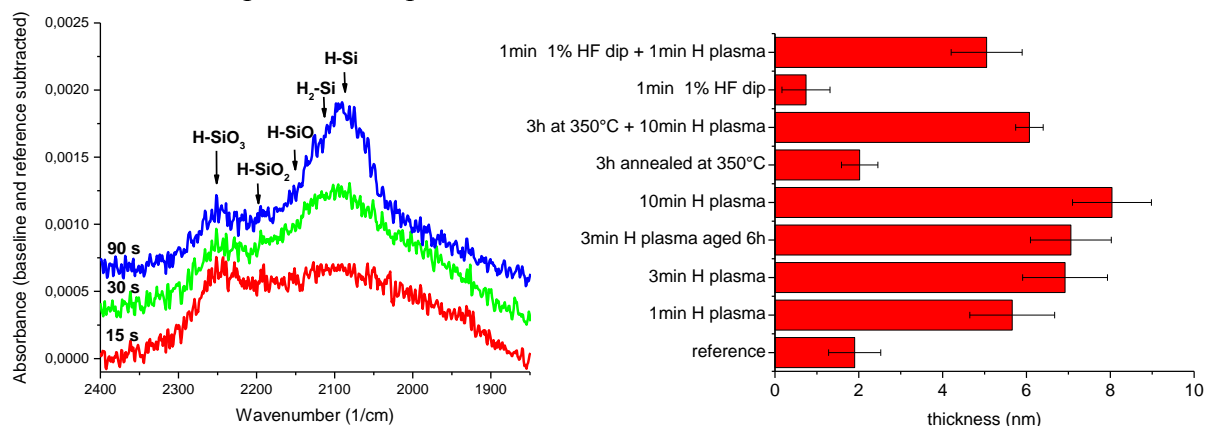
Fig. 2: Left - direct plasma treatment at 10 Wcm^{-3} 4% H_2 for different times, right – oxide thickness from ellipsometric measurements.

To know if the UV radiation irradiating SiO_x surfaces in contact with the direct DBD helps to react with H atoms, we used an additional on edge DBD reactor fed with nominally pure Ar. Over a width of 1-2 mm the sample was irradiated by UV emitted from this discharge. Again we saw no change in the Si-H peaks region. When we did separately first a UV treatment and then an H atom afterglow treatment the result was the same.
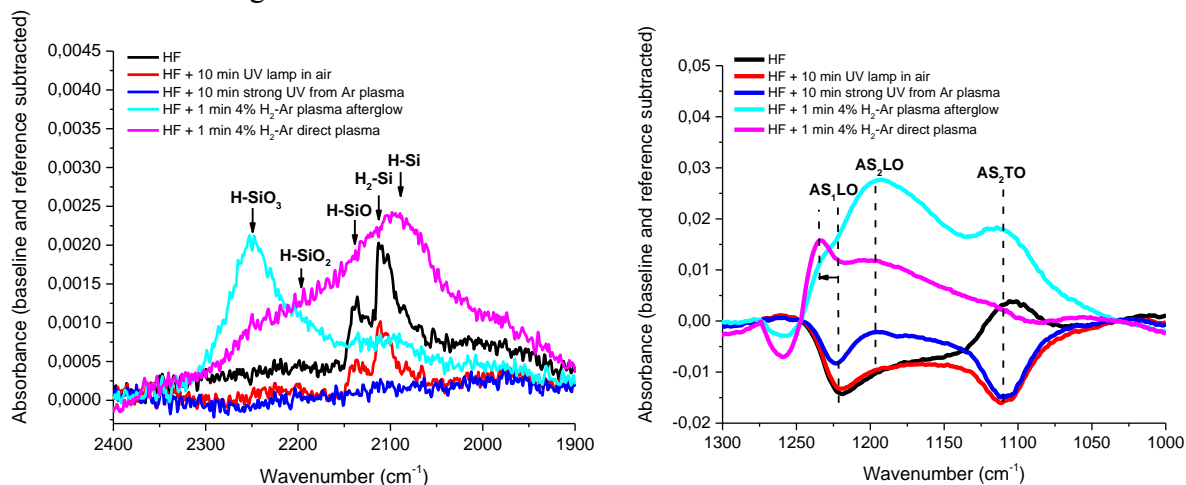
Fig. 3: Reference subtracted FTIR measurements of HF dipped Si wafer with additional post-treatment in UV, plasma afterglow and direct plasma: left – Si-H functional groups, right – Si-O functional groups.

In order to find out why we do not see Si-H bonds created in H atom afterglow even with simultaneous irradiation with UV light, we performed afterglow and/or UV treatment of HF-dipped Si wafer, where the surface is known to be terminated with Si-H bonds (Fig. 3). The UV radiation from an UV lamp (32 W radiation at 395 nm) in air for 10 min caused a decrease of the Si-H peak. But the UV radiation from Ar plasma side source, where the sample was placed in afterglow region as in Fig. 1., diminished it completely. This suggests that UV radiation probably dissociates Si-H bonds, leaving a reactive site behind, that could be later on oxidized, what we saw on FTIR measurement (Fig. 3 right). Afterglow treatment in an H atom stream from an Ar-H_2 DBD caused a decrease of peaks at 2090 and 2110 cm^{-1} and an increased peak at 2250 cm^{-1} that belongs to more oxidized Si in Si-H bond, but the Si-H bonds were still present. In direct plasma, that is a combination of H atom treatment, UV treatment but also contributions from other short-lived reactive species (electrons, ions, metastables, excited molecules), the peak at 2100 cm-1 become more intensive and broader, because some of Si-H bonds were partially transformed to more oxidized state.

4 Conclusion

During direct plasma treatment by an Ar-H_2 DBD plasma Si-H and Si-O groups were created on surfaces of as-received and also on annealed Si wafers, where a more stable thermal silicon oxide layer was present. The effect of UV from an Ar afterglow on already Si-H terminated surface obtained by an HF dip is that the hydrogen from Si-H bonds is completely removed and the surface is slightly more oxidized. The H atom afterglow treatment transferred the pure Si-H bonds to H-SiO$_x$ bonds introducing oxygen in proximity of Si, probably caused by a water impurity or water formed in discharge. The changes introduced by means of H plasma treatment sustained without changes in chemical composition, the plasma created Si-H and Si-O bonds were stable in time.

Acknowledgments

References
1. J. M. Buriak, Chem. Mater. 26, 763 (2014)
2. W. Cai et al., Biosens. Bioelectron. 19, 1013 (2004)
3. J. Borris et al., Plasma Process. Polym. 6, 258 (2009)
4. W. B. Choi et al., J. Korean Phys. Soc. 37, 878 (2000)
5. M. Green et al., Trans. Faraday Soc. 55, 2152 (1959)
6. H.-J. Tiller et al., Z. Chem. 14, 450 (1974)
7. Ch. Gerhard et al., Plasma Chem. Plasma Process. 33, 895 (2013)
8. M. Benedikt, Ph.D. thesis, Fraunhofer IST, Braunschweig, 2011
9. Y. Kato et al., Jpn. J. Appl. Phys. 27, L1406 (1988)
10. Y. J. Chabal, Fundamental aspects of silicon oxidation (Springer, Berlin, 2001)
11. A.-M. El-Sayed et al., Phys. Rev. Lett. 114, 115503 (2015)

A COMPARATIVE STUDY OF PTFE SURFACE TREATMENT USING LOW PRESSURE DISCHARGE (LPD) AND ATMOSPHERIC PRESSURE GLOW DISCHARGE (APGD)

M. Kogoma, K. Furuse, K. Takahashi, K. Tanaka

Department of Materials and Life Sciences, Faculty of Science and Technology, Sophia University

7-1 Kioi-cho, Chiyoda-ku, Tokyo, Japan

E-mail: m-kogoma@sophia.ac.jp

Advanced surface treatment of PTFE was studied in LPD and APGD systems. LPD treatment using NH_4-H_2O/He has shown a super hydrophilicity. On the other hand, APGD could not take any chemical effects with the same gas system. It seemed that the different results obtained in both plasmas are attributed whether the sputter induced chemical reaction is concerned or not in the plasma systems.

Keywords: PTFE; Surface treatment; LPD; APGD.

1 Introduction

Polytetrafluoroethylene (PTFE) is very useful material as an ultimate substance. However when we use in the industry, we perceive a need to refine the poor adhesion force and high water repellency on the surface. A large number of studies have been reported to increase the adhesion strength and hydrophilicity of the PTFE surface by low pressure discharge process (LPD) [1,2] but none of study attained the desired value to satisfy the request of industry. T. Moriuch and Ei Yamauchi [2] have discovered the better refinement of surface adhesion strength of PTFE with Ar sputtering system in LPD. In the case, the refinement of adhesion strength is not attributed to the increasing of the wettability but the increasing of the surface roughness. Because they found the sputter treated surface still keep -CF_2 bond which was measured by XPS. That means the surface wettability is hard to attain the super hydrophilicity by using the Ar-sputtering system. Therefore, at this moment, some chemical agents that contain metallic sodium are dominant for the surface treatment of the PTFE to improve the wettability and adhesion. However, this treatment needs a large amount of cleaning water and the disposal of much waste fluid. Moreover, their surfaces become blackish through the wet treatment. So a new dry process instead of the wet treatments has been desired. In 2010, APGD treatment with boron compounds was performed for defluorination of PTFE surface by M. Kogoma, K. Tanaka et al. [3]. Boron trifluoride (BF_3) is the gaseous fluorine compounds at room temperature and the bond enthalpy of fluorine with boron (757 kJ mol^{-1}) is much bigger than that of fluorine with hydrogen or carbon (570 or 552 kJ mol^{-1}) [4]. They have tried the defluorination by the combination of the diborane generation plasma system (DCDP) and the H_2/He plasma system to take the reaction between boron atom that produced by the dissociation of B_2H_6 and -CF_2 bond on the PTFE surface. Though they have succeeded to take good adhesion force on the treated surfaces, but it doesn't have super hydrophilicity. On the other hand, in 2016, new idea using NH_4-H_2O/Ar as the PTFE treating gas has been proposed in the low pressure glow discharge to take super hydrophilicity by T. Yajima et al. [5]. If it is possible to exchange the gas mixture with NH_4-H_2O/Ar instead of boron compound in the APGD, we will have a strong preference to obtain the super hydrophilicity in parallel with high adhesion force in APGD. So we will compare the surface effects between their processes to clear the difference of the kinetics. At final, we will consider that which system is better choice for the surface treatments of PTFE.

2 Experimental

RF discharge with parallel electrodes was used as a discharge system. Detaille of the schematics is shown in the recent published paper [3]. In the case of LPD, the chamber pressure was maintained at 0.6 Torr by pumping system and the treating gas (NH_3-H_2O/He) total flow-rate was 10sccm that supplied with bubbling system through the 10% NH_4OH in water (25°C) as same as in the reference [5]. In the total flow rate, the partial pressure were as follows; NH_3:0.35 Torr, H_2O: 0.05 Torr He: 0.2 Torr. The diameter of electrodes was 125 mm and the discharge power was 13.56 MHz, 100 W for both LPD and APGD. The electrode gap was changed with the operating pressure (LPD: 20 mm or APGD: 2 mm). In the case of APGD, NH_3-H_2O/He gas flow rate was the same as that of the LPD, except of the operating carrier gas flow rate of He (2 slm). We used He gas instead of Ar in reference [5] to maintain 1 atm, because He can keep much easier the glow condition than that of Ar. PTFE (0.5 mm × 2 cm × 3 cm) was placed on the grounded electrode. Water contact angle was measured by the contact angle meter. The adhesion force was measured using 180° peeling tester with epoxy resin adhesion. XPS (ULVAC, ESCA-5800ci) was used for the surface analysis.

3 Results and discussion

Figure 1 shows the surface wettability of PTFE as a changing of the treated time in LPD and APGD. In the case of the LPD, water contact angle (CA) is decreased with increasing of the elapse time. For treating time longer than 30 min, the contact angle is continually decreasing and going below 5 degrees. From the results, the appearance of the super hydrophilicity on the PTFE surface which is shown in the reference [5] has been demonstrated in LPD system. In contrary, in the APGD, the CA shows almost no change with changing of the elapse time even using the same gas composition and discharge power, except of the operating pressure. Figure 2 (a) (b) show the optical emission of LPD (a) and APGD (b) using NH_3-H_2O/He gas. In the spectrums, we can find many peaks of exited radicals. While we cannot find any different spectra between the figure (a) and figure (b). This probably means that almost same radicals will be produced in the LPD and APGD. Figure 3 show the XPS analysis of PTFE, treated in LPD (a) and treated in APGD (b). From the figure 3 (b), the plasma excited species such as O, H, OH and NH_n radicals could not react with the PTFE surface in APGD. In contrary, on the LPD treated sample, O1s or N1s spectra were found that for certain assigned as carboxyl or amide group. It seemed that extremely different quality was found on the LPD treated and APGD treated PTFE surfaces.

It is well known that some kinds of radicals cannot easy react with PTFE such as O
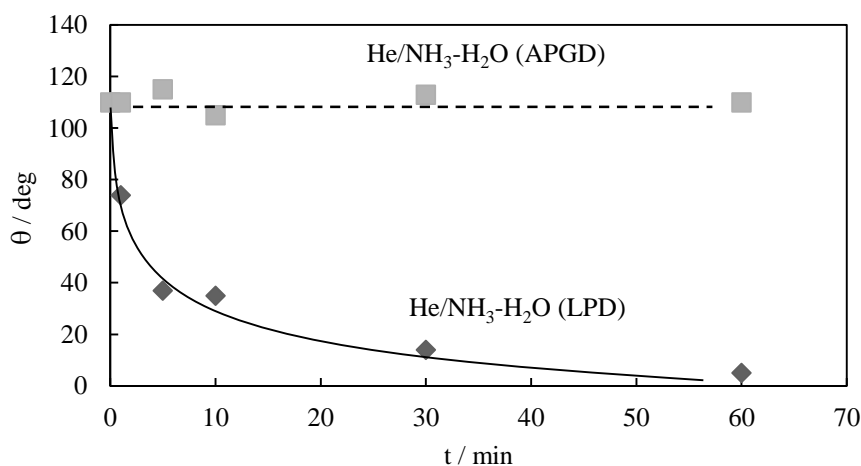
Fig.1 Water contact angle θ as a function of treatment time of PTFE that treated in LPD (0.6 Torr) and APGD discharge (1 atm)

atom, H atom, OH and NH_n, because $-CF_2$ bond is too strong to react with such radicals. So, some supporting reaction should be expected to enhance the radical reaction on the PTFE in
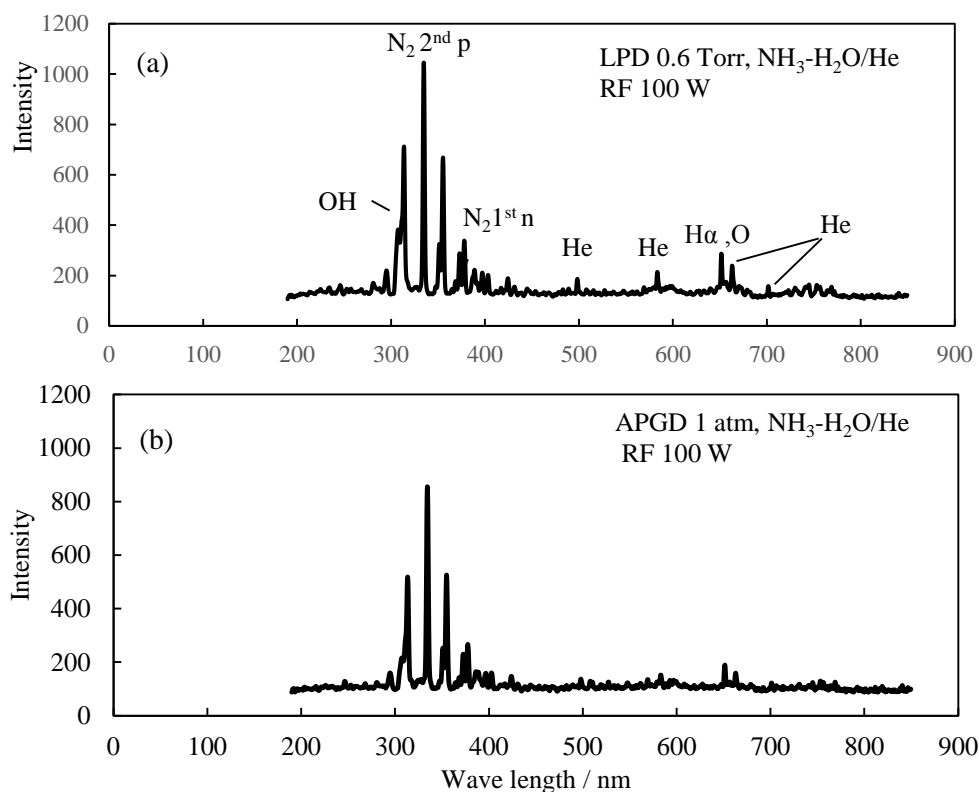
Fig. 2 Optical emission of LPD (a) and APGD (b) using NH_3-H_2O/He as a treating gas.

LPD. In the low pressure RF discharge, positive ion is accelerated by high bias voltage on the electrode that raises sputtering reaction [6]. It seemed that the sputter ablation and oxidation reaction or nitration reaction will be occurring even in NH_3-H_2O/He composition in LPD. Normally, an electro negativity of the carboxyl group is enhanced by containing of amide group that arise the enhancement of hydrophilicity in the molecule. This is one of the reasons why we see the super hydrophilicity at longer treatment time of PTFE in LPD in figure 1. On the other hand, in the atmospheric pressure, the sputtering reaction cannot take place in APGD, because ion energy is much lower than that of in LPD.

Figure 4 shows the peeling force of LPD treated PTFE with epoxy adhesion as a function of
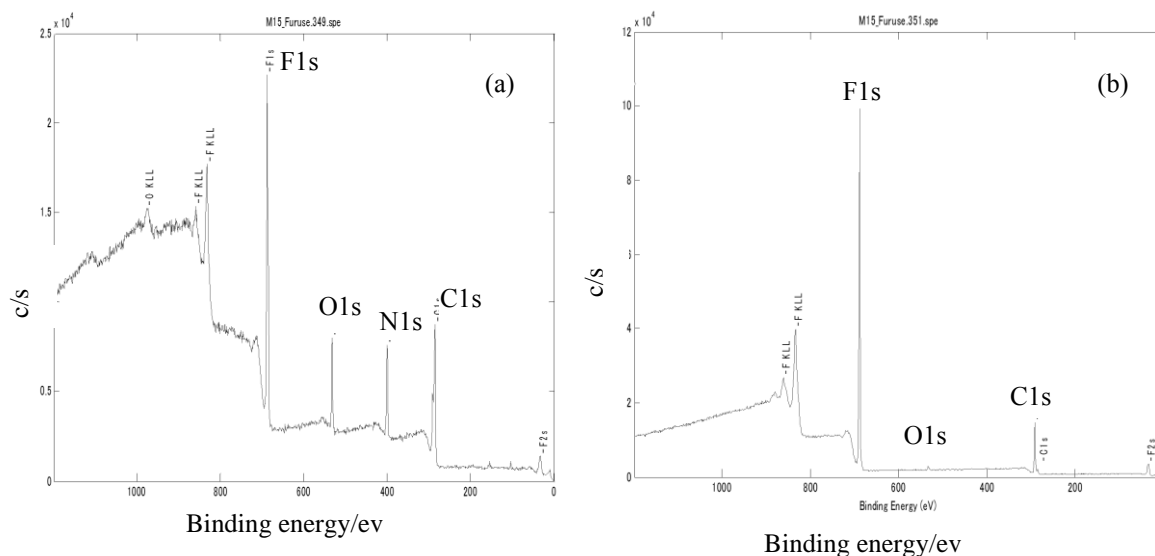
Fig. 3 The XPS analysis of PTFE, (a) treated in LPD and (b) treated in APGD.

the treating time in the different gas mixture. The peeling force which treated in APGD was the same as that of the untreated PTFE. Figure 4 also shows the PTFE surface treated in the boron compound-APGD system [3]. In the LPD treated surfaces, H_2O/He system shows faster increasing rate than that of NH_3-H_2O/He, but it shows much slower rate than that of the treated in boron compound-APGD system. Suppose the rate determining step will be attributed to the slow sputtering reaction on the PTFE in the low pressure. On the other hand, at the boron compound-APGD system, reactive metallic boron produced in APGD directly extracts the fluorine atom from -CF_2 bond of PTFE and then post oxidation will be occurred by the exposing in the air.
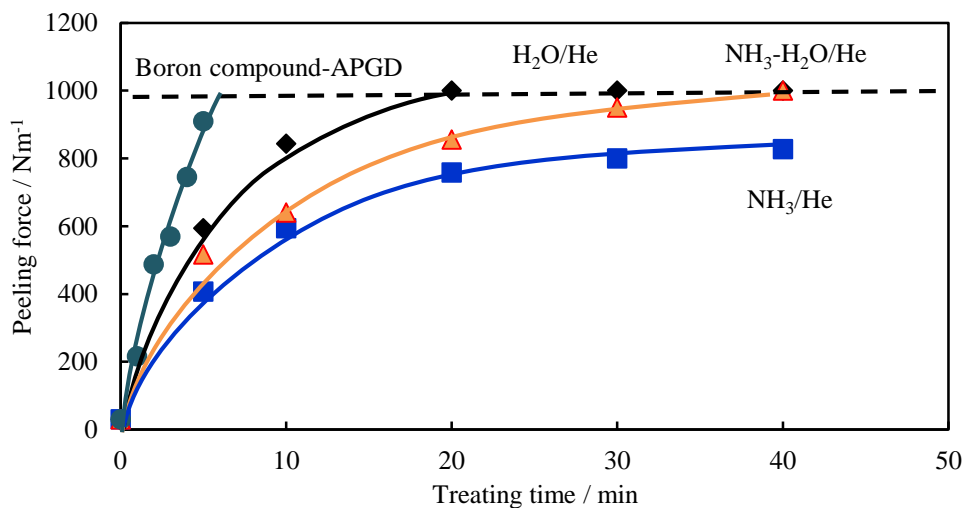
Fig. 4 The peeling force as a function of treatment time with epoxy adhesion treated in LPD and boron compound-APGD [3]. The dotted line shows the maximum force of the peeling tester.

4   Conclusion

LPD system using NH_4-H_2O/He or NH_4-H_2O/Ar [5] will be the best suited to achieve super hydrophilicity on the PTFE. But from the view point of the adhesion force refinement, APGD with boron compound system will be the recommended strategy for the industrial application.

References
1. H. Yasuda et.al, J. polym. Sci., Polym. Chem. ED., 15, 991 (1977)
2. T. Moriuch et al., Nitto-Gihou (In Japanies), 18 (1), 29 (1977)
3. M. Kogoma et al., *Proceedings of 29th ICPST*
4. D. R. Lide (ed.), Handbook of Chemistry and Physics, 81st edition, CRC Press, USA (2000).
5. H. Wenfeng et al., *Proceedings of 32nd ICPST-B2-12*
6. H. Yasuda, Plasma polymerization, pp.184, (Academic Press, Orlando 1985)

MODIFICATION OF POLYMER SURFACES BY ATMOSPHERIC PRESSURE PLASMAS

D. Kováčik, D. Skácelová, J. Kršková, M. Černák

Department of Physical Electronics, Faculty of Science, Masaryk University,
Kotlářská 2, 611 37 Brno, Czech Republic

E-mail: dusan.kovacik@mail.muni.cz

The surface of polyamide-12 (PA12), polypropylene (PP) and polyethylene (PE) foils was modified in order to improve their surface properties by two types of atmospheric pressure plasma sources - diffuse coplanar surface barrier discharge (DCSBD) and industrial corona discharge. A significant increase in wettability after plasma treatment was observed for all polymers. AFM measurement showed that the surface morphological changes due to plasma treatment strongly depend on the polymeric material. PE surface was significantly affected by plasma in comparison with PP and PA-12 surface.

Keywords: polymer foils; plasma surface treatment; atmospheric pressure plasma; coplanar discharge; industrial corona

1   Introduction

Polymers are increasingly used for many applications due to their unique properties. The surface properties of commercially used polymers are often more important to their function than their bulk properties and are determined by an extremely thin region that can be as small as a few atomic diameters. Atmospheric pressure plasma surface treatments represent widely used surface modification methods affecting only about 10 nanometres of the very surface layer, and have many potential benefits including minimal waste and control of surface functionality.

One of the most commonly utilized polymers are polypropylene (PP), polyethylene (PE) and polyamide (PA). PP is widely used in the packaging, automotive and textile industry due to its flexibility and economical benefit. Also PE belongs to the most common plastics due to its high ductility, impact strength and high mechanical and chemical stability. It is primary used in packaging industry as well as in medical engineering. The most used PA is polyamide-12 (PA12), which can be found in many industrial applications such as a protective covering, automotive industry or engineering. However, the poor hydrophilic properties of most polymers affect their printability, adhesion etc. thus a surface pre-treatment is required [1-5].
This paper deals with two types of atmospheric pressure plasma sources that were used to modified surface properties of PP, PE and PA12. Industrial corona (volume dielectric barrier discharge) represents the commonly used plasma source for in-line surface modification of polymer foils. The industrial demands on fast and efficient plasma treatment of flexible surfaces led to the development of a new type of atmospheric pressure plasma source suitable for very fast in-line treatment. Diffuse coplanar surface barrier discharge (DCSBD) [6-9], an unique type of dielectric barrier plasma source, was developed primary for low-cost in-line treatment of a wide scale of standard flat and web materials. This article studies the surface

modification of polymers by DCSBD and corona discharge in order to improve the wettability and adhesion. Modification of polymer surfaces was investigated by means of contact angle measurement and atomic force microscopy (AFM).

2   Experimental

Plasma treatment of the studied polymer foils (polyamide-12, polyethylene and polypropylene) was carried out in diffuse coplanar surface barrier discharge (DCSBD) and industrial corona discharge both operated in ambient air at atmospheric pressure. The cross-sectional schematics of both electrode systems are shown in Figs. 1a-b.

DCSBD[5,6,7] represents dielectric barrier discharge in coplanar geometry characterized by the generation of very thin, uniform, visually diffuse cold plasma with high non–isothermicity (Fig. 1c). The plasma reactor used in experiments is detailed described in [10]. Fig. 1c and Fig. 1d shows the flat and concave curved geometries of DCSBD electrode system, respectively. The thickness of DCSBD plasma layer is ~0.33 mm, the power density can vary from 50 to 100 $W.cm^{-3}$.
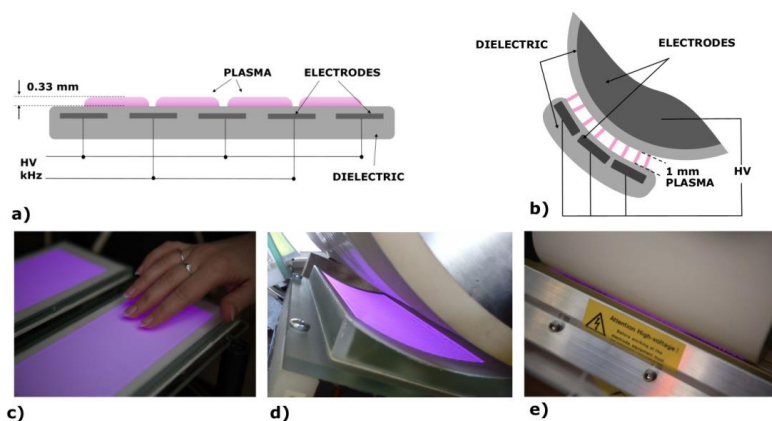
Fig. 1: a) the cross-sectional schematics of DCSBD electrode system, b) the cross-sectional schematics of corona system and the photography of c) the flat DCSBD electrode, d) the concave curved DCSBD electrode and e) corona discharge.

Corona treatments of polymer foils were carried out using a commercial device AHLBRANDT Industrial Corona System, which uses a volume configuration of electrodes isolated by a ceramic layer (Fig. 1e). Plasma burns between a grounded rotating cylinder and a detachable electrode with gaps, which serve as an air and ozone outlet. The plasma gap was adjusted to 1 mm, samples were treated 1, 3 and 5 seconds and plasma was generated at the same square power density (2.56 $W.cm^{-2}$) as in the case of DCSBD.

The analysis methods used for verification of the surface modification by DCSBD and industrial corona were the water contact angle (WCA) measurements to evaluate the wetting properties and AFM for determination of surface morphology.

3   Results and Discussion

Fig. 2 shows the water contact angle of the studied polymers modified in DCSBD and corona discharge for various exposure times. The wettability of all polymer surfaces was significantly

improved after plasma treatment. The water contact angles of untreated polymers are similarly close to the 100° (WCA$_{PP}$ =101.2°, WCA$_{PE}$ = 93.8° and WCA$_{PA12}$ = 99.9°). After plasma treatment the WCA significantly decrease. The 5 s modification of PP, PE and PA12 in DCSBD plasma decreased the WCA to 42.4°, 36.7° and 32.1°, respectively. The modification of polymers in corona discharge was less effective. The 5 s modification in corona discharge caused the WCA decrease of PP, PE and PA12 to the values 56.4°, 48.5° and 44.9°, respectively.
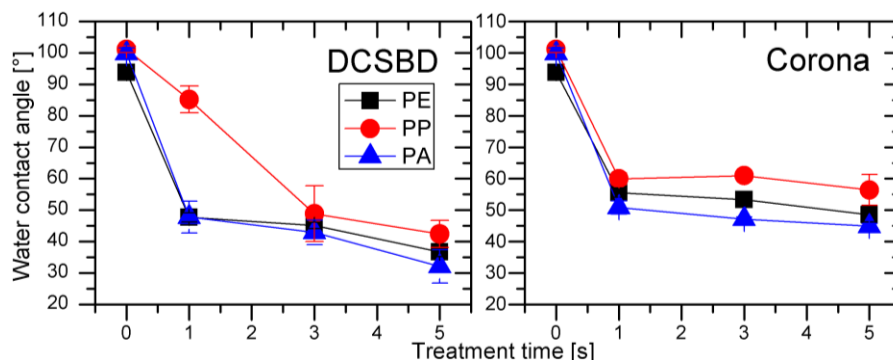
Fig. 2: Water contact angle of PE, PP and PA12 surface modified in DCSBD and corona discharge for 1 s, 3 s and 5 s in ambient air.

The morphology of untreated and plasma treated PP, PE and PA12 surface was examined using AFM. Fig. 3 shows the AFM images of reference samples and polymer surfaces treated in DCSBD and corona discharge for 3 s. It can be seen that plasma treatment significantly influences the surface morphology of PE while PP and PA12 surfaces remain almost unaffected. Plasma treated PE surface is characterized by smooth bubble-like areas randomly placed on the surface.
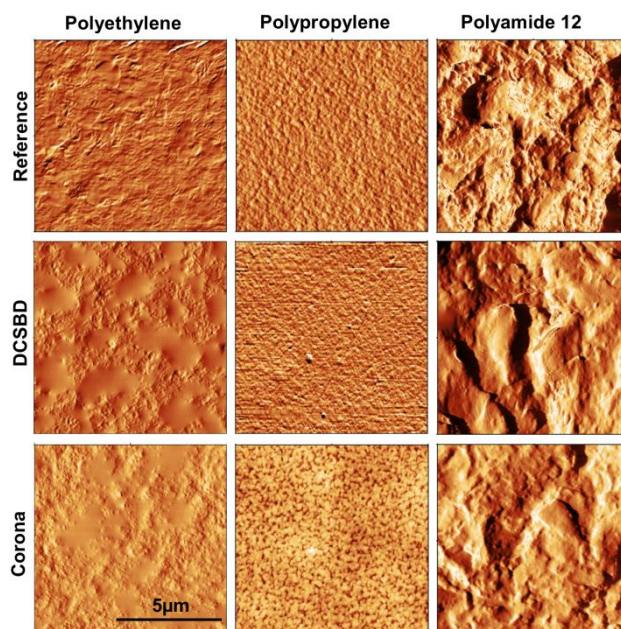
Fig. 3: AFM images of PE, PP and PA12 treated in DCSBD and corona discharge for 3 s. The scanned area is 10 x 10μm, non-contact scanning mode, processed in Gwiddion [11] software and applied filter.

Moreover, on the surface modified in corona discharge there are also observed a number of pinholes uniformly distributed on the surface. Such pinholes are characteristics for corona treatment and are caused by the interaction of surface and plasma filaments perpendicular to the treated surface.

PP surface modified in DCSBD plasma remains unchanged in comparison to reference characterized by the fine rough structure while the surface modified in corona discharge is very rough. This grain structure is also caused by the pinholing effect typical for corona discharge.

Surface of studied PA12 foil is very rough and inhomogeneous with rather sharp peaks and depths. Therefore, the effect of plasma treatment is not such obvious as in the case of PE and PP. Plasma treated surface seems to be unaffected by the plasma and comparable to reference surface.

4   Conclusion

In this work the surface modification of polyamide-12, polyethylene and polypropylene films using atmospheric pressure plasmas – diffuse coplanar surface barrier discharge and industrial corona discharge. Efficient hydrophilization of all polymer surfaces after plasma treatment have been observed. Surface morphology strongly depends on the polymeric material and its initial roughness. Moreover, the surface modification using industrial corona was characterized by typical pinholing effect compared to DCSBD plasma.

References

1. J. Friedrich, The plasma chemistry of polymer surface (Wiley-VCH Velrag, Weinheim, 2012)
2. M. Strobel et al., Plasma surface modification of polymers: Relevance to adhesion (VSPBV, Netherlands,1994)
3. E. M. Liston et al., J. Adhes. Sci. Technol. 7, 1091 (1993)
4. M. Noeske et al., Int. J. Adhes. Adhes. 24, 171 (2004)
5. J. Hanusová et al., Open Chem. 13, 382 (2015)
6. M. Šimor et al., Appl. Phys. Lett. 81, 2716 (2002)
7. M. Černák, Method and apparatus for treatment of textile materials, European Patent EP 1387901 B1, 2002
8. M. Černák et al., Eur. Phys. J-Appl. Phys. 47, 22806 (2009)
9. L. Černáková et al., Plasma Chem. Plasma Process. 25, 427 (2005)
10. M. Černák et al., Plasma Phys. Contr. F. 53, 124031 (2011)
11. D. Nečas et al., Gwyddion [Software] [on-Line] (access 6.5.2015) URL http://www.gwyddion.net

EFFECT OF METASTABLE-DRIVEN FILM DEPOSITION ON GROWTH-RATE PROFILES

J. Philipp, C.-P. Klages

Institute for Surface Technology (IOT), Technische Universität Braunschweig,
Bienroder Weg 54 E, 38108 Braunschweig, Germany

E-mail: jens.philipp@tu-braunschweig.de

DBD-based plasma-activated film deposition at atmospheric pressure has been studied employing a novel reactor for combinatorial studies. Gradient films were obtained by feeding the deposition reactor with a premixed precursor gas concentration gradient transverse to the direction of flow x using argon and argon doped with 2% xenon, respectively, as carrier gases. Characteristic film thickness profiles d(x) obtained as the main result were used to derive greatly simplified phenomenological models used for the simulation of three different typical thickness trends. We found experimental evidence that metastables and excimers play an important role in plasma polymerization processes from our DBD discharges.

Keywords: combinatorial surface technology; gradient surfaces; plasma-assisted deposition; plasma treatment; high throughput experimentation

1   Introduction

The present contribution focusses on the influence of monomer (precursor) concentration x_M in the carrier gas, one of the major experimental parameters, on film thickness distributions $d(x,y)$, with the gas flow direction taken as x direction, in order to demonstrate that the empirically found interrelation between x_M, varied in y direction perpendicular to x, and $d(x)$ is of significant diagnostic value for mechanistic studies, similar to the monomer pressure or flow rate in studies of low-pressure plasma deposition [1]. Systematic studies of x_M are still relatively rare for DBD-based PACVD processes, one example was published by Enache et al [2].

Within the scope of this work a new kind of flow reactors applicable for plasma-assisted chemical vapor deposition (DBD-PACVD) processes as well as surface treatment processes based on dielectric barrier discharges (DBDs) at atmospheric pressure (AP) was employed. This reactor utilizes a laminar gas flow with a premixed spatial concentration gradient $\partial c_i/\partial y$ transversal to the flow direction x and to the electric field (z direction) fed to a channel-like DBD reactor. The coordinates x and y, respectively, are planar coordinates in a Cartesian coordinate system. For deposition experiments polypropylene (PP) foils – placed within the discharge zone – were plasma-coated from a dielectric barrier discharge (DBD) which was fed with the obtained gas gradient. The development und experimental testing of these reactor has already been presented in a previous publication [3].

In this study we report results from experiments with hexamethyldisiloxane (HMDSO), tetramethylsilane (TMS), glycidyl methacrylate (GMA), furfuryl methacrylate (FMA), and trans-2-hexenal (hexenal) in different carrier gases and we will show that there are reasons to distinguish three different ideal types of precursor concentration dependencies, reflected in characteristic film thickness profiles d(x). Characterization of the plasma treated PP foils was usually carried out by means of FTIR-ATR spectroscopy. Furthermore, these three types of ideal deposition behavior were simulated by using greatly reduced phenomenological models deduced from the obtained deposition behavior.

2   Experimental

2.1 Deposition Experiments

To provide the necessary power for maintaining the discharge during film deposition process a high voltage generator was used in continuous wave (cw) or (for GMA and FMA, respectively) pulsed mode with a pulse/pause-ratio between 1/3 and 1/199 ms/ms. An excitation voltage of 3 kV $\pm$ 0.1 kV (amplitude) with a frequency of 86.5 kHz and 87 kHz, respectively, was applied. For all experiments presented here the treatment time was 60 s with exception for the experiments with FMA (treatment duration 300 s). Argon as well as argon doped with 2% xenon was used as a carrier gas with a total gas flow of 3 slm. A defined bypassed part of this carrier gas flow was bubbled through a flask containing the liquid precursor of interest. For some additional experiments the excitation voltage was set to 4 kV $\pm$ 0.1 kV and 5 kV $\pm$ 0.1 kV, respectively, the treatment time was varied from 6 s to 1200 s which was depending on the used pulse/pause-ration, and the total argon flow was changed in a range from 1.5 slm to 9 slm.

3   Results and Discussion

The main results from deposition experiments using plasma polymerization of HMDSO, TMS, GMA, FMA and hexenal are given in the following. To evaluate thickness trends in x direction d(X) FTIR-ATR spectra (diamond, 51°) were measured at different positions of a rectangular array on the plasma treated substrate in steps of 0.25, 5, or 10 mm, respectively. Comsol Multiphysics 5.1 was used to simulate the thickness trends d(x). It should be mentioned here that the simulation is actually without regard to plasma polymerization processes. For further detailed explanations of the experimental results and hypothesizes presented in this proceedings paper please look up our latest publication [3].

3.1 Plasma Polymerization from HMDSO, TMS, and Hexenal in Ar

Two characteristic features in the d(x) curves shown in Fig. 2 were attracting attention:

(i) Immediately behind the trailing edge of the discharge zone at x = 10 cm, there is a step increase of deposit thickness (typical width 0.5 to 1 cm). Scanning-electron-microscopic inspections show a nanoparticulate appearance (particle size 50 to 100 nm). (ii) The constancy of deposition thickness on the first few centimeters for a range of concentrations and formation of extended plateau regions with nearly constant film thickness at the highest x_M is observed.
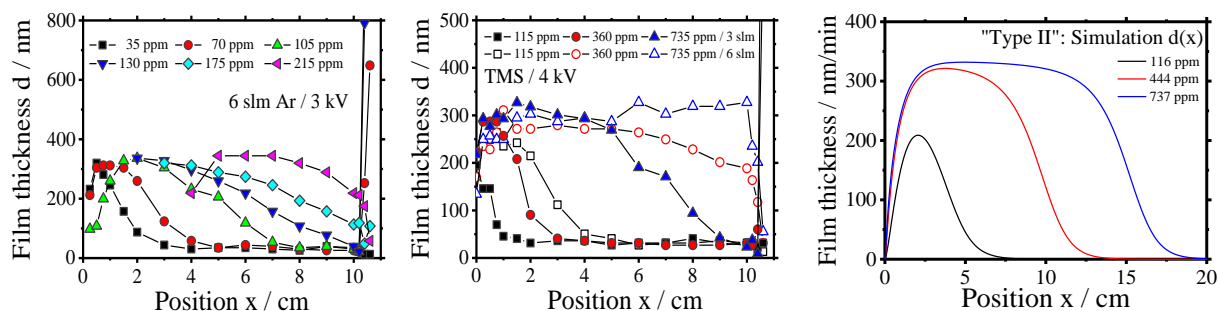
Fig. 1: Experimental film thickness profiles d(x) along flow direction of plasma polymers deposited from HMDSO in Ar (left) for a gas flow of 6 slm and 3 kV voltage amplitude. TMS curves for TMS in Ar (middle) are shown for 4 kV excitation voltage and gas flows of 3 slm (close symbols) and 6 slm (open symbols), respectively. A set of simulated curves (right) show a good agreement with thickness profiles obtained from TMS in Ar. Curve parameters for each set of d(x) curves are mole fractions of the precursor in the gas feed. "Position x" is the distance within the discharge zone (total length 10 cm) where 0 cm indicates the beginning of the discharge zone. Gas flow unit "slm" is in liters per minute at standard temperature and pressure (STP).

The remarkable d(x) dependence mentioned above is at variance with expectations based on a phenomenological deposition model in which the growth species, i.e., radicals and/or ions mainly contributing to film growth, are generated from the monomer M by electron collisions. Under the assumption that in the DBDs used here the temporal evolution of electron density and electron energy distribution function during an average transient discharge within one AC half-cycle is independent of the precursor concentration, the number of dissociation and ionization events within one discharge will be proportional to the precursor concentration. A linear scaling of d(x) with the initial monomer concentration should be the result. In the context of the present work we call this characteristic behavior "type-I" behavior.

The d(x) behavior ("type II") shown in Figure 1 can be reproduced by assuming that an x_M-independent number of energetic species $Ar^\#$ (i.e., Ar metastables and excimers) with a sufficient lifetime is generated from the carrier gas in every half-cycle of the DBD which subsequently react with the monomer under formation of a film forming product P. Averaged over many half-cycles a constant number of generated $Ar^\#$ per half-cycle corresponds to an x_M-independent generation rate of this species, and if the reaction with M is the only or at least the by far dominant decay channel of $Ar^\#$ this would result in an x_M-independent generation rate of film-forming species and yield to the observed d(x) characteristics.

3.2 Plasma Polymerization from HMDSO, TMS, and Hexenal in Ar/Xe

A substantially different dependence of film growth rates on monomer concentrations is observed for d(x) profiles of plasma polymerized films deposited from HMDSO, TMS and hexenal, respectively, from argon doped with 2% xenon (s. Figure 2):

(i) Film thickness maxima now tend to increase significantly with the precursor concentration, even though not strictly linear as expected for an ideal "type-I" behavior and (ii) there is never any evidence of plateau forming in the d(x) curves as it was observed especially clearly for TMS or hexenal in Ar.
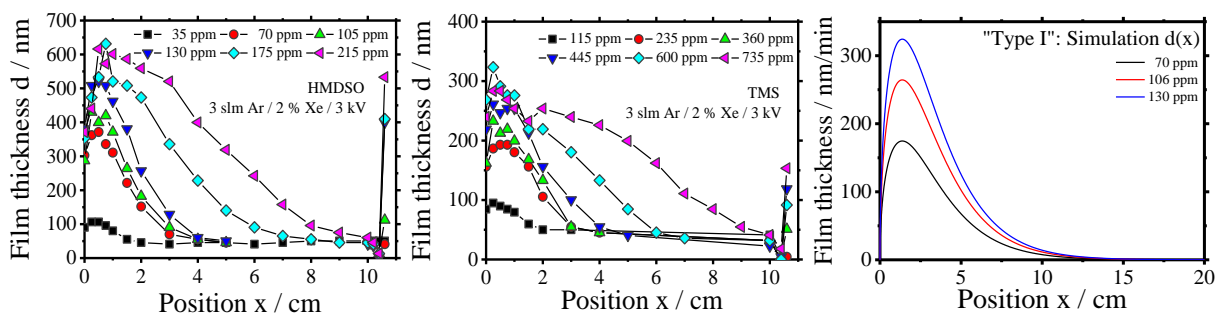
Fig. 2: Experimental film thickness profiles d(x) of plasma polymers deposited from HMDSO and TMS in a mixture of Ar mixed with 2% Xe. A set of simulated curves (right) show a good agreement with thickness profiles obtained from HMDSO in Ar doped with 2% Xe.

Assuming virtually unchanged generation rates of metastable Ar atoms (Ar^*) by direct electron-collisional excitation and radiative cascading from higher excited Ar states the addition of xenon will substantially reduce the concentration of Ar^* and metastable states of Xe may be formed. A tentative hypothesis which may explain why the Xe addition is able to give an enhanced deposition rate is that Ar^* are replaced by Xe metastables which seems to suppress ionization processes more strongly than dissociation processes, due to the lower energy of Xe metastables compared with metastable states of Ar.

The effect of a small amount of Xe in the carrier gas shown in Figure 2 is a clear indication of the role which metastables and excimers play in plasma polymerization processes from these discharges.

3.3 Plasma Polymerization from GMA and FMA in Ar

Thickness profiles d(x) which cannot be assigned to one of the idealized types of d(x) described above were obtained in experiments with GMA and FMA, respectively, carried out in pure Ar. The growth rates show an increase with x_M which is especially pronounced at high flow rates and, with exception of some of the data points including the leading edge of the plasma polymer film, growth rates are monotonously decreasing with x. The highest deposition rates are directly at the beginning of the plasma zone.
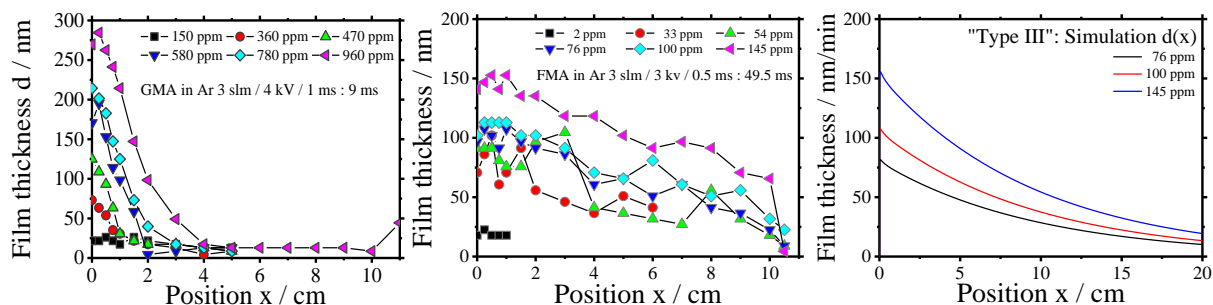
Fig. 3: Experimental film thickness profiles d(x) of plasma polymers deposited from GMA in Ar (left) at excitation voltages of 4 kV. FMA curves in Ar (middle) are shown for a frequency of 86.5 kHz with a treatment time of 300 s. Simulated curves (right) show already a good agreement with d(x) obtained from FMA in Ar.

Figure 3 shows a set of curves with monomer concentrations of FMA and GMA, respectively, as curves parameters for a varied excitation voltage (GMA). The discharge was pulsed (0.5/1 ms on; 9/49.5 ms off) in order to extend the range of film growth across a larger percentage of the substrate because with a cw discharge the deposition zone is scaled down to a narrow strip. This "type III" can be attributed to a plasma-induced polymerization of intact precursor M which is largely confined to the surface region, in agreement with previous investigations [4]. The simplest imaginable reaction scheme, involving a discharge-induced (re)activation of the substrate or the growing film, a propagation step, and a termination reaction should lead to an exponential decrease of d(x).

4   Conclusion

The usefulness of a DBD reactor fed with a premixed precursor gas concentration gradient transverse to the direction of flow x was indicated by results from DBD plasma deposition processes with the precursors HMDSO, TMS, GMA, FMA and hexenal, respectively, in argon as well as argon doped with 2% xenon. These experiments demonstrate the utility of such a combinatorial method for plasma-based surface science and technology, for example for investigations of deposition behaviors of different precursors at atmospheric pressure. As a main result from our investigations we have reasons to distinguish three different ideal types of deposition behavior, reflected in characteristic film thickness profiles d(x). The effect of a small amount of Xe in the carrier gas which leads to substantially different film growth rates for HMDSO, TMS and hexenal, respectively, is a clear indication of the important role which metastables and excimers play in plasma polymerization processes from our DBD discharges. Based on the experimental results and hypothesizes to explain the deposition processes we deduced reduced phenomenological models and used these model concepts for the simulation of the typical thickness trends. The first simulation results show already good agreements with thickness profiles d(x) obtained from experiments.

References

1. D. Hegemann, J. Phys. D: Appl. Phys. 46, 205204 (2013)
2. I. Enache et al., Plasma Process. Polym. 4, 806 (2007)
3. J. Philipp et al., Plasma Process. Polym. 13, 509 (2016)
4. C.-P. Klages et al., Plasmas and Polymers 5, 79 (2000)

FILM FORMATION FROM HMDSO: COMPARISON OF DIRECT PLASMA INJECTION WITH AFTERGLOW INJECTION USING AN ATMOSPHERIC PRESSURE DIELECTRIC BARRIER DISCHARGE

R. Wallimann, G. Oberbossel, D. Butscher, P. R. von Rohr

Transport Processes and Reactions Laboratory, Institute of Process Engineering, ETH Zürich, Sonneggstrasse 3, 8092 Zürich, Switzerland

E-mail: wallimann@ipe.mavt.ethz.ch

The afterglow of a dielectric barrier discharge plasma was used for the film formation on a silicon wafer. Argon was mixed as process gas with different amounts of oxygen and HMDSO. The silicon wafer was analyzed using white light interferometry and ATR-FTIR. Results show the influence of oxygen, HMDSO concentration and flow velocities on film formation. It is shown that afterglow injection of HMDSO yields film deposition comparable to direct plasma injection.

1   Introduction

Thin solid films from organosilane and organosiloxane monomers using plasma-enhanced chemical vapor deposition (PECVD) are produced mostly under vacuum conditions [1]. However, due to cost restrictions and setup complexity vacuum processes possess, atmospheric pressure discharges have been studied intensively in the past years [2]. Among others, applications of thin films from PECVD can be found in the micro-electronics industry [3], alteration of surface wettability [4,5], corrosion protection [6] and biomaterials [7].

In general, film deposition occurs in the reactor itself where reactive plasma species and electrons dissociate monomers and deposit a film on surfaces exposed to the discharge. Because of low gap size, such a setup is not feasible for treatment of powder, which is the predominant product form in chemical industry. Instead, plasma jets can be used to treat surfaces outside the plasma zone. Powders can be transported through the afterglow region whereas transportation through the discharge gap may cause channel clogging. Monomers can be injected into the plasma zone or into the afterglow. Afterglow treatment is seen to be less effective since reactive species recombine after exiting the plasma zone. High conversion rates are crucial for economic reasons, therefore, best parameters for film deposition in the afterglow need to be found. Moreover, the incorporation of particles into the thin-film has to be avoided.

In this study, argon is used as process gas since it guarantees stable plasma ignition and has been shown to be more efficient than helium in dissociating HMDSO [8]. As Fanelli [9] showed, film growth from MDSO using a molar ratio of O_2/MDSO up to 25 reduces methyl groups in the film. Because mostly SiO_x coatings are required, in this study, rates of 1 to 8 have been used to show the influence of oxygen admixture on film deposition.

2 Experimental

The setup used in this study is well described by Sonnenfeld [8] and shown in figure 1. The DBD exhibits a 1 mm gap with 60 mm length and 3 mm width and two PMMA barriers with 2 mm thickness (high voltage electrode) and 1 mm (ground electrode), respectively. The high voltage electrode is powered at a frequency of 7 kHz with a peak-to-peak voltage of 8 kV. In this study, a silicon wafer is mounted in front of the argon discharge with varying flow rates of argon (Pangas, 99.996%), HMDSO (SigmaAldrich, >98%) and oxygen (Pangas, 99.9999%). HMDSO was either injected into the plasma channel (injection point 1) or into the afterglow (injection point 2) together with argon.
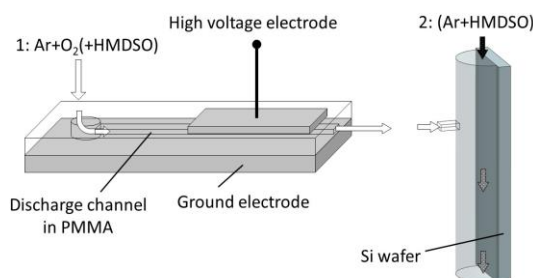
Fig. 1: Dielectric Barrier discharge setup used for film deposition. At point 1, argon and oxygen are injected into the discharge channel. For direct plasma injection, HMDSO is also injected. In case of afterglow configuration, argon together with HMDSO is injected at point 2. Films are collected downstreams on a silicon wafer.

The deposited films were analyzed using white light interferometry (WLI) (Zygo NewView 5000) to measure film volume and ATR-FTIR (PerkinElmer Spectrum Two) to evaluate the deposited species. Treatment time was 5 minutes for film volume measurements and 20 minutes for ATR-FTIR measurements.

3 Results and Discussion

In a first step, oxygen and HMDSO concentrations were optimized with respect to deposited film volume, whereby HMDSO was introduced at point 1. In a second step, these conditions were taken and HMDSO was introduced into the afterglow.

3.1 Direct plasma injection of HMDSO

Figure 2 shows the film volume and conversion rate for direct plasma injection in dependence of total gas flow rate while the percental admixture of oxygen (0.2%) and HMDSO (0.05%) was kept constant.
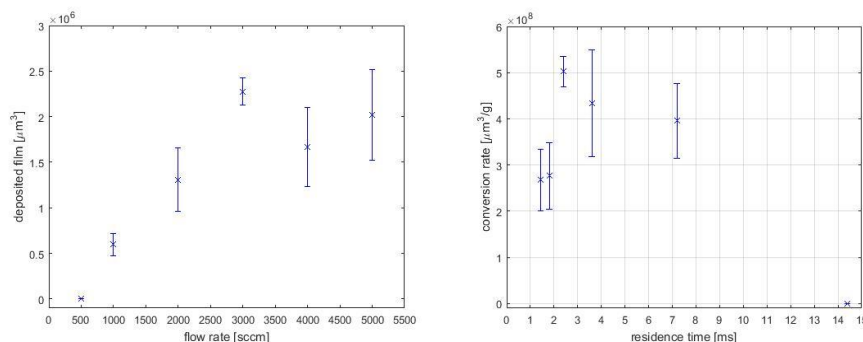
Fig. 2: Film volume as a function of total gas flow rate with admixture of 0.05 % HMDSO and 0.2 % oxygen (left) and conversion rate as a function of residence time of HMDSO in the plasma zone at 0.05% HMDSO and 0.2% oxygen admixture (right)

An increase in film volume with rising total gas flow rate is observed. Film formation levels off around 3000 sccm total gas flow rate. Film deposition at 500 sccm was not possible, presumably due to the unstable plasma discharge at low flow rates. Since the concentration of HMDSO in the gas flow was constant, the overall amount of HMDSO was increasing with increasing total flow rate and therefore film volume increased until 3000 sccm. The plateau after 3000 sccm can be attributed to the decreasing residence time shown in figure 2 (right). Conversion rate of injected HMDSO drops below the residence time of 2 ms whereas it is constant between 2 and 8 ms. Low residence time probably hinders the dissociation of HMDSO in the plasma zone. Moreover, the dissociated species are less likely to form films because residence time on the Si wafer is reduced at higher flow rates and shear forces interfere with the deposition process.

The development of the film volume with different oxygen admixtures is shown in figure 3. Maximum conversion is reached at 0.05% oxygen concentration. When introducing low amounts of oxygen, atomic oxygen is formed via the reaction $e^-+O_2 \rightarrow 2O+e^-$. A competing process is the formation of ozone via the three-body-reaction $O+O_2+M \rightarrow O_2+M$. At higher O_2 concentrations, ozone production becomes more effective [10]. Additionally, for molecular gases i.e. oxygen, collisional energy losses occur which reduces electron energy [11,12] and the electron density decreases with rising oxygen concentration because of molecular oxygen's electronegativity [10]. This explains the drop in film volume above 0.05 % oxygen. Lower atomic oxygen content, electron density and energy result in a lower dissociation capability of the plasma.
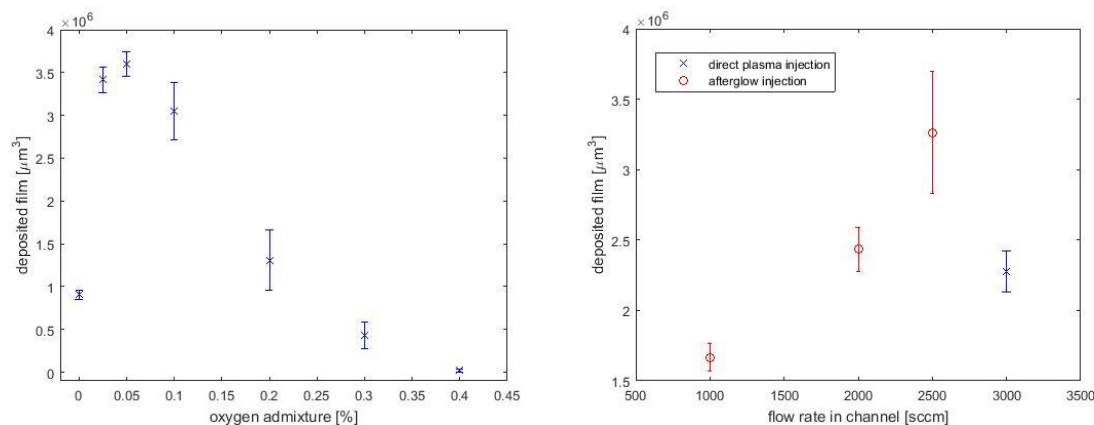
Fig. 3: Film volume as a function of oxygen admixture with 2000 sccm total flow and 0.05 % HMDSO (left). Deposited film as a function of the channel flow rate with HMDSO injected either into the plasma zone or into the afterglow. The total flow rate was kept constant at 3000 sccm, afterglow injection was chosen accordingly. The percental admixture of oxygen was 0.2 % of the total channel flow rate. HMDSO injection was 1.5 sccm in the afterglow (right).

3.2 Comparison of direct plasma and afterglow injection of HMDSO

Figure 3 shows the film deposition when introducing HMDSO into the afterglow at different discharge channel flow rates. In all cases, deposition from afterglow injection was higher than direct plasma injection. This is likely due to the deposition processes in the discharge channel itself i.e. dissociated HMDSO deposits on the channel walls before reaching the Si wafer. When increasing the flow rate through the channel, afterglow deposition increases since reactive species only have a limited lifetime and more of these can reach the afterglow zone.

In figure 4, absorption spectra of a film deposited during direct plasma injection as well as a film formed from afterglow injection are shown. The main peaks found are Si-O-Si a-stretching at 1034 cm^{-1}, CH_3 s-bending in $Si(CH_3)$ at 1260 cm^{-1}, CH rocking in $Si(CH_3)_3$ at 840 cm^{-1} and 760 cm^{-1}, Si-C (or Si-O) at 796 cm^{-1}, and C-H a-stretching at 2964 cm^{-1} [13]. The spectrum is similar to Raynaud at low pressure and low power, however C-H a-stretching are not present in the shown spectra. The afterglow injection yields a higher amount of Si-C (or Si-O) bondings than the direct plasma injection. Also, afterglow injection shows a slightly lower $Si(CH_3)$ content. Overall, afterglow injection shows more Si-O bonds and less incorporated methyl groups.
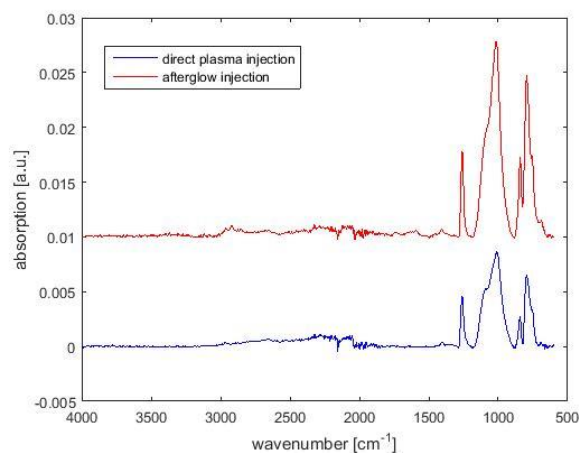
Fig. 4: FTIR absorption spectra of produced films using 0.2 % oxygen and 0.05 % HMDSO in 20 minutes.

4   Conclusion

We showed that dissociation of HMDSO injected into the afterglow of an atmospheric argon plasma yields similar film deposition compared to direct plasma injection. The deposition rate mainly depends on the concentration of reactive species present in the afterglow. Afterglow injection can slightly decrease incorporation of organic compounds and therefore should be favored when inorganic films are required. Treatment of powder outside the discharge channel even using afterglow injection of monomer seems feasible.

References

1. R. Thyen, Surf. Coat. Technol. 97 (1997)
2. U. Kogelschatz, Plasma Chem. Plasma Process. 23, 1 (2003)
3. M. Creatore, Mater. Sci. Semicond. Process. 7 (2004)
4. K.-S. Chen, Surf. Coat. Technol. 228 (2013)
5. D. J. Marchand, Surf. Coat. Technol. 234 (2013)
6. J. Bour, Plasma Process. Polym. 5 (2008)
7. T. Hayakawa, Biomaterials, 25 (2004)
8. A. Sonnenfeld, J. Phys. D: Appl. Phys. 44 (2011)
9. F. Fanelli, Plasma Process. Polym. 9 (2012)
10. D. Ellerweg, Ph.D. thesis, Ruhr-University Bochum, 2012
11. A. Schwabedissen, Plasma Sources Sci. Technol. 8 (1999)
12. K. Wagatsuma, Anal. Chim. Acta, 306 (1995)
13. P. Raynaud, Plasma Process. Polym. 2 (2005)

PLASMA MODIFICATION OF POLYESTER FABRICS WITH ULTRA HYDROPHOBIC AND OLEOPHOBIC PROPERTIES FOR IMPROVED LAMINATION

O. Beier[1], M. Ramm[1], B. Blechschmidt[2], J. Kelar[3], A. Pfuch[1]

[1]INNOVENT e.V. Technology Development, Pruessingstraße 27B, D-07745 Jena, Germany
[2] C.H. Müller GmbH, Gewerbering 1, D-08468 Heinsdorfergrund, Germany
[3]Dept. of Physical Electronics, Masaryk University, Kotlářská 2, CZ-61137 Brno, Czech Republic

E-mail: ob@innovent-jena.de

In this contribution we present results of an industrial initiated project, which aimed for improved lamination of polyester textile fabrics with ultra hydrophobic and oleophobic surface properties. These fabrics are functionalized with a fluoro-organic finishing and are generally used for automotive applications, like the interior of cars. Different atmospheric pressure plasma sources, like plasma jets, flames or surface barrier discharges (DCSBD) were investigated to improve the lamination ability of these fabrics only for one side, still remaining the antirepellent surface properties on the second side. Best results regarding one-sided textile modification and good lamination were obtained with DCSBD plasmas.

Keywords: atmospheric pressure plasma; textiles; surface modification; adhesion improvement; lamination

1   Introduction

Functional technical textiles have developed in the last decades to an essential part of the high-tech products available on many market areas. Especially, with view on the automotive industry more and more parts of the common interior of cars are substituted from plastics to textiles [1]. Besides car seats where technical fabrics are established, typical examples of new fields of applications are the pillars (A-, B-, C-pillar) or the car roof lining for finishing with textiles. Looking at the requirements these materials must have ultra hydrophobic and ultra oleophobic surface properties to ensure minimal pollutions from the environment or finger prints etc. and easy cleaning for the user. The corresponding textile finishing is normally performed by dip-coating with fluoro-organic solutions, resulting in functionalized surfaces of both the textiles upper and bottom sides. But, for further lamination or thermoplastic glueing these properties are unwanted for on one side, because of the bad wetting behaviour and low surface energies, respectively. In this case inhomogeneous distribution of resins and therefore insufficient adhesion can occur, which leads to more rejects in production lines.

The aim of these investigations was to characterise three areal, but fundamental different atmospheric pressure plasma systems and their efficiency in one-sided pre-treatment of ultra hydrophobic and ultra oleophobic polyester fabrics for improved lamination. DC-pulsed plasma jets, thermal flames and a special type of dielectric barrier discharge (surface barrier discharge) were used. Main results of these investigations are presented in this contribution.

2 Experimental

The experimental parts included three kinds of treatments shown in Fig. 1. These treatments were chosen because of their economic potential in industrial process conditions.

The first technical solution provides a propane / air gas flame (INNOVENT, Jena, Germany) which can be seen as a thermal plasma. Previously it was shown, that this technique can be applied successfully in the field of improvement of adhesion bonding strength between polymer bonding partners [2]. The advantage of this kind of source is the high quantity of substrates which can be treated in one run because of the burner width of up to 1.2 m. The treatment process itself is quite easy to handle in addition with the low sensitivity of changes in the parameter set. E.g. the gap between burner and textile substrate can differ 5 mm without significantly influencing the generated properties. The main parameters within this process are the velocity of the substrate and the number of treatments, which were investigated.

Speaking about polymer surface treatment the plasma technique, and in this context especially the atmospheric pressure plasma technique, is a very useful tool to influence the wettability and the polarity of a polymer surface [2-4]. So, the second plasma device supplied by TIGRES GmbH (Marschacht, Germany) provides 14 atmospheric plasma jets on an area of 2 x 10 cm^2. Unfortunately, with this source the amount of substrates, which can be treated in one run, decreases in comparison to the flame treatment. But on the other hand the thermal stress to the textile surface, which is occurring during flame treatment is not so strong even for moderate substrate velocities during plasma interaction. The electrical power can be tuned up to 200 W per nozzle, as process gas compressed air of 6 bar was used. Parameters which were varied are the substrate velocity between 100 und 200 mm/s and the number of treatments. Also a single jet plasma system with power values of 250 W was tested for these experiments, with the same process gas and velocities as described.

The third plasma system obtained from ROPLASS s.r.o (Brno, Czech Republic) was a Diffuse Coplanar Surface Barrier Discharge (DCSBD). This discharge type is characterised by a thin visible plasma layer of around 0.3 mm in thickness on top of the ceramic surface, with high plasma densities of up to 100 W/cm^3 [5, 6]. Areal dimensions for this type of source are 20 x 8 cm^2, but can be easily increased for high treatment width by connecting several ones together. Electrical power values were set to 400 W during the treatments, no specific working gas was used, only surrounding air. The fabrics were located stationary direct at the ceramic surface and different treatment times of up to 30 sec were tested. The plasma device itself is cooled by oil and no thermal stress or damage was observed at the textile surface.
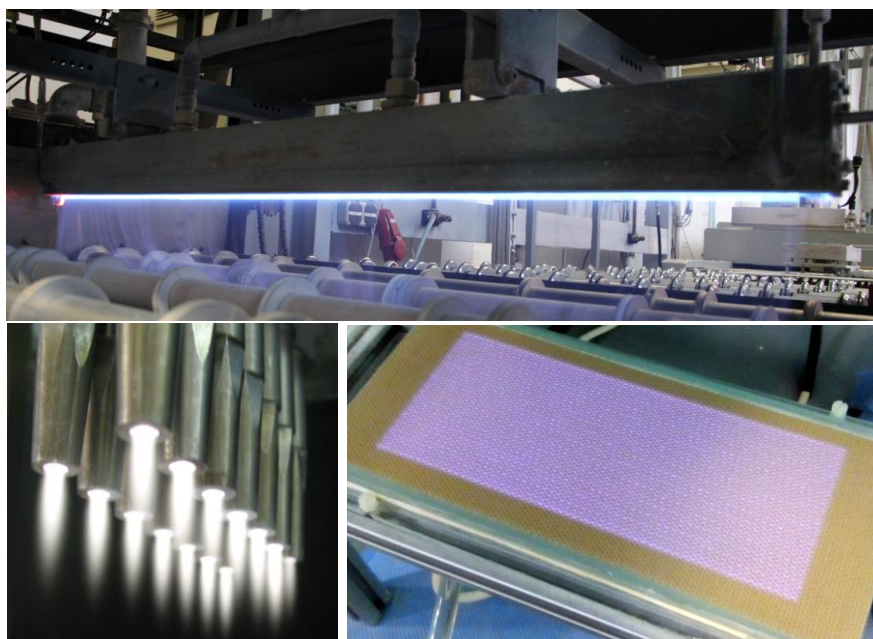
Fig. 1: flame system (top), multi plasma jet (bottom left), DCSBD system with textile on top (bottom right)

Surface analytics were focussed on X-ray photoelectron spectroscopy (XPS, Axis Ultra DLD, Kratos Analytical Ltd., United Kingdom), scanning electron microscopy (SEM, SUPRA 55 VP, Carl Zeiss NTS GmbH, Germany) with energy-dispersive X-ray spectroscopy unit (EDX), microscopy, water contact angle measurements, surface energy measurements and tear off tests based on DIN EN 13934 for the textile strength on one side. On the other side industry oriented methods were applied by C.H. Müller with oil and water repellence tests according to AATCC 118-2007 and lamination experiments after plasma treatment. The repellence test consists of two series of test fluids (oil and water) with different polarities. For each series of fluids graduated surface energies are used and overall 6 droplets are set onto the textile. The evaluation is performed by grades 0 – 6, which gives the number of droplets not sucked into the fabric. High values indicate hydrophobic or oleophobic properties, respectively.

3   Results and Discussion

In general, the tensile strength of the treated textiles was largely unaffected by the plasma treatments even when thermal damages already became visible. Values are spread around 25 MPa. Only extreme conditions like low velocities and a high number of treatment runs in case of flame and plasma jet treatment lead to a significant decrease in tensile strength. Furthermore, in common for all three methods a decrease in static water contact angles from 180° untreated to at least 100° after plasma treatment was observed, in case of plasma jets and DCSBD also ultra hydrophilic properties could be reached. XPS and EDX measurements also revealed a significant decrease in fluorine content at the surface. In Fig. 2 the elemental concentrations of carbon, fluorine and oxygen based on XPS measurements are shown for the plasma jet treatment with different velocities and for DCSBD with different treatment times.
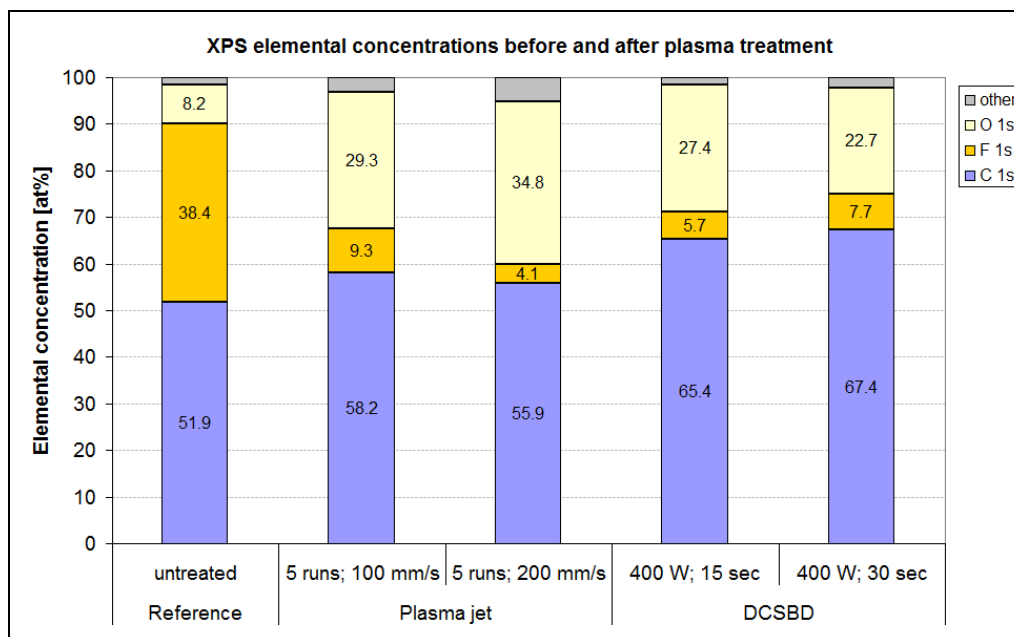
Fig. 2: XPS elemental concentrations of carbon, fluorine, oxygen and others of plasma treated polyester fabrics in comparison to untreated ones

For all plasma treatments a strong decrease in fluorine content at the textile surface can be observed and the same time higher accumulation of oxygen bondings in comparison to the untreated textile reference. A clear tendency in activation due to more intensive treatment parameters could not be determined here. But it has to be mentioned that for the initial textile material itself a significant spreading (not shown here) in elemental composition already occurs, which could be a cause. Fluorine contents between both plasma sources are in the same range. Only some differences for oxygen and carbon respectively its ratio can be noted, which hints to differences in storage conditions (e.g. time) prior to the XPS measurements.

For the industry oriented test methods the focus was set on the plasma jet technique and DCSBD because of higher tendency of thermal damages in the case of using the flame process. In lamination experiments a thermoplastic web was used as adhesive component between two treated textiles. Plasma treated fabrics showed an essential better distribution of the thermoplastic glue during lamination, which resulted also in a stable adhesion. Compound adhesion tests according to DIN 53357 showed no significant changes in adhesion values for plasma treated fabrics, in all these cases only cohesive failures inside the thermoplastic web occurred. Measurements regarding oil and water repellence as well as water contact angle revealed for plasma jet parameters, which led to a wanted hydrophilic behaviour on the treated side but also to an unwanted activation of the back side. In this case the DCSBD treatment was more suitable due to the thin plasma layer of 0.3 mm as can be seen in Fig. 3. Here, results from the repellence test for oil and water are shown for different treatment times and storage times before the measurement, which simulates the time before lamination.
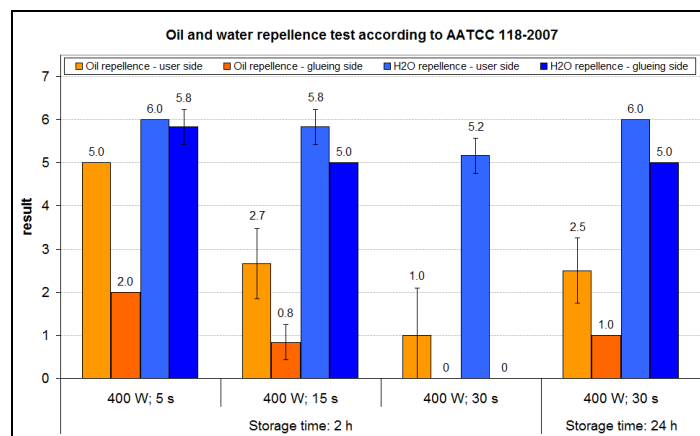
Fig. 3: Oil and water repellence test according to AATCC 118-2007 for DCSBD plasma treated fabrics with different processing times and storage times afterwards

Excellent hydrophobic properties at the user side (high values) as well as strong hydrophilic and oleophilic characteristics at the glueing side (low values) are especially important for the industrial application. This could be achieved in the best way with a DCSBD treatment time of 30 sec. Lower treatment times were insufficient for water as test medium. Also higher storage times of 24 h are leading again to much higher values. Following, the DCSBD application seems to be very useful for one-side treatment of ultra hydrophobic and ultra oleophobic polyester fabrics for improved lamination, but a certain aging effect after plasma treatment with time occurs. In consequence, the lamination has to be done as fast as possible after plasma interaction.

4 Conclusion

It could be shown in these investigations that atmospheric pressure plasmas are suitable to improve the lamination ability of fabrics with ultra hydrophobic / oleophobic finishing. For this the efficiency of the flame-treatment, the jet plasma technique as well as DCSBD was investigated. Best effects for one-sided treatment were achieved with a Diffuse Coplanar Surface Barrier Discharge (DCSBD).

References

1. W. Borgers, ATZ – Automobiltechnische Zeitschrift 105, 11, pp. 1100-1105 (2003)
2. A. Pfuch, Kunststoffe International 3, 16-19 (2007)
3. A. Pfuch, adhäsion KLEBEN & DICHTEN 09, 44-52 (2016)
4. A. Zille, Plasma Process. Polym. 12, 2, 98-131 (2015)
5. M. Černák, Eur. Phys. J. Appl. Phys. 47, 2, 1-6 (2009)
6. http://www.roplass.cz/technology/, accessed 13.04.2016

DEPOSITION OF THIN ZINC FILMS BY ATMOSPHERIC PRESSURE PLASMA JET IN AQUEOUS MEDIA

O. Galmiz, A. Brablec, V. Kudrle

Department of Physical Electronics, Masaryk University, Brno, Czech Republic
E-mail: abr92@sci.muni.cz

Argon plasma jet was operated at atmospheric pressure in contact with aqueous solution of a zinc salt in order to deposit thin films on silicon substrates immersed in the liquid. The thickness of the films was determined by a profilometer while the chemical composition was analysed by XPS technique. The experiments revealed the importance of the submersion depth of the substrate which strongly affects the energy and particle influx.

Keywords: atmospheric plasma jet; thin film deposition; zinc

1   Introduction

The non-equilibrium low-temperature plasma attracts attention due to its wide potential for interesting applications such as surface modification, bacterial inactivation, thin-film deposition, maskless etching, etc. [1, 2]. Among other approaches, capillary plasma jets (e.g. 'plasma pencil', 'plasma needle', APPJ) [2] represent a technique to generate and stabilize non-thermal plasmas at atmospheric pressure numerous. They all differ in design and size, working gas, frequency of applied voltage, etc., but the principle is the same. The plasma is produced inside a nozzle equipped with one or two electrodes and expanded outside the nozzle via a gas flow.

Compared to other non-equilibrium, atmospheric pressure plasmas, jet configurations are considered advantageous in particular for local film deposition or for the coating of 3D surfaces e.g. [3], inner walls of holes, trenches or cavities. Moreover, the jet geometry allows better flexibility in terms of substrate distance and electrical field, as the surfaces to be treated are not necessarily placed between electrodes.

For thin film deposition the use of plasma jets is very attractive since the substrate can reach big sizes. Deposition of different films such as TiO_2, SiO_2 and ZnO using various thin film techniques [2] including those using atmospheric plasma, were already reported.
In the present study the zinc nitrate hexahydrate $Zn(NO_3)_2 \cdot 6H_2O$ has been used as a precursor for deposition of Zn-containing films. The reason for choosing this salt is its low price and that during heating it forms zinc oxide, nitrogen dioxide and oxygen.

In all reported plasma experiments dealing with Zn film depositions these films were obtained only by additives and precursors in the gas phase or by sputtering, respectively. So far, the deposition of these films on substrates directly from liquid solutions by plasma method has not been reported.

2 Experimental set-up

The atmospheric pressure plasma jet "kINPen 09" (Neoplas GmbH, Germany) which generates cold, non-isothermal plasma was used as a plasma source in stationary mode. In Fig. 1 the principal schema of the plasma source is shown. A needle electrode with 1 mm diameter was fed from a radio-frequency (RF) generator (1.1 MHz, 2 - 6 kV peak-to-peak) and was axially mounted into a fused silica capillary with 1.6 mm inner diameter acting also as a dielectric barrier. The plasma ignited at the tip of the needle electrode and was blown outside the nozzle by the gas flow. The working gas was argon (99.99 % purity) at 2 l·min^{-1} or 5 l·min^{-1} flow rate. The length of the visible plasma plume depended on the RF power and was about 10 mm for the power of 7 W, while its diameter was about 1 mm. A detailed description and technical details of the kINPen 09 plasma source can be found e.g. in [4].
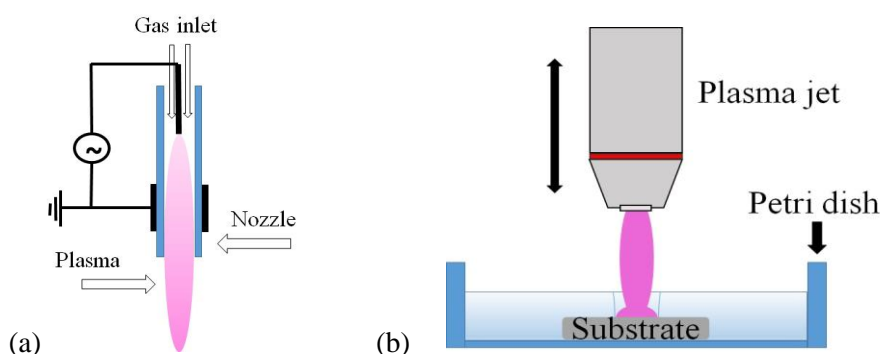
Fig 1: The principal schematics of the kINPen plasma source (a) and the principal drawing of thin film deposition by plasma jet (b), the substrate being completely immersed in the liquid.

3 Results and Discussion

Plasma jet can initiate a decomposition of a liquid solution, followed by the deposition on nearby substrate. A principal schema of such experiment is depicted in Fig. 1 right.

The zinc nitrate hexahydrate salt ($Zn(NO_3)_2.6H_2O$; 98% purity, supplied from Sigma Aldrich) was dissolved in distilled water with resulting concentrations in the 0.01 M (mol per litre) to 0.1 M range. Silicon wafers with 1.5×2 cm dimensions were used as the substrates. Prior to the deposition they were treated with isopropyl alcohol. At least 3 samples for each deposition condition were prepared, following the procedure described in [5].
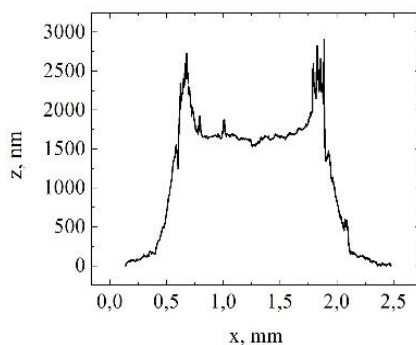
Fig. 2: Typical radial profile of the deposited film. Silicon substrate was treated 4 minutes in 0.01 M $Zn(NO_3)_2$•$6H_2O$ solution. Distance between the nozzle and the solution level was 3 mm, submersion was 3 mm, substrate-nozzle distance was 6 mm and RF power was 7 W.

The thickness of the deposited films was evaluated using a Dektak 8000 profilometer (Veeco). Several scans for each film were carried out in order to obtain average value. To test the stability of the films, the samples were ultrasonicated in distilled water for 15 minutes and then measured by profilometer again. The typical radial profile before ultrasonication is shown in Fig. 2.

Table 1: Thickness of the deposited thin film vs molar concentration of Zn salt in solution and treatment time. Other experimental conditions are the same as in Fig. 2

	$Zn(NO_3)_2.6H_2O$ solution			
	0.01 M	0.01 M after ultrasound	0.1 M	0.1 M after ultrasound
Deposition time [s]	Thickness [nm]	Thickness [nm]	Thickness [nm]	Thickness [nm]
60	221	200	1300	780
90	505	280		
120	800	450	3935	1650
180	1120	620		
240	1670	1140		
300	1800	1350	9040	3150

The chemical composition of the deposited films was analysed by X-ray photoemission spectroscopy (XPS) using ESCALAB 250Xi (ThermoFisher Scientific). In high resolution mode it gave the information about chemical state of Zn, too. Detailed results, including the spectra and atomic percentages, were published in [5] and so only a brief overview is presented here. The main peaks in the survey spectrum were at 1022 eV, 531 eV, 400 eV and 285 eV corresponding to Zn 2p, O 1s, N 1s and C 1s, respectively. Several Auger peaks of Zn (450 - 700 eV), C and O were also present.

In order to reveal the Zn bonds, a deconvolution of highly resolved Zn 2p peak was carried out. The peak was deconvoluted into 3 principal components, see Table 2. The components at binding energies 1021.4 eV, 1022.3 eV and 1023.2 eV were attributed to metallic Zn, ZnO and $Zn(OH)_2$, respectively [6].

Table 2: Relative areas of the main components of the deconvoluted Zn 2p peak

Chemical state	Zn	ZnO	$Zn(OH)_2$
Binding energy	1021.4 eV	1022.3 eV	1023.2 eV
Relative area,%	22	37	41

Taking into consideration the mechanisms and reactions for zinc nitrate decomposition and reduction formulated in [7] as well as mechanisms for direct reduction of the metal ions by the free plasma electrons and the presence of water, following plasma-chemical reactions should be considered:

$$Zn(NO_3)_2 + plasma \rightarrow Zn + NO_2, NO, NO_x \tag{1}$$
$$Zn(NO_3)_2 + plasma \rightarrow ZnO + NO_x \tag{2}$$
$$Zn + H_2O + plasma \rightarrow Zn(OH)_2 \tag{3}$$
$$Zn + H_2O + plasma \rightarrow ZnO \tag{4}$$
$$ZnO + H_2O + plasma \rightarrow Zn(OH)_2 \tag{5}$$
$$Zn(OH)_2 + plasma/temperature \rightarrow ZnO \tag{6}$$

Compared to work [7] it is reasonable to suppose that the same mechanisms (Eq. (1) and (2)) took place also in our experiment. The only difference is that in presence of water Zn oxidises and forms ZnO and $Zn(OH)_2$ as shown by the Eq. (3) - (6). The XPS results discussed above are therefore in agreement with the plausible outcome of these reactions.

4　Conclusion

Atmospheric pressure cold plasma jet kINPen 09 was successfully used to deposit Zn containing films from the hydrated zinc nitrate aqueous solution on a Si substrate. Varying the plasma deposition parameters (concentration of the solution, treatment duration and the distance between the nozzle and the substrate) it is possible to control the deposition quality, growth rate and resulting film thickness.

Acknowledgements

References

1. S. Samukawa et al., J. Phys. D. Appl. Phys. 45 (2012)
2. O. V. Penkov et al., Thin Solid Films 518, 6160 (2010)
3. S. Bornholdt et al., Eur. Phys. J. D 60, 653 (2010)
4. R. Foest et al., Plasma Phys. Control. Fusion 47, B525 (2005)
5. O. Galmiz et al., Open Chem. 13, 198 (2015)
6. B. Crist, Handbooks of Monochromatic XPS spectra-Vol. 2-Commercially Pure Binary Oxides, XPS International (1999)
7. A. Irzh et al., Langmuir 26, 5976 (2010)

IN SITU ATR-FTIR STUDY OF THE FORMATION OF HYDROPEROXIDES THROUGH POSTDISCHARGE TREATMENT OF THIN POLYMER FILMS

R. Duckstein, K. Lachmann, M. Thomas, C.-P. Klages
Fraunhofer Institute for Surface Engineering and Thin Films, Bienroder Weg 53 E, 38108 Braunschweig, Germany

E-mail: rowena.duckstein@ist.fraunhofer.de

Hydroperoxide groups on polymer surfaces are of interest as initiators for the grafting of polymers such as poly(*N*-ispropylacrylamide), forming thermoresponsive layers for biomedical applications. In the present study i*n-situ* ATR-FTIR measurements in combination with NO derivatization reactions are performed to investigate the formation of hydroperoxides on polyethylene surfaces after treatment with atmospheric-pressure dielectric-barrier postdischarges. Gas composition and plasma treatment time are varied in order to obtain a maximum density of hydroperoxide groups on the polymer surface.

Keywords: atmospheric pressure plasma; postdischarge; *in-situ* ATR-FTIR measurement; peroxides; grafting of pNiPAAm

1   Introduction

Surfaces with thermoresponsive properties have often been described in the literature in connection with biomedical applications to achieve, e. g., drug release or control of cell adhesion [1, 2]. The aim of this project is to deposit thin poly(N-ispropylacrylamide) (pNiPAAm) films on polyolefins using plasma activation of the polymer surfaces based on dielectric barrier discharges (DBD) at ambient pressure. Previous studies of DBD-based PECVD of pNiPAAm [3] have shown that a large pulse-pause ratio is necessary in order to obtain the thermoresponsive behavior. Unfortunately, thus deposited layers are not stable in water. This indicates that the polymer has not been covalently bonded to the surface. Therefore, a DBD-based surface activation for a subsequent covalent grafting is being studied. In the present investigation, polyethylene (PE) is treated with a DBD remote plasma in Ar or Ar/O_2 at atmospheric pressure to generate oxygen functional groups. *In-situ* ATR-FTIR measurements with a home-built set up [4] based on multireflectance ZnSe-ATR crystals are performed in order to obtain insight into the formation of hydroperoxide groups and to maximize their area density. Owing to the difficulty to detect and quantify hydroperoxide groups directly by ATR-FTIR spectroscopy and to distinguish these groups from hydroxy groups, chemical derivatization with NO is conducted [5]. It is planned to use the optimized parameters for hydroperoxide formation for modifying plastic films accordingly and then initiate gas phase grafting [6] of NiPAAM to the surface.

2 Experimental
2.1 Film Preparation
Ultrathin LDPE films are prepared as described previously [4].

2.2. *In-situ* ATR-FTIR Measurements

The experimental setup for the measurements has been described previously [4], however, instead of ZnS a ZnSe ATR crystal with the same dimensions was used in order to extend the usable wavenumber range below 1000 cm^{-1}. That way nitrates and nitrites, formed in the reaction of NO with hydroperoxides and hydroxides, respectively, can be detected and quantified, see below. ATR-FTIR measurements are done on a Nicolet 5700, equipped with an MCT detector using s-polarized light and 4 cm^{-1} spectral resolution. All other experimental parameters are listed in table 1. For a better understanding the process scheme is shown in figure 1. For the plasma treatment (**B**) a two-minute series measurement with small time intervals (2 s per spectrum) is performed. Thereafter, spectra are taken with growing intervals during O$_2$ exposure (**C**) (2, 4, 8, … 64 min) and NO exposure (**D**) (2, 4, 8, … 128 min).

Table 1: Experimental parameters of *in-situ* ATR-FTIR measurements on postdischarge-treated polymer thin films.

Gas composition	Gas flow/ L*min^{-1} STP	Treatment time/ s	O$_2$ exposure/ min	NO exposure/ min
Ar	16	8	64	254
Ar-O$_2$ (1000 ppm)	10	10	180	225
Ar-O$_2$ (1000 ppm)	10	30	180	234
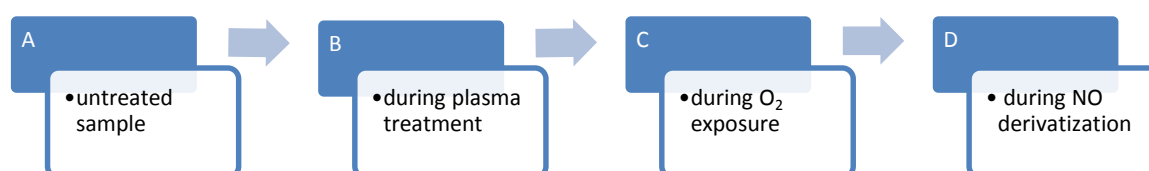
Fig. 1: Process scheme of atmospheric remote plasma treatment with subsequently NO derivatization.

3 Results and Discussion

The formation of hydroperoxides on the polymer surface was quantitatively evaluated based on the area of the secondary nitrates formed after derivatization with NO using the band of the asymmetric NO$_2$ stretching vibration of mostly secondary nitrates at 1630 cm^{-1}. The formula for the calculation of effective thickness d$_e$ for thin films measured with s polarization was taken from ref. [7]. The integrated intensity B [8] for organic nitrates can be found in a paper by Janni et al. [9]. Comparing the ATR-FTIR spectra measured on films treated with Ar plasma and Ar-O$_2$ plasma, respectively, regarding plasma treatment and exposure to O$_2$ it is seen (figure 2 and figure 3) that by Ar plasma treatment less characteristic oxygen bands are visible in the spectrum. After plasma treatment (B) only an OH peak (~ 3450 cm^{-1}) and a C=O peak (1716 cm^{-1}) were detected and after O$_2$ exposure (C) no intense bands could be seen. In

contrast after Ar-O$_2$ plasma treatment there were a lot of oxygen containing groups forming. The intensity of these bands increases with increasing plasma treatment time. An explanation could be that in the Ar-O$_2$ plasma more O atoms are formed [10]. The O atoms abstract H atoms from polymer chains resulting in C radicals which react with O$_2$ to peroxide radicals. However, more O atoms initiate secondary reaction and further oxidation reactions take place [11]. These processes seem to extend beyond the plasma treatment. Nevertheless, the Ar plasma treatment generates the larger amount of hydroperoxides compared to the Ar-O$_2$ (1000 ppm) plasma treatment. This is confirmed by NO derivatization (figure 4). On the one hand a more intense negative peak at 3400 cm^{-1} is obtained, indicating a decrease of hydroperoxide OH by resulting nitrate formation. On the other hand, all three characteristic bands (1630, 1277 and 863 cm^{-1}) for secondary nitrate groups are detected. For Ar-O$_2$ plasma treatment only the most intense nitrate band at 1630 cm^{-1} could be produced. The calculated values for the hydroperoxide density are shown in figure 5. It should be noted that after Ar plasma treatment only 1 h and for Ar-O$_2$ treatments 3 h O$_2$ exposure took place. Moreover, for Ar plasma treatment the NO derivatization time was 2 h and for Ar-O$_2$ plasma treatments it was totally 4 h. To compare the processes the peak intensities after 2 h derivatization were used. Also nitrites (1660 cm^{-1}) are obtained by derivatization of alcohols. But the quantification is somewhat more difficult because a broader peak is formed in front of the nitrate peak at 1630 cm^{-1}.
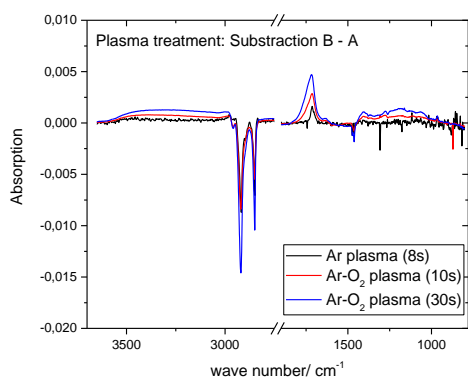
Fig. 2: Change of PE surface through post-discharge plasma treatment with different gas compositions and treatment times.
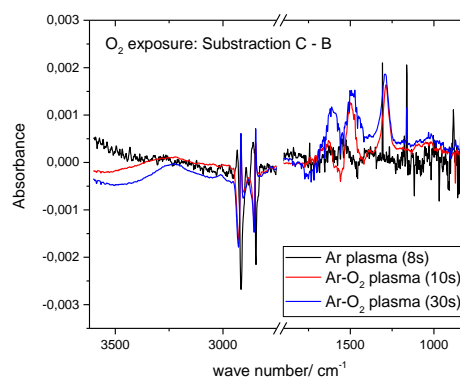
Fig. 3: Change of PE surface through O$_2$ exposure after postdischarge plasma treatment.
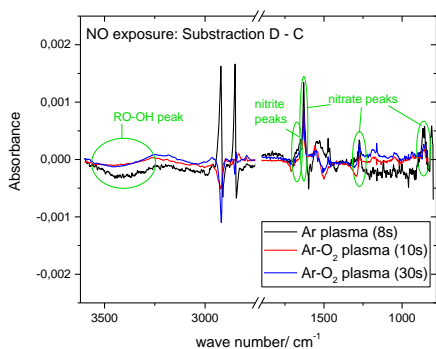
Fig. 4: Change of PE surface through NO derivatization after postdischarge plasma treatment and O$_2$ exposure.
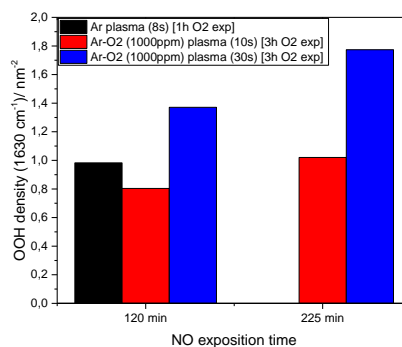
Fig. 5: Density of hydroperoxide groups using nitrate peak at 1630 cm^{-1} [4].

4   Conclusion

It could be shown that, within the studied parameter range, the largest hydroperoxide density is generated by postdischarge plasma treatment in nominally pure Ar. Oxygen in the gas mixture results in the formation of other oxygen species on the surface which may compete with the hydroperoxide in any form. However, such occurrence must be examined in more detail. Furthermore, it is planned to examine other possible oxygen-free gas compositions such as Ar-H_2 and N_2 in order to confirm the previous results.

References

1. E. Manek et al., Eur. Polym. J. 68, 657 (2015)
2. Y. Kumashiro et al., Colloid Surface B 106, 1977 (2013)
3. K. Lachmann et al., Plasma Med. 2, 127 (2012)
4. C.-P. Klages et al., Plasma Process. Polym. 10, 948 (2013)
5. D. J. Carlsson et al., Polym. Degrad. Stabil. 17, 303 (1987)
6. K. Olafsen et al., J. Appl. Polym. Sci. 46, 1673 (1992)
7. N. J. Harrick et al., Appl. Optics 10, 19 (1971)
8. A. S. Wexler, Appl. Spectrosc. Rev. 1, 1 (1967)
9. J. Janni et al., Spectrochim. Acta A 53, 1375 (1997)
10. S. Abou Rich et al., J. Phys. D.: Appl. Phys. 47, 1 (2014)
11. M. Mafra et al., Plasma Chem. Plasma Process. 28, 495 (2008)

WIDE-PRESSURE-RANGE COPLANAR DIELECTRIC BARRIER DISCHARGE FOR HYDROCARBON CONTAMINATION REMOVAL IN SCANNING ELECTRON MICROSCOPY

J. Dugáček, P. Sťahel, J. Čech, J. Jurmanová

CEPLANT – R&D Centre For Low-cost Plasma and Nanotechnology Surface Modifications, Masaryk University, Kotlářská 2, 611 37 Brno, Czech Republic

E-mail: 373920@mail.muni.cz

Unwanted organic contamination of the surface of SEM samples or vacuum chambers often causes reductions of the SEM image quality, e. g. brightness or contrast of image, which worsen over time. This is the reason why the regular cleaning of the surface of the sample or vacuum chamber is necessary. In the presented paper, a novel method for SEM samples organic decontamination based on wide-pressure-range coplanar dielectric barrier discharge was investigated. WPR-CDBD efficiency for various organic compounds' removal, including heavy hydrocarbons, was proved. Comparison with standard commercial plasma decontaminator XEI working with remote plasma was made.

Keywords: plasma; discharge; WPR-CDBD; decontamination

1   Introduction

Unwanted surface contamination of samples and surfaces is a large problem in various analytic methods like scanning electron microscopy (SEM). There are numerous existing methods of removing surface contaminants, like UHV RF discharge [1], DCSBD [2], plasma torch [3], corona discharge, dielectric barrier discharge, MW discharge, gliding arc or plasma jets [4]. The applicability of these methods is limited by the plasma source characteristics as the work pressure range (usually narrow), etching rate (usually slow), damage of samples suffered by plasma treatment, geometry limitations (thickness of active plasma), homogeneity or limited plasma source lifetime. In the presented work, we have tested a novel technique for removing the surface contamination using a wide-pressure-range coplanar dielectric barrier discharge (WPR-CDBD). The advantages of WPR-CDBD plasma source for organic contamination removal are its easy operability in wide pressure range of operation, from superatmospheric pressure to high vacuum, with damaging the samples and unwanted sputtering of material from electrode on the surface of the treated sample. Moreover, the geometry of this plasma source allows the treatment of objects with arbitrary thickness. The possibility to use this plasma in a large interval of pressures opens the door to in situ applications of plasma cleaning process of samples, as well as the whole reaction chamber.

2   Experimental

The wide-pressure-range coplanar dielectric barrier discharge (WPR-CDBD) consists of a pair of a pair of 1.5 mm wide interlocking comb electrodes embedded in 0.1 mm wide glass-ceramic dielectrics forming 5 interelectrode gaps of 45 mm length and 1 mm width. Its construction allows operation in a wide pressure range, from 10^{-4} Pa to 10^6 Pa what gives room for testing emerging applications. According to our previous research [5] the WPR-

CDBD at near to atmospheric pressure forms a sub-millimetre thin plasma layer with filamentary structure, that can in certain applications cause damage to the treated surfaces and the quality of decontamination may vary depending on the type of contamination and the surface structure of the treated sample. At lower pressures, the discharge shifts into 'low pressure' regime, where its structure becomes more homogeneous and less luminous. Decontamination in low pressure mode is more homogeneous and treatment range increases to 10 cm.

Plasma decontamination experiments were performed in the vacuum chamber. The decontamination efficiency was studied in a pressure range from 10 Pa to 130 kPa. The sub-atmospheric conditions were maintained using a scroll pump. The pressure was controlled using a needle valve.

The organic contamination was artificially deposited on a substrate of a c-Si wafer because c-Si has well known properties and no organic contamination comes in bulk. As model contaminants, oleic acid, stearic acid, cetyl alcohol, motor oil and sucrose were used. Oleic acid was dropped on the surface, stearic acid and cetyl alcohol were melted and poured on the surface, sucrose was dissolved in water and motor oil was dissolved in toluen.

The effect of sample cleaning was primarily tested using SEM, where contamination causes a reduction of brightness of samples. This effect becomes stronger over time while the same part of the sample is scanned. Beam deceleration mode was used to make this effect more visible. The effect was typically viewed by zooming in a part of the sample, scanning it for a fixed period of time, subsequently zooming out. Image of this surface shows the previously scanned area and its immediate surroundings, the previously scanned area is a dark square in the centre of the image. For comparison of results, these snaps have to be taken with the same brightness and contrast. This method is not quantitative because of the dependence of the lightness on the amount of contaminant is not known. Quantitative analysis of cleaning effects was done by weight measurement of the samples before and after subsequent decontamination process steps using an analytical balance. This allowed us to study the dependence of amount of contaminant removed as a function of cleaning time and correlate it with plasma conditions.

3   Results and Discussion

WPR-CDBD works in the pressure range from atmospheric pressure to high vacuum. In various pressures, the structure of the discharge and also its volume significantly change. Figure 1 shows the discharge performed at atmospheric pressure and at 10 Pa, both fed by the same power, 15 W. Discharge at atmospheric pressure is very short. At the pressure of 10 Pa, the discharge is uniform and its reach is much greater.

We have tested the cleaning efficiency of the discharge for various pressures. Figure 2 shows the decrease of weight of a sample contaminated with oleic acid after each subsequent cleaning step at two different pressures, atmospheric pressure and 10 Pa. Decontamination of

sample at the same condition i.e. the same pressure and power using XEI Zephyr Plasma Cleaner, a commercial plasma decontaminator, was taken as a reference.
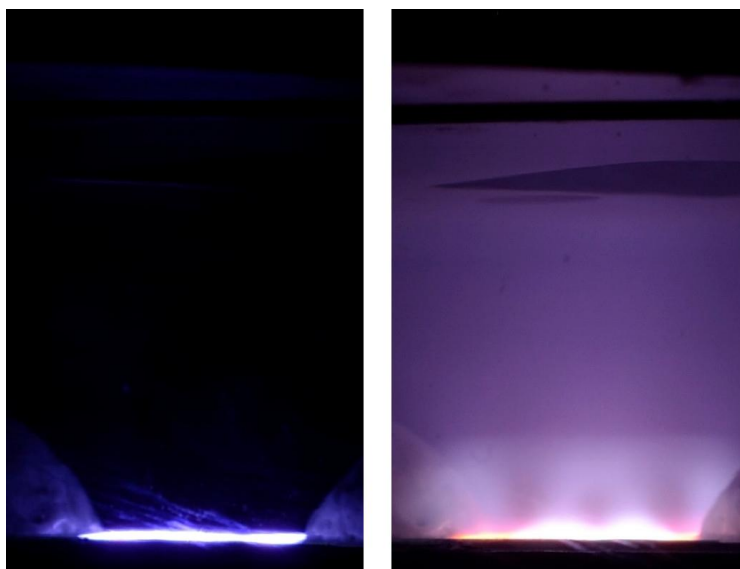
Fig. 1: Appearance of the WPR-CDBD discharge in atmospheric pressure (left) and 10 Pa (right).
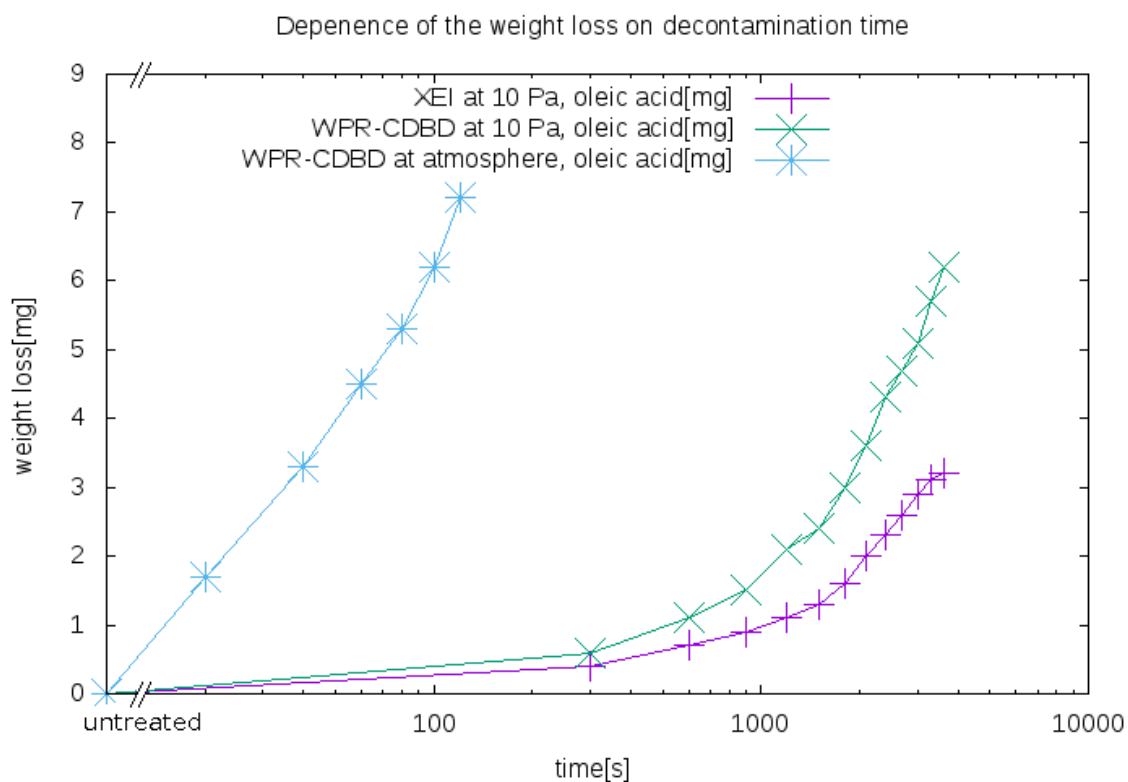
Fig. 2: Dependence of the weight loss of samples containing organic contamination as a function of plasma decontamination time.

Plasma decontamination in high pressure regime shows a fast decrease of weight during first two minutes of cleaning, i. e. 7 mg of oleic acid was decomposed in this time what corresponds with decontamination rate about 3,5mg/min. The process of decontamination in low pressure regime was slower, we obtained 6.2 mg of weight loss during first one hour of treatment, which corresponds to 0.1 mg/min. Cleaning process with commercial cleaner XEI

289

that uses remote plasma was much slower than WPR-CDBD, removing only 2.8 mg of contamination, which is approximately 0.04 mg/min.

The speed of the decontamination process depends strongly on pressure. This is most likely caused by the significant increase of the volume of the discharge at low pressure and with this related lower power density

4 Conclusion

We have shown that wide-pressure-range coplanar dielectric barrier discharge is a favourable tool for removal of organic contaminants from samples in range of pressure from atmospheric to high vacuum. The cleaning process at atmospheric pressure was very strong, the effect is clearly visible after 1 minute of cleaning, however cleaning range is very limited. The cleaning process in lower pressure is slower, but its ability to decompose various organic contaminants is superior to that of a commercial decontaminator using remote plasma. We showed that plasma decontaminator based on WPRCDBD works in a wide range of pressures, allowing to adapt it to various applications accordingly to their requirements.

References

1. M. González Cuxarta et al., Appl. Surf. Sci., 362 (2016)
2. T. Homola et al., Appl. Surf. Sci., 258 (2012)
3. G. Dinescu et al.., Fusion Eng. Des., 82 (2007)
4. V. Scholtz et al., Biotechnol. Adv., 33 (2015)

STUDY OF SURFACE PROPERTIES OF THE PLASMA-TREATED HIGH DENSITY POLYETHYLENE

H. Dvořáková, M. Stupavská, V. Buršíková, P. Sťahel

Masaryk University, Kotlářská 2, 611 37 Brno,Czech Republic

E-mail: hana.dvorakova@mail.muni.cz

Plasma treatment of polymers is frequently used for increasing the surface energy in order to improve wettability and adhesion properties. In this paper the changes of surface properties (surface energy, surface atomic composition, roughness) plasma modified polyethylene was studied. High density polyethylene was treated using Diffuse Coplanar Surface Barrier Discharge in ambient air. Surface energy was estimated using sessile drop contact angle measurement. Through this changes in chemical composition were analyzed via XPS. The surface roughness was investigated using AFM.

Keywords: plasma treatment; polyethylene; surface roughness; surface energy

1 Introduction

High density polyethylene (HDPE) is often used industrial polymer due to excellent mechanical properties and high chemical resistance. However a number of applications require a pre-treatment in order to increase surface energy. Plasma treatment is a universal method, which also enables to modify large scale of surface properties (e.g. surface energy, hardness, roughness, degree of crosslinking and chemical composition) without changing the bulk properties. [1, 2, 3, 4, 5, 6]

The aim of this work was to characterize the surface properties of plasma treated HDPE (surface energy, atomic composition and morphological parameters). Plasma modification was performed using Diffuse Coplanar Surface Barrier Discharge at atmospheric pressure in ambient air. The relationship between detected surface energy, concentration of oxygen and surface morphology is discussed.

2 Experimental

High density polyethylene plates manufactured by injection molding technology and with dimensions of 2.5 x 9.5 cm were used as substrate in this study.

Samples were modified using so called Diffuse Coplanar Surface Barrier Discharge (DCSBD) [7] operating at 30 kHz with power density 3.75 W/cm^2. Processing gas was an ambient air at atmospheric pressure and treatment times varied from 1.5 s up to 10 s. Distance between sample and plasma source was set at 0.2 mm.

Wettability and surface energy (SE) of samples was determined by measurement of static contact angle of two standard liquids (water and diiodomethan) using the sessile drop method. Surface energy was calculated using Owens, Wendt, Rabel and Kaelble model.

The surface atomic composition was analyzed by X-ray photoelectron spectroscopy (XPS) using spectrometer ESCALAB 250Xi. The system is equipped with 500 mm Rowland circle monochromator with microfocused Al Kα X-Ray source. An X-ray beam with power of 200 W and spot size of 650 microns was used. The spectra were acquired with pass energy of 20 eV and resolution of 0.1 eV and were referenced to the hydrocarbon type C 1s component set at a binding energy of 284.8 eV.

A surface morphology was investigated using atomic force microscope (AFM) Park NX 10 in semicontact mode. Dimensions of the analyzed areas were 4×4 μm and mean roughness (R_a) Root mean square roughness (R_q), Kurtosis (R_{ku}) and Skewness (R_{sk}) were used to quantify the surface morphology.

3   Results and Discussion

Hydrophilic modification is primarily the result of oxidative reactions between the surface of sample and plasma active species, which create new functional groups on the surface. In general, a higher concentration of oxygen on the surface causes higher values of SE [8]. Fig. 1 shows the value of SE and O/C ratio as a function of plasma treatment time. The value of SE increases rapidly with the treatment time in the course of the first 5 seconds of the plasma treatment. For the longer exposures the SE value did not change significantly. This corresponds with the increase of O/C ratio during the first 5 seconds of the treatment. The stagnation of SE value for longer exposure times indicates that the surface concentration of oxygen is not the only factor influencing the wettability of the plasma-treated samples in this case.
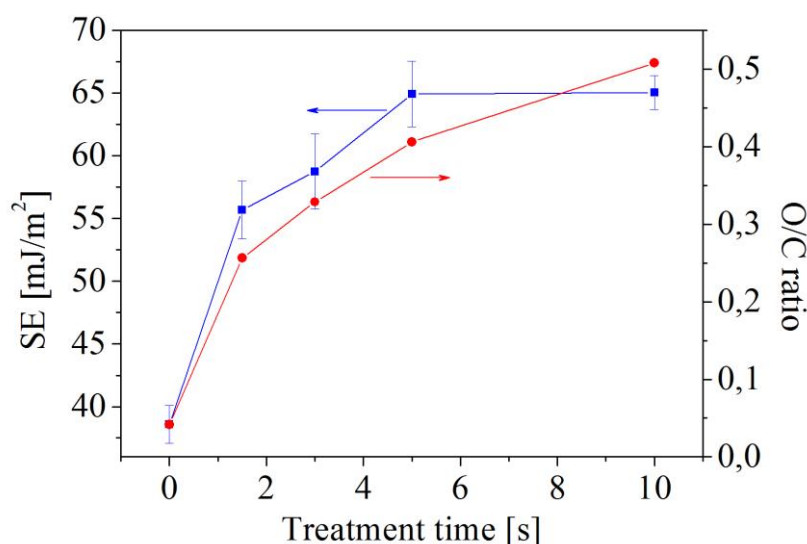
Fig. 1: Value of surface energy and O/C ratio as a function of the exposure time.

Besides the changes in the surface atomic composition, the plasma treatment can modify the surface topography by etching [9]. The increase of wettability with increasing roughness was originally described by Wenzel [10]. Generally, the hydrophilic rough surface has a better wetting than a smooth surface with identical value of SE. Morphological parameters as a function of treatment time are presented in Tab. 1. R_a and R_q decreased with increasing

treatment time. An increase of R_a and R_q was observed only on samples treated for 10 seconds. Kurtosis and Skewness decreased with an increasing treatment time, which indicates more rounded peaks and more plateau-like surface. The slope of peaks influences the wetting properties, therefore R_{ku} and R_{sk} can affect the value of SE, determined using the measurement of contact angle. In nanometres range, the roughness did not affect the surface wettability. Nevertheless, the R_a and R_q belong among significant factors affecting adhesion properties. [11, 12, 13]

Tab. 1: Morphology parameters determined by AFM analysis as a function of the exposure time.

Treatment time [s]	R_a [nm]	R_q [nm]	R_{ku} [nm]	R_{sk} [nm]
0	25 ± 2	31 ± 3	3.1 ± 0.3	0.67 ± 0.07
1.5	21 ± 2	26 ± 3	2.3 ± 0.2	0.40 ± 0.04
3	20 ± 3	25 ± 2	2.2 ± 0.3	0.28 ± 0.05
5	16 ± 2	20 ± 2	2.1 ± 0.1	0.28 ± 0.04
10	25 ± 1	30 ± 1	2.0 ± 0.1	0.23 ± 0.03

4 Conclusion

The changed wettability after the plasma treatment is the result of chemical and morphological changes of the treated surfaces. Their contributions are difficult to be distinguished due to their simultaneous formation. Surface energy increases with increasing treatment time, however for longer treatment times its value increases only slightly. AFM measurement shows that the wettability could be affected by decreasing of parameters R_{ku} and R_{sk} concurrently with an increasing treatment time.

Acknowledgements

References

1. C. M. Chan et al., Surf. Sci. Rep. 24, 1 (1996)
2. J. Peyroux et al., Appl. Surf. Sci. 315 (2014)
3. S. Wu et al., Polymer. Int. 52, 9 (2003)
4. M. Noeske et al., Int. J. Adhes. Adhes. 24, 2 (2004)
5. M. R. Sanchis et al., Eur. Polymer. J. 42, 7 (2006)
6. G. Borcia et al., Appl. Surf. Sci. 221, 1 (2004)
7. M. Šimor et al., Appl. Phys. Lett. 81, 15 (2002)
8. R. Dorai et al., J. Phys. Appl. Phys. 36, 6 (2003)
9. N. Y. Cui et al., Appl. surf. sci. 189, 1 (2002)
10. R. N. Wenzel, Ind. Eng. Chem. 28, 988 (1936)
11. J. D. Miller et al., Polymer. Eng. Sci. 36, 14 (1996)
12. H. J. Busscher et al., Colloid. Surface. 9, 4 (1984)
13. Y. Y. Wang et al., Thin Solid Films 485, 1 (2005)

FAST LOW-COST HYDROPHILIZATION OF SURFACES USING PLASMA POLYMERISATION

H. Dvořáková, M. Štipl, J. Čech, J. Jurmanová, P. Sťahel

Masaryk University, Kotlářská 2, 611 37 Brno,Czech Republic

E-mail: hana.dvorakova@mail.muni.cz

Plasma modification of surfaces is often used method in different applications. The aim of this work is to find the way to solve two main disadvantages of plasma activation of surfaces- aging effect and limited surface hydrophilicity by means plasma deposition. High precursor consumption was compensated by use of cheap propane-butane in volume concentration 0.75%. Highly hydrophilic layers were created for deposition times in the order of seconds.

Keywords: plasma polymerisation; propane-butane; polyethylene; surface energy; wettability

1 Introduction

Atmospheric pressure plasma discharges are often used for modification of surfaces in order to wettability improvement. Plasma treatment in pure gasses and their mixtures (e.g. argon, oxygen, air) introduces new functional hydrophilic groups onto the substrate surface [1, 2, 3]. The disadvantage of this method is only the limited hydrophilicity of surface depending of type of functional groups and so called aging effect, which decreases the wettability in time after the plasma treatment due to the post-plasma surface reactions with gases of ambient atmosphere and due to the molecular mobility (reorientation and diffusion of plasma-created functional groups) [4]. Hydrophilization via plasma deposition enables creation of layers with high surface energy, selective cell adhesion, high adhesion and barrier properties with good time stability. [5, 6, 7]

Plasma deposition using low pressure plasma sources is traditionally in a large scale of industrial applications [5, 8, 9]. The disadvantage of these methods is requirement of expensive and unpractical vacuum system. Hence the solutions to plasma polymerisation at atmospheric pressure (AP) are investigated nowadays. Atmospheric pressure deposition methods do not require expensive vacuum system. However, in comparison with vacuum deposition it has significantly higher consumption of the precursor.

Our new hydrophilization technique based on atmospheric pressure discharge in nitrogen with small admixture of non expensive monomers propane and butane (PB) in volume concentration below 1%. This non toxic and non expensive gas has great potential for preparation of hydrophilic surfaces with high adhesion strength [9, 10]. The aim of this work was fast and cost effective preparation of high hydrophilic surfaces using PB plasma polymerisation. Wettability of deposited layer was characterized using water contact angle (WCA) and surface energy (SE). Surface morphology was investigated via scanning electron microscopy.

2 Experimental

High density polyethylene (HDPE) plates with dimensions 2.5 × 9.5 cm were used as substrate in this study. The surface energy of untreated samples was 38.6 mJ/m^2.

Plasma deposition was performed using Diffuse Coplanar Surface Barrier Discharge (DCSBD) at atmospheric pressure [11]. Discharge was generated using sine-wave high voltage generator with the frequency of 30 kHz and with power density of 3.75 W/cm^2. Processing gas was pure nitrogen with small admixture of propane and butane (volume concentration propane 0.25% and butane 0.5%). Total gas flux was kept at 2 L/min. The distance 0.1 mm between sample surface and electrode was kept in this study and deposition times were varied from 0.5 s up to 15 s.

Wettability and surface energy of samples was calculated using static contact angles of water and diiodomethane measurement. Surface energy was calculated by Owens, Wendt, Rabel and Kaelble model.

Surface morphology was investigated by Scanning Electron Microscope (SEM) at the voltage of 15 kV. Samples were covered with a thin gold layer.

3 Results and Discussion

Fig. 1 shows WCA and SE as the functions of deposition time. DCSBD was used as plasma source. SE sharply increased already after the first second of deposition, however for longer deposition time it increased only slightly. The minimum WCA (13°) was achieved for deposition time 5 seconds. A comparison of the progress of WCA and SE suggests that the increase of SE value is mainly the result of the acid-base component gain. The surface properties become more homogenous with increasing deposition time. This manifests itself by significant reduction of error of WCA measurement. The increase of surface homogeneity with deposition time could be a consequence of the filamentary character of the DCSBD [6].
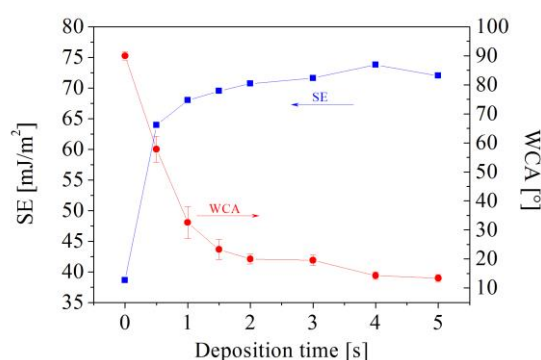
Fig. 1: Dependence of SE and WCA value on time of plasma deposition. Time 0 s represents untreated HDPE sample.

Fig. 2 shows the SEM images representing the changes in the surface morphology after plasma deposition using DCSBD.

Surface of untreated samples showed the lamellar structure typical for polyethylene [12]. After 5 seconds of deposition the surface became smoother and the lamellar structure partially

vanished. This can be the result of both plasma etching and overlapped with a new polymer layer.
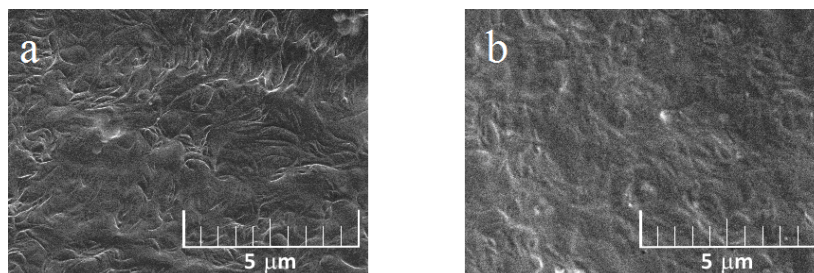
Fig. 2: SEM images of surface morphology of untreated HDPE (a) and HDPE after 5 seconds of deposition (b).

4   Conclusion

HDPE samples were modified by means of deposition of hydrophilic thin layers of plasma polymer using DCSBD plasma sources. Processing gas was nitrogen with a negligible admixture of propane-butane (less than 1 %), selected owing to its low cost and non toxicity. Wettability and homogeneity of the deposited layer increased with increasing deposition time. The saturated values of WCA and SE were 14° and 74 mJ/m^2. For comparison, plasma treatment in the pure nitrogen produces the surfaces with values of SE around 55 mJ/m^2 and WCA around 40° [13]. This means, that plasma deposition provides the surfaces with significantly better wetting properties, although the treatment time was in order of seconds in both cases.

SEM images showed that the sample surface became smoother and deposited layer was without pinholes or structural defects.

References
1. M. Noeske et al., Int. J. Adhes. Adhes. 24, 2 (2004)
2. M. Lehocký et al., Colloid. Surface. A 222, 1 (2003)
3. R. Dorai et al., J. Phys. D Appl. Phys. 36, 6 (2003)
4. Y. Ren et al., Surf. Coat. Tech. 202, 12 (2008)
5. H. Biederman, Vacuum, 37, 3 (1987)
6. M. Lehocky et al., J. Mater. Process. Tech. 209, 6 (2009)
7. M. Lehocky et al., J. Chem. Technol. Biot. 82, 4 (2007)
8. F. Massines et al., Plasma Process. Polym. 9, 11 - 12 (2012)
9. I. Amir et al., Chem. Listy 103 (2009)
10. M. Jasso et al., Source: Surf. Coat. Tech. 201, 1 (2006)
11. M. Šimor et al., Appl. Phys. Lett. 81, 15 (2002)
12. A. Peacock, Handbook of polyethylene: structures: properties, and applications (CRC Press, 2000)
13. M. Šíra et al., J. Phys. D: Appl. Phys. 38, 4 (2005)

ELIMINATION OF DIAZINON INSECTICIDE FROM CUCUMBER SURFACE WITH LOW TEMPERATURE PLASMA TREATMENT

H. Ghomi[1], N. Dorraki[1], N. N. Safa[1], V. Mahdavi[2], A. Ghasempour[2]

[1]Laser and Plasma Research Institute, Shahid Beheshti University, Evin1983963113,Tehran, Iran

[2]Medicinal plants and drugs Research Institute, Shahid Beheshti University, Evin1983963113,Tehran, Iran

E-mail: h-gmdashty@sbu.ac.ir

Food industry constantly searches for new technologies to improve commercial sterilization process of agricultural commodities. The plasma application may offer a novel and efficient method for removal pesticide from agricultural product surfaces. The degradation effects of plasma opens up a novel route for the development of advanced technologies for the elimination of pesticide contamination. Cucumber, as a popular vegetable, is the fourth most widely cultivated vegetable crop in the world after tomato,cabbage, and onion. Diazinon residue remain in greenhouse cucumber in fruit and vegetable markets and most of the time by washing it will not remove. We have studied degradation of diazinon on the surface of cucumber by air dielectric barrier discharge. The concentration of diazinon before and after plasma treatment were analyzed by gas chromatography/mass spectrometry (GC/MS) to determine plasma degradation effect. It was found that by 15 minutes plasma treatment , all diazinon (50 PPM) on the surface of cucumber are approximately degraded. Experimental results indicate degradation efficiency by air-DBD plasma depends on plasma treatment time, discharge power and diazinon concentration.

Keywords: plasma; DBD; diazinon; cucumber

1   Introduction

Pesticides are widely present in the environment, including water and soils, agricultural products and foodstuffs, as a result of the application of phytosanitary products in modern agriculture. In the last years, new pesticides, which show a more specific mode of action and have a higher polarity and lower persistence than old ones, have Diazinon (O,O-Diethyl O-[4-methyl-6-(propan-2-yl)pyrimidin-2-yl] phosphorothioate) is a phosphorothioate insecticide with a pyrimidine ring attached to it with widespread agricultural and non agricultural uses in Iran.

Various physic-chemical methods like photocatalysis , ozonation , ultrasonication , ionizing radiation and non-thermal plasmaus have been used for organoposphate pesticides decomposition. The present of electrone, UV radiation, excited and reactive species such as O, O_2^+, O_3, OH^-, NO, NO_2 in the plasma which have oxidative effects, make it more efficient in comparision with the other methods [1, 2].

In these recent years, only a few number of studies have indicated successful pesticides degradation by non-thermal plasma. Mirsa et al. demonstrated the successful degradation of pesticide residues on strawberries by dielectric barrier discharge plasma [3]. They decreased

the levels of azoxystrobin, cyprodinil, fludioxonil and pyriproxyfen after 5min plasma treatment at 80 kV. Bai et al. also demonstrated O_2 plasma-induced degradation of dichlorvos and omethoate mechanisms onto maize samples [4] and in an another work, they illustrated successful degradation of dichlorvos pesticides coated on glass slides by radio frequency O_2 oxygen [5]. In this work, in order to have an effective and economical method, atmospheric-pressure air-DBD has been used as the plasma source.

Cucumber, as a popular vegetable, is the fourth most widely cultivated vegetable crop in the world after tomato,cabbage, and onion. Per capita consumption of cucumbers in Iran is 32 Kg/ year because of high and fresh consumption of cucumber that shows the importance of cucumber sterilization. In this study, a QuEChERS (acronymic name for quick, easy, cheap, effective, rugged and safe) method used for extraction of diazinon from cucumber samples. The method is based on the extraction with acetonitrile, followed by an induced liquid–liquid partition after the addition of salts and a dispersive solid-phase extraction (d-SPE) cleanup step [6].

2 Experimental

1.1. Cucumber sample preparation

An individual diazinon stock solution containing 1000 mg L^{-1} was prepared in acetone and stored at -18 °C. The surface of a fresh cucumber was coated by using spray-out with the diazinon insecticide standard solution at 0.032 and 0.020 ppm, respectively. The cucumbers were then exposed to the plasma.

1.2. Experimental plasma apparatus

An arrangement of DBD plasma was used for this study. Upper electrode was made of copper which was covered by 1 mm-thick quartz as dielectric barrier. A stainless steel grounded mesh was used as the second electrode in contact with the quartz to make a homogenous DBD plasma. The sample was put on the sample holder which was grounded at a distance of 2 mm from the grounded mesh. A 6 kHz DC-pulsed high voltage which is variable from 0-14 kV was applied to the electrodes. Fig 1(a) shows current voltage digram at 14 kV. This study has been done for two different discharge powers which determined by lissajous curves (Fig 1(b)).
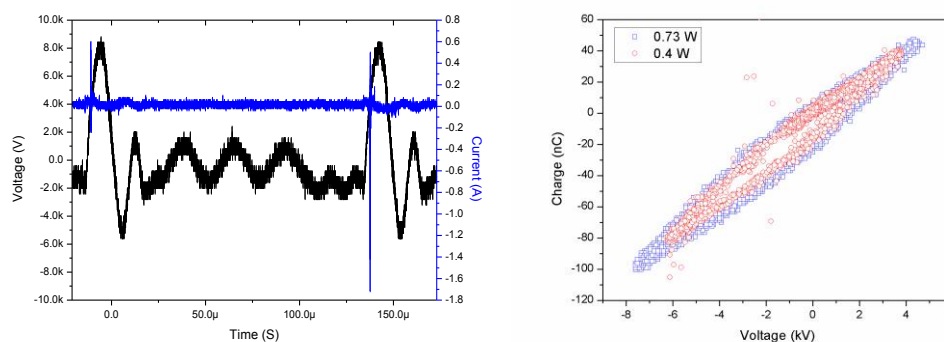
Fig 1. (a) Current and voltage waveforms of the DBD discharge generated at 14 kV, (b) Lissajous curve a 0.73 and 0.4 W.

1.3. Quenchers extraction and cleanup

The QuEChERS procedure for cucumber samples was as follows: (1) weigh 10 g homogenized and blended cucumber into a 50 ml polypropylene centrifuge tube; (2) 15 ml of ACN (Acetonitrile) with 1% Acetic acid (3) shake with a wrist action shaker for 1 min; (4) add 6 g $MgSO_4$, 1 g NaCl and 1.5 g $C_6H_5O_7Na_3.2H_2O$; (5) shake the tube immediately and vigorously for 1 min by vortex; (6) centrifuge the tube at 3450 rpm for 5 min; (7) transfer 5 ml of the ACN extract to a 15 ml PTFE d-SPE clean-up tubes containing 4 g of anhydrous $MgSO_4$ + 1.2 g of primary and secondary amine (PSA) + 0.06 g of GCB for sample cleanup; This procedure is of crucial importance to maximize the sensitivity of diazinon extraction and to minimize the presence of interfering compounds in the extract. The mixture was shaken in a vortex and centrifuged for 2 min at 3450 rpm. Then, all (4.5ml) aliquot of the extract was evaporated under a gentle stream of nitrogen to near dryness and the residue was taken up with 0.25 ml of aceton and was filtered through a 0.22 μm Millipore PTFE filter membrane prior to GC/NPD analysis.

3   Results and Discussion

To show the effects of plasma treatment on the reduction of diazinon on the surface of cucumbers, the diagram of diazinon residue (solute concentration of 0.033 ppm) as a function of plasma treatment time is shown in Fig 2(a). Plasma effects on diazinon residues with two different concentration; 0.033 and 0.020 ppm, are shown in Fig 2(b).
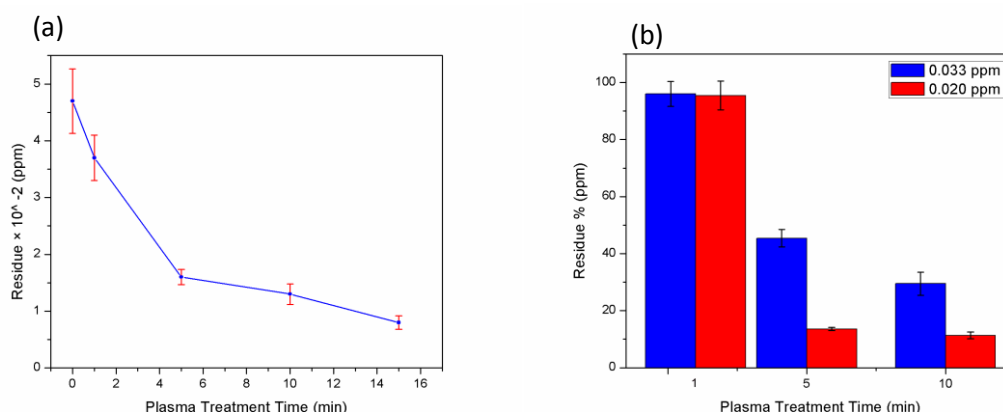
Fig 2. (a)Effect of plasma treatment time on diazinon residue (diazinon concentration of 0.033 ppm), (b) comparison of plasma treatment on two different diazinon concentration (0.033 and 0.020 ppm).

It can be noticed that the diazinon residue decreases sharply with increasing plasma treatment. This indicates that the treatment time is the most influential parameter and the longer treatment time can speed up the reduction efficiency of pesticide.
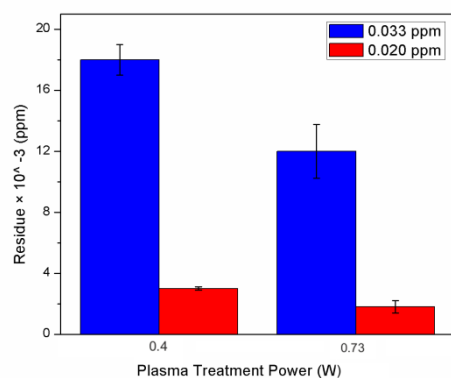
Fig 3. Effects of plasma power on diazinon residue with two different concentration at 10 minutes plasma treatment time on the surface of cucumbers.

In this way, we examined effects of plasma discharge power on the reduction of diazinon on the surface of cucumbers at 10 minutes plasma treatment time for two different concentration of diazinon on the surface of cucumbers. The remaining fraction of diazinon versus discharge power is shown in Fig 3. The results show further increasing the discharge power enhances degradation of diazinon. These results can show the reduction effects of reactive species in air plasma like oxygen reactive species which can increase reduction speed of diazinon.

4   Conclusion

Dielectric barrier discharge as an atmospheric pressure cold plasma type can offer a novel method for removal pesticide from agricultural products. In this study, reduction of diazinon on the surface of cucumber by dielectric barrier discharge are shown. Increasing plasma treatment time shows reduction enhancement in diazinon residue on the surface of cucumbers. This reduction can be a reason of chemical reaction of reactive species in air plasma like oxygen reactive species which increase reduction of diazinon. Furthermore, improving plasma discharge power can reduce plasma treatment time. More research effort must be undertaken to evaluate the projected cost of the treatment for large quantities of agricultural products.

References

1. A. Moghadamnia et al., *An epidemiological study of poisoning in northern Islamic Republic of Iran,* 2002
2. N. Scialabba, *Factors influencing organic agriculture policies with a focus on developing countries*. in *IFOAM 2000 Scientific Conference,* Basel, Switzerland, 2000
3. N. Misra et al., J. Hazard. Mater. 271, 33-40 (2014)
4. Y. Bai et al., J. Agr. Food Chem. 57(14), 6238-6245 (2009)
5. Y. Bai et al., Chemosphere 81(3), 408-414 (2010)
6. M. Anastassiades et al., J. AOAC Int. 86(2), 412-431 (2003)

PLASMA MODIFICATION OF POLYCARBONATE SURFACE BY ATMOSPHERIC PLASMA SOURCES

J. Kelar, T. Homola, R. Krumpolec, P. Slavíček, M. Černák

R&D Center for Low-Cost Plasma and Nanotechnology Surface Modification (CEPLANT), Department of Physical Electronics, Faculty of Science, Kotlářská 2, 611 37 Brno, Czech Republic

E-mail: Jakub.kelar@mail.muni.cz

In short study below we report effects of ambient air atmospheric pressure plasma treatment of polycarbonate surface. Atmospheric plasma treatment was done by two different plasma sources. First was special type of dielectric barrier discharge called Diffuse Coplanar Surface Barrier Discharge (DCSBD). Second one was glide arc like plasma APC 500. We report significant changes in surface free energy, water contact angle and hysteresis calculated from dynamic contact angle (advancing, receding).

Keywords: DCSBD; glide arc; surface free energy; dynamic contact angle; plasma modification

1   Introduction

As material a Polycarbonate (PC) is highly prized for many useful properties such as: excellent transparency, high temperature resistance (Tg ~ 145°C), relatively small density (light weight material), mechanical strength, biocompatibility, acid resistance and on a top of that relative low cost. This particularly useful material is used for example in automotive production for cars wind shield and/or rear windows [1] and microfluidics [2].

However, surface of PC has relatively low surface energy and therefore is not suitable for direct surface processing: e.g. painting, printing, gluing or application of functional coatings [3]. Mainly for this reason, an appropriate surface modification is in need for this material. Plasma modification is well known technique for not only increasing of free surface energy but also in increasing of adhesive properties of various materials. In presented work we have successfully used two different atmospheric plasma sources, glide arc like plasma and dielectric barrier discharge. Ambient air was used for surface modifications due its low operation cost. In this paper we are going to show significant increase of free surface energy after plasma treatment by both sources and interesting dynamic contact angle behavior.

2   Experimental setup

In this study a 2 mm thick semi-crystalline sheets of polycarbonate (PC) were treated by two atmospheric plasma sources. Before plasma treatment was applied PC sheets were cut to approximately 15 x 100 mm samples. Polycarbonate was equipped by protective foils which were removed before plasma treatment.

Plasma treatment was done by two atmospheric plasma sources: Diffuse coplanar surface barrier discharge (DCSBD) (Roplass s.r.o, Czech Republic) with frequency of 15 kHz and input power of 400 W [4-6] and by Plasma APC 500 (APC) (Diener electronic GmbH + Co.

KG, Germany) that is based on gliding arc discharge principle and uses 40 kHz frequency and power of 500 W [7].
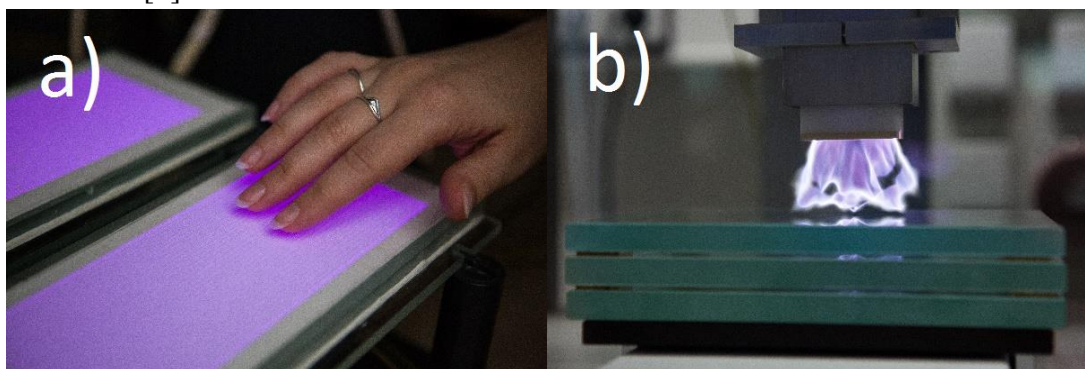
Fig. 1: Photo of a) DCSBD and b) APC 500 plasma.

The surface of polycarbonate plates has been analyzed via two surface energy diagnostic tools (DSA30 and See System). The DSA30 (Kruss GmbH, Germany) was used for dynamic water contact angle measurements (advancing and receding). We have used cycle with increasing and decreasing volume of water droplet from 1 μl to 5 μl and back to 1 μl.

For static contact angle and free surface energy a See System(Advex Instruments) device with three calibrated liquids (water, diodomethane, ethylene glycol) was used. Free surface energy was calculated by Owens-Wendt regression model. The effect of plasma treatment on the stability of free surface energy after 72 h was measured as well.

3 Results and Discussion

Plasma treatment of PC surface by both atmospheric plasma sources resulted in decrease of water contact angle (advancing, receding, static) and significant increase of free surface energy as shown on Fig. 2.
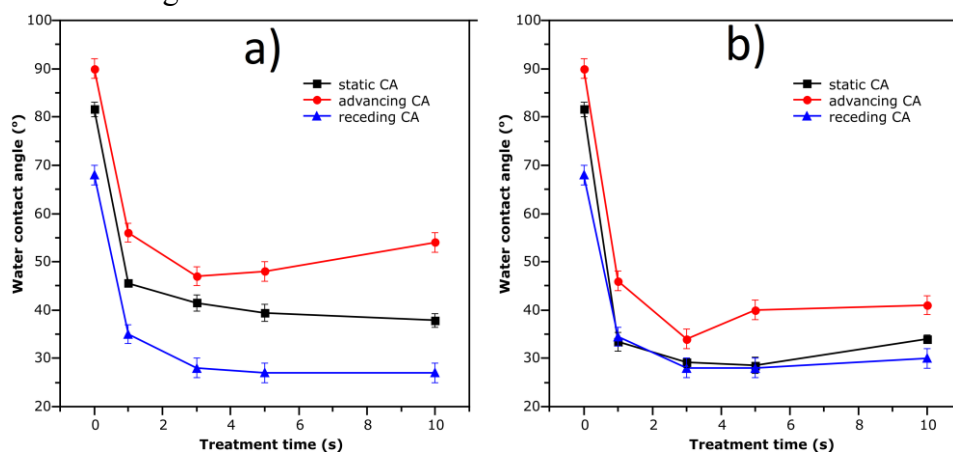
Fig. 2: Water contact angle (WCA) for treated PC with a) DCSBD, b) APC 500 plasma .

As was expected by theory static contact angle is below advancing and above receding part of water contact angle. Hysteresis in this case is between 19 and 27 degrees. For untreated sample hysteresis was 22 degrees and due to error of measurement we can say that hysteresis of WCA for surface modified by DCSBD is more or less constant and same as for untreated

sample (27 degrees was measured for 10s treatment, in other cases, we cannot distinguish between reference and treated sample hysteresis due to error of hysteresis estimation).

In case of WCA after plasma treatment by APC 500 plasma source, once again, results are predictable by theory and static contact angle is below advancing and slightly above of receding WCA. In this case hysteresis of WCA for treated surfaces was measured in range between 6 and 12 degrees which is significantly different from DCSBD and reference sample. We believe that this is due to macroscopic changes of sample surface and significant roughness changes as well as melting phenomena for longer treatment times (APC 500 plasma source has significantly bigger temperatures of neutral particles than DCSBD plasma source). Both assumptions needs to be compared with atomic force microscopy (AFM) and X-ray photoelectron spectroscopy (XPS) measurements.

Results of free surface energy (FSE) estimation with use of Owens-Wendt regression model are shown on Fig. 3 for both atmospheric plasma sources. As was expected, plasma treatment by DCSBD plasma source significantly changes polar part of free surface energy. Samples were stored in glass Petri-dish, in air-conditioned room and in relative darkness. The values of FSE stored for 72 hours after treatment are shown on the Fig 3 with empty points. Free surface energy was still higher than for reference sample but was also smaller than for sample measured immediately after the treatment. Same behavior was observed for samples treated by APC 500 plasma. The only notable difference is steeper increase of surface energy than for DCSBD plasma source.
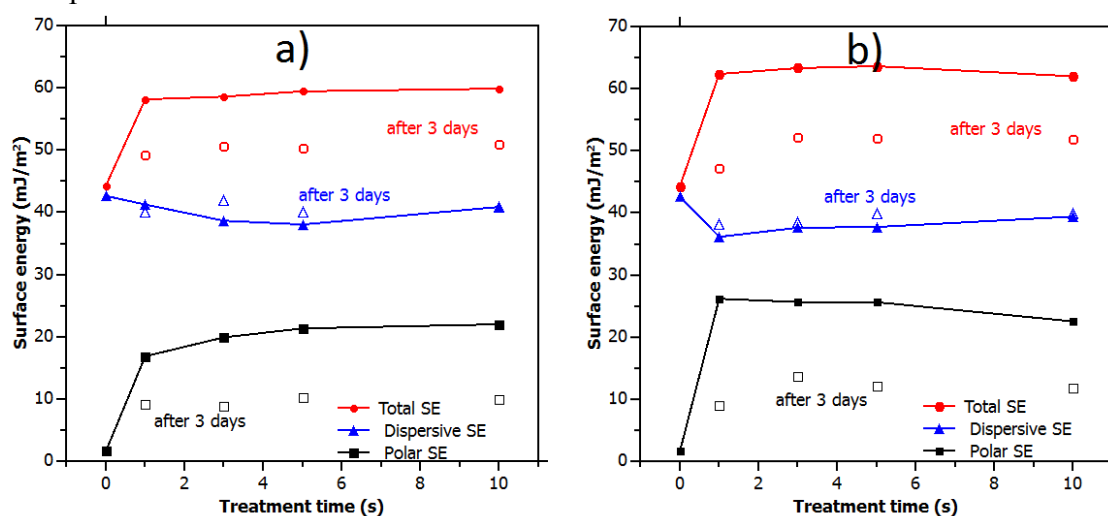
Fig. 3: FSE of treated PC with a) DCSBD, b) APC 500 plasma.

4   Conclusion

In conclusion it can be stated that plasma modification in ambient air by both plasma sources presented in this work is suitable for increasing of surface free energy. Main result of this paper is difference in hysteresis of WCA between two plasma sources, which differs significantly (APC 500 hysteresis is half of DCSBD hysteresis value). Further and more precise research of this phenomena and theoretical background would be published in the nearest future.

References
1. N. De Vietro et. al., Sensors Actuators A Phys. 206 (2014)
2. J. Chen et al., Anal. Chem. 77 (2005)
3. H. Yaghoubi et al., Appl. Surf. Sci. 257 (2011)
4. U. Kogelschatz, Plasma Chem. Plasma Process. 23 (2003)
5. C. Liu et al., Surf. Coatings Technol. 185 (2004)
6. T. Homola et al., J. Adhes. 90 (2014)
7. A. Fridman et al., Prog. Energy Combust. Sci. 25 (1999)

PLASMA ASSISTED CALCINATION OF POLYMER/PRECURSOR FIBERS

V. Medvecká[1], D. Kováčik[1,2], A. Zahoranová[1], E. Múdra[3], M. Strečková[3], P. Ďurina[1], M. Černák[1,2]
1Department of Experimental Physics, Faculty of Mathematics, Physics and Informatics, Comenius University in Bratislava, Mlynská dolina F2, 842 48 Bratislava, Slovak Republic
2CEPLANT, Faculty of Science, Masaryk University, Kotlářská 2, 611 37 Brno, Czech Republic
3Institute of Materials Research, Slovak Academy of Sciences, Watsonova 47, 040 01 Košice, Slovak Republic

E-mail: veronika.medvecka@fmph.uniba.sk

The effect of non-thermal plasma on composite precursor nanofibers (NF´s) was studied for application by preparation of nickel zinc ferrite NF´s as an alternative to conventional annealing. The composite metal nitrates/polyvinyl alcohol NF´s prepared by electrospinning were exposed to atmospheric pressure plasma generated by Diffuse Coplanar Surface Barrier Discharge in ambient air for 1-30 minutes. The changes in chemical bonds were studied by ATR-FTIR analysis. The chemical composition before and after plasma treatment was characterized using EDX. The influence of plasma on fibers morphology was observed by SEM.

Keywords: plasma assisted calcination; ferrite nanofibers; atmospheric pressure plasma; DCSBD

1   Introduction

High resistivity, low dielectric loss, excellent chemical stability and mechanical hardness make nanosized ferrites attractive for microwave and high frequency applications and as ferro-fluids and biomedical materials [1]. Nickel zinc ferrites find applications as the electronic sensor materials, for example, sensor for humidity measurement and ethanol detection [2]. Electrospinning has rapidly changed fiber making from a capital intensive, large scale process to a low cost, broadly applicable method that manufactures fibers on a laboratory bench, to serve diverse needs ranging from materials science and technology to life sciences and clinical medicine. The high ratio of surface area to mass is a primary characteristic of nanofibers [3]. The needle-less electrospinning technology was used in the present work as economically viable to produce ferrite fibers in a mass of industrial scale [4].

To obtain ferrite NF´s, as-spun polymer/precursor nanofibers NF´s are annealed at high temperature in the order of 100°C for several hours to transform them into ferrite nanofibers [5–7]. High temperatures and long calcination times cause that conventional thermal calcination is very energy and time-demanding process. Plasma assisted calcination provides a promising low-temperature, low-cost and time-saving method for preparation of inorganic fibers. The low-temperature, non-equilibrium plasma generated in working gases with high oxidative effect, e.g. oxygen and air, appears to be a suitable tool for the oxidation and removing of organic base polymer at low temperature by reactive oxygen species produced in plasma. This type of plasma, generated at low or atmospheric pressure has already been used

for plasma calcination by producing nanopowders, inorganic thin layers and inorganic fibers [8–11].

In present work, we used atmospheric pressure plasma generated by Diffuse Coplanar Surface Barrier Discharge (DCSBD) [12, 13] for plasma assisted calcination (PAC) of the composite fibers. DCSBD generates strongly non-equilibrium homogeneous plasma in thin layer on the surface of dielectric alumina plate in ambient air without the need of any working gas. This source of plasma has been studied for surface modification of various types of materials for the purpose of activation, cleaning, plasma assisted deposition of layers, ozone production, etc. [14–19] and also for plasma assisted calcination by the preparation of cerium oxide fibers in submicron scale [20].

2   Experimental

The precursor solution for the electrospinning was prepared by mixing of 7% wt. water solution of polyvinyl alcohol (PVA, Acros Organic, Mw = 146 - 186,000 g.mol^{-1}) with appropriate amount of metal nitrates (Acros Organic, $Ni(NO_3)_2$. $6H_2O$, $Zn(NO_3)_2$. $6H_2O$, $Fe(NO_3)_3$. $9H_2O$). The molar ratio of $Ni^{2+}/Zn^{2+}/Fe^{3+}$ was 0.3/0.7/2 due to maintain of the molar ratio in the resulting ferrite $Ni_{0.3}Zn_{0.7}Fe_2O_4$. Subsequently, 0.03% vol. of acetic acid (Sigma Aldrich, 99.7%) was added to the prepared solution. The prepared solutions were spun by Nanospider TM NS Lab from ELMARCO equipped by needle-less electrospinning technology. The applied voltage was 80 kV, the spinning distance between both spinning and collector electrodes was in a range 130 - 140 mm. The electrospinning was performed at ambient temperature with a relative humidity of 50%.

Composite NF´s were treated by atmospheric pressure ambient air plasma generated by diffuse coplanar surface barrier discharge detailed described in [12,13,16,21]. The distance between the sample and planar ceramic plate of DCSBD was fixed to 0.3 mm by the moveable sample holder. The plasma exposure time was in the range of 1-30 min at input power 400 W.

Attenuated Total Reflectance - Fourier Transform Infrared (ATR-FTIR) spectra were obtained using Bruker Vector 22 FT-IR spectrometer with the additional accessories Pike MIRacle^{TM} in the range of 4500 to 500 cm^{-1}, during 20 scans, with 2 cm^{-1} resolution. Morphology of fibers was studied by Scanning Electron Microscope (SEM) Vega II SBH (Tescan, CZ). Energy-disperse X-ray Spectroscopy (EDX) measurements were realized using Vega I TS 5136 MM (Tescan, CZ) with EDX spectrometer INCA x-sight (Oxford Instruments, UK).

3   Results and Discussion

In Fig. 1 the spectra of composite fibers and fibers treated by DCSBD plasma at different exposure time are present. The broad bands found in the region 3100-3500 cm^{-1} and around 1650 cm^{-1} are linked to O-H stretching and bending vibrations in PVA base polymer and also due to the presence of water in hydrated precursors [22, 23]. At 2900-2950 cm^{-1} and around 1420 cm^{-1} were observed bands assigned as symmetric and asymmetric stretching and bending of CH_2 group, respectively [22, 23]. Peak at 1100 cm^{-1} was attributed to stretching

vibration of C-O bond. Typical bands of nitrates salts can be visible at 1300 cm^{-1} (symmetric stretching of NO$_2$), 1550 cm^{-1} (asymmetric stretching of NO$_2$) and 825cm^{-1} (bending of N-O) [6, 23].
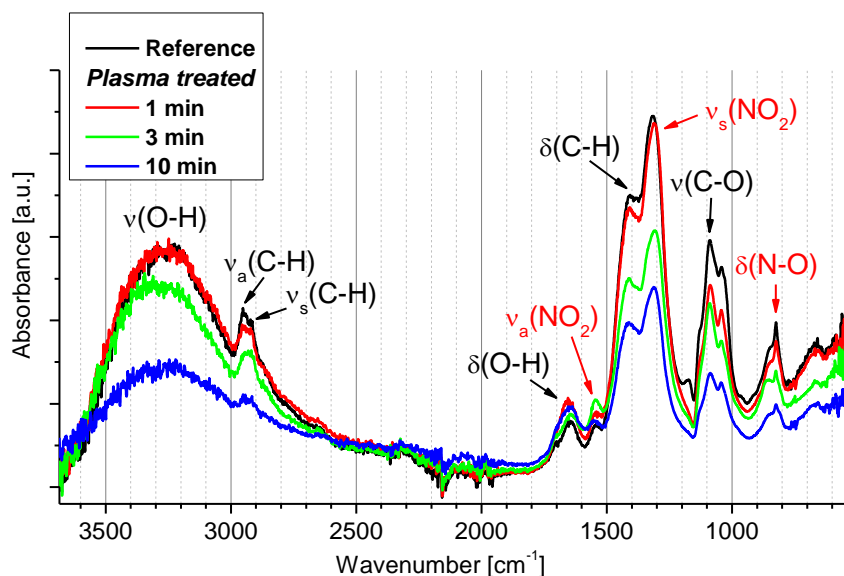
Fig. 1: ATR-FTIR spectra of as-spun fibers and fibers treated by plasma at exposure time 1, 3 and 10 minutes.

The decline of the bonds attributed to organic polymer as well as nitrate ion bonds, which form the precursors, was observed. The degradation of polymer matrix and nitrate parts of precursor was confirmed by EDX analysis, where we detected high decrease of carbon and nitrogen and increase of the content of nickel, zinc and iron.
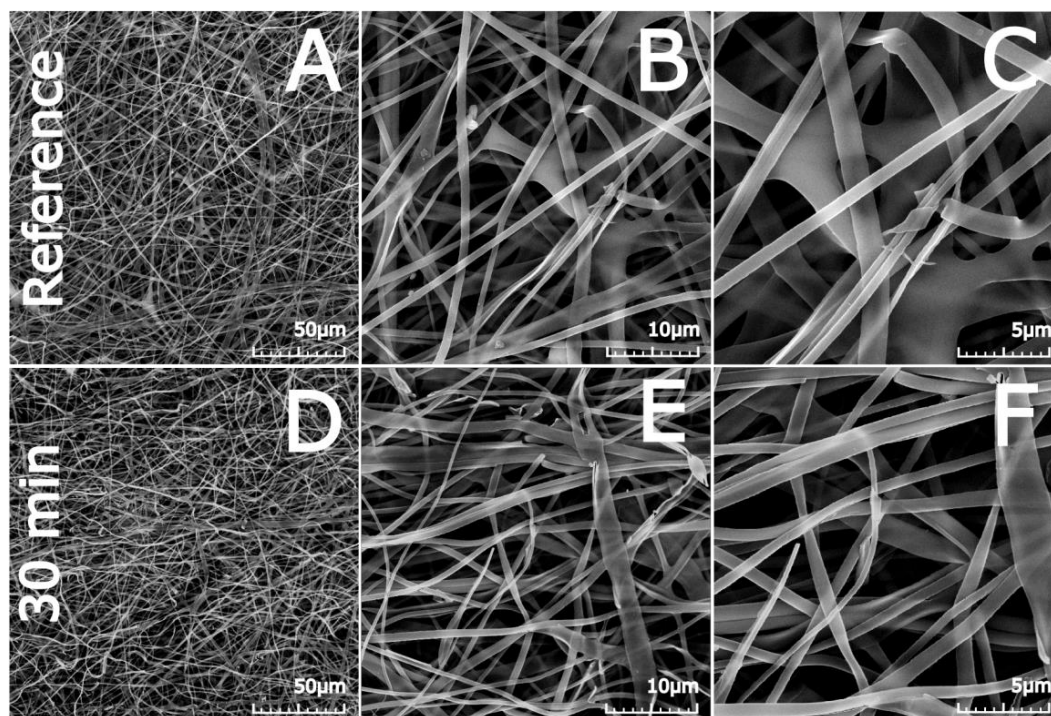
Fig. 2: SEM micrographs of reference sample of as-spun composite fibers (A, B, C) and sample after plasma treatment for 30 minutes in ambient air (D, E, F).

In Fig. 2, SEM micrographs of samples before and after plasma treatment with exposure time of 30 min are presented. PAC using DCSBD caused no degradation of fibrous structure or breaking of fibers and the length of fibers was remained after plasma treatment. The diameter of composite fibers is in the range from 150 – 500 nm. On the sample exposed to plasma, we can see slight shrinking of fibers. The effect is caused by the removal of polymer matrix.

4 Conclusion

In this work the low-temperature plasma assisted calcination of composite metal nitrates/polyvinyl alcohol fibers intended for the preparation of ferrite nanofibers was studied. PAC was carried out at atmospheric pressure and ambient air in dynamic mode by using diffuse coplanar surface barrier discharge. The advantage of DCSBD is optimal characteristics of generated plasma (high power density related to high density of active species, macroscopic plasma uniformity and diffusiveness) for application for the decomposition of polymeric matrix by low-temperature ambient air PAC without degradation of the fibrous structure.

References
1. O. A. Li, J. Magn. Magn. Mater. 408, 206 (2016).
2. A. P. Kazin, J. Solid State Chem. 184, 2799 (2011).
3. D. H. Reneker et al., Polymer (Guildf). 49, 2387 (2008).
4. O. Jirsak et al., Int. J. Nanotechnol. **9**, 836 (2012).
5. X. Huang, J. Alloys Compd. 627, 367 (2015).
6. H. Qiao, Electrochim. Acta 160, 43 (2015).
7. O. Saensuk, Ceram. Int. 41, 8133 (2014).
8. J. M. Gomez-Vega, Surf. Coatings Technol. 169-170, 504 (2003).
9. Z. Károly, Powder Technol. 110, 169 (2000).
10. P. Baroch et al., Thin Solid Films 515, 4905 (2007).
11. H. Wang, Mater. Res. Bull. 44, 1676 (2009).
12. M. Šimor, Appl. Phys. Lett. 81, 2716 (2002).
13. M. Černák et al., Plasma Phys. Control. Fusion 53, 124031 (2011).
14. L. Černáková et al., Plasma Chem. Plasma Process. 25, 427 (2005).
15. T. Homola et al., Polym. Degrad. Stab. 97, 2249 (2012).
16. T. Homola et al., Appl. Surf. Sci. 258, 7135 (2012).
17. A. Pamreddy et al., Surf. Coatings Technol. 236, 326 (2013).
18. D. Skácelová et al., Mater. Sci. Eng. B 178, 651 (2013).
19. M. Šimek et al., *icpig2007.ipp.cas.cz* 450, 934 (2007).
20. V. Medvecká et al., Mater. Lett. 162, 79 (2016).
21. M. Černák et al., Eur. Phys. J. Appl. Phys. 47, (2009).
22. A. Shehap, Egypt. J. Solids 75 (2008).
23. G. Socrates, Infrared and Raman Characteristic Group Frequencies, 3rd edn. (John Wiley & Sons, 2004).

MODIFICATION OF POLYETHYLENE TUBES SURFACE IN DIELECTRIC BARRIER DISCHARGE REACTOR

M. Młotek, A. Błaszczyk, B. Ulejczyk, K. Krawczyk
Warsaw University of Technology, 3 Noakowskiego Street, 00-664 Warsaw, Poland

E-mail: mmlotek@ch.pw.edu.pl

The influence of gas composition and power supply on the properties of the tubes surface was studied. The exposure time and gas flow rate were constant but the gas composition and discharge power varied. The treated samples were examined by water and diiodomethane contact angle measurement. The surface energy was calculated using Owens-Wendt method. After treatment time of 30 s the water contact angle was reduced from the initial value of 55° to the 27°. The surface energy increased from 46.8 mJ/m^2 to 65.7 mJ/m^2.

Keywords: nonequilibrium plasma; surface modification; dielectric-barrier discharge

1   Introduction

Plastics are prevalent in daily life and provide one of the most important materials in the industry. Nowadays scientific research focuses not only on macroscopic properties of materials such as strength or flexibility but also on surface properties. Innovations in the preparation of the materials determine the development of new methods for modifying of the outer surface [1, 2]. During the recent years, many studies have been focused on finding new plasma methods for plastic surface treatment [3, 4]. Many methods for modification of the surface of films or flat panels are used in the industry, but the treatment of irregular surfaces is still tested.

In order to modify a material's surface multiple techniques are used: mechanical, chemical, plasma or radiation. Often it is necessary to change only the surface properties for corrosion protection, sealing and adhesion improvement. The surface of plastics is very often too smooth and difficult to wetting. This causes problems for such treatment as printing, painting, gluing, laminating or coating deposition of layers on such materials. This could be due to the polymer structure, deposition of impurities on the surface of plastics or migration of plastic components on its surface [5]. The surface free energy (SFE) and contact angle are the parameters that characterize the properties of surfaces [5]. The aim of this work was to study the effect of power supply mode and gas composition on properties of the polymer surface.

2   Experimental

The dielectric-barrier discharge reactor for modification of the 2 mm diameter polyethylene (PE) tubes (Fig. 1A) was used [6]. The cross section of the reactor is shown in Fig. 1B. The reactor consisted of the top and bottom, two dielectric barriers of polycarbonate, high-voltage and grounded stainless steel electrodes and the plate made of polycarbonate with an S-shaped passage, where the dielectric barrier discharge was generated. The modified tube was placed in the channel. In this solution the discharge was generated only in the space where the tube was placed. This increased the energy density in the discharge gap and reduced power consumption. Two dielectric barriers made of a 0.3 mm thick PC film were used (Fig. 1A). To separate modified material from the surface of the electrodes the use of two dielectric barriers is required. This is important when the modified material will be used for medical purposes.

The DBD reactor was used for the modification of the plastic tube surface in the atmosphere of numerous gases. The reactor worked in a horizontal position.
Three kinds of power supply were used:
1) HF - 7 -9 kV AC 6.5 kHz;
2) LF - 8 kV 50Hz 37 mA neon transformer;
3) PPS - pulse power source where the frequency and duration of pulse could be varied.
Current and voltage characteristics and discharge power were measured in the high voltage circuit using Tektronix DPO3034 oscilloscope with probes: P6015A and TCP0030.
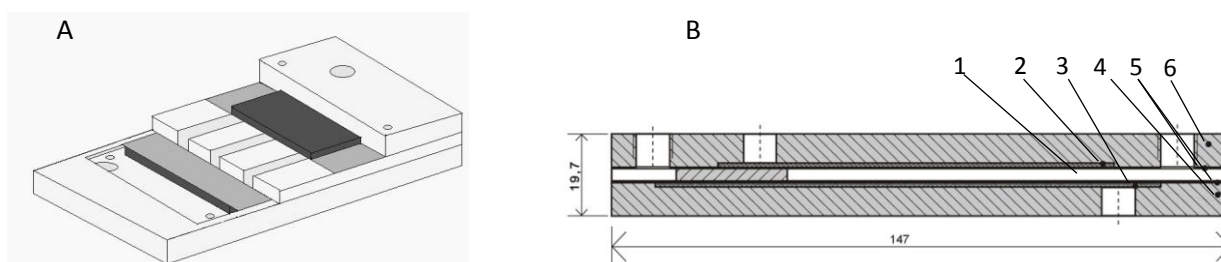
Fig. 1. Reactor for polyethylene tube modification. A - general view of the reactor; B - cross-section: 1 – discharge channel, 2 – high voltage electrode, 3 – grounded electrode, 4 - bottom part 5 – dielectric barriers, 6 – top cover [6].

3 Results and Discussion

Measurements were conducted for four gaseous mixtures: air + H_2, air + CO_2, Ar + H_2 and Ar + CO_2. Concentrations of added gas (H_2 or CO_2) were 5%, 10%, 15%, 25% and 50%. The contact angles were measured for a raw sample and after the modification. Distilled water and diiodomethane were used as liquids. Surface free energy was calculated using Owens – Wendt method [5], which is based on the assumption that the surface free energy (SFE) is the sum of the dispersive (γ_s^d) and polar component (γ_s^p).

Results obtained with a neon 50Hz transformer (power supply 2) were much lower than those obtained with a pulse or high frequency power supply (3 or 1). The lowest value of the polar component, i.e. 25 mJ/m^2, was obtained for the neon power supply, whereas the highest (39 mJ/m^2) for power supply 1. Moreover, the polar component was higher when high frequency power supply (1) was used than the pulse one (3). While the dispersive component for each power supply was rather constant, in the range 23-27 mJ/m^2, higher polar components resulted in higher surface free energy. Therefore, for further experiments power supply 1 of a high frequency sinusoidal voltage and current was used.

The carrier gas had a significant influence on the values of dispersive and polar component and surface free energy. The value of the polar component was raised with increasing concentration of doping gas for all studied gas mixtures. The highest value of the polar component (33.4 mJ/m^2) was observed after the modification in 50 %vol. of argon and 50 %vol of CO_2. The biggest differences of the polar components of the modified sample compared to those of the unmodified sample were obtained using the mixture containing CO_2 + Ar (Fig. 2 A). The hydrogen present in the gas mixture had a lower impact on the modification of the surface than the carbon dioxide. The values of the polar component in H_2 + Ar were lower than the values obtained in the gas containing CO_2. Plasma modification of PE tube surface resulted in an increase of the surface free energy in all experiments. The highest surface free energy, i.e. 52.5 mJ/m^2, was obtained for the gas containing 50 vol. % Ar + 50 vol. % CO_2. A high value of the surface free energy (51.4 mJ/m^2) was also obtained for air + H_2, but this value was associated with a high value of the dispersive component, which

did not affect the increase in the hydrophilicity of the surface. The lowest increase of the surface free energy was observed for gas containing air and CO_2 (Fig. 2B).

Surface free energy of the raw material was 48-50 mJ/m^2. For all used power supplies SFE was higher after modification (Fig 3A).
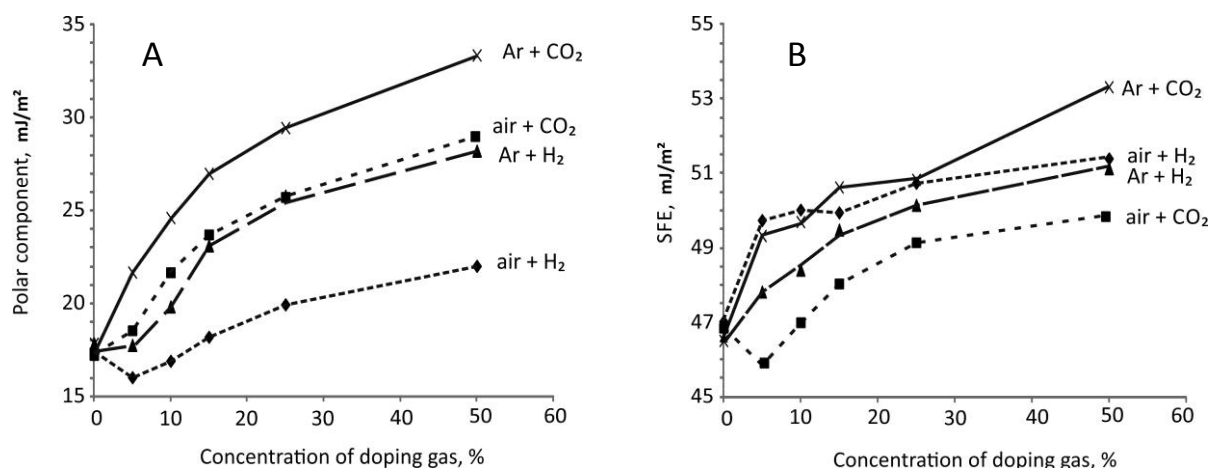
Fig. 2. The effect of doping gas concentration on A - polar component, B - surface free energy. Gas flow rate 20Nl/h, discharge power 17 W power source HF, modification time 30s.

At the power discharge of 10 W only a slight increase of the polar component (1.5 mJ/m^2) was observed with increase of voltage (Fig 3B). When the discharge power was increased to 23 W, influences on modification process was more distinct. At 7 kV, the polar component was higher. In contrast, the dispersive component was lower when 23 W discharge power was used. However, increasing the voltage to 9 kV at the discharge power of 23 W resulted in the melting of the modified tube, making it impossible to measure contact angles.

The modification provided with the 8 kV and power discharge of 23 W was the most effective. Under these conditions the largest increase of the polar component, i.e. 19.3 mJ/m^2, was achieved. It was almost two times more than that of the unmodified sample. This also caused a significant increase of surface free energy of the tube to 64 mJ/m^2. The outer tube's surface was not bearing any traces of destruction of distortion or melting.
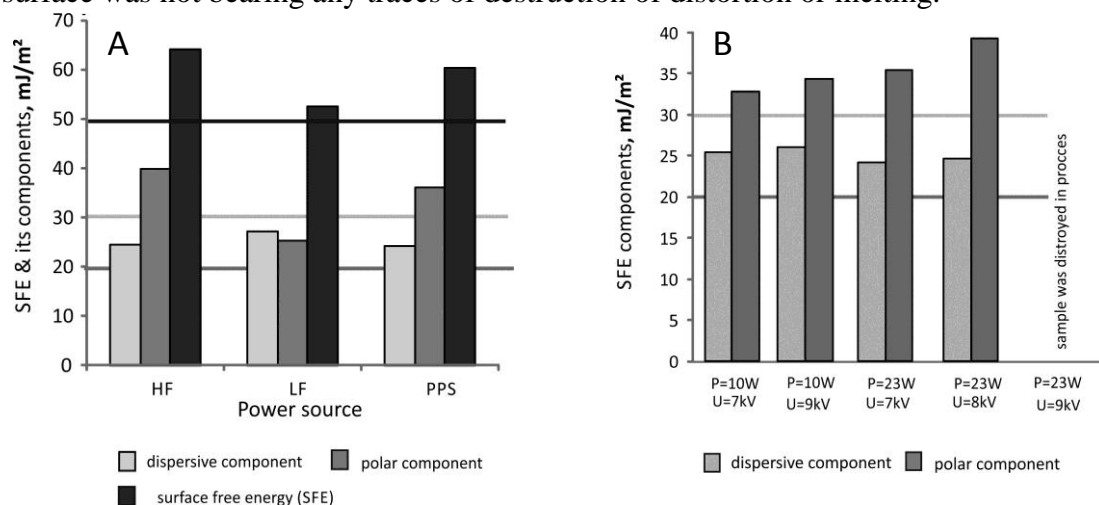
Fig. 3. Effect of power supply on surface free energy and its components. Discharge power A - 23 W, B - 10 or 23 W, gas flow rate 20 Nl/h, gas composition 50% Ar + 50% CO_2. Lines indicate values for raw sample.

The long-term stability of modification was tested (Fig 4). Measurements were conducted just after modification and after 21 days. Modification was provided using power supply HF (sin line and high frequency) and PPS (pulse) (Fig. 4A). After 21 days SFE decreased when both power supplies were used. However, for sin line high frequency power supply surface free energy reduced only by 3 mJ/m^2, whereas when the pulse power supply was used the value of the surface energy decreased more than 5 mJ/m^2. Moreover, SFE of the tubes modified in the reactor supplied with power source 1 is higher than the SFE of those supplied with power source 3 for the entire duration of the measurement.

The results of measurements conducted in dry air and argon indicate differences in changes of surface properties in time (Fig. 4B). Surface free energy and the polar component of samples, stored in dry air or argon, decreased. The changes of the dispersive component were negligible. After 21 days samples stored in argon had higher SFE and the polar component. This could be the reason of limitations of the chemical reactions and recombination on the active surface of the tube.
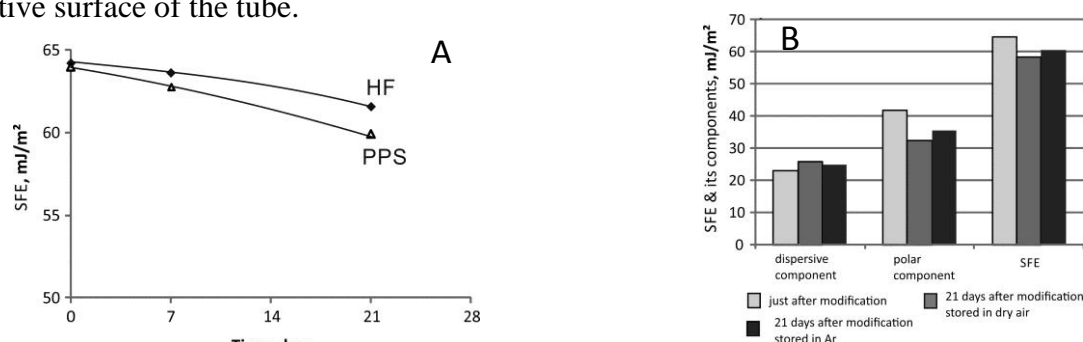
Fig. 4. Effect of time on stability of surface modification. A – power source HF or PPS, B – power source HF. Discharge power 23 W, gas flow rate 20 Nl/h, gas composition 50% Ar + 50% CO$_2$.

4   Conclusion

Scientific research focuses not only on macroscopic properties of materials such as strength or flexibility but also on surface properties, which are of major importance for many industrial processes. Nonequilibrium plasma of the dielectric-barrier discharge is a convenient method for surface modification of polymers. Carrier gas composition and characteristic of power source had significant influence on the modification process. In the DBD reactor surface free energy and the polar component were increased; however, this modification was not permanent. After three weeks SFE decreased, but this effect depended on many parameters i.e. power source used during modification or condition of sample storage. Noble gases could be an environment, in which the chemical reactions and recombination on the active surface of the tube is limited.

References
1. T. Opalinska et al., Polimery 49(4), 257, (2004)
2. A. Van Deynse et al., Plasma Process. Polim. 11, 117, (2014)
3. C. S. Ren, et. All., Appl. Surf. Sci. 255(2), 3421 (2008)
4. R. Mix et al., Plasma Process. Polym. 9, 406 (2012)
5. M. Żenkiewicz,: Adhezja i modyfikowanie warstwy wierzchniej tworzyw wielkocząsteczkowych, (WNT Warszawa, 2000).
6. M. Młotek et al., in *Proceedings of the Int. Sym.on High Pressure Low Temperature Plasma Chemistry „Hakone 14"* Greifswald 2014.

DBD TREATMENT OF PVC TUBES TO REDUCE PLASTICIZER MIGRATION

T. Neubert, K. Lachmann, C.-P. Klages, M. Thomas

Fraunhofer IST, Bienroder Weg 54 E, 38108 Braunschweig, Germany

E-mail: thomas.neubert@ist.fraunhofer.de

In this work we discuss the dielectric barrier discharge (DBD) treatment of soft polyvinylchloride (PVC) tubes in an argon atmosphere. The migration of the plasticizer diethylhexyl phthalate (DEHP) was measured by washing it out from the treated PVC surface and then quantifying it with infrared spectrometry. Thus we could observe a reduction of the migration of DEHP of up to 95%.

Keywords: dielectric barrier discharge; migration; polyvinylchloride; plasticizer; cross-linking

1 Introduction

Plasticizers play a very important role in the mechanical properties (i.e. stiffness, flexibility) of many polymers such as polyvinylchloride (PVC). Soft PVC contains a significant amount of plasticizer (in the range of 40 wt% [1]) and is often used for medical devices like blood bags and flexible tubes [2]. Unfortunately, plasticizers are not chemically bound to the polymer molecules so they can migrate freely and will be transferred into the surrounding environment [3, 4]. Commonly used plasticizers like diethylhexyl phthalate (DEHP) are problematic for human health [5, 6]. Thus, there is a big demand for alternatives [1] or at least for methods to reduce the mobility of the plasticizer. Lakshmi et al. described a reduction of DEHP plasticizer migration in PVC by light induced cross-linking [7]. Audic et al. showed that migration of plasticizers in PVC can be minimized by low pressure plasma treatment with argon gas causing crosslinking of the PVC at the surface [8]. In this work a dielectric barrier discharge at atmospheric pressures is used for the treatment of PVC tubes to carry out a more cost effective way to reduce the migration potential of plasticizers.

2 Experimental

The experiments were performed on 110 mm long pieces of PVC tubes with approx. 34 wt% DEHP as plasticizer. The tubes had an inner diameter of 3.9 mm and an outer diameter of 5.4 mm. There was no cleaning of the tubes to avoid changes in the plasticizer concentration on the inner tube surface.
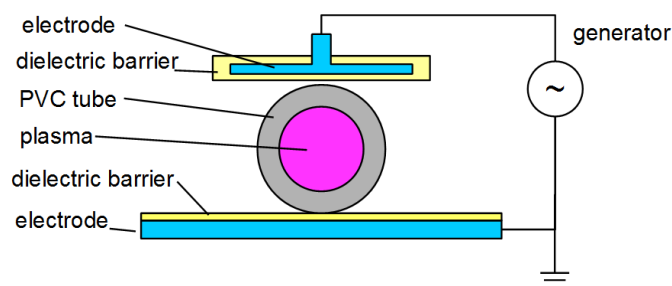
Fig. 1: Setup for DBD plasma treatment

For the plasma treatment, the tube was placed between two electrodes: the upper one covered with about 2 mm ceramic and the lower one covered with about 1 mm silicone rubber as dielectric barriers (Fig. 1). 5 slm argon (99.999%) gas was guided through the tubes. The discharge was powered using a 7010 R high voltage AC generator from Softal Electronic GmbH with a frequency of about 25 kHz. The distance between the electrodes was about 8 mm.

To measure the barrier effect of the plasma treatment, a 50 mm segment from the center of the tubes was filled with decane (purity 98%, Sigma Aldrich) and then was shaken for 2 h at room temperature. The mass of the filled decane was measured by weighing the empty and the filled tubes and is in the range of 0.4 g. The decane was then analyzed with ATR infrared measurements with a Nicolet iS10 infrared spectrometer from Thermo Scientific. The area of the carbonyl peak of the DEHP at 1730 cm^{-1} can be taken as a measure of the amount of DEHP migrated into the decane. A barrier efficiency ε can by defined by the following equation 1 (M_1 is the amount of plasticizer migrated from the treated sample, M_2 is the amount of plasticizer migrated from the non-treated reference sample) [3].

$$\varepsilon = 1 - \frac{M_1}{M_2} \tag{1}$$

Since for the relatively low concentrations used here there is a linear correlation between concentration and carbonyl peak area, the barrier efficiency ε can be calculated directly from the peak areas A and the decane mass m of treated samples and a non-treated reference sample with equation 2.

$$\varepsilon = 1 - \frac{A_{sample}}{A_{reference}} \cdot \frac{m_{sample}}{m_{reference}} \tag{2}$$

3   Results and Discussion

We found that the carbonyl peak at about 1730 cm^{-1} in the infrared absorption spectra of the decane solutions almost vanished with treatment times above 60 s (Fig. 2). The barrier efficiency for DEHP molecules calculated from the peak areas increased up to 95% after 60 s treatment time (Fig. 3). So for the treated samples there is much less DEHP dissolved in the decane. There are different possible explanations for this behavior. The plasma treatment could have cleaned the surface from DEHP molecules. Thus washing out the plasticizer is hindered by a longer diffusion path. ATR infrared spectra of untreated and treated PVC surfaces showed no significant difference. Thus the changes caused by the treatment seem to be limited to an ultrathin region close to the surface.

We repeated the measurements with samples stored for 1 week at room temperature and for samples stored for 1 week at room temperature and heated for 1 h at 80 °C. Under these conditions, we assumed that the plasticizer should be distributed uniformly again in the PVC material. However, the results for the barrier efficiency did not change much (Fig. 4).
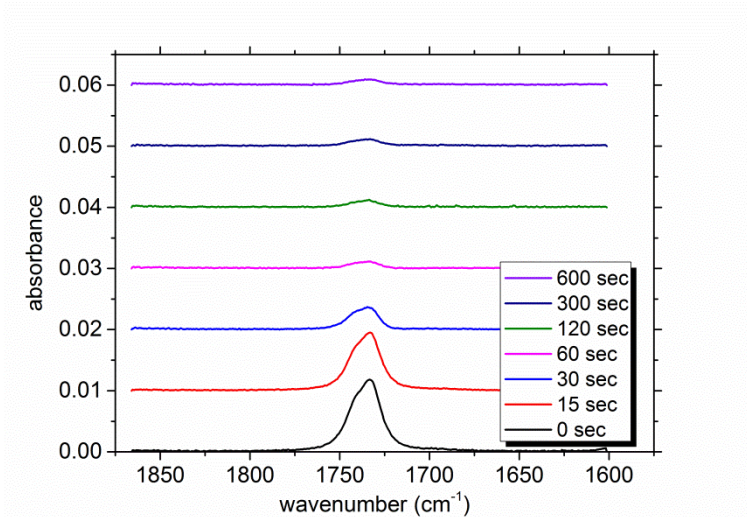
Fig. 2: Carbonyl peak in infrared absorption spectra of the decane solutions for PVC tube samples treated for different times
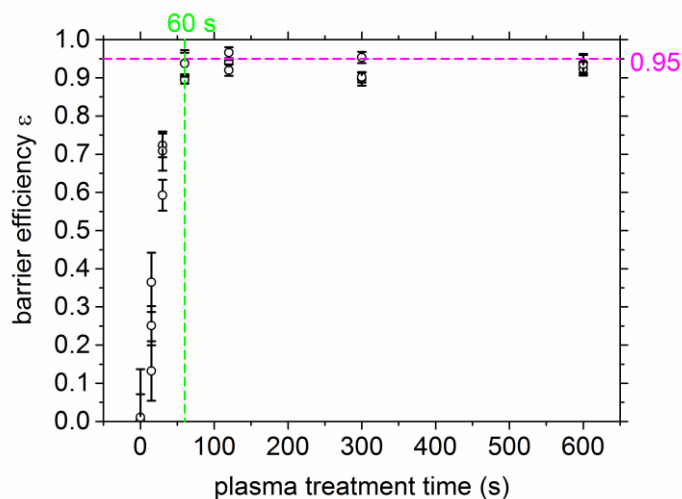
Fig. 3: Barrier efficiency as a function of treatment time
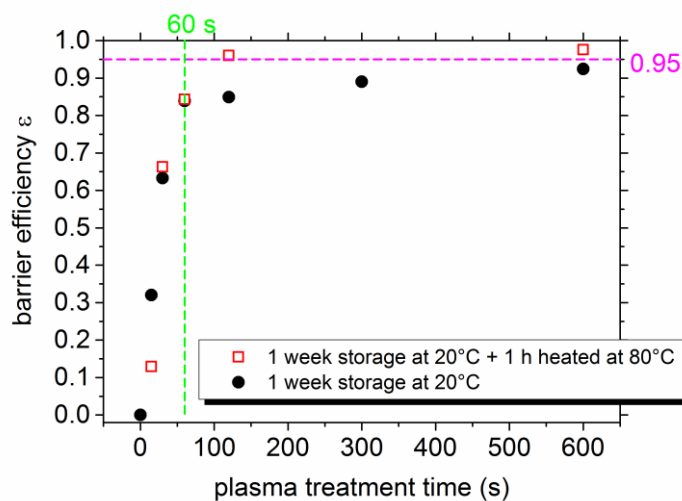
Fig. 4: Barrier efficiency as a function of treatment time for stored and heated samples

The other possible explanation for the reduction of the solved plasticizer is some kind of cross-linking of the PVC chains by the argon plasma. Audic et al. [8] reported a reduced plasticizer migration by cross-linking for plasma treatment of PVC in argon at low pressures. The comparison of plasma treatments at low pressures and at atmospheric pressures is difficult since the ion energies and the mean free path of particles were very different. However, cross-linking and other molecular structural changes of PVC can also be caused by processes involving only UV radiation [9-12]. Shorter wavelengths tend to have a bigger influence [12]. Typical durations for UV irradiation studies were in the range of several hours up to weeks using UV lamps with 254 nm to 365 nm wavelength and intensities in the range of about 5 mW/cm² [11,12]. It is known that dielectric barrier discharges in pure argon can be a very efficient way to generate short wavelength excimer radiation at 126 nm with intensities up to 100 mW/cm² [13]. Thus in our case, it could be possible that the structural changes of the PVC reducing the DEHP migration were caused by these type of radiation.

4 Conclusion

We showed that a DBD treatment of PVC tubes with pure argon gas can reduce the migration of plasticizers like DEHP significantly without any coating as diffusion barriers. The barrier efficiency increases with the treatment time up to 95% and can be measured by leaching the plasticizer in decane for a defined period. As possible explanation for the reduced DEHP migration cross-linking of the PVC was suggested.

References
1. L. Bernard et al., Talanta 129, 39-54 (2014)
2. D. Bourdeaux et al., J. Pharmaceut. Biomed. 118, 206-213 (2016)
3. M. Cerezuela Barreto et al., Plasma Process. Polym. 9, 1208-1214 (2012)
4. A. Marcilla et al., Polym. Test. 27, 221-233 (2008)
5. J. C. Caldwell, Mutat. Res. 751, 82-157 (2012)
6. R. Li et al., J. Hazard. Mater. 241-242, 231-240 (2012)
7. S. Lakshmi et al., Polymer 39, 151-157 (1998)
8. J.-L. Audic et al., J. Appl. Polym. Sci. 79, 1384-1393 (2001)
9. G. Arias et al., J. Vinyl Addit. Techn. 49-54 (2006)
10. H. Sobue et al., J. Polym. Sci. 27, 596-597 (1958)
11. R. Ito et al., Int. J. Pharm. 303, 104-112 (2005)
12. J. M. Hankett et al., J. Phys. Chem. B 117, 16336-16344 (2013)
13. U. Kogelschatz, Appl. Surf. Sci. 54, 410-423 (1992)

EFFECT OF AIR IONS ON PRODUCTION OF METAL NANOPARTICLES VIA SPARK DISCHARGE GENERATOR

D. H. Park, Y. H. Joe, J. Hwang

[1] School of Mechanical Engineering, Yonsei University, Seoul 120-749, Republic of Korea

E-mail: dhoonpark@yonsei.ac.kr

In this study, the effects of air ions on the spark discharge generation (SDG) system were inspected. Positive and/or negative air ions were generated by carbon brush type air ionizer and injected upstream of spark regime. The switching circuit including pulse current network was fabricated and used as test circuit. The characteristics of generated particles, such as mass and number concentrations and mode diameter were investigated with various concentrations of air ions. The mass concentration of the generated particles evidently decreased, while slight reduction was observed in number concentration. The mode diameter of generated particles decreased.

Keywords: air ion; spark discharge; nanoparticle; synthesis; particle generation

1 Introduction

Recently, researches of nanoparticles are increasing. Among the nanoparticles generation methods, the spark discharge generation (SDG) method is well known as a simple, and environment-friendly technology to generate nanoparticles from bulk materials with high surface purity [1-3].

The SDG system can be performed at room temperature and atmospheric pressure. A power source charges a capacitor, and when voltage reaches the breakdown voltage which causes a carrier gas to form a conductive line, the spark occurs. The temperature on the spark regime extremely rises and the electrode is vaporized. Because the period of spark is very short, the metallic vapor is cooled rapidly, consequently, nanoparticles are generated through nucleation, condensation, and coagulation processes [4].

These days, many researches are trying to achieve the stability of nanoparticle generation from SDG system. In this study, when an air ionizer was located at upstream of the spark region, the effect of air ion on the stability of spark discharge was studied. In order to control the recurrence of a spark, a personal circuit including switching network was used. The voltages between two electrodes and across the capacitor were measured with different ion concentration. The characteristics of generated particles, such as mass and number concentrations and mode diameter were measured.

2 Experimental
2.1 Spark discharge generation system

Test circuit was fabricated with the concept of switching circuit, which is suggested from Pfeiffer et al. [5]. The circuit consisted of a high voltage capacitor which has 1 nF of capacitance (SV15JA102JAR, AVX corp.), a pair of silver electrodes (diameter is 10 mm, length is 100 mm, Ag-402651, Nilaco Corp.), two switch elements (S_1 and S_2), and a power

supply (customer order, UltraVolt). In order to discrete charging and discharging phases of SDG system, two insulated gate bipolar mode transistors (IGBT, IXBH12N300, IXYS) were used as switch elements. The frequency of charging and discharging phases period is 1 millisecond.
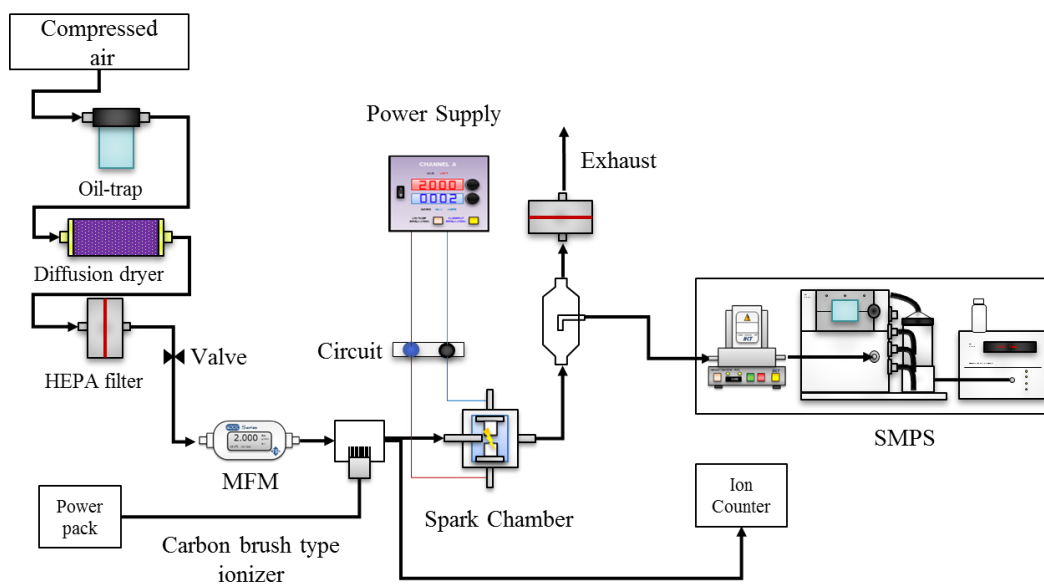
Fig. 1 Schemetics of experiment

2.2 Particle generation and voltage curve

The experimental system consisted of a clean air supply system, a lab-made SDG system, an ionizer, and a particle measurement system (Fig.1). The clean air was passed through carbon brush type ionizer (Sejin Electronics). The ion concentrations with varying rheostat resistance were measured as follows; An ion counter (AIC20M, AlphaLab, USA) was located downstream of the SDG chamber, after two electrodes being removed. 5 lpm of air entered the chamber and the ionizer was operated with varying rheostat resistance. The ion concentration increased with decreasing resistance, then, five different cases were selected for main experiment. The generated nanoparticles were delivered by carrier gas and 0.3 lpm was sampled to measurement. The number and mass concentrations of the generated nanoparticles were measured using a scanning mobility particle sizer (SMPS, TSI Inc.). The maximum and minimum measuring sizes of the DMA were 4.61 nm and 156.8 nm respectively. An oscilloscope (6050A, LeCroy) including high voltage proves (P6015A, Tektronix) was parallel connected with the electrodes and the capacitor.

3   Results and Discussion

Number concentration and mode diameter of the generated particles with various air ion concentrations are shown in Fig. 2(a). The number concentration and mode diameter slightly decreased with increasing air ion concentration but there was no significant difference as ion polarity.

Mass concentration of generated particles precipitously decreased with increasing air ions as shown in Fig. 2(b). Moreover, breakdown voltage decreased when positive or negative ions were injected.
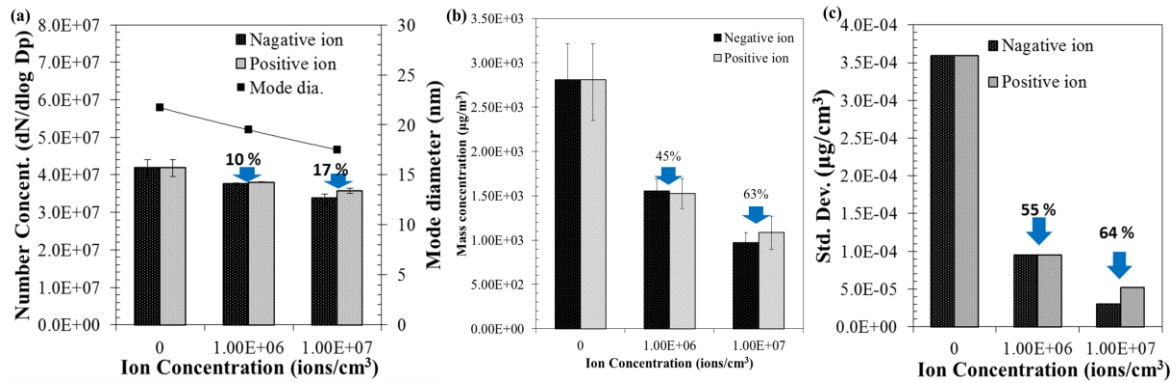
Fig. 2 (a) Number concentration and mode diameter, (b) Mass concentration of generated particles with air ion injection, (c) Standard deviation of mass concentration generated particles for 30 minutes operation.

The SDG system was continually operated for 30 minutes and standard deviation of generated particles in mass base was evaluated (Fig. 2(c)). Without ion injection, standard deviation of generated particles was approximately 3.6×10^{-4} μg/cm^3, while the value precipitously decreased to approximately 3.0×10^{-5} μg/cm^3 when 1×10^7 ions/cm^3 of negative ions was injected. It indicates that air ions can lead to decrease cross section for ionization and expedite electron avalanche inside the electrical field, finally, lead to stable spark ignition.

4 Conclusions

The effects of air ion injection upstream of spark regime on SDG system can be summarized as follows: 1) The probability of ionization on impact decreased 2) Townsend's first ionization coefficient increased. 3) Agglomeration between generated particles was interrupted. By these effects, the breakdown voltage of the carrier gas decreased and stable spark ignition was observed. The mass concentration of the generated particles evidently decreased, while fine reduction was observed in number concentration. Moreover, mode diameter of generated particles decreased. Even though air ion injection in front of spark regime has disadvantages in mass production of the particles, the system can be applied to the process which demands high number concentration of fine particle and stable particle generation.

References
1. C. Roth et al., Aerosol Sci. Tech. 38, 3 (2004)
2. J. P. Borra, Appl. Phys. 39, 2 (2006)
3. N. S. Tabrizi et al., J. Nanopart. Res. 11, 2 (2009)
4. J. H. Byeon et al., J. Aerosol Sci. 39 (2008)
5. T. V. Pfeiffer et al., Adv. Powder Technol. 25 (2014)

APPLICATION OF PLASMA TREATMENT
IN THE NANOFIBERS PROCESSING

D. Pavliňák, J. Kelar, O. Galmiz, M. Zemánek, J. Hnilica, V. Kudrle, M. Alberti
Department of Physical Electronics, Faculty of Science, Masaryk University,
Kotlářská 2, 611 37 Brno, Czech Republic

E-mail: d.pavlinak@mail.muni.cz

The nanofiber carriers (PP foil or paper) were treated by a novel convexly curved coplanar DBD electrode. The surface of polyamide-6 nanofibers on PP foil and paper carriers were oxidized in order to improve their surface properties by of microwave atmospheric pressure plasma jet. The increasing of adhesive properties to carrier substrate as well as surface plasma functionalization of polyamide nanofibers were confirmed.

Keywords: nanofibers; adhesion; plasma treatment

1   Introduction

Among various techniques of fabrication, the electrospinning technique plays a key role in commercial production of nanofibers because it is simple, effective and low-cost method. The electrospinning utilizes high electrostatic field stress to a flowing polymer, either melted or dissolved in electrically conductive solvent. If the applied electrostatic force exceeds the surface tension of polymer solution, a charged liquid jet is ejected towards the opposite electrode and can be collected on suitable substrate. Nanofibers fabricated via electrospinning technique have an uncommonly great length/diameter ratio. Such fiber properties as length (centimeters), fiber diameter (tens to hundreds of nanometers) and great porosity make this material interesting for applications focusing on filtration, fibrous reinforcements in synthetic or biological composites, electronic devices or tissue engineering [1-4]. Unfortunately, like in other areas of technological development, the application potential of electrospinning is degraded by adverse processing effects. One of disadvantages represents the bad adhesion of produced nanofibers to substrate. The other disadvantages are bad surface properties such as a weak hydrophilicity, an absence of suitable chemical groups for chemical derivatization and grafting of other functional materials. These weaknesses are based on the origin properties of the used polymer and are commonly known to the whole sector of polymer industry. At present, many efforts are being addressed to modify the surface properties of polymer fibers in order to improve the performance of these materials and to pave the way to new technological applications. Nowadays a plasma treatment is widely used as an effective tool for physical and chemical modification of polymer surfaces, leaving the internal bulk material unchanged [1-3]. Under the bombardment of active species generated by the plasma, the polymer surface can be modified, removing the surface contamination, introducing new chemical functional groups or depositing a thin coating. In this work the atmospheric plasma sources are used to improve properties of the nanofibers. The main goal of the work is to induce a modification /functionalization of the carrier substrates and/or the nanofibers itself.

2   Experimental

2.1   Nanofibres processing

Polyamide 6 (PA6) as a model polymer was chosen for preparation of polymer nanofibers. Polymer solution was made from granulated polymer Ultramid B24 (BASF Company, Germany) dissolved in the solution of glacial acetic acid (CH_3COOH, 99%) and formic acid (HCOOH, 98%) (Sigma Aldrich). For fabrication of nanofiber mats a Nanospider[TM] NSLAB 500 (Elmarco, Czech Republic) was used. The solution for electrospinning was prepared by dissolving 4.5 g of polymer pellets in 50 ml of acetic and formic acid mixture in ratio 17/33 (v/v). After mixing the solution was tempered for 1h at 40°C and later 23h at 25°C. Conditions of electrospinning were as follows: 50kV applied HV, 170 mm electrode to collector distance, 4 rpm rotating speed of the working electrode. As the working electrode was used the 10 cm rotating wire electrode. The nanofiber mats were collected on paper or polypropylene substrates with a 15 mm/min shift speed.

2.2   Plasma treatment

Plasma treatment of nanofibers carriers was carried out by an experimental DBD plasma devices developed at the Department of Physical Electronics, Masaryk University and closely described in Czech utility model PUV-28677 – "Device for plasma surface treatment of material being selected from the group comprising film, paper, fabric, non-woven fabric" [5]. The main advantage of this devices is the novel convexly curved coplanar DBD electrode enables in-line industrial application. The nanofiber carrier (paper and PP foil) was treated 60 s in ambient air and discharge power 400 W. Then the plasma activated substrate was inserted to electrospinning machine and a layer of nanofibers was deposited on the treated surface. Plasma treatment of nanofibers was carried out by an atmospheric pressure microwave jet (2.45 GHz) – surfatron (commercial SAIREM SURFATRON 80 with integrated matching unit). The microwave generator operated in continuous mode with 150 W of power. The surfatron design consists of a coaxial resonant cavity with a 1 mm wide wave launching gap around a fused silica discharge tube. Argon was chosen as a working gas with flow rate set to 1.45 slm. The admixture 2% oxygen was added to the main gas. During the plasma surface treatment, the PA6 samples were fixed on planar holder with 15 mm distance from the end of the plasma discharge tube. The holder was motorized, mowing rate at 12 mm/s, and the number of passings through the plasma determined the total exposure time.

3   Results and Discussion

In Fig. 1 a SEM image of PP carrier with electrospunned PA6 nanofibers is shown. On the left side (A) is clearly visible bad adhesion of nanofiber mats to polymeric substrate. There is no apparent interaction that could promote the adhesion properties. In the contrast, the side (B) demonstrate the effect of plasma treatment on adhesion improvement. The whole surface of nanofiber mats is in tight contact to PP carrier which significantly increased the mechanical properties of deposited nanofibers. Similar results were observed when the paper was used as carrier substrate.
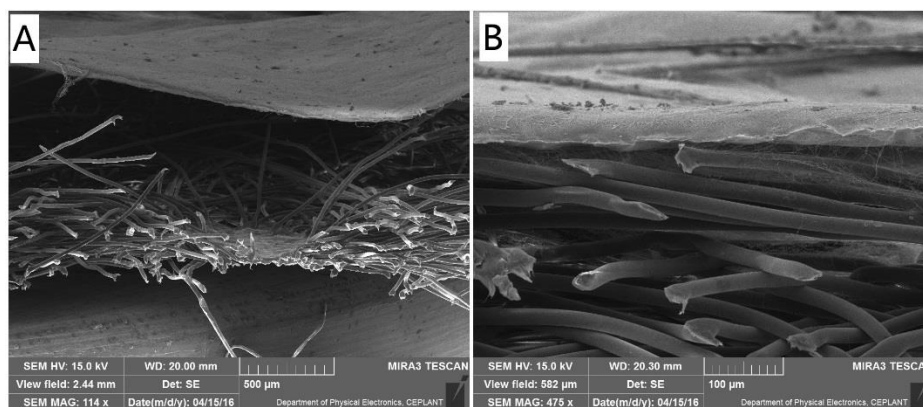
Fig. 1: SEM images of the adhesion effect to non-treated (A) and plasma treated (B) polypropylene carrier. Magnification: Image A – 114x, Image B – 475x.

In Fig. 2 a SEM images of electrospun polyamide nanofibers are shown. After the plasma treatment, sintering of nanofibers was observed. The sintering can be quantified by apparent porosity, which decreases with increasing treatment time. The porosity of samples was calculated from SEM images using ImageJ software. The values for Ar+O_2 plasma treatment are following: for 1x treatment the porosity is 22.8%, for 2x it is 6.0% for 4x it is 2.0% for 8x it is 1.6% and for 16x it is 0.35%. It can be seen that for 16 treatments, which is the maximum in this study, there are almost no pores left on the surface of the nanofiber mat.
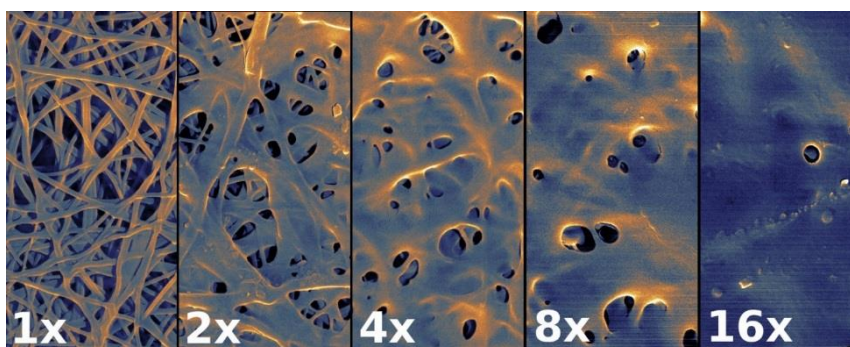
Fig. 2: SEM images of the PA6 fibers for increasing number of plasma (Ar + 2% O2) treatment repetitions. (Firstly published in [1].).

In Fig. 3 the ATR-FTIR spectra of treated PA6 fibers are shown. All particular absorption lines of the spectra revealed a fundamental chemical composition of polyamide-6. The chemical changes induced by plasma discharge were studied in two regions. While the absorptions in the region A (around 750 cm^{-1}) can be assigned to the internal structural changes of the γ-crystalline form, the absorptions in the region B are predominantly caused by polymer surface oxidation. Especially the absorbance band at 1714-1650 cm^{-1} can be interpreted as an increased abundance of carbonyl groups (C=O). It is well known that the absorbance of carbonyl, carboxyl (COOH) and ester (COOR) functional groups occur most often in this infra-red region [1, 6, 7].
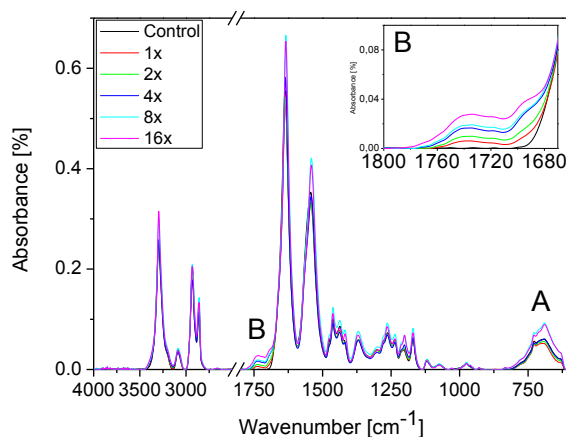
Fig. 3: ATR-FTIR spectrum of plasma treated PA6 nanofibers. In the right-upper corner is maximized the absorbance region of carbonyl functional groups. (Firstly published in [1].)

4   Conclusion

In summary, the results of above mentioned experiments show the advance of used plasma technologies to improve the properties of electrospunned nanofibers. The increasing of adhesive properties to carrier substrate as well as surface plasma functionalization of polyamide nanofibers were confirmed.

Acknowledgement

References

1. D. Pavliňák et al., Polym. Degrad. Stab. 108, 48-55 (2014)

2. A Manakhov et al., Thin Solid Films 581, 7-13 (2015)

3. E. Kedroňová et al., Plasma. Process. Polym. 12.11, 1231-1243 (2015)

4. V. Švachová et al., Mater. Sci. Eng., C 67, 493-501 (2016)

5. J. Ráheľ, M. Černák, D. Kováčik. *"Zařízení pro povrchovou plazmovou úpravu materiálu ze skupiny fólie, papír, textilie, netkaná textilie."* Czech Republic, utility model PUV 28677 (2015).

6. Y. Liu et al., Macromolecules 40.17 6283-6290 (2007)

7. D.W. Mayo et al., Course notes on the interpretation of infrared and Raman spectra. (New York: Wiley-Interscience) 2004.

CHANGE OF SURFACE CONTACT ANGLE OF POLYMERIC MATERIALS EXPOSED ON PLASMA GENERATED IN DBD PLASMA JET REACTOR

M. Kwiatkowski, P. Terebun, J. Diatczyk, J. Pawlat

Institiute of Electrical Engineering and Electrotechnologies of Lublin University of Technology, ul. Nadbystrzycka 38a, 20-618 Lublin, Poland

E-mail: askmik@hotmail.com

One of the characteristics, defining the physicochemical surface properties of material surfaces is its wettability. Wettability can be determined by measurements of the contact angle. This work describes a method of changing the contact angle of polymeric materials using a plasma jet type reactor with dielectric barrier discharge.

Keywords: atmospheric pressure plasma; dielectric barrier discharge plasma jet; surface modification; polymer

1 Introduction

Materials made from plastics such as acrylonitrile-butadiene-styrene (ABS), polypropylene homopolymer (PP-H), and high impact polystyrene (HIPS) are characterized by different mechanical and thermal properties. Their common feature is the ease of heat and mechanical processing, as well as high resistance to chemical compounds. They are widely used in many fields, eg. buildings, advertising, food industry (packaging and pallets for food products), etc. Possibility of atmospheric pressure plasma application in bioindustrail fields is widely investigated by many research groups [1-6].

2 Experimental

Study the properties of materials treated with non-thermal plasma was carried out using a plasma jet type reactor, which construction is shown in Fig. 1. The reactor was supplied by voltage of 3.7 kV with frequency of 17 kHz, distance between plasma jet and sample was 20 mm. All test samples had a size of 30 mm × 40 mm with a thickness of 2 mm. Softening temperatures of HIPS, ABS and PP-H ranged 90, 94 and 95°C, respectively. All measurements were made for gas temperature below the softening temperature of material with the smallest thermal resistance.
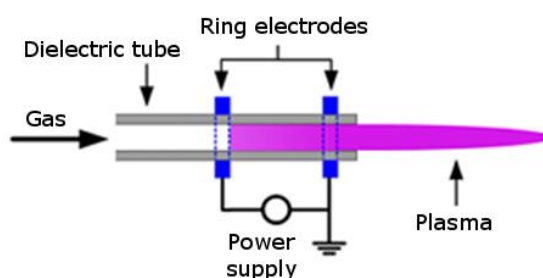
Fig. 1: Diagram of DBD reactor in system of two ring electrodes on a ceramic tube.

3   Results and Discussion

The contact angle of the control sample for PP-H was 82 degree and it decreased after 30 s of plasma treatment. The change in flow or increased air addition had no significant effect. For ABS (control contact angle of 75 degrees) results showed higher discrepancy with increased flow rate of helium (1.67 l/min). The contact angle for the control sample of HIPS was 90 degrees. During the plasma treatment, slightly increasing trend in contact angle value with increasing air flow could be observed. Fig. 2 shows the comparison of contact angles with three materials treated with plasma jet during 120s. The smallest contact angles were achieved for HIPS material and the greatest for the PP-H material. For this case slight angle increase with increasing addition of air was observed.
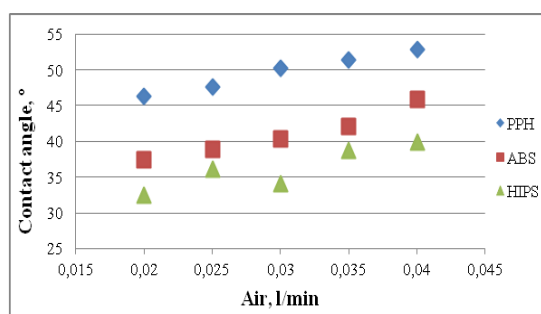
Fig. 2: Comparison of surface contact angle for different materials in dependence on air flow. Plasma treatment time- 120s, helium flow rate-1.33 l/min.
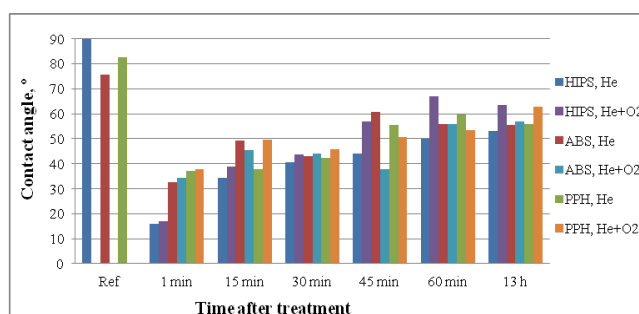
Fig. 3: Surface contact angle dependence on time elapsed since plasma treatment.

Fig. 3 depicts contact angle values and time elapsed from the end of plasma treatment of polymeric materials. It can be seen that the longer time elapsed from the end of treatment, the material surface contact angle increase approaching to the measured initial value.

4   Conclusion

The results show that the use of non-thermal plasma generated in the barrier discharge reactor significantly reduced the hydrophobicity of the tested materials. Increase in the gas flow rate or in air addition did not significantly affect these properties. Much more important is the time elapsed since completion of the materials treatment. The results show that with time the surface contact angle value increased, which may indicate the reversibility of process.

References

1. N. Škoro et al., J. Phys. D: Appl. Phys. 46(47) 475206 (2013)
2. K. Hensel et al., Biointerphases 10(2) 029515 (2015)
3. M. Fialová et al., Chem. Listy, 106, 1439 (2012)
4. J.-L. Brisset et al., Plasma Chem. Plasma Proc., 36(2), 355 (2016)
5. J. Pawlat, Eur. Phys. J. Appl. Phys. 61 (2) 24323 (2013)
6. J. Pawłat et al., IEEE Trans. Plasma Sci. (99)1, (2015)

BORON-BASED THIN LAYERS DEPOSITED BY RF PLASMA JET WITH SLIT NOZZLE

B. Pijáková, M. Alberti, M. Klíma

Department of Physical Electronics, Masaryk university, 267/2 Kotlářská,
CZ-61137 Brno, Czech Republic

E-mail: barbora.pijakova@mail.muni.cz

An atmospheric pressure slit plasma jet system was used to prepare thin layers using trimethyl borate. Organic precursor was introduced to plasma in a form of vapor. Observation of produced layers was focused on chemical composition, surface structure and friction coefficient measurements. Smooth surface exhibits low RMS roughness and friction coefficient of 0.05, enabling the potential industrial application.

Keywords: friction coefficient; RF plasma jet; trimethyl borate

1 Introduction

Boron-based compounds have wide variety of use. Ranging from the flame retardants [1], up to products with remarkable mechanical properties such as cubic boron nitride exhibiting high hardness [2] or low friction coefficient surface layers based on boric acid [3, 4].

For this purpose, trimethyl borate is appropriate for partial conversion to boric acid, because of possible hydrolytic reaction in contact with moisture [5], affecting the change of surface mechanical properties.

Herein, we report the deposition of thin layers from trimethyl borate vapors used as precursor by atmospheric pressure plasma jet system. The resulting product demonstrates low friction coefficient and RMS roughness.

2 Experimental

2.1 Materials

Microscope slides by Paul Marienfeld GmbH & Co.KG (76x26x1 mm) were used as substrates. Boron trioxide ($\geq$98%), methanol ($\geq$99.9%), sulphuric acid ($\geq$95%) and calcium chloride ($\geq$93%) were purchased at Sigma Aldrich. Deionized water (conductivity 18.18 μS/cm at 13°C) was prepared at Masaryk University using demineralization unit RO1-1CC (MEMSEP Ltd.).

2.2 Methods

Chemical composition was detected by EDX analysis (Oxford Instruments). Surface topography was observed by scanning electron microscope Tescan MIRA3 with BSE, SE and InBeam detectors (Tescan). Scratch tests and calculation of friction coefficient and roughness were executed on Hysitron TI950 Tribo Indenter operating with software TriboScan and TriboView.

2.2.1 Synthesis of trimethyl borate

Reaction of boron trioxide and methanol, catalyzed by sulphuric acid was realized at higher temperature using heating mantle and reflux condenser for 60 min. Subsequently, the reflux condenser was replaced by Liebig condenser. Distillation was proceeding up to vapor temperature of 68 °C, reducing the liquid in heated bulb flask to minimum. Extraction of the trimethyl borate was realized by mixing condensate with calcium chloride, causing the mixture to separate into two layers. The upper layer containing the trimethyl borate was collected using separatory funnel.

2.3 Experimental setup

Fig. 1 shows the jet system composed of double vapor jet (1) mounted in between two plasma jets (2). Plasma jet with slit nozzle was equipped with grounded electrode (3) and working electrode (4), connected to RF source Caesar (5; 0-1000 W; Dressler) operating at 13.56 MHz. RF signal from source was transferred via coaxial cable (6) to LC matching unit (7) for limitation of reflected power.

Transport of carrier gas, argon, and precursor vapors was managed by hosing system (8), connecting jet inlet with the argon bottle (9). Control of gas flows were managed by separated flow meters (10). Introduction of precursor vapors was realized by using bubbler (11).

2.4 Deposition conditions

Jet system for deposition of layers was using power supply of 450 W, argon flow to single plasma jet of 50 l/min, argon flow of 1.7 l/min to bubbler with trimethyl borate and 3 l/min for bubbler with deionized water. Precursors were transported to vapor jet separately. The distance between substrate and slit edge was stated to 10 mm. Covering of whole sample surface by deposit was realized by conveyor working at speed of 1.4 m/min. The deposition cycle was repeated 6 times.

For structure comparison, glass substrate was dipped in boric acid trimethyl ester and retained in a fume hood for hydrolysis caused by air moisture.
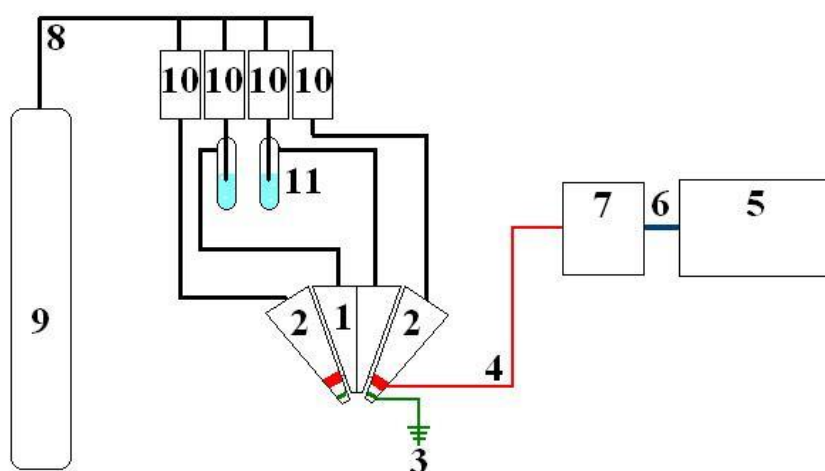
Fig. 1: Apparatus

3   Results and Discussion

3.1 Chemical composition

EDX analysis accompanying the SEM performed the presence of boron on both types of samples, specifically 2.62 at.% for P1 and 28.18 at% for D1. However, signal for deposited samples is very weak. This significant loss of signal strength could be caused by depositing very thin layer and collection of signal predominantly from glass substrate.

3.2 Structure

Surface structure of sample P1 prepared using jet system in comparison to sample D1 prepared by dipping method is depicted on Fig.2a). Using the magnification of 50kx, the significant differences are observable. Despite of fact, that sample P1 exhibits presence of crackles, the surface is relatively homogeneous. On the other hand, surface of sample D1 is covered by crystalline material with large variety of crystal sizes. Individual crystals are aggregated to microscopic formations.

3.3 Tribology

Realized scratch tests on P-type samples allowed the determination of friction coefficient, wear resistance and roughness. In Fig.2b), measured area of sample P1 before and after scratch test is presented. The friction coefficient is 0.05, corresponding to friction coefficient of boric acid layer described in [6]. RMS roughness before scratching is stated to 0.94 nm, while the RMS roughness after test was only 0.27 nm. Decreasing RMS roughness is related to moderate wear resistance of layers and caused by surface smoothening during the mechanical material loss. Nevertheless, the RMS roughness lower than 1 nm refers to very smooth surface.
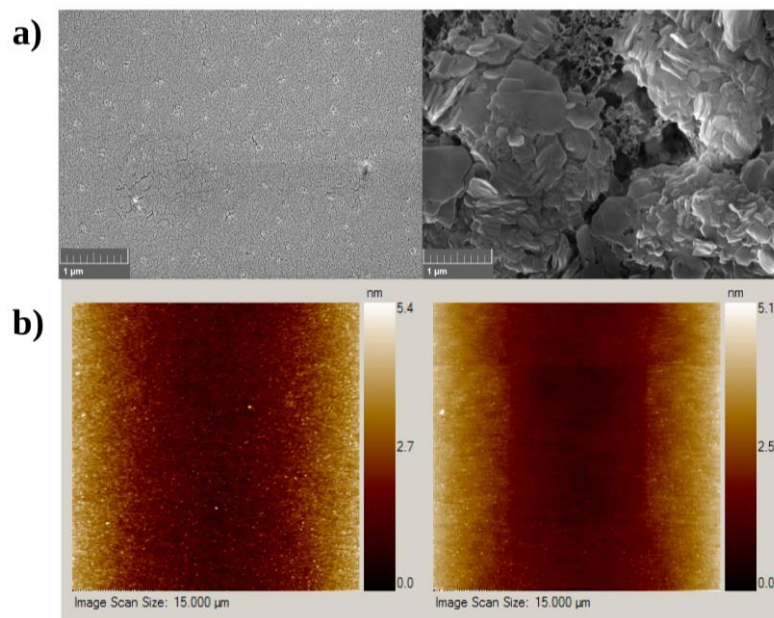
Fig.2: a) SEM images of surface structure; magnification 50kx; left – P1 (InBeam); right – D1 (SE); b) P1 surface image from Hysitron TriboIndenter; left – before scratch test; right – after scratch test

4   Conclusion

We reported the simple preparation of boron based thin layers using plasma jet system equipped with vapor jet enabling to inlet the precursor in the form of vapors to plasma. Resulting products exhibited structure homogeneity, characteristic low friction coefficient of 0.05 and RMS roughness lower than 1 nm.

References

1. M. Dogan et al., Polym. Degrad. Stab. 99, 12-17 (2014)
2. P. B. Mirkarimi et al., Mater. Sci. Eng. R 21, 47 (1997)
3. A. Erdemir et al., Wear. 205, 236-239 (1997)
4. A. Erdemir et al., Surf. Coat. Technol. 87, 507–510 (1996)
5. P. Turner, Wood Sci. Technol. 29, 385-395 (1995)
6. D. Kurapov et al., Plasma Chem. Plasma Process. 25, 613-623 (2005)

PLASMA TREATMENT OF NATURAL LEATHER WITH DIFFUSE COPLANAR SURFACE BARRIER DISCHARGE IN AMBIENT AIR

V. Štěpánová[1], J. Kelar[1], P. Slavíček[1], S. Chlupová[1], J. Jurmanová[1],
M. Stupavská[1], M. Zvonař[2], M. Černák[1]

*[1]Department of Physical Electronics, Faculty of Science, Masaryk University,
Kotlářská 2, 611 37 Brno, Czech Republic*
*[2]Department of Kinesiology, Faculty of Sports Studies, Masaryk University,
Kamenice 5, 625 00 Brno, Czech Republic*

E-mail: vstepanova@mail.muni.cz

Natural leather was plasma treated with Diffuse coplanar surface barrier discharge (DCSBD) at atmospheric pressure. The aim of plasma treatment was activation of leather surface and improvement of wettability. Samples of bovine leather were plasma treated for few seconds and analyzed with SEM, XPS, and contact angle measurement. Surface morphology was not affected with plasma treatment. Plasma treatment caused wettability change at the half value of contact angle in comparison with untreated leather. Wettability change is relative stable in the first 24 h after plasma treatment. Change in percentage of chemical bonds containing carbon and oxygen was observed.

Keywords: natural leather; plasma treatment; DCSBD; contact angle measurement

1   Introduction

The aim of this contribution is to activate the surface of natural leather with low temperature plasma and improve its hydrophilicity. Plasma treatment of leather at low-pressure in different gas mixtures is described in literature [1]. Low temperature plasma generated by radio frequency (rf) discharge in different gases is used for change of surface properties of natural leather [2].

Potential of this application is in improvement of dyeing ability, adhesion before gluing and better printability of natural leather. Mechanical properties of leather, like elasticity and tensile strength, are important parameters which should not be ruined due to plasma treatment.

2   Experimental

Plasma treatment was provided with Diffuse coplanar surface barrier discharge (DCSBD) at atmospheric pressure in ambient air. DCSBD operates at the frequency of 15–50 kHz in ambient air with discharge power in the range 100-600 W. Power of 400 W and frequency of 15 kHz were used in this work. The discharge area produced by the DCSBD is 8 × 20 cm and the thickness of generated plasma is about 0.3 mm. This type of discharge has already found application in treatment of nonwoven textiles [3], glass [4], metals [5], rabbit fibres [6], etc. Exposure time of 10 seconds was used for plasma treatment.

Contact angles were measured with See System (Surface Energy Evaluation) analyzer (Advex Instruments). Detailed images of natural leather were done on the scanning electron microscope Mira3 (Tescan) and XPS spectra were obtained from the ESCALAB 250Xi (Thermo Fisher Scientific).

Natural bovine leather from our industrial partner commonly used in footwear production was used for experiments.

3   Results and Discussion

Surface morphology observed using SEM (scanning electron microscope) shows no difference between untreated and plasma treated surface of leather (Fig. 1). Leather contains a lot of pores on the surface and average diameter of pore is 39 μm.
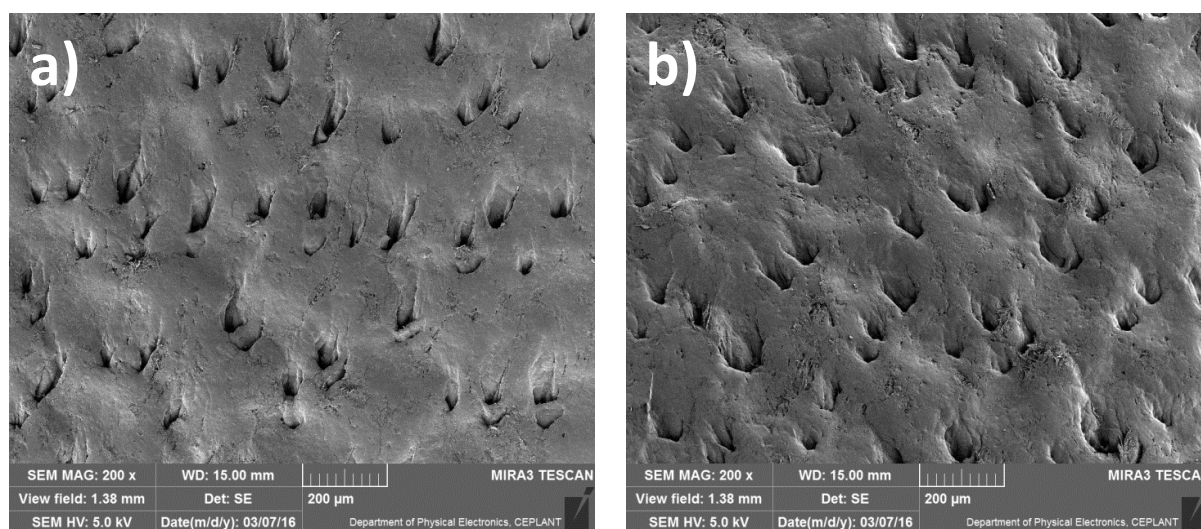
Fig. 1: Surface morphology of a) untreated and b) plasma treated leather. Magnification 200x and accelerating voltage 5 kV was used.

Influence of plasma treatment on the wettability of leather was investigated via water contact angle measurement. Plasma treatment caused wettability change from 89.6 ± 0.9° for untreated to 40.8 ± 0.9° for plasma treated (10 s) leather. Aging effect of plasma treatment was examined because the hydrophilization of leather is not stable in time. Contact angles were measured immediately after plasma treatment, then 2 h, 8 h, 24 h, 48 h, and 120 h after plasma treatment. Aging effect of plasma treatment is shown in Fig. 2. Wettability change is relative stable in the first 24 h after plasma treatment. Contact angle increased to the value of 80.3 ± 1° during 48 h after plasma treatment. After 5 days from plasma treatment the value of contact angle increased almost to the value of the untreated leather.
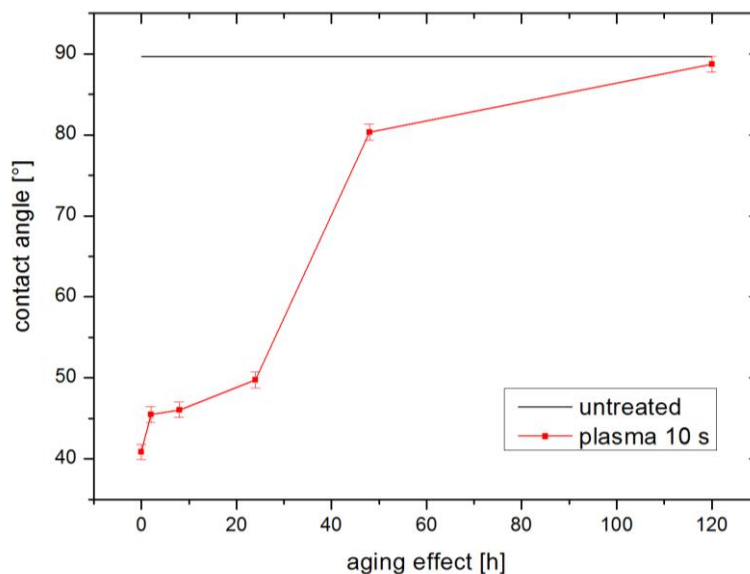
Fig. 2: Water contact angle in dependence on aging effect of plasma treatment.

Tab. 1: Chemical composition of untreated and plasma treated leather.

sample	Atomic percentage [%]			Bonding type percentage [%]				
	C	O	N	C-C/C-H	C-O	C=O	O-C=O	C-N
untreated	74.03	17.95	3.01	76.63	7.85	1.11	4.25	10.16
10 s plasma	67.18	22.06	4.54	68.38	11.81	3.64	4.76	11.4

Chemistry of plasma treated leather was determined using XPS (X-ray photoelectron spectroscopy). The surface composition and carbon chemistry of treated and untreated leather is presented in Tab.1. Main difference in chemical composition of leather after plasma treatment was in contain of carbon and oxygen – carbon decreased and oxygen increased. The peak fitting routines were done in order to evaluate the changes in the bond structure and, therefore, explain the observed changes after plasma treatment. The high resolution C 1s peak was fit with 5 principal components: C-C/C-H (binding energy at 284.8 eV), C-N (285.9 eV), C-O (287.0 eV), C=O (288.0 eV), and O-C=O (289.0 eV). The results of the fits are presented in Table 1. Percentage of oxygen containing bonds was higher after plasma treatment, in contrast with percentage of C-C/C-H bond, which decreased after plasma treatment.

4   Conclusion

Plasma treatment of leather caused its hydrophilization. Wettability change was not stable in time, contact angle reached the value of untreated sample after 5 days. Surface morphology of leather was not affected with plasma, no changes between untreated and plasma treated leather were observed. Percentage of chemical bonds was different after plasma treatment: C-C/C-H bond decreased in comparison with C-O, C=O, and O-C=O bonds, which increased. DCSBD is a suitable device for hydrophilizaiton of natural leather without damage of the surface.

References

1. X. You et al., App. Surf. Sci. 360 (2016)
2. J. H. Choi et al., Surf. Coat. Tech. 171 (2003)
3. M. Černák et al., Eur. Phys. J-Appl. Phys. 47 (2009)
4. V. Štěpánová et al., Chem. listy 106 (S) (2012)
5. V. Prysiazhnyi et al., Thin Solid Films 550 (2014)
6. V. Štěpánová et al., App. Surf. Sci. 355 (2015)

CARBON FIBER SURFACE TREATMENT WITH ATMOSPHERIC PRESSURE GLOW PLASMA FOR NEW CFRP FABRICATION

K. Tanaka[1], M. Ohkoshi[2], H. Hamada[2], M. Kogoma[1]
[1]Department of Materials and Life Sciences, Sophia University, Tokyo, Japan
[2]Future-Appliedd Conventional Technology Center, Kyoto Institute of Technology, Kyoto, Japan

E-mail: tanaka@mls.sophia.ac.jp

Carbon fiber surface treatment methods with atmospheric pressure glow plasma were investigated to develop new carbon fiber reinforced plastics used polycarbonate or polyethylene. Amine groups on the carbon fiber surface introduced by $O_2/H_2/He$ plasma treatment and chemical reaction with 3-(2-aminoethylamino) propyltrimethoxysilane improved the adhesiveness between the treated carbon fiber and polycarbonate. Convexoconcaves of the carbon fiber surface made by the silica deposition via dimethoxydimethylsilane/O_2/He plasma improved the adhesiveness between the treated carbon fiber and polyethylene.

Keywords: carbon fiber reinforced plastic; polycarbonate; polyethylene; atmospheric pressure glow plasma

1 Introduction

Carbon fiber reinforced plastic (CFRP) with a thermosetting resin, such as epoxy resin, is widely used for some constructional materials (e.g. jumbo jet aircraft's body) because of its light weight and high strength. However, since current CFRP needs a thermosetting resin, it has low productivity and high cost. So a new CFRP used a thermoplastic resin (e.g. polycarbonate, polyethylene, nylon and so on) has been desired.

Before producing current CFRP, carbon fiber (CF) surfaces are treated with some agent (e.g. silane coupling agent) to improve the adhesiveness between CF and epoxy resins. The adhesiveness between untreated CF and almost all thermoplastic resins is also low. Thus, new CFRP production needs some surface treatments, but there is no suitable agent for any thermoplastic resins. Therefore, in this study, we tried to develop a new CF surface treatment method with the Atmospheric Pressure Glow (APG) plasma, and polycarbonate (PC) and polyethylene (PE) were used as the thermoplastic resins.

2 Experimental

Fig. 1 shows the dielectric barrier discharge apparatus for 1 m CF ribbon treatment. The discharge area was a quartz glass tube (ϕ_{id} = 7 mm, ϕ_{od} = 9 mm) and was cooled by cooling liquid (Fluorinert FC-40, 3M). Both the ring electrode thickness and the electrode distance were 3 mm. PAN (polyacrylonitrile) type CF ribbon was used in this study. An about 1 m length and 5 mm width CF ribbon was set in the apparatus, and then the CF was treated by the APG plasma. We supposed that amine groups (NH2-) react with PC and amide bonds (R-CONH-R') are generated. Thus, the CF for PC was treated by $O_2/H_2/He$ plasma to generate hydroxy groups (-OH) and then plasma treated CF reacted with 3-(2-aminoethylamino)

Table 1 The plasma treatment conditions.

Discharge frequency	300 kHz
Discharge power	250 W
He flow rate	6 slm
O_2 flow rate	20 sccm
H_2 flow rate	2 ~ 6 sccm
DMS flow rate	1 sccm
O_2 flow rate	20 sccm
Pressure	atmospheric pressure

Table 2 The heat press conditions.

Temperature	120ºC
Pressure	0.2 MPa
Press time	15 s
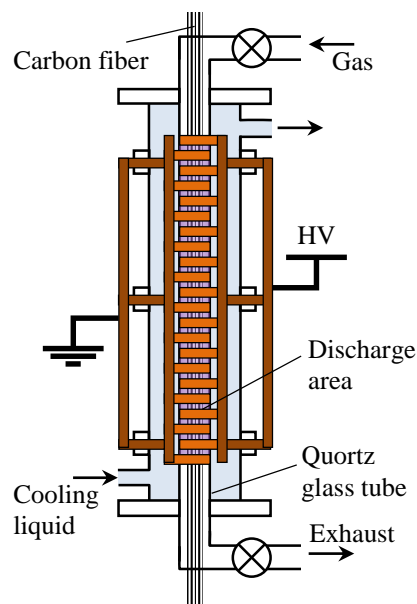
Fig. 1: Schematic diagram of the discharge apparatus.

propyltrimethoxysilane (AS): treated CF ribbon dipped into AS ethanol solution in a fixed soaking time. In the case of PE, since it is quite difficult to bring a chemically reaction between CF and PE, we tried to make some convexoconcaves on the CF surface. First, the CF for PE was treated by dimethoxydimethylsilane (DMS)/O_2/He plasma to deposit some silica and was treated by O_2/He plasma continuously. [1] Table 1 shows the plasma treatment conditions.

The treated CF ribbons were examined with XPS and SEM. The adhesiveness between the treated CF and thermoplastic resins were measured by the pull-out test. The test pieces for the pull-out test was prepared by a heat press of treated CF ribbon and thermoplastic resin plate. the heat press conditions are show in Table 2.

3 Results and Discussion

3.1 CF treatment for PC

Fig. 2 shows the Si/C and N/C atomic ratios obtained from XPS measurement. Silicon and nitrogen atoms proceeded from AS, and their amount was not decreased by washing with any solvents. Thus, AS reacted with CF completely. Fig. 3 shows the pull-out test results of treated CF and PC test pieces. The pulling resistance value was increasing as the increasing AS on CF. Therefore, the adhesiveness between the treated CF and PC was improved by introducing amine groups onto CF surface.

3.2 CF treatment for PE

Fig. 4 shows the pull-out test results of treated CF and PE test pieces. Only the pulling resistance of 5 min treated CF indicated quite high value. Fig. 5 shows SEM photographs of untreated and silica deposited CF. While silica depositions on 5 min treated CF surface were sparse, those of 20 min treated CF covered CF surface completely. These results indicated

that convexoconcaves on the 5min treated CF caught PE molecules, and the adhesiveness between the treated CF and PE became strong.
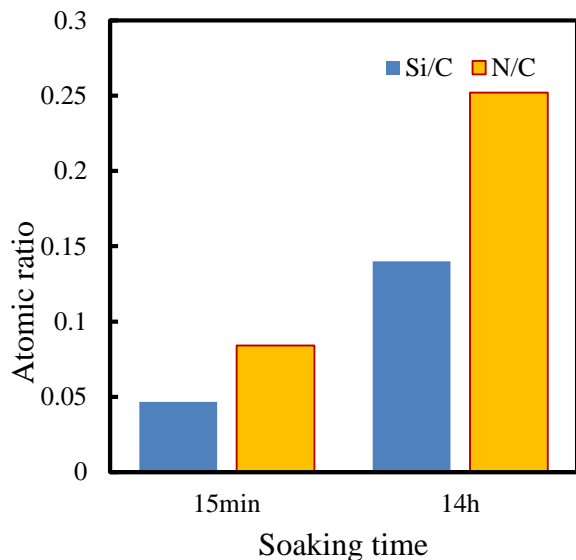
Fig. 2: Atromic ratios of CF surfaces reacted with AS.
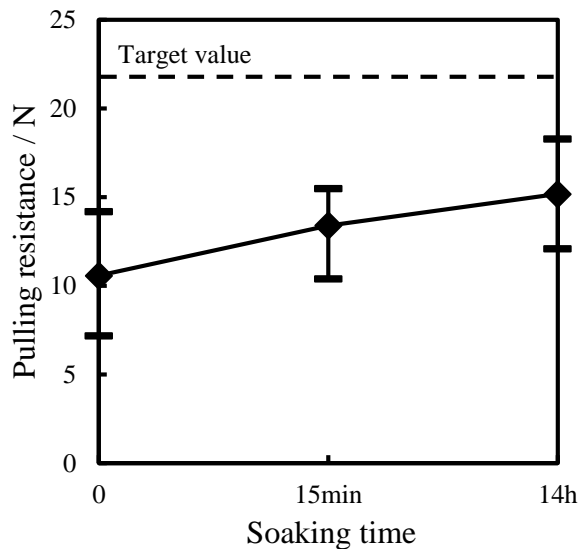
Fig. 3: The pull-out test results of treated CF and PC test pieces.
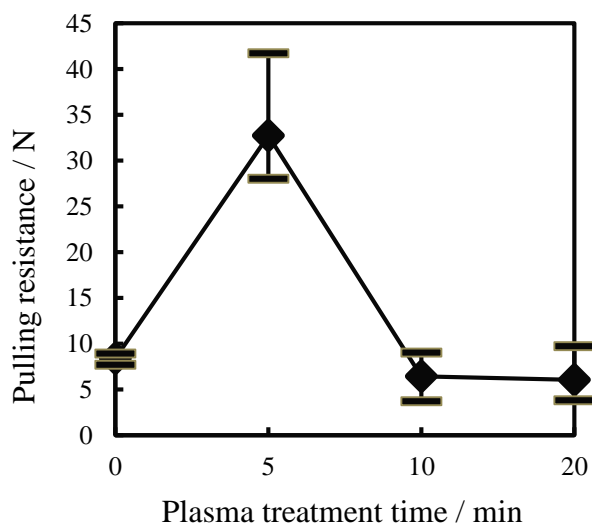
Fig. 4: The pull-out test results of treated CF and PC test pieces.
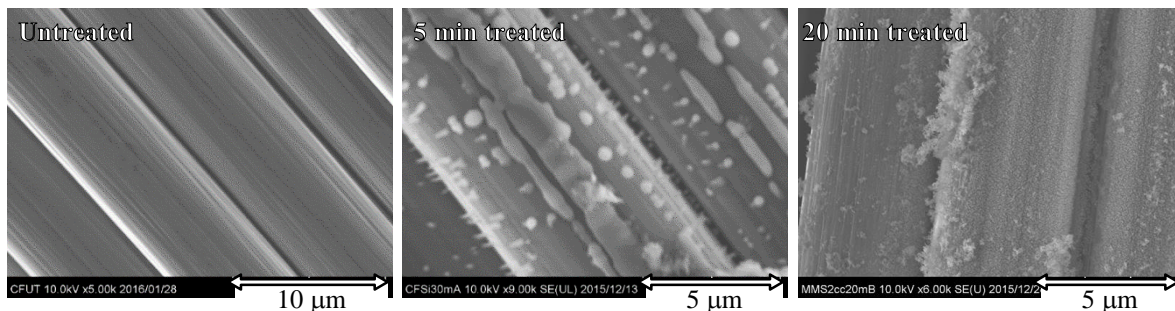
Fig. 5: SEM photographs of untreated and silica deposited CF.

4   Conclusion

The APG plasma treatment improved the adhesiveness between the treated CF and PC or PE. These strengths were not enough. So we will try to introduce more amine groups and convexoconcaves onto CF surface.

References

1. L. Hooseok et al., Appl. Surf. Sci. 328, 241-246 (2015)

TOPIC 8: BIOLOGICAL APPLICATIONS

POWER MEASUREMENT FOR AN ATMOSPHERIC PRESSURE PLASMA JET AT DIFFERENT FREQUENCIES – DISTRIBUTION IN THE CORE PLASMA AND THE EFFLUENT

T. Gerling, R. Brandenburg, C. Meyer, C. Wilke, K.-D. Weltmann

Leibniz Institute for Plasma Science and Technology (INP Greifswald), Felix-Hausdorff-Str 2, 17489 Greifswald, Germany

E-mail: gerling@inp-greifswald.de

The characterization of electrical power distribution in an atmospheric pressure plasma jet operated at six different frequencies is investigated by measurement of input power and voltage-charge plots for the 'core' plasma and the plasma in the effluent. The frequency change is further characterized by measuring the temperature in the effluent at different positions and input power levels. The power input into the 'core' plasma is limited to about 1 W for a wide range of frequencies while the total input power and thus the power input into the effluent increases continuously with frequency.

Keywords: electrical characterization; atmospheric pressure; plasma jet; power measurement

1   Introduction

Cold atmospheric pressure plasma jets cover a wide range of potential applications, e.g. plasma medicine, where these devices offer a high potential for therapeutic use [1]. While the basic research on biological effects in this field is meanwhile well established, the physics of the plasma sources itself is handled quite differently in the community [2]. For example, the aspect of the medical restrictions is not widely addressed [3].

During many cycles of plasma source development for potential medical applications we encountered several challenges in the source optimization. One of them resulting from addressing legal regulations is the reduction of the plasma efficacy due to implementation of a duty cycle for the applied high voltage, as encountered in the development chain for first plasma jet to be certified as a medical product, the kINPenMED (neoplas tools GmbH) [4]. The stability and reproducibility of the plasma source is an important aspect for the evaluation of biological tests as well as the transfer of in-vivo results to more praxis-oriented investigation and clinical applications. One important value, also for the comparison of different plasma sources is the input power, as it is typically used in combustion research or exhaust gas treatment to scale efficiency.

In plasma medicine, the aspect of efficacy is yet a topic for discussion, since the classification of effective agents is difficult due the variety, the individual response of the treated object and the difficulties to measure them. Nevertheless, the approach in this contribution is aimed to measure one live parameter that is supposed to scale with efficacy. Here the focus is on the electrical input power, which was determined for different frequencies of applied voltage by

means of voltage-charge plots. Finally, we will discuss the distribution of power in the discharge between the 'core' discharge in the nozzle and the effluent plasma leaving the electrode configuration. Therefore, the temperature is measured in the effluent.

2   Experimental setup

The experimental setup is shown schematically in figure 1. A sinusoidal power supply is connected to different inductances to match a range of frequencies. A list of the chosen values is given in table 1. Attached to the inductance is a kINPen plasma nozzle ("head") as described in [4]. An inner needle electrode is connected to the high voltage and a gas flow of 5 slm argon is supplied to the head. A dielectric capillary (steatite, 1.6 mm inner and 2.4 mm outer diameter) surrounds the needle and shields the high voltage electrode from the grounded housing of the head. Attached to the head is a measurement capacitor for the voltage-charge plots (also referred to as Lissajous figures). The input voltage U_P, the high voltage U_{S1} and voltage over the capacitor U_C are measured with voltage probes (Tektronix P6015A and P6139A) and the current I_P as well as the current to the ground I_{S2} are measured with current probes (Pearson 2877 and Tektronix CT 1). In order to further characterize the difference between different frequencies, the temperature in the effluent was measured by an optical fiber as described in [5].
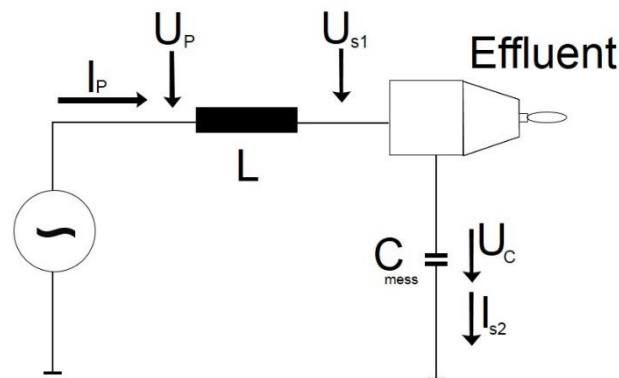
Fig. 1: A scheme of the experimental setup with the measurement values.

Tab. 1: Overview of parameters in this study. The input voltage was varied from 40 V to 65 V, the frequency was adapted for every applied voltage to be in resonance

Input voltage U_P	61V	63V	42V	44V	57V	47V
Input current I_P	12mA	21mA	40mA	53mA	66mA	109mA
High voltage U_{S1}	3,8kV	3,4kV	3,2kV	3,1kV	3kV	3kV
Frequency f	80kHz	233kHz	380kHz	573kHz	814kHz	1500kHz
Inductance L	151mH	32mH	12,6mH	5,78mH	2,9mH	0,96mH
Measurement capacitor C_{mess}	4,2nF					

The input power as well as the plasma power are calculated from the respective measurements. In addition, the input power without plasma is measured every time to estimate power losses e.g. heat loss at the inductance [6]. The difference between input power with and without plasma results in the plasma power consumption in the device head. With the value from the voltage-charge plots the consumption of the head can be separated into two

parts: the 'core' plasma (discharge inside the head onto the dielectric) and the effluent. Hence the difference of the two power values should result in the power going into the effluent. Thus the following set of equations is used:

$$P_{In} = U(t) \cdot I(t), \text{ (plasma on)} \tag{1}$$
$$P_0 = U(t) \cdot I(t), \text{ (plasma off by switching off gas)} \tag{2}$$
$$P_{Plasma} = P_{In} - P_0, \tag{3}$$
$$P_{Liss} = A_{Liss} \cdot C_{mess} \cdot f \tag{4}$$
and
$$P_{Effluent} = P_{Plasma} - P_{Liss}. \tag{5}$$

3 Results and Discussion

Measured temperatures are presented in figure 2a for the frequencies of 0.8 MHz and 1.5 MHz. For each coordinate (see colors of corresponding lines), the temperature increases with the plasma power but is independent on the frequency.

Along with the change of frequencies, the input current steadily increased at similar input voltages (see figure 2b). Due to the device head being attached to the inductance, an increased frequency reduces the parasitic resistance of the head capacity and results in a higher current. Therefore, the input power is increased for higher frequencies.

(a)

(b)

(c)
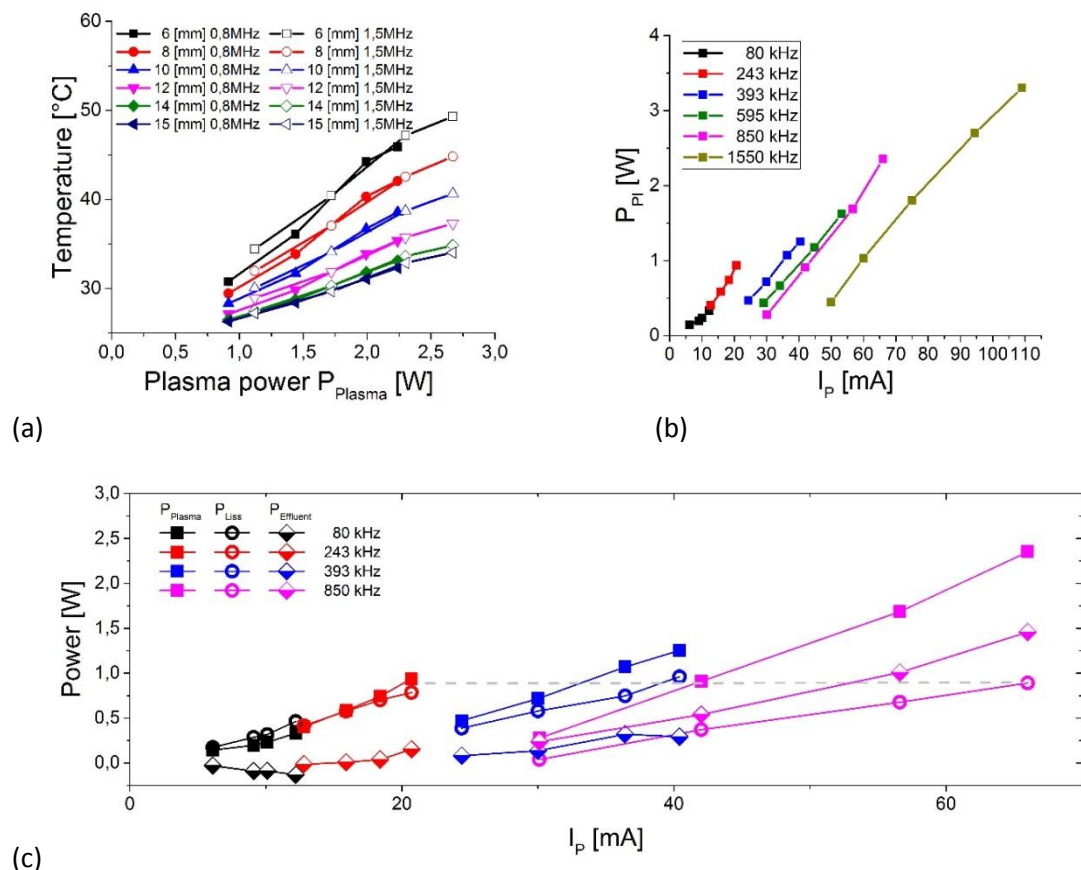
Fig. 2: (a) measurement of temperature for different distances from the capillary edge, frequencies and powers, (b) plasma power as a function of input current and frequency, (c) distribution of plasma power (P_{Plasma}, rectangular) between core plasma (P_{Liss}, circle) and effluent ($P_{Effluent}$, trapezial)

With the set of equations (1) – (5), the values in figure 2c were calculated for the investigated frequencies. At 850 kHz the Lissajous figure was nearly a straight line, therefore the value at 1.5 MHz could not be resolved. For the frequencies 243 kHz, 393 kHz, 595 kHz (not shown) and 850 kHz, the value of P_{Liss} reaches the same peak value around 1 W. Meanwhile the input power P_{Plasma} and the effluent power $P_{Effluent}$ increase steadily up to values of 2.5 W and 1.5 W. It seems that for higher frequencies and hence higher input currents, the power in the core plasma is saturated and additional input power is mainly delivered into the effluent.

Considering the measurement for the frequency of 80 kHz, the value of P_{Liss} is between 20 % and 30 % above the input plasma power P_{Plasma}. Thus, with previous observation, this would indicate a nonexistent effluent. Yet, the effluent is well observed and the deviation of the values require a more detailed discussion. One issue would be the possibility to apply the Lissajous figure for a strongly non-asymmetric geometry with an additional electrical connection outside through the effluent. This method is not limited to symmetric barrier discharge geometries and examples for non-symmetric barrier discharges can be found [7,8]. For further understanding of the deviation a further characterization of the effluent by optical and thermal measurements is planned.

4   Conclusion

The power distribution in an atmospheric pressure plasma jet operated at different frequencies is investigated by means of electrical measurements, similar as established for barrier discharges. The dissipated power of the 'core' plasma and the effluent can be determined. In the range of frequencies being investigated a saturation of power in the 'core' plasma at 1 W and a further increase of the input power and the effluent power is obtained. This observation is in contradiction with an observation for the lowest frequency, where the measured power in the 'core' plasma was greater than the input power. Further investigations on the method used for the power estimations is needed and a more detailed characterization of the effluent is planned to further understand these observations.

References
1. Th. von Woedtke et al., Physics Reports 530, 291 (2013)
2. J. Winter et al., Plasma Sources Sci. Technol. 24, 064001 (2015)
3. M. Mann et al., in *IEEE International Conference on Plasma Science*, Antalya, (2015)
4. S. Bekeschuss et al., Clinical Plasma Medicine, in print (2016)
5. K.-D. Weltmann et al., Contrib. Plasma Phys. 49, 631 (2009)
6. S. Hofmann et al., Plasma Sources Sci. Technol. 20, 065010 (2012)
7. U. Kogelschatz, Plasma Chem. Plasma P. 23, 1 (2003)
8. S. Pekárek, Eur. Phys. J. D 67, 94 (2013)

PROPAGATION OF ARGON SURFACE DISCHARGE IN LONG TUBES AT ATMOSPHERIC PRESSURE, ITS BACTERICIDAL EFFECT AND THE EFFECT OF UV EMISSION

Z. Kovalova[1,2], M. Leroy[1], C. Jacobs[1], M. J. Kirkpatrick[1], Z. Machala[2], F. Lopes[3], C. O. Laux[4], M. S. DuBow[5], E. Odic[1]

[1] *GeePs—Group of electrical engineering—Paris UMR CNRS 8507, CentraleSupélec, Univ Paris-Sud, Sorbonne Universités, UPMC Univ Paris 06 91192 Gif-sur-Yvette, France*

[2] *Faculty of Mathematics, Physics and Informatics, Comenius University in Bratislava, 84248 Bratislava, Slovakia*

[3] *Laboratoire de Génie des Procédés et Matériaux LGPM, CentraleSupélec, 92295 Châtenay-Malabry, France*

[4] *Laboratoire d'Energétique Moléculaire et Macroscopique, Combustion EM2C, CNRS UPR 288, CentraleSupélec, 92295 Châtenay-Malabry, France*

[5] *Laboratoire de Génomique et Biodiversité Microbienne des Biofilms, Institute for Integrative Biology of the Cell (I2BC), CEA, CNRS, Université Paris-Saclay, Université Paris-Sud, Bâtiment 409, 91405 Orsay, France*

E-mail: kovalova@fmph.uniba.sk

The objective of the presented work is the bio-decontamination of small diameter long tubes by direct exposure of the tube inner surface to the plasma of a pulsed corona discharge in dry or humid argon. Bactericidal tests were conducted with *Escherichia coli* strain DH-1 for various exposure times. Up to ~5.5 $\log_{10}$ reduction was observed for *E. coli* exposed 44 cm away from the HV electrode, for a 20 minute treatment. The factors contributing to the observed bactericidal effect include desiccation, reactive oxygen species (OH), H_2O_2 accumulation in the liquid phase, and UV B (and possibly VUV) in dry argon.

Keywords: low-temperature plasma; bio-decontamination; UV emission; argon plasma; pulsed corona discharges

1 Introduction

In the domain of surface sterilization of thermally sensitive materials, the decontamination of the interior of small diameter tubes (e.g. catheters, endoscopes) is an important issue. In previous studies, the inner surfaces of tubes were exposed to different plasma processes at atmospheric pressure in direct [1-3] or remote exposure modes. For the remote exposure mode, a flowing post-discharge was passed through the tube inlet. The plasma source was either a pure nitrogen corona discharge producing an emissive afterglow [4], or a humid argon dielectric barrier discharge [5]. In the latter case, argon was preferred to air as a feed gas in order to avoid the formation of ozone and nitrogen oxides that may damage the treated surface. Furthermore, water dissociation in the argon discharge is much more efficient than in air or nitrogen [6].

2   Material and methods

2.1   Plasma device

Pulsed corona discharges were propagated on the inner surfaces of a quartz tube (8 mm inner diameter, 49 cm long), in which argon (3.9 slm) or humid argon (4.7 slm, 760 ppm water vapor/argon mixture) was flowing at atmospheric pressure, from a tungsten needle connected to a pulsed high voltage power supply placed at the tube inlet to a grounded counter electrode located at its outlet (Fig. 1). A voltage probe (Tektronix P6015A) connected to the needle electrode and a current transformer (Tektronix CT-2) connected to the counter electrode were used for voltage and current measurements respectively. Signals were recorded using a LeCroy WaveRunner 62 Xi digital oscilloscope. For all bactericidal tests, the plasma was generated with a 2-2.2 µs voltage pulse at 500 pulses/s with a 20.6-27.9 kV peak voltage depending on the sample and the gas humidity.
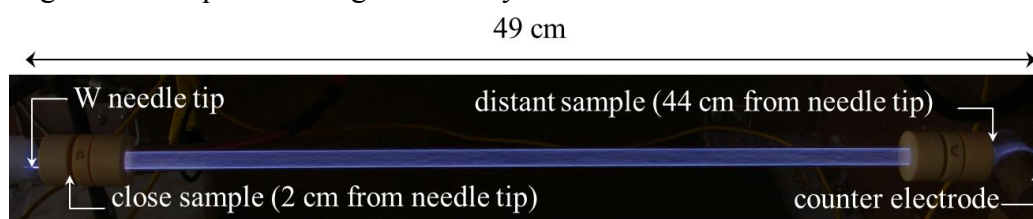
Fig. 1: The pulsed corona discharge propagating in argon gas inside an 8 mm inner diameter quartz tube over 49 cm. The bacterial sample locations at 2 and 44 cm are indicated.

2.2   Optical emission spectroscopy

OES was performed in the 250–850 nm range using an Acton Standard Series SP-2758 imaging spectrograph of a focal length 750 mm. Two ruled gratings were used in the measurements; a 2400 gr/mm blazed at 240 nm and a 300 gr/mm blazed at 300 nm. This spectrograph was coupled to a Princeton Instruments PI-MAX4:1024f-RB intensified CCD. For all spectroscopic measurements, a fiber optic cable with a collimator adjusted to collect light from a 1cm diameter disk centered on the tube axis was pointed perpendicularly at the tube from a distance of 38 cm. This fiber was moved along the tube's length in order to collect light from different positions.

2.3   Bacterial sample and test conditions

Escherichia coli strain DH-1 was used for all experiments. The culture in stationary phase was frozen with 20% (v/v) glycerol in 20 µl aliquots tittered at ~10^9 colony forming units (CFU)/ml. Before experiment aliquots were thawed and resuspended in 110 µl 1/3X LB. Droplets of 10 µl volume were placed inside or outside the quartz tube (to evaluate the UV B effect on bacteria viability), and either immediately treated as droplets (liquid) or dried at room temperature (2 – 4 h). Samples were positioned 44 cm from the needle electrode (Fig. 1) and treated by the plasma up to 20 min, samples exposed for the same duration to the argon flow alone were included as controls. Bacterial cells were recovered with rinsing of the inner or outer quartz tube surface with 100 µl sterile distilled water and resuspended in 1/3X LB. Recovered samples were serially diluted, plated on LB agar, incubated at 37°C overnight, and quantified by colony counting.

3   Results and Discussion

3.1   Optical emission spectroscopy

Optical emission spectra of the pulsed corona discharge plasma in dry and humid argon (Fig. 2) showed the presence of emissive OH radicals. In the presence of water (even traces, as it is for "dry" Ar condition), the argon plasma generates ultraviolet (UV B, 280–315 nm) emission through the de-excitation of OH* [A$^2\Sigma^+$ - X$^2\Pi$] radicals (305–311 nm), mainly produced by a water dissociation mechanism involving Ar*: Ar* (4p) + H$_2$O → Ar (3p) + OH* (A$^2\Sigma^+$) + H
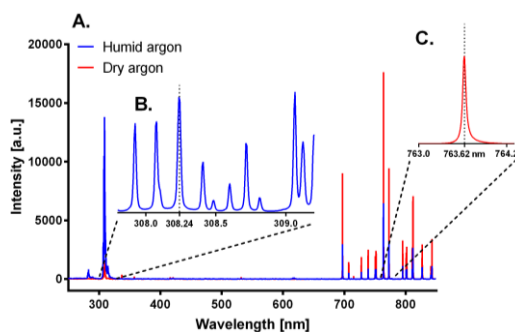
Fig. 2: A) Optical emission spectra of the pulsed corona discharge in and humid argon acquired at 5 cm from the HV electrode. Detector integration time 600 ns, grating 300 lines/mm. B) Spectrum of the rotational bands of OH [A^{2}S$^+$ - X^{2}P] measured in humid argon (760 ppm water vapor), grating 2400 gr/mm. C) Ar emission line in dry argon, grating 1800 gr/mm.

The relative intensity of the OH band depends on the humidity present in the feed gas and it is greater in argon with 760 ppm of water vapor than in dry argon [7]. This water vapor concentration is slightly below the optimum value, above which increasing the water vapor content does not lead to a further increase in the OH line intensity, but on the contrary leads to its decrease. This result was previously observed and was found to be caused by quenching mechanisms that become the dominant phenomena in high water vapor concentration conditions [7, 8] as per: OH* (A$^2\Sigma^+$) + H$_2$O → OH (X$^2\Pi$) + H$_2$O. The presence of humidity in the feed gas has thus a dual benefit of producing both reactive OH radicals and UV B emission.

3.2   Bio-decontamination efficiency of the discharge and its UV B emission

We investigated the decontamination efficiency of the pulsed corona atmospheric pressure argon plasma at the inner and outer surfaces of the quartz tube 44 cm from the HV needle electrode. The water content (in argon gas or at the sample level) was shown to be a key parameter that strongly influenced the generation of reactive species [9]. Two extreme combinations are presented in Fig. 3 - combination with the highest water content of humid argon gas and liquid bacterial samples and dry argon gas with dried samples as dried combination. The bactericidal effect of the treatment is presented in terms of "reduction factor", defined as: $log_{10}(N_0/N)$ where N_0 is the control sample CFU and N the sample after plasma treatment CFU.

The biocidal activity of emission at 308 nm is cumulative, and the decontamination efficiency tends to increase with treatment time in all conditions, reaching a maximum efficiency of 1.24 reduction factor for 20 min treatment of a liquid sample with a humid argon feed gas at 44 cm (Fig 3.). The discharge in humid argon with a liquid sample, while not the most efficient when

looking at the decontamination efficiency of the overall plasma treatment process inside the tube (In), generated the best efficiency of decontamination for UV B radiation alone outside the tube (Out). In the case of dry argon/dry sample inside the tube, VUV can have high contribution to the decontamination efficiency. For the outside samples this is not the case because the quartz does not allow VUV to pass, although we still have the effect, probably of residual humidity, that produces UV B. In the case of humid argon/liquid sample, the inside samples are exposed to higher VU B emission, OH radical production, and there is accumulation of H_2O_2 in the liquid of sample. Outside samples are exposed to higher doses of UV B originated also from sample evaporation, therefore there is higher decontamination efficiency. In the case of liquid samples, there is a dilution of the reactive species and so a delay in the bactericidal effect compared to the dried samples.
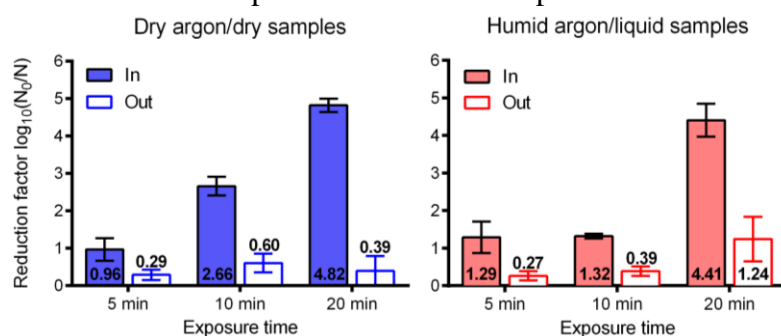
Fig. 3: Reduction factor measured after the argon plasma treatment (In) and the argon plasma-generated UV B radiation (Out) for increasing exposure times at 44 cm in humid and dry argon with liquid and dried samples. Assays were carried out in triplicates. Graphed: mean ± SEM.

4   Conclusion

We report biocidal results obtained with and atmospheric pressure non-thermal pulsed corona discharge source adapted for inner surfaces of long narrow tubes. Within 20 min exposure time 5 $\log_{10}$ reduction of bacterial population was reached at the end of the quartz tube. We showed that the UV B emission played important role in discharge bio-decontamination efficiency.

References
1. Z. Kovalova, et al., J. Phys. D: Appl. Phys. 48.46, 464003 (2015)
2. J. Pollak, et al., Plasma Process. Polym. 5.1, 14-25 (2008)
3. M. Polak, et al., Plasma Process. Polym. 9.1, 67-76 (2012)
4. S. Limam, et al., Plasma Process. Polym. 10.8, 679-685 (2013)
5. E. Odic, et al., Plasma for bio-decontamination, medicine and food security, NATO ASI Series, Z. Machala ed., 93-106 (Springer, 2012)
6. B. Dodet, J. Adv. Oxid. Technol., 8, 91-97. (2005)
7. K. V. Kozlov et al., in *Book of Contributed Papers of 10th International Symposium on High Pressure Low Temperature Plasma Chemistry,* Saga, Japan (2006)
8. C. Hibert, et al., J. Appl. Phys. 85, 7070-7075 (1999)
9. J. Winter, et al., J. Phys. D: Appl. Phys. 46, 295401 (2013)

CORONA SOFT PLASMA POLYMERISATION OF LACCASE ENZYME FOR BIO-ACTIVE COATINGS

Sz. Malinowski[1], P. A. F. Herbert[2], J. Rogalski[3], J. Jaroszyńska-Wolińska[1]

[1]Lublin University of Technology, Department of Geotechnical Engineering
[2]Plasma Ireland, Cork, Ireland
[3]Maria Curie-Skłodowska University, Faculty of Biology and Biotechnology

E-mail: s.malinowski@pollub.pl

Soft Plasma Polymerisation (SPP) by Corona plasma has been previously shown to achieve the important combination of cross-linking without damage to the primary structure of large organic molecules. This work attempts to extend Corona SPP to bio-active molecules ~x 200 heavier. The plasma deposited coatings have been shown to exhibit fragmentation of the laccase molecule but also significant polymerisation imparting a high degree of coating durability to water wash in comparison to non-plasma control coatings. Furthermore, this was achieved with a sufficiently high degree of retention of laccase bio-activity so as to ensure that the retained activity after elution in plasma deposited coatings was always higher than that of non-plasma coatings.

Keywords: laccase; immobilization; SPP; coating; corona plasma polymerization

1   Introduction

Plasma polymerisation is a well-established route to surface functionalisation but has been limited due to fragmentation of the precursor molecules by aggressive, high energy plasma species so that complex chemistry could not be deposited. SPP, however, has been shown to deliver coatings of large organic compounds without affecting their primary structure [1]. It was found that the low specific energy and room temperature Corona plasma type was able to achieve SPP and to produce solid coatings from gas phase organic precursors which were well cross-linked while largely retaining the chemical structure of the precursor monomers. Thus, Corona SPP appeared to reconcile the conflicting aims of polymerisation with negligible damage to or denaturing of the monomer molecule.

In this work we aim to extend our investigation of Corona SPP beyond organic molecules to bio-active species, specifically the enzyme laccase. Such molecules are phenol oxidoreductases which belong to the multi-copper oxidase family [2]. They have a structure of four copper atoms bound to 3 redox sites (T1, T2, T3) and are glycoproteins with average molecular mass of 60-70 kDa [3]. Industrial applications of laccases include clinical, environmental and food industries [4]. Immobilization of laccase on various solid supports has found numerous applications in the biotechnological industry such as biosensors used in clinical, environmental and food sampling.

2   Experimental

Two experimental methods were carried out. In both cases a solution was prepared comprising laccase dissolved in a mix of de-ionised water and 10% by volume ethyl alcohol.

In the first experiment the solution was placed in a syringe and injected into a Burgener type T2100 nebuliser using a syringe pump. The presence of the alcohol greatly reduces the surface tension of the water and, thus, reduces the size of the atomized particles emitted by the nebuliser to approximately 1/10th of the pure water size. We believe that the emission from the nebuliser is a mix of atomized droplets < 1 μm diameter and vapour.

The nebuliser emission was injected into a stream of helium carrier gas contained within a vertical glass cylinder of internal diameter 17 mm and length 60 mm open at the bottom end. At the top end of the cylinder were two side-by-side sharp pins to which voltage of up to 10 kV was applied at 20 kHz. The stream of gas is subjected to the high electric field at the point of the pins which breaks down the gas to form the Corona-type plasma.

Prior to deposition a glass slide 50 mm x 10 mm was surface cleaned and sterilised with ethyl alcohol followed by immersion for 10 minutes in a standard low pressure 'barrel asher' type reactor using an oxygen/argon plasma. The slide was then placed on a stage immediately below and 10 mm from the open end of the glass cylinder containing the plasma. The stage was moved in 1 dimension at a constant speed of 1.67 mm/s so that the glass slide surface was exposed to the plasma emitted from the cylinder starting at one end of the slide and finishing at the other end over a period of 30 s. This constituted 1 coating 'cycle'.

Immediately on completion of the plasma deposition, the coated slide was immersed in de-ionised water for 3 minutes, removed and allowed to dry. The purpose of this elution was to test one of the key response parameters of the process, namely the durability of the coating, i.e. the degree of cross-linking and polymerisation achieved by exposure to the plasma. Control samples were generated in the same way but in the absence of plasma so that these could act as a reference enabling comparison between plasma and no plasma treated laccase.

The other key response parameter of the process was the degree of bio-activity in the plasma deposited laccase coating. As-deposited laccase activity deposited on the glass surface was performed according to [11] on a Shimadzu 1800 spectrophotometer (Tokyo, Japan) using syringaldazine as the substrate in 0.1M McIlvaine buffer, pH 5.5. The protein concentration was determined at 280 nm using the Nanodrop ND-1000 spectrophotometer (NanoDrop Technol. Inc., Wilmington, USA).

In the second experiment the syringe pump and nebuliser were not used. A thin film of the laccase solution was manually spread over the glass slide and the corona plasma jet was then played onto the slide surface as the slide was moved through one cycle. The treated coating was then characterised for molecular size with a Zetasizer Nano ZS (Malvern Instr., UK) using 175 degree scattering optics for particle size determination.

In the first experiment the control parameters varied (factors) were applied voltage to the pins and carrier gas Helium flow rate. The response measured was laccase activity. Again, a control slide not plasma treated was measured. In the second experiment the factors were voltage and exposure time to plasma and the measured response was particle size.

3 Results and Discussion

From experimental method 1, Figure 1 shows the dependency of laccase activity on Corona generation voltage at a fixed Helium carrier gas flow rate of 10 L/minute:
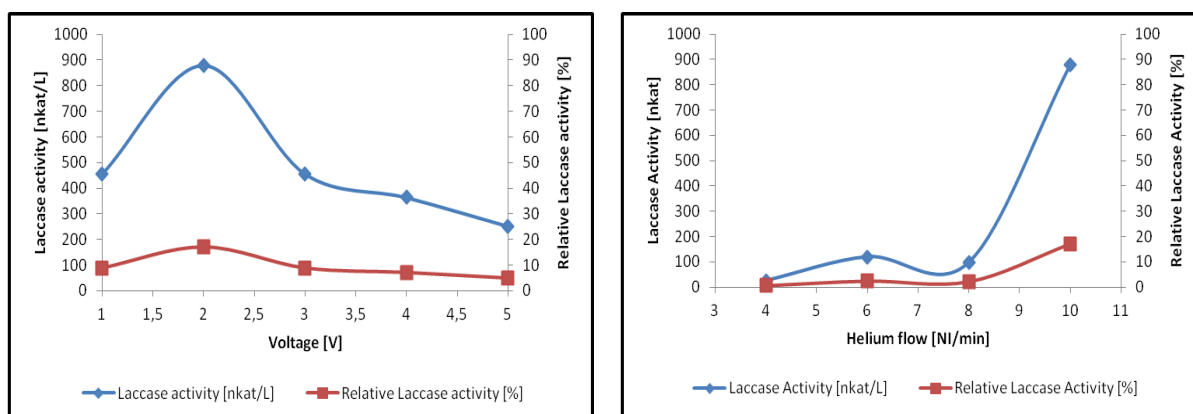
Fig. 1 (left): Laccase activity in the as-deposited coating after elution vs. Corona applied voltage
Fig. 2 (right): Laccase activity in the as-deposited coating after elution vs. Helium carrier gas flow rate

The peak of activity at 2 kV suggests the interplay of two competing mechanisms. Plasma energy density increases with applied voltage. Higher energy density will generate greater polymerisation and, thus, coating durability to the washing process (increasing activity) but will also generate greater molecular damage thus reducing measured activity. It appears that beyond 2 kV the molecular damage to the laccase caused by the plasma outweighs the advantage of greater cross-linking.

Figure 2 shows the dependency of laccase activity on helium flow rate at a fixed voltage of 2 kV. Helium flow rate determines the residence time that unit volume of the laccase remains in the plasma and, thus, the energy to which it is exposed. Again, the same two competing mechanisms seem likely to be operating but, within the range of helium flow investigated, the reduced damage to the laccase molecules resulting from the lower plasma energy input at higher flow rates appears to be dominating over reduced polymerisation.

Following these results, the plasma process was fixed at 2 kV and 10 L/min. Figure 3 compares plasma deposited laccase against non-plasma deposited coatings. The plot shows laccase activity after 3 minutes elution comparing with and without plasma. The number of coating cycles, 1, 2 or 3, is used as a parameter:
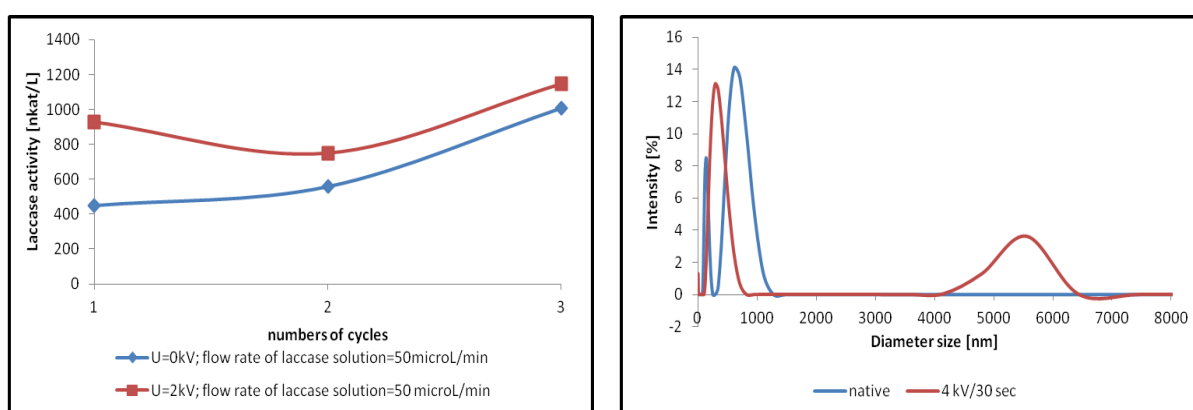
Fig. 3 (left): Laccase activity in the as-deposited coating after elution comparing with (red) and without (blue) plasma with the number of coating cycles as a parameter
Fig. 4 (right): Size distribution of laccase particles in coating with (red) and without (blue) Corona plasma treatment

It is clear that the retained activity in the coating after water elution is always greater with plasma treatment indicating that, despite the damage done to laccase molecules in the corona

plasma, the durability of the coating due to plasma induced cross-linking enables retention in the coating of greater activity under the stress of elution. Thus, it appears that this Corona plasma process can, indeed, achieve a measure of SPP of bioactive molecules reconciling polymerisation, inevitably involving some chemical alteration to the laccase molecule, with retention of essential bio-functionality.

From experimental method 2, Figure 4 shows the size distribution of laccase particles in 0.1M McIlvaine buffer pH 5 both with (red) and without (blue) plasma treatment. Two important features appear. Firstly, it is seen that part of the plasma treated laccase has undergone significant molecular fragmentation following exposure to the 4 kV plasma for 30 s. The large blue peak at about 700 nm in the untreated laccase distribution drops to a peak size of about 400 nm after plasma treatment. However, in addition to fragmentation, there is also agglomeration of particles under plasma as shown by the new red peak at around 5,500 nm. This could indicate that significant cross-linking is being achieved by the plasma process as further evidenced by the durability under water wash seen in the results of experimental method 1.

4   Conclusions

A pin-to-plane type Corona plasma has been applied to a mix of nebulised droplets and vapour containing the copper-containing oxidase enzyme laccase within a stream of Helium carrier gas from which the plasma was generated. Coatings were deposited on glass and measured for two properties, namely durability and bio-activity. Durability was tested by eluting the coatings in a water wash and laccase activity measured with a standard procedure. The plasma deposited coatings were measured against non-plasma treated coatings for reference.

Two factors were optimised, namely voltage applied to the Corona generation pins and Helium flow rate. Both factors control the energy density coupled into unit volume of the laccase. A comparison was then made of coatings fabricated with and without plasma by measuring laccase activity of the coating after 3 minutes water elution. In all tests it was found that the laccase activity of the plasma-deposited coating was greater than that of the non-plasma coating by up to a factor of ~x 2.2.

In a second experiment, a film of laccase solution on glass was exposed to a Helium Corona plasma jet. The size of laccase particles in the coating was then measured. While a substantial proportion of the laccase molecules were fragmented and reduced in characteristic size, another significant portion were greatly increased in size by a factor of ~8.

We believe that the data shows clear evidence of SPP of the enzyme laccase by Corona plasma in a single step process. The plasma process achieves substantial cross-linking/polymerisation of the molecules enabling coating durability whilst retaining sufficient bio-activity to deliver coatings superior in activity after wash to non-plasma coatings.

We believe that this is the first reported evidence of the retention of enzyme activity following a plasma polymerisation process. We hypothesise that the key parameter in the optimisation of such process is the energy per unit volume coupled by the plasma into the monomer precursor. The Corona type plasma appears well placed to deliver energy at the required level.

The results indicate the possibility of using the Corona SPP method for the preparation of bioactive coatings possibly eliminating the need for toxic or harmful solutions in lengthy wet chemistry processes currently necessary for the immobilization of bio-molecules.

Acknowledgements

References

1. J. Jaroszyńska-Wolińska et al., Chem. Mater. 21, 4401-4406 (2009)
2. J. Abenojar et al., Surf. Coat. Tech. 203, 2173-2180 (2009)
3. K. Szot et al., Elecrochim. Acta 54 4620-4625 (2009)
4. B. Bertrand et al., J. Mol. Catal. B-Enzym. 122, 339-347 (2015)

EFFECT OF VUV RADIATION ON MICROORGANISMS

<u>G. Zvereva</u>[1,3], I. Kirtsideli[2], A. Vangonen[3]

[1] State University of Civil Aviation, 38 Pilotov st., St.Petersburg, 196210, Russia
[2] Komarov Botanical Institute RAS, 2 Professor Popov st., St.Petersburg, 197376, Russia
[3]Vavilov State Optical Institute, 5-2 Kadetskaya line, St.Petersburg, 199053, Russia

E-mail: zvereva@soi.spb.ru

The work is devoted to the effect of vacuum ultraviolet (VUV) radiation ($\lambda = 172$ nm) of xenon barrier discharges on different species of microscopic fungi spores being at exponential phase of growth. In the work survival probability (SP) values were obtained for VUV dose interval 0-40 mJ/cm^2. Doses of 90% SP was found to have values 4-30 mJ/cm^2 depending on type and age of spores. FTIR transmission spectra indicate that the VUV radiation leads to degradation of proteins and polysaccharides.

Keywords: vacuum ultraviolet emission; VUV; spore; micromycetes; DNA

1   Introduction

VUV spectral region lays in wavelength interval 10 nm< λ <190 nm. VUV radiation can occur in a gas discharges in mixtures containing, for example, hydrogen or inert gases. Since VUV radiation photons energy (*hv* > 6.4 eV) is equal or exceeds the average energy of electrons in many types of gas discharges, VUV radiation can produce photochemical effects comparable to plasma-chemical ones.

Our work is devoted to the effect of VUV radiation on microorganisms. As model microorganisms were used spores of various species of microscopic fungi (microfungi). As a source of VUV radiation was used plasma of dielectric barrier discharges (DBD) in xenon.

Biological potential of VUV radiation is of interest, because it is efficiently absorbed not only by water and oxygen molecules with formation of highly reactive oxygen-containing species (ROS), but also by such biologically important molecules as: DNA, proteins, polysaccharides. VUV radiation leads to another types of DNA molecules destructions than UV radiation: to single- and double-strand breaks [1]. VUV radiation absorption by polysaccharides [2] and protein [3] may lead to degradation of spore's cell walls.

Possible biological application of VUV radiation includes: disinfection of surfaces, effect on biological objects in scientific researches, astrobiological studies related to origin of life on the Earth, investigation of microorganisms transfer in space, development of microflora in spacecrafts.

Relatively small number of scientific papers are devoted to a effect of VUV radiation on microorganisms. Series of studies devoted to effect VUV radiation on *Saccharomyces cerevisiae* spores has been carried out by Ito et al [4]. The authors have come to the

conclusion that mechanism of inactivation of wet spores is associated with the destruction of the spore's cell wall by highly reactive products of VUV photolysis of water.

Most of the works devoted to the effects of UV radiation on microorganisms are connected with astrobiology [5, 6]. These studies have shown that effect of the VUV radiation, along with the action of the vacuum, is one of the factors determining the survival of microorganisms in space.

2   Experimental Conditions

As sources of VUV radiation were used laboratory samples of DBD excimer lamps (Xe, p = 300 Torr, discharge gap d = 1 cm, length L = 10 cm, applied voltage f = 12 kHz, U = 3,5 kV). Output window was made of MgF_2 to allow withdrawal of VUV radiation (emission band $\lambda = 166$-180 nm with maximum at $\lambda = 172$ nm, surface power P=1-2 mW/ cm^2). The absolute intensity of the VUV radiation was measured by a photodetector HAMAMATSU H8025.

Spores of various types of microfungi derived from Antarctic habitat: *Aureobasidium pullulans, Geomyces pannorum, Rhodotorula colostri, Cladosporium herbarum, Penicillium aurantiogriseum* were irradiated. Samples of the spores had age 5-12 days, that corresponds to exponential phase of growth. Monolayers of spores dried on the surface of the slide were used to eliminate the effect of the mutual shielding of layers. The slides had direct contact with lamp's window. After irradiation, the spores were cultivated 10-15 days at t =14 °C in Petri dishes in agar medium. After cultivation the number of fungi colonies was counted and survival probability (SP) was defined.

An AFM microscope NTegra Aura (NT-MDT) in semicontact mode with cantilever NSG10 was used for microscopic examination of spore's surface.

FTIR spectrometer FSM (Infraspek) was used to register the infrared transmission spectra of spores.

3   Results and Discussion

Figure 1 shows SP curves for the different types of spores being at the exponential phase of growth. SP values of figure 1 are less than the values obtained in [7] for the spores at stationary phase of growth. The analysis shows that the degree of difference between the doses obtained in stationary and exponential phase of the spores is correlated with the difference in their size (table 1). The latter, in turn, is determined by the speed of growth of the spore.

Data of [7] indicates on decrease of SP with absence of pigmentation. Thus, the greatest reduction (60 times) of the survival probability in exponential phase compared to the stationary one, have spores *Cladosporium herbarum*, whose protective pigment melanin is accumulated with age and has maximal concentration at stationary phase.

Figure 1 shows, that doses of inactivation have equal or even lower values in comparison with usually used germicidal UV light sources ($\lambda = 254$ nm) ones. Thus, VUV dose of SP = 10% of the species *Saccharomyces cerevisiae* spores equal I = 4 mJ/cm^2, which is 1.5 times less than the same UV dose I = 6 mJ/cm^2 [8].

Figure 2 shows the infrared transmission spectra of spores obtained using FTIR spectrometer for *Aureobasidium pullulans* spores. IR spectra show that VUV radiation leads to the destruction of proteins and polysaccharides. The intensity of their absorption bands decreases noticeably with VUV dose increasing: spectral range 1000-1100 cm^{-1} corresponds to the absorption of polysaccharides, 1200-1600 cm^{-1} - to absorption of proteins.

At the same time AFM images doesn't reveal the difference in the surface of the irradiated and control spores for doses of VUV irradiation less 60 mJ/cm^2.

Table 1. Doses, leading to 90% inactivation ($\lambda = 172$ nm).

Type of microfungi	Dose of 90% inactivation, (mJ/cm^2)		average size, (μm $\times$ μm)	
	A	B	A	B
Aureobasidium pullulans	15	3	5 x 5.4	2.5 x 4.5
Geomyces pannorum	20	20	3.5 x 3.5	3.5 x 3.5
Rhodotorula colostri	20	8	4.2 x 5.6	3 x 4
Cladosporium herbarum	240	4	5 x 9	2.5 x 6
Saccharomyces cerevisiae	45	4	6 x 9	2.5 x 3.5
Penicillium aurantiogriseum	10	7	4 x 4	4 x 4

A-stationary phase , B- exponential phase
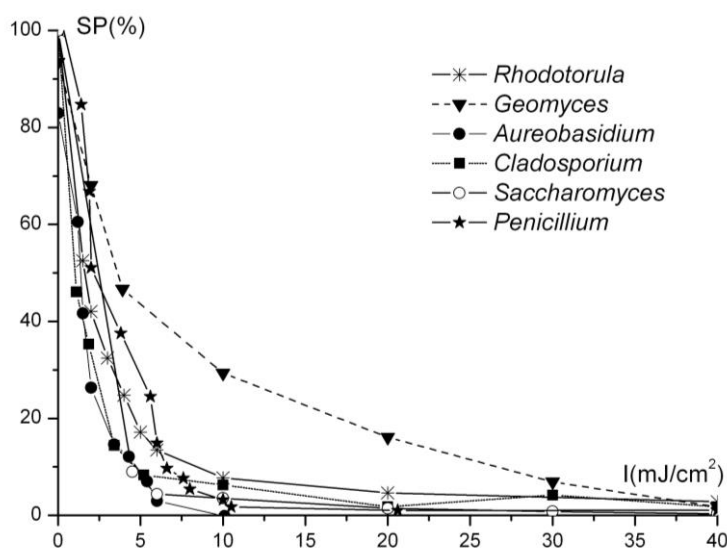
Fig.1: Dependence of the survival probability of different types of spores.
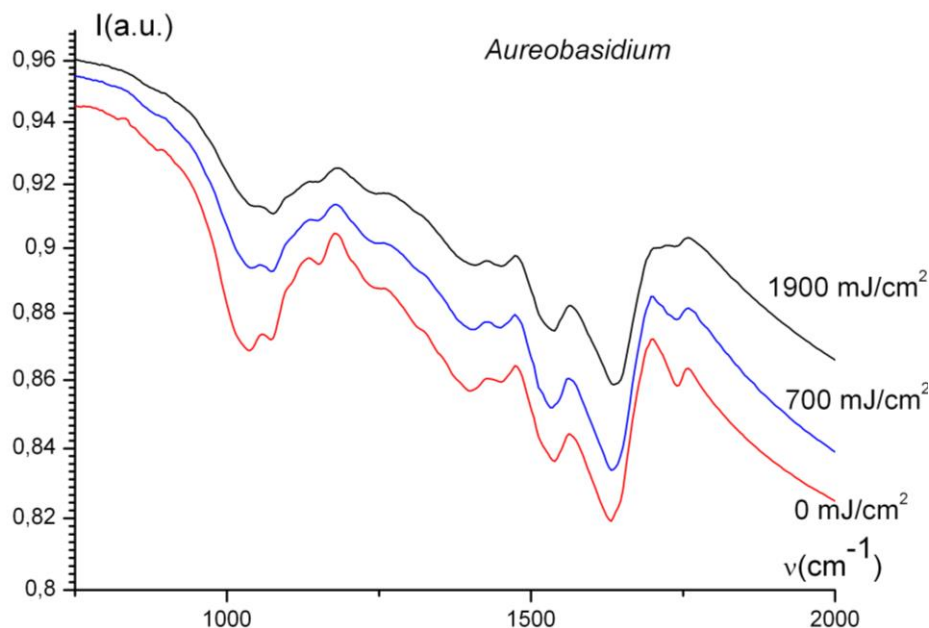
Fig. 2: FTIR transmission spectra of *Aureobasidium pullulans* at different doses of VUV irradiation ($\lambda = 172$ nm).

4   Conclusion

Experiments have shown that VUV irradiation leads to inactivation of the spores. Survival probability grows with age increasing, that could be caused by: 1) spore size increasing, 2) cell wall thickness increasing and 3) appearance of pigmentation. FTIR transmission spectra indicate that the VUV radiation leads to degradation of proteins and polysaccharides.

References

1. B. D. Michael et al., Int. J. Radiat. Biol.66, 569 (1994)
2. H. R. Dickinson et al., J. Am. Chem. Soc. 96, 5050 (1974)
3. T. Inagaki et al., Biopolymers 14, 839 (1975)
4. T. Ito et al., Rad. Res. 96, 532 (1983)
5. G. Horneck et al., Microb. Molec. Biol. Rev. 74, 121 (2010)
6. E. Sarantopoulou et al., J. Appl. Phys. 116, 104701 (2014)
7. G. Zvereva et al., in *Proc. of SPIE*, 9810, 98101W-1 (2015)
8. UV Light Disinfection Technology in Drinking Water Application – An Overview. Report of EPA Contract N68-C3-0365,1996

PLASMA DEPOSITION OF DRUG CONTAINING COMPOSITE COATINGS

P. Jelinek[3], F. Palumbo[2], C. Lo Porto[1], L. Zajickova[3,4], G. Camporeale[1], P. Favia[1]

[1]*Department of Chemistry, Università degli Studi di Bari "A. Moro", Via Orabona 4, 70126 Bari, Italy*

[2]*Istituto di Nanotecnologia, CNR, Bari, Via Orabona, 4 70126 Bari, Italy*

[3]*Department of Physical Electronics Faculty of Science, Masaryk University, Kotlářská 2,61137 Brno, Czech Republic*

[4] *Plasma Technologies, CEITEC — Central European Institute of Technology, Masaryk University, Kotlářská 2, Brno 61137, Czech Republic*

E-mail: fabio.palumbo@cnr.it

This contribution presents our last outcomes on an atomizer-assisted atmospheric-pressure plasma process for the production of coatings obtained by the co-deposition of an organic precursor and water or water solution containing a bioactive molecule - vancomycin. The purpose of this process is to deposit a coating for the controlled release of the bio-active molecule. It has been demonstrated that changing the deposition parameters can lead to tune the release at a certain extent.

Keywords: vancomycin; dbd; bio-composite

1   Introduction

Bio-composite coatings can be defined as interlayers made of at least two components: an organic/inorganic synthetic matrix, well adherent to substrates and working as supporting network, and biological compounds (such as proteins, nucleic acids, lipids, and even cells, viruses or their fractions) embedded, conjugated or mixed to the matrix. They are usually employed to improve the biological activity (antibacterial, cell-adhesive, biomolecule-sensing, etc.) of an underlaying material without altering its bulk properties.

Bio-composite films can be used in a wide range of technological applications including biosensors, cell growth enhancing coatings for tissue engineering, antibacterial films for food packaging. [1-3] Many techniques, such as drop-casting, dip coating and painting, [4-6] layer-by-layer deposition of polyelectrolytes, [7, 8] electrochemically induced deposition, [9] sol-gel, [10] many wet chemical reactions [11-13] have been developed for their preparation. Unfortunately, all of them have some drawbacks (e.g. large use of solvents and reactants, long tedious multi-step procedures, need for sample pretreatments). Therefore, plasma-based method can be a suitable alternative overcoming some drawbacks. So far, two main strategies based on reactions in plasma phase have been set up. One consists in a two-step process, in which substrates are firstly functionalized by atmospheric or low-pressure plasmas and then grafted with biomolecules in a wet chemistry step. [14, 15]

Recently, many efforts have been devoted to set up one-step atmospheric-pressure plasma-based processes embedding biomolecules in polymeric thin films. This strategy can be carried

out by coupling dielectric barrier discharge (DBD) reactors with atomizing systems spraying nano-droplets of biomolecule solution directly in the plasma chamber.

2   Experimental Arrangement

The investigated method is based on a one-step deposition process in the DBD reactor schematically shown in Fig. 1. It consisted of two parallel plate silver electrodes, 5 mm apart, both covered by thick alumina sheets. Helium (carrier gas, 99.999% Air Liquide) and ethylene were fed into the chamber via electronic mass flow controllers (MKS Instruments).

Substrates samples were placed between two parallel-plate electrodes covered with alumina. Helium plasma was ignited in the inter-electrode gap, while ethylene was added in constant amounts and water Vancomycin aqueous solution droplets were injected through an aerosol generator (atomizer). The coatings were characterized by SEM and FT-IR analysis.

For the Vancomycin containing films, C_2H_4 was used as the precursor of the matrix at the flow rate of 20 sccm. In this case water was replaced with a Vancomycin solution. Before each deposition process complex cleaning procedure was performed and He was added to the reactor chamber for 5 min for conditioning and purging.
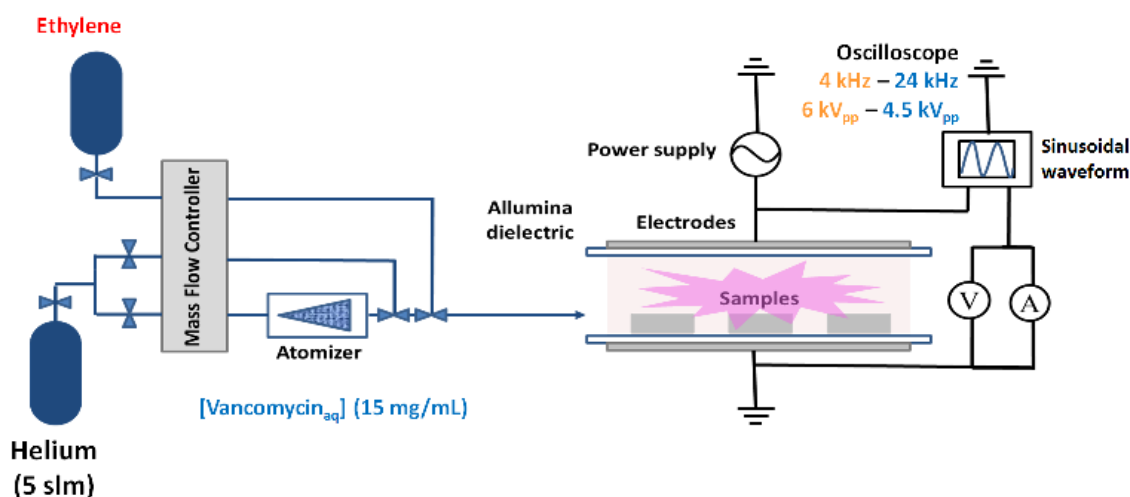
Fig. 1: Schematic diagram of aerosol-assisted atmospheric-pressure DBD deposition system.

3   Results and Discussion

The deposition process of the vancomycin containing composite films has been optimized, working in continuous and pulsed mode. In Fig. 2, the FTIR spectra of vancomycin containing coatings deposited in continuous and pulsed mode at the same peak power are reported together with that of the pure antibiotic (drop casting of vancomycin) and deposited layer without Vancomycin (water aerosol + ethylene). It can be observed that in continuous mode the presence of bands that can be attributed to vancomycin is lower than in the pulsed mode. This observation is further confirmed by release test of bancomycin from deposited samples into water (measured with UV-VIS spectrometry) whose results are depicted in Fig. 3. It has been estimated that the total amount of biomolecule embedded in the coating is

$40\mu g/cm^2$. Furthermore, coatings containing Vancomycin deposited onto Ti disk have shown proper antibacterial activity.
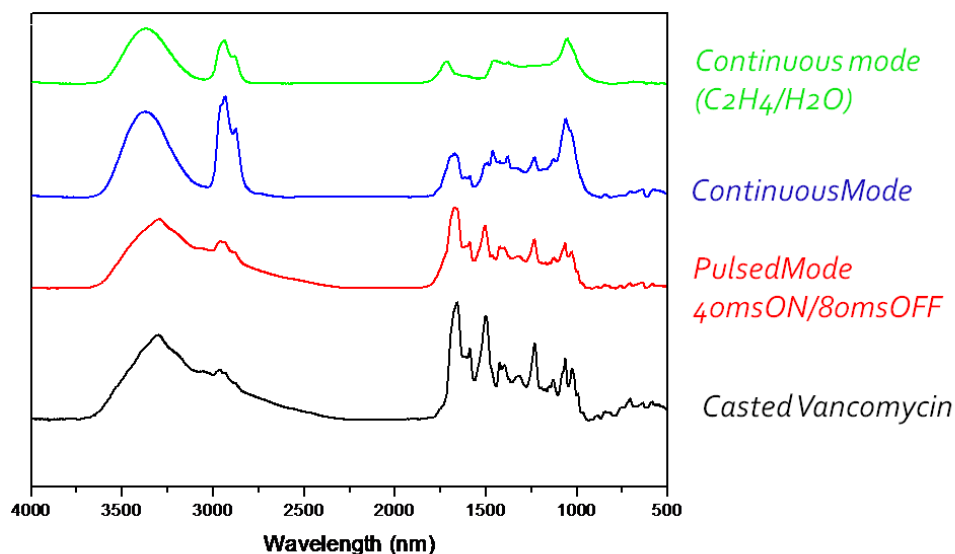
Fig. 2: FTIR analysis of films deposited with no Vancomycin (green), continuous mode with Vancomycin aerosol (blue), pulsed mode with Vancomycin (red), drop casted Vancomycin (black).
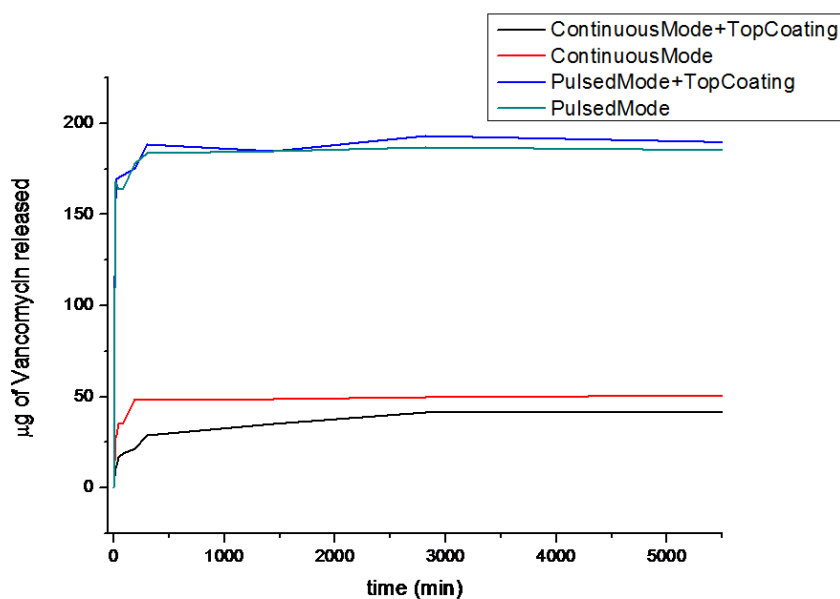
Fig. 3: Results of release tests performed on deposited samples.

4   Conclusion

An aerosol-assisted atmospheric-pressure plasma deposition process has been used to deposite vancomycin/CH_x coatings. It has been found that Vancomycin containing coatings were deposited using DBD in pulsed mode contains significantly higher amount of Vancomycin then layers with similar thickness deposited with continuous mode. It was also shown that the

deposition of top coating, a pure CH$_x$ film, could influence release rate of vancomycin and, therefore, allow tuning the release rate in a specific way.

Wide possibilities of optimizing this process for further development in drug delivery systems can be envisioned.

References
1. K. Kojima et al., Anal. Chem. 75, 1116 (2003)
2. M.-J. Kim et al., Biomaterials 34, 7236 (2013)
3. J. L. Quintieri et al., Innov. Food Sci. Emerg. Technol. 20, 215 (2013)
4. J. Heuts et al., J. Biomed. Mater. Res. A 92A, 1538 (2010)
5. S. Dobretsov et al., Mar. Biotechnol. 9, 388 (2007)
6. C. Melander et al., Int. Biodeterior. Biodegrad., 63, 529 (2009)
7. O. Etienne et al., Antimicrob. Agents Chemother. 48, 3662 (2004)
8. E. Faure et al., Adv. Funct. Mater. 22, 5271 (2012)
9. P. Lisboa et al., Micro Nanosyst. 3, 83 (2011)
10. H. Haufe et al., J. Sol-Gel Sci. Technol. 45, 97 (2008)
11. F. Patolsky et al., Proc. Natl. Acad. Sci. U. S. A. 101, 14017 (2004)
12. P. Appendini et al., Packag. Technol. Sci. 10, 271 (1997)
13. A. Caro et al., J. Colloid Interface Sci.,349, 13 (2010)
14. P. Favia et al., Plasmas Polym. 3, 77 (1998)
15. D. Duday et al., Surf. Coat. Technol. 218, 152 (2013)

THE INFLUENCE OF PLASMA PARAMETERS ON THE INACTIVATION OF DIFFERENT BACTERIAL SPECIES

M. Modic[1], N. Hojnik[1], M. Djurović[2], V. Vuksanović[2], D. Vujošević[2], U. Cvelbar[1]

1Department of Surface Engineering and Optoelectronics, Institute »Jozef Stefan« Jamova cesta 39, 1000, Ljubljana, Slovenia
2Institute of Public Health of Montenegro, Dzona Dzeksona, 81000 Podgorica, Montenegro

E-mail: martina.modic@ijs.si

The inactivation effects of helium atmospheric pressure plasma jet (APPJ) on four different bacterial species; *Bacillus stearothermophilus, Bacillus subtilis, Staphylococcus aureus* and *Escherichia coli* were investigated. Treatments were performed under changing plasma conditions, i. e. gas flow rate, treatment time and power.

Keywords: cold atmospheric plasma; plasma parameters; reactive plasma species; bacterial inactivation

1 Introduction

Cold atmospheric plasma (CAP) is an emerging technology for different biomedical applications. Plasma can be an efficient source of ions, electrons, UV, electric field and free radicals, which are all known to have bactericidal effects, therefore making plasma as a promising tool for microbial inactivation [1-3]. The inactivation efficiency of CAP depends on various factors; from plasma parameters, environmental conditions to the type of microorganisms, their characteristics and their concentration.

The purpose of our study was to evaluate the influence of different parameters on the efficiency of plasma inactivation of different bacterial strains. Helium atmospheric pressure plasma jet (APPJ) presented in the Figure 1a was used in this study. Gas flow rate, power and time of exposure were the parameters applied on 4 different bacterial strains.
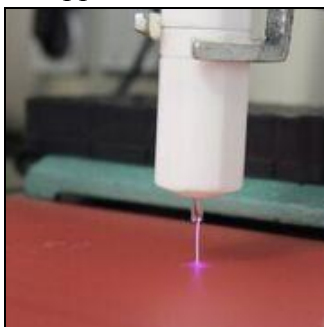
Fig. 1: Helium atmospheric plasma jet (APPJ) used in experiments.

2 Experimental

2.1 Bacterial strains used in experiments

Four different bacterial strains were used in our study; *Bacillus stearothermophilus* ATCC No. 7953 (Gram-positive bacteria), *Bacillus subtilis* ATCC No. 6633 (Gram-positive

bacteria), S*taphylococcus aureus* ATCC No. 25923 (Gram-positive bacteria) and *Escherichia coli* ATCC No. 25922 (Gram-negative bacteria).

2.2. Preparation of bacterial culture

Bacterial cultures were grown overnight on Columbia (COS) agar plates (bioMérieux SA, Marcy l'Etoile, France) at 55°C for *B. stearothermophilus* and 37°C for *B. subtilis, S. aureus* and *E. coli*. Cells were picked up with a loop and re-suspended in sterile saline to obtain 0.5 McFarland (1-2 x 10^8 CFU/ml) initial bacterial suspensions. The 100 µl of these initial 0.5 McF bacterial suspensions, as well as their 100-fold dilutions were evenly transferred in 96-wells microtiter-plate with flat bottom.

2.3. Plasma treatment

Suspensions with concentration of ~10^6 bacteria were exposed to the He atmospheric plasma reactor designed as end-field jet, with 0.1 mm copper wire, which was inserted inside of a 50 mm long and 4 mm outer diameter borosilicate glass tube. Electrode was connected to a 30 kHz high voltage AC power supply. Treatments were performed in a stationary mode at a constant distance of 15 mm at different gas flow rates (0.5, 1, 1.5 and 2 slm) and different powers (3, 4.5, 6, 9 and 12 V). Different bacteria concentrations (10^8, 10^6, 10^4 and 10^3 CFU/ml) were also investigated. The survival of bacteria was evaluated using Miles-Misra enumeration method. All experiments were performed in triplicates.
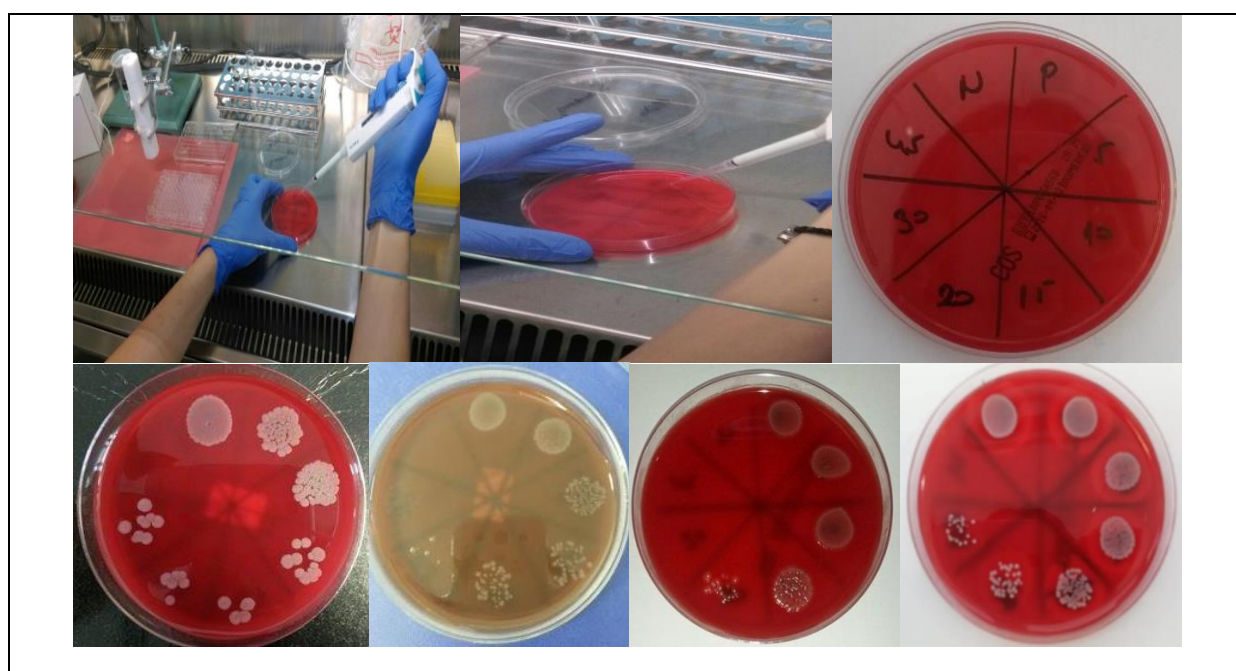
Fig. 2: Representative images of Columbia blood agar plate incubated with different plasma treated samples: 5 s, 10 s, 15 s, 20 s, 30 s, 45 s, negative control (N) and positive control ((P) untreated sample).

3   Results and Discussion

3.1 Influence of gas flow rates on bacterial survival

Bacterial solutions were exposed to He gas flows at 0.5, 1, 1.5 and 2 slm. The results showed that the gas flow rate affected the inactivation rate of bacteria. Higher flow rates significantly shortened the time needed for complete inactivation of all four bacterial strains used in the study.

3.2 Influence of power on bacterial survival

The effect of different powers on the bacterial inactivation was investigated with changing the input voltage from 3 to 12 V. The inactivation rate strongly related to the powers used for plasma treatments. The time needed for complete bacterial inactivation was shortened with increasing the input voltage. The longest treatment times were used for the input voltage of 3 V in all study cases.

3.3 Influence of bacterial concentration on plasma efficiency

Figure 3 shows the efficiency of plasma treatment on bacterial solutions with different bacterial concentrations. The results showed that the inactivation efficiency of plasma also depends on the concentration of bacteria present in the solution. While the complete inactivation of solutions with concentrations of 10^4 CFU/ml was achieved for all four bacterial strains, the solutions with concentrations of 10^8 CFU/ml were not affected after 4 min exposure in the case of *B. subtilis, S. aureus* and *E. coli*.
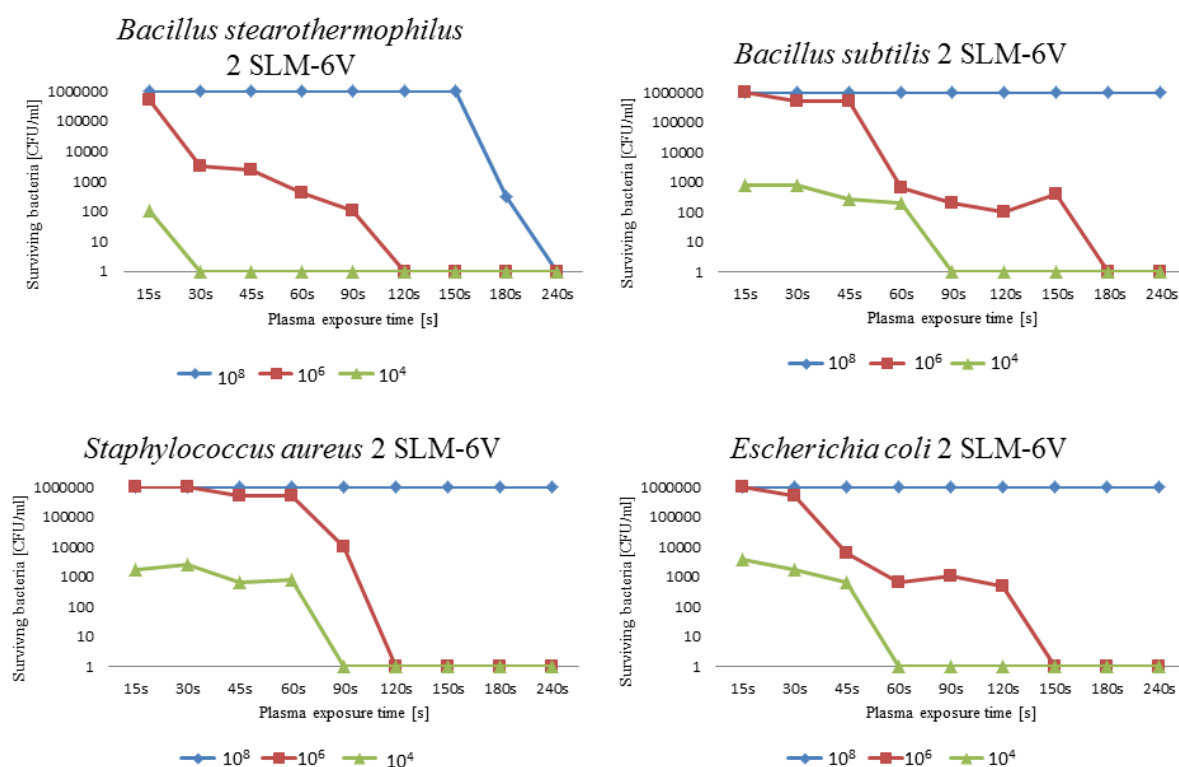
Fig. 3: Survival curves for solutions with different concentrations of bacteria (10^8, 10^6, 10^3 CFU/ml), exposed to He APPJ (6 V, 2 slm).

4   Conclusion

The study demonstrates that the Helium atmospheric pressure plasma can be used as an efficient tool for inactivation of different bacterial species, even highly resistant and spore-forming bacteria. The results showed that the bacterial survival strongly depends on used plasma parameters, bacterial strain and bacterial concentrations. We also observed the difference in susceptibility between bacterial strains, where the *E. coli* was the most susceptible and *S. aureus* was the most resistant to He APPJ exposure.

Acknowledgments

References

1. J. Guo et al., Food Control 50 (2015)
2. V. Scholtz et al., Biotechnol. Adv. 33 (2015)
3. J. Shen et al., Jpn. J. Appl. Phys. 53 (2014).

INTERACTION OF LOW-TEMPERATURE PLASMA WITH GRAINS OF MAIZE (*ZEA MAYS* L.)

M. Henselová[1], Ľ. Slováková[1], M. Martinka[1], A. Zahoranová[2], M. Černák[2]

[1]Department of Plant Physiology, Faculty of Natural Sciences, Comenius University, Ilkovičová 6, 842 15 Bratislava, Slovak Republic
[2]Department of Experimental Physics, Faculty of Mathematics, Physics and Informatics, Comenius University, Mlynská dolina, 842 48 Bratislava, Slovak Republic

E-mail: henselova@fns.uniba.sk

The grains of maize (*Zea mays* L). var. KWS were exposed to low-temperature plasma (LTP) by using Diffuse Coplanar Surface Barrier Discharge (DCSBD) in the range from 10 to 600 seconds. The treatment of maize grains with LTP induced visible structural changes on the surface of grains. Increasing plasma exposure time reduced the weight of grains and increased grains' water uptake. The protein content significantly increased with the age of maize seedlings and exposure time of LTP. SOD and CAT enzyme activities were significantly increased mainly after 3 days, but in contrast G-POX activity decreased only after 6 days of seedling cultivation.
Keywords: low-temperature plasma; treatment; maize grains; water uptake; protein; enzyme

1 Introduction

In recent years many physical methods have been used in the field of agricultural science [1]. One of the physical methods which offer a broad range of potential industrial applications is low-temperature plasma [2]. Experimental studies by many authors have reported the predominantly positive effects of LTP on germination, as well as on the development and growth of plants [3–5]. It is also known that the use of plasma activates enzyme complexes in the seed [6, 7], which ensures the faster growing of the germ, increases germination energy, and speeds up rooting. According to [8] in high-pressure non-equilibrium plasma discharges, reactive species are generated through various colliding pathways, such as electron impact excitation and dissociation. Reactive species play an important role in all plasma-surface interactions. For example, air plasmas are excellent sources of reactive oxygen-based and nitrogen-based species, such as O, O_2^*, O_3, $OH^\bullet$, NO, NO_2, etc. Plants have evolved protective mechanisms including enzymatic and non-enzymatic antioxidants [9] against environmental and physical stresses [10, 11] that generate reactive oxygen species (ROS). ROS are highly reactive in the absence of any protective mechanism; they can seriously disrupt the normal metabolism of plants through oxidative damage to membrane lipids, proteins, pigments and nucleic acids.

In this work, we studied the effect of LTP on the modification of seed surface structure, changes in the weight and dynamics of water uptake by grains, as well as the protein content and antioxidant enzyme activities of maize germinating seedlings.

2 Experimental

2.1 Characteristics of plasma source – DCSBD

The treatment of maize grains was carried out using Diffuse Coplanar Surface Barrier Discharge (DCSBD), non-thermal plasma source at atmospheric pressure in the ambient air [2]. On an alumina plate the DCSBD generates a thin uniform layer of macroscopically homogeneous plasma with high plasma power density (up to ~100 W/cm^3) in ambient air and without any inert gas admixture. The discharge was powered by 14 kHz sinusoidal voltage

with the amplitude of approximately 10 kV, supplied by HV Plasma Power Supply. Input power of 370 W was used for plasma processing, which allows short treatment times and the possible incorporation of DCSBD directly in continuously working production lines. The movement of maize grains on the electrode surface was carried out mechanically to ensure uniform treatment. For experiments, the grains were treated with exposure times ranging from 10 to 600 sec. The grains were taken from the plasma area after treatment and exposed to the atmosphere for 24 hours before the biological experiments started.

2.2 SEM analysis

The grains of maize after LTP treatment (0, 60, 120, 600 sec.) were coated with a 10 nm layer of carbon and observed with a scanning electron microscope (JXA 840A, JEOL, Japan) at an accelerating voltage of 15 kV.

2.3 Loss of weight and water uptake by grains

Maize grains were exposed to LTP for 0 (control sample) and 10–200 sec, and 100 seeds for one variant in three repetitions were used. Grains before and after LTP treatment were weighed on an electronic balance. Control and treated grains were submerged in beakers containing distilled water at 25°C for 2- and 8-hours. The grain samples after an imbibition interval were blotted dry and weighed to the nearest 0.1 mg. The amount of water uptake by the grains was determined as the actual increase in grain weight according to the following equation: Water content (WC) (mg grain^{-1}) = (FW-DW)/100, where FW is fresh weight and DW is dry weight. The loss weight of grains after LTP treatment was determined as the actual decrease in grain weight according to the formula: Loss of weight (LW) (μg grain^{-1})/100 = (Wt$_0$ − Wt$_n$)/100, where Wt$_0$ is the weight of grains before LTP treatment and Wt$_n$ is the weight after LTP treatment at 10–200 sec exposure time.

2.4 Plant material and growth conditions

In the experiments we used dried grains of maize (*Zea mays* L.) var. KWS (obtained from the Sedos Co. in Krakovany, Slovakia). Control (untreated) and treated seeds after 10-hours imbibition were immediately placed on two layers of filter paper soaked with 10–15 ml distilled water in Petri dishes. Seeds were germinated in darkness at 26°C for 6 days.

2.5 Protein and enzyme determination

The shoots were sampled 3 and 6 days after sowing to study various enzymes and proteins. Frozen shoots, which were ground in liquid nitrogen with mortar and pestle, and the powder suspended in 50 mM sodium phosphate buffer (pH 7.5) containing 1mM EDTA, filtered and centrifuged at 15 000 g for 20 min, were used for proteins extraction. Supernatant was used as an enzyme source in the determination of enzymatic activity. The soluble protein concentration was determined according to Bradford's method [12] using bovine serum albumin as standard. Superoxide dismutase (SOD), peroxidase (G-POX) and the catalase (CAT) activities were determined according to methods [13, 14].

3   Results and Discussion

SEM analysis showed that LTP significantly modifies the seed surface structures of maize grains and morphological differences depending on the exposure time of plasma. Disruption or loosening of the original structure in the coat areas of grain was observed.

Our results showed that the plasma-treated grains had a lower weight of 80.63 to 830.23 μg grain^{-1} at exposure times in the range of LTP 10–200 sec (Fig.1). The control and LTP treatment samples grain showed different values of water uptake by grains (Fig.2). It was

found that the water content of the LTP treated samples, after keeping them in beakers with water for 2- and 8-hours of the imbibition period, increased from 44.37 to 80.40 mg·grain^{-1} at 10 sec and from 50.40 to 102.40 mg grain^{-1} at 100 sec LTP, while that of the control samples was only 44.27 or 79.43 mg·grain^{-1}. Similar curves were obtained for wheat in [15].
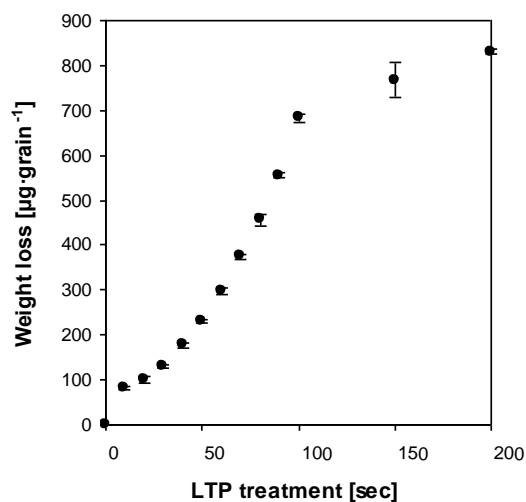
Fig.1: Changes in the weight of grains after treatment by LTP. The range of weights obtained is indicated by bars. Average weight of single grain was 323.6 ± 0.58 mg.
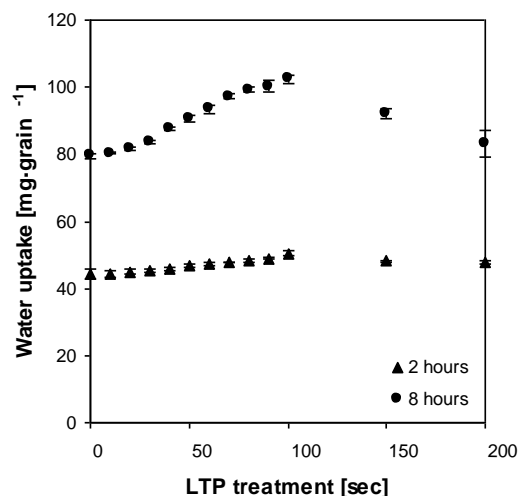
Fig.2: Changes in water uptake after 2 and 8-hours of imbibition at 25°C for LTP treated and untreated maize grains. Values are means of 3 measurements. Bars represent $\pm$ SE.

As seen from Fig.2, higher plasma exposure times of 150 and 200 sec reduced the water uptake by grains, which may be associated with the longer inactivation of the embryo. The biophysical changes induced with LTP on the grain surface and dynamics of water uptake, causes the increased germinating power of grains and affects the post-germination growth of maize seedlings [16]. Changes in the protein content and activity of some antioxidant enzymes during the early growth of seedlings are documented in Fig.3. The protein content significantly increased with the age of seedlings and exposure time of LTP from 6.4 to 41% at 60 sec and from 13.0 to 60% at 120 sec compared to the control (Fig. 3 A). The activity of SOD in the shoots significantly increased from 79 to 87% after only 3 days, and in contrast after 6 days of cultivation it decreased from 9 to 23% compared to the control (Fig. 3B). CAT activity in 3 day old shoots significantly increased in both exposure times from 68 to 137% over the control, and after 6 days of cultivation decreased to about 16% at only 120 sec exposure time (Fig. 3C). G-POX activity significantly decreased from 15 to 20% in only 6-day-old shoots in comparison to the control seedlings (Fig. 3D).

4 Conclusion

The results showed that the LTP affects grain surface modifications by changing the relief pattern of the maize grain coat with the surface becoming smoother. The changes of grain surface under LTP treatment had an influence not only on decreasing grain weight, but mainly on increasing the dynamics of imbibition and water uptake into the grains. These biophysical changes probably also involved several biochemical pathways inside the grains and seedlings. The high metabolic activity of grain germination and early seedling growth is accompanied by the generation of reactive oxygen species (ROS).
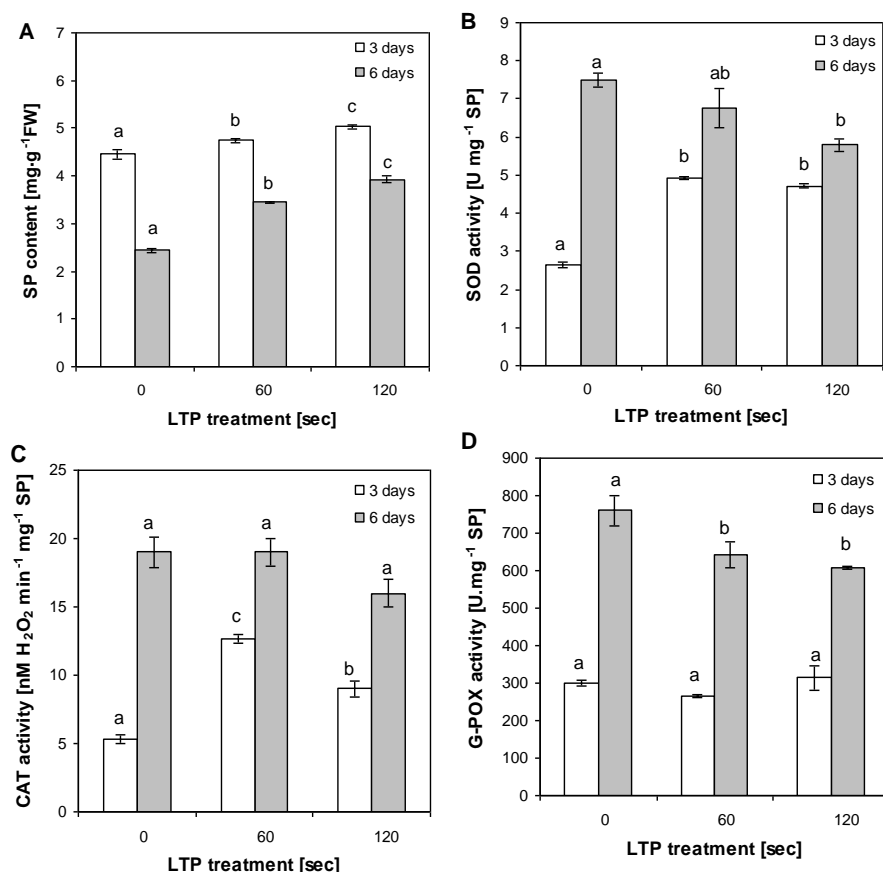
Fig.3: Total soluble protein content (A) and enzyme activities in extracts from shoots of 3- and 6-day-old maize seedlings grown from grains treated with LTP for 60 and 120 sec. B- SOD activity, C – CAT activity, D – G-POX activity. Values are the means ± SE of three replicates. Bars with different letters are statistically different at ($P < 0.05$).

References
1. L. Bari et al., J. Food Protec. 66, 767 (2003)
2. M. Černák et al., Eur. Phys. J. Appl. Phys. 47, 22806 (2009)
3. J. C. Volin et al., Crop Sci. 40, 1706 (2000)
4. S. Lynikiene et al., Int. Agrophysics 20, 195 (2006)
5. B. Šerá et al., Plasma Sci. Technol. 10, 506 (2008)
6. M. Q. Yin et al., Plasma Sci. Technol. 7, 3143 (2005)
7. A. Vashist et al., J. Agric. Physics. 9, 50 (2009)
8. M. Laroussi, Plasma Process. Polym. 2, 391 (2005)
9. Ch. Foyer et al., Physiol. Plant. 92, 696 (1994)
10. J. L. Donahue et al., Plant Physiol. 113, 249 (1997)
11. A. Hammed et al., Pak. J. Bot. 40,1033 (2008)
12. M. M. Bradford, Anal. Biochem. 72, 248 (1976)
13. N. R. Madamanchi et al., Plant Mol. Biol, 26, 95 (1994)
14. D. M. Hodges et al., J. Exp. Bot, 48, 1105 (1997)
15. A. Zahoranová et al., Plasma Chem. Plasma Process, 36, 397 (2016)
16. M. Henselová et al., Biologia, 67, 490 (2012)

TOPIC 9: MISCELLANEOUS

ATMOSPHERIC JET BASED ON SURFACE STREAMER DIELECTRIC BARRIER DISCHARGE

M. Šimek, V. Prukner

Institute of Plasma Physics of the CAS, Department of Pulse Plasma Systems,
Za Slovankou 1782/3, Prague 8, Czech Republic

E-mail: simek@ipp.cas.cz

We designed novel axisymmetric atmospheric jet formed by effluents produced by surface streamers suitable for various applications. Filamentary streamers are produced by the amplitude-modulated AC surface dielectric barrier discharge. The SDBD-based jet makes use of the tangential injection of the working gas into a cylindrical chamber that induces a fast vortex flow through the discharge zone and expells excited/ionized/reactive species out of the discharge area through the axial orifice in the form of a jet spinning around its axis. The jet may be easily used to treat surfaces, expose biological samples or even be injected in liquids.

Keywords: atmospheric pressure; jet; surface barrier discharge

1   Introduction

Highly reactive environment produced by atmospheric-pressure streamers generated by surface dielectric barrier discharges (SDBDs) may be used for various applications (e.g. pollution control, sterilization, ozone generation, surface modification). In this work, we present novel SDBD based jet which differs from the standard SDBD electrode geometry based on parallel metallic strips used as the exposed high-voltage (HV) electrode and employed in our previous works [1-3]. The SDBD-based jet makes use of the tangential injection of the working gas into a cylindrical chamber that induces fast vortex flow through the discharge zone, expelling discharge products out of the discharge volume through the axial orifice in the form of a jet spinning around its axis. We present microscopic images capturing characteristic features of a newly designed rotating atmospheric jet based on axisymmetric SDBD electrode geometry and fed by pure nitrogen, oxygen, synthetic air and argon.

2   Experimental

The SDBD electrode geometry of the jet is formed by a pair of concentric planar ring electrodes. The smaller exposed high-voltage Ni electrode (thickness of ~30 μm, inner/outer diameter of 9/14 mm) is deposited on the surface of MACOR® glass-ceramic disk (diameter 25 mm, 5 mm thick with a ϕ=2.8 mm hole drilled in the center). The larger grounded Ag back electrode (4/16 mm inner/outer diameter) is embedded inside the disk and separated from HV electrode by 0.5 mm thick dielectric layer. The disk surface with HV electrode is closed inside a cylindrical chamber containing two tangential gas inlets and one quartz window. The window is placed parallel to the disk surface providing an access for optical diagnostics. Working gas which symmetrically injected through the two tangential inlets forces whirlwind dragging streamers produced and propagating on the ceramic surface above back electrode. The SDBD was powered by an AC power supply composed of a TG1010A

Function Generator, a Powertron Model 250A RF Amplifier and a step-up transformer. The driving AC frequency (in this work 500 Hz, 1 kHz, 5 kHz) was amplitude-modulated to produce sine-wave T_{ON}/T_{OFF} periods with a variable duty cycle $D=T_{ON}/(T_{ON}+T_{OFF})$.
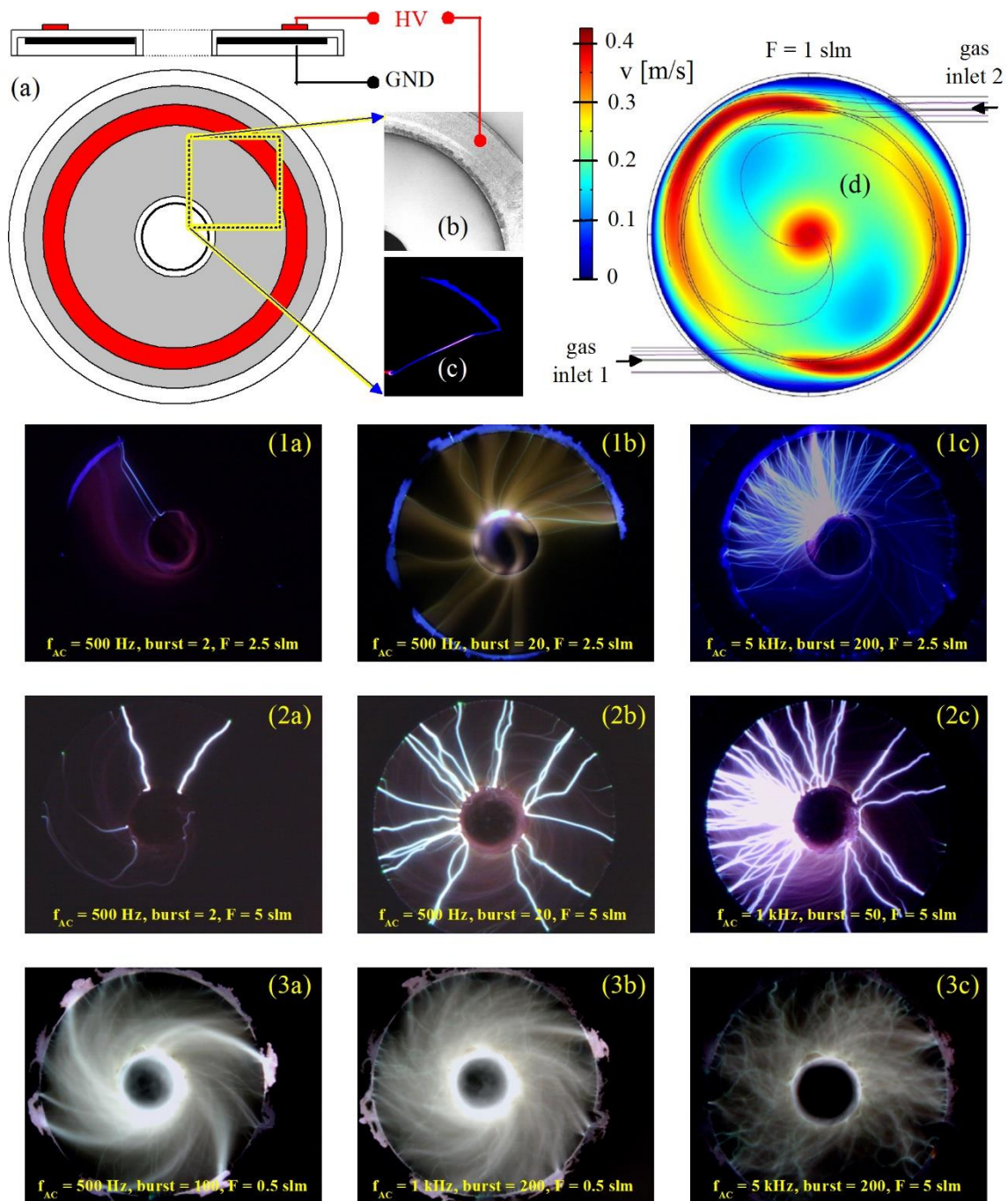
Fig. 1: Microscopic images of SDBD streamers produced at various discharge conditions. Inserts in the upper part show simplified scheme of the SDBD electrode geometry (a), snapshot of the section of discharge exposed HV electrode without (b) and with (c) single nitrogen streamer discharge event. Insert (d) shows model predictions of the flow field velocity with streamlines in the plane close to the discharge surface. Nine microscopic images capture whole surface of the SDBD driven in atmospheric pressure nitrogen (1a-1c), synthetic air (2a-2c) and argon (3a-3c). Specific discharge conditions are indicated in the lower part of each image. Thin and bright filaments are streamers propagating on dielectric surface between the HV electrode and central hole during positive AC half-cycle.

3   Results and Discussion

Selected microscopic images of SDBD streamers produced at various discharge conditions (gas flow F=0.5-5 slm) are displayed in figure 1. Insert (a) in the upper left part of the figure shows simplified sketch of the SDBD electrode geometry together with two snapshots of the section of real discharge exposed HV electrode without (b) and with (c) single streamer discharge event occurring in pure nitrogen. Insert (d) in the upper right part of the figure presents model predictions of the flow field velocity (induced by the total flow of 1 slm) with streamlines in the plane close to the discharge surface. Nine microscopic images capture whole surface of the SDBD driven in atmospheric pressure nitrogen (1a-1c), synthetic air (2a-2c) and argon (3a-3c). Specific discharge conditions are indicated in the lower part of each image. Thin and bright filaments are streamers propagating on dielectric surface between the HV electrode and central hole during positive AC half-cycle producing excited/ionized/reactive species. However, the discharge works well also in pure oxygen (ozone generator) or even in gases saturated with water vapors (OH/H_2O_2 generator).

References

1. P. F. Ambrico et al., Plasma Chem. Plasma Process. 28, 299 (2008)
2. M. Šimek et al., Plasma Chem. Plasma Process. 30, 607 (2010)
3. I. Gordeev et al., Plasma Process. Polym. 9, 83, (2012)

COST TD1208 CONTRIBUTIONS: NON-EQUILIBRIUM PLASMAS WITH LIQUIDS FOR WATER AND SURFACE TREATMENT

STREAMERS SLIDING ON A WATER SURFACE

Yu. Akishev[1,2], V. Karalnik[1], A. Petryakov[1], N. Trushkin[1]

[1]SC SRC RF TRINITI, Moscow, Troitsk, 142190, Pushkovykh Str., 12, Russia.
[2]NRN University MEPhI, Moscow, Kashirskoe shosse 32, 115409, Russia.

E-mail: akishev@triniti.ru

Pulsed discharge from a pin electrode located slightly above a liquid appears in a form of thin current filaments (streamers) spreading on surface of liquid. The features of electrical interaction between streamer and liquid are still unknown in many details. This report presents the results of 3-D numerical calculations on spatial distribution of the electric field and current lines in/around the streamer and in liquid medium in dependence on deepness of a liquid. It is shown that diameter of streamer strongly influences both the strength and spatial structure of the electric field in gas-plasma interface around streamers.

Keywords: streamers on liquid; plasma-liquid system; numerical calculations

1 Introduction

Initiation of the needed chemical processes in a liquid by reactive species (atoms, radicals, UV, excited atoms and molecules, ions) generated by non-thermal plasma at atmospheric pressure is a greatly wanted process for various applications in biomedicine, chemical and civil engineering, environmental protection, production of novel materials. At present different plasma-liquid systems are developed for production of reactive species in liquids. Many of them are based on the use of transient streamer or spark discharges generated on surface of a liquid to be treated. In such a case, non-thermal plasma on a liquid appears in a form of thin current filaments (streamers) which tightly adjoin the liquid and spread along its surface. However many aspects of electrical interaction between streamer and liquid are still unknown. The results of 3-D numerical calculations of spatial distribution of the electric field and current lines in/around surface streamer and in liquid medium as well in dependence on deepness of a liquid are presented. It is shown also that the streamer diameter strongly influences both the spatial structure and strength of the electric field in gas-plasma interface around streamer.

2 Description of the mathematical model

We used the simplified model to describe mathematically the complicated 3-D configuration of streamer - liquid system. Despite its simplicity, this model takes into account all physical peculiarities related to the streamer propagation on liquid surface. The main of them are low velocity of streamer propagation (10^5 - 10^6 cm/s) and rather high conductivities of both the streamer's plasma and liquid medium. In such a case the contribution of a displacement current in total electric current flowing through streamer-liquid system is negligible. We assumed additionally that the streamer conductivity is constant in time and does not depend on the coordinate along streamer length. In reality this assumption is not completely satisfied, nevertheless it allows us to find out some fundamental properties of the streamer propagation on liquid. In total, all mentioned above leads to that the 3-D spatial distribution of the electric fields and currents in plasma-liquid system at every length of streamer can be described in quasi-stationary approximation.

The set of Master Equations includes the equation of the electric current conservation for liquid and plasma medium with given their conductivities and Laplace equation for the electric potential in gas medium (ambient air).
These equation look as follows:
(plasma and liquid medium):

$$\nabla \cdot \boldsymbol{J} = 0 \qquad (1)$$

$$\boldsymbol{J} = \sigma \boldsymbol{E},$$

$$\boldsymbol{E} = -\nabla V,$$

where $\boldsymbol{J}$ is the electric current density, V is the electric potential, σ is the electrical conductivity.
Boundary conditions for potential V at the high voltage electrode and grounded electrode are $V_0 = 10$ kV and $V = 0$ respectively. Normal components of the electric current at the streamer-gas, liquid-gas and liquid-dielectric walls boundaries are equal to zero. In other words, the electric current does not penetrate into gaseous and dielectric media from plasma and liquid. Mathematically, this boundary condition looks as follows:

$$\mathbf{n} \cdot \boldsymbol{J} = 0,$$

here $\mathbf{n}$ is a normal vector to the surface.
(gas medium):

$$\nabla \cdot (-\nabla V) = 0 \qquad (2)$$

The electric potentials in gaseous domain at the plasma-gas and liquid-gas boundaries are determined by the electric potentials at these boundaries formed by the electric currents in liquid and plasma medium. In calculations, the design gaseous domain has a spherical form, and electric potential at its external boundary is equal to zero. In order to exclude the influence of the external boundary conditions on the results of calculations, the chosen radius of the gaseous domain exceeds drastically all sizes of the rectangular dielectric basin.

A general sketch of the plasma-liquid system configuration that was treated mathematically is shown in figure 1. The chosen liquid cell is the rectangular dielectric basin filled with water. The shape of surface streamer chosen for calculation is the semi-cylinder with a semi-spherical head. The streamer locates symmetrically in cross-section of basin and propagates along coordinate x. Variable parameters were the conductivity σ and deepness h of the liquid and diameter d and length l of the streamer. The parameters of plasma-liquid system chosen as the basic (or reference) parameters for modeling are as follows: liquid cell dimensions are 25 mm in length, 15 mm in width and 2.5 mm in depth; liquid conductivity is $\sigma_w = 0.1$ S/m; streamer diameter and length are $d = 1$ mm and $l = 5$ mm; streamer conductivity is $\sigma_s = 100$ S/m (the concentration of plasma in a hot streamer is equal approximately to $n \sim 3 \cdot 10^{15}$ cm^{-3})
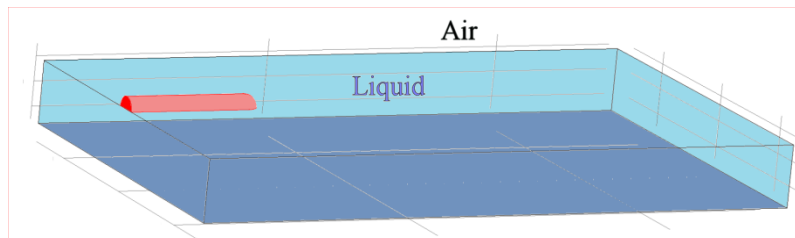
Fig. 1. Configuration of plasma-liquid system with the streamer spreading on surface of liquid. The streamer shape is the semi-cylinder with a semi-spherical head. High voltage potential is delivered to the left end of streamer. The grounded electrode is a metallic plate located at the bottom of rectangular dielectric basin filled with liquid. The gaseous domain has a spherical form with radius drastically exceeding the dimensions of the basin and therefore is not shown in this figure. The used coordinate system is the right Cartesian one. Coordinate x is directed along streamer from left to right, coordinate y is directed upward.

3 Results and Discussion

Some results of 3-D calculations of surface streamer on liquid are shown in figure 2.
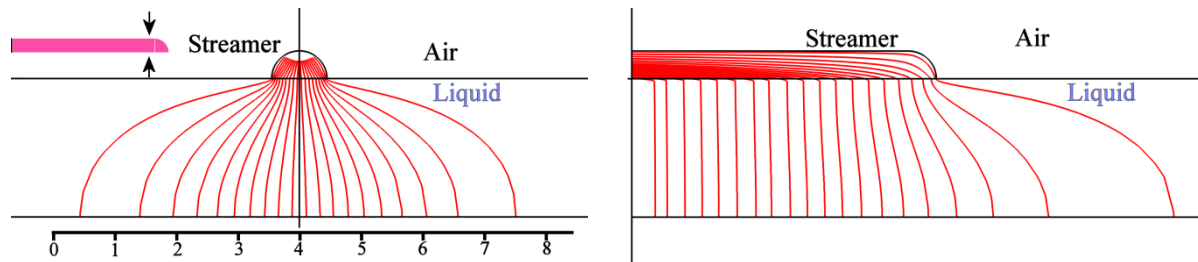
Fig. 2. The map of the current streamlines in plasma-liquid system with surface streamer. Liquid is tap water with σ_w=0.1 S/m. Streamer diameter and length are 1 and 5 mm. The basin sizes: deepness is 2.5mm, width is 15 mm, length is 25 mm. Left picture is the map in plane YZ, x=4.75 mm; right picture is the map in plane YX, z=0. The applied voltage amplitude is 10 kV, total electric current flowing trough streamer is 2.2 A.

One can see in figure 2 that the current density in streamer body increases toward the high-voltage end of streamer due to collection of the current from liquid through lateral side of the streamer. The area of liquid from which streamer collects the current exceeds essentially the sizes of streamer in both directions - transverse and longitudinal. So, inhomogeneity of the current density along the streamer length is inherency of surface streamer. This property is in contrast to volume streamer in which the current density along its length is constant.

Note the ionization mechanism providing a high conductivity of surface streamer is beyond the scope of this article - we only postulate that streamer has a high conductivity. If to ignore the inhomogeneity of the electric field distribution in the streamer cross-section, one can prove that the electric potential $V(x)$ along the streamer-liquid boundary satisfies this diffusion equation (the coordinate x=0 corresponds to high-voltage electrode):

$$\frac{\partial^2 V}{\partial x^2} = \frac{\sigma_w}{\sigma_s} \frac{V(x)}{S_s \int_0^h \frac{dy}{a(y)}}, \tag{3}$$

here S_s is the streamer cross-section; $a(y)=3\sqrt{y}$ is the transverse size (in plane YZ) of liquid taking a part in collection of the current flowing into streamer through its lateral side. One can see that equation (3) contains all parameters characterizing the plasma-liquid system: V_0, σ_s, σ_w, d_s, h. Note that this equation is not applicable to description of the area around streamer head. It means the longer surface streamer, the more realistic description of the electric potential distribution $V(x)$ by equation (3) will be.

The solution of equation (3) gives the exponential decrease of the electric field toward the streamer head that is connected with the decrease of the current density in streamer with a distance from high-voltage electrode (see figure 2). This circumstance leads to that the streamer eventually will stop its extension.

4 Conclusion

We have done 3-D numerical calculations of surface streamer on conductive liquid and found out the spatial structure of both the electric field and current in and outside the streamer. We estimated also the maximum length of surface streamer in dependence on the parameters of plasma-liquid system.

DEGRADATION OF PARACETAMOL IN AQUEOUS SOLUTION BY NON THERMAL PLASMA

Y. Baloul[1], O. Aubry[1], H. Rabat[1], C. Colas[2, 3], B. Maunit[2], D. Hong[1]

[1]GREMI, UMR 7344, Univ.of.Orleans, CNRS, Orléans, France
[2]ICOA, UMR 7311, Univ.of.Orleans, CNRS, Orléans, France
[3]CBM, UPR 4301, CNRS, Orléans, France

E-mail: yasmine.baloul@univ-orleans.fr

In this study, the paracetamol degradation in water was investigated using Non Thermal Plasmas (NTP) created by Dielectric Barrier Discharges. The effects of the operating conditions (applied voltage, inlet gas composition) on the degradation were studied. A conversion rate higher than 90% was reached with an energy yield of 1 g/kWh. We showed that the efficiency of the process highly depends on electrical parameters and gas composition injected in the reactor containing the aqueous solution. The main produced species in water were nitrogen compounds, carboxylic acids and aromatic compounds.

Keywords: wastewater treatment; drug residues; emergent pollutants; non thermal plasma; advanced oxidation process

1   Introduction

Pharmaceutical substances like paracetamol are frequently present in groundwater, and present a long-term risk for the environment and health [1]. We propose to use Advanced Oxidation Processes (AOPs) using Non Thermal Plasmas to degrade these drug residues. AOPs generally refer to a specific subset of processes which produces oxidizing species such as O, O_3, $OH^\bullet$ and H_2O_2. AOPs can also involve TiO_2 catalysis, Fenton's reaction, and Non Thermal Plasma (NTP) [2, 3]. Here, we use a NTP process which was generated by Dielectric Barrier Discharge, because they have proved to be effective for the production of oxidizing species. These processes have already been applied for the treatment of pharmaceutical compounds in aqueous media but differed in the type of plasma reactor [3, 4]. To get a better understanding of degradation mechanisms, it is important to study the effects of the electrical parameters of the reactor and operating conditions on the treatment of pollutants and the generated products. So, in this work which deals with the treatment of paracetamol in liquid by non-thermal plasma process, the effects of the nature of the working gas into the solution and the plasma reactor operating parameters (voltage, power) on the conversion rate and the generated products were studied.

2   Experimental

The plasma reactor used was a multiple needle-to-plate configuration. The schematic diagram of the experimental setup has been previously described [5]. The volume of the treated solution was 40 mL of tap water with an initial paracetamol concentration of 20 mg/L. The initial pH of the solution was 7.2. The electrical discharge was powered by a high voltage amplifier driven by a function generator. The electrical measurements were performed using a high voltage and current probes and were displayed on an oscilloscope. Lissajous's method [6] was used to evaluate the consumed power. To quantify the paracetamol concentration in

the solution, analyses were performed using an absorption UV-Visible spectrophotometer. The range concentrations of H_2O_2, NO_2^-, NO_3^-, were estimated during the treatment times with semi-quantitative test strips QUANTOFIX®. The degradation products were identified by High-Resolution Mass Spectra (HRMS) on a Q-TOF maXis mass spectrometer (Bruker®) [7].

3 Results and Discussion

3.1 Effects of operating conditions

In a previous paper [5], the effects of the amplitude of applied voltage on the conversion of paracetamol have been presented. It was shown that in an oxidative gas, a better conversion rate is obtained when the applied voltage is high, whatever the treatment times. The discharge regime must be streamer one [5], since the spark regime may lead to the disruption of the functioning of the reactor. The conversion rate, τ, and the energy yield, EY (g/kWh), of paracetamol degradation were calculated from equations (1) and (2), respectively, with C_0, C_t concentrations ($g.L^{-1}$) of paracetamol in the solution at the beginning and the end of the time interval Δt (h), V is the volume of the solution (L) and P, the consumed power (kW).

$$\tau = \frac{C_0 - C_t}{C_0} x100 \tag{1}$$

$$EY = \frac{(C_0 - C_t).V}{\Delta t.P} \tag{2}$$

Figure 1.a shows the conversion rates for various injected gas mixtures in function of the treatment time. Theses curves show that the composition of the injected gas plays an important role on the paracetamol degradation in the liquid. The highest conversion rate is obtained for 90% Ar+10% O_2 mixture, because the dissociation of O_2 enables the generation of oxidizing species such as O or O_3 in the gas phase and also $OH^\bullet$ in the liquid phase to degrade the pollutant. Furthermore, the interest to combine an oxidative gas with argon, is to generate more easily the discharge, and to reduce the necessary applied voltage (*i.e.* $\pm$ 5 kV for the mixture 90% Ar + 10% O_2, $\pm$ 3.6 kV for the mixture 90% Ar + 10% air, and $\pm$ 6.8 kV for 100% air) due to a lowest breakdown voltage [8]. In absence of oxygen in the injected gas, no paracetamol degradation was observed [5]. The energy yield of the process therefore depended on the nature of the working gas and the diffusion of the produced species (figure 1b).
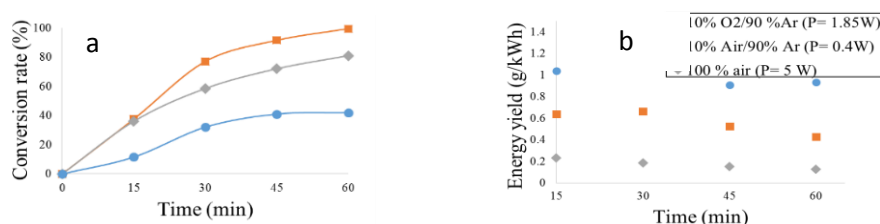
Fig. 1: Effects of the injected gas composition and treatment duration on a) Paracetamol conversion rates and b) energy yields.

We observe that the injected power strongly depends on the injected gas. With the mixture 10% O_2+90% Ar, we obtained the highest τ, but its EY is lower than the one in the mixture 10% air+Ar, because of a higher power injected. The plasma process used in this work is not yet fully optimized, and this study allows to obtain a good paracetamol degradation with an energy yield in the range of 0.2 and 1.4 g/kWh. Brillas *et al* [9] obtained an energy yield of 0.82 g/kWh, in good agreement with our results.

3.2   Generated products

The concentrations of NO_3^-, NO_2^-, H_2O_2 and pH were estimated every 15 min during one hour of paracetamol treatment, the results obtained after 60 minutes of treatment are displayed in Table 1. H_2O_2 is an oxidizing species which can react non-selectively [10]. In this work, we observe that the measured concentrations of H_2O_2 in the treated solutions are similar in all the studied conditions. An increase of the treatment duration leads to a higher concentration of H_2O_2. The production of NO_3^- and NO_2^- does not seem to be linked to the degradation of paracetamol. Indeed in Ar-O_2 mixtures, these species are not produced despite the high conversion of paracetamol obtained. In presence of air, the concentrations of NO_3^- and NO_2^- increase over time, reaching values of 100 and 5 mg/L, respectively, after one hour of treatment.

Table 1: Ranges of concentrations of NO_3^-, NO_2^-, H_2O_2 and pH measured in the liquid.

Time (min)	90% Ar + 10% O₂				90% Ar + 10% air				100 % Air			
	$[NO_3^-]$ mg.L^{-1}	$[NO_2^-]$ mg.L^{-1}	$[H_2O_2]$ mg.L^{-1}	pH	$[NO_3^-]$ mg.L^{-1}	$[NO_2^-]$ mg.L^{-1}	$[H_2O_2]$ mg.L^{-1}	pH	$[NO_3^-]$ mg.L^{-1}	$[NO_2^-]$ mg.L^{-1}	$[H_2O_2]$ mg.L^{-1}	pH
60	0	0	10-25	6.9	25-50	5-10	10-25	5.7-6	50-100	0-1	10-25	6-6.3

Figure 2 shows the absorption spectra of the paracetamol for different treatment time, and various inlet gas. An absorption band, observed around 210 nm, corresponds to the presence of NO_3^- and NO_2^- in the treated liquids [11]. These results are in agreement with the concentrations of NO_3^- and NO_2^- previously measured. These compounds are not produced in the absence of N_2 in the injected gas as shown in Figure 2b.
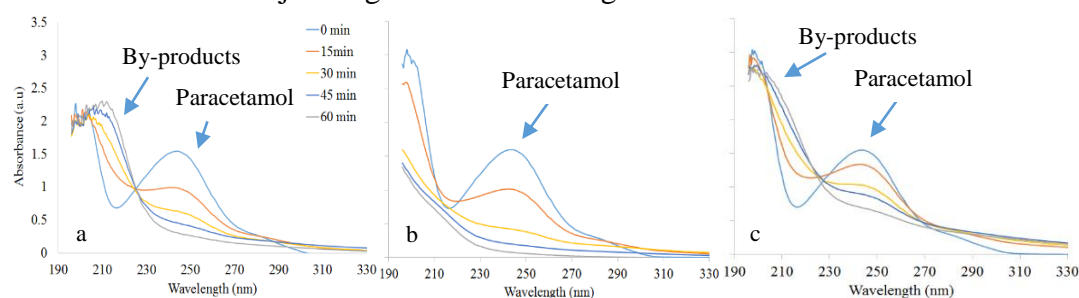
Fig. 2. Absorption spectra in function the composition of the injected gas a) air (U = ± 6.8 kV); b) 90% Ar + 10% O₂ (U = ± 5 kV); c) 90% Ar + 10% air (U = ± 3.6 kV).

A complete analysis of the generated products was performed by HRMS. Table 2 presents a non-exhaustive list of the main detected degradation products among about 70 ones. All the compounds presented in table 2 are common to the treatments using three gas compositions. Different families of molecules from paracetamol degradation have been identified, including compounds similar to those observed from the degradation of paracetamol in some AOPs [12-15] and also in NTP processes [3]. In addition to the aromatic compounds listed in Table 2, nitrophenol, aminophenol, and hydroquinone were also detected and carboxylic acids (*i.e.* acetic, succinic, muconic, and maleic acids) were identified. Nitrites and nitrates were also detected only for the 100% air and 10% air + 90% Ar. The formation of carboxylic acids during the degradation of paracetamol can explain the acidification of the samples as reported in Table 1.

Table 2. List of identified compounds by HRMS which are similar to literature.

mode	experimental m/z	Attempt of identification	Molecular formula	formula
Negative	103.004	Malonic acid [12,13]	$C_3H_3O_4^-$	
Negative	145.014	acetonedicarboxylic acid	$C_5H_5O_5^-$	
Negative	166.051	hydroxy-4-(Nacetyl)-aminophenol [12]	$C_8H_8NO_3^-$	
Positive	200.055	[12,14]	$C_8H_{10}NO_5^+$	
Negative	214.035	[12]	$C_8H_8NO_6^-$	
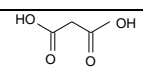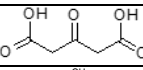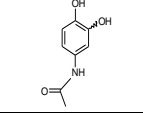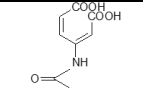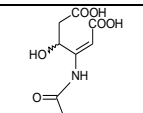
4 Conclusion

This study was about the treatment of paracetamol in aqueous solution by non-thermal plasma. The effects of the nature of the working gas on the conversion rate and the produced species were presented. The highest conversion close to 99% was obtained for a gas mixture of O_2-Ar with an EY of 0.7 g/kWh. A better energy yield of 1.4 g/kWh was obtained for gas mixture of air-Ar. The dissociation of O_2 in the plasma and the diffusion of produced species in the liquid are necessary steps in the process. The energy yield of the process, strongly depends on the experimental conditions as the consumed power which in turn depends on the composition of injected gas. In the liquid phase, analysis shows that nitrites, nitrates, carboxylic acids, and aromatic compounds are the main degradation products. The perspectives of this work will be to optimize the process with the study of the influence of the concentration and the volume of the solution. A comparison of this process to another one in post-discharge, like an ozone generator, is scheduled to find out the influence of other generated species in addition to ozone.

References

1. D.W. Kolpin et al., Sci. Total. Environ. 328, 119 (2004)
2. O. Jimoh et al., Water. Air. Soil. Poll. 225, 2102 (2014)
3. M. Magureanu et al., Water. Res. 45, 3407 (2011)
4. I. Panorel et al., Ozone: Sci. Eng. 35,116 (2013)
5. Y. Baloul et al., IJPEST. (to be published)
6. Z. Falkenstein et al., J. Phys. D. Appl. Phys. 30, 825 (1997)
7. H. Belghit et al., Inter. J. Environ. Anal. Chem. 95, 2 (2015)
8. J. Park et al., J. Appl. Phys. 89, 1 (2001)
9. E. Brillas et al., Chemosphere.58, 399 (2005)
10. M. Magureanu et al., Plasma. Chem. Plasma. Process. 27, 589 (2007)
11. J. S. Oh et al., in *Proceedings of 22nd International Symposium on Plasma Chemistry*, Antwerp, 2015, edited by A. Bogaerts and R. van de Sanden
12. L. Zhang et al., Chem. Eng. J. 276, 185 (2015)
13. R. Andreozzi et al., Water. Res. 37, 993 (2003)
14. M. Torun et al., Environ. Technol. 8, 970 (2014)
15. E. Moctezuma et al., J. Hazard. Mater. 243, 130 (2012)

PULSED ATMOSPHERIC PRESSURE PLASMA REFORMING OF ETHANOL

H. Baránková, L. Bardos

Uppsala University, Ångström Laboratory, Division of Electricity, Plasma Group, Box 534, SE-751 21 Uppsala, Sweden

E-mail: hana.barankova@angstrom.uu.se

The plasma source with a coaxial geometry was used for generation of plasma inside water and the ethanol-water mixtures. The hydrogen-rich synthesis gas with hydrogen content up to 60% was produced in submerged dc pulsed plasma. The effect of various plasma generation regimes on the performance of plasma, on the hydrogen production efficiency and on the reaction rise-time was examined. A role of the solution temperature, composition of the mixture and current delivered to the discharge are investigated.

Keywords: plasma discharge in liquids; hydrogen production; ethanol reforming

1   Introduction

Plasma reforming of ethanol represents an area of a great potential because bioethanol is easily accessible from biomass and also its transport is safe. Small plasma reactors powered by renewable electric power sources can then be used for production of hydrogen on demand. [1-3]. The paper presents results of hydrogen production from ethanol-water mixtures by submerged pulsed dc plasma at low average power.

2   Experimental

A coaxial diode system with a negative outer electrode terminated by a slit and with a central grounded anode is installed inside the stainless steel cylindrical reactor, filled by the mixture of deionized water and ethanol. The experiments were carried out without an auxiliary gas brought into the reactor. The reactor is closed hermetically and its outlet is connected to the pressure gauge, hydrogen detector (HY-Alerta), gas flow meter (glass rotameter) and an outlet nozzle for igniting the flame. The reactor is equipped by the thermometer, densitometer, pH meter and conductivity meter. Optical emission from the plasma is detected by a quartz optics connected to the PLASCALC-2000-UV-VIS-NIR Plasma Monitoring & Process Control System. Several types of power generators were tested in the system with pure water, the 13.56 MHz and 27.12 MHz rf generators, 2.4 GHz microwave generator, 0.1 µs pulsed dc generator and 9 ns pulsed dc generator with variable repetition frequencies, in order to select the best generation with minimum heating of the water. The reforming experiments were performed with 9 kV negative pulses at the repetition frequency of 15 kHz. The root mean square value of the pulsed current delivered to the plasma from the generator was measured by oscilloscope. The content of hydrogen in the produced gas was measured continually by a HY-Alerta[TM] detector and measured values were checked by and compared with the GC-406 (Agilent Technologies) measurements of gas samples using Tedlar® Gas Sampling Bags.

3 Results and Discussion

The photograph from the discharge in the ethanol-water mixture is shown in Fig.1. The rise-time of the high hydrogen content synthesis gas production is very short and the flame can be
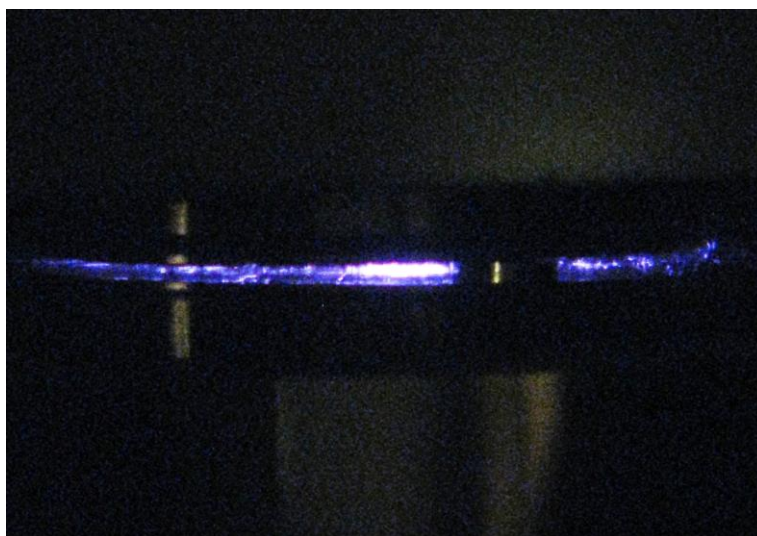
Fig. 1: Pulsed dc discharge in the mixture of water with ethanol

ignited at the gas outlet nozzle almost immediately. No auxiliary/carrier gas was admitted into the reactor. The temperature of the liquid increases very slowly for the low average power generation, even without reactor cooling. The optical emission spectra from the discharge feature hydrogen lines, atomic oxygen lines and CO band. The forming of the synthesis gas and hydrogen content were studied for different compositions of the ethanol-water mixtures, always starting with a fresh low conductivity mixture of about 2 μS/cm. The maximum hydrogen content observed in the produced gas was 60% and the maximum production rate appeared around 30 - 35% of ethanol in the bath. The hydrogen production efficiency corresponds to 12 kWh/kg H_2.

4 Conclusion

The pulsed dc plasma source was used for generation of plasma inside ethanol-water mixtures. The hydrogen-rich (60%) synthesis gas was produced at a low average power of 10 W, with the production efficiency of 12 kWh/kg H_2. The optimum regimes were reached for 30 - 35% ethanol-water mixtures.

References

1. J. H. Chaffin et al., J. Energy Engineering 132, 104 (2006)
2. Z. Yan et al., J. Phys. D, Appl. Phys. 41, 155205 (2008)
3. D. Czylkowski et al., Int. J. Hydrogen Energy 40, 14039 (2015)

APPLICATION OF SURFACE DIELECTRIC BARRIER DISCHARGE GENERATED FROM LIQUID ELECTRODE FOR SURFACE TREATMENT OF TUBES

O. Galmiz, D. Pavlinak, M. Zemanek, A. Brablec, M. Cernak

Department of Physical Electronics, Masaryk University, Kotlarska 2, Brno 60200, Czech Republic

E-mail: oleksandr.galmiz@gmail.com

A new type of SDBD generating thin layers of plasma which propagate along the treated polymer surfaces was used to achieve permanent hydrophilization of inner and outer surfaces of polytetrafluoroethylene (PTFE) and polyvinyl chloride (PVC) tubes. Diagnostic of the discharge using the conventional and high-speed photography as well as optical emission spectroscopy were summarized.

Keywords: surface dielectric barrier discharges; plasma treatment; diagnostic

1 Introduction

Combining basic features of discharges generated in contact with water with surface dielectric barrier discharges (SDBD) by using water-solutions as discharge electrodes, a new type of SDBD generating thin layers of plasma which propagate along the treated polymer surfaces has been designed. The technique was aimed to achieve uniform atmospheric pressure plasma treatment of inner and/or outer surfaces of polymeric tubes and other hollow bodies. This method can bring a cost effective process of uniform and easy treatment with reduced or totally absent damaging of electrodes and/or dielectric body [1]. To illustrate the application potential of this configuration and to summarize its basic physical properties a set of experiments were realized making possible to achieve permanent hydrophilization of inner and outer surfaces of polytetrafluoroethylene (PTFE) and polyvinyl chloride (PVC) tubes.

Here, results using the conventional and high-speed photography on differences in discharge structures of four technologically relevant gases: air, argon, nitrogen and oxygen, are summarized. Optical emission spectroscopy (OES) has been used for characterization of excited species in case of concrete working gas which appears useful while treating materials sensitive to temperature (in order not to damage it) and the chemical reactions, which could take place during treatment or deposition [2]. Changes in water contact angle (WCA) as well as long-time aging are also discussed.

2 Experimental setup

Schematic drawing of the discharge, including photos without and with plasma recorded at the discharge power of 6 W are presented in the figure 1. All three possible electrode configurations which can be used for the inner, outer as well as for both tube surfaces simultaneous treatment are shown. The PTFE tube (outer diameter of 8 mm, inner diameter of 7 mm) is inserted vertically into the oxalic acid solution and filled with the identical

solution. Both electrically insulated spaces volumes serve as liquid electrodes (5 % solution of oxalic acid in distilled water with conductivity of 50 mS·cm^{-1}).

Electrical characteristics of the discharge were monitored by a digital oscilloscope Hewlett Packard Infinium (500 MHz; 2 GSa/s) connected to a voltage (Tektronix P 6015A) and current (Pearson Electronics 2877) probes. To make electrical current measurement more sensitive, the capacitive (displacement) current waveform component was eliminated by method described in [3]. The polarity of outer liquid electrode determines the polarity of discharge.
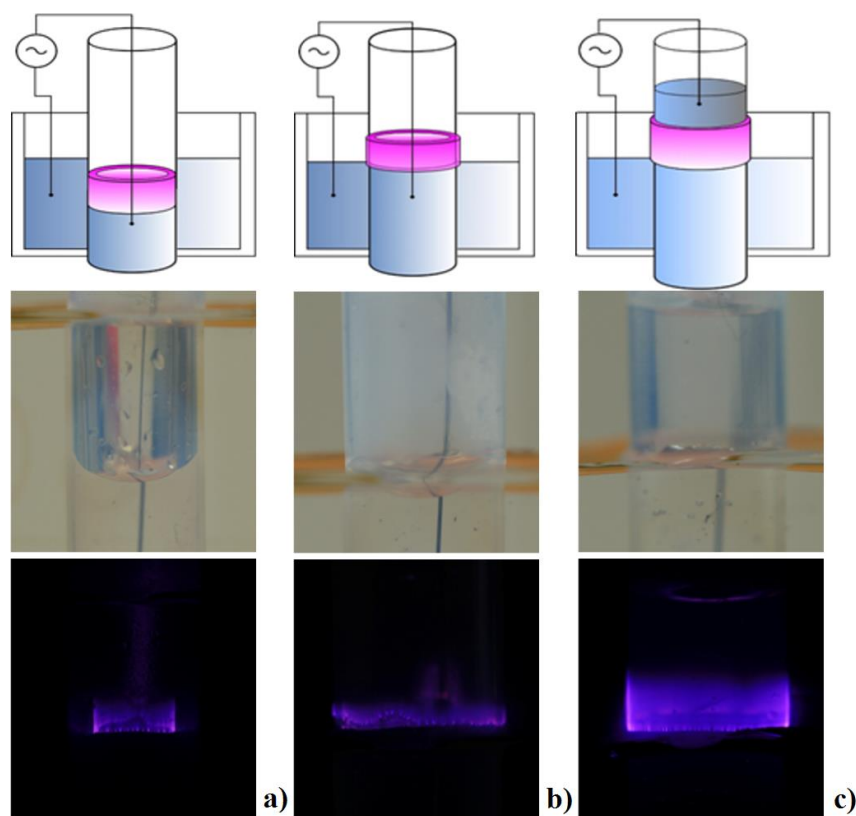
Fig. 1. Schema of the discharge, photos without and with plasma taken at the discharge power of 6 W. All three possible electrode configurations are shown - the treatment of inner side a), both tube surfaces simultaneously b) and outer side c).

3   Results and Discussion

Figure 2 shows the hydrophilic changes on the surface of PTFE tube after the plasma treatment. It was found that the PTFE surface treated in plasma region gained significant hydrophilic properties. Namely, while the WCA of the surface that was in contact with the oxalic acid solution did not change and was about 100°±7° (taken as reference sample), in case of plasma treatment the contact angle decreased to 65°±5° .

As to the time evolution of plasma treated PTFE material (aging) it was found that the long-time aging was very slow and even after one hundred days (average WCA was 70°±10°). That is the difference of almost 30° against the original state. Thus, it can be summarized,

that the treatment with plasma generated from oxalic acid solution is stable over time and retains the gained hydrophilic properties.

The discharge ignited in air generates visually almost diffuse surface plasma layers. However, the conventional and ICCD cameras study has revealed rather complex discharge structures [2].
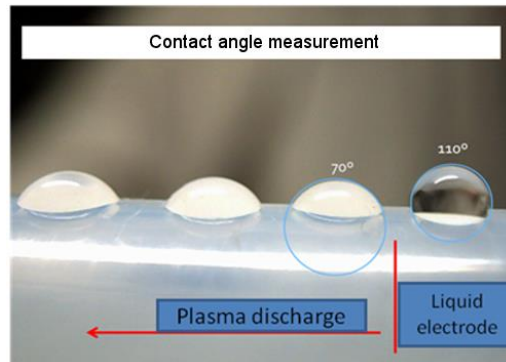
Fig. 2. The hydrophilic changes on the surface of PTFE tube after the plasma treatment (left) and the effect of oxalic acid solution (right). The vertical line indicates the boundary level of solution during treatment.

Very important for the surface treatment applications feature of the discharge is the increase of the discharge uniformity with the increase of the input power. This feature was observed for all used gases with exception for argon where filamentary structure was present even for powers higher than 80 W.

The discharge consists of short-lived filamentary microdischarges (MD) appearing randomly at both polarities of the applied voltage. Nevertheless, for each half cycle of the applied voltage the visual appearance of MD is different. Behaviour of discharge's current and voltage waveforms with time and in different atmospheres was studied. Obtained waveforms are different in shapes of current peaks, quantity and position (figure 3).
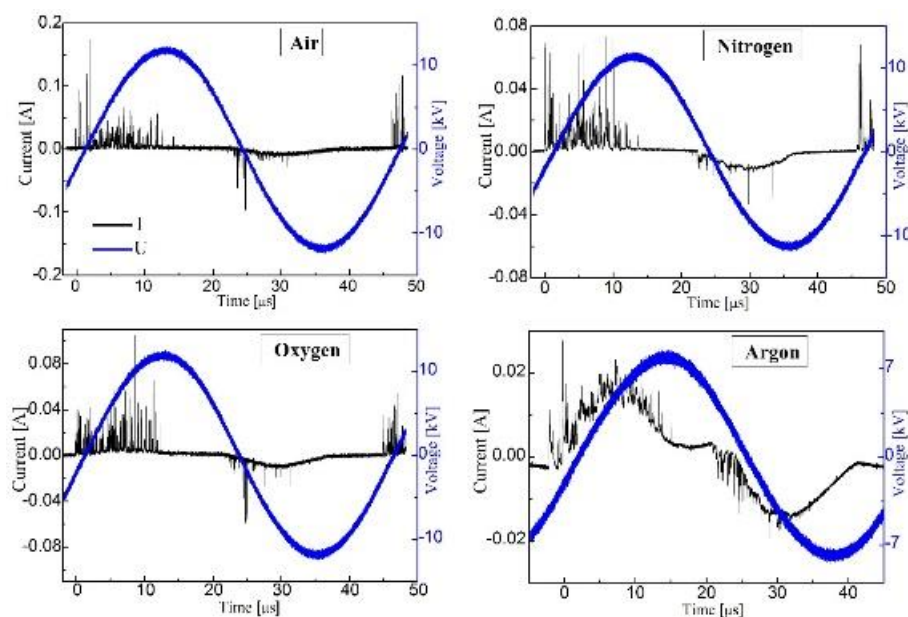
Fig. 3. The voltage and current waveforms for discharges in different gases and applied power of 80 W [2].

It was found that in emission spectra of the discharge generated in air at atmospheric pressure and influenced by water vapours (even in argon) one can identify that the most intensive bands belongs to the second positive system of nitrogen $C^3\Pi_u(v') \rightarrow B^3\Pi_g(v'')$, the 306.3 nm ($A^2\Sigma^+ \rightarrow X^2\Pi$, $\Delta v = 0$) system of OH radicals and first negative system N_2^+ (FNS, $B^2\Sigma_u \rightarrow X^2\Sigma_g$). The same bands were also observed in case of nitrogen was used as a feed gas. While using nitrogen gas the intensity of nitrogen lines increased as it was expected.

For air, nitrogen and argon the rotational temperatures calculated from the OH system were in range 540-660 K, 550-640 K and 425-625 K, respectively. In our experiments the molecule of OH plays important role as one can found also in argon and so this temperature can be used for mutual comparison of discharges in different gases.

For air and nitrogen, the rotational temperatures calculated from the second positive system of nitrogen were in range 365-445 K and 333-425 K, respectively. The vibrational temperatures in case of our experimental conditions were around 2240-2540 K and 1950-2270 K for air and nitrogen, respectively.

While using argon gas the excitation temperature was in range of 3180-4200 K depending on the applied power.

4   Conclusion

It can be concluded that plasma-chemical treatment of PTFE and PVC tubes led to the chemical modification of the surface. Hydrophilic properties of the treated surface were gained immediately after the treatment and were stable in time.

To gain a better insight into this still little known gas discharge phenomenon, basic characteristics of SDBDs generated from water-solution electrodes at atmospheric pressure in several technologically important working gases were investigated.

Obtained results show that the configuration of electrodes appears to be viable and technically simple alternative to other plasma surface treatments of dielectric hollow bodies. It is flexible, employs simple high-voltage power supplies operated at low frequencies, and can be easily modified. The low energy consumption of this technique is suitable for industrial use together with the absence of any expensive gases or electrode solutions.

References
1. D. Pavliňák et al., Appl. Phys. Lett. 105, 154102 (2014)
2. O. Galmiz et al., J. Phys. D. Appl. Phys. 065201, 65201 (2016)
3. J. Ráheľ et al., Contrib. to Plasma Phys. 47, 34-9 (2007)

CROSS-CORRELATION SPECTROSCOPY STUDY OF THE BREAKDOWN MECHANISM IN ATMOSPHERIC PRESSURE AIR TRANSIENT SPARK DISCHARGE

M. Janda[1], T. Hoder[2], A. Sarani[3], R. Brandenburg[3], Z. Machala[1]

[1]*Faculty of Mathematics, Physics and Informatics, Comenius University in Bratislava, Mlynská dolina F2,842 48 Bratislava, Slovakia*
[2]*Faculty of Science, Masaryk University, Kotlarska 2, 611 37 Brno, Czech Republic*
[3]*INP Greifswald e.V., Felix-Hausdorff-Str. 2, 17489 Greifswald, Germany*

E-mail: janda@fmph.uniba.sk

A streamer-to-spark transition in a self-pulsing transient spark (TS) discharge of positive polarity in air was investigated using cross-correlation spectroscopy. The entire temporal evolution of the TS, including the primary streamer, the secondary streamer, and the transition to spark was recorded at several wavelengths of spectral bands or lines corresponding to the second positive system of N_2 (337.1 nm), the first negative system of N_2^+ (391.4 nm), and to atomic oxygen (777.1 nm) and nitrogen (746 nm). The obtained results contribute to a deeper understanding of the breakdown mechanism in air at high repetition frequencies.

Keywords: cross-correlation spectroscopy; transient spark; breakdown mechanism

1   Introduction

The Transient Spark (TS) is a dc-driven self-pulsing discharge with the typical repetition frequency 1-10 kHz [1-3]. The TS is initiated by a primary streamer, followed by a secondary streamer generating a short spark current pulse with a maximum amplitude in the range of a few Amps. The TS spark current pulses are sufficiently short (~10-100 ns), thus significant heating of the gas in the generated plasma is avoided. Plasma generated during the spark phase of the TS is therefore highly reactive with the electron density as high as 10^{17} cm^{-3} [4]. These reactive plasma properties predetermine the TS for several biomedical and environmental applications [5, 6]. However, further basic research of TS is needed, e. g. for the explanation of TS peculiarities changes with increasing repetition frequency [7].

Based on the significant shortening of the streamer-to-spark transition delay time [7], a change of the breakdown mechanism in the TS with the increasing frequency is assumed. There are probably several 'memory' effects (especially pre-heating, residual ions and changes of the gas composition by previous TS pulses) in the gap. Residual space charges also influence the development of single dielectric barrier discharges [8].

2   Experimental

In this paper we explore the entire evolution of the TS discharge from the primary streamer to the spark breakdown at a repetition frequency in the range 8-10 kHz. Cross-correlation spectroscopy was used [9], since it is very sensitive and suitable for the investigation of self-pulsing discharges unless other techniques like iCCD cameras, which require precise synchronization with the discharge event. Figure 1 shows the schematic of the used

experimental setup. A novel CCS device as described in [10] was used. It enables multi-dimensional TC-SPC and thus automatic scanning of the discharge gap via imaging on a rotating mirror.
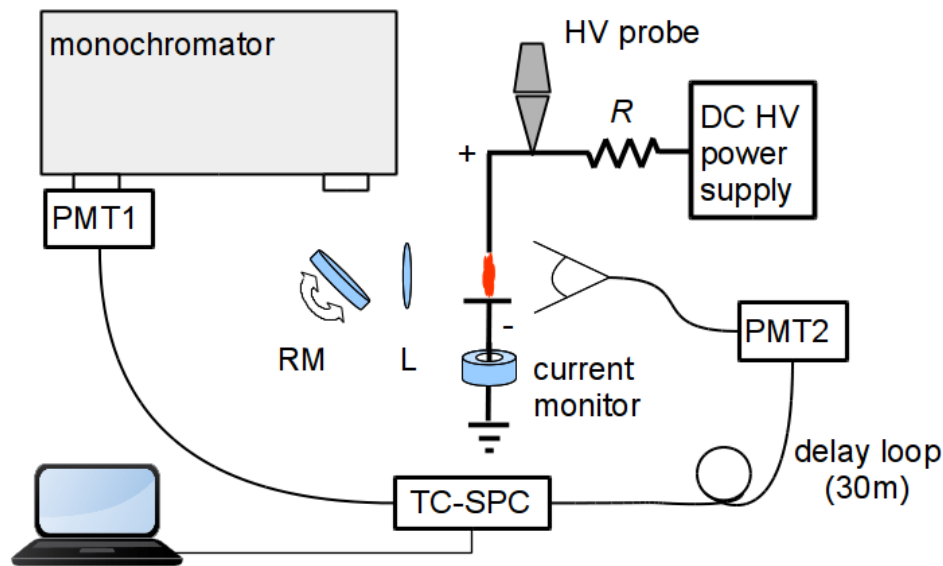
Fig. 1: Schematic of the experimental setup, PMT – photo multiplier, TC-SPC – time correlated single photon counting board, RM – rotating mirror, L – lens, R – external resistor.

The positive polarity TS was generated in atmospheric pressure air between steel electrodes in point-to-plane configuration with the gap length $d = 4$ mm, by a DC HV power supply connected to the electrodes via a series resistor $R = 6.85$ MΩ (Figure 1). The discharge voltage was measured by an HV probe (Tektronix P6015A) and the discharge current was measured by a current monitor (Pearson Electronics 4100 1V/A). Both voltage and current signals were recorded by a 1 GHz digitizing oscilloscope (Tektronix DPO 4104).

3   Results and Discussion

The entire temporal evolution of the TS, from the primary streamer to the transition to spark was obtained. The emission from the discharge at several wavelengths was recorded (Figure 2), corresponding to the second positive system (SPS) of N_2 (0-0 transition at 337.1 nm), the first negative system (FNS) of N_2^+ (0-0 transition at 391.4 nm), and the emission lines of atomic oxygen (777.1 nm) and nitrogen (746 nm).

During the primary streamer (time ~0-8 ns in Figure 2), the emission of the SPS dominates, but the emission of the FNS was also observed. The interesting fact of the FNS being constantly ahead of the SPS signal during the streamer propagation was discussed and clarified in detail in [11].

A transition to the spark (developed at time ~13-27 ns) within ~5 ns after the primary streamer was observed. The spark itself was preceded not only by the primary streamer, but also by a feature (time ~8-11 ns in Figure 2) that probably represents a secondary streamer [12]. During this period, only the emission of the 2nd positive system of N_2 was observed.

During the spark phase, only the emission of the 1st negative system of N_2^+ and atomic lines were detected. This can be partially attributed to a high degree of ionization and dissociation of molecular species during the spark phase. Moreover, the lack of the SPS emission could be explained by lower electron mean energy during the spark phase, so that the direct electron impact excitations are not efficient. On the other hand, the emitting atoms and N_2^+ ions are probably populated by different stepwise mechanisms.
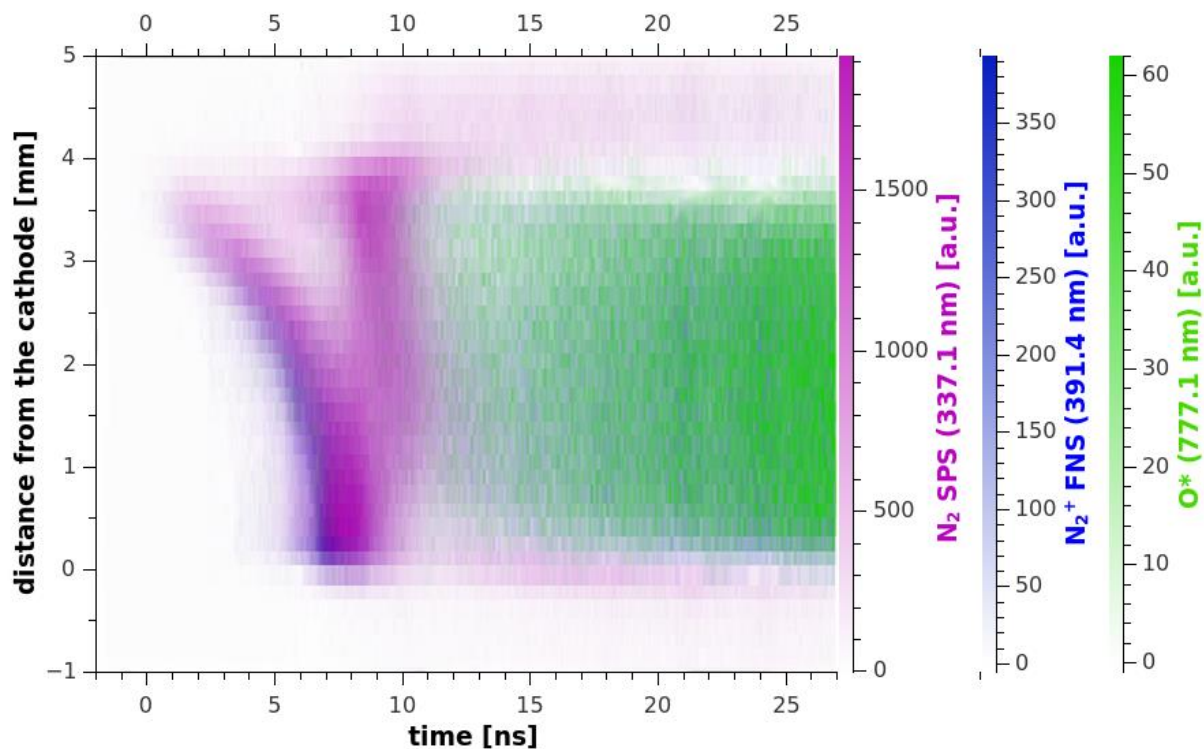
Fig. 2: Cross-correlation spectroscopy record of the TS evolution, positive polarity (anode at the top), repetition frequency 8-10 kHz, gap 4 mm.
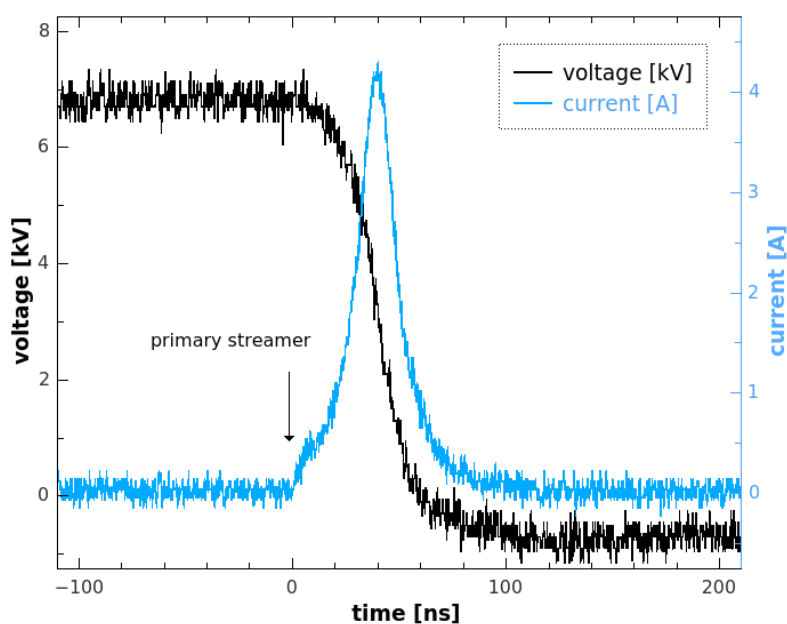
Fig. 3: Typical waveforms of transient spark discharge, repetition frequency 8-10 kHz, gap 4 mm.

The high degree of ionization results from a narrow discharge channel (~50-150 μm [4]) and a high current (Figure 3) during the TS spark phase. Subsequently, the high density of electrons and ions can significantly contribute to the dissociation of the molecular species via dissociative electron-ion recombination reactions:

$$e + O_2^+ \rightarrow O + O\ (O^*), \qquad (1)$$
$$e + N_2^+ \rightarrow N + N\ (N^*). \qquad (2)$$

4   Conclusion

We investigated the streamer-to-spark transition mechanism in the Transient Spark (TS) discharge in atmospheric pressure air using cross-correlation spectroscopy. The TS is a self-pulsing discharge initiated by a primary streamer followed by short spark current pulse. The TS repetition mean frequency can be controlled in the range 1-10 kHz by the applied voltage, but the self-pulsing frequency is not regular, which makes the synchronized diagnostics of the TS difficult. The cross-correlation spectroscopy proved to be a suitable technique for the investigation of such self-pulsing discharges.

Our obtained results show that the transition from the streamer to the spark proceeds within about 10 ns. This could be attributed to the fast propagation of the secondary streamer through the whole gap, probably due to memory effects – the pre-heating of the gas in the gap, or the accumulation of species such as oxygen atoms generated by the previous TS pulses. Further research is required, including kinetic modeling to verify this hypothesis.

References

1. Z. Machala et al., J. Mol. Spectrosc. 243, 194 (2007)
2. M. Janda et al., Plasma Sources Sci. Technol. 20, 035015 (2011)
3. T. Gerling et al., Plasma Sources Sci. Technol. 22, 065012 (2013)
4. M. Janda et al., Plasma Sources Sci. Technol. 23, 065016 (2014)
5. Z. Machala et al., J. Phys. D: Appl. Phys. 43, 222001 (2010)
6. E. Hontanon et al., Nanopart. Res. 15, 1957 (2013)
7. M. Janda et al., Plasma Sources Sci. Technol. 21, 045006 (2012)
8. H. Hoeft et al., J. Phys. D: Appl. Phys. 47, 465206 (2014)
9. H.-E. Wagner et al., Vacuum 71, 417 (2003)
10. R. Brandenburg et al., in *Proceedings of 22nd International Symposium on Plasma Chemistry*, Antwerp, 2015, edited by A. Bogaerts and R. van de Sanden
11. T. Hoder et al., J. Appl. Phys. 117, 073302 (2015)
12. R.S. Sigmond, J. Appl. Phys. 56, 1355, (1984)

GAS DISCHARGE EXCITED BY STRONG SUBTHRESHOLD MICROWAVE BEAM IN A HIGH PRESSURE LARGE VOLUME GAS. PHYSICAL BASIS AND TOPICAL PLASMACHEMICAL APPLICATIONS

I. A. Kossyi, G. M. Batanov, N. K. Berezhetskaya, A. M. Davydov,
K. A. Sarksyan, N.K. Kharchev

Prokhorov General Physics Institute of Russian Academy of Sciences, Moscow, Russian Federation, 119991, Vavilov Street 38

E-mail: kossyi@fpl.gpi.ru

Physical basis of an unusual and insistent type of microwave discharge (SNS discharge) excited by strong subthreshold microwave beam in a high pressure gas is under discussion. First results of SNS applications in a plasmachemical reactor put into operation in GPI are presented.

Keywords: microwave discharge; ionization-thermal instability; plasmachemistry; methane conversion; CO2 utilization

1   Introduction

Overview of experimental and theoretical researches in which for the first time the new type of microwave discharge received such a denomination as SNS (Self/Non-Self sustained) discharge [1-6] – is presented. This type of discharges are exciting in the high-pressure gases ($veff > \omega$) by a pulse microwave beams at a strong subthreshold conditions relative to the self-sustained microwave discharges excitation in the free-space ($E/nm << [E/nm]thr$). Hear $veff$ – is effective frequency of electron-neutral collisions, ω – is cyclic frequency of microwave radiation, E – is microwave electric field and nm – is concentration of molecules in the gas medium. Typical photography of such a type of discharge in a free space in atmospheric pressure air is shown on the Fig. 1
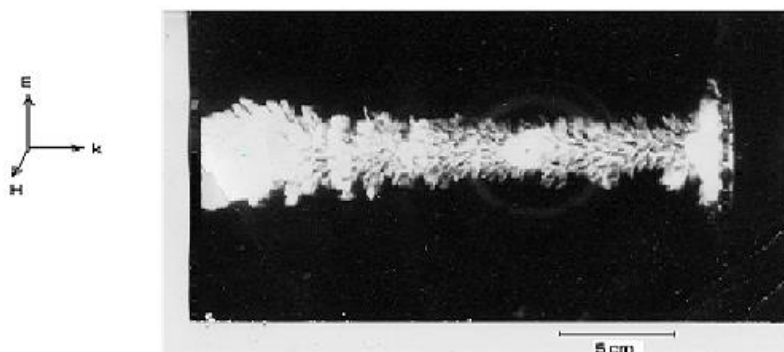
Fig. 1. Typical photography of SNS discharge in the atmospheric pressure air.

2   Model and Results

Physical model of phenomenon appearing at conditions where the fact of gas-discharge plasma formation looks rather paradoxical is presented. SNS discharge is generated in a high-pressure gases under conditions when value of reduced electric field in a convergent microwave beam is lower (or much lower) than the breakdown field in a free space. Initiation

of discharge in a focal plane leads to the occurrence of ionizing wave propagating toward the microwave beam and occupying major part of it. Initiation of discharge and its propagation represents alternation of self-sustained and non-self-sustained discharges where the changing over from one form to another proceeds through the ionization-overheating instability. Strong space uniformity of the SNS discharge is a consequence just of this type of instability getting to a strong nonlinear phase. Discharge looks like a multitude of channels (filaments) stretched along the microwave electric field. Plasma in filaments has extremely high density (up to $n_e \cong 10^{16} - 10^{17}$ cm^{-3}) that is much higher than the "critical" one for producing it microwave radiation. Typical parameters of channels and near-the-channel space are presented on the Fig. 2.
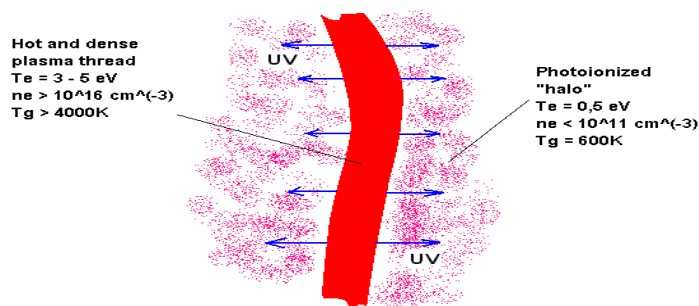
Fig. 2. Typical parameters of plasma "thread" and photoionized "halo".

Wide area of applications of a new variety of microwave discharge (plasma-chemistry, aeronautic engineering, space techniques, high-power UV-lamps, etc.) is under discussion.

3   Conclusion

New type of plasmachemical reactor based on the SNS discharge has been designed and put into operation in the GPI. As a microwave generator powerful GIROTRON has been applied (pulse power $\leq$ 1 MW, pulse duration $\leq$ 20 ms, wavelength 0,4 cm). Results of the first experiments dedicated to the topical plasmachemical applications are presented. Among them such ones like methane conversion in a Sin-gas, CO_2 utilization, cleaning of industrial waste gases. Results of these experiments are demonstrating unqualified attractiveness of SNS discharges for solution of topical applications problems.

References

1. G. M. Batanov, S. I. Gritsinin, I. A. Kossyi, A. N. Magunov, V. P. Silakov, N. M. Tarasova, High-pressure microwave discharges in Plasma Physics and Plasma Electronics, edited by L. M. Kovrizhnykh, (Nova Science Publishers, 1985)

2. G. M. Batanov, S. I. Gritsinin, I. A. Kossyi, J. Phys. D: Appl. Phys. 35, 20 (2002)

3. V. G. Avetisov, S. I. Gritsinin, A. G. Kim, I. A. Kossyi, Pis'ma v Zhurnal Experim. I Teoretich. Fiziki. 51, 6 (1990) In Russian

4. A. G. Kim, G. M. Fraiman, Fizika Plasmy. 9, 3 (1983) In Russian

5. Generation of Nonlinear Waves and Quasi-Steady Currents in Plasma. Transact. GPI. 16. (Moscow: Nauka. 1988) In Russian

6. I. A. Kossyi, in *Proceedings of 44th AIAA Aerospace Sciences Meeting and Exhibit*, Reno, Nevada, 2006, Report AIAA-2006-1457

TREATMENT OF THE GLASS ARCHAEOLOGICAL ARTEFACTS BY UNDERWATER DISCHARGE

L. Hlochova[1], W. G. Graham[2], D. Janova[1], F. Krcma[1]

[1]*Brno University of Technology, Faculty of Chemistry, Institute of Physical and Applied Chemistry, Purkynova 118, Brno, 612 00, Czech Republic*
[2]*Queen's University Belfast, School of Mathematics and Physics, Centre for Plasma Physics, Belfast, BT7 1 NN, Northern Ireland, United Kingdom*

E-mail: krcma@fch.vut.cz

This work focuses on the removal of corrosion product layers from the glass made archaeological artefacts. The reactive species and physical effects generated by the underwater discharge in multielectrode configuration were used as reducing agents. Original archaeological artefacts were treated for three minutes per square cm at the applied power of 5 W. Surface changes were visible by the naked eye and visualized using scanning electron microscopy. The relative concentrations of the elements were monitored by X-ray microanalysis on the objects surfaces and from the object core. Very good corrosion removal using this new low stressing technique was fully confirmed.

Keywords: plasma generated in liquid; surface cleaning; ancient glass

1   Introduction

The application of plasma in the field of conservation/restoration of archaeological objects is studied during the last few decades. The first application was described by the group around V. D. Daniels [1]. A few years later, the group of S. Veprek developed a new technology [2] based on RF low pressure plasma. The samples were significantly heated up to 400°C and thus their procedure was applicable for iron and silver objects, only. More studies focused on treatment of metallic objects and model samples were carried out recently by our group [3, 4]. The results showed that successful corrosion removal can be reached using much lower temperatures that allows treatment even of more temperature sensitive materials like bronze. Unfortunately, the thermal stress by low pressure plasma application is still relatively high and it does not allow safety treatment of glass objects that can have easily breakable microcrystalline structure, especially at older objects.

The research in the field of electrical discharges interacting with liquids or generated directly in liquids opens new possible ways for the application in conservation/restoration. The plasma interacting with liquids is typically of low temperature and at atmospheric pressure (so there is no additional stress to object due to decreased pressure). The discharges with water environment produce a huge amount of atomic hydrogen and extremely reactive hydroxyl radicals that are able to react with corrosion products at the object surface. These heterogeneous reactions are well operating at ambient temperature and are further supported by UV radiation generated by the discharge. Some under liquid discharges also generates acoustic of shock waves at different frequency and intensity that can additionally help to the corrosion layers removal [5]. Various water solutions of alkali salts like NaCl, Na_2HPO_4, KCl are typically used in these systems.

The mechanism of the corrosion formation on the glass objects is meaning exchange alkali ion from the glass matrix to ion H^+ from the environment. The elements from the environment participate in this process. They are adsorbed to the damaged matrix and object surfaces is devaluated by the corrosion [6]. Therefore, corrosion removal means elimination of all elements which are not presented in the original glass object bulk. Free radicals generated by discharges with or in liquids can play the main role in this process. Corrosion layers on the object surface is "bombarded" by these active particles (OH·, H·, O· a HO$_2$·). OH· and H· can effectively react with hydrogen contained in the corrosion layer that can be easy substitute by alkali metal ions (sodium, potassium) from the solution. Thus discharges with liquids are able not only remove the layers of corrosion products but they are also able partially restore the original object surface elementary composition.

The first application of gaseous RF plasma jet interacting with water for surface cleaning of ancient glass was described by M. Klima [7]. The current study brings detailed description of the multi-electrode system (which is commonly used in medicine) application on the ancient glass surface cleaning.

2   Experimental

Plasma was generated by special multi-electrode device (see Fig. 1) directly in NaCl water solutions.
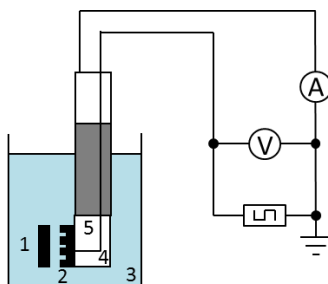
Fig. 1: The multi-electrode system scheme: 1 – sample, 2 – power electrode, 3 – liquid, 4 – insulator, 5 – grounded electrode.

The plasma head is very small (3.5 mm in diameter) and thus allows very local application at the surface and it is possible to apply it also at non-smooth surface. The plasma is flowing from the interelectrode gap to the front of head up to distance about a few mm. This high-performance instrument is commonly used in biomedicine for the treatment of diseased tissues so it is clear that it is a soft tool and can be applied for the ancient glass objects treatment. The thermal effect on the sample is minimized due to the presence of the cooling water solution in whole treated object surrounding. The system operates as a multi-electrode setup with driving circuit producing 100 kHz RF bipolar square wave voltage signals. The main factor for the treatment is obviously the solution conductivity which in turn depends on the temperature and concentration. The optimal experimental conditions for the archaeological glass artefacts treatment were found as 0.9% water solution of sodium chloride (solution conductivity of 13 mS·cm^{-1}), the optimal distance of the treated surface from the plasma head was about 1 mm at applied power of 5 W.

The original ancient glass samples from the 17th – 18th century excavated at Hutsky pond, Josefov, South Moravia (GPS: 49°18'28.6"N 16°41'19.8"E). The wastes of blowing glass (3 samples) were used for the current study. The objects were treated for 3 minutes over selected small area of 1 cm² at constant power of 5 W. After the plasma treatment, all objects were dried at ambient air and finally they were individually packed in aluminium bags with oxygen and humidity absorbers (Long life for art). To verify the surface structure changes as well as changes in the surface elementary composition, the scanning electron microscopy with EDS detector (SEM-EDS) was used on the same areas of these objects before and after the plasma treatment. The analysis of the bulk material was added for comparison of the surface/bulk elementary composition.

3   Results and Discussion

The corrosion layers were removed from the objects surface during the plasma treatment and the original surfaces were excavated (see Fig. 2, parts A1 and A2). The area treated by plasma is marked on the object body. The elementary surface composition before and after the plasma treatment and composition of the bulk material (obtained from the quarry) is given in Fig. 2 on right side. The EDS analysis is not only surface sensitive (in contrary to XPS) and thus strong signals of Si and O atoms from the bulk material are dominating in all EDS spectra. Al, Fe and partially Na are presented mainly on the objects surface and they were partially or even fully removed by plasma treatment. All these elements are typical for the soil from object's surrounding at given location. Contents of Ca and K were significantly increased closely to their content in the bulk material due to the plasma treatment. Small content of Mg and P show the same trend. All these elements are typical additives presented in the ancient glass and have melt function. They were originally added as potash and lime during the manufacturing process.
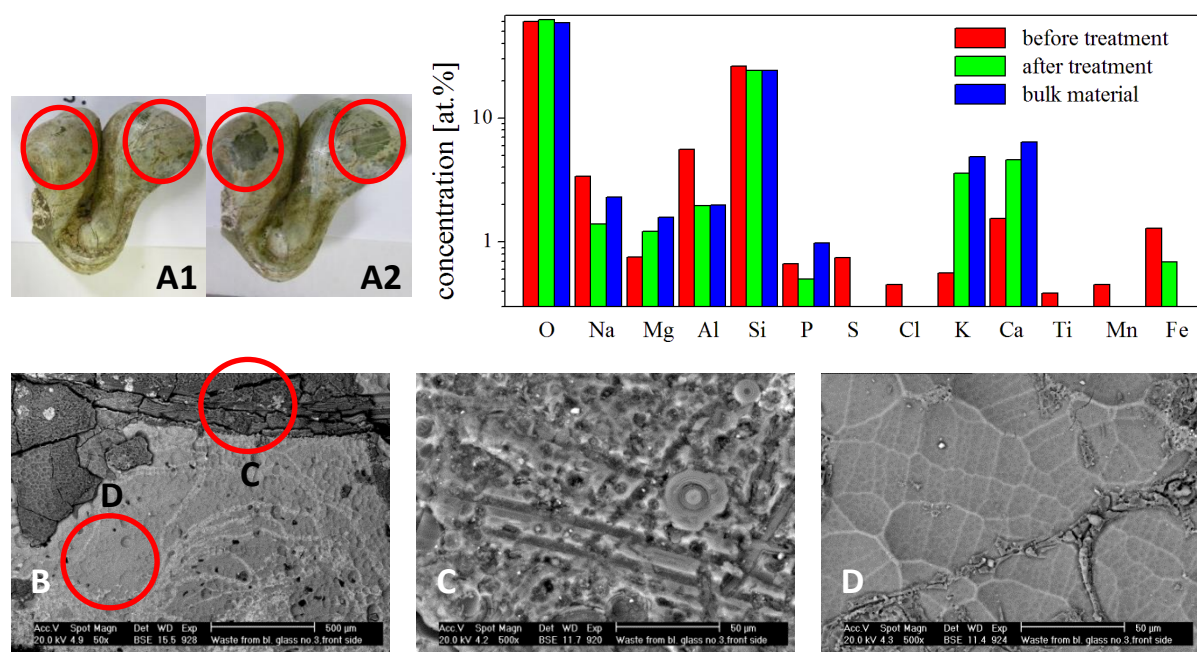
Fig. 2: A/ Waste from blowing glass III: before (A1) and after (A2) the plasma treatment. Graph shows EDS analysis results. B/ SEM image at the boundary of non-treated and treated surface. C/ SEM image of surface before the plasma treatment. D/ SEM image of surface after the plasma treatment.

The other elements are at the trace amount, only, and their detected concentrations are close to the detection limit, so it is impossible to discuss any clear changes in their concentrations due to the plasma treatment. As partial conclusion, the elementary composition studies showed that elements originating from corrosion product layers at object surfaces were successfully removed. The current EDS analyses did not allow distinguishing the potential surface layers (a few nm) changes due to implantation of sodium or other elements in ionic state originated from the water solution.

The scanning electron microscopy was used for the surface microstructure visualization. The original excavated object surface structure is non-smooth with high density of cracks and contains some soil grains (see Fig. 2C). The sample surface after the plasma treatment is generally smooth with no soil grains and a few of crack lines (see Fig. 2D) and the microcrystalline character is well visible. The microcrystallization of ancient glass is well known for many years [8].

4   Conclusion

The presented work showed the application of the plasma multi-electrode system generated directly in water solutions as a new soft tool for very soft and also fast local surface cleaning of ancient glass objects. The corrosion layers were successfully removed from ancient original glass object surface at treatment speed of about 0.3 cm^2/minute at applied power of 5 W in physiologic water solution (0.9% NaCl water solution). The SEM images showed discovering of the smooth surface structures after the plasma treatment with visible microcrystalline structures. The elementary composition of the plasma treated surface was close to the bulk material composition, so the corrosion layers were removed successfully. No treated object was damaged during the plasma treatment, so we can conclude that this technique should be applied in the practice but further experiments will be needed mainly with respect to the treatment condition optimization.

Acknowledgement

References

1. V. D. Daniels et al., Studies in Conserv. 24, 85 (1979)
2. S. Veprek et al., Plasma Chem. Plasma Proces. 5, 201 (1985)
3. L. Radkova et al., Romanian Rep. Phys. 67, 586 (2015)
4. P. Fojtikova et al., Open Chem. 13, 362 (2015)
5. P. H. Ceccato et al., J. Phys. D: Appl. Phys. 47, 175202 (2010)
6. A. Tournie et al., Solid State Ionics 179, 2142 (2008)
7. M. Klima, P. Slavicek, Plasma pencil - high-universal plasma source for local treatment. Brno, Czech Republic: Masaryk University, 2006. CTT, Plasma Pencil
8. J. G. Morley, Br. J. Appl. Phys. 12, 10 (1961)

IDENTIFICATION OF THE REACTIVE SPECIES PRODUCED BY TRANSIENT SPARK DISCHARGE IN GAS AND LIQUID PHASE AND ITS EFFECT ON *ESCHERICHIA COLI*

K. Kučerová, M. Janda, K. Hensel

Faculty of Mathematics, Physics and Informatics, Comenius University, Bratislava, Slovakia

E-mail: katarina.kucerova@fmph.uniba.sk

We used the self pulsing transient spark discharge driven by DC power supply at atmospheric pressure above the circulating water solution in various gas mixtures of nitrogen and oxygen. For better understanding the plasma induced chemical and biological changes in solutions we analyze both the gas and the liquid phase. We detected NO, NO_2, O_3 molecules in the gas phase by FTIR, while in the liquid phase we measured H_2O_2, NO_2^- and $^\cdot OH$ radical concentrations by UV-VIS and fluorescence spectroscopy. The results from gas and water analysis were put in a correlation with the bactericidal effect of TS on *E. coli* in water solution.

Keywords: transient spark discharge; reactive oxygen and nitrogen species; bacteria

1 Introduction

The electrical discharges generated in gasses at atmospheric pressure are the source of low temperature plasma. Their properties predetermine them for many industrial, environmental and even biomedical applications. Low temperature plasma generated in air like mixtures in contact with water induces numerous reactive species in the gas phase, which could subsequently diffuse into liquid phase and induce further chemical reactions. These chemical changes in the liquid also affect the biological matter inside the treated liquid. There is number of publications dedicated to research of chemical changes in plasma treated solutions also studying the effects of the plasma on bacteria, eukaryotic cells and tissues [1-5]. Although a great research effort has been dedicated to elucidate the role of the plasma interaction with biological matters, the exact mechanisms of their interaction are still not enough clear. Therefore, we investigate the transient spark (TS) discharge generated in various gas mixtures of nitrogen and oxygen in contact with water solutions. We separately explore the products generated in the gas phase and in the liquid phase and relate these results with bactericidal effects on *E. coli*.

2 Experimental

In Figure 1 is schematically depicted the principle of water electrode system (side view). The transient spark (TS) discharge was generated in point to plane geometry (inter-electrode distance 1 cm) driven by DC high voltage of positive polarity [6]. Downstream, the grounded electrode, through the discharge zone a liquid was repetitively circulated (flow rate 14 mL/min). The discharge system was enclosed in a small chamber (volume 12.5 mL) to allow variation of O_2/N_2 gas mixtures (flow rate 2 L/min). As a liquid, we used 2 mM phosphate buffer (**PB**, 550 µS/cm, pH 7) and its non-buffered counterpart the solution of monosodium dihydrogen phosphate $NaH_2PO_4.2H_2O$ (**W,** "water", 600 µS/cm, pH 5) to study the pH dependent changes. In these solutions were Gram-positive bacteria *Escherichia coli*

were dissolved with initial concentration $\sim 10^7$ CFU/mL. The bacterial inactivation was evaluated by standard colony counting method. The chemical species produced in the gas phase by the TS discharge were measured by FTIR absorption spectroscopy (*IRAffinity-1S, Shimadzu*). In the liquid phase we measured the concentration of hydroxyl radical (˙OH) by fluorescence spectroscopy using terephthalic acid as a probe. For the analysis of the other reactive species in water solution we used UV-VIS absorption spectroscopy (*UV 1800, Shimadzu*). The H_2O_2 concentration in the liquid was evaluated by titanyl ions from titanium oxysulfate (TiOSO$_4$) forming yellow-colored complex. The NO_2^- and NO_3^- were measured by commercial kit (*Cayman*) based on reaction with Griess reagents.
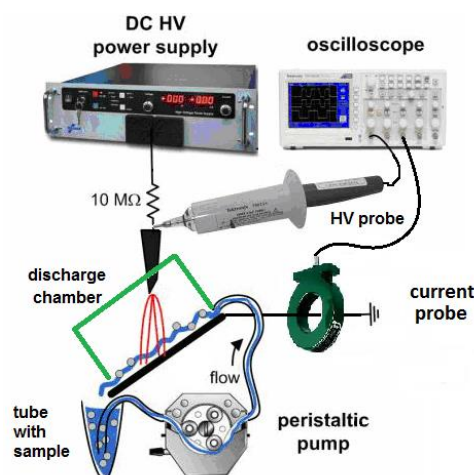
Fig. 1. Scheme of the experimental setup.

3   Results and Discussion

We present the results of self-pulsing TS discharge effect on buffered (PB) and non-buffered (W) water solutions containing bacteria. The TS discharge was generated in various O_2/N_2 gas mixtures. The typical amplitude of the applied voltage was $U_{max} = 10 - 13$ kV, amplitude and frequency of the discharge current pulses were $I_{max} = 5 - 18$ A and f = 1.5 − 4 kHz, respectively. The character of the TS discharge was slightly different and depended on the ratio of O_2/N_2 gas mixtures; however the total mean power was nearly the same ~5-7 W.

The reactive molecules in the gas phase and the subsequent effect on reactive chemical species produces in water and effect on bacteria were observed. We detected NO and NO_2 molecules in gas mixtures containing both O_2 and N_2 molecules by FTIR measurements. The NO and NO_2 concentrations were increasing with O_2 ratio up to 50%, where the concentration of NO and NO_2 achieved maximum, 264 ppm and 60 ppm respectively. In pure O_2 we detected only O_3 molecules (~ 110 ppm).

The concentrations of H_2O_2, NO_2^- and ˙OH radical in solutions depended on O_2/N_2 ratio in gas mixture. In the case of mixtures containing both O_2 and N_2, the most significant pH decrease and the relatively high concentration of reactive species (0.4-0.5 mM) was observed compared to pure N_2 and O_2. When the discharge was generated in pure O_2, the NO_2^- concentration was negligible, but the concentration of H_2O_2 was relatively high due to higher formation of ˙OH radicals in the gas phase that subsequently forms and accumulates H_2O_2 in water solution and also due to lack of NO_2^- that could potentially react with it. In pure N_2 the discharge produced only a small amount of NO_2^- because of lack of O_2, therefore only a small decrease of pH was observed.

The gas composition above the treated water solution affected the production of reactive species in liquid solutions and subsequently also inactivation of bacteria. Even the differences among respective gas mixture were not significant, the bacterial inactivation rate expressed as a logarithmic reduction was highest in air like mixture ~ 2.5 log reduction. In gas mixtures where O_2 and N_2 are present in relatively equal rate, also H_2O_2 and NO_2^- are present equally in solution. Synergetic effect of H_2O_2 and NO_2^- in acidic conditions can lead to formation of peroxinitrites ($ONOO^-$) and is responsible for overall strong bactericidal effect [5]. The difference between the effect in buffered (PB) and non-buffered (W) solution can be seen in the Fig. 2. which shows that bacterial inactivation is more efficient in W solution, where pH decrease and conductivity increase were more pronounced than in PB.
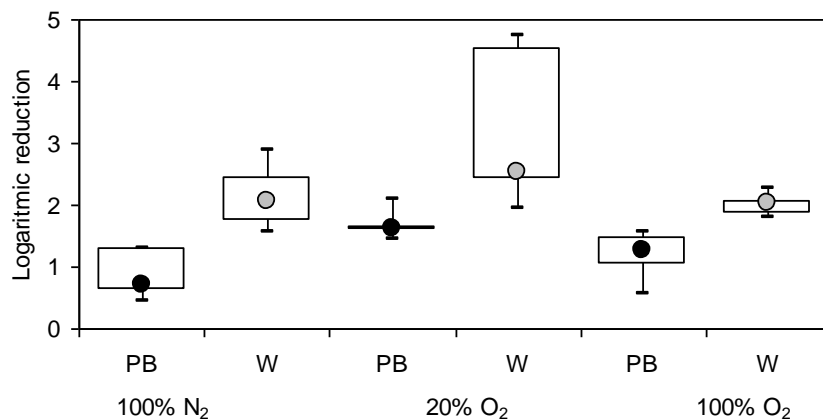
Fig. 2. The logarithmic reduction of *E. coli* in phosphate buffer (PB) and "water" (W) 5 min treated by TS discharge generated in various gas mixtures (100% N_2, 20% O_2, 100% O_2), data shown as maximum, upper quartile, median, lower quartile, minimum, from 5 independent measurement.

4   Conclusion

The low temperature plasma generated by the TS discharge at atmospheric pressure were generated in various O_2/N_2 gas mixtures in contact with water solutions in order to explore the relationship between reactive species generated in the gas and liquid phase and subsequent effect on bacteria *E. coli*. FTIR spectroscopy dominantly showed NO and NO_2 molecules in most of the gas mixtures, while O_3 was observed only in pure O_2. In the liquid phase H_2O_2, NO_2^- and $^\bullet OH$ reactive species were detected. The *E. coli* inactivation was more pronounced in mixtures in non-buffered solution. In conclusion, for the efficient *E. coli* inactivation both H_2O_2 and NO_2^- need to be present in the treated water solution.

References
1. A. Fridman et al., Plasma Medicine, 1st edn. (Wiley, UK, 2013)
2. Y. Gorbanev et al., Chem. Eur. J. 22, 11 (2016)
3. H. Wu et al., Plasma Process. Polym. 9, 417-242 (2012)
4. K. Hensel et al., Biointerphases 10, 029515 (2015)
5. Z. Machala et al., Plasma Process. Polym. 10, 649-659 (2013)
6. M. Janda, et al., Plasma Sources Sci. Technol. 21, 045006 (2012)

NEGATIVE CORONA DISCHARGE IN A TWO-PHASE FLUID

J. Mizeraczyk[1], A. Berendt[2], J. Podliński[2], M. Domaszka[1]

[1] *Department of Marine Electronics, Gdynia Maritime University, Morska 81-87, 81-225 Gdynia, Poland*

[2] *Centre for Plasma and Laser Engineering, The Szewalski Institute of Fluid Flow Machinery,*
Polish Academy of Sciences, Fiszera 14, 80-231 Gdansk, Poland

E-mail: jmiz@imp.gda.pl

The process of temporal and spatial development of negative corona discharge and corresponding electrohydrodynamic (EHD) flow of dust particles (cigarette smoke) suspended in still air in a needle-to-plate negative DC corona discharge arrangement just after the corona inception, i.e. in the very beginning of the unsteady state of the EHD two-phase (air- dust particles) flow induced by the negative corona is presented. The experiment showed that just after the corona inception in the air-dust particles the negative corona has the form of irregular pulse trains, each consisting of several Trichel pulses. They induce mushroom-like dust particle minijets travelling along the interelectrode gap.

Keywords: dc corona discharge; EHD flow; time-resolved imaging

1 Introduction

Electrohydrodynamics (EHDs) is devoted to the investigation of motion of electrically charged fluids (gaseous or liquid) subjected to an electric field, usually external. In a single-phase fluid, for example such as air, the forces exerted by the external electric field on free or polarization charges present in the fluid are transferred during collisions to the neutral molecules, changing their previous motion (which is called a primary flow). As a result a secondary molecular flow appears. The secondary flow causes a redistribution of the electrical charges (electrons and ions) in the fluid, which in turn modifies the electric field in the fluid. Such a coupling of the electric field, the space charge formed by the electrical charges [1-5] and the fluid flow causes that the EHD phenomena in the single-phase fluid are complicated [6-8]. An example of the single-phase fluid with complicated EHDs is a single- or multicomponent gas in which a corona discharge has been induced. The EHD phenomena become even more complicated when the fluid consists of two or more matter phases (the so-called multi-phase fluid). An example of the two-phase fluid is the flow of flue gas in electrostatic precipitators (ESPs), which can be regarded as a mixture of an after-combustion gas (a carrier fluid) and dust (a particulate matter) suspended in it. In this case, in the presence of corona discharge the particulate matter become charged by the gaseous ions and get subjected to the electrical field. Due to it the charged particles form its own secondary flow, usually different from that of the molecular secondary flow. As a result the EHD interactions include the electric field, the molecular space charge, the dust particle space charge, and the flows of the carrier-fluid (the gas) and suspended dust particles. This makes the EHDs of such a two-phase fluid very complex.

Most aspects of EHD phenomenon in gaseous two-phase fluids (carrier gas and minority of particulate matter) may be illustrated using an example of ESPs [9-11] where the EHD forces play a major role in collecting the dust particles. The majority of EHD effects present in ESPs [12-21] are typical of other gaseous EHD systems.

The ESPs have received the intensive study in their hundred-year history [9-11]. Nowadays they operate with high overall dust particle collection efficiency (99.5 %), however, they are not effective in removing the fine particles (below 1 um). The present industrial ways of increasing the fine particle collection are limited. This is mainly attributed to poor understanding of the performance of ESPs, operation of which depends on EHD phenomena.

Large precipitators are usually designed with negative high-voltage polarized discharge electrodes because this allows a higher voltage to be applied (without an arc). However, small precipitators, such as those designed for the removal of cigarette smoke in rooms, may have positive high-voltage electrodes, to minimise the production of ozone. Apart from forming a high electric field the negative or positive high-voltages applied to the discharge electrodes induce the so-called negative or positive corona, respectively, in the ESP chamber through which the post-combustion gas carries the dust particles suspended in it. The ions produced by the corona serve to charge the dust particles while the electric field pushes the charged dust particles towards the grounded electrodes, where they are collected. This short description of the operation principle of ESPs shows how the characteristics and parameters of the corona discharges are important for the performance of ESPs. The corona discharges energized by the positive high-voltage are called negative coronas while the positive coronas are those energized by the positive high-voltage.

There are many varieties of electrical coronas. This paper is limited to the negative coronas in two-phase fluid resembling the combustion gas-particle matter fluid typical of the ESPs. Fortunately, due to the usually low concentration of the dust particles the ESP flue gases one may expect (at least as a first-order assumption) that in principal the mechanisms of forming the corona discharge should be similar in "pure" air (i.e. in a single-phase fluid) and in air with suspended dust particles (a two-phase fluid) of low concentration. Therefore, the knowledge acquired on the corona discharges in the single-phase fluids is an essential background for the investigations of corona discharges in the gaseous two-phase fluid with low concentration of the particulate matter component.

The negative corona discharges similar to that induced in ESPs have been subjected to intensive experimental and theoretical studies for more than 80 years. The vast majority of this work concerned the negative coronas in the single-phase fluids, mainly in air. It is known that the discharge in air at corona threshold (i.e. in the unsteady conditions) consists of usually irregular pulses in the kHz range, with a mean current on the order of a microampere. A small increase in voltage results in the establishment of regular current pulses the frequency range of which may extend to the megahertz range. The early (1938-1962) basic studies of the regular current pulses (later named the Trichel pulses) of negative corona in air, were carried out by Trichel [22], Loeb's group and others (Loeb's and other studies have been

comprehensively described in [23]). The main results of these early studies were analytically summarized and experimentally verified by Lama and Gallo [24]. The basic data and results of negative corona studies till 1980s were also collected in [25, 26]. Afterwards hundreds on new contributions to the negative coronas have been published.

The behaviours of negative coronas and relevant EHD flows were studied by many researchers mainly in terms of practical aspects relevant to the performance of precipitators (breakdown voltage, ozone production, collection efficiency). However, the investigations of the fundamentals of the both phenomena in a two-phase fluid similar to that of the ESP flue gas are scarce. The ESP performance undoubtedly depends on the understanding of physics of the corona discharge which energizing the ESP two-phase fluid and is responsible for the EHD effects. (e.g. influence of the EHD flow turbulences on the dust particle collection efficiency in the ESP is still unclear).

In this paper we present the temporal and spatial development of negative corona discharge and corresponding electrohydrodynamic flow of dust particles (cigarette smoke) suspended in still air in a needle-to-plate negative DC corona discharge arrangement just after the corona inception, i.e. in the very beginning of the unsteady state of the EHD two-phase (air - particle dust) flow induced by the negative corona.

2 Experiment and results

The experimental apparatus for our study of the negative corona inception and EHD flow onset consisted of a discharge chamber (an acrylic box with a needle-to-plate electrode arrangement inside), high voltage power supply and time-resolved EHD imaging system based on 2D Time-Resolved Particle Image Velocimetry equipment. Before applying the voltage, the particle-seeded air in the discharge chamber was still. Before each measurement, the discharge chamber was filled with new air with homogeneously distributed dust particles (cigarette-smoke) in it. The initial concentration of the homogeneously-distributed dust particles was about 450,000 particles/cm^3 $\pm$ 50,000 particles/cm^3. The needle electrode was made of a stainless-steel rod (1 mm in diameter), the end of which had a tapered profile with the tip having a radius of curvature of 75 μm. The interelectrode gap was 25 mm. The negative high-voltage was applied to the needle electrode through a 3.3 MΩ resistor. The plate electrode, also made of stainless-steel, was grounded. For the precise setting a desired DC high voltage on the discharge electrode a rectangular negative high voltage pulse rising linearly to a certain value and then remaining constant was applied. The negative high voltage pulse reached its ultimate amplitude of - 6.5 kV with a rise rate of 6.5 V/ms.

We found that the first Trichel pulse appeared when the rising voltage pulse has reached a value of about - 4.23 kV. The first Trichel pulse was followed by several subsequent Trichel pulses, which formed a pulse train of a time duration of 5.5 ms (Fig. 1). Then the Trichel pulses disappeared for a period of about 60 ms. At a time of about 66 ms, a new Trichel pulse train formed, and disappeared similarly as the first Trichel pulse train. The third Trichel pulse train formed after a period of about 50 ms, and disappeared shortly after. The process of forming and the disappearance of Trichel pulse trains recurred, as shown in Fig. 1. As seen,

generally every Trichel pulse train contained different numbers of Trichel pulses (from several to a few dozens) and lasted several milliseconds. The Trichel pulse trains occurred in irregular intervals with a tendency of shortening these intervals with the rising voltage on the needle electrode. The duration of Trichel pulse trains and the numbers of Trichel pulses in them seem to be a result of stochastic processes occurring in the very early development stage of the EHD flow in the two-phase fluid.

Fig. 1 shows images of the EHD particle flow. Each image is a recording (by the time-resolved EHD imaging system) of the instantaneous map of the laser green light scattered by the dust particles in the observation plane. High light intensity recorded in a given area of the image corresponds to a high dust concentration in this area. Dark spots or areas in the image
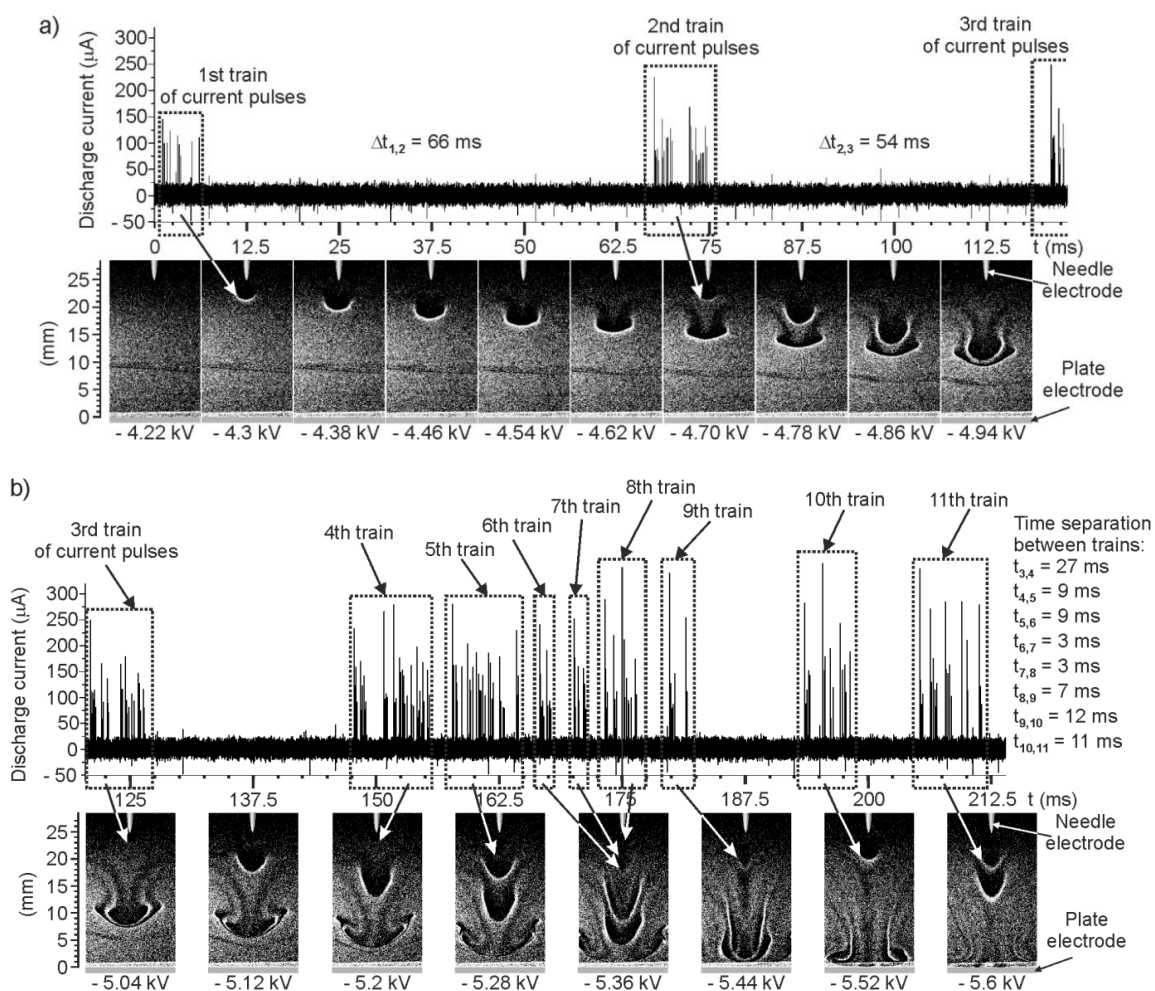
Fig. 1: Trichel pulses trains and EHD minijets. The black-and-white arrows connect the Trichel pulse trains and the corresponding minijets. Time of 1 ms before onset of the first Trichel pulse is assumed as a reference time t = 0 [27].

mean that there is no or little dust particles there. The image captured at a time of t = 0 (Fig. 1a), i.e. just before the first Trichel pulse train indicates that the dust particles are uniformly distributed between the needle and the plate electrodes. As mentioned above, at a time of t = 1 ms the first Trichel pulse train began and lasted for 5.5 ms. In the image captured at a time of t = 2.5 ms (at a voltage of - 4.23 kV) we noticed a slight movement of the dust particles in the close vicinity of the needle electrode (the blurred image is not

presented in this paper). It meant that the EHD particle flow had just started. At a time of t = 12.5 ms, the dust particles pushed from the vicinity of the needle electrode have already formed a very bright surface on the dark (i.e. dust particle-free) mushroom-like moving object which is pushed from the needle electrode towards the collecting electrode. The pushed-down particles are seen as a bright layer on the surface of the dark mushroom cap. The image captured at a time of t = 75 ms (Fig. 1a), corresponding to the time interval in which the second Trichel pulse train has occurred, shows that a second mushroom cap structure has been generated at the needle tip. Both structures, the first and second one are moving downwards as mushroom cap-like minijets. It is worth noting the bright layer between both these mushroom minijets, formed by the pushed-down seeding particles. Both mushroom minijets are growing when moving downwards. This and the subsequent images of Trichel pulse trains and minijets, shown in Fig. 1b, suggest that there exists a correlation between the Trichel pulse trains and the generation of mushroom-like minijets. Fig. 1b shows the generation of 9 consecutive Trichel pulse trains which have induced 9 subsequent mushroom-like minijets.

Summarizing, the experimental results showed that the very early stage of the negative corona discharge in particle-seeded air in the needle-plate electrode arrangement has the form of Trichel pulse trains, consisting of Trichel pulses (which number was from several to a few dozens). Every Trichel pulse train induces a mushroom-like minijet, which travels towards the plate electrode. Several minijets can be simultaneously present in the gap. Although a Trichel pulse train (consisting of several Trichel pulses) was needed for inducing a minijet, as shown in Fig. 1, an additional experiment showed that also a single Trichel pulse is capable of inducing a minijet.

3   Conclusions

In this paper we presented the experimental results concerned the evolution of the negative corona discharge and the induced EHD flow of dust particles suspended in still air in the needle-to-plate negative DC corona discharge arrangement just after the corona inception, i.e. in the very early stage of development of the EHD particle flow. The experiment presented in this paper is one of the first temporal and spatial resolved researches on the behaviour of the negative corona and EHD phenomena in a two-phase fluid. Our experiment showed that in the very early stage of the negative corona discharge in particle-seeded air has the form of Trichel pulse trains, which induce a mushroom-like minijet, which travels towards the plate electrode. Several minijets can be simultaneously present in the gap. The series of mushroom-like objects moving along the interelectrode gap looked like a series of mushroom-like minijets shot from the needle electrode vicinity toward the collecting electrode. The simultaneous presence of mushroom-like minijets in the interelectrode gap in the corona discharge in the particle-seeded air resembles the negative-ion-charged clouds (induced by the Trichel pulses) traversing simultaneously the interelectrode gap of the corona discharge in air (as predicted a long time ago by Loeb [23] and Lama and Gallo [24], and recently by Dordizadeh et al. [28]).

Next experiments aiming at explanation of the mechanism responsible for the observed phenomena in the presented experiment are needed.

Acknowledgment

References

1. R. Leny et al., in *Proceedings of the 4th Int. Conf. Gas Discharges*, Swansea, 1976, p. 246

2. R. S. Sigmond, Electrical breakdown of gases, edited by J.K Meek, J.D. Craggs, (J. Wiley & Sons, 1978)

3. A. Yabe et al., J. AIAA 16, 340-345 (1978)

4. G. C Crichton et al., in *Proceedings of the 14th Int. Conf. Phenomena in Ionized Gases*, Grenoble, 1979, p. C7-287

5. J. S. Chang, J. Aerosol Sci. 12, 19-26 (1981)

6. J. S. Chang et al., IEEE Trans. Plasma Sci. 19, 1152-1166 (1991)

7. J. S. Chang et al., IEEE Trans. Diel. Electr. Insul. 1, 871 895 (1994)

8. R. J. Peterson et al., in *Proceedings of the IEEE Ind. App. Soc. Ann. Meeting*, Denver, 1994, p. 1513-1518

9. H. J White, Industrial electrostatic precipitation (Addison-Wesley, 1963)

10. A. Mizuno, IEEE Trans. Diel. Electr. Insul. 7, 615 624 (2000)

11. A. Jaworek et al., J. Electrostatics 65, 133-155 (2007)

12. G. L. Leonard et al., J. Fluid Mech. 127, 123 140 (1983)

13. P. Atten et al., IEEE Trans. Ind. Appl. 23, 705-711 (1987)

14. C. L. Chang et al., J. Aerosol Sci. 30, 325-340 (1999)

15. B. Hoferer et al., Conf. Electrical Insul. Diel. Phenomena, 93-96, 2000

16. N. T. Parasram et al., in *Proceedings of the 8th Int. Conf. Electrostatic Precipitation*, Birmingham, 2001, p. A1-2

17. D. Blanchard et al., in *Proceedings of the 8th Int. Conf. Electrostatic Precipitation*, Birmingham, 2001, p. A1-4

18. T. Yamamoto et al., Conf. Electrical Insul. Diel. Phenomena 228-231 (2002)

19. H. Fujishima et al., J. Electrostatics 62, 291-308 (2004)

20. H. Fujishima et al., IEEE Trans. Diel. Electr. Insul. 13, 160-167 (2006)

21. K. Adamiak et al., IEEE Trans. Dielectr. Electr. Insul. 16, 608-614 (2009)

22. G. W. Trichel, Phys. Review 54, 1078-1084 (1938)

23. L. B. Loeb, Electrical coronas, their basic physical mechanisms (University of California Press, 1965)

24. W. L. Lama et al., J. Appl. Phys. 45, 103-113 (1974)

25. R. S. Sigmond et al., in Electrical Breakdown and Discharges in Gases Part B, edited by E. Kunhardt (Springer, US, 1981)

26. R. S. Sigmond, in Electrical Breakdown of Gases, edited by J.M. Meek and J. D. Craggs (Wiley, New York, 1978)

27. J. Mizeraczyk et al., J. Phys. D: Appl. Phys. 49, 205203 (2016)

28. P. Dordizadeh et al., J. Phys. D: Appl. Phys. 48, p. 415203 (2015)

EVOLUTION OF POINT-TO-PLANE NANOSECOND DISCHARGE IN DEIONIZED WATER

M. Šimek[1], B. Pongrác[1], M. Člupek[1], V. Babický[1], P.Lukeš[1]
Institute of Plasma Physics of the CAS, Department of Pulse Plasma Systems,
Za Slovankou 1782/3, Prague 8, Czech Republic

E-mail: simek@ipp.cas.cz

We employed techniques of time-resolved ICCD microscopy and spectroscopy to register basic morphologic and emission fingerprints of micro-discharges produced in deionized water. Fast rise-time high-voltage pulses (duration of 5 ns and amplitude of ~110 kV) applied in a point-to-plane electrode geometry produced micro-discharges either periodically or in a single-shot regime. Time resolved ICCD images evidence typical streamer-like branched filamentary morphology while emission spectra show a broad-band continuum evolving during the first few nanoseconds followed by the well-known H^I/O^I atomic lines (tens of ns).

Keywords: nanosecond discharge; water; ICCD imaging

1 Introduction

Fundamentals of electrical discharges generated in aqueous liquid solutions are much less understood compared with gaseous discharges [1-6]. Discharges inside liquids can be initiated through bubbles (gas breakdown) that can be formed due to the local heating of the liquid. The bubble breakdown in water typically occurs in the discharge systems driven by slow high-voltage (HV) waveforms (such as AC or pulsed waveforms of microsecond duration) [1-3, 5]. However, in the case of discharges driven by short HV waveforms of nanosecond duration applied at low repetition rate it is frequently assumed that the discharge develops due to the presence of voids or that direct ionization of water without phase change (no bubbles) takes place [4, 6]. In this work, we have explored emission characteristics of the discharge produced in deionized liquid water by applying fast-rising positive HV pulses of nanosecond duration in point-to-plane electrode geometry. We employed techniques of time-resolved ICCD microscopy and spectroscopy to register basic morphological and emission fingerprints with high spatial (few micrometers) as well as temporal (from 0.2 to 2 ns) resolutions. The ICCD based diagnostics were complemented by detecting evolution of emission waveforms through the fast photomultiplier (PMT) to determine average propagation velocity of luminous discharge filaments.

2 Experimental

The discharge reactor consists of a needle-plane electrode system with an inter-electrode gap distance of 5 mm, completely immersed in deionized water (conductivity of ~2 μS/cm). The HV needle anode and grounded plane cathode were made from mechanically sharpened tungsten and from stainless steel, respectively. The whole electrode system is then enclosed in a cylindrical glass vessel equipped with side arms fitted with quartz windows to enable access for optical diagnostics [5]. The HV pulse power generator (FID) was used to produce short HV pulses of ~110 kV in amplitude and of 5 ns in duration (FWHM), either with the

repetition rate of 1 Hz or in a single-shot regime. The single-shot regime was used to make sure that no bubbles created during the collapse of previous discharge cycle could remain in the vicinity of the pin electrode thus forcing/enabling the gaseous bubble breakdown mechanism.

A fast DH740i-18U-03 iStar ICCD camera (Andor) was utilized to register either images (2048x512, effective pixel size 13.5x13.5 μm, minimum intensifier gate width 2 ns) or spectrally-resolved plasma induced emissions (PIE) of individual micro-discharges synchronously with the HV pulses. The frontal window of the discharge reactor was used to register time-resolved magnified ICCD images of individual micro-discharges through a Questar QM-1 long-distance microscope. The calibration of the images was made using a glass slide with an engraved micrometer reticle scale. The spatial resolution of the QM-1+ICCD setup was limited by the given microscope's magnification and by the size of the ICCD pixel.

In this work, all presented images were taken at a fixed spatial resolution of 3.25 μm/pixel. To register time and spectrally-resolved PIE, the micro-discharge emission was collected by the quartz optical fiber bundle through the pair of lenses and a band pass filter. Optical axis of the PIE collection system was perpendicular to the propagation trajectory of the discharge with the field of view selecting small area close to the tip of the needle [5]. The output of the fiber bundle was coupled to the iHR-320 (Jobin-Yvon) imaging spectrometer (spectral dispersion 2.31 nm/mm @ 500 nm for 1200G/mm grating) and registered by the ICCD. The ICCDs' intensifier was triggered by the photomultiplier (PMT) pulse generated by the integral emission of the discharge itself. Alternatively, UV-vis emission waveforms were registered through the set of selected band-pass filters by the fast PMT (Hamamatsu H10721).

3   Results and Discussion

Typical time-resolved ICCD images of a single discharge event occurring in de-ionized water acquired using the single-shot regime of the discharge are shown in figure 1. The sequence of single-shot images (a) − (d) was captured with the shortest possible gate of the ICCD intensifier (2 ns). The intensifier's gate was appropriately delayed with respect to the onset of the HV pulse. The image (a) captures inception of three isolated micro-discharge filaments evolving on the needle surface (the dotted white line indicates the position and shape of the HV needle anode). The next image (b) shows the discharge phase of about 0.8 nanoseconds later, when the length of luminous filaments reaches about 0.2 mm and the onset of primary filament branching becomes clearly visible. Further discharge evolution (about 2 ns after the onset) leads to the extension of the tree-like structure with the luminous length reaching about 0.4 mm and characterized by evident branching of secondary filaments. The maximum length of luminous branches (0.6-0.9 mm) is reached approximately 3 ns after the onset (coinciding more or less with the peak of the HV pulse) followed by the collapse of the length of the discharge filaments towards the needle anode.

Thanks to the calibration of the images it is possible to estimate characteristic diameter of primary and terminal filaments to be about 50 and 20 μm, respectively. Furthermore, by

comparing the geometrical length of luminous filaments captured in figure 1, it is also possible to make a very rough estimation of an average propagation velocity of the luminous part of the discharge (2-3 $\times$ 10^5 m/s). Such a high propagation velocity (together with registered progressive narrowing and branching of few initial filaments) supports the idea of the discharge evolution controlled by a streamer-based mechanism. Spectral analysis of the discharge luminosity is of crucial importance for further understanding of the obtained images. Consequently, the time–resolved emission spectra were acquired in the 300-800 nm spectral range during the discharge evolution starting from its onset [7]. The growing phase of the discharge (as captured in figure 1) is characterized by broadband emission which peaks in UV between 350-400 nm. After ~20 ns, when the broadband emission disappears, some low-intensity atomic line emission (H^I/O^I), which is typical for water discharges initiated through the bubble breakdown mechanism, occurs [1, 5].
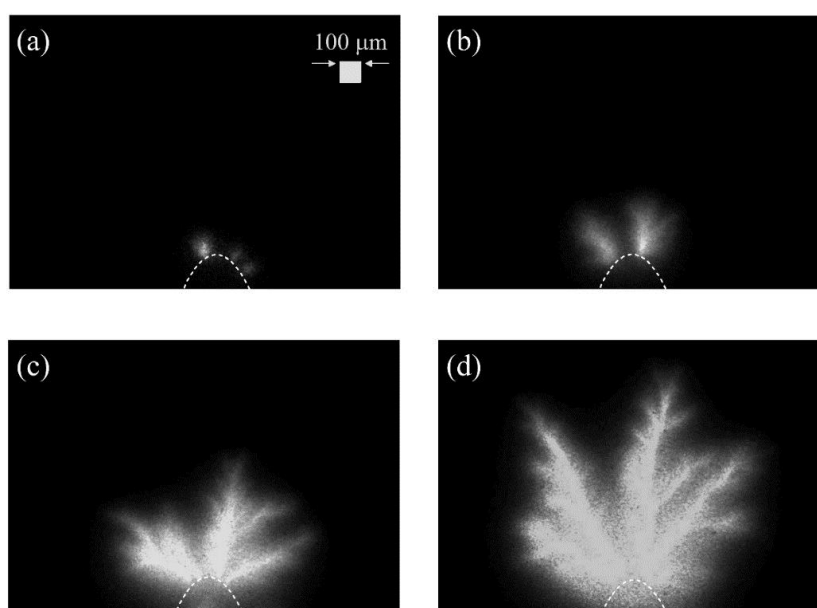
Fig. 1: Time-resolved ICCD images of a single discharge event occurring in deionized water. The sequence of single-shot images (a) – (d) was captured with the shortest gate of the ICCD intensifier (2 ns). The intensifier's gate was appropriately fixed with respect to the onset of the HV pulse. The dotted white line indicates the position and shape of the HV needle electrode.

References
1. P. Šunka et al., Plasma Sources Sci. Technol. 8, 258 (1999)
2. F. De Baerdemaeker et al., Plasma Sources Sci. Technol. 16, 341 (2007)
3. B. R. Locke et al., Ind. Eng. Chem. Res. 45, 882 (2006)
4. A. Starikovskiy et al., Plasma Sources Sci. Technol. 20, 024003 (2011)
5. M. Šimek et al., Plasma Sources Sci. Technol. 21, 055031 (2012)
6. D. Dobrynin et al., J. Phys. D: Appl. Phys. 46, 105201 (2013)
7. B. Pongrác et al., in *Book of Contributed Papers of the 15th Int. Symposium on High Pressure Low Temperature Plasma Chemistry*, Brno, 2016

ATMOSPHERIC PRESSURE PLASMA IN CONTACT WITH LIQUID AND ITS APPLICATION FOR NANOPARTICLES FABRICATION

V. Burakov, M. Nedelko, V. Kiris, N. Tarasenka, A. Nevar, N. Tarasenko

B.I. Stepanov Institute of Physics of National Academy of Sciences of Belarus,
2Nezalezhnasti Ave. 68, 220072 Minsk, Belarus

E-mail: n.tarasenko@ifanbel.bas-net.by

The capabilities of the atmospheric pressure gas-liquid interfacial discharge plasma for synthesis of metallic, oxide and composite nanoparticles are discussed. The main characteristics of the discharge plasma were studied by varying the discharge current, gas flow rate and solution composition. The morphology and composition of the generated particles were found to be dependent on both plasma parameters and plasma induced processes in solution.

Keywords: electrical discharge in contact with liquid; ZnO nanostructures; optical properties

1 Introduction

Among the different discharge systems for generation of non-thermal, atmospheric-pressure plasmas a more recent direction is connected with plasmas produced inside or in contact with liquid. When discharge is formed at the liquid surface the energetic species from the microplasma are capable to initiate electrochemical reactions such as anodic dissolution of solid electrodes or electroreduction of dispersed metal salts and subsequent particles nucleation or modification of their surfaces. Atmospheric pressure plasma in contact with liquid has therefore initiated a new synthetic approach that is different from both standard liquid electrochemistry as well as from the submerged discharge method.

Recently, several groups used microplasmas generated between a hollow capillary cathode and liquid anode for nanoparticles (NPs) synthesis [1-4]. Despite the significant growth of interest to this type of discharge, the obtained results are not enough to explain all the variety of physical and chemical phenomena accompanying the discharge. It should be noted that parameters of NPs synthesized by this method depend on the plasma parameters such as electron density, electron and gas temperature that in turn, are largely dependent on the discharge current and gas flow rate. Therefore there is a necessity for further studies of processes involved in the formation of NPs by the electrical discharge in contact with liquid aiming to optimize the conditions for NPs formation with the desired characteristics.

In this paper atmospheric pressure plasma of the gas-liquid interfacial discharge was used for synthesis of metallic, oxide and composite NPs. The formation of metal (Au, Ag or Zn) NPs with a possibility of changing their properties and average size by varying the solution composition and discharge parameters as well as a formation of composite Zn@ZnO and ZnO/Ag structures by using sequential discharges with Zn and Ag electrodes was demonstrated. Zinc oxide (ZnO) nanostructures have received a great interest in recent years due to potential applications in transparent electrodes, solar cells, blue/UV light emitting diodes, gas sensors, etc. [5]. Based on the spectroscopic measurements, the plasma composition, electron density and temperature was evaluated depending on the discharge parameters. It was found that the main features of the glow discharge with the liquid electrode are connected with plasma-liquid interface interactions.

2   Experimental

A schematic diagram of the experimental set-up is shown in Fig. 1. In our experiments one electrode (metallic, or graphite) acting as anode was placed inside liquid (distilled water, HAuCl₄ solution, colloidal solutions of NPs). In some experiments the aqueous solution consisting of 1 mM HNO₃ with 10 mM glucose (fructose) or without these stabilizers were used as working liquids. The acid was used to increase the solution conductivity; glucose and fructose are stabilizers that prevent uncontrolled particle growth and agglomeration. The discharge was ignited between a stainless-steel capillary (or rod) electrode served as cathode and the surface of liquid. The stainless steel capillary tube (500 μm inside diameter, 5 cm length) was located at a distance of 1-8 mm above the liquid surface. The experiments were carried out at atmospheric air with a rod cathode and with argon flowing through the capillary tube. The discharge was ignited by applying a high voltage (above 3 kV) using a dc power supply. A high-current power supply ($V_{max} = 600$ V, $I_{max} = 600$ mA) ensures operation at high discharge currents (up to 100 mA).
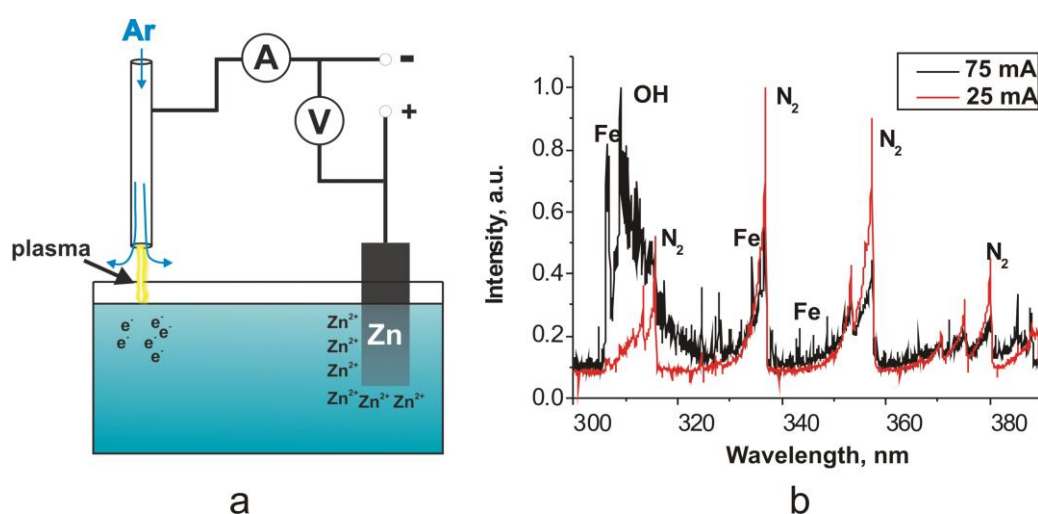
Fig. 1: Schematic diagram of the gas–liquid interface discharge used for synthesis of NPs (a) and emission spectrum of the discharge plasma (b)

3   Results and Discussion

Information about the properties of a gas-discharge plasma transport processes and plasma parameters was obtained on the basis of spectroscopic, electrical and spatial resolved investigation of the glow discharge. The main characteristics of the discharge plasma were studied by varying the discharge current, gas flow rate and solution composition. The measured current-voltage characteristics showed that the discharge was in a glow-like mode.

It was found that at low currents (about 4 mA) and with argon flowing through the cathode the plasma spectrum does not contain spectral lines of the cathode material. The main components of the spectra were found to be spectral lines originated from the anode material, OH and N₂ bands. Most likely, OH bands are due to the vapor phase at the plasma-water interface while the nitrogen bands are caused by interaction of plasma with the surrounding air. N₂ bands disappeared when the argon flow rate was increased from 15 to 60 sccm. But starting from approximately 25 mA iron lines caused by cathode sputtering appeared in the discharge plasma spectrum (Fig.1b) increasing in intensity with current increasing. At the current of 75 mA iron lines were observed not only in plasma emission spectrum, but also in the laser-induced emission spectra of the produced NPs.

Thus, at high currents sputtering of the cathode material should be taken into account. In some cases this fact may be used for doping of the produced particles. Furthermore, with the

discharge current increase the rate of solution evaporation also increases, resulting in the nitrogen bands intensity decrease with simultaneous increase in the OH radical bands intensity. Plasma electron temperature was evaluated using relative intensity values of silver lines Ag I λ=3280.7 and 3382.9 nm. According to the evaluation data the plasma temperature decreases from 4000 to 2000 K with the increase of the argon flow rate (at the current of 4 mA). The vibrational temperature (0,15 - 0,33 eV) determined based on the measured emission from the N_2 second positive system rises with the discharge current increase and was more than twice higher than the rotational temperature. The rotational temperature of the microplasma was determined by fitting the measured OH emission spectrum with the corresponding synthetic spectrum. The difference between the vibrational and rotational temperatures indicates the non-equilibrium state of the microplasma.

Typical UV–visible absorption spectra of the colloids prepared by gas–liquid interfacial discharge are shown in Fig. 2. TEM analysis shows that the particles are non-agglomerated, quasi-spherical with a mean size of about 12-15 nm. The spectral features of the colloid prepared using zinc electrode in pure water are characterized by a sharp absorption increase at 385 nm which is indicative of a semiconducting nature of the formed NPs in this case and most probably, corresponds to the excitonic absorption of ZnO. The optical band-gap estimated from the absorption spectrum confirmed the formation of ZnO NPs (E_g = 3.36 eV). As can be seen from the Fig. 2 the UV–visible absorption spectrum of NPs produced in the glucose solution has a band at 266 nm while the excitonic band is absent in the spectrum. We suggest that the band at 266 nm corresponds to the surface plasmon resonance of Zn NPs in the glucose aqueous solution [6]. For silver NPs the absorption spectrum exhibited the characteristic plasmon absorption band located at 400 – 417 nm.

In the case of the sequential discharges with silver and zinc electrodes, as can be seen from Fig.2 the spectra are dependent on a sequence of electrode dissolution: discharge with the Zn electrode immersed into the cell with colloid previously prepared with Ag electrode (Zn-Ag sequence), or vice versa (Ag-Zn). For the Zn-Ag sequence, optical absorption spectra of the synthesized NPs (curve 4, Fig. 2) exhibited two absorption peaks. The first peak around 350 nm is attributed to the excitonic absorption peak of ZnO NPs. A weak and broad band around 410 nm was found to be red shifted, broadened and increased in intensity with longer reaction times. For the Ag - Zn sequence the spectra of the solutions do not exhibit the pronounced features attributable to the Ag or ZnO particles (curve 5, Fig. 2)
Most probably, composite ZnO/Ag structures are formed by these two-step synthesis approaches. One possible way is the reduction of Ag ions to metal Ag on ZnO surface and formation of Ag shell layer around ZnO nanocrystals.

It should be noted that the plasma induced processes in solution at the plasma-liquid interface are responsible for the synthesis of NPs. This could be confirmed by a comparison of the results of experiments with plasma above the solution and without plasma (performed with two electrodes immersed in the solution). The electrical conditions were kept the same in both experiments, but, for example, gold NPs from the $HAuCl_4$ solution could not be formed in the second experiment. At the same time after the discharge ignition above the $HAuCl_4$ solution surface the formation of gold NPs was observed.

Solution chemistry induced at the plasma-liquid interface can be used for NPs surface engineering. Absorption spectra of the solutions after plasma treatment indicate that intermediate products can exist. Plasma electrons initiate the reactions in the bulk liquid resulting in the formation of a range of radicals and ions. The experimental evidence

indicates the possibility of using the plasma for the colloidal solution treatment and surface modification of NPs.
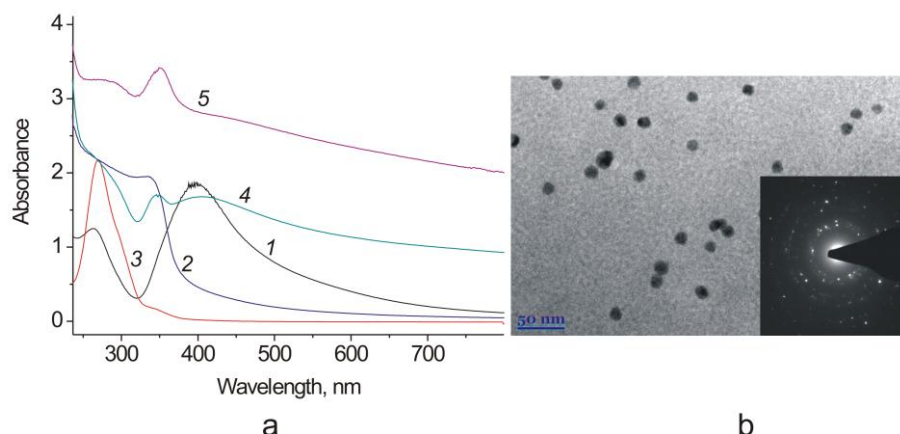
Fig.2. Typical UV–visible absorption spectra of samples prepared by gas–liquid interfacial discharge (a): with silver electrode in the 0.01 M glucose solution (1), zinc electrode in distilled water (2) and in the 0.01 M glucose solution (3) and by sequential Zn-Ag (4) and Ag-Zn (5) discharges. (b): TEM photograph of the Zn NPs prepared in the 0.01 M glucose solution, the inset shows the SAED pattern of the selected group of nanoparticles

4   Conclusion

A gas-liquid interfacial microplasma generated between a capillary and liquid surface in ambient air with flowing argon as a working gas was characterized by optical emission spectroscopy. The main parameters of the plasma generated were studied by varying the gas flow rate and the discharge current.

The formation of metal (Ag or Zn) nanoparticles with a possibility of changing their composition and average size by varying the solution composition and discharge parameters as well as a formation of composite ZnO-Ag structures by using sequential discharges with Zn and Ag electrodes were demonstrated. The morphology and composition of the prepared NPs were examined at different experimental conditions. It was established that the presence of the reducing and stabilizing agents in liquid such as glucose can change a composition of the produced particles, for example, in the glucose aqueous solution metallic Zn NPs were formed instead of zinc oxide NPs that are formed in pure water.

Acknowledgment

References
1. D. Mariotti et al., J. Phys. D: Appl. Phys. 44, 174023 (2011)
2. J. Patel et al., Nanotechnology, 24 245604 (2013)
3. V.Burakov et al., Plasma Phys. Technol. 1, 127 (2014)
4. N. Shirai et al., Jap. J. of Appl. Phys. 53, 046202 (2014)
5. C. F. Klingshirn et al., Zinc Oxide: From Fundamental Properties towards Novel Applications (Springer, New York, 2010)
6. H. Zeng et al., J Phys. Chem. B 109, 18260 (2005)

HYDROGEN PEROXIDE GENERATION IN CORONA DISCHARGE ABOVE LIQUID IN THE PRESENCE OF ORGANIC COMPOUNDS

D. Dobrin[1], M. Magureanu[1], C. Bradu[2], N. B. Mandache[1], V. I. Parvulescu[3]

[1]*National Institute for Lasers, Plasma and Radiation Physics, Department of Plasma Physics and Nuclear Fusion, Atomistilor Str. 409, 077125 Magurele-Bucharest, Romania*
[2]*University of Bucharest, Faculty of Biology, Department of Systems Ecology and Sustainability, Splaiul Independentei 91-95, 050095 Bucharest, Romania*
[3]*University of Bucharest, Faculty of Chemistry, Department of Organic Chemistry, Biochemistry and Catalysis, Bd. Regina Elisabeta 4-12, 030016 Bucharest, Romania*

E-mail: daniela.dobrin@infim.ro

The formation of hydrogen peroxide (H_2O_2) in a pulsed corona discharge in contact with liquid is investigated in the absence and in the presence of an organic compound (methyl paraben, MeP) in solution. It is found that low concentrations of MeP can favor H_2O_2 production, by suppressing its decomposition in radical reactions, while high MeP concentration inhibit H_2O_2 generation, by reducing the concentration of $^\bullet$OH radicals. The degradation of MeP is enhanced when combining plasma with ozonation, using ozone generated in the discharge. In this plasma+O_3 configuration H_2O_2 decomposition in reactions with O_3 becomes important, especially after MeP removal from the treated solution.

Keywords: corona discharge; ozone; hydrogen peroxide; methyl paraben

1 Introduction

In all advanced oxidation processes investigated for water treatment hydroxyl radicals ($^\bullet$OH) are regarded as the most useful reactive oxygen species due to their highly oxidative nature and to the high reactivity with most organic compounds. In electrical discharges produced in gas-water environment $^\bullet$OH radicals are generated by electron dissociation of H_2O molecules in the contact area between the plasma and the liquid. Recombination of $^\bullet$OH radicals leads to the formation of hydrogen peroxide (H_2O_2), which is the main stable oxidative species formed in water exposed to plasma, and has been considered as an indicator of $^\bullet$OH production. Most investigations report measurements of H_2O_2 formation in discharges in water or gas-water environments [1]. In water treatment experiments a number of organic compounds (the parent compound and its degradation products) are simultaneously present in the solution and can affect the production of H_2O_2.

In this work, measurements of H_2O_2 formed in a pulsed corona discharge above an aqueous solution of methyl paraben (MeP) are compared with the data obtained in the absence of the organic compound. Correlation of these measurements with the results on MeP removal leads to an improved understanding of the contaminants degradation process under plasma conditions.

2 Experimental

The corona discharge is generated in oxygen between a multi-wire electrode (20 copper electrodes, 100 μm×36 mm, 6 mm distance between adjacent wires) and the surface of the liquid [2]. The discharge gap is 4 mm and the height of the liquid in the plasma reactor is approximately 5 mm. The aqueous solution is continuously circulated between a reservoir and

the plasma reactor with 160 mL/min flow rate. The total volume of liquid is 330 mL and the solution volume in the plasma reactor is 90 mL. The effluent gas containing ozone produced in the plasma can be either bubbled through a porous ceramic into the solution reservoir (plasma+ozonation configuration) or vented (plasma alone configuration).

The discharge is operated in pulsed mode with high voltage pulses of 18 kV amplitude, rise time of 55 ns (10-90%) and duration of 416 ns (FWHM). The pulses are generated by discharging a 6 nF capacitor using a solid-state thyristor switch, triggered by a variable frequency pulse generator. The pulse frequency is set to 25 Hz and the average power dissipated in the discharge is 32 W.

The methyl paraben solution is prepared in tap water with conductivity 250 µS/cm and pH 7. The initial concentration of MeP is in the range 10-100 mg/L. Analysis of the treated solutions is done by high performance liquid chromatography (HPLC) to evaluate MeP removal and by total organic carbon (TOC) analysis to determine the mineralization degree. The concentration of H_2O_2 in the liquid was determined by the spectrophotometric titanium sulfate method [3].

3   Results and Discussion

Improved efficiency of organic compounds removal in a combined plasma+ozonation system was evidenced in previous experiments [2]. In the present work the results obtained with plasma alone and in plasma+O_3 configuration are compared under identical conditions. Fig. 1 shows the removal of MeP (1a) and its mineralization (1b) as a function of treatment time in both configurations.
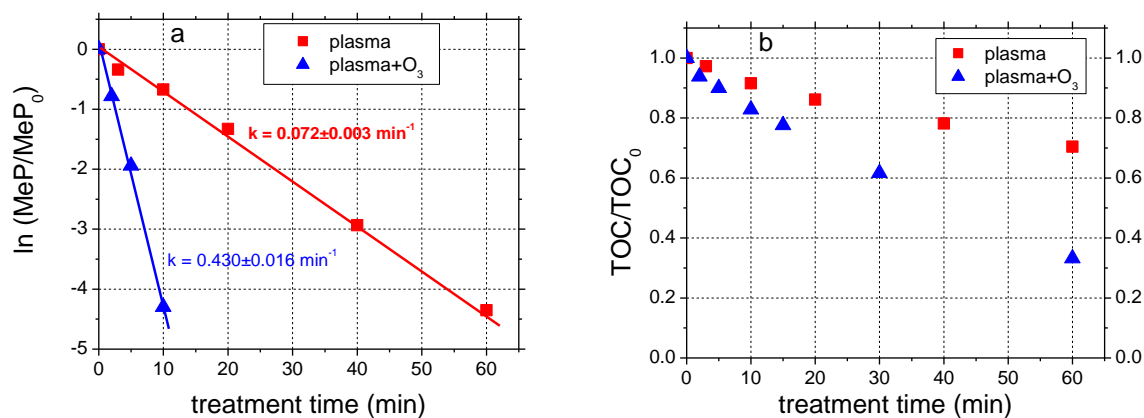
Fig. 1: (a) Degradation of MeP; (b) TOC removal as a function of treatment time in plasma alone and in the plasma+O_3 configuration (initial MeP concentration 50 mg/L)

In both configurations MeP degradation is described by first-order kinetics (Fig. 1a), but the removal is considerably faster in the plasma+O_3 experiments, where 15 minutes are sufficient for complete elimination of the target compound. However, the comparison should take into account that the effective contact time between the plasma and the solution is only 16 minutes for a 1 hour experiment, due to the circulation of liquid through the plasma reactor. Mineralization is also faster in plasma+O_3 configuration (Fig. 1b), reaching 66.5% after 60 minutes of treatment, while by plasma alone TOC is reduced with 29.5% during the same period. The results clearly show that good contact between the plasma-generated oxidative species and the solution (by bubbling ozone produced in the discharge through the solution) significantly enhances system performance with respect to the degradation of the target organic compound.

Measurements of H_2O_2 formed during plasma treatment of the liquid with and without MeP are plotted in Fig. 2. The concentration of H_2O_2 formed in water and in MeP solutions increases approximately linearly with time (Fig. 2a). Higher amounts of H_2O_2 are detected in the presence of the organic compound (up to 44 mg/L H_2O_2 in the 50 mg/L MeP solution) as compared to pure water data (up to 28.4 mg/L). The formation of H_2O_2 depends on the initial concentration of MeP, showing a clear maximum at 50 mg/L MeP in solution (Fig. 2b). Further increase in MeP amounts is expected to lower the H_2O_2 concentration below the values obtained in water, however above 100 mg/L MeP the degradation products interfere with the H_2O_2 measurements.
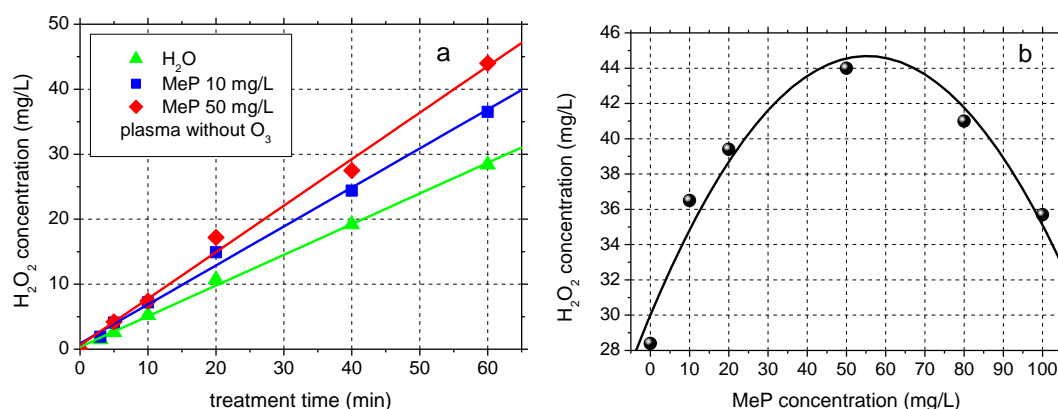
Fig. 2: (a) Concentration of H_2O_2 formed by plasma treatment of water and MeP solutions (initial MeP concentrations 10 mg/L and 50 mg/L), as a function of treatment time; (b) Concentration of H_2O_2 measured after 60 minutes plasma treatment of water and MeP solutions (initial MeP concentration 10-100 mg/L)

In analyzing this behavior two effects should be taken into account: (i) formation of H_2O_2 mainly by recombination of $^\bullet OH$ radicals, and on the other hand (ii) radical decomposition of H_2O_2.

An organic compound present in solution acts as $^\bullet OH$ scavenger and thus negatively affects H_2O_2 production by reducing $^\bullet OH$ concentration. Indeed, the reactions of $^\bullet OH$ radicals with organic compounds have high rate constants (10^7-10^{10} $M^{-1}s^{-1}$). Tay et al. [4] reported rate constants for the reaction of $^\bullet OH$ with parabens in the range 6.8-9.2×10^9 $M^{-1}s^{-1}$, similar with the rate constant for $^\bullet OH$ self-reaction with formation of H_2O_2 (5.5×10^9 $M^{-1}s^{-1}$ [5]). Franclemont et al. [6] found that the presence of organic compounds diminishes the concentration of H_2O_2 generated by an underwater corona discharge as compared to pure water. At the very high concentration of organic compounds used in their work the formation of H_2O_2 is obviously inhibited.

On the other hand, radical decomposition of H_2O_2 should not be neglected. Locke and Shih [1] stressed the importance of suppressing these reactions for enhancing the efficiency of H_2O_2 generation in plasma. Therefore, the scavenging effect of the organic compound can actually have a positive influence on H_2O_2 generation, through inhibiting its decomposition by radicals. Increased production of H_2O_2 in the presence of alcohols as compared to the results in pure water was reported by Kuzmicheva et al. [7] in a discharge above liquid. The authors also observed a dependence of the H_2O_2 yield on the concentration of alcohols.

The present results confirm that the presence of an organic compound affects the production of H_2O_2 by plasma. Depending on the concentration of the organic compound, its presence influences either the formation rate of H_2O_2 or its decomposition rate.

Fig. 3 shows the concentration of H_2O_2 during plasma+O_3 treatment of water and of MeP solutions. In this configuration, besides the above-mentioned reactions, ozone also plays an important role. This is obvious from the results obtained in pure water, where no H_2O_2 is detected, most likely due to its decomposition by O_3 with formation of $^\bullet OH$ radicals.

For short treatment time (below 10 minutes) the H_2O_2 concentrations are similar to the values obtained with plasma alone. Ozone reactions with MeP and its degradation intermediates are favored here, since O_3 reacts well with aromatics, while the reaction with H_2O_2 is slower, so H_2O_2 formation is not likely to be affected by ozone in the beginning of treatment. As the treatment time increases MeP is gradually eliminated and the resulting are detected and the decline in H_2O_2 concentration starts later. In this case MeP degradation consumes larger amounts of ozone and requires longer treatment time, so less O_3 is involved in reactions with H_2O_2, which explains the concentration profiles in Fig. 3.
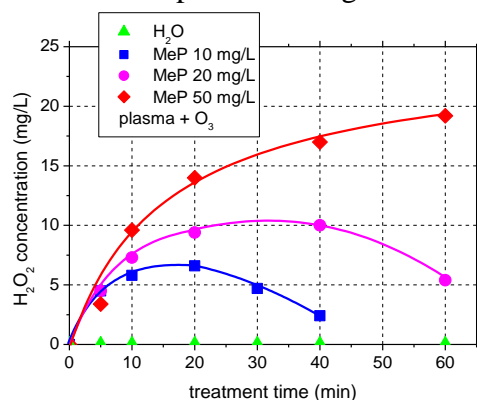
Fig. 3: Concentration of H_2O_2 formed by plasma+O_3 treatment of water and MeP solutions (initial MeP concentrations 10-50 mg/L), as a function of treatment time

4   Conclusion

A pulsed corona discharge in contact with liquid was evaluated from the point of view of organic compounds degradation and generation of H_2O_2. Ozone produced in the plasma can be used more efficiently by bubbling it through the solution, which leads to enhanced removal and mineralization of the target compound. Thus, in the plasma+O_3 configuration complete removal of MeP is achieved after 15 minutes treatment, and the mineralization reaches 66.5% after 60 minutes. The concentration of H_2O_2 produced in plasma is affected by the presence of MeP. On one hand the organic compound can inhibit H_2O_2 decomposition in reactions with other oxidizing species ($^\bullet OH$, O_3). On the other hand high concentrations of organic compounds can suppress H_2O_2 formation by reducing $^\bullet OH$ concentration.

References

1. B. R. Locke et al., Plasma Sources Sci Technol 20, 034006 (2011)
2. D. Dobrin et al., Environ. Sci. Pollut. Res. 21, 12190 (2014)
3. G. M. Eisenberg, Ind. Eng. Chem. Anal. Ed. 15, 327 (1943)
4. K. S. Tay et al., Chemosphere 81, 1446 (2010)
5. G. V. Buxton et al., J. Phys. Chem. Ref. Data 17, 513 (1988)
6. J. Franclemont et al., Plasma Chem. Plasma Process. 34, 705 (2014)
7. L. A. Kuzmicheva et al., Surf. Eng. And Appl. Electrochem. 44, 281 (2008)

COLD ATMOSPHERIC PLASMA TREATMENT OF CANCER CELLS *IN VITRO* AND THE MECHANISMS OF ITS CYTOTOXICITY

N. Hojnik[1,2], S. Kos[3], M. Modic[1], A. Kaucic[4], L. Prosen[3], G. Sersa[3], U. Cvelbar[1,2]

[1]Department of Surface Engineering and Optoelectronics, Jozef Stefan Institute, Jamova cesta 39, SI-1000 Ljubljana, Slovenia

[2] Jožef Stefan International Postgraduate School, Jamova cesta 39, SI-1000 Ljubljana, Slovenia

[3]Department of Experimental Oncology, Institute of Oncology Ljubljana, Zaloska 2, SI-1000 Ljubljana, Slovenia

[4]University Clinic of Respiratory and Allergic Diseases Golnik, Golnik 36, SI-4204 Golnik, Slovenia

E-mail: natasa.hojnik@ijs.si

The cold atmospheric plasma (CAP) technology showed promise in various fields, including cancer cell treatment. The inhibitory effects against cancer cells are the results of the presence of charged particles, reactive species, UV and many others, which interact with liquid media surrounding the cells and change the cell dynamics. The aim of this study was to explore the mechanism behind the CAP produced cytotoxicity.

Keywords: cold atmospheric plasma; cancer cell treatment; plasma-liquid interactions; reactive species determination

1   Introduction

The cold atmospheric plasma (CAP) technology is a very promising tool for the diversity of applications in the field of medicine, where it was already applied for sterilization, dental care, skin diseases and wound healing [1-3]. Recently, the research is focused on the CAP implementation in the cancer treatment in terms of cell growth arrest and apoptosis. The ability of CAP to produce oxidative stress in the cancer cells is the result of the presence of different charged particles, reactive oxygen and nitrogen species (ROS and RNS), UV and many others. Nevertheless, the exact mechanism is still unexplored in detail, despite that the different studies already indicated that CAP treatments were capable of inducing selective inhibitory effects towards the cancers cells [4].

During various experimental approaches *in vitro*, the cancer cells are usually covered with liquids like cell culture medium. Similarly, tumors are surrounded by the various corporal fluids in *in vivo* cases. The interaction between CAP gas species and liquid media may result in the modification of the initial liquid media composition and consequent change of cancer cell dynamics [5-7].

The focus of our recent study was to investigate the nature of the damage on cancer cells which is caused by CAP treatment. As a priority we wanted to examine the effects on the viability of the cancer cells and content of the cell culture media, which was followed by a more detailed look at the damage caused on a cellular level.

2   Materials and Methods

Murine melanoma cell line B16F1 was used for the first set of experiments. The cells were plated in 96-well microtiter plate one day prior the CAP treatments. The CAPs were operated by a generator set at 5 kV and 25 kHz AC discharge frequency. The flow rate of helium gas was 700 sccm, where the distance between the end of the glass tube and the bottom of the well-plate was 2 cm. Three different plasma set-ups were used: single electrode jet and two DBD jets (with grounded upper or lower electrode). Cell culture media was changed with the fresh one right before the treatments. The exposure times were 10 s, 30 s, 60 s, 180 s, 300 s and 600 s. Cell viability was tested 24 h and 72 h after the treatment. Moreover, the production of lipid hydroperoxides and the presence of intercellular ROS and RNS were examined as well. Separately, with the higher number of cells per well, the intake of dextran (sizes: 4 kDa, 10 kDa, 40 kDa and 70 kDa) after the plasma treatment was observed as well.

The second set of experiments was focused on CAP-induced modifications of the treated liquid. AMEM cell culture media with 5 % fetal bovine serum (FBS), antibiotics (penicillin and gentamicin) and L-gluthamine (10 mM) was used. As for melanoma cells before, the same experimental set-up was applied. UV-VIS spectrometry was performed to track the modifications of the AMEM with the focus on significant peaks. The concentrations of newly produced hydrogen peroxide were examined with the assay based on xylenol orange dye in the acidic solution. Also, the concentrations of nitrites were determined with the Griess reagent.
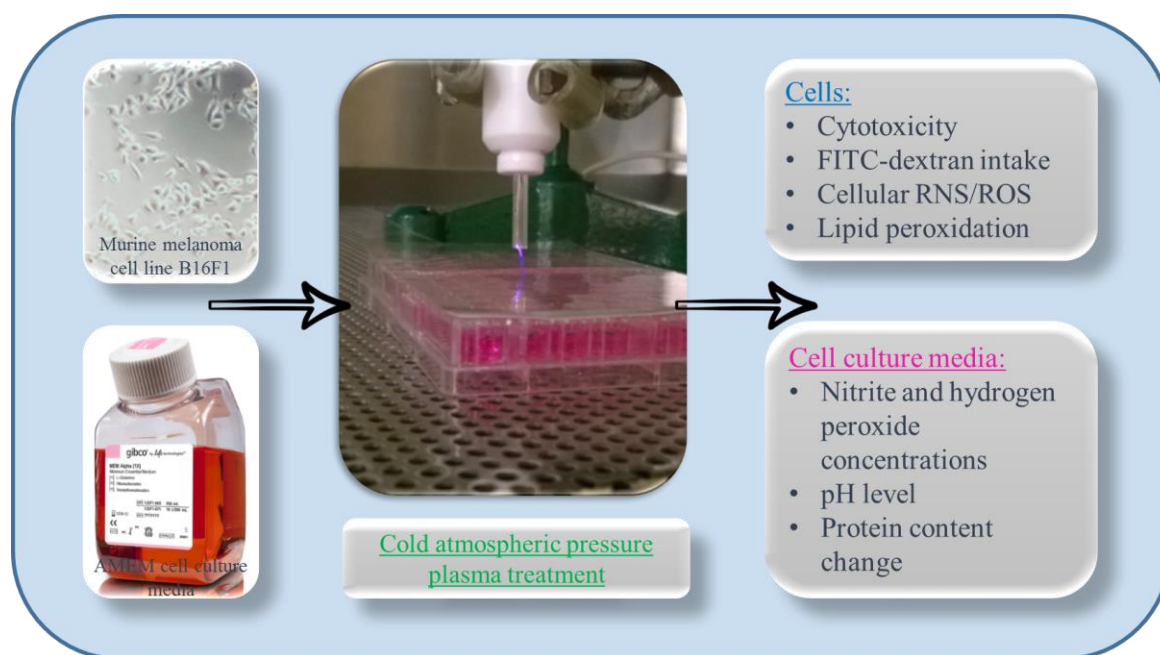
Fig. 1: The experimental set-up of the CAP treatment of cancer cells (murine melanoma line B16F1) and AMEM cell culture media and the examination of the CAP produced cancer cell damage

3   Results and Discussion

The results showed that all three CAP set-ups produced resembling inhibitory effects on cancer cells. As expected, the more significant cytotoxic effect was achieved with longer

exposure times, namely 180 s, 300 s and 600 s. Hence, 72 h after the treatments the cytotoxicity rate was around 55 % for 180 s, 65 % for 300 s and 70 % for 600 s. Among these, both DBD set-ups were capable of producing 45 % cytotoxicity already after 60 s exposure (72 h after the treatment). As control experiment, we confirmed that exposure of cancer cells to gas only had no cytotoxic effect (Fig. 2a and 2b).

Furthermore, CAP treatments also produced comparable effects on dextran intake of the cancer cells. The results demonstrated that the highest intake rate was achieved with 10 kDa dextrans at an exposure time of 5 min, suggesting that all 3 CAP set-ups triggered the formation of the membrane damage in the form of specifically sized pores. The most significant intake effect was observed at DBD jet with grounded upper electrode.

Considering the CAP treatments of liquid media only, longer exposure times produced more significant modifications of AMEM cell culture media. In addition, the concentrations of both hydrogen peroxide and nitrites were increasing with longer exposure times. The highest concentration of hydrogen peroxide was observed after 600 s of treatment with DBD jet (grounded lower electrode) when on the other hand the highest amount of nitrites was produced after the longest exposure time to single electrode jet (Fig. 2c and 2d).
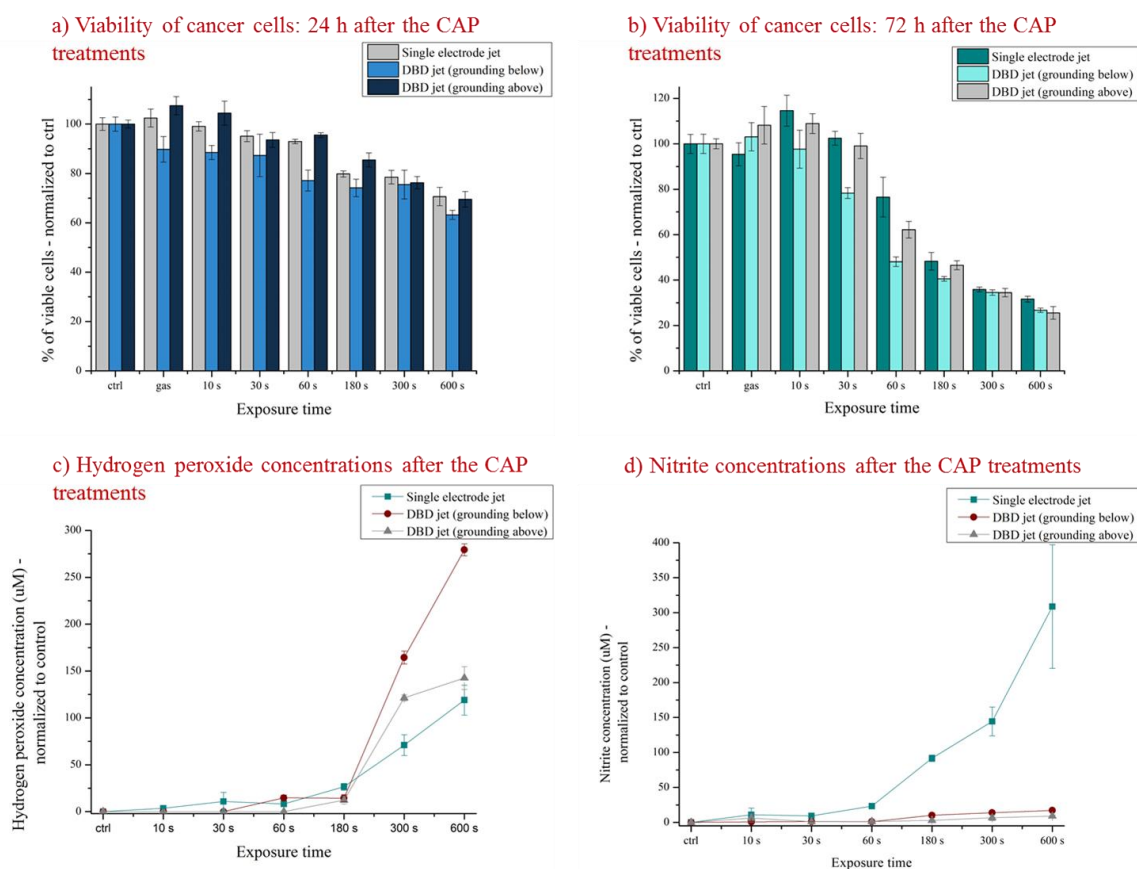
Fig. 2: a) The viability of cancer cells 24 h after the CAP treatments. b) The viability of cancer cells 72 h after the CAP treatments. c) The concentrations of hydrogen peroxide produced after the CAP treatments. d) The concentrations of nitrites produced after the CAP treatments.

4   Conclusion

To sum up, all CAP set-ups used for this purpose demonstrated the comparable cytotoxic effect on cancer cells. The changes in cancer cell dynamics were most likely induced by the CAP-related modifications of cell culture media and the production of liquid reactive species. Both of them also contributed to the formation of the cell membrane pores, letting the reactive species into the cell. For a more detailed look, further analysis of the cellular ROS, RNS, and lipid peroxidation is necessary.

References

1. J. Guo et al., Food Control. 50 (2015)
2. B. Haertel et al., Biomol. Ther. 22, 6 (2014)
3. N. Chernets et al., Tissue Eng. Part A. 21, 1-2 (2014)
4. M. Keider, Plasma Sources Sci. Technol. 24 (2015)
5. M. Hoentsch et al., PLoS One. 9, 8 (2014)
6. F. Utsumi et al., PLoS One. 8, 12 (2013)
7. R. Laurita et al., Clin. Plasma Med. 3 (2015)

APPLICATION OF WATER FALLING FILM DBD FOR DEGRADATION OF NICOTINE IN WATER SOLUTIONS

V. V. Kovačević[1], B. Dojčinović[2], J. Krupež[3], M. Jović[3], M. Natić[3], G. B. Sretenović[1], D. Manojlović[3], B. M. Obradović[1] and M. M. Kuraica[1]

[1]University of Belgrade, Faculty of Physics, PO Box 44, 11001 Belgrade, Serbia

[2] University of Belgrade, Institute of Chemistry, Technology and Metallurgy, Studentski trg 12, Belgrade, Serbia

[3] University of Belgrade, Faculty of Chemistry, Studentski trg 12-16, Belgrade, Serbia

E-mail: vesna@ff.bg.ac.rs

In this paper we present plasma-based degradation of nicotine in water solutions. Water falling film dielectric barrier discharge (DBD) was used as plasma source operating in air at atmospheric pressure. Solutions containing 50 ppm and 300 ppm of nicotine in distilled or tape water were treated directly and indirectly by plasma. Influence of homogeneous catalysts Fe^{2+} and H_2O_2 was also tested. *Artemia Salina* organisms were used for toxicity tests of treated solutions. Degradation efficiency was the highest in direct plasma treatment of nicotine with Fe^{2+} as a catalyst and in this case the toxicity test showed the lowest mortality.

Keywords: water falling film DBD; water purification; nicotine degradation

1   Introduction

Nicotine (3-substituted pyridine, $C_{10}H_{14}N_2$) is one of the mostly known alkaloids, and despite of its toxicity (LD_{humans} 40-60 mg) it is still widely consumed by humans mainly through cigarette smoke. Primarly, nicotine is present in tobacco industry wastes, it is used as insecticide and also present in pharmaceutical products. Solubility of nicotine in water is very high. This fact represents a major risk during waste disposal and storage because nicotine can be washed out and transferred into aquifers. If the products that contain nicotine are not properly stored and discarded this alkaloid can easily dissolve in water becoming a risk for enivornment, especially for ground and underground water. Methods used for removing nicotine from water solutions include advanced oxidation processes, aerobic and anaerobic degradations and solid phase adsorption. Non-thermal plasmas in and in contact with liquids have been recognized as an emerging technology for water purification processes [1, 2]. This is primary due to formation of reactive nitrogen species (RNS) and reactive oxygen species (ROS) in plasma treated liquids, such as highly reactive radicals (OH•, O_2•-, NO•) and molecular species (O_3, H_2O_2, NO_3^-, NO_2^-). Their existence in a liquid exposed to plasma allows a wide range of applications, particularly bio-medical applications [3–5] and degradation of pollutants in water [2, 6, 7]. Oxidation of nicotine in plasma processes has been poorly investigated [8]. Water falling film DBD has already been used in numerous applications for water purification and gas cleaning proceses [9–12]. In this study, the reactor was applied for degradation of different nicotine solutions. The influence of initial nicotine concentration, homogeneous catalysts and treatment methods is presented.

2   Experimental

Water falling film DBD is an atmospheric pressure non-thermal plasma reactor which was developed to allow direct treatment of the solution in plasma. The reactor configuration is cylindrical and it consists of inner tube electrode, glass tube and outer electrode mounted concentrically on a plastic holder and centered with a plastic lid, as illustrated in schematics in Fig. 1, and it has been described in detail in [11]. Outer electrode was connected to a high

voltage power supply and inner electrode was grounded and discharge was generated in the 4.5 mm gap between the glass tubes. The discharge voltage and frequency were set to 17 kV and 300 Hz. The working gas was air at atmospheric pressure with a flow rate of 5 L/min. The solution was pumped with a flow rate of 125 mL/min from a vessel by a peristaltic pump through the inner glass tube and when it reaches the top of the tube it falls down making a thin film over the outer surface of the tube.
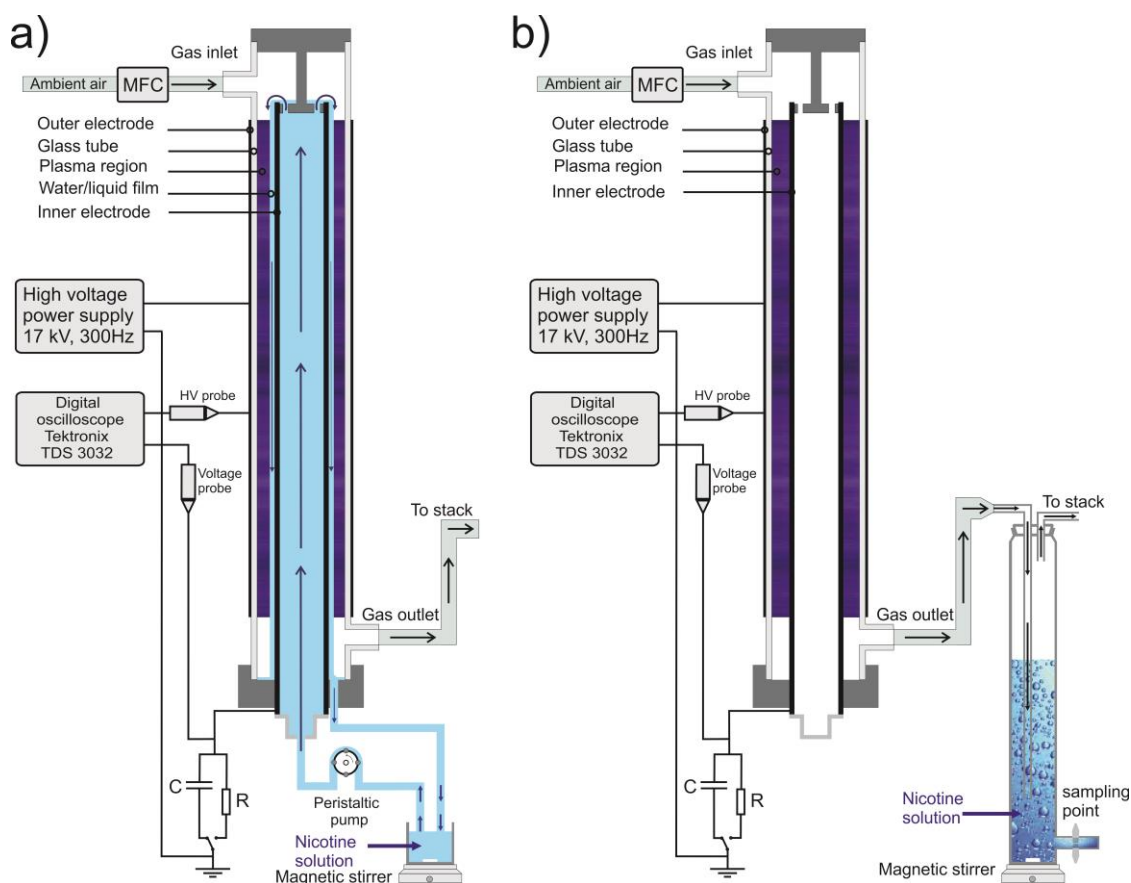
Fig. 1: The scheme of the experimental set-up for a) direct treatment and b) indirect treatment.

In the experiment two methods of treatment, direct and indirect, were applied. In direct treatment, shown in Fig. 1 a), water solution with different initial concentrations of nicotine was circulating through the reactor and therefore it was directly exposed to plasma and short-living as well as long-living chemically active species. In this setting plasma parameters were kept constant, while the composition of the solution was modified. Namely, the treatment was applied to the following solutions: distilled water with 50 ppm and 300 ppm of nicotine and tap water with 300 ppm of nicotine. In direct treatment the influence of homogenous catalysts on the degradation efficiency was also tested on distilled water containing 50 ppm of nicotine and 0.5 mmol/L of Fe^{2+}, and distilled water containing 50 ppm of nicotine and 10 mmol/L of H_2O_2. Indirect treatment, shown in Fig. 1 b), refers to the bubbling of the effluent gas from plasma containing long-living chemical species through the nicotine solution in a cylindrical glass vessel 1 m in height and 5 cm in diameter. Degradation efficiency of this method was tested on distilled water containing 50 ppm and 300 ppm of nicotine and tap water containing 300 ppm of nicotine. In each experiment initial volume of the solution was 500 mL and treatment time was 60 minutes, while degradation kinetics was monitored by sampling of 30 ml on every 10 minutes. Degradation efficiency was followed using HPLC analysis

(Dionex UltiMate 3000, Thermo Fisher Scientific, Bremen, Germany). Characterization of degradation products was conducted using UHPLC-LTQ OrbiTrap MS (ThermoFisher Scientific, Bremen, Germany). Eggs of *Artemia salina* (Artemia-mix) and sea salt (Tropic Marin® Sea salt) that were used for toxicity test were a product of company Sera®, Germany.

3 Results and Discussion

The results of the nicotine degradation are presented in Fig. 1. Fig. 1 (a) shows degradation of 50 mg/L of nicotine in distilled water and with addition of catalysts and Fig. 1 (b) shows degradation of 300 mg/L of nicotine.
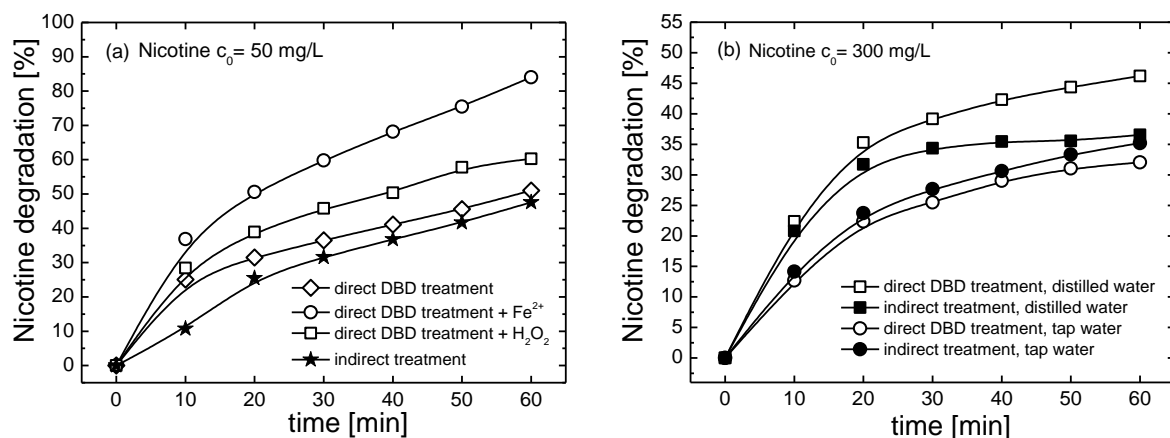
Fig. 2: Nicotine degradation efficiency in direct and indirect treatment: (a) in distilled water with 50 mg/L of nicotine with addition of homogeneous catalysts (0.5 mmol/L of Fe^{2+}, 10 mmol/L of H_2O_2) and (b) in distilled and tap water with 300 mg/L of nicotine.

From Fig. 1 (a) it is clear that catalysts significantly contribute to overall efficiency of the process and direct treatment of 50 mg/L of nicotine with addition of 0.5 mmol/L of Fe^{2+} achieved the highest efficiency of degradation among all processes reaching degradation of 84 %. Addition of Fe^{2+} increases the oxidation power since it participates in Fenton reaction and contributes to additional generation of hydroxyl radical which non-selectively reacts with pollutant molecules. Higher concentration of 300 mg/L of nicotine reduces degradation to 46%, with higher efficiency in distilled water compared to tap water, which could be expected since tap water contains other compounds like calcium-carbonate which react with hydroxyl radical and other species acting as scavenger. Analysis of mass spectra showed total of 18 nicotine degradation products (not shown here). In direct treatment only small volume of the liquid is exposed to plasma at a particular moment and the rest of the volume is in vessel and in hoses without any contact with plasma, unlike the indirect treatment where the total volume is treated with effluent gas for overall treatment time. In order to display the real treatment efficiency and to compare the applied methods the residence time of the solution per one pass through the reactor is estimated to be 2.5 s per one pass through the reactor. This allowed estimation of rate constants for different degradation processes, showing that direct treatment provides two orders of magnitude higher efficiency of depollution (50 mg/L of nicotine in distilled water, k= 0.014 s^{-1}) compared to indirect treatment (50 mg/L of nicotine in distilled water, k= 1.76×10^{-4}s^{-1}). Results of *Artemia Salina* toxicity test are shown in Fig. 3. The lowest mortality of *Artemia Salina* organisms was observed in nicotine solution with Fe^{2+} directly treated by DBD. Increase of nicotine concentration increases mortality of organisms, and comparison of the results in deionized and tap water gives advantage to the indirect treatment, which is closely related to degradation mechanisms and degradation products of each process.
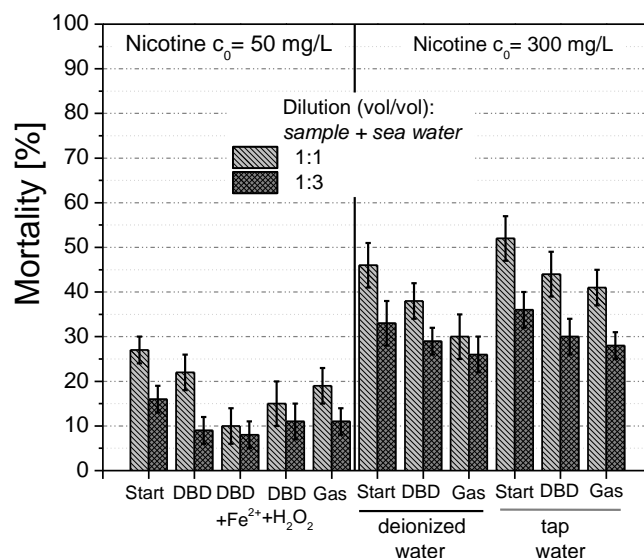
Fig. 3: *Artemia Salina* toxicity test (Gas- refers to indirect treatment)

4 Conclusion

Plasma-based treatment of nicotine solutions and toxicity of its byproducts was studied. It was shown that direct treatment of solutions in plasma provides significantly higher efficiency compared to indirect treatment. Efficiency can be further increased by addition of catalysts which also affects mechanisms of degradation and contributes to decrease of *Artemia Salina* mortality.

Acknowledgements

References

1. P. Bruggeman et al., J. Phys. D. Appl. Phys. 42, 053001 (2009)
2. B. R. Locke et al., Ind. Eng. Chem. Res. 45, 882 (2006)
3. J. Ehlbeck et al., J. Phys. D. Appl. Phys. 44, 013002 (2011)
4. D. B. Graves, J. Phys. D. Appl. Phys. 45, 263001 (2012)
5. T. von Woedtke et al., Phys. Rep. 530, 291 (2013)
6. M. A. Malik et al., Plasma Sources Sci. Technol. 10, 82 (2001)
7. B. Jiang et al., Chem. Eng. J. 236, 348 (2014)
8. E. B. Tsagou-Sobze et al., J. Hazard. Mater. 152, 446 (2008)
9. M. M. Kuraica et al., Vacuum 73, 705 (2004)
10. B. P. Dojčinović et al., J. Hazard. Mater. 192, 763 (2011)
11. M. S. Jović et al., Chem. Eng. J. 248, 63 (2014)
12. R. Brandenburg et al., Contrib. Plasma Phys. 54, 202 (2014)

DC CORONA DISCHARGE FOR BACTERIAL BIOFILM DECONTAMINATION

Z. Kovalova[1,2], M. Leroy[1], Z. Machala[2], E. Odic[1]

1 GeePs—Group of electrical engineering—Paris UMR CNRS 8507, CentraleSupélec, Univ Paris-Sud, Sorbonne Universités, UPMC Univ Paris 06 91192 Gif-sur-Yvette, France
2 Faculty of Mathematics, Physics and Informatics, Comenius University in Bratislava, 84248 Bratislava, Slovakia

E-mail: kovalova@fmph.uniba.sk

DC corona discharges in air were tested for the eradication of 48-hour Escherichia coli biofilms on glass slides. Thermostatic cultivation and confocal laser scanning microscopy of the biofilm stained with fluorescent dyes were used for biocidal efficiency quantification. Up to $5.7 \log_{10}$ reduction of bacterial concentration in the biofilm was measured after exposure to DC corona discharges for 15 min. CLSM showed that live/dead ratio in the biofilm was decreasing after plasma treatment and that the biofilm thickness was reduced for both corona polarities. The biofilm biomass loss was supported by crystal violet assay.

Keywords: bacterial biofilm; non-thermal plasma; corona discharge; water electrospray, fluorescence.

1 Introduction

Bacteria on surfaces exist predominantly in the form of biofilms, which are populations of microorganisms concentrated at an interface (usually solid-liquid) and encased in a hydrated matrix of exopolymeric substances (EPS), polysaccharides, and proteins that are produced by the resident microorganisms [1]. EPS protects cells from the outer environment and facilitates cell-to-cell communication (quorum sensing) [2]. Bacteria in the biofilm are protected from harsh conditions (high temperature, low pH, ultraviolet radiation, dehydration, etc.), and therefore are more resistant than their planktonic (suspended cells) counterparts [2]. In order to avoid using toxic chemicals or high concentrations of antibiotics to achieve the desired decontamination efficiency in biofilms, a search for new alternative methods of decontamination is required; one of these is low-temperature plasma.

2 Materials and Methods

2.1 DC corona discharges in air

Corona discharges in atmospheric pressure air were generated in open air in a point to plane geometry. The needle electrode was a sharp or a clipped hypodermic syringe needle connected to a DC high-voltage (HV) power supply. Opposite to the needle HV electrode, a copper plate was grounded through a $50\,\Omega$ resistor. Some experiments were performed with sterile distilled water electrosprayed onto the sample, through a hollow clipped HV needle electrode; this was supplied to the needle by pumping with NE-300 SyringePump. Electrical characteristic of the discharge are presented in [3].

2.2 Biofilm on glass

Escherichia coli strain BW25113 F+ was used to form biofilm on glass cover slides (2×2 cm) for 48 hours. One mL a stationary phase culture was diluted 1/100 in buffered M63 medium was placed into each well of a homemade 6-well plate. The samples were incubated without agitation at 30°C for 48 hours with media refreshment after 24 hours.

The biofilms on glass cover slides were taken out from the 6-well plates after 48 hours. The excessive liquid was removed, the samples were dried for 20 min at 35°C, and then placed onto the grounded electrode 0.5 cm from HV electrode. The control samples were dried using the same procedure but not treated with plasma. Cultivability was determined by repetitive rinsing and scraping of the biofilm into 5 mL of 0.85% NaCl saline solution. The solution with recovered bacterial cells was vortexed, serially diluted and spread over LB agar in petri dishes and incubated at 37°C overnight, then the bacterial colony forming units (CFUs) were counted.

For imaging using confocal laser scanning microscopy (CLSM), the treated biofilms were stained with a solution of three fluorescent dyes: Syto9, Propidium iodide (PI) and DAPI (4',6-diamidino-2-phenylindole) in phosphate buffered saline (PBS, pH 7.4), and incubated for 25 min in the dark. CLSM images were acquired with an inverted confocal laser microscope OLYMPUS IX81.

Biofilm biomass was evaluated using crystal violet (CV) staining following the established microbiology protocol [4]. The control and plasma-treated biofilms were resealed in the 6-well plate after treatment and 200 µL of 0.1% crystal violet was introduced into each well. After 10 min incubation the CV solution was carefully removed by pipetting and biofilms were rinsed with deionized water until the waste liquid was clear. The 6-well plate was dried overnight at room temperature. When fully dried, 200 µL of 33% acetic acid was added to each well to solubilize the CV for 15 min, then recovered and diluted in 1/10 deionized water and the absorbance measured at 550 nm.

3 Results and Discussion

3.1 Biofilm cultivation

The initial bacterial concentration in the biofilm was $3.1 \pm 6.6 \times 10^7$ CFU per mL. In both corona polarities (Fig. 1), the decontamination efficiency increased with exposure time and
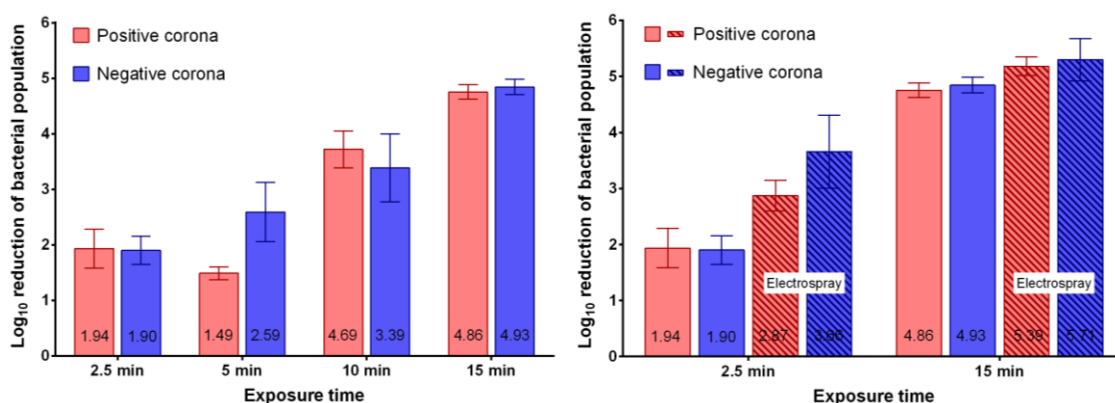
Fig. 1: Logarithmic reduction of bacterial concentration in the biofilm on the cover glass by cold plasma treatment of the corona discharges. Left: Reduction with inctreasing plasma treatment time. Right: The effect of water electrospray 0.01 mL/min on the sample - hatched bars (mean±SEM, 5–6 repetitions).

reached up to 4.9 log$_{10}$ reduction for positive and negative corona within 15 min. The electrospray increased bactericidal effect of plasma, for the 2.5 min exposure from 1.9 log$_{10}$ in both polarities to 2.9 and 3.7 log$_{10}$ for PC and NC, respectively. For longer exposure time 15 min this increase was from 4.9log$_{10}$ to 5.4 and 5.7 log$_{10}$ for PC and NC, respectively.

3.2 Confocal laser scanning microscope results

The fluorescence was acquired from four random examined spots on the biofilm. Examples of reconstructed three-dimensional examined spots of the biofilm are presented in Fig. 2. From this representation we can see that the plasma treated biofilms contain more dead cells (red stained by PI) than the controls (green cells stained by Syto9). The structure of the biofilm also changed with plasma treatment: the biofilm seems denser with more compact cellular structure. After plasma treatment with the water electrospray, the biofilm became thinner and patchy.

Fig. 2: Three-dimensional reconstruction of the biofilm *z*-stacks from CLSM. Red indicates dead cells and green live cells. From the left: control dried 20 min at 35°C, DC corona discharge treated samples for 15 min with or without water electrospray (magnification 60×, section size 211.2×211.2 μm).

From the third fluorescent dye – DAPI, which stains all cells, the biofilm thickness was calculated (Fig.3). It was calculated for all *z*-stacks in all biofilms and the resulted mean values are presented in Fig. 3 (left). There is a trend of reduction of the biofilm thickness with the rising exposure time and it is enhanced by adding the water electrospray to the discharge. The only significant difference was found for NC 15 min with electrospray (12.3 μm) in comparison with the control sample (18.1 μm).
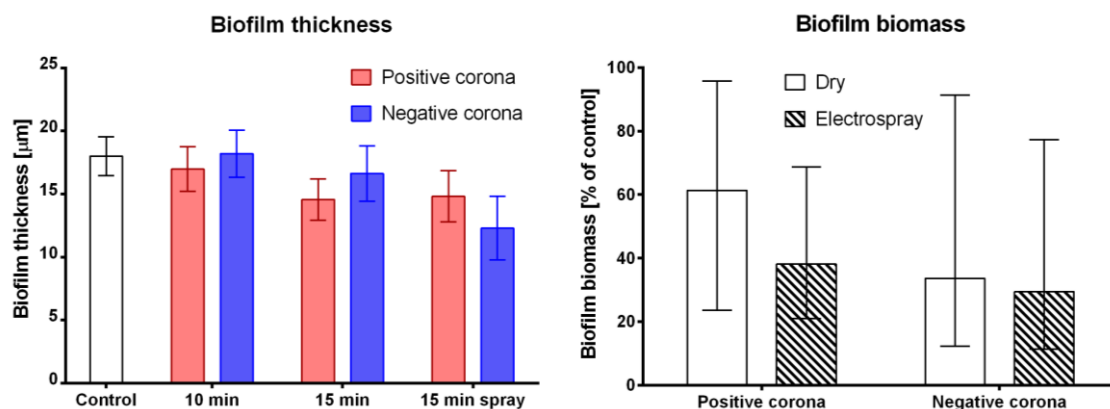
Fig. 3: Left: The biofilm thickness calculated from DAPI fluorescence integrated over the entire biofilm thickness for samples treated (plotted mean ±SEM, 8≤n≤16 in each group). Right: The biofilm biomass calculated as percentage of controls (100%) from crystal violet absorbance after 15 min PC and NC treatment with or without water electrospray. (Median with IQR, n = 10 in each group).

Biofilm biomass after plasma treatment was calculated as the percentage of the control sample absorbance (control sample biomass is equal to 100%), taking into consideration the dispersion in biofilm (controls) thickness over all experiments. Experiments were done for 15

min exposure time, because of the most significant decrease in the attached biomass was expected (Fig.3, right). For PC 61.3% and NC 32.7% of the biomass remained attached to the surface after exposure to those discharges. When the water electrospray was added to the discharge, stronger bacteria detachment occurred and only 38.1% and 29.5% of the biomass remained attached to the cover glass in PC and NC treatment, respectively.

4   Conclusion

Low-temperature (cold) atmospheric pressure plasmas represent a new promising method for surface decontamination from bacterial biofilms. Within 15 min $5.7 \log_{10}$ reduction in population of the bacterial biofilm was achieved by using DC corona discharges with water electrospray. With CLSM we observed increase in red fluorescence of biofilm after plasma treatment, and the DAPI staining showed thinning of biofilms after plasma treatment (negative corona with electrospray for 15 min), with its thickness decreased from 18.1 μm in the control samples to 12.3 μm after treatment. A substantial biofilm biomass loss was confirmed by the Crystal Violet assay.

Acknowledgement

References

1. K. Sauer, Genome Biol. 4 (6), 219 (2003)
2. L. Hall-Stoodley et al., Nature Rev. Microbiol. 2 (2), 95-108 (2004)
3. Z. Kovalova et al., Bioelectrochemistry (to be published)
4. J. H. Merritt et al., Curr. Protoc. Microbiol. 1B−1 (2005)

ELECTRIC FIELD MEASUREMENT IN HELIUM PLASMA JET CONTACTING THE WATER SURFACE

V. V. Kovačević[1], G. B. Sretenović[1], A. Sobota[2], O. Guaitella[3], I. B. Krstić[1],
B. M. Obradović[1], M. M. Kuraica[1]

[1]University of Belgrade, Faculty of Physics, PO Box 44, 11001 Belgrade, Serbia
[2]Eindhoven University of Technology, EPG, Postbus 513, 5600MB Eindhoven,
The Netherlands
[3]LPP, Ecole Polytechnique, Route de Saclay, 91128 Palaiseau, France

E-mail: kuki@ff.bg.ac.rs

In this paper we present electric field distribution in He plasma jet impinging the liquid surface. Dielectric barrier discharge (DBD) plasma jet with constant He flow of 1000 SCCM, operating at applied voltage of 2 kV and 30 kHz, was positioned above the water surface. Electric field measurement was performed using Stark polarization spectroscopy for different positions (5 mm and 10 mm) of plasma jet nozzle above the water surface. Obtained axial distribution of the electric field shows that maximal value of the field slightly increases with increase of distance, but it's also notably higher compared to the values found in jet without target.

Keywords: plasma jet; electric field; plasma-liquid interaction

1   Introduction

In recent years atmospheric pressure plasma jets have been extensively investigated and recognized as an emerging tool in the field of plasma medicine and biology [1]. Plasma jets are source of reactive oxygen and reactive nitrogen species which play important role in redox biology and medical applications [2]. Among reactive species, it is known that electric field can be the cause of various effects observed in experiments on biological samples [3]. In our previous study of spatio-temporal development of the plasma jet in helium for two different electrode configurations it was found that without the grounded electrode downstream from the nozzle the maximal value of electric field was about 10 kV/cm. Contrarily, when a grounded electrode is present, a maximal electric field of 20 kV/cm is obtained [4]. This suggests great influence of target on jet properties.

2   Experimental

In this study, we present our recent research on helium plasma jet interacting with the liquid surface. Here we focus on spatially resolved measurements of electric field strength along the jet axis when water is positioned at different distances from the jet nozzle. The atmospheric pressure plasma jet in use has already been described in detail [5, 6]. Powered electrode is needle with the inner diameter of 0.8 mm centered inside the Pyrex capillary (inner diameter 2.5 mm, outer diameter 4 mm). Metal ring on the outer side of the capillary is used as the grounded electrode. The thickness of the ground was 3 mm, and the gap between the two electrodes was 5 mm, while the distance from the grounded electrode to the end of capillary was 20 mm. Helium flow was set to 1000 SCCM by mass flow controller. The power supply provided a sine voltage at 2 kV in amplitude and 30 kHz frequency. Petri dish filled with

distilled water was positioned at two distances, 5 mm and 10 mm, downstream from the jet nozzle. Electric field strength was measured by non-perturbing method based on Stark effect of helium lines developed by Kuraica and Konjević [7], and it was already applied for the electric field measurements in He plasma jets [4, 8, 9].

3 Results

The electric field measurements are presented in Fig. 1. Figure 1 shows the distribution of the electric field along the plasma plume as a function of the distance of the water surface from the capillary. It is clear that measured electric field rises with the distance from the capillary reaching the maximum value of about 20 kV/cm at the water surface when the distance is 5 mm and about 25 kV/cm when the distance is 10mm. Also, decrease of the distance leads to steeper increase of the electric field.
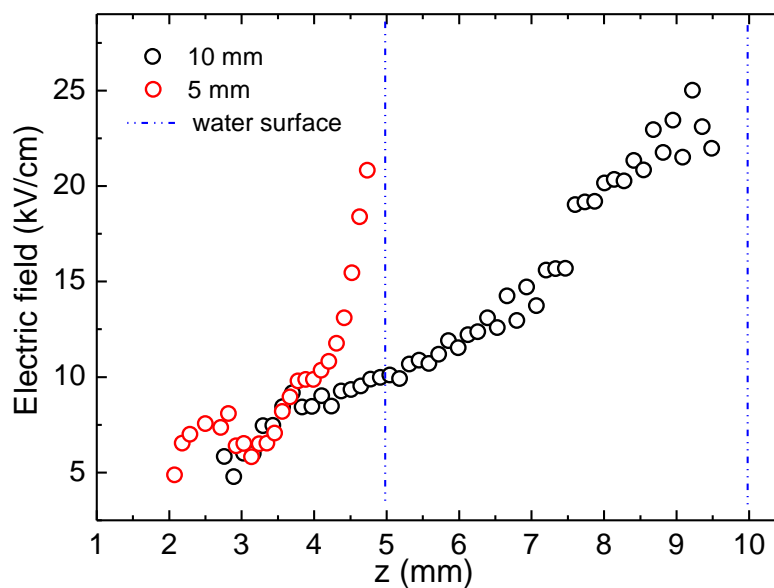
Fig. 1: Electric field strength in the plume of the plasma jet as a function of the distance between jet nozzle and distilled water surface as a target.

Acknowledgements

References

1. T. von Woedtke et al., Phys. Rep. 530, 291 (2013)
2. D. B. Graves, J. Phys. D. Appl. Phys. 45, 263001 (2012)
3. M. Moisan et al., J. Phys. D. Appl. Phys. 47, 285404 (2014)
4. G. B. Sretenović et al., J. Phys. D. Appl. Phys. 47, 102001 (2014)
5. A. Sobota et al., Plasma Sources Sci. Technol. 23, 025016 (2014)
6. O. Guaitella et al., J. Phys. D. Appl. Phys. 48, 255202 (2015)
7. M. M. Kuraica et al., Appl. Phys. Lett. 70, 1521 (1997)
8. G. B. Sretenović et al., Appl. Phys. Lett. 99, 161502 (2011)
9. G. B. Sretenović et al., IEEE Trans. Plasma Sci. 40, 2870 (2012)

DETECTION OF PLASMA-JET-GENERATED PRESSURE WAVES IN GAS AND LIQUID PHASES USING FIBERED OPTICAL WAVE MICROPHONE MEASUREMENT

S. Kusumegi[1], F. Mitsugi[1], T. Kawasaki[2], T. Nakamiya[3], Y. Sonoda[3]

[1]Kumamoto University, 2-39-1 Kurokami, Kumamoto, Kumamoto 860-8555, Japan
[2]Nippon Bunri University, 1727 Ichigi, Oita, Oita 870-0397, Japan
[3]Tokai University, 9-1-1 Toroku, Kumamoto, Kumamoto 862-8652, Japan

E-mail: kusumegishota@gmail.com

When irradiated atmospheric plasma jet to liquid target, induces a stream of reactive oxygen or nitrogen radicals generated by plasma jet from the liquid surface to the bottom under limited conditions. Pressure waves can be considered to be one of possible forces that concern with the stream in liquid targets because we succeeded to detect pressure waves generated by plasma jets in air with a fibered optical wave microphone. In this work, the fibered optical wave microphone measurement was done in gas and liquid phases to investigate frequency properties of the plasma-generated pressure waves.

Keywords: plasma; plasma jet; pressure wave; fibered optical wave microphone

1 Introduction

Reactive oxygen and nitrogen species generated by atmospheric pressure plasma jets is about to be applied for microbes treatment, bacteria inactivation, protein destruction, wound healing, plasma medicine, cancer treatment, and plant's growth. We have focused particularly on an energy transfer from plasma to atmosphere in the form of shock waves or sound waves [1-3]. In this work, as a fundamental study, frequency and gas flow dependence on the generation of pressure waves at the downstream of plasma jets in atmosphere was investigated with the fibered optical wave microphone.

2 Experimental Methods

A schematic illustration of the experimental setup for the fibered optical wave microphone measurement on pressure changes caused by plasma jets was shown in Fig. 1. Principles of optical wave microphones were described in other references [4-8]. The device of a dielectric barrier discharge plasma jet [9] was made of a glass tube (8.0 mm in outer diameter, 2.5 mm in inner diameter) with wrapped powered and grounded electrodes (13 mm in width) separated each other by 20 mm on the tube. The powered electrode was located at 10 mm away from the tip of the glass tube. Helium gas was supplied into the glass tube with the flow rate of 1-10 L/min. Sinusoidal high voltage (10 kV) was applied to the powered electrode. The applied voltage and current waveforms were monitored through a high voltage probe and a current sensor, respectively using an oscilloscope.

3 Results and Discussion

Adjusting the frequency of applied voltage to a specific frequency at a gas flow rate enhances the generation of relatively strong pressure waves with a single-frequency. Optimum frequencies of the applied voltage to generate single-frequency pressure waves from plasma

jets were decided using Fast Fourier Transform (FFT) analysis of fibered optical wave microphone waveforms at different gas flow rates.
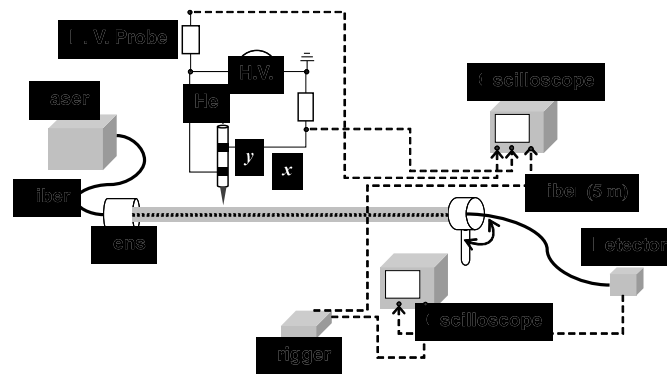
Fig. 1: A schematic illustration of the experimental setup of the dielectric barrier discharge plasma jets and the fibered optical wave microphone system.

One of typical examples of single-frequency pressure waves is introduced here. The probe laser of the fibered optical wave microphone passed at 1 mm below the tip of the glass tube. When the frequency of the applied voltage was set to the same frequency as the specific frequency of the glass tube (3.9 kHz), stronger pressure waves with a single-frequency (3.9 kHz) could be observed at the downstream of the device, as shown in Fig. 2.
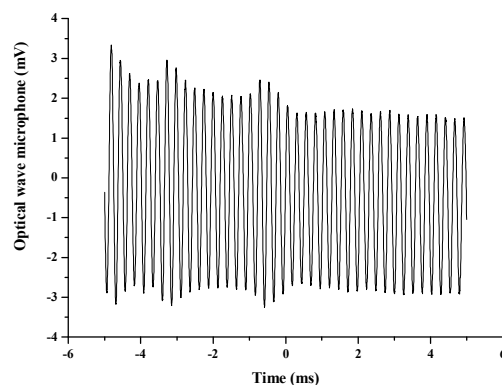
Fig. 2: Typical fibered optical wave microphone waveforms with a single-frequency observed in atmosphere for 3.9 kHz at the He gas flow rate of 10 L/min.

4   Conclusion

In this work, the fibered optical wave microphone measurement was used in atmosphere to investigate frequency properties of the generation of pressure waves from plasma jets in advance of measurement of pressure waves in water irradiated by plasma jets. Optimum frequencies of the applied voltage to generate single-frequency pressure waves from plasma jets should be adjusted to specific frequencies of the glass tube that depend on gas flow rates. Based on these results, investigation on the detection of pressure waves in water is now in progress. We are simultaneously trying to observe flows in water induced by pressure waves.

References
1. T. Nakamiya et al., J. Adv. Oxid. Tech. 14, 63 (2011)
2. F. Mitsugi et al., Przeglad Elektrotechniczny 88, 105 (2012)
3. T. Nakamiya et al., Eur. Phys. J. Appl. Phys. 61, 24310 (2013)
4. D. E. Evans et al., Plasma Phys. 24, 819 (1982)
5. Y. Sonoda et al., Jpn. J. Appl. Phys. 21, L372 (1982)
6. D. E. Evans et al., Plasma Phys. 25, 617 (1983)
7. Y. Sonoda et al., Jpn. J. Appl. Phys. 23, 1412 (1984)
8. Y. Sonoda et al., Jpn. J. Appl. Phys. 33, 3110 (1994)
9. T. Kawasaki et al., Jpn. J. Appl. Phys. 54, 086201 (2015)

OPTIMIZATION OF KINETIC SCHEMES FOR HELIUM APPJs WITH HUMID AIR IMPURITY FOR TWO-DIMENSIONAL FLUID MODELS USING THE ELEMENTARY EFFECTS METHOD

A. Obrusník[1], Z. Bonaventura[1]

[1]*Dept of Physical Electronics at the Faculty of Science, Masaryk University, Kotlarska 2, Brno, CZ*

E-mail: adamobrusnik@physics.muni.cz

This contribution focuses on simplification of a reaction scheme for atmospheric pressure plasmas using the elementary effects method which is well established in various fields. The aim is, first of all, to reduce the number of species that have to be included in the model and secondly to reduce the number of reactions by neglecting reactions that are comparably slower in the relevant range of conditions. Such reaction schemes should then enable development of 2D or 3D fluid models of plasma chemistry, which would otherwise be too computationally expensive.

Keywords: helium APPJ; reaction kinetics; reaction scheme; elementary effects method

1   Introduction and state of the art

Numerical modelling of atmospheric-pressure plasma jets (APPJs) and the plasma chemistry therein is currently very desirable especially in the light of recently reported promising applications of these sources [1, 2]. Additionally, the number of empirical works dealing with the applications of these discharges dramatically exceeds the number of works on their characterization, meaning that the chemical reaction pathways in these plasmas remain largely unknown. Furthermore, a concise model capable of capturing both the plasma ignition mechanism and the detailed chemistry leading to production of the active species of interest (e.g. hydroxyl radical, superoxide, nitrite or nitrate) in close-to-real geometry is not yet available.

For a proper description of the plasma-chemical processes taking place in the APPJs, at least a two-dimensional model is required. This is due to the fact that the plasma is ignited in helium with an admixture of molecular gases and subsequently discharged into ambient air. The admixing of ambient air does speed up certain reactions in the plasma afterglow, which cannot be captured using a zero-dimensional or one-dimensional codes. The two-dimensional models published so far focus predominantly on the plasma sustainment mechanism and do not contain the complete reaction scheme leading to active species formation [3, 4] while available models of the full plasma chemistry are only zero-dimensional, containing over a thousand reactions [5].

In order to develop a two-dimensional model which would, at reasonable computational costs, describe both the processes in the active plasma and the pathways leading to generation of active species, the reaction schemes have to be strongly optimized, leaving out particularly those species which are not of interest for the applications and exhibit negligible

concentrations. Subsequently, it is also desirable to reduce the number of reactions. At the same time, it has to be taken into account that many of these species and reactions can have nonlinear effect (e.g. species that act as intermediate species). The first study of this kind in plasma physics has been published very recently [6] and focuses on simplification of a reaction scheme of helium/oxygen plasma.

2 The method

The method that is incorporated for the simplification of the reaction scheme is the Elementary effects method according to Morris [7], which has been further developed and refined by Campolongo *et al* [8]. The fundamental idea is to carry out a number of runs of the complete 0D numerical model and then perform statistical analysis of the quantities called elementary effects. An elementary effect of *i*-th model input on the model output is defined as

$$d_i = \frac{[Y(\mathbf{X} + \Delta \mathbf{e}_i) - Y(\mathbf{X})]}{\Delta}$$

where *Y* is any of the model outputs, $\mathbf{X}$ is the vector of model inputs normalized to the interval 0 and 1, $\mathbf{e}_i$ is a vector which has zero in nearly all positions and one on *i*-th position and Δ is a number between 0 and 1. For each input parameter, several elementary effects have to be calculated and from their standard deviation and mean value, the importance of this particular input parameter is assessed.

As already mentioned, the aim of this work is to reduce both the number of species and the number of reactions in the kinetic scheme. To that end, the following two-step procedure is applied:

1. **Elimination of unimportant species**
   The model will have *N* input parameters denoted m_i where *N* is the number of species. The parameter m_i is either increasing or decreasing the rates of all reactions producing *i*-th species and the influence of these changes on the remaining species is analyzed.

2. **Elimination of unimportant reactions**
   Similar to [6], the sensitivity of the model to individual rate coefficients will be studied. This will help to identify reactions, to which the model is insensitive.

Once the reaction scheme is optimized and validated against their complete counterpart, it can be incorporated in 2D fluid models. The simplified reaction scheme in this work is derived from the very comprehensive scheme by Murakami *et al* [5,9].

References

1. A. R. Gibson et al., Plasma Process. Polym. 11, 1142 (2014)
2. D. B. Graves, Plasma Process. Polym. 11, 1120 (2014)
3. G. V Naidis, J. Phys. D. Appl. Phys. 44, 215203 (2011)
4. X. Y. Liu et al., Plasma Sources Sci. Technol. 23, 035007 (2014)
5. T. Murakami et al., Plasma Sources Sci. Technol. 23, 025005 (2014)
6. M. M. Turner, Plasma Sources Sci. Technol. 24, 035027 (2015)
7. M. D. Morris, Technometrics 33, 161 (1991)
8. F. Campolongo et al., Environ. Model. Softw. 22, 1509 (2007)
9. T. Murakami et al., Plasma Sources Sci. Technol. 22, 045010 (2013)

CHARACTERIZATION OF ATMOSPHERIC NANOSECOND DISCHARGE UNDER HIGHLY INHOMOGENEOUS AND TRANSIENT ELECTRIC FIELD IN AIR/WATER MIXTURE BY OES AND PLIF

K. Ouaras, P. Tardiveau, L. Magne, P. Jeanney, B. Bournonville

Laboratoire de Physique des Gaz et des Plasmas, Paris-Saclay University, 91400, Orsay, France

E-mail: karim.ouaras@u-psud.fr

We report the studies of a centimeter range pin-to-plane nanosecond repetitively discharge (< 30 ns and 10 Hz) in standard conditions of pressure and temperature under very high positive voltage pulses (20 to 100 kV). This kind of discharge is not well understood and requires a fine description of plasma dynamic and behavior under relevant context (air depollution) using pertinent gas (humid air). Thus, after a brief description of the discharge, we will focus on determination of rotational and vibrational temperature (OES) and preliminary results concerning the production and evolution of OH radical in temporal post-discharge in air/water mixture (PLIF).

Keywords: nanosecond pulsed discharge; pin-to-plane discharge; OH dynamics; imaging

1   Introduction

Atmospheric plasma improvement for environmental issues [1-2] but also for biomedical [3] and material processing [4] is highly desirable. In depollution context, it is necessary to: (i) enhance pollutant degradation by improve plasma device characteristics and (ii) better understand the role of radicals (*e.g.* OH) which play a major role in non-thermal plasma reactions paths [5-7]. In our case, we use a non-equilibrium centimeter range gap air (or humid air) discharge based on the use of five or ten times higher voltage than classical steady-state breakdown levels. This kind of discharge is still an understudied area [9-13]. Thus, our general motivation is to understand plasma physics which governs the formation of this particular diffuse discharge (cf. fig.2) obtained in these extreme conditions and apply it as an eventual environmental plasma process considering its high potentials features (stabilized, diffuse and radially extended discharge). Thus, in parallel of sub-nanosecond discharge imaging used for study plasma propagation and behavior, we undertake OES measurements to determine typical plasma parameters and PLIF (Planar Laser Induced Fluorescence) in order to study spatially and temporally the OH radical behavior in humid air conditions.

2   Experimental

The fig.1 shows a schematic of the experimental set-up including the pin-to-pin reactor (with high voltage power supply) and all implemented diagnostics (described in following section).
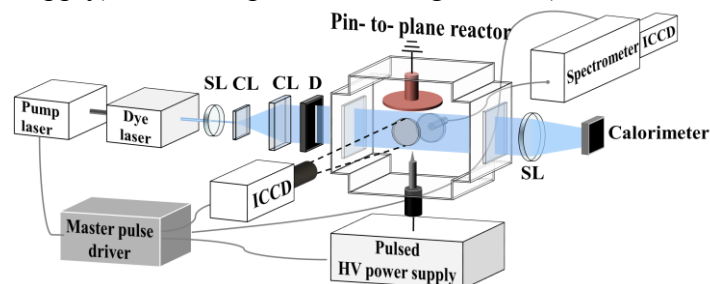
Fig. 1: Schematic description of the experimental set-up: SL=spherical lens; CL=cylindrical lens; D= diaphragm.

2.1 Discharge reactor and characteristics

The discharge is generated between a grounded copper plane (ø =80 mm) and a molybdenum pin with curvature radius of 10 µm. The pin is connected to pulsed nanosecond high voltage (HV) supply which ensures a frequency range between 5 to 100 Hz and voltage between 20 to 100 kV. This reactor presents a large range of flexible parameters: (i) material nature (Tungsten, Copper, Molybdenum) and curvature radius (10, 50, 100 and 200 µm) of the pin; (ii) pin-to-plane distance (d_{p-p}=10 to 30 mm). Moreover, the HV supply is composed of three channels (Channel 1 to 3) and each one offers the possibility to access to a couple of voltage rise time and discharge duration (2 ns/~ 10 ns: Channel 1; 2.8 ns/~ 20 ns: Channel 2 and 5.2 ns/~ 30 ns: Channel 3). A complete study and description of the device can be find in [13]. With this reactor set-up and characteristics, we obtain a more diffuse and stabilized discharge in space and time as comparison with classical streamers [13]. The fig.2 shows a picture of the discharge in typical condition of stabilized air plasma obtained with sub-nanosecond (time gate of 200 ns) imaging (4-picos ICCD from Stanford Computer Optics).
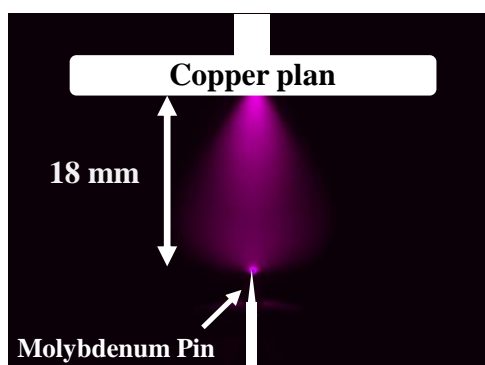
Fig. 2: Picture of plasma discharge. Experimental conditions: Channel1/65 kV/10 Hz/Air/d_{p-p}=18 mm.

2.2 Diagnostics

In addition to systematic discharge imaging, synchronized spectroscopic characterizations are conducted in order to describe and qualify plasma properties. OES was used to determine rotational and vibrational temperature and PLIF measurements were recently undertaken in order to determine OH radical creation and evolution in temporal post discharge (humid air).

2.2.1. Optical Emission Spectroscopy

Experiments were conducted using a 75 cm focal length imaging spectrometer (Acton SP 2750 PI) equipped with an ICCD camera (PI-MAX 2 of Princeton instruments) which allows time gate resolution of 3 ns. The optical system (lens+fiber) is located to collect light perpendicular to the plasma. We principally use a 2400 groove.mm $^{-1}$ grating to maximize spectral resolution (down to 0.04 nm) in order to describe rotational lines of the second positive system (C-B) of N_2 (which is the most intense system in our conditions). For rotational temperature (T_{rot}) determination we use the emission of the (0,0) vibrational band of N_2 (C-B) with a fitting procedure given by [14]. For vibrational temperature (T_{vib}), we use the emission of (3,5), (1,3) and (0,2) bands of N_2 (C-B) with a procedure (Boltzmann plot's) described in [15].

2.2.2 Planar Laser Induced Fluorescence

A frequency-doubled pulsed Nd:YAG laser (YG 980 Quantel) was used to pump a dye laser (TDL 90 Quantel) with Rhodamine 590. The $P_1(2)$ transition (well isolated line) of the OH (X-A) system is used to obtain temporally and spatially LIF measurements. Before passing the discharge the laser beam is extended into a sheet by means of cylindrical lenses and its

size was modulated with a diaphragm in order to coincide with inter electrode space. The OH profile is obtained by the same ICCD which was used for discharge imaging and was equipped with a UV filter (308 nm +/- 10 nm). Because of time limitation induced by the pulser system, the post discharge can be probed only after ~ 400 ns.

3   Results and Discussion
3.1   Temperature determination
Temperature was determined as function of: (i) gas mixtures (pure air; 0.5 and 1.5 % of water diluted in air); (ii) voltage (65, 75 and 85 kV); (iii) Channel 1 and 2 which correspond respectively to discharge duration of ~ 10 and 20 ns; (iv) for fixed frequency (10 Hz), gas flow rate of 1 l.min^{-1} and pin-to-plane distance of 18 nm. We consider here that rotational temperature is equal to the gas temperature (fast rotational-translational relaxation at atmospheric pressure) [16]. The fig.3 presents results obtained in conditions mentioned above. The fig.3.a and b represent respectively the rotational and vibrational temperature evolution. In fig.3.a, we can observe that the gas temperature (T_{rot}) is mostly strongly influenced by the discharge duration (i.e. Channel used). For lower time duration (channel 1), T_{rot} is quite similar for all experimental conditions. For higher time duration (channel 2), we can note that the evolution of gas temperature is closely related to water content, especially when the voltage is high (85 kV).
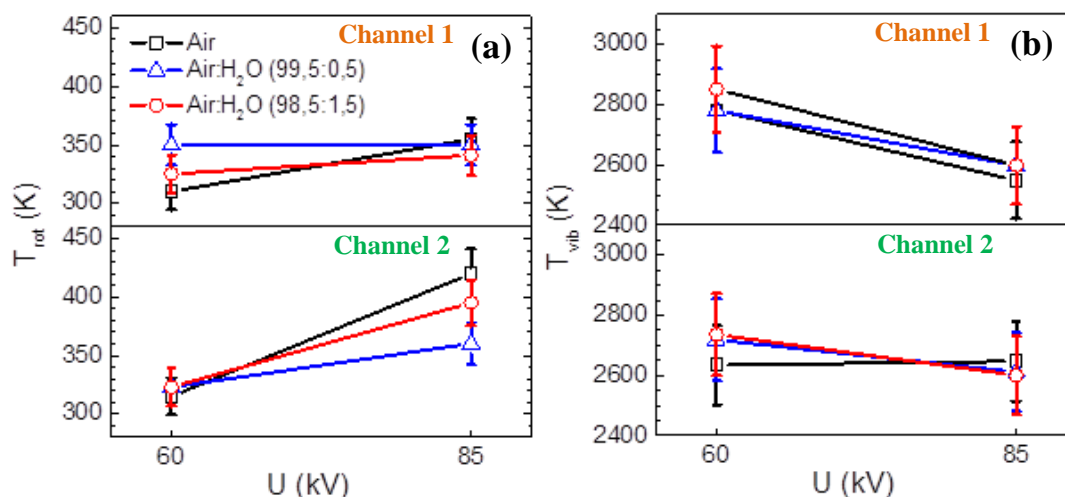
Fig.3: Evolution of T rot (a) and Tvib (b) as function of channel, voltage and gas mixture.

For vibrational temperature (cf. fig.3.b), the trend is reversed. The channel 1 is the most conducive to strongest evolutions. Even if T_{vib} are in same range (2600 to 2800 K) for all conditions, we can note a net decrease of T_{vib} for lower time duration when the voltage increases. This is quite difficult to ascertain an explanation because of vibrational temperature evolution can be correlated to a number of plasma parameters (n_e, T_e, ionization degree…). Furthers investigations will be undertaken to determine plasma parameters (n_e by stark broadening) as well as reduced electric filed (using N_2^+ and N_2 emission lines ratio) in order to give an objective interpretation of these evolutions.

3.2 OH profile: preliminary results
As a preliminary result, we present in fig.4 a profile of OH intensity obtained approximately 400 ns and 10 μs after plasma extinction for typical conditions of stabilized discharge with 0.5 % of water diluted in air. This image is obtained by the treatment of three images: (i) the image of the fluorescence; (ii) the image of laser without fluorescence and (iii) the image of the sheet profile obtained with acetone without plasma. We observe that OH intensity is

higher in pin and plane region (creation zone). This experimental works will serve to validate future kinetic modeling of the discharge for pollutant abatement context.
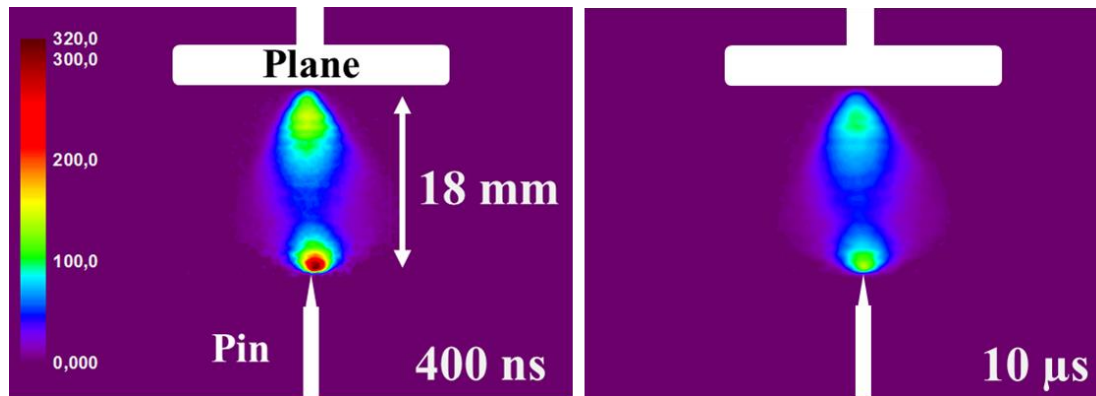
Fig4: Temporal post discharge OH profile obtained by PLIF measurements (400 ns and 10 μs after plasma extinction). This figure is presented with same intensity scale for a better direct comparison. Experimental conditions: Air/Water (99.5:0.5) / 65 kV/10 Hz / Channel 1 / d_{p-p}=18 mm.

References

1. S. Pasquier et al., Plasma. Phys. Control. Fusion. 55, 12 (2013)
2. G. J. J. Winands et al., J. Phys. D: Appl. Phys. 39, 14 (2006)
3. G. Y. Park et al., Plasma Sources Sci. Technol., 21, 4 (2012)
4. D. Mariotti et al., J. Phys. D: Appl. Phys. 44, 17 (2011)
5. L. Magne et al., J. Phys. D: Appl. Phys. 40, 10 (2007)
6. L. Magne et al., J. Phys. D: Appl. Phys. 42, 16 (2009)
7. T. Verreycken et al., J. Phys. D: Appl. Phys. 42, 16 (2012)
8. E. G. Danchenko et al., Tech. Phys. 50, 876-880 (2005)
9. I. D. Kostyrya, Tech. Phys. Lett. 31, 457-460 (2005)
10. I. D. Kostyrya, Tech. Phys. 50, 881-885 (2005)
11. A. G. Rep'ev et al., Plasma Phys. Rep. 32, 72-78 (2006)
12. P. Tardiveau et al., J. Phys. D: Appl. Phys. 42, 175202 (2009)
13. P. Tardiveau et al., submitted to Plasma Sources Sci. Technol. 2016
14. R. P. Cardoso et al., J. Phys. D: Appl. Phys. 40, 5 (2007)
15. K. Gazeli et al., J. Appl. Phys., 117, 093302 (2015)
16. M. Capitelli, Plasma Kinetics in Atmospheric Gases (Springer, 2000)

A COMPARATIVE STUDY OF AIR PLASMA INDUCED DEGRADATION OF PERFLUOROOCTANOIC ACID (PFOA) IN WATER UNDER DIFFERENT DISCHARGE REGIMES

E. Marotta[1], L. Nani[1], A. Giardina[1], F. Tampieri[1], R. Gobbo[2], C. Paradisi[1]

[1]*Department of Chemical Sciences, University of Padova, Via Marzolo 1, 35131 Padova, Italy*
[2]*Department of Industrial Engineering, University of Padova, Via Gradenigo 6/A, 35131 Padova, Italy*

E-mail: cristina.paradisi@unipd.it

Perfluoroalkyl substances (PFAs) are very inert and thus persistent organic pollutants presently causing great concern for the water reservoirs in northern Italy. We report here and discuss the results of a comparative study in which air non-thermal plasma is produced above PFAs-contaminated water by different types of discharges (DC, positive or negative, and AC in a dielectric barrier electrode configuration).

Keywords: perfluoroalkyl substances (PFAs); perfluorooctanoic acid (PFOA); water treatment by air NTP; comparison of different discharge regimes

1 Introduction

Perfluoroalkyl substances (PFAs), notably sulfonates and carboxylates, are man-made chemicals widely used in or released by many different processes and products including surface treatment of textiles and paper, production of fluoropolymers, paints, cosmetics [1]. Due to their great chemical and photochemical stability and solubility in water they are highly resistant to degradation in the environment and undergo very efficient transport. These combined features lead to diffusion and persistence [1]. Although some of these compounds have been in use for a long time, their capillary presence in major water reservoirs in Italy, especially in its northern Veneto region, has only recently been detected and quantified raising great concern in the governance and the public [2]. The toxicity of these compounds and their removal from contaminated waters are still issues of study and debate. The normal stages used for the degradation of organic matter in water treatment plants are not effective in the removal of PFAs which are usually eliminated by filtration on active materials [2]. We will report the results obtained in a study in which we subjected PFOA (perfluorooctanoic acid), used as model PFA, to air plasma treatment under different discharge conditions (DC of either positive or negative polarity and DBD discharge by AC voltage). The results will be discussed also with reference to previously reported plasma based treatments, including work by Yasuoka et al. [4] and Takeuchi et al [5].

2 Experimental

Two plasma reactors have been used (Fig. 1). In both HV is applied to parallel wires (2 [6] or 7 wires, depending on the reactor) placed in the air volume above the water to be treated at a few mm distance from the liquid surface. For experiments with AC voltage (50 Hz), the external bottom surface of the reactors was painted with colloidal silver and connected to

ground through a metal plate. In addition, experiments with DC voltage of positive or negative polarity were carried out the the 7-wires reactor. For these experiments the bottom part of the 7-wires reactor was substituted with one having an inox plate connected to ground placed inside directly in contact with the solution. Experiments were carried out at constant applied voltage and the decay of the organic pollutant monitored by LC-ESI-MS analysis of aliquots withdrawn at different treatment times.
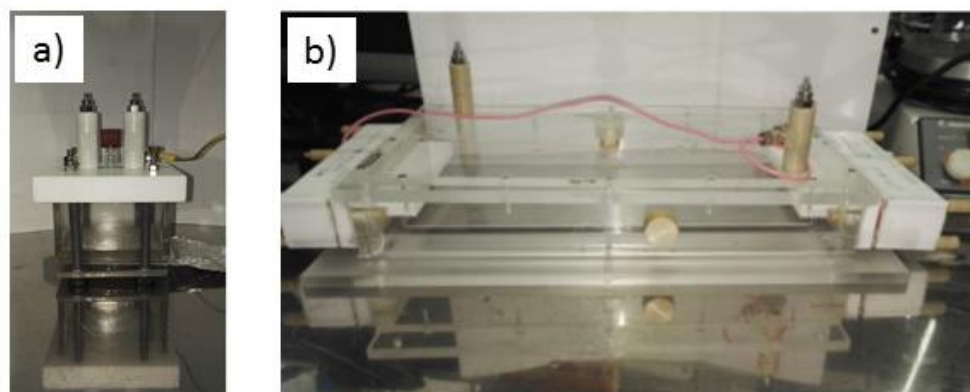
Fig. 1: Plasma reactors used in this work: a) 2-wires reactor [6] and b) 7-wires reactor.

3   Results and Discussion

Experiments were carried out using different initial concentrations of PFOA ($1 \cdot 10^{-4}$, $1 \cdot 10^{-5}$ and $5 \cdot 10^{-6}$ M) in MilliQ water and applying the discharge for long treatment times. LC-ESI-MS analysis of aliquots of the solution withdrawn at different treatment times provided concentration vs time profiles which in turn yielded conversion and kinetic data. LC-MS analysis showed that decay of the PFOA occurs by C-C bond cleavage yielding homologues of the precursor with shorter chain lengths. One example is shown in Fig. 2 for an experiment run with DC- and an initial PFOA concentration of $1 \cdot 10^{-5}$ M.
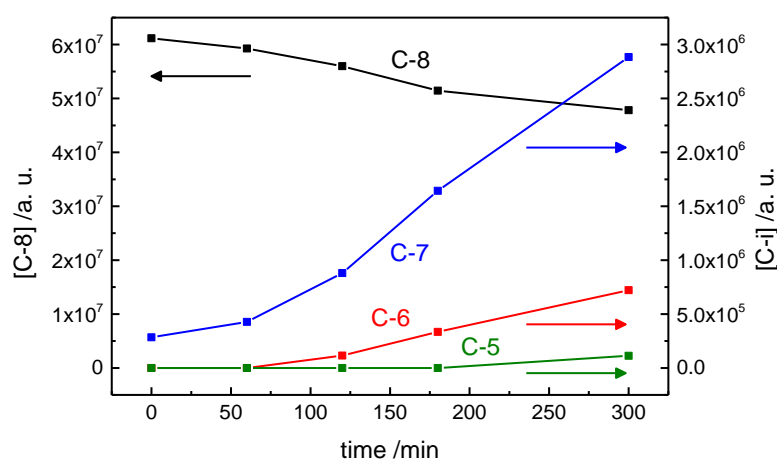
Fig. 2: Time profile for decay of PFOA (initial concentration $1 \cdot 10^{-5}$ M) and for formation of degradation products during treatment with DC- in MilliQ water in the 7-wires reactor. C-7, C-6 and C-5 are short notations for $C_nF_{2n+1}COO^-$ with n = 6, 5 and 4, respectively.

Our results show that with DC- the initial concentration of PFOA does not influence much the efficiency of the process. Treatment with DC+ the 7-wires reactor is completely ineffective in decomposing PFOA. In the case of DBD discharges in the 2-wires reactor, the removal efficiency depends inversely on the PFOA initial concentration. With an initial concentration of $5 \cdot 10^{-6}$ M about 50% of PFOA is removed in 5 hours.

The results will be discussed with reference to possible reaction mechanisms and compared with previously published data [4, 5].

4   Conclusion

Our study confirms that PFAs are recalcitrant substrates also under the harsh oxidizing conditions of non-thermal air plasmas. The degradation proceeds by cleavage of C-C bonds along the alkyl chain producing homologues of the precursor pollutant characterized by shorter chain length. The process efficiency depends on the type of discharge applied, a result attributed to the different distributions and densities of short-lived reactive species achieved under the different regimes.

Acknowledgments

References

1. K. Prevedouros et al., Environ. Sci. Technol. 40, 32 (2006)
2. M. F. Rahman et al., Water Research 50, 318 (2014)
3. S. Valsecchi et al., Chemosphere 129, 126 (2015)
4. K. Yasuoka et al., Plasma Sources Sci. Technol. 20, 034009 (2011)
5. N. Takeuchi et al., IEEE Trans. Plasma Sci. 39, 3358 (2011)
6. E. Marotta et al., Chem. Eng. J. 292, 35 (2016) and refs. cited therein.

PLASMA PROCESSING OF DRY AND WET CELLULOSE-BASED MATERIALS

J. Pawlat[1], P. Terebun[1], M. Kwiatkowski[1], U. Cvelbar[2], M. Modic[2], H. Puliyalil[2],

[1]*Institiute of Electrical Engineering and Electrotechnologies of Lublin University of Technology, ul. Nadbystrzycka 38a, 20-618 Lublin, Poland*
[2]*Jozef Stefan Institute, Department of Surface Engineering and Optoelectronics, Teslova 30, 1000 Ljubljana, Slovenia*

E-mail: askmik@hotmail.com

Cellulose-based paper of 90 g/mm^2 grammage as a perspective platform for antibiotic sensitivity tests was selected as a model material for plasma treatment for enhancement of wettability. Influence of the flow rate and gas type, power of the discharge, and distance from the nozzle was examined. Dry-treated and wet-treated paper properties were compared using goniometric tests, XPS and AFM tools. RF plasma jet allowed to decrease surface contact angle in both cases without drastic changes in other features of tested material.

Keywords: atmospheric pressure plasma; RF plasma jet; surface modification; paper

1   Introduction

Atmospheric pressure plasma based methods with their flexibility and variety of reactor constructions offer many application possibilities for instance in environmental engineering, agriculture, medicine and technology [1-3]. Plasma can clean, activate and further modify several tens of nm depth surface and offer great flexibility combining many active factors including ions, radicals, electrons, neutrals, metastables and photons in dependence on the substrate gas, treated substrate (in gaseous, liquid or solid state), geometry of the reactor and electric power supply parameters [4-9]. Thus, environmental friendly plasma process can be tailored to the product, decrease number of steps in operation cycle and reduce cost of treatment. In this work, influence of RF atmospheric pressure plasma jet treatment on basic surface properties of dry-treated and wet-treated paper.

2   Experimental

A biodegradable polymer preserves its mechanical strength and other material performance characteristics during practical application, after which is degraded to low molecular weight compounds such as H_2O, CO_2 and other non-toxic by-products. Cellulose (Fig. 1.) and cellulose-derivatives based natural polymers fulfill above conditions and are one of most abundant natural materials on earth as they can be obtained from various algae, bacteria and plants.
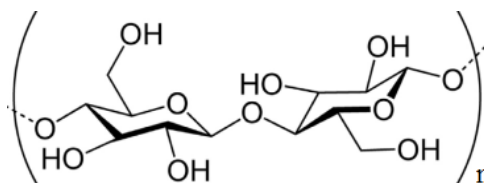
Fig. 1: Molecular structure of cellulose.

In this study, the measurements were performed using radio frequency plasma jet with stainless steel, high voltage electrode inside the nozzle. Experimental set-up configuration is depicted in Fig. 2. The reactor operated at the atmospheric pressure, which facilitates the plasma treatment and can allow a significant reduction in cost of the process in industrial applications. Power supply used a resonant circuit that allowed adjust the discharge power up to 50 W. Cellulose-based, elemental chlorine free paper of 90 g/mm^2 grammage with calcium carbonate as a filler was used as a sample. Samples' transparency and thickness ranged 93% and 98 μm, respectively. Pure water was used as sample liquids for dipping paper for 60 s prior to treatment and as a liquid in Kruss DSA25E goniometer. The chemical modifications on the surface were analyzed with X-ray photoelectron spectroscopy - XPS (TFA XPS Physical Electronics).

3   Results and Discussion

Surface contact angles were measured for paper in dry state and for paper, which was dipped for 60 s in pure water prior to plasma treatment. The results obtained for paper treated in dry state and the different working gases indicated that the smallest increase of wettability was observed for a mixture of helium and air, where the contact angle remained almost unchanged regardless of the time of treatment. Enhancement of wettability obtained for mixtures containing oxygen can be explained by greater amount of oxygen radicals (like ozone) which can influence the behavior of the sample surface. Paper, which was dipped in pure water for 60 s prior to the treatment shows similar tendency as paper treated in dry state. XPS survey spectra (Fig. 2, Tab. 1,) showed that plasma treatment increased oxygen content as well as nitrogen content compared to the reference dry sample, which is expected to be as an after effect of plasma functionalization. At the same time, carbon content was decreased after various plasma treatments. Interestingly, 50 W He/O_2 treated wet paper sample had less nitrogen compared to all other plasma treated samples. Probably the water somehow quench nitrogen incorporation during this treatment.
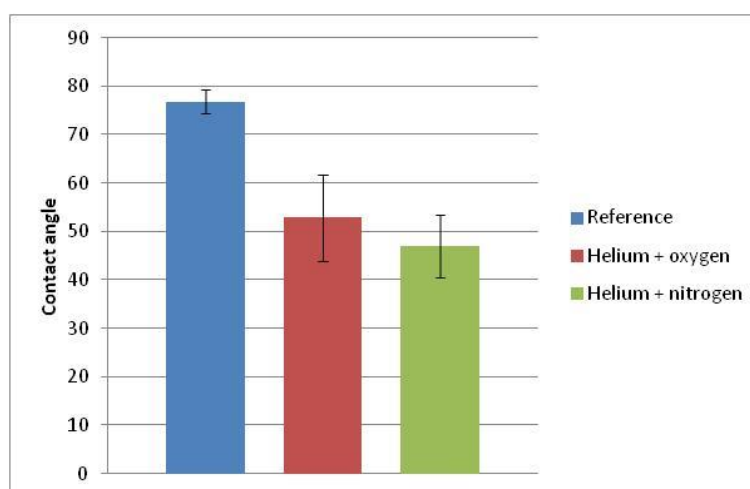
Fig. 2: The contact angle change after 60 s dipping in pure water prior to 1 min plasma treatment in dependence on substrate gas (distance 3 cm).

Tab. 1: Elemental composition from the XPS survey spectrum.

Sample	Carbon (%)	Oxygen (%)	Nitrogen (%)	Calcium (%)
Sample without treatment	67.9	30.7	0.9	0.5
Wet paper	64.5	34.5	0.8	0.2
Dry paper treated with 50 W He/O_2 plasma	63.3	34.2	1.8	0.7
Dry paper treated with 50 W He/N_2 plasma	61.2	36.4	1.8	0.6
Wet paper treated with 50 W He/O_2 plasma	61.6	37.5	0.4	0.7
Wet paper treated with 50 W He/N_2 plasma	61.8	36.1	1.7	0.5

4   Conclusion

RF atmospheric pressure plasma jet operating with various gas mixtures can be a flexible tool for increasing of paper's surface wettability. Treatment of paper dipped in pure water prior to the plasma treatment revealed different functionalization paths. RF plasma jet can be used for a non destructive surface treatment of cellulose based materials for biotechnological application.

References

1. K. Hensel et al., Biointerphases 10(2) 029515 (2015)
2. H. Stryczewska et al., JAOTs, 1(16), 23 (2013)
3. J.-L. Brisset et al., Plasma Chem. Plasma Proc. 36(2), 355 (2016)
4. J. Pawlat, Eur. Phys. J. Appl. Phys. 61 (2) 24323 (2013)
5. N. Škoro et al., J. Phys. D: Appl. Phys. 46(47) 475206 (2013)
6. J. Pawłat et al., IEEE Trans. Plasma Sci. PP (99)1, (2015)
7. M. Fialová et al., Chem. Listy, 106, 1439 (2012)
8. R. Krumpolec et al., Chem. Listy, 106, 1450 (2012)
9. A. Vesel et al., Surf. Interface Analysis 40(1), (2008)

SPECTROSCOPIC STUDY OF UNDERWATER ELECTRICAL DISCHARGE GENERATED BY NANOSECOND PULSES

B. Pongrác, M. Šimek, M. Člupek, V. Babický, P. Lukeš
*Institute of Plasma Physics of the CAS, Department of Pulse Plasma Systems,
Za Slovankou 1782/3,182 00 Prague 8, Czech Republic*

E-mail: pongrac@ipp.cas.cz

Underwater electrical discharge generated by high voltage pulses with nanosecond duration (~110 kV amplitude on the needle, ~5 ns duration (FWHM), 1 Hz repetition rate) has been investigated. Time–resolved optical emission spectroscopy showed different emission spectra profile of the ns–pulsed discharge compared to the μs–pulsed discharges investigated previously. Some characteristic peaks typical for water discharges (H_α, O^I) were clearly visible in the spectra. In addition, the integral light emission of the discharge was recorded by photomultiplier tube.

Keywords: nanosecond discharge; water discharge; time-resolved emission spectroscopy

1   Introduction

Phenomena of high voltage (HV) electrical discharges generated in liquid phase are still less explored in comparison to the relatively known gas discharges. It is caused mainly due to the differences between physical properties of gas and liquid media (e.g. electrical permittivity, higher density of the liquid and specific conductivity) [1−6].

Recently, electrical discharges in liquids have been extensively studied for various environmental and medical applications. Electric fields of sufficient strength applied to a liquid can initiate physical and chemical processes, thus leading to generation of various reactive species, radicals and ultraviolet (UV) radiation. Underwater electrical discharges can be used also for generation of strong shock waves propagating inside the liquid media [3].

Pulsed electrical discharges in liquids can be generated mostly by microsecond (μs) HV pulses. However, currently with the improving of electric devices capability, it is possible to generate this kind of discharges by nanosecond (ns) or even sub−ns HV pulses. According to the theory and experimental observations, the μs−pulsed discharges in liquids are basically initiated in the gas phase (bubbles) which are formed due to the local Joule heating of liquid or even other possible mechanisms (e.g. cavitation). However, some details are still not well understood and recently some works [4, 6] have indicated that ionization in pure water without phase change can also be possible. These works report a fundamentally different type of water discharge generated without bubble formation by application of ns or sub−ns HV pulses. On such short time scale there is not enough time to form bubbles and thus the mechanism of discharge development in the liquid phase is similar to the ionization wave propagation in gases.

2   Experimental

In this experimental work we investigated the liquid-phase electrical discharge generated by HV pulses with 5 ns pulse duration (FWHM). As a liquid medium we used deionized (DI) water with conductivity ~2 µS/cm. We used a point–to–plane electrode geometry, with tungsten needle anode, and stainless steel plate cathode. Both metallic electrodes were immersed in water, with an interelectrode gap distance of 5 mm. FID HV pulse power generator was used to produce HV pulses of ~110 kV in amplitude on the HV electrode, at the repetition rate of 1 Hz. The voltage on the HV needle was estimated from the shunt measurement technique of the HV pulse propagating in the coaxial cable.

We used time-resolved optical emission spectroscopy (OES) as the main diagnostic tool. During the OES, the iCCD camera (Andor iStar) intensifier was triggered by photomultiplier tube (PMT) voltage pulse generated by discharge light emission. The complete experimental set-up is described in more details elsewhere [7].

3   Results and Discussion

The time–resolved emission spectra were measured during the discharge ignition with 3 ns or 20 ns acquisition time and with 3 ns or 20 ns time resolution, respectively. Some results for 20 ns time resolution (3 ns time resolution is not shown here) can be seen in Fig. 1. In the region 320–750 nm, we observed almost broadband emission spectra profile occurring only during the first ~20 ns. The origin of this emission is unclear and identification of the spectra is still in progress. After 20 ns, this almost continuum spectra profile gradually disappeared and some known peaks typical for water discharges initiated through bubble breakdown mechanism (e.g. H_α ~656.3 nm, O^I ~771.1 nm) emerged from the continuum [1, 5]. As can be seen also from the PMT signal of the integral light emission (sub-image of the Fig. 1), the discharge has the higher light intensity only during the first ~25 ns.
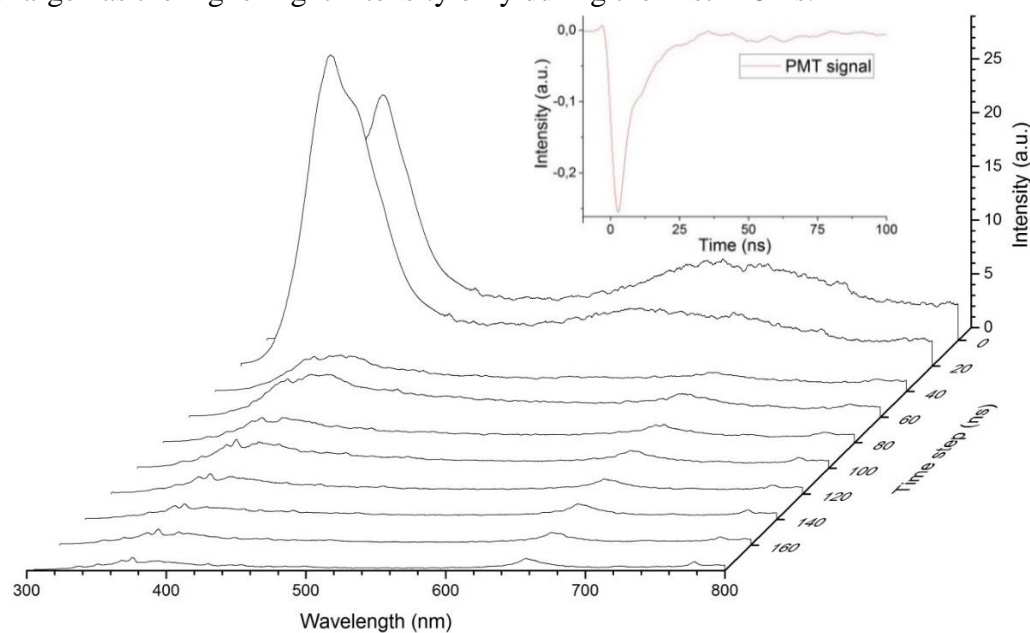
Fig. 1: Time–resolved emission spectra of the ns–pulsed discharge generated in DI water (U_{max}~110 kV, U_{width}=5 ns, f_{pulses}=1 Hz, gap= 5 mm) supplemented with the PMT signal of discharge light emission. The acquisition time of the spectra is 20 ns with time step 20 ns. Spectra are averaged over 50 accumulations. Time 0 ns approximately correspond to the ignition of the discharge.

We have not detected any other hydrogen atomic lines of the Balmer series in our spectra. The OH (A–X) molecule spectrum was also not observed, although the presence of OH radicals in water was detected by chemical analysis.

The emission spectra of a needle–to–plane streamer corona–like discharge generated by μs HV pulses in aqueous solutions were investigated in previous work [5]. Some continuum spectra profile in the region 320–750 nm observed in the present work dealing with the ns–pulsed water discharge (Fig. 1) was present also for μs–pulsed discharges (e.g. see Fig. 6 in [5]). However, there are some differences when compared these two spectra. We can notice that ns discharge spectra profile investigated in this paper is much more prominent than μs discharge spectra profile investigated previously. Moreover, the emission of the most important electronically excited species (H^I, O^I, O^{II} and OH species) were clearly visible for μs corona–like discharge.

Additional time-resolved iCCD imaging measurements of the discharge light patterns evolution are shown elsewhere [7].

4   Conclusion

This short paper deals with the experimental study of underwater electrical discharge generated by HV pulses with ns duration. Time-resolved OES showed interesting results of broadband emission spectra profile occurring only during the first ~20 ns in the region 320–750 nm. As can be seen also from the PMT signal, during the first ~25 ns the discharge has the highest light intensity. For the μs–pulsed discharge investigated previously, this kind of broadband emission spectra profile was significantly less prominent.

References
1. P. Šunka et al., Plasma Sources Sci. Technol. 8, 258 (1999)
2. P. Šunka, Phys. Plasmas 8, 2587 (2001)
3. B. R. Locke et al., Ind. Eng. Chem. Res. 45, 882 (2006)
4. A. Starikovskiy et al., Plasma Sources Sci. Technol. 20, 024003 (2011)
5. M. Šimek et al., Plasma Sources Sci. Technol. 21, 055031 (2012)
6. D. Dobrynin et al., J. Phys. D: Appl. Phys. 46, 105201 (2013)
7. M. Šimek et al., in *Book of Contributed Papers of the 15th Int. Symposium on High Pressure Low Temperature Plasma Chemistry*, Brno, 2016

INFLUENCE OF THE GAS FLOW RATE ON THE ELECTRIC FIELD STRENGTH IN HELIUM PLASMA JET

G. B. Sretenović[1], A. Sobota[2], O. Guaitella[3], I. B. Krstić[1], V. V. Kovačević[1],
B. M. Obradović[1] and M. M. Kuraica[1]

[1]*University of Belgrade, Faculty of Physics, PO Box 44, 11001 Belgrade, Serbia*
[2]*Eindhoven University of Technology, EPG, Postbus 513, 5600MB Eindhoven,
The Netherlands*
[3]*LPP, Ecole Polytechnique, Route de Saclay, 91128 Palaiseau, France*

E-mail: sretenovic@ff.bg.ac.rs

The presented paper focuses on the influence of the gas flow rate on the electric field distribution in the capillary and plume of the helium plasma jet. 30 kHz AC-driven He jet with the coaxial geometry is used in this study. For the fixed amplitude of the applied voltage of 2 kV, electric field strength is measured using Stark polarization spectroscopy for several gas flows in range of 700-2000 SCCM. It was found that the increase of gas flow doesn't change the maximal value of the electric field, but it stretches measured profile in space.

Keywords: plasma jet; electric field measurement; Stark spectroscopy

1   Introduction

Studies of breakdown and development of plasma jets, their interaction with different media and also production of active chemical species is in the focus of nonthermal plasma community in the last decade [1, 2]. The reasons for interest are physical properties of such a discharge [3] and its possible applications in the field of medicine [4, 5]. It is known that plasma jets produce streamers in noble gas (helium, argon or neon) and air mixtures, often called plasma bullets. One of the most important features of streamer is high value of the electric field in its strength [6–8]. Streamer in noble gas is also characterized by the high electric field, which is about one order of magnitude lower than the field in streamer in air [9–11]. With the knowledge of the value of the electric field in the streamer head, many other features of the streamer e.g. streamer velocity and the electron density can be determined [12].

In this study, electric field in helium plasma jet is measured by means of Stark polarization spectroscopy for different gas flows. The results of the influence of gas flow rate on the electric field in the capillary and the plume of He plasma jet are presented.

2   Experimental

The plasma jet studied in this article is coaxial configuration used in LPP-TUE collaboration [13,14]. Powered electrode is needle with the inner diameter of 0.8 mm centered inside the Pyrex capillary (inner diameter 2.5 mm, outer diameter 4 mm). Metal ring on the outer side of the capillary is used as the grounded electrode, as illustrated in the schematics in Fig. 1. The thickness of the ground was 3 mm, and the gap between the two electrodes was 5 mm, while the distance from the grounded electrode to the end of capillary was 20 mm for the entire

study. Helium flow through the capillary is regulated using mass flow controller in range of 700-2000 SCCM. The jet is powered by sine voltage at 30 kHz, 2 kV in amplitude.
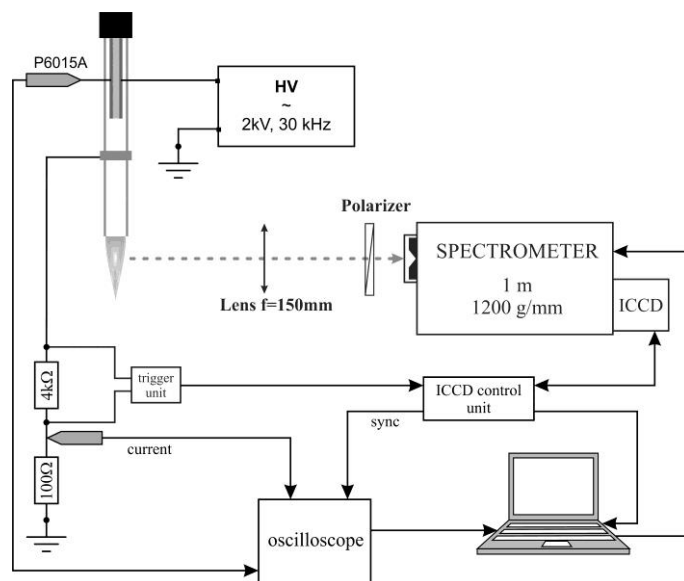
Fig. 1: The scheme of plasma jet configuration and the experimental set-up of the electric field measurements.

Noninvasive spectroscopic method based on Stark effect of helium lines is used for the determination of the electric field values along the plasma jet in the glass tube and in the plume. The method developed by Kuraica and Konjević [15], based on early work of Foster [16], is previously used for diagnostics of low pressure glow discharge [15], then for dielectric barrier discharge in helium [17], and finally for the electric field measurements in He plasma jets [9–11].

3   Results and Discussion

The results of the electric field measurement are presented in Fig. 1. Fig. 1 (a) shows distribution of the electric field in the capillary and Fig. 1 (b) shows distribution of the electric field in the plume for different gas flow rates.
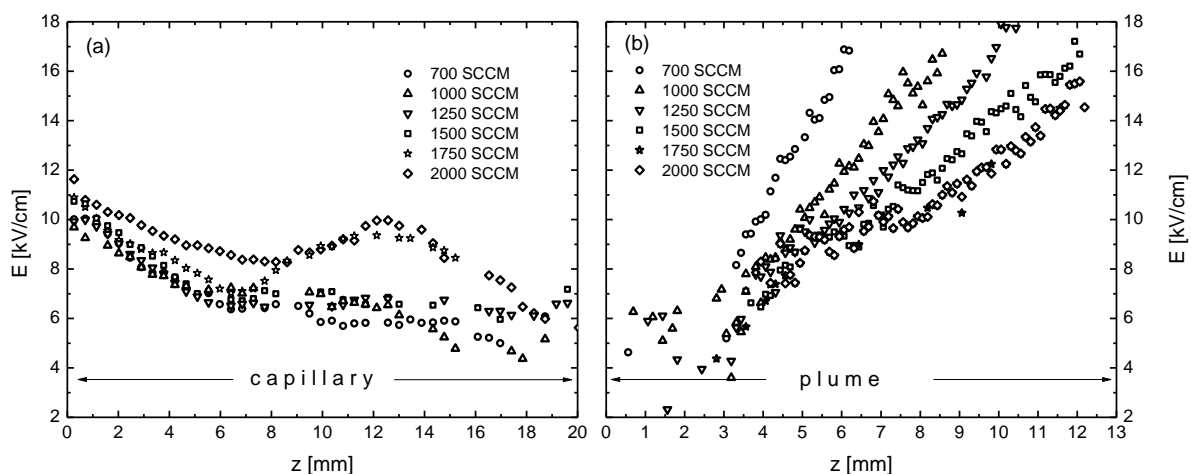
Fig. 2: Electric field strength as a function of the gas flow: (a) in the plume of the plasma jet and (b) in the capillary.

Electric field in the capillary has the maximal value close to the grounded electrode for all gas flows. These values are in range of 10-12 kV/cm. Electric field strengths linearly decrease for all gas flows along the first half of the capillary for 20-30 %. Also, one could notice that the value of the electric field strength is slightly higher for the higher gas flow. For the lower gas flow rates, electric field riches the plateau at the values of 5-7 kV/cm, and that is the mean electric field of the streamer at the very exit of the capillary. For the higher flow rates, the dependence of the electric field on the distance from the grounded electrode is not monotonous function, but it has the maximum in the second part of the capillary. Such a behavior is observed for the gas flows of 1750 and 2000 SCCM. The rise of the electric field strength in the tube for higher gas flows coincides with the constrictions of the discharge channel in the tube, visible by a naked eye. This is probably due to the turbulences which are induced with the higher gas velocity in the tube. In case of the constriction of the discharge channel in the tube, density of the charges in the streamer head raises which results with the increase of the electric field strength. Nevertheless, the electric field in the streamer head has a value of 5-7 kV/cm at the exit of the tube for higher gas flows also.

When the streamer/ionization wave exits the tube, electric field has the value between 5-7 kV/cm which corresponds to the value at the very end of capillary. The field rises almost linearly along the plume for all gas flows, but with different slopes. For lower gas flow rates electric field strength grows faster, e.g. for the flow of 700 SCCM, electric field strength reaches the maximum of about 17 kV/cm at the distance of 6 mm from the tube, while for the 1500 SCCM it comes to the same value at about 12 mm. The gas flow is several orders of magnitude slower than ionization wave velocity, thus the movement of the gas can be considered as negligible and cannot directly influence the charge carrier transport. On the other hand, gas flow is responsible for the gas composition. It can be shown by the simulation of gas composition, that the molar fractions of air in helium are the same for maximal values of the electric field for different flow rates. This leads to the conclusion that the value of the electric field is in direct correlation with the Townsend ionization coefficient which determines the number of ions in streamer head. More details about this analysis will be given in some of the following publications.

Observing the graphs in Fig. 1 one could see that the electric field in the plume reaches much higher values than in the capillary, which means that the ions of nitrogen and oxygen are main ions in the ionization wave. Further, the electric field strength in the streamer head rises in order to prolong streamer propagation in regions with higher air fraction in helium, which request higher electric field for the same ionization coefficient. The radius of the streamer decreases at the same time as a consequence of He/air mixing.

4 Conclusion

This article shows new results of the influence of the gas rate on the electric field distribution in helium plasma jet. The electric field values are measured in the capillary of the plasma jet and in its plume. The distributions of the electric field are obtained for different gas flow rates in range of 700-2000 SCCM. The electric field strength decreases for all gas flows in the first part of the tube, which can be a consequence of the loss of the charge on the inner walls of the

tube. In the second part electric field reaches a plateau for lower gas fluxes and for all gas flows the streamer exits the tube with the electric field of 5-7 kV/cm in its head. It is observed that the electric field has a second maximum for high flow rates, probably due to turbulences and constriction of the discharge in the capillary. When streamer exit tube, the electric field in its head raises almost linearly up to values of 17 kV/cm. The linear increase of the electric field strength is observed for all gas flows, but the slopes of these growths are different and they are lower for higher gas flow rates.

Acknowledgements

References

1. X. Lu et al., Phys. Rep. 540, 123 (2014)
2. X. Lu et al., Plasma Sources Sci. Technol. 21, 034005 (2012)
3. M. Teschke et al., IEEE Trans. Plasma Sci. 33, 310 (2005)
4. G. Y. Park et al., Plasma Sources Sci. Technol. 21, 043001 (2012)
5. T. von Woedtke et al., Phys. Rep. 530, 291 (2013)
6. Y. P. Raizer, Gas Discharge Physics (Berlin: Springer, 1991)
7. E. M. Bazelyan and Raizer Yu P, Spark Discharge (CRC Press, Boca Raton FL, 1998)
8. G. Naidis, Phys. Rev. E 79, 057401 (2009)
9. G. B. Sretenović et al., Appl. Phys. Lett. 99, 161502 (2011)
10. G. B. Sretenović et al., IEEE Trans. Plasma Sci. 40, 2870 (2012)
11. G. B. Sretenović et al., J. Phys. D. Appl. Phys. 47, 102001 (2014)
12. J.-P. Boeuf et al., J. Phys. D. Appl. Phys. 46, 015201 (2013)
13. A. Sobota et al., Plasma Sources Sci. Technol. 23, 025016 (2014)
14. O. Guaitella et al., J. Phys. D. Appl. Phys. 48, 255202 (2015)
15. M. M. Kuraica et al., Appl. Phys. Lett. 70, 1521 (1997)
16. J. S. Foster, Proc. R. Soc. London. Ser. A 117, 137 (1927)
17. B. M. Obradović et al., Appl. Phys. Lett. 92, 191501 (2008)

COLD AIR PLASMA PASTEURISATION OF FRESH APPLE JUICE

B. Tarabová, A. Žilková, Z. Machala

Division of Environmental Physics, Faculty of Mathematics, Physics and Informatics,
Comenius University in Bratislava, Mlynská dolina, 84248 Bratislava, Slovakia

E-mail: tarabova@fmph.uniba.sk

Transient spark and streamer corona discharges were tested for a non-thermal pasteurization of fresh apple juice. The juice was treated in two systems – electro-spray system and static (batch) system. The inactivation rate of model pathogens (*Escherichia coli*) of contaminated juice showed high efficiency for the transient spark, especially for the static treatment. The presence of food borne pathogens and their effect on the juice life time was also tested. A minimal effect of cold plasma on juice chemical and sensory properties (pH, color) was shown. Measured concentrations of nitrites and nitrates formed in the juice by plasma treatment were shown to be lower than the acceptable daily income dose.

Keywords: cold air plasma; non-thermal pasteurization; apple juice

1   Introduction

Sterilization is one of the most important technologies in food processing and food safety. The traditional methods for inactivation of food borne pathogens in different types of food are based on thermal processes, typically referred to as pasteurisation. Unfortunately, the use of high temperatures is not convenient for heat-sensitive products and may lead to the loss of food quality (loss of nutrition values and vitamin content, changes in sensory properties like taste or color, and others). Therefore in recent years, non-thermal methods of food processing have been investigated – such as high hydrostatic pressure, pulsed electric fields, ionizing radiation and non-thermal plasma [1-2]. Cold plasmas are known for bactericidal effects on variety of bacteria, bacterial spores, biofilms or yeasts [3]. These properties predetermine cold plasma for the applications in sterilization/pasteurization of fresh food products or food packaging [4-6].

Consumers demand for the freshly squeezed fruit juices with high nutritional values that were not thermally pasteurized. The object of this work was to test the use of cold plasma generated by transient spark and streamer corona for fresh apple juice non-thermal pasteurization. The apple juice was selected, because is the most consumed fruit juice (together with orange juice).

2   Experimental set-up and methods
2.1 Cold plasma discharges

DC discharges used in this study - transient spark discharge (TS) and streamer corona (SC) were generated in ambient air at atmospheric pressure in point-to-plane geometry producing cold plasma. SC is typical with small current pulses of streamers (~ tens of mA) with a repetitive frequency ~ 10-30 kHz, during which the discharge voltage remains fairly constant. TS is a self-pulsing repetitive streamer-to-spark discharge with the duration of spark current pulse (~ 5-30 A) shorter than 100 ns. The repetitive frequency is ~1 kHz [7-8]. Two different systems with TS or SC for juice treatment were used – the electro-spray system (ES) and the static system (SS). High voltage electrode was represented by the hypodermic hollow needle. In the electro-spray system, juice was pushed by the syringe pump directly through the needle, which enabled the direct contact of the discharge with sprayed droplets of the treated juice.

The effect of electro-spraying of juice to the micrometric size droplets occurred due to the applied high voltage. This set-up allows increasing the contact of the discharge with the juice surface. The static system is based on the static, i.e. batch treatment by the discharge generated directly over the juice surface, in which the grounded electrode was submerged.

2.2 Juice preparation and treatment, microbial handling
Ripped apples (old Slovak variety Ontario) were harvested and after being washed, they were squeezed by using common juicer (Bosch MES3500). The fresh juice containing the pulp was stored in the freezer at -20°C. We performed several experiments focused on:

a) Inactivation rate of bacteria by cold plasma – juice was thawed at the room temperature and centrifuged to remove the pulp. Subsequently it was inoculated by model pathogens - *Escherichia coli* ATCC 25922 and *Saccharomyces cerevisiae* S228C with the initial concentration $\sim 10^6$ -10^7 CFU/mL.

b) Effect of cold plasma on shelf life time of juice – thawed juice containing pulp contained only its native pathogens.

In every experiment, the juice was treated by TS and SC in electro-spray and static system. The juice flow rate in ES was 1mL/min and the treatment condition in SS was 1 min treatment per 1 mL of juice. The number of living microbial/yeast cells in the juice after plasma treatment and in the control was evaluated immediately after plasma treatment by classical thermostatic cultivation on Petri dishes. We followed either the inactivation rate or the spoilage rate of treated juice in post treatment time (from 0 up to 21 days). Meanwhile, the juice was stored at 4°C in the refrigerator to simulate the behavior of consumers. Furthermore, we focused on the effects of cold plasma on the chemical, nutrient and sensory properties of treated juice, like pH changes; nitrites/nitrates (measured by Griess assay) and hydrogen peroxide H_2O_2 (measured by Amplex red assay); color changes by measuring juice transmittance and °Brix (content of sugar).

3   Preliminary results
3.1 Effect of cold plasma on juice properties
Cold air plasmas in contact with liquids are known for the formation of short-lived reactive oxygen and nitrogen species (RONS) that lead to formation of long-lived RONS in water, especially nitrites, nitrates and hydrogen peroxides. All these substances may be harmful for human health; therefore their content in foods is regulated. The Joint Expert Committee on Food Additives (JECFA) of the Food and Agriculture Organization of the United Nations/World Health Organization and the European Commission's Scientific Committee on Food have set an acceptable daily intake (ADI) for nitrate of 0-3.7 milligrams nitrate ion per kilogram body weight and for nitrite of 0-0.06 milligrams nitrite ion per kilogram body weight [9]. We calculated the ADI of nitrites and nitrates per average 60 kg person: 36 mg NO_2^- and 222 mg NO_3^-. Concentrations of measured nitrites and nitrates in plasma treated juice in comparison with the ADI are shown in Fig. 1a). Both nitrites and nitrates concentrations are lower than ADI doses and their concentration is decreasing to minimum after 2 days.

The sensory properties of the juice (color, taste, smell) are indicated by the values of total acidity, pH, transmittance and °Brix. We detected no significant changes of pH after plasma treatment of juice – pH dropped from 3.28 to 3.19. Furthermore, measuring of the transmittance showed a slight decrease in the juice treated by transient spark discharge (Fig. 1b).
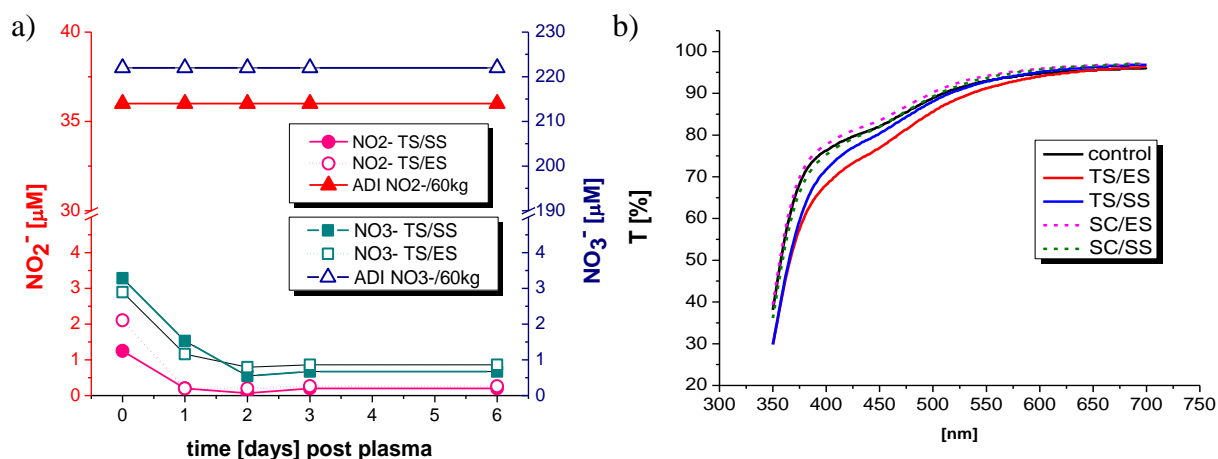
Fig. 1. a) Nitrites and nitrates concentrations measured in cold plasma treated juice compared with the acceptable daily intake (ADI) doses; b) Transmittance [%] of the untreated and treated juice by transient spark and streamer corona.

3.2 Effect of cold plasma on inactivation rate and shelf life time of the fresh juice

The efficiency of cold plasma treatment of the fresh apple juice on the inactivation rate was tested. Juice without pulp was inoculated by model microorganism *E. coli* ATCC 25922 and treated by streamer corona and transient spark in both systems. Fig. 2 shows the bacterial population growth up to 7 days post plasma treatment. In general, streamer corona treatments reached very low efficiency (less than 1 log reduction), which remained in post treatment time without significant change. Transient spark treatment also showed low efficiency (< 1 log) directly after plasma treatment, but the efficiency was increasing with days post TS treatment. TS treatment in static system reached the maximal efficiency (6 log reduction) after 2 days of storage of the juice in the fridge.
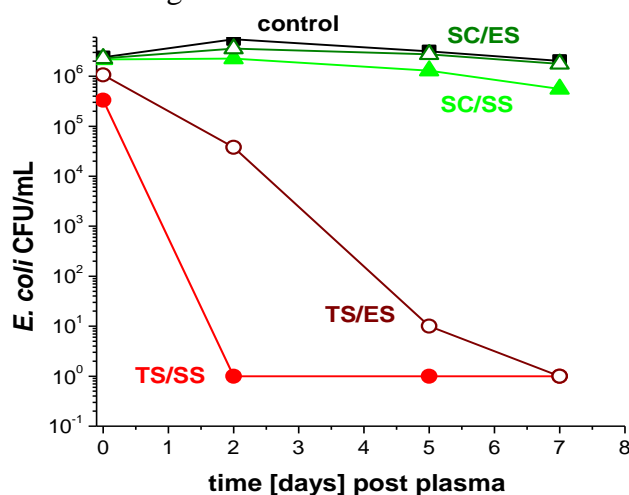
Fig. 2. The inactivation rate of the treated juice contaminated by *E.coli* by streamer corona and transient spark.

Fresh apple juice may contain native food borne pathogens. At first, we tested their presence. The juice containing pulp was kept for 24 hours at 30°C and 24 hours at 35°C to cultivate the native pathogens and then cultivated on Petri dishes. We detected 3 different strains of yeasts and bacteria. These pathogens are responsible for the spoilage of the fruit juice and shortening of the shelf life time. The plasma treated natural juice demonstrated no bacterial or yeast growth up to 7 days post plasma treatment. Further experiments are planned to test the treated juice up to 21-28 days post treatment.

4   Conclusion

Cold plasma is a promising alternative food processing technique for non-thermal pasteurization. Preliminary results with cold air plasma treatment of fresh apple juice are very optimistic: a significant decontamination rate, shelf life time extension, and no chemical and sensory modifications were observed. Further investigation is needed to improve the treatment conditions and treat larger volume of a fresh juice.

References

1. B. H. Lado, Microbs & Infections. 4, 433-440 (2002)
2. B. Niemira, Annu. Rev. Food Sci. Technol. 3, 125-142 (2012)
3. B. Surowsky et al., Int. J. Food Microbiol., 174, 63-71 (2014)
4. K. Lee, J. Microbiol. 44 (2006)
5. D. Ziuzina et al., Food Microbiol. 42 (2014)
6. P. Basaran, Food Microbiol. 25 (2008)
7. Z. Machala et al., Eur. J. Phys. D 54 (2009)
8. Z. Machala et al., Plasma Process. Polym. 10 (2013)
9. European Commission's Scientific Committee for Food Science and Techniques, Opinion of the Scientific Committee for Food on Nitrites and Nitrates, 38th series (1997)

FORMATION OF RONS IN COLD AIR PLASMA ACTIVATED WATER AND THEIR EFFECTS ON CELL MEMBRANES OF *ESCHERICHIA COLI*

B. Tarabová[1], E. Doležalová[2], P. Lukeš[2], Z. Machala[1]

[1]*Faculty of Mathematics, Physics and Informatics, Comenius University in Bratislava, Mlynská dolina, Bratislava, Slovakia*

[2]*Institute of Plasma Physics of the CAS, v.v.i., Za Slovankou 3, Prague, Czech Republic*

E-mail: tarabova@fmph.uniba.sk

In this work, we focused on the detection of secondary reactive oxygen and nitrogen species (RONS) formed by cold plasma induced gas-liquid chemistry in air discharge activated water and liquids. Plasma induced chemical changes in plasma activated water (PAW) were correlated with the antibacterial effect, sublethal injury of bacterial cells and peroxidation of membrane lipids. The contribution of the electric field induced by the plasma treatment was evaluated by the detection of membrane permeabilization. The bactericidal effects of direct (plasma and PAW) and indirect (only PAW) treatments were compared with long-term preservation of the PAW with its antibacterial properties.

Keywords: cold air plasma; plasma activated water; sublethal injury; lipoperoxidation

1   Introduction

Nowadays, cold atmospheric pressure plasmas generated by electrical discharges in gas-liquid interface or directly in water are studied. Plasmas generated in air and in contact with liquids generate a number of primary reactive species in the gas phase, which induce formation of secondary reactive species in the liquid phase through the gas-liquid interface. Reactive oxygen and nitrogen species (RONS) such as hydrogen peroxide, hydroxyl radical, superoxide, nitrites/nitrates, hypochlorites and peroxynitrites induce chemical changes in water solutions and the plasma activated water (PAW) and liquids are created. Thanks to the synergistic effects of the plasma agents (electric field, electrons and ions, RONS) and the induced chemical changes in the liquid, cold air plasmas and PAW lead to various biocidal effects on microorganisms and cytotoxic or growth stimuli effect on cells [1-2]. The investigation of the effects on cells induced by plasma agents or PAW is very important for further bio-medical applications. Therefore the aim of our work was to detect the chemical changes induced via the formation of RONS in air plasma activated liquids and their effects on bacterial cells and cell membranes.

2   Experimental set-up and methods
2.1   Transient spark with electrospray

Transient spark (TS) discharge was generated in ambient air at atmospheric pressure in point-to-plane geometry (Fig. 1). TS is a self-pulsing repetitive streamer-to-spark discharge with the spark current pulse (20-30 A) duration shorter than 100 ns. Due to the short pulse duration, the plasma cannot reach the thermal equilibrium conditions and remains at low gas temperature. A positive high voltage (10-12 kV) was applied on the hollow needle electrode. The water solutions/bacterial suspensions were pushed through the high voltage electrode by a syringe pump. This allowed the water solutions to flow directly through the active zone of the discharge. Furthermore, due to the applied high voltage, we observed the effect of the electrospray. This electrospraying enhanced the mass transfer of reactive oxygen and nitrogen species into the treated liquid solutions [3].
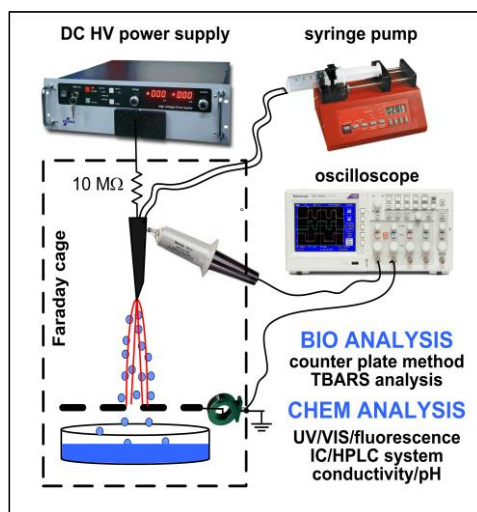
Fig. 1. Experimental set-up of the transient spark discharge with electrospray.

2.2 Chemical methods

Aqueous solutions with different initial pH and electrolytic conductivities σ were used for plasma treatment by the dissolution of different salts in deionized water: water (NaH_2PO_4 solution), phosphate buffer (NaH_2PO_4/KH_2PO_4 solution), saline solution (0.85% NaCl) and phosphate buffered saline. RONS in plasma treated water (plasma activated water PAW) were detected mostly by colorimetric methods (UV/VIS absorption spectrometer UV-1700 SHIMADZU) or fluorescent spectroscopy:

1. Analysis of H_2O_2: Titanyl ions Ti^{4+} react with H_2O_2 in the presence of NaN_3 and create pertitanic acid with the absorption maximum at 407 nm.
2. Analysis of NO_2^-: Nitrites NO_2^- react with Griess reagents and create azo-dye with the absorption maximum at 540 nm (Nitrate/Nitrite Colorimetric Assay Kit, Cayman Chemical).
3. For qualitative detection of peroxynitrites was used the fluorescent dye H_2DCFDA (2,7-dichlordihydrofluoresceine diacetate).
4. Superoxide O_2^- was detected indirectly as the increase of H_2O_2 concentration after superoxide dismutation by the superoxide dismutase enzyme.

2.3 Microbial handling

The antibacterial effect was tested on suspensions of planktonic form of *Escherichia coli* ATCC 25922. The number of living microbial was evaluated by classical thermostatic cultivation on Petri dishes. Furthermore, the effects of the chemical changes of PAW on the bacterial cells were detected – sublethal injury of outer and cytoplasmic membrane, the peroxidation of membrane lipids, the loss of membrane integrity and the metabolic activity [4-5]. To study the presence of sublethally injured cells, samples were plated on two selective media: TSAYE (tryptone soya agar enriched with yeast extract) with 3.1% of sodium chloride (TSAYE-SC) and TSAYE with 0.3% of bile salts (TSAYE-BS). Cells become sensitized and unable to grow on the selective media containing bile salts if their outer membranes are damaged, whether the loss of tolerance to the presence of sodium chloride is linked with the loss of the functionality and/or integrity of cytoplasmic membrane. To evaluate the cell permeabilization, we tested the fluorescent staining - propidium iodide or DAPI (4'6-diamino-2-phenylindole). Reactive species forming during the plasma treatment in PAW cause the peroxidation of cell membrane lipids, which was detected by the thiobarbituric acid test (TBA). Thiobarbituric acid reacts with secondary product of lipid peroxidation – malondialdehyde forming the pink colored $MDA-TBA_2$ complex.

3 Preliminary results

The transient spark discharge was generated in ambient air at atmospheric pressure in the direct contact with treated liquid solutions. Changes of pH, conductivity and formation of RONS were observed in water or PB solutions. In non-buffered water solution was observed the decrease of pH ($5 \rightarrow 3.2$) instead of PB buffered solution, where pH remained at 6.9. Dissolution of NO_x along with the formation of NO_2^-, NO_3^- was responsible for the acidification of the plasma treated solution. Measured concentration of long-lived species such as H_2O_2, NO_2^- and NO_3^- in PAW on post-treatment time showed the ongoing post-discharge chemistry – acidic decomposition of nitrites and decreasing concentrations of H_2O_2 and NO_2^- because of the peroxynitrite formation. The higher bactericidal effect (Fig. 2a) was observed in non-buffered solutions and it was linked with the different RONS chemistry associated with acidification (pH ~ 3). At acidic pH radicals like $OH^.$, $NO^.$ and $NO_2^.$ are formed by acidic decomposition of nitrites and also peroxynitrites, which posses a strong cytotoxic effects on cells. Bactericidal effect of PAW remained for some time post plasma treatment, as shown in Fig. 2b, where indirect treatment means 10 min incubation of PAW with bacteria. Furthermore, the longer incubation times were tested and the preservation of bactericidal effect of PAW by long-term storage by deep freezing was investigated.
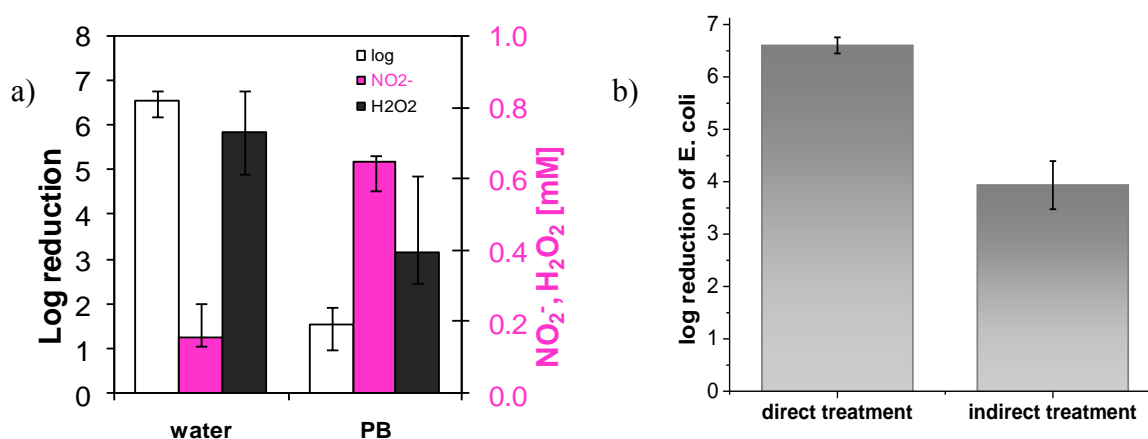
Fig. 2. a) Bactericidal effect of direct treatment of E. coli suspension linked with the nitrites and hydrogen peroxide concentrations. b) Comparison of bactericidal effect of direct plasma treatment and indirect PAW treatment (10 min incubation).

Reactive species (mostly $OH^.$, $NO^.$, $NO_2^.$ and $O_2^{.-}$) forming during the plasma treatment in PAW are responsible for the oxidative damage of the cell membrane due to the peroxidation of membrane lipids. The significant increase of the MDA-TBA$_2$ complex was measured on bacteria in non-buffered solutions after plasma treatment. Due to the minimal amount of detected sublethally injured bacterial cells in buffered solutions, we found out that the sublethal injury was also accompanied with the acidification and formation of the cytotoxic radicals in PAW.

References

1. M. Laroussi, IEEE Trans. Plasma Sci. 30, 1409-1415 (2002)
2. S. Bekeschus et al., Oxid. Med. Cell. Longev. 2016, 5910695 (2016)
3. Z. Machala et al., Plasma Process. Polym. 10, 649-659 (2013)
4. C. Arroyo et al., Lett. Appl. Microbiol. 51, 525-531 (2010)
5. E. Doležalová et al., J. Phys. D: Appl. Phys. 49, 074501 (2016)

CARBON NANODOTS SURFACE TREATMENT BY NON-EQUILIBRIUM PLASMA CONTACTING WITH SOLUTION

V. Kiris, N. Tarasenka, A. Nevar, N. Tarasenko, F. Krcma
B.I. Stepanov Institute of Physics of National Academy of Sciences of Belarus,
2Nezalezhnasti Ave. 68, 220072 Minsk, Belarus
2Faculty of Chemistry, Brno University of Technology,
Purkynova 118, Brno 612 00, Czech Republic

E-mail: n.tarasenko@ifanbel.bas-net.by

The capabilities of the non-equilibrium gas-liquid discharge plasma for surface modification and improvement of photoluminescent properties of carbon nanoparticles are discussed. Microplasma generated at the surface of a colloidal solution is used to induce low-temperature liquid-based non-equilibrium chemistry and promote their surface functionalization

Keywords: electrical discharge in contact with liquid; carbon nanodots; photoluminescence

1   Introduction

In recent years carbon nanoparticles (NPs) with sizes below 10 nm, so called carbon nanodots (C-dots), owing to their excellent biocompatibility, chemical inertness, and size-selective photoluminescence properties have received a great interest for the potential applications in biotechnology as more suitable alternatives to the traditional semiconductor quantum dots. Much progress has been achieved in the synthesis and characterization of C-dots [1]. Nevertheless, the origin of the photoluminescence (PL) in C-dots is not well understood yet, though many mechanisms have been proposed lately. However, the understanding of emission origins and control over C-dots luminescence are of great importance for their successful applications and for development of methods for the improvement of the C-dots PL quantum yield. It should be noted that the particle surface passivation or surface functionalization are the most popular approaches to enhance the luminescence of C-dots. Surface groups, such as, e.g., C-O, C=O and COOH, can introduce trapping states with different energy levels on NPs surfaces, that are considered to be responsible for their luminescent properties. Thus, in case of C-dots with poor fluorescent intensity, the proper surface passivation is required to enhance their fluorescence intensity. Among the different surface passivating agents, amino-groups could be effective candidates to achieve the controlled photoluminescence properties of C-dots.

Post-synthesis surface modification of C-dots has so far largely relied on traditional or enhanced (e.g. thermally, by illumination) solution chemistry and only very recently alternative approaches have been used [2]. Therefore, a development of new approaches for preparation of C-dots and increasing their photoluminescence properties is still of interest. Among the new approaches a treatment of colloidal NPs by reactive non-equilibrium plasmas can offer more opportunities for their surface engineering and an improvement of photoluminescent properties. In this paper we report an approach based on the two-jet direct current (dc) discharge system generating the non-equilibrium plasma in contact with colloidal

solution. The capabilities of the developed approach for surface modification and an improvement of photoluminescent properties of carbon nanoparticles are discussed.

2   Experimental

The initial colloidal C-dots were prepared via an electrical discharge between two graphite electrodes submerged into water. The power supply provided an alternating current (ac) spark discharge with a repetition rate of 100 Hz. The discharge was initiated by applying a high voltage pulse of 11 kV. The peak current of the high-voltage spark in the form of high-frequency oscillations was about 17 A with a duration of a single discharge pulse of 50 μs. The optimal distance between the electrodes was 0.3-0.5 mm.

The typical TEM images of the prepared carbon NPs showed separate and quasi-spherical particles, sometimes they were partly agglomerated. The sizes of the freshly prepared NPs were mainly distributed in the range of 2–5 nm with an average value of 3 nm (Fig. 1 b).
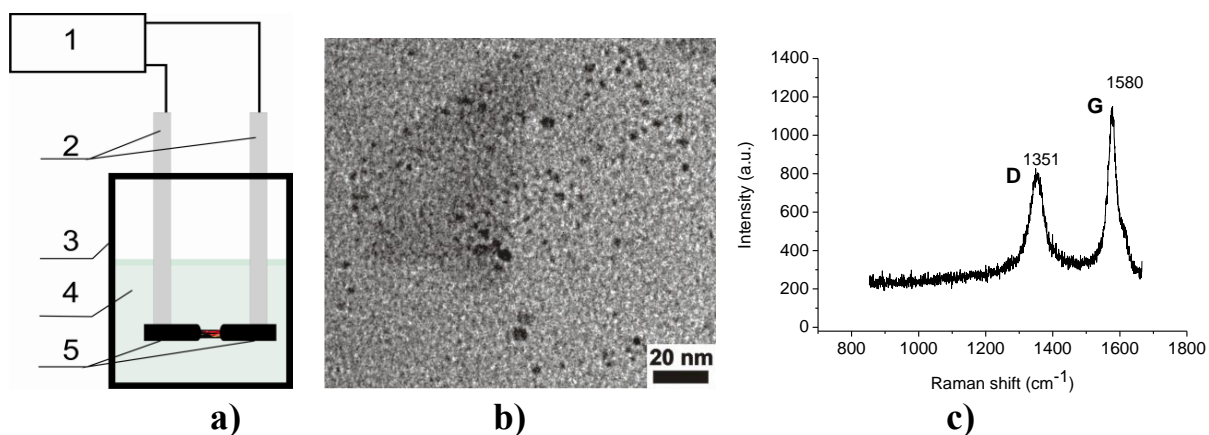
Fig. 1. (a) Schematic diagram of the setup for NPs synthesis by electrical discharge in liquid: 1-power supply, 2-electrode holders, 3-reactor cell, 4-liquid, 5-electrodes; (b) typical TEM image of generated carbon NPs; (c) Raman scattering spectrum of carbon NPs deposited on silicon substrate

Typical Raman spectra of the synthesized carbon nanodots are presented in Fig. 1c. The Raman spectrum of the prepared carbon NPs contains two distinct peaks which could be assigned to the D-band at 1351 cm^{-1} arising from the disorder in sp^2 hybridized carbon and indicating the presence of sp^3 defects, and the G-band at 1580 cm^{-1} corresponding to graphitic structures (due to the in-plane stretching vibration of carbon atom pairs).

The I (D)/ I (G) ratio has been extensively used for the quantification of defects in carbon-based materials. In our case the I (D)/I(G) for the carbon NPs obtained via electrical discharge in water method was around 0.70, indicating that, most probably, they have a graphitic-like structure.

To tailor surface properties of the carbon nanoparticles, the prepared colloids, practically immediately after the preparation, were treated by atmospheric pressure two microplasma jets

generated over the colloidal solution and coupled to the colloid. A schematic diagram of the microplasma-liquid system with two plasma jets is shown in Fig. 1.

Two stainless steel capillary tubes (500 μm inside diameter, 5 cm length) that served as electrodes were located at a distance of 1-5 mm above the liquid surface. The experiments were carried out with argon flowing through the capillary tubes. The gas flow rate was measured with a mass flow controller and can be varied from 10 to 45 sccm. The discharge was ignited by applying a high voltage (above 3 kV) using a dc power supply. The dc voltage applied between the two nozzle electrodes by a regulated power source with a constant current mode, resulted in the generation of two glow discharges that were in contact with the liquid surface. A ballast resistor (0.1 - 0.4 MΩ) limited the current and provided the stability of the discharge in the range of 1 - 5 mA. Visible images of the discharge and liquid were taken by a charge-coupled device (CCD) camera. The pH value was measured by using a pH meter (Hanna Instruments HI 83141). The composition, morphology and optical properties of the synthesized and plasma treated NPs were studied by TEM, EDX, PL, FT-IR, Raman and ultraviolet–visible spectroscopy.
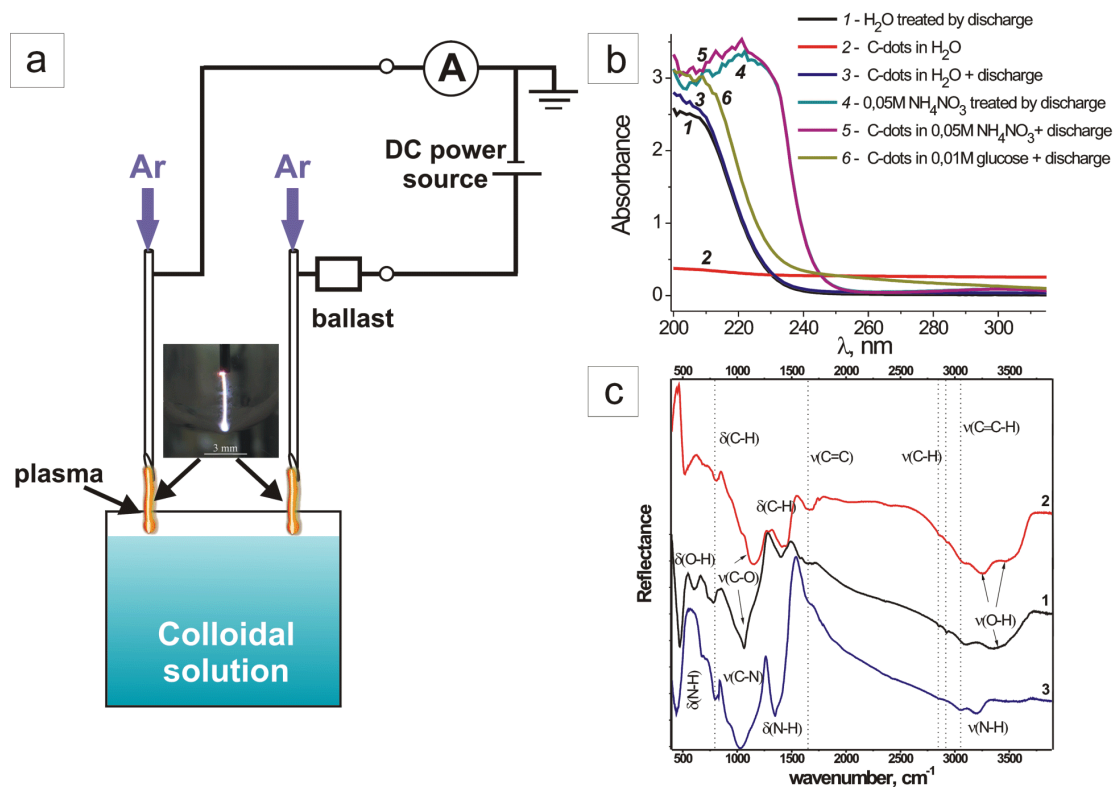
Fig. 2: (a) Schematic diagram representing the double plasma–liquid systems for surface engineering of NPs; (b) optical absorption spectrum of the C-dots in different solutions; (c) FT-IR spectra of as-prepared (1) and plasma processed C-dots in water (2) and in ammonia solution (3).

3 Results and Discussion

It is known that microplasmas generated at the surface of the colloidal solution induce low-temperature liquid-based non-equilibrium chemistry and therefore promote NPs surface functionalization [2].

Fig. 1b illustrates the absorption spectra of C-NPs before and after processing by dc-discharge plasma in different aqueous solutions. The absorption spectra of the solutions after plasma treatment indicate that intermediate products are formed during the treatment process. Plasma electrons initiate reactions in the bulk liquid resulting in formation of a range of radicals and ions.

To examine the chemical composition of the C-dots FT-IR was used to identify the surface functional groups of pristine and processed C-dots. The analysis of the surface properties by FT-IR revealed the following characteristic features of the samples: 1640 cm^{-1} – C=C bond in aromatic carbon, 1430 cm^{-1} – C–H bending, 3050 cm^{-1} –C=C–H stretching, peak at 1045 cm^{-1} is from C−O vibrations. The FTIR results confirm a presence of oxidation and H-terminations after the dc-microplasma treatment, however the surface bonds are qualitatively different.

It should be noted that dc-microplasma processing of C-dots in aqueous glucose and ammonia solutions demonstrated that a different type of surface engineering can be achieved by changing the liquid media. The surface characteristics of C-dots treated in the ammonia nitrate solution showed that terminations of C–N–H type are likely to be formed in this case. We suggest that the different surface chemistry activated in different solutions could be due to different reactions induced by plasma-electrons at the plasma–solution interface compared to plasma–water surface. Changing the surface groups is believed to be effective in improvement of photoluminescence properties of the synthesized C-dots. Indeed, our preliminary experiments showed an enhancement of PL of the plasma treated C-dots: after plasma processing the nanoparticles exhibited a luminescence visible by the naked eye under UV light excitation (266 nm). The more detailed studies of luminescent properties of the plasma treated samples are in progress.

4   Conclusion

The capabilities of the non-equilibrium gas-liquid discharge plasma for surface modification and an improvement of photoluminescent properties of carbon nanoparticles have been demonstrated. The interaction of plasma-electrons with the colloidal solution initiates liquid-based non-equilibrium chemistry that results in surface functionalization of the particles present in the solution. Although experimental evidence indicates the possibility of PL enhancement after plasma treatment, still detailed studies are required to understand the reaction kinetics of microplasma-induced processes and plasma-induced mechanisms that contribute to the surface modification of NPs.

References

1. H. Li et al., J. Mater. Chem., 22, 24230 (2012)
2. D. Mariotti et al., Nanoscale, 5, 1385 (2013)

THE PARAMETERS OF DIFFUSE COPLANAR SURFACE BARRIER DISCHARGE GENERATED IN PURE WATER VAPOUR AT ATMOSPHERIC PRESSURE

Z. Tučeková[1], J. Antalík[1], V. Procházka[2], P. Slavíček[2], P. Dvořák[2], D. Kováčik[1,2], A. Zahoranová[1], M. Černák[1,2]

[1] Department of Experimental Physics, Faculty of Mathematics, Physics and Informatics, Comenius University in Bratislava, Mlynská dolina F2, 842 48 Bratislava, Slovakia

[2] R&D Center for Low-Cost Plasma and Nanotechnology Surface Modifications, Faculty of Science, Masaryk University, Kotlářská 2, 611 37 Brno, Czech Republic

E-mail: zlata.tucekova@fmph.uniba.sk

The contribution deals with Diffuse Coplanar Surface Barrier Discharge (DCSBD) that was successfully generated in pure water vapour at temperature 400 K at atmospheric pressure. The parameters of plasma were investigated by measurement of electrical characteristics and by means of optical emission spectroscopy. The weak Hα line and OH radicals were observed in emitted spectra.

Keywords: atmospheric pressure plasma; dielectric barrier discharge; water vapour; OH radicals

1   Introduction

The potential applications of atmospheric-pressure plasma sources producing highly reactive species for surface treatment of various materials are nowadays widely investigated. Diffuse Coplanar Surface Barrier Discharge (DCSBD) belongs to the sources of non-equilibrium plasma generated at atmospheric pressure. The macroscopically homogeneous plasma of the DCSBD and variability of used working gases are main advantages in the field of surface treatment [1, 2, 3]. The considerable disadvantage of using gaseous mixtures such as air is the occurrence of various types of polar functional groups on the plasma treated surfaces. The desirable solution could be the surface modification exclusively by the OH-functional groups generated by the DCSBD atmospheric pressure plasma. Therefore, for this purpose we designed and constructed the diagnostic apparatus – plasma reactor capable to generate the DCSBD plasma in pure water vapour at atmospheric pressure. We studied the parameters of such plasma by optical emission spectroscopy (OES) and the electrical characteristics by oscilloscopic measurement.

2   Experimental

The DCSBD electrode system consisted of several silver strip 1.5 mm wide electrodes with 1 mm gap. The strips were placed on the 0.6 mm thick planar ceramics on the opposite side to the generation of plasma layer. To prevent the undesirable sparkling between adjacent electrodes, the insulating oil was circulating in direct contact with the electrode system. The DCSBD was supplied by AC (14 kHz) high voltage source *LIFETECH GENERATOR VF 700* (from *LIFETECH*, Brno, Czech Republic) and the input power was set to 250 W, 300 W and

350 W. For the atmospheric pressure plasma generation in water vapour, a unique double-shell heated plasma reactor was built (Fig. 1). The components of plasma reactor were continually heated to prevent the condensation of the water vapour on chamber walls and the ceramics. The temperature of ceramics was regulated to more than 390 K by oil thermoregulator. The atmosphere in the chamber of the plasma reactor was heated to 400 K by separate thermoregulator.
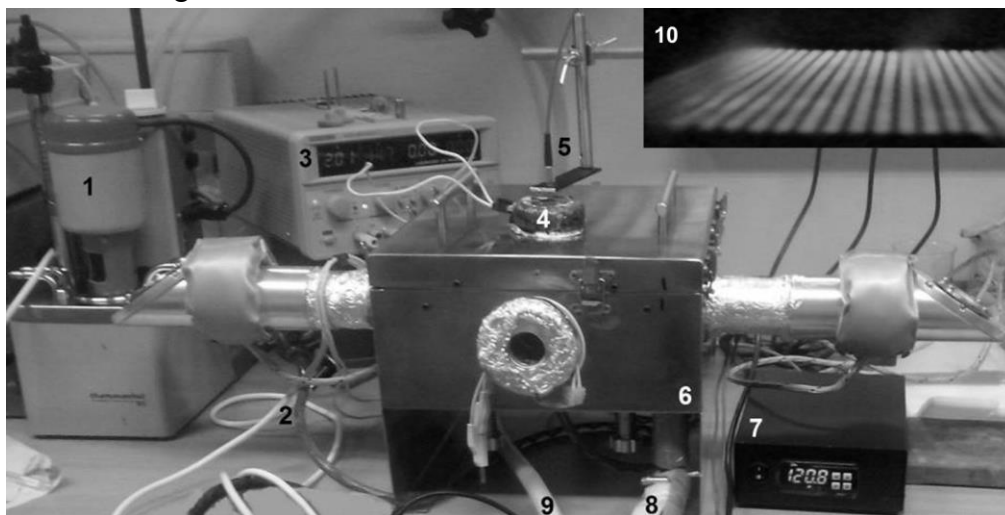
Fig. 1: The heated reactor for DCSBD plasma generation in pure water vapour: 1- oil thermoregulator, 2- oil and electric power inlet, 3- power source for additional heating, 4- additional heating of quartz glass, 5- optical fiber, 6- heated chamber, 7- chamber air thermoregulator, 8- water vapour input, 9- water vapour output, 10- the detail front view of the DCSBD plasma generated in pure water vapour.

The electrical characteristics of DCSBD water vapour plasma was measured using *Tektronix 2024B* oscilloscope. The voltage *U(t)* was estimated as the subtraction of voltage signals measured by *Tektronix P6015A* (1:1000) high voltage probes and the current *I(t)* was measured by Rogowski's coil *Pearson electronic 4100*.

The generated OH(A-X) system was detected by the means of standard OES. To measure the emission of OH(first order, ultra-violet) system bands (0,0) and (1,1) in range 305-340 nm we used the monochromator *FHR-1000 by Jobin-Yvon-Horiba* (2400 gr/mm, CCD detector Symphony cooled by four stages Peltier cooler, spectral resolution of 0.05 nm, spectral range 200-750 nm). The emission of OH(second order) system and Hα in range 555-663 nm was detected by *Andor Shamrock 750* spectrometer (1200 gr/mm, CCD detector *DU940P-BU2 Andor*, spectral resolution 0.04 nm, spectral range 200-1000 nm). The optical fiber was positioned perpendicularly to the plasma layer to scan the emission from several microdischarges and the acquisition time for recorded spectra was set to 100 s. The OES were processed using *Spectrum Analyzer* [5] in order to estimate the characteristic temperatures of the DCSBD water vapour plasma.

3   Results and Discussion

The character of DCSBD plasma generated in pure water vapour at atmospheric pressure was defined by the highly uniform thin channels of the microdischarges (Fig. 1). The pure water vapour effect on microdischarge character was also observed in the detail of current

waveform (Fig. 2). Our investigation correlates with the densification and spatial stabilization of filamentary part of the discharge pattern observed with increasing humidity in [6].
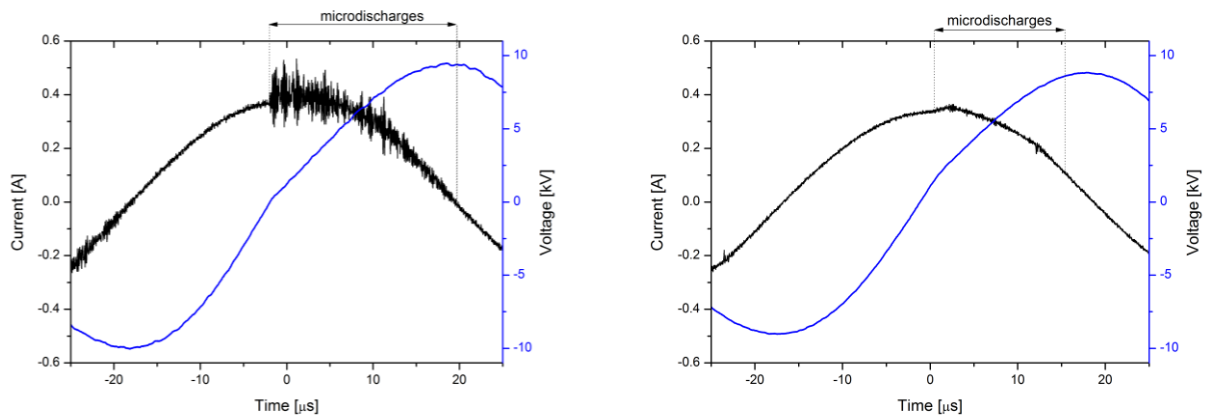
Fig. 2: The details of current and voltage waveforms of DCSBD discharge generated in ambient air (left) and in pure water vapour (right) at power 350 W. The shown waveforms are an accumulation of the signal from several periods of discharge ignition.

The recorded spectra of DCSBD plasma generated in water vapour at atmospheric pressure were characterized by emission of OH radical and weak Hα line (data not shown). No O atomic lines were detected during the OES measurement what corresponds with the decrease of O emission intensity with water content increase reported in [6].

The previous works [7,8] have shown the need of complicated model of OH excited species generation by different independent mechanisms (i.e. electron impact excitation of ground state OH, direct dissociation of water vapour, positive and negative ion recombination, etc.) resulting in non-Boltzmann behavior of OH rotational population at rotational numbers J>13 [9]. In our study, the non-Boltzmann behavior of the OH radical rotational population was also observed. The rotational numbers $J(Q_1)$<13 of OH(A-X) molecular band at 308 nm according to method suggested by Bruggeman [7, 10] were used to calculate T_{Rot} to approx. 720±150 K (Fig. 3). The estimation of unified T_{Rot} using only OH emission spectra is nowadays under discussion of many authors [7-11].
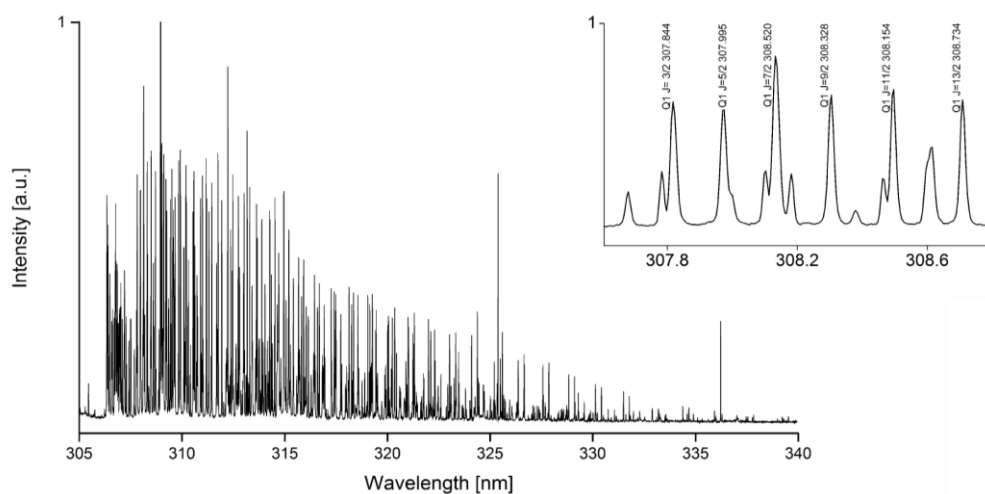
Fig. 3: Emission spectrum of OH(A-X) generated in pure water vapour DCSBD plasma (left) and rotational lines of OH band Q_1 used for T_{Rot} estimation (right).

4   Conclusion

The pure water vapour DCSBD plasma was proven to be the efficient source of OH radicals. The further investigation using e.g. time resolved OES and/or laser induced fluorescence spectroscopy is needed to analyze the parameters of DCSBD water vapour plasma for the potential surface treatment application.

Acknowledgments

References

1. L. Bónová et al., App. Surf. Sci. 331, 79 (2015)
2. Ľ. Černáková et al., Open Chem. 13 (1), 457 (2015)
3. R. Krumpolec et al., in *Scientific Program and Book of Abstracts of 6th Central European Symposium on Plasma Chemistry*, Bressanone, Italy, 2015, p. 58
4. Z. Tučeková et al., in *Book of Contributions of 14th International Symposium on High Pressure Low Temperature Plasma Chemistry*, Zinnowitz, Germany, 2014, p. 461
5. Z. Navrátil et al., Czechoslov. J. Phys. 56, B944 (2006)
6. J. Čech et al., Plasma Phys. Technol. 2(3), 307 (2015)
7. P. Bruggeman et al., J. Phys. D: Appl. Phys. 42, 053001 (2009)
8. T. Verreycken et al., Plasma Sources Sci. Technol. 19, 045004 (2010)
9. L. Li et al., J. Phys. D.: Appl. Phys. 45, 125201 (2012)
10. O. Motret et al., J. Phys. D.: Appl. Phys. 33 (12), 1493 (2000)
11. T. Krähling et al., Spectrochim. Acta Part B 114, 20 (2015)

AUTHOR INDEX

Hakone XV: International Symposium on High Pressure Low Temperature Plasma Chemistry
with joint COST TD1208 workshop Non-Equilibrium Plasmas with Liquids for Water and Surface Treatment

Book of Contributed Papers

11th – 16th September 2016
Brno, Czech Republic